

ADVERTIMENT. La consulta d'aquesta tesi queda condicionada a l'acceptació de les següents condicions d'ús: La difusió d'aquesta tesi per mitjà del servei TDX (www.tesisenxarxa.net) ha estat autoritzada pels titulars dels drets de propietat intel·lectual únicament per a usos privats emmarcats en activitats d'investigació i docència. No s'autoritza la seva reproducció amb finalitats de lucre ni la seva difusió i posada a disposició des d'un lloc aliè al servei TDX. No s'autoritza la presentació del seu contingut en una finestra o marc aliè a TDX (framing). Aquesta reserva de drets afecta tant al resum de presentació de la tesi com als seus continguts. En la utilització o cita de parts de la tesi és obligat indicar el nom de la persona autora.

ADVERTENCIA. La consulta de esta tesis queda condicionada a la aceptación de las siguientes condiciones de uso: La difusión de esta tesis por medio del servicio TDR (www.tesisenred.net) ha sido autorizada por los titulares de los derechos de propiedad intelectual únicamente para usos privados enmarcados en actividades de investigación y docencia. No se autoriza su reproducción con finalidades de lucro ni su difusión y puesta a disposición desde un sitio ajeno al servicio TDR. No se autoriza la presentación de su contenido en una ventana o marco ajeno a TDR (framing). Esta reserva de derechos afecta tanto al resumen de presentación de la tesis como a sus contenidos. En la utilización o cita de partes de la tesis es obligado indicar el nombre de la persona autora.

WARNING. On having consulted this thesis you're accepting the following use conditions: Spreading this thesis by the TDX (www.tesisenxarxa.net) service has been authorized by the titular of the intellectual property rights only for private uses placed in investigation and teaching activities. Reproduction with lucrative aims is not authorized neither its spreading and availability from a site foreign to the TDX service. Introducing its content in a window or frame foreign to the TDX service is not authorized (framing). This rights affect to the presentation summary of the thesis as well as to its contents. In the using or citation of parts of the thesis it's obliged to indicate the name of the author

UNIVERSITAT POLITÈCNICA DE CATALUNYA (UPC)

**Characterization and Design
of Multifunction Photonic Devices
for Next Generation
Fiber-to-the-Home
Optical Network Units**

Author

Bernhard Schrenk

Advisors

**Josep Prat Gomà
José A. Lázaro Villa**

**A thesis submitted in fulfillment for the
degree of Doctor of Philosophy**

at the

**Optical Communications Group (GCO)
Signal Theory and Communications Department (TSC)**

March 2011

The work described in this thesis was performed at the Signal Theory and Communications department of the Universitat Politècnica de Catalunya / BarcelonaTech. It was funded, in part, by the Spanish ministry of science and innovation by the FPU grant AP2007-04116 and supported by the European Commission through the FP7 Projects SARDANA, EURO-FOS and BONE.

Bernhard Schrenk

*Characterization and Design of Multifunction Photonic Devices
for Next Generation Fiber-to-the-Home Optical Network Units*

Subject Headings: Optical fiber communication

Copyright © 2011 by Bernhard Schrenk

All rights reserved. No part of this publication may be reproduced, stored in a retrieval system, or transmitted in any form or by any means without the prior written consent of the author.

Printed in Barcelona, Spain.

ISBN: 9788469443651

Reg: B. 25779-2011



INFO ABOUT RIGHTS



1 103158 713828

www.safecreative.org/work

To my parents

Abstract

Optical access technology has experienced a boost in the last years, thanks to the continuously migrating multimedia services that are offered over the internet. Though the devices used for deploying *Fiber-to-the-Home* instead of traditional copper-based solutions are still based on micro-optics, an evolution towards photonic integration can be foreseen. What remains is the question about the exact designs for this important step of integration, which should be optimized in terms of transmission performance, energy efficiency and cost to address all requirements of *next-generation* photonic networks.

As the most critical element in optical access, the customer premises equipment is in primary focus of this discussion. The covered topics span over a wide range and include wavelength recycling for full-duplex data transmission on a single optical frequency, the generation of advanced modulation formats with low-cost semiconductor modulators with small form factor, support for optical amplification by means of seeding techniques and the support of higher layer functionality at the physical layer.

Next to the principal proof of the proposed techniques, the benefits, impediments and upgrade paths towards *multifunctional photonic systems* are highlighted in different case studies, while the most representative designs are further discussed in their capability of being photonicallly integrated.

Acknowledgements

First of all I have to look towards my roots and thank my parents, who supported my stay abroad during all the years of my PhD study and my academic career development during the years before. I understand that it was not completely easy for them, not only because of my long absence and the few trips back to Austria, but also due to the attitude a scientific researcher has when he is stressed. I fear, however, that the time for the return to my homeland has still not come.

Next, I want to gratefully acknowledge the opportunity that Prof. Josep Prat gave me to join his team and the good infrastructure he provided for us. His broad knowledge in optical access networks allowed me to settle in a completely different field of research that has its own rules, especially when looking back at my academic origins in microelectronics, semiconductor physics and quantum cryptography – though the main focus was always concentrated on optical telecommunications.

The most work deriving from my PhD study had probably Dr. Jose A. Lazaro, who had the pleasure of sitting opposite of my workplace and thus directly in front of me. With this, he got permanently into scientific discussions about many different topics. He never had problems to tune from one to the next topic though being appointed also to other research and administrative problems, and indeed he always had good answers and suggestions for me, especially during the process of writing the right words in the paper manuscripts.

The climate in the group wouldn't have been the same without my other colleagues who were mostly obtaining their PhD degree as I did. Here I want to mention Francesc Bonada and Josep M. Fabrega first, who shared the table on the left-hand side of mine and in the second case most of the early morning hours. I will keep not only the funny lunch times but also the fruitful and relaxed discussions in the morning hours from 7-9am, next to a coffee, in mind (the emphasis here is on “next to”). In fact, most of the ideas I had during my work were developed in these early hours that provided some inspiring and unique atmosphere. At this point I also want to mention the time that Francesc spent in several experiments we performed together, most of them having a productive outcome, leading also to a relative high number of journal publications and conference visits.

Since it is always a paralyzing shock when jumping into cold water the first time, I would like to acknowledge the support from Victor Polo and Mireia Omella, helping me to get into the handling of the lab instrumentation and RF stuff. Especially Victor, who

did his job as lab chief well during all the years, received many questions for many times and had always an open ear for them. Eduardo Lopez and Ivan Cano as well as the colleagues from the “software level” shall be acknowledged for the good atmosphere they provided during the many working hours.

Finally I want to acknowledge the support by our collaborators outside of UPC. Without the continuous support with photonic devices there would not have been the same amount of positive outcome. Christophe Kazmierski, but also Guilhem de Valicourt and Romain Brenot from Alcatel-Thales III-V Lab guaranteed a steady flow of new samples for me, and I hope that we have done well in turning that support into successful experimental proofs for different techniques that can be used for future research.

In addition, I want to express my gratitude to Prof. Hercules Avramopoulos and his team at NTUA for his point of views before and at the end of my PhD study, as well as for their support and good atmosphere during my long-term mobility end of 2010 to Athens. Back at the roots, I also want to thank Prof. Walter Leeb for his regular opinion during my academic career.

At last it has to be mentioned that good work is only possible with appropriate funding. For this reason, I want to express my thanks to the Spanish Ministry of Science, MICINN, for granting my FPU scholarship that allowed me to work on my PhD degree without worrying about monetary issues and also for accepting my long-term mobility to Athens.

Further, many trips have been made thanks to the interest in scientific research by the European Commission. Without funding from the EU, many additional aspects of a life as PhD would get lost, including not only the possibility to join project meetings for discussing with other European colleagues, but also to visit congresses where one can see researchers from worldwide from face to face and enjoy a unique atmosphere when presenting the own contribution to the big or, in case of optical telecommunication, actually small “world of research”. In course of that I would also like to mention the IEEE Photonics Society who funded my trip to OFC 2010. All these additional tools, mostly constituted by congress participations, strengthen the possibilities that one as ordinary “student” has and are indispensable for a good PhD work.

Now, as these acknowledgements already span over two pages, let me mention that the idea of Networks of Excellences is not bad at all, though they are going to become extinct in near future – a pity that the next generation of PhDs will not have that pleasure! One shall also recall that the EU is not a hole where money disappears as many narrow-minded people might think, but that it provides a lot of possibilities and chances that are not seen at first glance, allowing to work effectively with many friends beyond the borders of the own country. This is at least one important aspect I have learnt during the last 3 years and I invite all prospective PhD students to give that experience a chance.

Table of Contents

Abstract	v
-----------------------	----------

Acknowledgements	vii
-------------------------------	------------

Table of Contents	ix
--------------------------------	-----------

Chapter I – The Rise of Optical Access

1.1	Introduction	1
1.2	State-of-the-Art.....	2
1.2.1	Active and Passive Access Networks.....	2
1.2.2	Access Network Architectures	3
1.2.3	Standards for Optical Access.....	11
1.2.4	Customer Premises Equipment and Key Components.....	12
1.3	Thesis Outline.....	17

Chapter II – Fundamental SOA Models

2.1	Introduction	19
2.2	Amplification: Gain and Noise.....	21
2.2.1	Energy Band Structure of Direct Semiconductors	21
2.2.2	Analytical SOA Model	25
2.2.3	Simulation.....	35
2.3	Electro-Optical Modulation Bandwidth	45
2.3.1	Electro-optical transfer function.....	45
2.4	Patterning and Optical-Optical Transfer Function	52
2.5	Chirp.....	57
2.6	Summary.....	59

Chapter III – A Practical Perspective of SOAs

3.1	Introduction	61
3.2	Principal Amplifier Design.....	62
3.3	Packaged Devices and Chips-on-Carriers	64
3.4	Optical Properties and Characterization	68
3.4.1	ASE Spectrum and Gain Ripple	68
3.4.2	Polarization Dependent Gain.....	69
3.4.3	Gain Saturation and Transparency Threshold	69
3.4.4	Gain Spectrum and Gain Bandwidth	70
3.4.5	Noise Figure	71
3.5	SOAs in Applications as Intensity Modulators	72
3.5.1	Operational Bias Point.....	72
3.5.2	Electro-optical Response and Modulation Bandwidth	74
3.5.3	Optical Response and Patterning	79
3.6	Chirp	80
3.6.1	Measurement	80
3.6.2	Assistance for Transmission at Higher Data Rates	82

Chapter IV – Full-Duplex ASK-Transmission on a Single Wavelength

4.1	Introduction	85
4.2	Wavelength Reuse in Bidirectional Transmission	86
4.3	Gain Saturation of a SOA.....	92
4.3.1	Natural Suppression of Bit Patterns due to Gain Saturation	92
4.3.2	Selection of the Optimum Modulation Index	96
4.4	Electrical Feed-Forward Downstream Cancellation.....	98
4.4.1	Functional Scheme of Operation	98
4.4.2	Principal Proof of Concept	103
4.4.3	Optimum Reception Bandwidth for the Upstream	110
4.4.4	Experimental Validation.....	113
4.5	All-Optical Downstream Cancellation by Carrier Recovery.....	134
4.5.1	Principal Scheme	134
4.5.2	Analytical Model	135
4.5.3	Simulation.....	138
4.5.4	Experimental Validation.....	141
4.5.5	Possibilities for Photonic Integration	150
4.6	All-Optical Downstream Cancellation with Pulse Shaping	151
4.6.1	Simulation.....	152
4.6.2	Experimental Validation.....	154
4.7	Additional Aspects for Wavelength Reuse.....	157
4.7.1	Wavelength Shifting due to Clock Tone Extraction.....	158
4.7.2	Wavelength Generation due to Four-Wave Mixing	163

Chapter V – Orthogonal and Advanced Modulation Formats for Access

5.1	Introduction	173
5.2	Integrated FSK Demodulator and Detector for FSK/ASK	173
5.2.1	Gain Ripple of a SOA	174
5.2.2	Demodulation of FSK Signals	175
5.2.3	Experimental Validation	182
5.2.4	Possibilities for Photonic Integration	187
5.3	Advanced Downstream Data Rates with FSK+ASK/ASK	188
5.3.1	Colorless ASK+FSK Demodulation	188
5.3.2	ASK+FSK / ASK Transmission Performance	190
5.4	QAM with Integrated InP-based Modulators	192
5.4.1	SOA as Phase Modulator	192
5.4.2	Experimental Validation	193

Chapter VI – Seeding Techniques

6.1	Introduction	197
6.2	Self-Seeded Upstream Transmission	197
6.2.1	PON Architecture and Seed Loop Design	198
6.2.2	Characterization of ONU and Upstream Carrier	200
6.2.3	Signal Evolution	202
6.2.4	Relative Intensity Noise	205
6.2.5	Transmission Performance	207
6.2.6	Comparison between Self-Seeded and Conventional PON	210
6.3	Seeding of an EDF Pump for Transparent Power Splitting	211
6.3.1	Noise-Pumped Extender Box	211
6.3.2	Experimental Proof of Concept	220
6.3.3	Scenario 1: Reflective ONU based on SOA and REAM	225
6.3.4	Scenario 2: ONU based on Gated EML	228
6.3.5	Scenario 3: ONU based on a RSOA	235
6.3.6	Comparison with Other Amplification Schemes	239

Chapter VII – ONU Designs Supporting Higher Layer Functionality

7.1	Introduction	241
7.2	Multi-Operability and Dynamic Bandwidth Allocation	241
7.2.1	Principal Scheme	242
7.2.2	Considerations for the Modulation Bandwidth	245
7.2.3	Applicability to Access Networks	246

Chapter VIII – Conclusions

8.1	Technical Conclusion	253
8.2	Outlook for the Future	254

A. List of Acronyms	I
----------------------------------	----------

B. List of Symbols	V
---------------------------------	----------

C. Research Publications	XIII
---------------------------------------	-------------

D. Bibliography	XIX
------------------------------	------------

Biography	XXXVII
------------------------	---------------

Chapter I

The Rise of Optical Access

The advantage of optical telecommunication eases the daily life though it is so far not really transparent to the mankind since it is hidden in the core networks and therefore not touchable. The worldwide penetration of optical fiber into the last extents of communication networks, the so-called access networks, is very low and just common in a few countries. However, with the expected deployment of fiber till the customer premises in the coming years, this initially small field of telecommunication has attracted the research community.

This chapter provides a short overview about ongoing research and standardization, as well as the different architectures and components used for the communication subsystems of access networks.

1.1 Introduction

Optical fiber communications is one of the drivers to enable broadband services for the end-users of nowadays telecommunication networks, which will then also be able to spread over larger geographic areas. According to the reach of the transmission links, one speaks about core, metro or access network [1]. Optical fiber is thereby used as transmission medium since it offers several advantages compared to the copper wires such as the traditional twisted pair cable.

Fiber-to-the-X (FTTX) technology has been extensively studied worldwide, aiming at the delivery of high bandwidth to users and for converging wireless and wireline communication. The ‘X’ can stand for Curb, Node, Building, Home or any other implementation of FTTX.

An important point for FTTX is the capability for building future-proof broadband networks with low installation and operating expenditures: unless a “killer” application is found, customers will not be willing to pay more for higher data rates and, as a consequence, the cost per user can be raised just marginally. In addition to a cost-efficient deployment, upgrade paths for a later expansion – in terms of reach extension and increased number of customers – have to be considered, demanding scalable and flexible network architectures and subsystems. Although networks can thereby grow and absorb the metro segment, as illustrated in Fig. 1.1, the term “access” network is still common for such long-reach networks. The aim is thereby to consolidate multiple

central offices (CO) at a single location or to expand the access network into a “green” field where no telecommunication solution is present so far [2].

With the growth of the access segment, additional functionalities such as multi-operability, dynamic bandwidth allocation and resiliency are demanded by the operators.

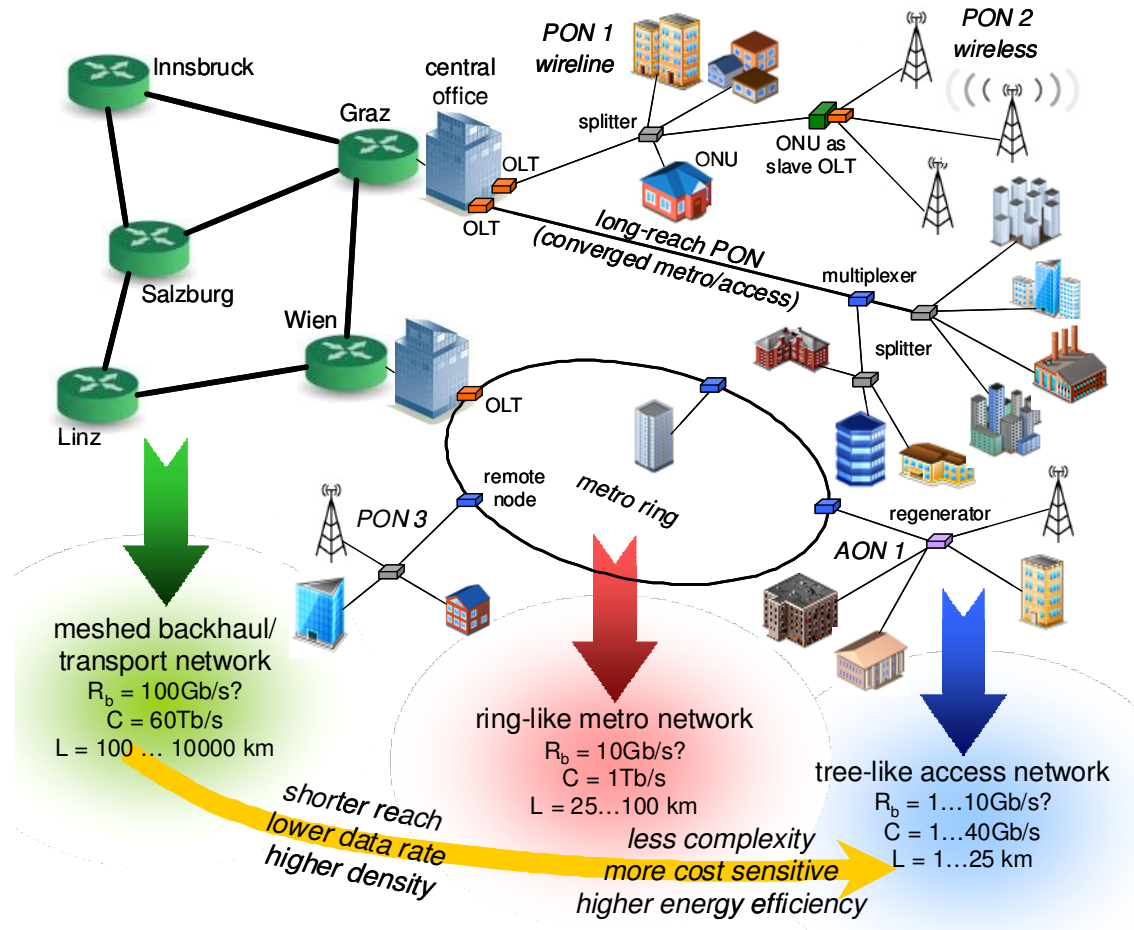


Fig. 1.1. Telecommunication infrastructure. Next to the long-haul transport network a metro/access convergence takes place.

1.2 State-of-the-Art

The following sections highlight access network architectures and their multiplexing techniques, standards, commonly used electro-optical devices and research activities of the last years, while support will be given by references to fundamental and recent research literature.

1.2.1 Active and Passive Access Networks

While active optical access networks (AON) exist and take advantage of repeaters in the form of o/e/o-regenerators as well as switches for reach extension and routing [3-5], passive optical networks (PONs) are also gaining attention due to the fact that no active

components are deployed in the distribution plant between the operator and the customers [6-8]. In this way, cost deriving from maintenance of active devices can be kept low as they are situated either at the CO of the provider or located at the customer premises. A third kind of access networks can be found in the middle between AONs and PONs, where the fiber plant is in principle subject to passive components but contains service nodes referred to as local exchanges, where electrically powered equipment such as amplifiers may be found [9-12]. Although such networks are still called PONs due to the absence of higher layer functionality in these network nodes, they are not considered in this thesis since they are strictly spoken not passive at all.

In general, the capital and operating expenditures (Capex / Opex), which can be seen as a figure of merit for a network architecture in the view of an operator, are lower in the case of truly passive PONs when compared to AONs or PONs that both incorporate electrically powered elements at the optical distribution network [13].

1.2.2 Access Network Architectures

Over the past years, a series of network architectures have been shown up, mainly inspired by wavelength and time division multiplexing (WDM, TDM) [14]. The architectures are classified in their multiplexing technique that is employed to expand the number of customers, regardless if they are from active or passive nature, and further distinguished by a coarse set of network parameters, which contains

- customer density
- loss budget
- delivered data rate
- Capex and Opex
- energy efficiency

Customer Density

The user density reflects the share of network equipment and has therefore impact on cost considerations for the Capex: the higher the number of users served by a PON, the less the marginal cost increase when additional components such as amplifiers are required at the common infrastructure. If a long reach can be covered in addition, the closer location of the access network head-end to the core network not only simplifies the overall network hierarchy but safes also cost.

Depending on the multiplexing technique that is used, different subsystems inside the network can be shared among a certain number of users. While the optical line terminal (OLT) at the premises of the network operator is always shared between all customers, network nodes might be dedicated to a smaller subset of users, and therefore subject to increased cost-sensitivity. An extreme case is the optical network unit (ONU), which has direct impact of the cost for each customer – considering a scenario without multiple dwelling units as end-nodes. On the other hand, the Opex is determined by the

steady power consumption and operational cost of several electrically powered components, where the impact of the customer density is reduced. However, the required number of closets for hosting networks components and with them, the Opex that derive from the rent of housing or environmental conditioning, are reduced for dense PONs due to the share of infrastructure.

Loss Budget

Together with the loss budget, the customer density determines the geographical coverage by a single OLT. The optical loss budget includes several optical losses that can be found between OLT and ONU, including the intrinsic loss of the multiplexing technique that is required to expand the customer density (i.e. the power splitting loss or the insertion losses of wavelength multiplexers), additional prospected losses that may arise during the lifetime of the PON (i.e. splicing losses), and the loss that derives from the fiber spans that are required to achieve the desired network reach. Care has to be taken for the case of bidirectional transmission, since the loss budget is then limited by the worse transmission direction. Especially for the uplink, this can cause stringent restrictions: although the upstream reception can benefit from the use of optical amplifiers in contrary to the downstream reception that is bound to low-cost components at the ONU, the seed of reflective modulators requires a certain optical signal condition at the input of the ONU, which results in a third limitation for the overall PON loss budget [15].

Delivered Data Rate

For the delivery of services, the multiplexing technique has big impact on the guaranteed data rate. The principal idea of access networks relies on data transmission on a single wavelength. Since the spectral window for fiber-optic telecommunication is limited by the fiber loss spectrum and the availability of optical amplification, a certain number of wavelengths can be used. Considering the third telecommunication window around 1550 nm where the fiber loss is low, around 80 wavelengths in the conventional and long wavelength band (C+L) are found to be compatible with rare earth-doped fiber amplifiers [16, 17].

A wavelength can be dedicated to each of the customers according to the strategy of WDM-PONs. Although a limit for the user density of the network arises, a fixed data channel for each of the customers can be provided [18]. For this reason the data rate depends then only of the subsystems at the OLT and the ONU, and on the transmission impairments that derive with higher data rate.

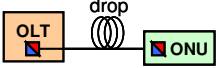
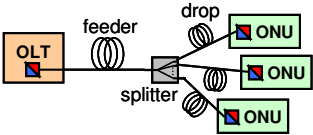
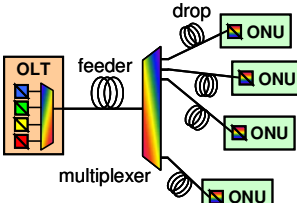
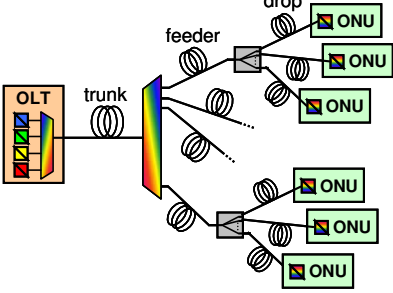
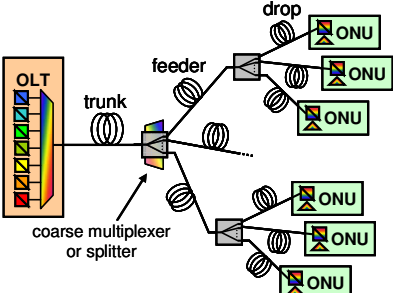
<div style="text-align: center;">Characteristics</div> <div style="text-align: center;">Architecture</div>	principal RX/TX	typ. loss budget [dB]	typ. user density	min. granted data rate [Gb/s]	max. data rate [Gb/s]	cost per user
P2P 	CM-IM/DD	10	1	10	10	very high
TDM [19] [20] [21] 	BM-IM/DD	28	32	0.3	10	low
WDM [18] [22] 	CM-IM/DD	20	40	10	10	high
Hybrid WDM/TDM [23] [24] 	BM-IM/DD	32	1000	0.3	10	very low
UDWDM [25] 	CM coherent	40	1000	1	1	high

Table 1.1. Common PON architectures and their typical parameters.

On the contrary, when a single wavelength channel is shared among a certain number of users in terms of a TDM basis [19], the time-slot that is dedicated to each of the customers can be from short duration once the customer density of the PON increases. This in turn means that the minimum granted data rate is just a fraction (corresponding to the TDM duty cycle) of the nominal data rate, for which the subsystems have to be drawn for.

The delivered data rate has to be therefore traded-off with the customer density. An exception are ultra-dense WDM (UDWDM) PONs that employ techniques of coherent detection, which allow to slice the available wavelength spectrum with a significantly higher granularity. However, limits are then given for the maximum data rate.

Energy Efficiency

With the permanently increasing power consumption of the telecommunication sectors, special attention has been drawn on the access segment, which aims at a mass deployment of future-proof customer premises equipment. One of the goals for development has to be therefore the minimization of the energy consumption for electrical subsystems of the ONU. Since that includes not only electro-optical aspects such as driving circuitry for modulators or other active components but also the subsystems that are used for electrical (real-time) signal processing and medium access control (MAC) [26], the thesis does not focus on optical frequency division multiplexing (OFDM) [27] which nowadays requires heavy signal processing in digital signal processors or field-programmable gate arrays in contrary to the simpler, conventional multi-channel transmission systems [28].

The common network architectures are further discussed in their principal advantages and technical challenges. An overview with typical parameters is given in Table 1.1.

Point-to-Point Connection

Similar to meshed networks that are found in the transport segment, point-to-point (P2P) access solutions require a dedicated fiber span between each OLT and ONU. This corresponds to a worst case where no infrastructure is shared, neither in the fiber plant nor at the central office.

This exclusive connection, which typically utilizes one or two wavelengths for half- or full-duplex bidirectional data transmission for the end-user, allows thereby high transmission capacities with simple transmitters and receivers, as it is the case in optical intensity modulation / direct detection (IM/DD) transmission systems. However, since such solutions are not considered to be cost-efficient for access, this kind of architecture is not further targeted in this thesis.

TDM-PON

A simple solution to overcome the cost-inefficiency of P2P connections is to share the fiber plant among a higher number of customers. The fiber span is thereby commonly used to connect several ONUs to a single OLT, by splitting the signal in its power to a bunch of customers instead of only one [19, 29]. This in turn requires a TDM scheme to avoid crosstalk between the data streams sent by the users, which have to be also allocated with the help of some MAC intelligence due to the different drop span lengths. Each user obtains a time slot in this way, which is dedicated solely to its own data transmission. The allocation of time slots can vary over time to incorporate a dynamic bandwidth allocation mechanism between the users.

Although this procedure leads to a reduction in the data rate per user, the naturally high data rates that can be achieved thanks to the maturity of optical transmitters ensures that the net data rates for the single customers is still higher than conventional telecommunication standards such as the very high speed digital subscriber line (VDSL) can offer – by increasing the possible network reach at the same time.

Besides the typical splits in the order of 1:32, much higher split values up to 1:4000 have been reported in scientific literature [20-21,23]. Although this would be practically useless due to the low guaranteed bandwidth per customer, the splitting loss can be re-attributed towards a reach extension. The idea hereby is to place the splitter as close as possible to a bunch of users that are connected by drop fibers with a length of up to 10 km, while the feeder fiber that constitutes the trunk is extended up to 100 km. Such reach extensions have been reported mainly by using Raman amplification [30]. The maximization of the common fiber link leads to a higher share of infrastructure and therefore to higher cost-efficiency. Due to backscattering effects in the optical fiber, the trunk is sometimes composed by a dual-feeder fiber, especially when longer fiber spans and higher loss budgets are targeted. However, for a green-field deployment, the cost of the additional fiber has to be seen in contrast with the digging cost and is likely to be negligible.

In contrary to P2P links where a continuous-mode (CM) data stream is delivered, the TDM scheme requires burst-mode (BM) electronics at the ONU transmitter and the OLT receiver. Although this does not introduce a significant cost increase since it has in principle no effect on the optical and electro-optical components, the required timing demands short preambles in the order of a few nanoseconds for synchronization and threshold detection. Different standards such as Ethernet PON (EPON) and Gigabit PON (GPON) derived from that problem of defining an optimum TDM scheme for the access segment and are discussed briefly later in this chapter.

With nowadays progress in research, it is not clear if TDM and the included BM transmission will be carried to standards of next-generation optical access networks.

WDM-PON

Another approach to increase the share of common infrastructure can be the multiplexing in the optical frequency domain [18,29]. The optical power splitter of TDM-PONs is thereby replaced by a WDM multiplexer. Besides the reduced optical losses of the multiplexing stage, the WDM-PON increases the spectral efficiency of the access network by taking advantage of the high optical bandwidth of optical fibers: instead of sending just one or a pair of wavelengths to the users connected to the OLT, the available transmission spectrum of the optical fiber is filled with data signals. Although this might be not compliant with the wavelength allocation of existing standards such as analog wireline video transmission, the low commercial impact of these conflictive standards provides strong arguments for an efficient deployment of WDM-PONs in future.

The CM data transmission can accommodate high guaranteed data rates up to 10 Gb/s, without the introduction of additional intelligence in the MAC layer due to the exclusive wavelength channel that each network possesses.

Typical customer densities are 40 per employed waveband, while up to 3 wavebands in the short (S-), C-, and L-band could be effectively used to maintain low optical losses in the distribution fiber. The request for wavelength-agnostic ONUs, which may contain reflective active remodulators, can thereby limit the spectral window for wavelength deployment due to the optical gain response of the low-cost components used in the ONUs. In addition, the granularity of nowadays commercial components for WDM multiplexers is limited, so that a fine channel grid that provides a larger number of wavelengths per waveband cannot be achieved. A typical channel spacing is 100 GHz, but are still expected to decrease which is also confirmed by research where a spacing of down to 1 GHz has been demonstrated [31,32]. In turn, a larger number of data channels would also require powerful and electrically powered optical amplifiers that are placed inside the optical distribution network, since Raman amplification or remotely pumped EDFs at the common trunk span are not able to provide significant gain for a dense comb of data signals in contrary to the reach extension of single- or dual-wavelength TDM-PONs.

Hybrid WDM/TDM-PON

A hybrid PON architecture maximizes the customer density by incorporating WDM and TDM techniques [6,8,10-11,23,29]. A set of wavelengths is thereby fed together via a common and in general long trunk or ring segment, and a WDM demultiplexer then spreads the single data channels towards a bunch of TDM trees – sometimes referred to as “spurs”, each of them containing a feeder fiber, a power splitter and a short drop fiber. In this way, the multiplexing factors of WDM and TDM segment are multiplied and a high number of customers can be served by the operator. A hybrid PON can be seen as an overlay of TDM-PONs, whose trunk segment is partially shared over a single fiber span.

The loss budget of hybrid PONs is typically extended to far beyond the budget of a TDM-PON, since a metro-access convergence is targeted at the same time. Due to the highly non-centric loss distribution, meaning a placement of the TDM splitting stage (i.e. in general the largest concentrated loss element) very close to the ONU, problems are very likely to arise due to Rayleigh backscattering in the feeding fibers when a single wavelength is reused for down- and upstream transmission.

The junction between the WDM and the TDM segment is often used to incorporate some network intelligence or means of amplification. While in networks that contain electrically powered equipment these so-called remote nodes include routers [4,33] or protocol terminators [5], other approaches, which provide optical amplification by remotely pumping rare-earth doped fibers, exist [6,8].

The guaranteed bandwidth of hybrid PONs equals the one of TDM-PONs and the necessity of the more complex BM electronics is given too.

UDWDM-PON

An emerging type of access network are WDM-PONs with ultra-dense wavelength allocation [25]. The idea is not only to increase the customer density of the PON, but also to avoid narrow-band WDM multiplexers. The latter is gained by placing passive splitters as signal distribution elements, as it is the case in TDM-PONs, and in turn coherent detection to overcome the introduced high loss budget of the network. Alternatively, a coarse WDM multiplexer with drop channel widths much wider than the spectral width of a single data channel can be used as first distribution element.

Coherent detection of a specific data channel requires a tunable laser source [34] at the ONU and is in principle contradictory to cost-effective mass deployment. However, progress has been made on the development of lower cost tunable lasers, that can be also used for data modulation at bit rates up to 2.5 Gb/s [35].

A typical data rate would be 1 Gb/s that is compatible with a channel spacing of 3 GHz [36]. Considering the spectral windows defined before, this would assure a customer density of 1000 users or more, however, with the restriction of having a limited maximum data rate for which no simple upgrade path is given. The large number of individual transmitters and receivers that are required at the OLT is another problem to be solved in UDWDM systems and demands progress in photonic large-scale integration.

The principal idea of sending ~1000 wavelengths to all users, which in turn select just a single one, is questionable from the viewpoint of energy efficiency. In addition, the reception sensitivity has to be very low to avoid nonlinear effects at the fiber span close to the OLT where many wavelengths are present with average to high overall optical power.

An illustration of the coverage and maximum transmission data rates of the aforementioned access network architectures is shown in Fig. 1.2 together with conventional local and core telecommunication networks.

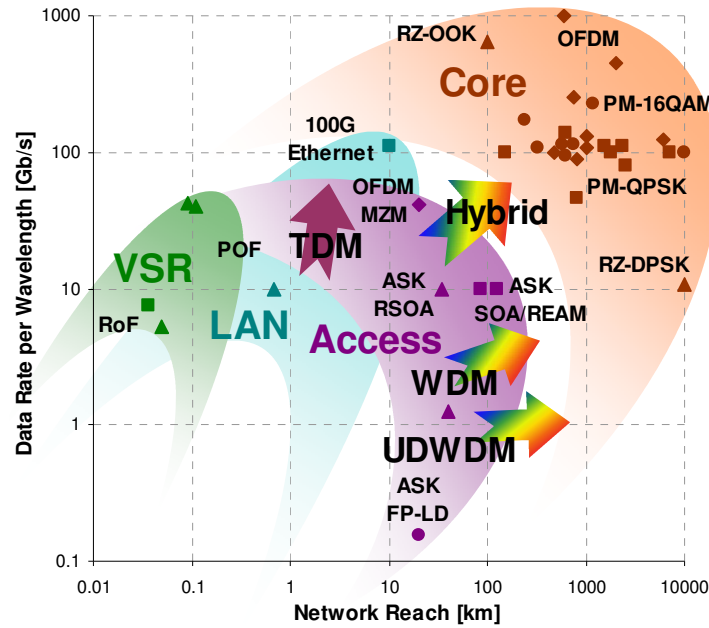
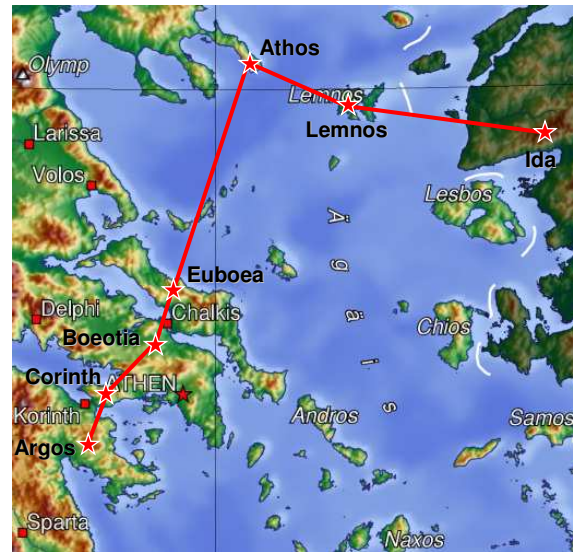


Fig. 1.2. Reach and maximum data rate per wavelength for access networks as well as for local and core telecommunication networks.

Note. The origins of optical communication root deep in history. The first reported optical transmission of information dates back to 1184 B.C., to the fall of Troy. After years of war, the ancient Greeks urged to send a short notice about the successful siege to Mycenae. According to Homer's *Ilias*, a chain of fires were lighted, started by Agamemnon on mount Ida next to Troy, towards Lemnos, Athos, Euboea, Boeotia and Corinth. After passing this repeated 518 km long transmission link with six hops, the message, containing just a single bit, arrived after a little bit more than three hours on mount Argos next to Mycenae.



Much later in human history, in 1880 A.D., Alexander Graham Bell invented the Photophon, which came already close to a communication equipment suitable for mass deployment. On the contrary to the telephone, it allowed to transmit voice with the help of bundled light rays. Sun light was used as the optical source and was modulated by the voice that was directed on a mirror. In accordance with directional link systems, a parabolic mirror collected the transmitted light and directed it towards a selenium cell that acted as transducer.

Although telecommunication was in its infancy in these early days, Bell already had a sense for the impressive strides that optical telecommunication would made. He expressed that with some words about the Photophon: "It's the greatest invention I have ever made; greater than the telephone!"

1.2.3 Standards for Optical Access

Two main access standards have emerged from the evolution of access networks. While EPON (IEEE 802.3ah) [37] derives from the world of Ethernet and provides a net data rate of 1 Gb/s, GPON (ITU-T G.984) [38] provides a wider functionality regarding MAC and higher layers while the data rate is 2.5/1.25 Gb/s for down- and upstream.

The increasing demand for broadband services – considering the shared fiber media and the therefore reduced minimum guaranteed data rate – led to the successors 10G-EPON (IEEE 802.3av) [39] and XGPON [40], the 10 Gb/s capable PON. Both standards aim at symmetrical data rates of 10 Gb/s. While the 10G-EPON standard was ratified in September 2009, the XGPON standard is still in progress and not approved so far. Both standards declare the 1490 nm region for the downstream and the 1310 nm window for the upstream, to be compatible with a video overlay around 1550 nm.

The following table summarizes the PON standards that are currently in consideration.

<i>Access Standards</i>	EPON	GPON	10G-EPON	XGPON (10G-GPON)
Standard	IEEE 802.3ah	ITU-T G.984.x	IEEE 802.3av	ITU-T (2010)
Max. Link Loss [dB]	20 (A) 24 (B) 28 (C) 32(D)	28 (B+) 30 (C) 33 (C++)	20 (PR10) 24 (PR20) 29 (PR30)	30-32 (tbd)
Symbol Rate [Gbaud] Down/Upstream	1.25	2.48832/1.24416	10.3125 (also 1.25)	tbd
Framing	IEEE 802.3	125 μ s, fixed	IEEE 802.3	tbd
Line Coding	8B10B	only frame scrambling, run length of 72 bits	64B66B	tbd
Forward Error Corr.	Reed-Solomon (255,239)	RS (255,239)	RS (255,233)	tbd

Table 1.2. Access standards and some of their characteristic parameters.

The line coding affects not only the MAC layer but impacts also the physical layer since it determines the number of consecutive identical bits and therefore the required low-frequency cutoff. This in turn is strongly related with bit pattern dependent distortions in semiconductors and also with scattering effects in optical fibers, where the optical carrier in a bidirectional transmission is backscattered into the counter-propagating data stream. A further interesting parameter at the physical layer is the robustness to a reflection, which is defined with a maximum of -20 dB.

1.2.4 Customer Premises Equipment and Key Components

As the key element of the access network, the ONU has strong impact on the transmission performance, cost and energy efficiency of the PON. Depending on how the downstream signal is re-used for upstream transmission, three categories of ONUs can be distinguished regarding their upstream transmitter design, which can be based on

- laser diodes
- injection-locked light sources
- reflective modulators

Although it is in principle desired to avoid laser sources at the customer premises, proposals, for which the use of a laser at the ONU is mandatory, exist. An example are receivers in UDWDM systems that are typically based on coherent detection where a local oscillator is required. While fast tunable lasers are still expensive, cheaper derivatives that follow a set-and-forget adjustment would suit.

On the other hand, the EPON or GPON standard foresees the use of light sources at the customer premises of TDM-PONs too, since the fixed down- and upstream wavelength are far detuned and not suitable for wavelength reuse. In the latter case a directly modulated laser (DML) is used as upstream transmitter. Such devices not only save cost by avoiding external modulators, but suffer also from parasitic effects of the semiconductor such as chirping.

A slightly different approach is to use a multi-wavelength laser, such as Fabry-Pérot laser diodes (FP-LD) or Vertical Cavity Surface Emitting Laser diodes (VCSEL). A specific laser mode can thereby be selected by locking the downstream to one of the modes [41-43]. With a proper injection into the laser, the upstream wavelength then follows the one of the downstream.

Although commercial deployment of optical access will most probably focus on reflective modulators [44], first commercial demonstrations of WDM-PONs were indeed relying on FP-LDs [45]. However, problems still arise when the comb of the FP-LD has to be tuned to the incident optical signal, since the tuning range of these devices is limited. Modulation at high data rates has been reported lately with a VCSEL in a chirp-managed transmission scheme [46].

The most versatile and from the first view also simplest solution is to avoid light sources at the customer premises equipment; A centralized light generation not only concentrates the wavelength management at the central office, it eases also the maintenance of the light sources. In addition, the ONU, which holds a semiconductor modulator [47], becomes colourless. This in turn allows to port it to another location of the PON without being reconfigured as it would be the case for a tunable laser that is used as light source of the upstream transmitter.

The incorporation of reflective modulators that are integrated together with optical amplifiers is a promising solution for the ONU [48-50]. In this way, the loss over the network can be at least partially overcome while the upstream data is imprinted on the

incoming signal. A spectrally efficient network does not dedicate a second wavelength for the upstream besides the one that is allocated for the downstream, but uses a single wavelength as optical input signal for an ONU. This signal not only carries the downstream data but is recycled for the purpose of upstream transmission. In the extreme case of full-duplex transmission, the two counter-propagating data streams are then present on this wavelength at the same time.

Wavelength reuse in terms of remodulating the downstream can be achieved either by using orthogonal modulation formats for down- and upstream or by suppression of the amplitude shift keyed (ASK) downstream pattern before the optical carrier is again modulated with ASK upstream data. A trade-off has to be made between the introduced complexity when orthogonal formats with frequency or phase shift keying (FSK, PSK) for the downstream have to be detected, and the residual penalty when means of imperfect downstream suppression techniques for simple modulation formats such as ASK are employed.

The performance of the receiving and mainly the transmitting subsystem of the ONU depends strongly on the used components and technology. Extensive research work has been focusing on reflective upstream transmitters. Promising candidates for this purpose are the reflective semiconductor optical amplifier (RSOA), the reflective electro-absorption modulator (REAM) or integrated versions of SOA and REAM, short SOA/REAM.

These components can be realized within the Indium-Phosphide semiconductor material system. Compared to Lithium-Niobate based solutions such as the Mach-Zehnder modulators (MZM), the III-V semiconductor components provide a by far smaller form-factor and are therefore in course of the miniaturization of future customer premises equipment [51]. However, parasitic side effects during modulation, such as chirp and in case of RSOAs also the limited electro-optical bandwidth, penalize the data transmission for the cheaper and smaller semiconductor-based modulators. It is therefore often required to compensate these unwanted effects by additional electronic means like passive or adaptive electronic equalization.

Within the research, several ONU designs and modulation formats for down- and upstream have been proposed. In the beginning most of them were focused on simple realizations for the subsystems of the ONU, since means of photonic integration were not available and not expected to be available in the following years. Although nowadays commercial products are therefore still based on micro-optics, advances have been made in research, especially in the field of optical interconnects [52], and it can be expected that soon added complexity that allows significant extra functionality will come at just marginal cost. Due to that, the required simplicity of the electro-optical subsystems has prevented to exploit the whole variety of modulation formats for optical telecommunication [53].

However, up to now discrete components are employed in the receiving and transmitting subsystems at the OLT and the ONU. Table 1.3 compares the complexity and performance of representative modulation formats for down- and upstream.

complexity and cost shifted towards DS subsystems

		NRZ/NRZ	IRZ/NRZ	FSK/ASK	DPSK/ASK
Downstream (DS)	TX	simple, ER reduced	twice the modulation bandwidth required	complex, eventual residual ASK	complex, bulky
	RX	simple, ER penalty	simple, but eye width reduced	requires optical filter	requires delay interferometer and stabilisation
Upstream (US)	TX	DS pattern erasure required	simple, just bit synchronisation required	simple	simple
	RX	simple, but penalty from DS crosstalk	simple, but eye width reduced	simple, good reception performance	simple, good reception performance

← US reception worsens with simple DS subsystems

Table 1.3. Access standards and some of their characteristic parameters.

While the ASK-based modulation formats with simple subsystems suffer mainly from penalties that derive from the non-orthogonal nature of the down- and upstream modulation format, orthogonal modulation formats such as FSK/ASK or DPSK/ASK benefit from the good remodulation in upstream direction, though they introduce cost and complexity at the downstream-related subsystems. Although ASK can provide a time-multiplex solution with inverse return-to-zero (IRZ) – to be orthogonal in its two time slots per bit period, the requirements for the modulation bandwidth double, which is often not acceptable in case of a nominal 10 Gb/s transmission system.

Fig. 1.3 shows the reported data rates for full-duplex down- and upstream transmission on a single wavelength, achieved by different ONU designs over arbitrary distance [54].

As can be seen, the EPON standard fuelled the efforts of employing RSOA based solutions [55]. First solely for pure upstream transmission, the efforts have then moved towards full-duplex 1 Gb/s transmission on a single wavelength, suitable for EPON. Advantage has been thereby taken from the saturation effect of the amplified remodulator, which allows to compress the downstream pattern to recover a slightly degraded optical carrier for upstream modulation [56], or by adapting the modulation format towards orthogonality between down- and upstream. A good candidate for this second approach at low data rates is sub-carrier multiplexing (SCM) [57-59]. Later, these techniques have been proven in their feasibility for GPON data rates [60].

Alternatively, differential PSK (DPSK) and ASK for down- and upstream [61,62] were applied to obtain orthogonality for penalty-free upstream transmission. The introduction of GPON and the foreseen increase in the data rates roots in symmetrical 2.5 Gb/s experiments that have been performed by still keeping a RSOA as reflective modulator [49,63]. With the further increase of the downstream data rate towards 10 Gb/s, orthogonal DPSK/ASK formats allowed for bidirectional transmission at the significant cost of adding a delay interferometer at the ONU receiver [64]. In this case, also the DPSK/DPSK format can be used since the remodulation just requires a feed-forward path from the downstream receiver and a bit synchronization mechanism [65].

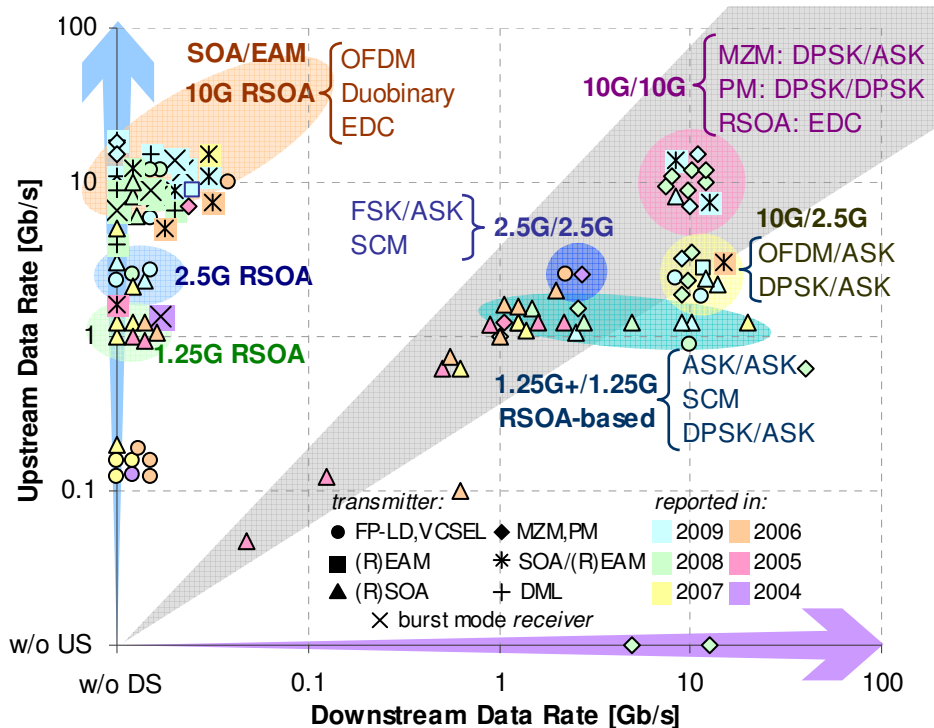


Fig. 1.3. ONU solutions and corresponding full-duplex data rates obtained on a single wavelength, reported in scientific literature. The cone represents symmetrical data rates for down- and upstream.

Upstream transmitters at 10 Gb/s were finally found with the help of SOA/REAMs [50,66-67] or spectrally compressed modulation formats such as duobinary [68] or quaternary amplitude modulation [69] while keeping the RSOA. However, the RSOA-based transmitters were just suitable for a low loss budget and suffered from strong performance degradation already with short fiber spans.

Even with the incorporation of electronic dispersion compensation (EDC) [70,71] and optical offset filtering at the upstream receiver [72] to convert the chirp into supportive amplitude modulation [72], the seeding budget for the RSOA restricted to reach the loss budgets that are proposed in the GPON standard. Besides the simple ASK modulation format, RSOAs and DMLs have been also found the attraction of OFDM [73-75], which was performed offline at this point of time. However, a first real-time implementation was demonstrated in 2010 [76,77].

Finally, full-duplex transmission at 10 Gb/s with RSOA- and SOA/REAM-based ONUs was obtained without the help of MZMs or phase modulators (PM). In Dezember 2009, the first RSOA that is capable for reaching a nominal electro-optical bandwidth for 10 Gb/s ASK transmission without offset filtering or EDC has been demonstrated, providing also a respectable increase in the loss budget due to its capability to operate with input power values as low as -20 dBm [15]. In a later experiment [24], full-duplex transmission at 10 Gb/s was achieved, taking advantage of the high gain and high saturation output power of the RSOA [49]. A loss budget of 30 dB was achieved in a hybrid PON, without the need for optical amplification stages that are either electrically powered or remotely pumped from the OLT.

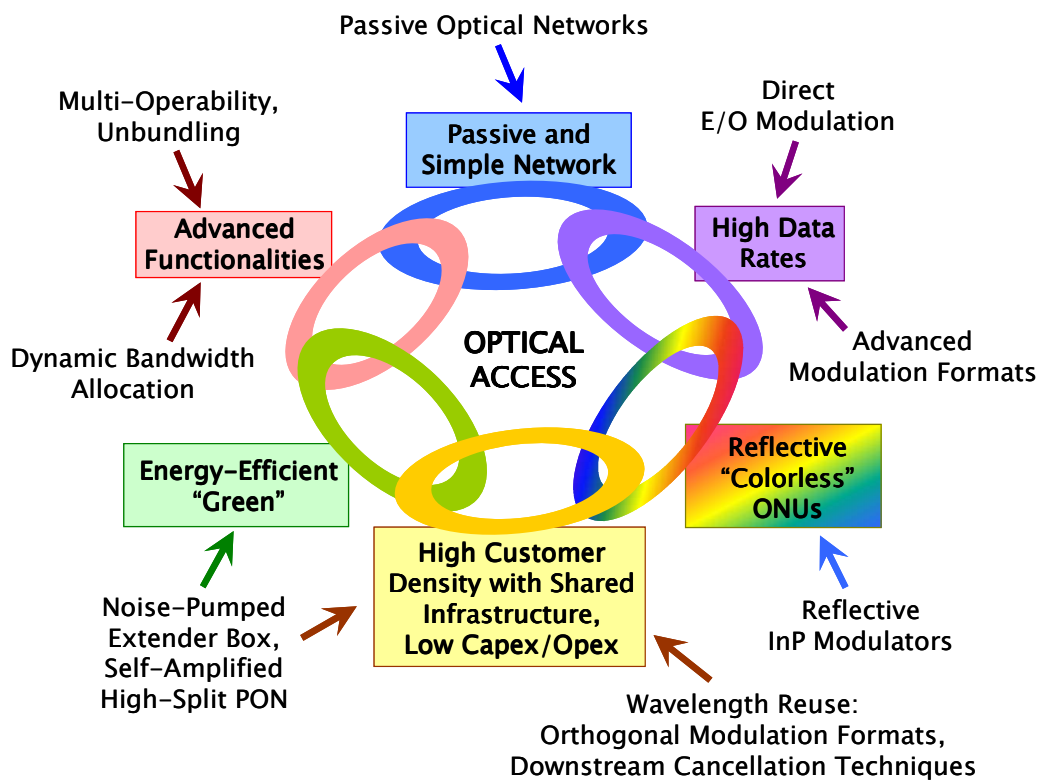


Fig. 1.4. Main research topics under investigation in this thesis.

1.3 Thesis Outline

The rest of the dissertation is organized as following.

Chapter II aims in a theoretical investigation about SOAs, which are key elements in next-generation ONU designs due to their multiple functionalities. Besides its capability to act as an optical amplifier, attention is also given on the modulation characteristics.

Chapter III introduces some practical aspects when working with SOAs and acquires experimentally the static and dynamic characteristics when using a RSOA as 10 Gb/s upstream modulator.

Chapter IV focuses on operational aspects in a PON. Next to the investigation of downstream cancellation techniques for wavelength reuse with the simple ASK/ASK modulation format, transmission aspects in such spectrally efficient PONs are highlighted.

Chapter V contrasts the developed downstream cancellation techniques with an orthogonal modulation scheme, in which the complexity of the downstream receiver is avoided by incorporating an integrated colorless demodulator and detector that is based on a SOA/REAM. In a further step, advanced functionalities of SOA-based upstream transmitters are gathered with the re-use of intrinsic device impairments.

Chapter VI applies novel seeding techniques to overcome the high loss budgets of a PON. Next to the self-seeded upstream transmission which generates an optical upstream carrier out of the natural noise emission of a SOA element inside the ONU, also a pump for a remote rare-earth doped fiber amplifier is seeded. High splitting ratios beyond 1:1000 and hybrid PONs with extended loss budgets >30 dB are presented while no pump delivery from the OLT is required for the sparsely deployed fiber amplifiers.

Chapter VII explains how the physical layer of the ONU can support higher layer functionalities. Approaches for multi-operability and dynamic bandwidth allocation are discussed and demonstrated with electrically reconfigurable ONU designs.

A short summary and a prospective outlook conclude the thesis with a list of published contribution to scientific congresses and archival journals.

Chapter II

Fundamental SOA Models

This chapter presents a couple of analytical models to characterize the principal SOA performance. Included are a model for the signal gain and the noise emission, which derives from the energy band diagram of the semiconductor. Further, a small signal analysis regarding the electro-optical response is given, showing the capability but also the limitations of a SOA to act as intensity modulator. Finally, the patterning effects of the SOA and the effect of chirping are briefly investigated.

How the theoretical concepts discussed here relate to practical aspects is addressed in chapter III, where the realization of an amplified reflective 10 Gb/s upstream transmitter based on a SOA element will be presented.

2.1 Introduction

Optical amplification constitutes a fundamental cornerstone of optical telecommunication. The continuously increasing reach and optical link loss of transmission spans make amplifiers a key component in nowadays communication networks. The demand in several fields of optical networks, let it be the core, metro or even access segments, leads at the same time to a rapid evolution of their performance. Especially for residential broadband, where reflective customer premises equipment is desired, means of amplification are indispensable. In this special case, big benefit can be taken if the reflective modulator can incorporate optical wide-band amplification as well, to act as an amplified and colorless upstream transmitter.

Optical amplification has been widely adapted in transport networks. With the introduction of rare-earth doped fiber amplifiers, the golden age of WDM was introduced, avoiding big farms of electrical-optical-electrical regenerators. At the same time, bandwidth-transparent amplification was achieved. However, such fiber amplifiers have never reached the small form-factor of semiconductor-based devices and are still not suitable for technological platforms that are used for photonic integration although progress has been made towards the chip level [78].

The SOA provides a good trade-off between its small form-factor and its slightly worse performance as amplifier. Especially for low-cost applications with a single or few wavelength channels, the SOA offers a series of additional functionalities that are mostly based on carrier density modulation or non-linear effects [79]. This added value

of the SOA has attracted for research and has been exploited extensively during the last two decades.

Mainly the capability as intensity modulator and its adaptation to nearly the complete wavelength range that is intended to be used for telecommunications enable the SOA to penetrate commercial territory that was originally occupied by fiber amplifiers. Due to the similarity with its relative, the laser diode, the physical processes that lies behind the macroscopic optical amplification, namely the stimulated emission of light, is well known. This plays an important role in the history of the SOA, which was always a competitor to the Erbium-doped fiber amplifier (EDFA) for different applications such as booster in transmitters [80,81], repeater in transmission links [82], or preamplifier in receivers [83].

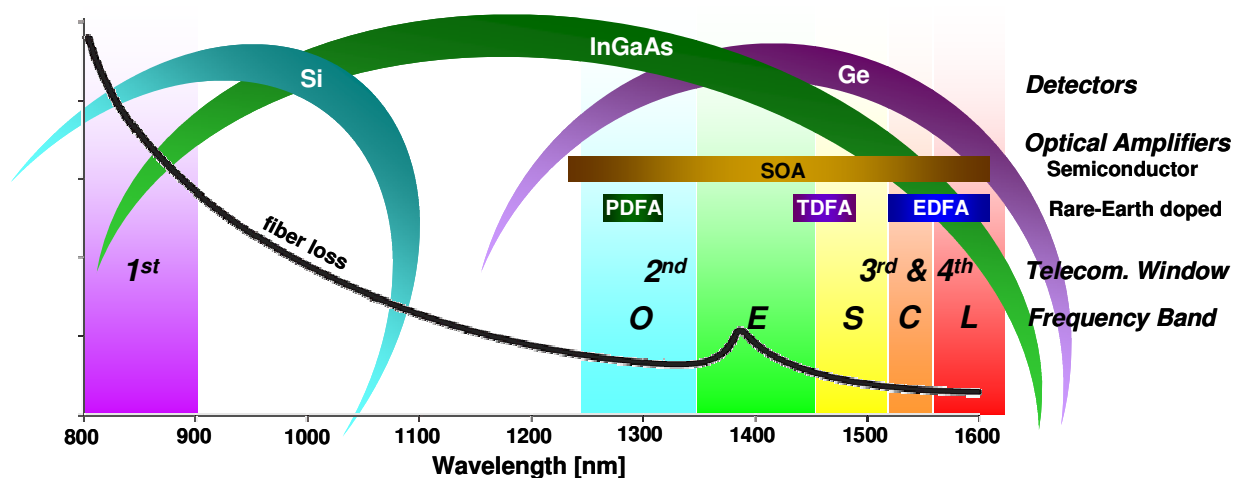


Fig. 2.1. Spectral response of fiber, optical amplifiers and detectors.

With the invention of semiconductor laser diodes in the early 1960s, which can be seen as a SOA having degraded facets, first thoughts about the application as optical amplifier appeared as well [84]. In the mid 70s, semiconductors with hetero-junctions were available and proposals for SOAs as repeaters in core networks were found on papers. Despite the advances in modeling and design and available AlGaAs SOAs for the 830 nm band [85,86], the SOA-bubble exploded in the mid 80s due to the introduction of the EDFA. At the same time, InP/InGaAsP SOAs for the 1.3 and 1.55 μm band became available and the processing of anti-reflection coatings at the end of the 80s [87] allowed the introduction of the travelling-wave SOA before the 90s [88], though with asymmetrical waveguides and high polarization dependent gain. Soon the polarization dependence was understood and effort on photonic integration started. Although years passed by since the begin of the 90s, there are still no commercially available photonic integrated circuits – showing that there is still a huge step to be made to lift SOAs out of their commercial infancy.

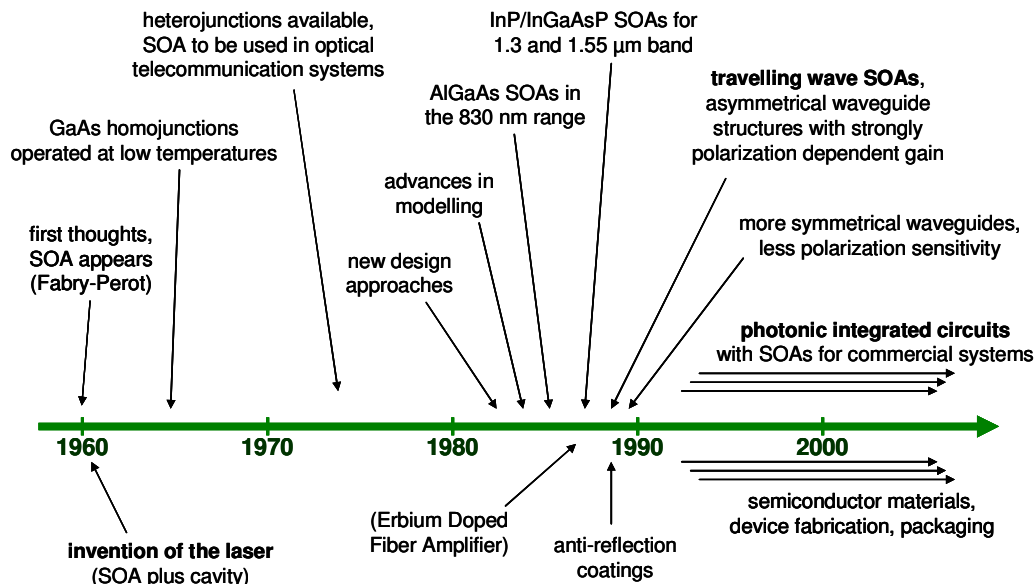


Fig. 2.2. Advances in the history of the semiconductor optical amplifier.

2.2 Amplification: Gain and Noise

The main characteristics of an optical amplifier, namely the signal gain and noise emission, were examined with the help of an analytical model for bulk SOAs. This model derives from the material gain of the semiconductor devices, which in turn allows, with a set of travelling-wave equations for the signal and the noise and the rate equation for the carrier density, to deduce the macroscopic measures for gain and noise figure. The model was evaluated with the help of Matlab.

2.2.1 Energy Band Structure of Direct Semiconductors

Optoelectronic semiconductor devices are always bound to specific spectral windows, according to the material used during the fabrication process. The spectral response is derived from the energy levels in the semiconductor, which are described with the help of the band structure.

The energy band diagram is related to the last energy level that is occupied by carriers, the so-called valence band, and the first empty energy level, referred to as the conduction band. Between these two levels an energy gap can be found, which is characterized by the semiconductor material of the active region, where amplification by means of stimulated emission is intended to take place. Transitions between these two bands typically occur between the minimum of the conduction and the maximum of the valence band.

According to this extrema of the bands, two classes of semiconductors are distinguished (Fig. 2.3). While indirect semiconductors require phonons for transitions due to shifted extrema, direct semiconductors allow transitions without additional

contribution to satisfy the conservation of momentum. The class is given by the groups of chemical elements; Semiconductors used for telecommunications typically stem from a III-V compound for direct band-gaps and from group IV materials for indirect gap.

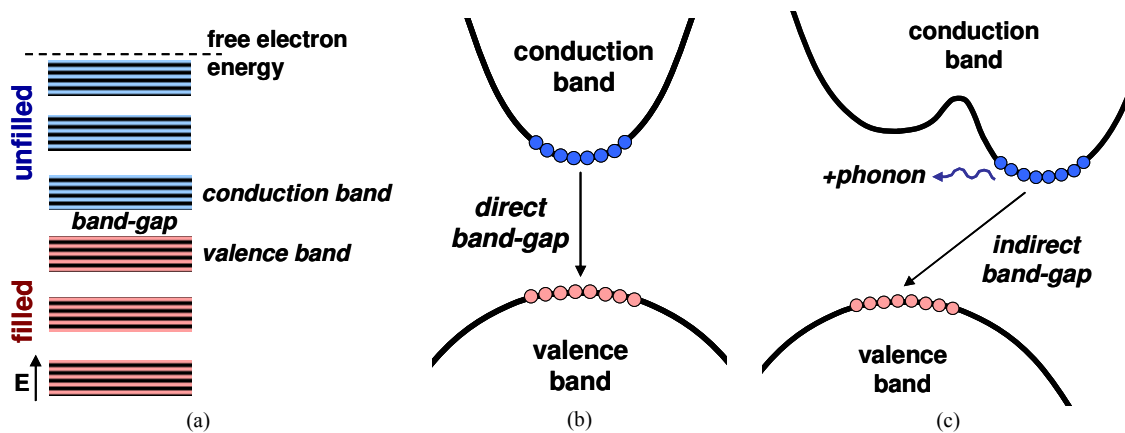


Fig. 2.3. (a) Energy levels in a semiconductor and band diagram for (b) a direct and (c) an indirect semiconductor.

Since the lifetimes of carriers in these bands is related with the transition probability, these two types are subject to different applications for telecommunication. The beneficial co-location of the extrema for conductance and valence band in the momentum space of direct semiconductors makes them attractive as optical amplifiers or light sources, whose transition probability is then given by Fermi's golden rule that respects amongst others the overlap between the initial and final electron state and the coupling between the electrical field and the electron states – which makes it polarization dependent. On the other hand, indirect semiconductors are typically used for photo detectors.

The material gain coefficient, which is a more accessible measure for analytical models, is related to the energy band structure according to

- the compounds used for the semiconductor, since this will determine the band-gap energy,
- how the active region was grown, since this will determine the shape of the valence and conduction band, and the density of allowed energy states that can be found within them,
- the carrier density and the temperature inside the semiconductor, since this will determine the filling of energy bands with carriers

As will be addressed later in this chapter, the differential gain coefficient is closely related with the modulation bandwidth of a semiconductor device. Different possibilities exist to increase the differential gain coefficient of a SOA so that the modulation bandwidth is increased. Next to cooling [89] or operation at shorter wavelengths off the peak gain wavelength [90], a confinement of the electrons in one or more dimensions that increases the density of states can be beneficial. Alternatively, compressive strain can be applied to push the light hole valence band down. A trivial

method is to increase the doping of the active region though this affects the threshold carrier density negatively.

The gain spectrum of a SOA can be modified by means of band structure tailoring [91], which aims mainly in optimization of the molar fractions for several compounds of the semiconductor alloy. The semiconductor is thereby designed for a specific pump, which will determine the occupation of energy states inside the conduction and valence band, and thus the spectral dependence of the gain coefficient. The principle behind this idea can be illustrated via the density of allowed energy states and the Fermi-Dirac distribution (Fig. 2.4).

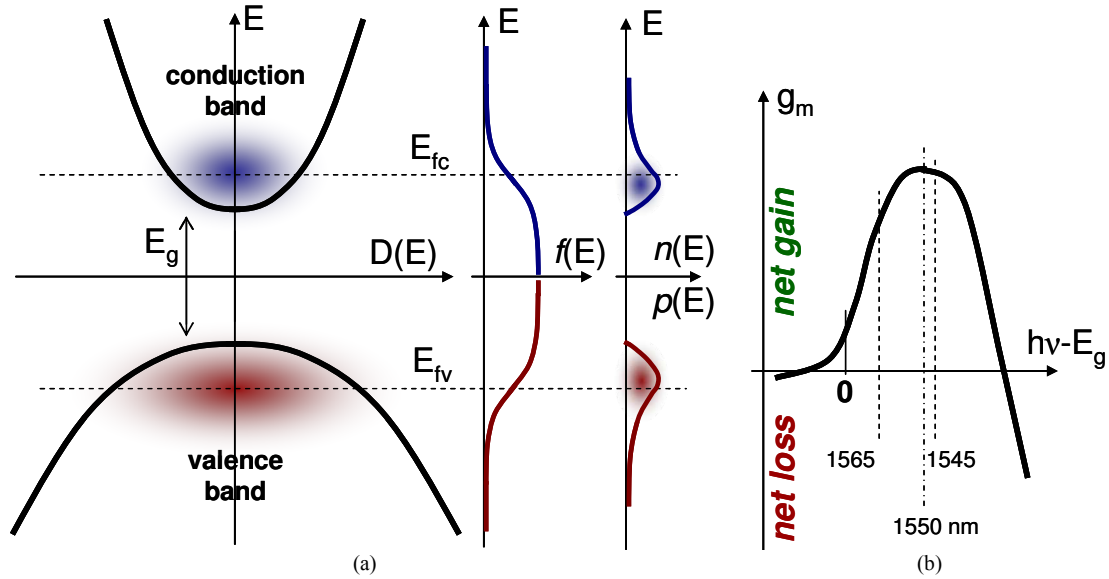


Fig. 2.4. Energy band diagram with the allowed density of states $D(E)$, Fermi-Dirac distribution $f(E)$ for conduction and valence band, carrier densities $n(E)$ and $p(E)$ for electrons and holes inside these bands, and material gain coefficient g_m as function of the detuning from the band-gap for a certain electrical pump.

The density of states is determined by the possible states that can be occupied for a given energy E and the volume V of the semiconductor. Both possible spins have to be taken into consideration.

$$D(E) = 2 \frac{d}{dE} \left(\frac{N(E)}{V} \right) \quad D_{bulk}(E) \propto \sqrt{E} \quad (2.1)$$

For a bulk device, the density inside the conduction and valence band follows a square root function, which shapes the bands towards parabolic ones.

The electrical pump that is applied through the bias current of the SOA causes non-equilibrate conditions in the semiconductor, so that no common Fermi level for electrons and holes is given anymore. Instead, two quasi-Fermi levels E_{fc} and E_{fv} of the conduction and valence band are defined [92]. For each of the bands, the Fermi-Dirac distribution for a certain temperature is

$$f(E) = \frac{1}{e^{\left(\frac{E-E_f}{kT}\right)} + 1} \quad (2.2)$$

and the relation between the two Fermi-Dirac distributions of conductance and valence band is

$$f_v(E) = 1 - f_c(E) \quad (2.3)$$

The carriers that are present in the conductance and valence band according to the overlap between the allowed density of states $D(E)$ and the Fermi-Dirac distribution $f(E)$ will determine the population of carriers inside the bands. The density for electrons and holes are therefore

$$n = \int_{E_c}^{\infty} f_c(E) D(E) dE \quad (2.4)$$

$$p = \int_{-\infty}^{E_v} f_v(E) D(E) dE$$

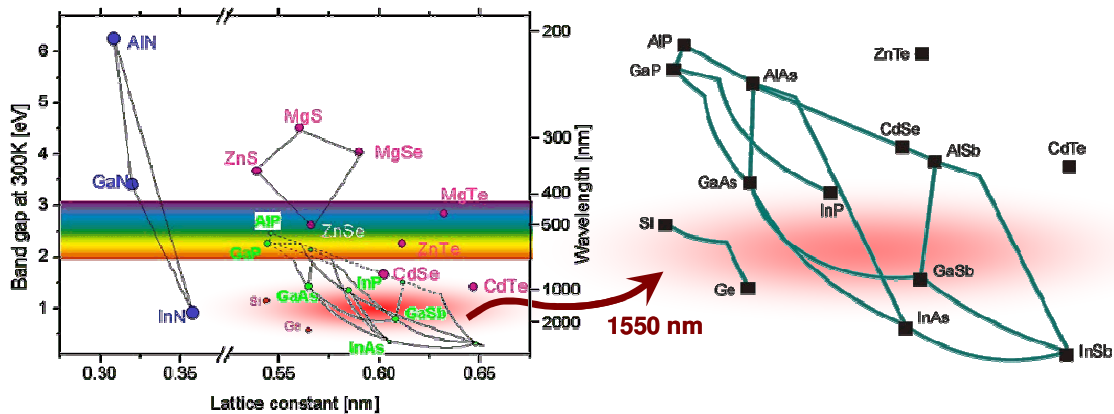
Since the spectral location of the SOA gain peak is given by this carrier population, the peak is in principle not found at the wavelength that corresponds to the band-gap energy E_g .

Note. Appropriate semiconductor materials can be engineered by using compounds of different chemical elements. The benefit of doing so can be easily understood when looking at the different band-gap energies of elements and compounds, which relate directly to their different emission spectra.

The band-gap energy is thereby a combination of the gaps of the different elements. For a ternary alloy for example, the band-gap energy can be found with

$$E_g(A_{1-x}B_x) = (1-x)E_g(A) + xE_g(B) - x(1-x)C$$

whereby the bowing parameter C takes the non-linear combination of the individual band-gap energies in account.



Furthermore, the geometry of the atomic layers inside the active region is optimized to obtain a higher efficiency. Quantum-mechanical structures such as quantum wells, wires or dots are incorporated in the active waveguide, resulting in a modified density

of allowed energy states, which becomes more discrete and sharper since carriers are then confined in certain energy levels. The employed hetero-structures of different semiconductor alloys, used to force the carriers into these states, require usually similar lattice constants for the materials used to avoid physical strain in these structures.

2.2.2 Analytical SOA Model

The following model [93] originates from the methodology presented in the previous chapter. Since the basic equations of the semiconductor material are employed for the model, it is suitable for a wide range of wavelengths. The semiconductor waveguide was chosen to be a buried InGaAsP active waveguide on an InP substrate, which is a typical design for SOAs due to the good heat dissipation and the spectral response in the third telecommunication window. Amplified spontaneous emission is taken into account by travelling wave equations for the noise power, while the emission of the input signal uses equations that treat the signal coherently.

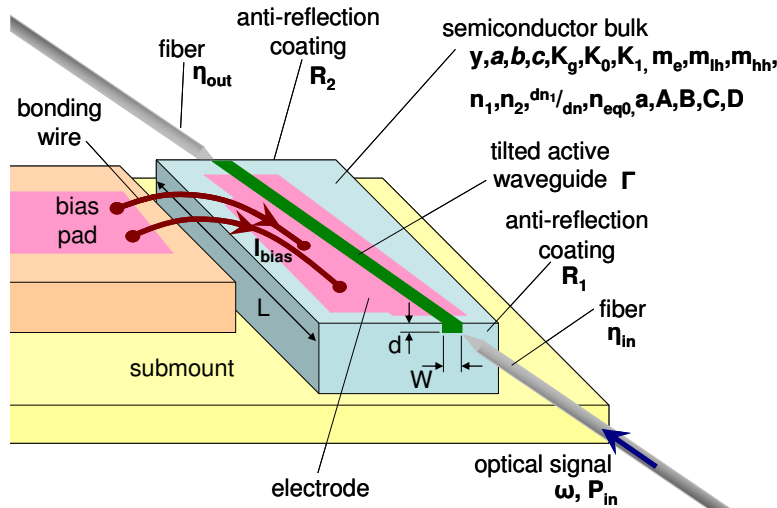


Fig. 2.5. Definition of the geometrical and operating parameters of the SOA.

The material gain coefficient can be expressed as a function of wavelength and carrier density n of electrons in the conductance band [94]

$$g_m(\nu, n) = \frac{c^2}{4\sqrt{2}\pi^2 n_1^2 \tau_e \nu^2} \left(\frac{2m_e m_{hh}}{h(m_e + m_{hh})} \right)^{\frac{3}{2}} \int_0^{\infty} \left[\sqrt{\nu' - \frac{E_g(n)}{h}} (f_c(\nu') - f_v(\nu')) \cdot \left(\frac{2T_0}{1 + (2\pi T_0)^2 (\nu' - \nu)^2} \right) \right] d\nu' \quad (2.5)$$

where c is the speed of light and ν the optical frequency, n_1 is the refractive index of the active region. τ_e is the radiative carrier recombination lifetime that is determined by the radiative carrier recombination rate R_{rad} and is approximated by

$$\tau_e = \frac{n}{R_{rad}(n)} = A_{rad} + B_{rad} \cdot n \quad (2.6)$$

where A_{rad} and B_{rad} are the linear and bimolecular radiative recombination coefficients. m_e and m_{hh} are the effective masses of the electrons in the conduction band and heavy holes in the valence band, respectively. h is the Planck constant and T_0 the mean lifetime for coherent interaction of electrons with a monochromatic field.

According to the Lorentzian lineshape for optical amplification processes [95], which result from the gain reduction in case that the wavelength of the incident optical signal does not correspond to the transition energy of the (homogeneously broadened) two-level system, a short lifetime T_0 in the order of 1 ps leads to a broad amplification spectrum. The second term in the integral of equation 2.5,

$$\frac{2T_0}{1+(2\pi T_0)^2(\nu'-\nu)^2} \simeq \delta(\nu-\nu') \quad (2.7)$$

can be therefore approximated as a Delta function as it has a much narrower spectrum than the other functions in the integral so that the material gain coefficient becomes dependent only on the structure of the energy band diagram.

$$g_m(\nu, n) = \frac{c^2}{4\sqrt{2}\pi^{\frac{3}{2}}n_1^2\tau_e\nu^2} \left(\frac{2m_em_{hh}}{\frac{h}{2\pi}(m_e+m_{hh})} \right)^{\frac{3}{2}} \cdot \sqrt{\nu - \frac{E_g(n)}{h}} (f_c(\nu) - f_v(\nu)) \quad (2.8)$$

The band-gap energy E_g can be written as

$$E_g(n) = E_{g0} - \Delta E_g(n) \quad (2.9)$$

where E_{g0} is the band-gap energy without injected carriers and given by the approximation

$$E_{g0} = e(a + by + cy^2) \quad (2.10)$$

with the electron charge e and the quadratic coefficients a , b , c for the band-gap energy. The coefficient y determines the molar fraction of Arsenide in the active region. The term ΔE_g takes the band-gap shrinkage due to injected carriers into account and is determined by the band-gap shrinkage coefficient K_g according to

$$\Delta E_g(n) = eK_g n^{1/3} \quad (2.11)$$

Due to this contribution of carriers in the band-gap energy, the spectra for gain and amplified spontaneous emission (ASE) are shifted towards longer wavelengths. f_c and f_v are the Fermi-Dirac distributions that depend on the photon energy and are given in accordance with equation 2.2 by

$$f_c(\nu) = \frac{1}{e^{\left(\frac{E_a - E_{fc}}{kT}\right)} + 1} \quad E_a = (h\nu - E_g(n)) \frac{m_{hh}}{m_e + m_{hh}} \quad (2.12)$$

$$f_v(\nu) = \frac{1}{e^{\left(\frac{E_b - E_{fv}}{kT}\right)} + 1} \quad E_b = -(h\nu - E_g(n)) \frac{m_e}{m_e + m_{hh}} \quad (2.13)$$

where T is the absolute temperature and k the Boltzmann constant. The quasi-Fermi levels E_{fc} and E_{fv} of the conduction and valence band are referenced to the bottom and top edge of those bands, respectively. A simple approximation of those energy levels can be retrieved from the Nilsson approximation [96]

$$E_{fc} = \left[\ln \delta + \delta \left[64 + 0.05524 \delta (64 + \sqrt{\delta}) \right]^{\frac{1}{4}} \right] kT \quad \delta = \frac{n}{n_c} \quad (2.14)$$

$$E_{fv} = - \left[\ln \varepsilon + \varepsilon \left[64 + 0.05524 \varepsilon (64 + \sqrt{\varepsilon}) \right]^{\frac{1}{4}} \right] kT \quad \varepsilon = \frac{p}{n_v} \quad (2.15)$$

Fig. 2.6 shows the location of these quasi-Fermi levels as function of the present carrier density for typical values of the semiconductor material (as they will be reported later in Table 2.1).

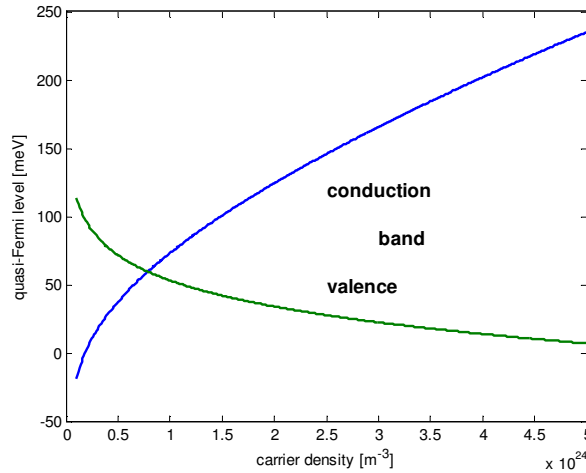


Fig. 2.6. The location of the quasi-Fermi levels as function of the carrier density.

The carrier densities n for electrons and p for holes are normally equal for the levels that are present in the SOA. The constants n_c and n_v in equations 2.14 and 2.15 are determined by

$$n_c = 2 \left[\frac{m_e kT}{2\pi \left(\frac{h}{2\pi}\right)^2} \right]^{\frac{3}{2}} \quad (2.16)$$

$$n_v = 2 \left[\frac{m_{dh} kT}{2\pi \left(\frac{h}{2\pi} \right)^2} \right]^{\frac{3}{2}} \quad m_{dh} = \left(m_{hh}^{\frac{3}{2}} + m_{lh}^{\frac{3}{2}} \right)^{\frac{2}{3}} \quad (2.17)$$

where m_{lh} is the effective mass of light holes in the valence band.

The material gain coefficient can be decomposed into a gain coefficient g'_m and an absorption coefficient g''_m which are both positive per following convention,

$$g_m = g'_m - g''_m \quad (2.18)$$

with

$$g'_m(\nu, n) = \frac{c^2}{4\sqrt{2}\pi^{\frac{3}{2}} n_1^2 \tau_e \nu^2} \left(\frac{2m_e m_{hh}}{\frac{h}{2\pi} (m_e + m_{hh})} \right)^{\frac{3}{2}} \cdot \sqrt{\nu - \frac{E_g(n)}{h}} f_c(\nu) (1 - f_v(\nu)) \quad (2.19)$$

$$g''_m(\nu, n) = \frac{c^2}{4\sqrt{2}\pi^{\frac{3}{2}} n_1^2 \tau_e \nu^2} \left(\frac{2m_e m_{hh}}{\frac{h}{2\pi} (m_e + m_{hh})} \right)^{\frac{3}{2}} \cdot \sqrt{\nu - \frac{E_g(n)}{h}} (1 - f_c(\nu)) f_v(\nu) \quad (2.20)$$

How the spectral gain coefficient relates to the material gain – for the same values that will be used for the later simulation – can be seen in Fig. 2.7. The gain peak shifts to higher energy levels (shorter wavelengths) for an increased pump [97].

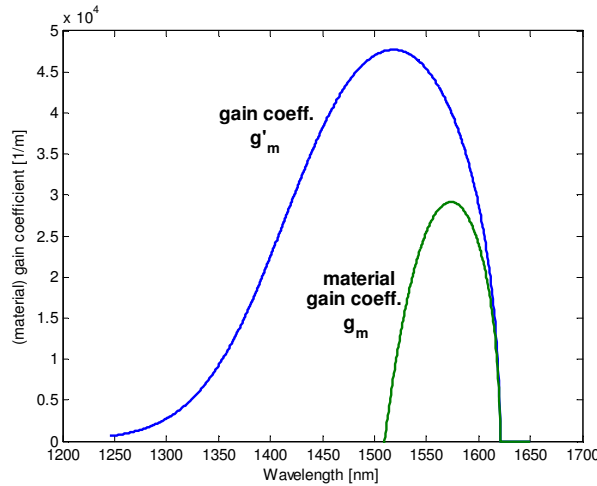


Fig. 2.7. The relation between the gain coefficient and the net material gain as function of the wavelength.

The material loss coefficient α depends on the carrier density via the carrier-independent and carrier-dependent absorption loss coefficients K_0 and K_1 , which take the intrinsic material loss and the inter-valence band absorption into account.

$$\alpha(n) = K_0 + \Gamma K_1 n \quad (2.21)$$

The constant Γ is the confinement factor for the optical radiation and is determined by the transverse waveguide-mode distribution $F(x,y)$ of the electrical field inside the SOA,

$$\Gamma = \frac{\int_0^w \int_0^d |F(x,y)|^2 dx dy}{\int_{-\infty}^{\infty} \int_{-\infty}^{\infty} |F(x,y)|^2 dx dy} \quad (2.22)$$

The spatial evolution of the signal and the noise inside the SOA is described by a pair of travelling-wave equations. These equations can be formulated for the parts propagating in positive and in the negative direction to take reflections from the end facets into account.

An ensemble of N_s optical signals S_k are launched into the waveguide and amplified by the SOA, whereby the interaction between the photon rates and the carrier density are described by a set of coupled differential equations. As the active region is narrow, transversal variations of these measures are considered to be negligible.

The propagation axis z is chosen to originate from the left (input) facet. The field of each signal is decomposed in a component that travels into the positive and another one that propagates into the negative z -direction, whereby the photon rates Ψ_{S_k} of the light flux are in relation with the field amplitude according to

$$\Psi_{S_k}^{\pm} = |E_{S_k}^{\pm}|^2 \quad k = 1 \dots N_s \quad (2.23)$$

The signal has to be treated coherently to consider effects on facets on its transmission through the amplifier that depends on its phase and frequency. The differential equations and their boundary conditions are

$$\frac{dE_{S_k}^+(z)}{dz} = \left(-j\beta_k + \frac{1}{2}(\Gamma g_m(v_k, n) - \alpha(n)) \right) E_{S_k}^+(z) \quad (2.24)$$

$$\frac{dE_{S_k}^-(z)}{dz} = \left(j\beta_k - \frac{1}{2}(\Gamma g_m(v_k, n) - \alpha(n)) \right) E_{S_k}^-(z) \quad (2.25)$$

$$\begin{aligned} E_{S_k}^+(0) &= (1-r_1) E_{in} + r_1 E_{S_k}^-(0) \\ E_{S_k}^-(L) &= r_2 E_{S_k}^+(L) \end{aligned} \quad (2.26)$$

whereby the signal propagation coefficient β_k is given by the equivalent refractive index n_{eq} of the amplifier waveguide,

$$\beta_k = \frac{2\pi n_{eq} \nu_k}{c} \quad (2.27)$$

The input signal is coupled into the SOA from the left side ($z = 0$) and the output signal is retrieved at the right facet ($z = L$), always respecting the fiber coupling efficiencies η_{in}

and η_{out} as well as eventual residual facet reflectivities r_1 and r_2 for the field amplitudes at the input and output which are given by the power reflectivities R_1 and R_2 ,

$$r_{1,2} = \sqrt{R_{1,2}} \quad E_{ink} = \sqrt{\frac{\eta_{in} P_{ink}}{h\nu_k}} \quad (2.28)$$

$$E_{outk} = (1 - r_2) E_{Sk}^+(L) \quad P_{outk} = h\nu_k \eta_{out} |E_{outk}|^2$$

To obtain the equivalent refractive index n_{eq} ,

$$n_{eq} = \sqrt{\left(n_1^2 - n_2^2\right) \frac{\Gamma}{2 - \Gamma} + n_2^2} \quad (2.29)$$

a linear model [98] is used where n_{eq} depends on the carrier density n ,

$$n_{eq} = n_{eq0} + \frac{dn_{eq}}{dn} n \quad (2.30)$$

in which n_{eq0} is the equivalent refractive index without carrier injection and n_2 is the refractive index of the InP material that surrounds the active region. The dependence on the carrier density is given by the change of the refractive index n_1 of the active waveguide with the carrier density,

$$\frac{dn_{eq}}{dn} = \frac{n_1 \frac{\Gamma}{2 - \Gamma}}{\sqrt{\left(n_1^2 - n_2^2\right) \frac{\Gamma}{2 - \Gamma} + n_2^2}} \frac{dn_1}{dn} = \frac{n_1 \Gamma}{n_{eq0} (2 - \Gamma)} \frac{dn_1}{dn} \quad (2.31)$$

As the generated noise drains the injected carriers and also has impact on the saturation of the gain, it affects the amplification of the signal and has to be taken into account for accurate modeling. However, due to its distribution over a wide wavelength range it does not have to be treated coherently.

The remaining reflectivities of the facets form a cavity so that the ASE spectrum will show longitudinal modes. Noise photons will then be generated according to those modes with discrete frequencies ν_j that are separated in frequency by the mode spacing $\Delta\nu_m$,

$$\nu_j = \nu_c + \Delta\nu_c + jK_m \Delta\nu_m \quad j = 0 \dots N_m - 1$$

$$\nu_c = \frac{E_{g0}}{h} \quad \Delta\nu_m = \frac{c}{2 \int_0^L n_{eq} dz} \quad (2.32)$$

The cut-off frequency ν_c is given by the band edge E_{g0} (equation 2.10) and the constant $\Delta\nu_c$ is used as offset to match the first discrete frequency ν_0 to a resonance. The constants K_m and N_m depend on the gain bandwidth and desired accuracy of the model.

The ASE generated in the SOA is described in terms of power by averaging the noise signals of two adjacent cavity modes. The noise photon rates Ψ_j^+ and Ψ_j^- for a particular polarization refer to a frequency range of $K_m\Delta\nu_m$ that is centered on the frequency ν_j , travelling in the positive and negative propagation direction, respectively. The travelling-wave equations for the ASE and their boundary conditions are

$$\begin{aligned}\frac{d\Psi_j^+(z)}{dz} &= (\Gamma g_m(\nu_j, n) - \alpha(n))\Psi_j^+(z) + R_{sp}(\nu_j, n) \\ \frac{d\Psi_j^-(z)}{dz} &= -(\Gamma g_m(\nu_j, n) - \alpha(n))\Psi_j^-(z) + R_{sp}(\nu_j, n)\end{aligned}\quad (2.33)$$

$$\begin{aligned}\Psi_j^+(0) &= R_1\Psi_j^-(0) \\ \Psi_j^-(L) &= R_2\Psi_j^+(L)\end{aligned}$$

where R_{sp} represents the spontaneously emitted noise that is coupled into those noise signals. This contributing term can be determined by comparing the emitted noise of an ideal amplifier with the quantum mechanical model [94],

$$N_{out} = (G-1)h\nu_j K_m \Delta\nu_m \quad (2.34)$$

An ideal amplifier works without gain saturation and therefore a constant carrier population along the amplifier. Furthermore, it has no intrinsic losses, no facet reflectivities and no coupling losses. Therefore in the travelling-wave equations the loss coefficient α can be set to zero and the output noise power centered on frequency ν_j for a single polarization and frequency band $K_m\Delta\nu_m$ is

$$N_{out} = \frac{G-1}{\Gamma g'_m(\nu_j, n)} h\nu_j R_{sp}(\nu_j, n) \quad (2.35)$$

with gain G at this center frequency. Compared to the previous mentioned quantum mechanical expression the term R_{sp} can be found with

$$R_{sp}(\nu_j, n) = \Gamma g'_m(\nu_j, n) K_m \Delta\nu_m \quad (2.36)$$

Injected noise photons are by their nature not centered on the resonant frequencies but uniformly spread over the appropriate frequency band of a resonance. Therefore, this generated noise will be partially filtered by the cavity and a normalization factor for the noise photon rates Ψ_j^+ and Ψ_j^- has to be taken into account.

For the case that the cavity round trip time is much smaller than the inverse of the highest frequency component of the input signal – which is typically the case for the considered dimensions and data rates – the gain around a resonant frequency ν_j in a band $\Delta\nu_m$ around this resonance is

$$G(\nu) = \frac{(1-R_1)(1-R_2)G_s}{(1-\sqrt{R_1 R_2} G_s)^2 + 4G_s \sqrt{R_1 R_2} \sin^2(\varphi)} \quad (2.37)$$

where G_s is the single-pass gain at ν_j and φ is the single-pass phase shift.

$$G_s(\nu) = \exp \left[\int_0^L [\Gamma g_m(\nu, n) - \alpha(n)] dz \right] \quad \varphi = \frac{2\pi\nu}{c} \int_0^L n_{eq}(z) dz \quad (2.38)$$

The gain at the resonance is given by

$$G(\nu_j) = \frac{(1-R_1)(1-R_2)G_s}{(1-\sqrt{R_1R_2}G_s)^2} \quad (2.39)$$

and a gain ripple can be observed in the gain spectrum $T(\nu)$ due to the difference for resonant and anti-resonant frequencies.

$$G_{res}(\nu_{res,j}) = \frac{(1-R_1)(1-R_2)G_s(\nu_{res,j})}{(1-\sqrt{R_1R_2}G_s(\nu_{res,j}))^2} \quad j = 0 \dots K_m(N_m - 1) \quad (2.40)$$

$$\nu_{res,j} = \nu_c + \Delta\nu_c + j\Delta\nu_m \quad j = 0 \dots K_m(N_m - 1)$$

$$G_{ares}(\nu_{ares,j}) = \frac{(1-R_1)(1-R_2)G_s(\nu_{ares,j})}{(1+\sqrt{R_1R_2}G_s(\nu_{ares,j}))^2} \quad j = 1 \dots K_m(N_m - 1) \quad (2.41)$$

$$\nu_{ares,j} = \nu_{res,j} - \frac{\Delta\nu_m}{2} \quad j = 1 \dots K_m(N_m - 1)$$

The gain ripple is not static in its spectrum: the comb-like transmission function is red-shifted in the presence of an input signal due to the carrier reduction that takes place with the amplification of the signal in the active waveguide. This in turn leads to an increase in the refractive index in the active region and thus to the experienced shift in the optical spectrum of the gain ripple.

An enhanced gain ripple can be critical since the information bandwidth of the signal can be comparable to the spectral period of the ripple. Especially for optical data signals that are located at the positive edge of the ripple, severe degradation can be suffered [99]. A more detailed analysis of the gain ripple will be presented in chapter V.2, where also an application that takes benefit of this natural impairment is presented.

Note. Residual facet reflectivity introduces also backward gain. This effect is unwanted and critical in transmission systems with cascaded amplification without isolation of the single stages. The gain of the backward travelling signal is [100]

$$G_{bw}(\nu) = \frac{(\sqrt{R_1} - \sqrt{R_2}G_s(\nu))^2 + 4\sqrt{R_1R_2}G_s(\nu)\sin^2(\varphi)}{(1 - \sqrt{R_1R_2}G_s(\nu))^2 + 4\sqrt{R_1R_2}G_s(\nu)\sin^2(\varphi)}$$

A ratio of 20 dB between forward and backward gain alone requires therefore a facet reflectivity of $3 \cdot 10^{-5}$ or less for the case of a forward gain of 25 dB.

The noise output for a noise input spectral density σ_{in} that is distributed uniformly over the noise band $\Delta\nu_m$ is obtained via a substitution of $d\nu$ in the integral via equation 2.32.

$$d\nu = \frac{c}{2\pi n_{eff}} d\phi \quad n_{eff} = \int_0^L n_{eq} dz \quad (2.42)$$

$$N_{out} = \sigma_{in} \int_{\nu_j - \Delta\nu_m/2}^{\nu_j + \Delta\nu_m/2} G(\nu) d\nu = \sigma_{in} \Delta\nu_m \frac{1}{\pi} \int_0^\pi G(\phi) d\phi$$

For the case of having this input noise concentrated at the resonance frequency ν_j , the noise photon rate would be

$$N_{res,out} = \sigma_{in} \Delta\nu_m G(\nu_j) K_j \quad (2.43)$$

The normalization factor K_j equates those two noise outputs and can be expressed by

$$K_j = \frac{\int_0^\pi G(\phi) d\phi}{\pi G(\nu_j)} = \frac{1}{\pi} \int_0^\pi \frac{d\phi}{1 + \gamma^2 \sin^2(\phi)} \quad \gamma = \frac{4G_s(\nu_j) \sqrt{R_1 R_2}}{(1 - \sqrt{R_1 R_2} G_s(\nu_j))^2} \quad (2.44)$$

and is identical to unity if there are no facet reflectivities present.

Taking coupling losses η_{out} , two polarizations and a bandwidth of $K_m \Delta\nu_m$ into consideration, the spectral noise density for the photon rate centered on ν_j is

$$\sigma_N(\nu_j) = \frac{2\eta_{out} (1 - R_2) K_j \Psi_j^+(L)}{K_m \Delta\nu_m} \quad j = 0 \dots N_m - 1 \quad (2.45)$$

Together with the gain spectrum $T(\nu)$ the spectral output power for the noise can be determined by

$$\sigma_{ASE}(\nu) = \frac{h\nu \sigma_N(\nu_{res,j}) T(\nu)}{\frac{1}{\Delta\nu_m} \int_{\nu_{ares,j}}^{\nu_{ares,j+1}} T(\nu') d\nu'} \quad P_{ASE}(\nu) = \int_{\nu - \Delta\nu/2}^{\nu + \Delta\nu/2} \sigma_{ASE}(\nu') d\nu' \quad (2.46)$$

where the spectral density of the noise photon rate σ_N of the closest cavity mode, where noise is pronounced, is multiplied by the photon energy and the ratio of actual gain for the desired frequency and the average gain of the closest cavity mode. For a bandwidth of $\Delta\nu$, the ASE power can be easily calculated via this spectral density.

The noise figure can be obtained [101] by considering negligible input signal noise via

$$NF_{dB} = 10 \log \left(\frac{\sigma_{ASE}(\nu)}{h\nu G(\nu)} + \frac{\eta_{out}}{G(\nu)} \right) \quad (2.47)$$

Both, signal and noise photon rates drain the carrier population. This is taken into account by a rate equation for the carrier density n . Carriers are injected via the bias current I that is assumed to pass uniformly only through the active region defined by the geometrical parameters L , d and W . Further, the rate equation takes the recombination covered by the term R and the amplification of signal and noise into account, which all lead to depletion of carriers.

$$\frac{dn(z)}{dt} = \frac{I}{edLW} - R(n(z)) - \frac{\Gamma}{dW} \left[\sum_{k=1}^{N_s} g_m(\nu_k, n(z)) (\Psi_{Sk}^+(z) + \Psi_{Sk}^-(z)) \right] - \frac{2\Gamma}{dW} \left[\sum_{j=1}^{N_m-1} g_m(\nu_j, n(z)) K_j (\Psi_j^+(z) + \Psi_j^-(z)) \right] \quad (2.48)$$

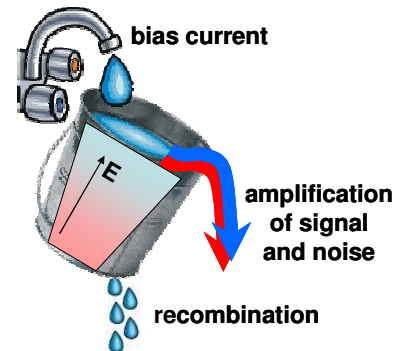
Noise is generated in two orthogonal polarization modes (TE, TM) and the fraction of amplified photons that resides in the active region is determined by the confinement factor.

The recombination rate R is given by radiative and non-radiative processes that can be expressed by polynomials [102,103] of the carrier density, incorporating the coefficients A_{rad} and B_{rad} for linear and bimolecular radiative processes. The non-radiative recombination is comprised of linear recombination due to traps in the semiconductor material that are given by the coefficient A_{nrad} , bimolecular recombination that is taken into account by B_{nrad} , Auger recombination which is determined by the coefficient C_{aug} and D_{leak} covers leakage effects.

$$\begin{aligned} R(n) &= R_{rad}(n) + R_{nrad}(n) \\ R_{rad}(n) &= A_{rad}n + B_{rad}n^2 \\ R_{nrad}(n) &= A_{nrad}n + B_{nrad}n^2 + C_{aug}n^3 + D_{leak}n^{5.5} \end{aligned} \quad (2.49)$$

Note. An interpretation of the rate equation as leaky bucket with higher energy carriers on the top reveals the wavelength-dependency of the saturation. When carriers are poured out of the bucket, higher energy carriers will deplete faster than the carriers on the bottom.

In so-called “reservoir” models, the SOA behavior is reduced to the solution of a single differential equation for a single state variable. The most appropriate state



variable of a SOA is given by the carrier density, since it allows – once its (dynamic) behavior is found – to predict the behavior of several WDM channels. Due to the similarity with excited Erbium ions in Erbium-doped fiber amplifiers, the term “reservoir” is used.

2.2.3 Simulation

The SOA is discretized in space for a numerical implementation in Matlab as it is also done for the desired wavelength range. The latter allows to obtain the gain and noise figure spectra, while investigating effects such as the gain ripple.

Several semiconductor related parameters were taken from literature [93] and the analysis performed was carried out for a wavelength of 1550 nm if there should not be another condition mentioned. The parameters used for the analytical model as well as for the simulation are listed in Table 2.1.

SOA – Gain

The spatial carrier density distribution goes hand in hand with the spatial distribution of the optical power within the SOA and is related via the pump depletion (Fig. 2.8). Foremost, the backward propagating signal is small compared to the forward propagating one thanks to the small facet reflectivities. Further, the spatial distribution of the carriers shifts towards the input facet with increasing input power, since the ratio between signal and noise emission is more beneficial. This means that more carriers are devoted for the amplification of the signal while the concurrently raising spontaneous emission stays at a low level. This is the case for Fig. 2.8, where an input power of -10 dBm was set for the simulation.

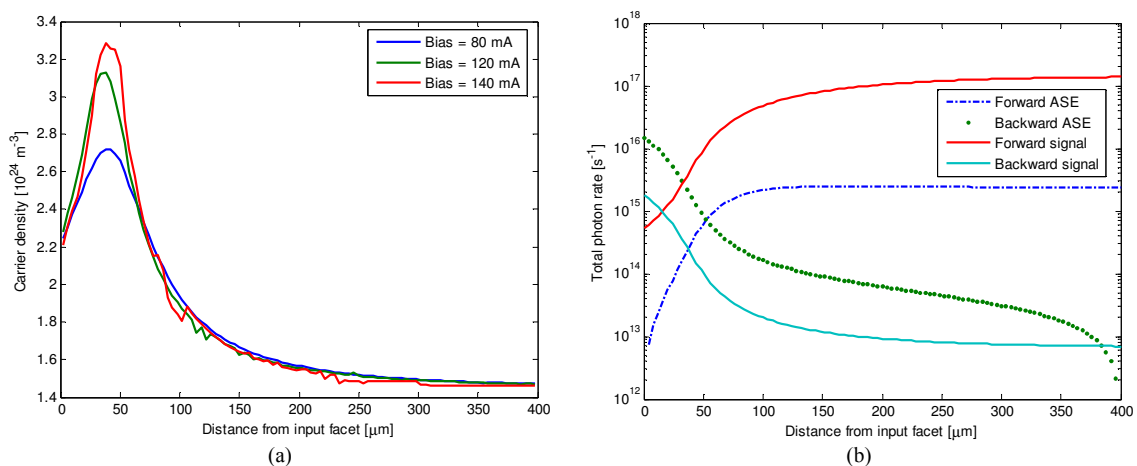


Fig. 2.8. Spatial distribution of (a) the carrier density and (b) the photon rates for forward- and backward propagating signal and noise for a signal input of -10 dBm, the latter for a SOA bias current of 120 mA.

parameter		value chosen	attributed to	
L	length	400 μm	SOA geometry	
d	thickness	0.4 μm		
W	width	0.4 μm		
Γ	confinement factor	0.3		
y	molar fraction of Arsenide in the active region	0.892	semiconductor material	
a	quadratic coefficients for the band-gap energy	1.35 eV		
b		-0.775 eV		
c		0.149 eV		
K_g	band-gap shrinkage coefficient	$0.9 \cdot 10^{-10}$ eVm		
m_0	electron rest mass	$9.11 \cdot 10^{-31}$ kg		
m_e	effective mass of electron in the conduction band	0.045 m_0		
m_{hh}	effective mass of a heavy hole in the VB	0.46 m_0		
m_{lh}	effective mass of a light hole in the VB	0.056 m_0		
n_1	active region refractive index	InGaAsP, 3.22		
n_2	bulk region refractive index	InP, 3.167		
dn_1/dn	differential of active region refractive index with respect to the carrier density	$-1.8 \cdot 10^{-26}$ m^{-3}		
n_{eq0}	equivalent refractive index at zero carrier density	3.22		
A_{rad}	radiative recombination rate	10^{-7} s^{-1}		
A_{nrad}	non-radiative recombination rate	10^8 s^{-1}		
B_{rad}	radiative recombination coefficient	$5.6 \cdot 10^{-16}$ m^3/s		
B_{nrad}	non-radiative recombination coefficient	0 $\text{m}^3 \text{s}^{-1}$		
C_{aug}	Auger recombination coefficient	$3 \cdot 10^{-41}$ m^6/s		
D_{leak}	leakage recombination coefficient	0 $\text{m}^{13.5} \text{s}^{-1}$		
K_0	carrier independent absorption loss coefficient	6200 m^{-1}		
K_1	carrier dependent absorption loss coefficient	7500 m^2		
a	differential gain	$0.8 \cdot 10^{-20}$ m^{-2}		
T	absolute temperature	300 K		
η_{in}, η_{out}	fiber coupling loss	1.5 dB		fiber to chip coupl.
R_1	input facet reflectivity	$5 \cdot 10^{-5}$		
R_2	output facet reflectivity	$5 \cdot 10^{-5}$		
ω	optical frequency	193.1 THz	opt. signal	

Table 2.1. Parameters chosen for the simulation of the SOA.

On the contrary, if the input signal level is low, as in Fig. 2.9 that shows the results for an input of -25 dBm, the spatial distribution of the power levels and carrier density show a symmetry in the middle of the SOA. For this signal input, the ASE is already dominating over the signal, leading also to a symmetrical ASE distribution along the SOA.

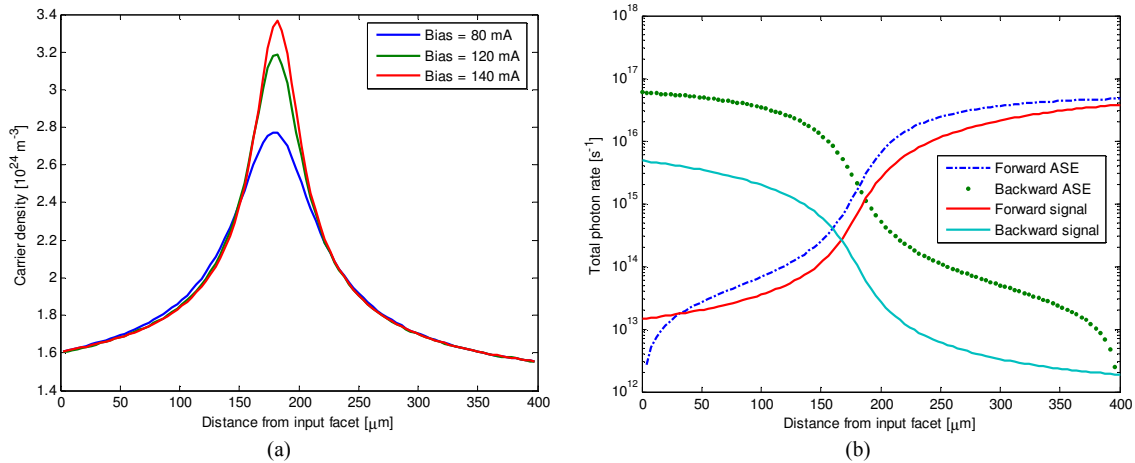


Fig. 2.9. Spatial distribution of (a) the carrier density and (b) the photon rates for forward- and backward propagating signal and noise for a signal input of -25 dBm, the latter for a SOA bias current of 120 mA.

The SOA can be also used to simultaneously amplify signals on different wavelengths. Fig. 2.10 shows an example for three input signals at wavelengths of 1540, 1550 and 1555 nm and power values of -15, -10 and -15 dBm, respectively. However, when modulated signals are amplified in a SOA, care has to be taken that the amplifier is operated in the linear regime since otherwise cross-gain modulation occurs, which will lead to cross-patterning effects between the individual data signals.

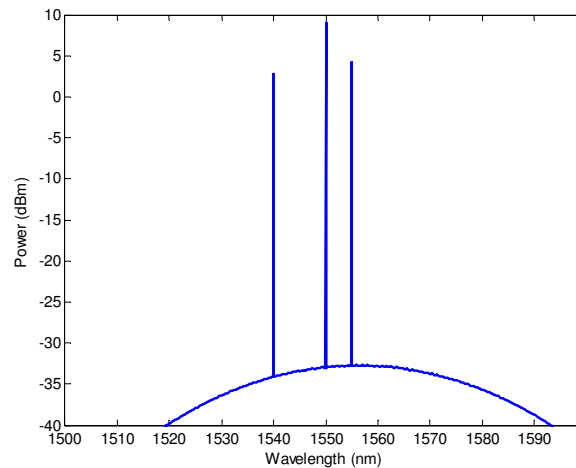


Fig. 2.10. Amplification of multiple wavelengths with a common SOA. The resolution bandwidth is 0.1 nm.

The spectrum shows the usual ASE peak that derives from the parabolic band structure (Fig. 2.11). The ASE background has some gain ripple that is caused by the residual facet reflectivities. Especially for low signal input power, the ASE background enhances together with its gain ripple due to the shared carrier reservoir. Note that in

Fig. 2.11, the signal peak with its high optical power level has been suppressed for the sake of enhancing the visibility of the gain ripple.

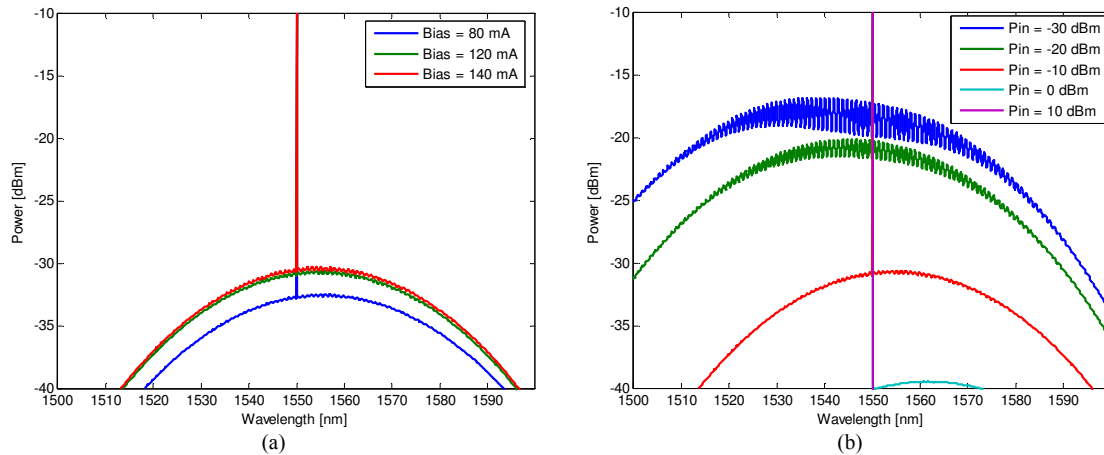


Fig. 2.11. Optical spectrum at the SOA output for a resolution bandwidth of 0.1 nm, for (a) a signal input of -10 dBm and (b) a bias current of 120 mA.

In the pure ASE spectrum, shown in Fig. 2.12, nonlinear gain compression can be deduced for the application of the SOA as amplifier. A slight shift of the ASE peak can be seen when the bias current increases. This is related with the change in the optical density (i.e. the refractive index) inside the SOA, caused by the higher carrier density. An increase of the bias current from 60 to 100 mA shifts the peak by ~ 4 nm. Residual facet reflectivities due to a good but not perfect anti-reflection coating lead to gain ripple. The magnitude of the ripple is related to the in general high gain provided by the SOA medium. As can be seen in Fig. 2.12(b), the gain ripple for the chosen facet reflectivities of $5 \cdot 10^{-5}$ and a bias current of 100 mA is already 1.9 dB at the ASE peak.

The gain ripple is especial critical for the reflective derivatives of the SOA, the RSOA. This anchors in the high reflective facet on the back of the device, which requires a high quality for the front facet that is typically coated with a dielectric multi-layer anti-reflection coating.

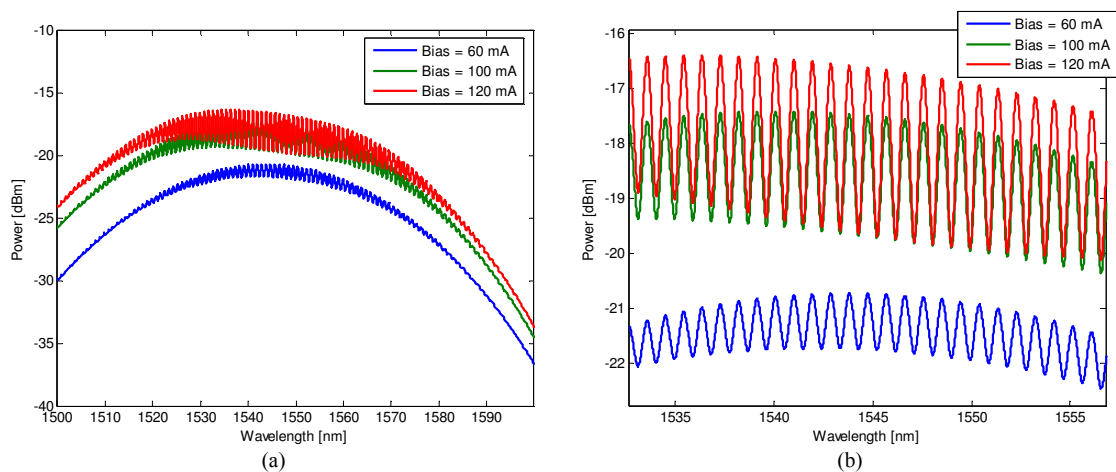


Fig. 2.12. (a) ASE spectrum and (b) gain ripple and shift of the ASE peak for different SOA bias currents and a resolution bandwidth of 0.1 nm.

Although nonlinear gain compression can be deduced from Fig. 2.12(a), a more proper investigation of the gain saturation effect that is introduced by a raised bias current is

focused on the signal amplification itself. Fig. 2.13 and 2.14 show this gain-current relation for the signal wavelength.

Once transparency is achieved by injecting a bias current of ~ 25 mA, a small signal gain up to 24 dB can be obtained for a bias as high as 120 mA. However, this gain cannot be provided as the input power level raises. This saturating effect is shown in Fig. 2.13 as function of input as well as output power for different bias currents. For a typical pump of 100 mA the small signal gain of 23 dB starts to saturate when the input power reaches -13 dBm, corresponding to an output power of 6.7 dBm. This shows that for input power levels that are typically considered in access applications, at least weak gain saturation has to be taken into account. For higher bias values the saturation output power shifts to higher values.

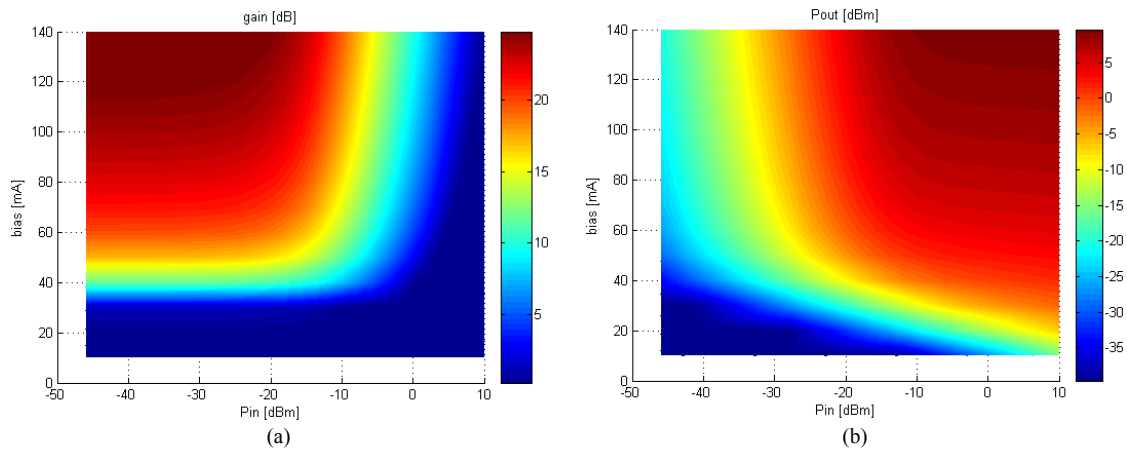


Fig. 2.13. (a) Gain and (b) output power of a SOA as function of the bias current and optical input power.

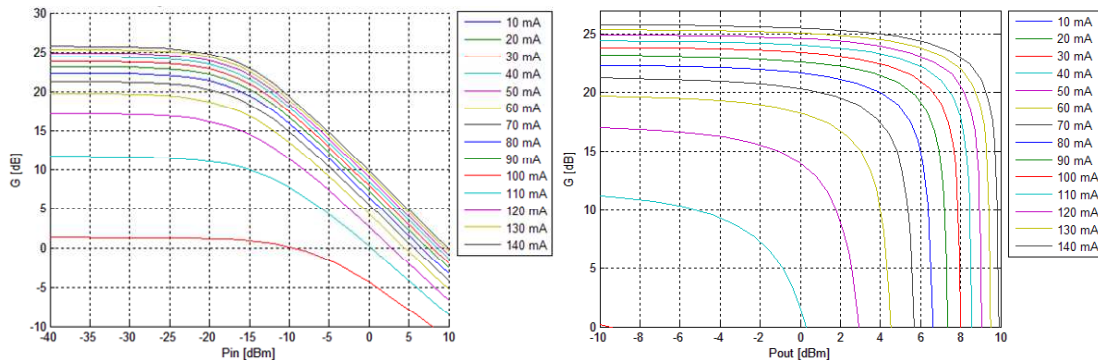


Fig. 2.14. The effect of optical gain saturation occurs for higher values of optical input power.

Note. The effect of optical gain saturation is in principle not wanted for optical amplifiers. The origin of saturation is found in the carrier depletion, which is pronounced for high signal input power values. For EDF-based amplifiers, saturation occurs at higher power values, which is one of the reasons why booster amplifiers are typically employing EDFAs. However, the pumps required for such boosters can be very strong compared to small signal amplifiers for single wavelengths. Nonetheless, saturation is not always a bad thing. Many applications, primarily related with all-optical signal processing, derive from the beneficial use of saturation. Since

data streams have to be handled by the amplifier, the dynamic behavior of the gain saturation plays an important role. An important measure for the dynamics is the gain recovery time, which strongly depends on the SOA design. For commercially available bulk components, this time constant is in the order of 200 ps but can be decreased to a few picoseconds by introducing quantum dots in the active region [104]. Such dots are semiconductor particles with a scale of nanometers – in the order of tens to hundreds of atoms – and allow to catch single carriers that are then confined in a well-defined specific energy level. With the introduction of such quantum mechanically enhanced devices, high bit rates of 40 Gb/s and beyond can be supported without introducing patterning effects.



SOA - Noise generation

Interband transitions in semiconductors not only result in stimulated emission. A small portion of recombined electron-hole pairs lead to spontaneous emission, as it is also the case for laser diodes that are driven below their threshold. The spontaneously emitted photons are partially coupled into the signal and amplified together with the signal.

The noise figure of SOAs is comparable with the one of EDFAs, but suffers from the fact that part of the signal is lost during the fiber-to-chip coupling. The coupling efficiency appears therefore in the analytical expression for the noise figure NF so that

$$NF_{SOA} \approx \eta_{in} NF_{EDFA} \quad (2.50)$$

Although the theoretical noise figure could in principle reach the 3-dB limit, it is typically in the order of 6 dB due to the fiber coupling.

However, considering photonic integrated circuits where light is inserted and extracted once, the integration of SOAs into photonic subsystems does not introduce devastating noise accumulation.

The RSOA is subject to an increased noise figure due to the mirror at its back facet. The ASE that raises in forward propagating direction is reflected back towards the input facet, so that a more rapid ASE build-up is given compared to the SOA.

The impact of the ASE, which is coupled into the signal, on the noise figure depends on the signal gain that is experienced on the way through the amplifier. Fig. 2.15 shows a typical characteristic for different bias currents and optical input power values.

The noise figure spectrum of the SOA is shown in Fig. 2.16. The minimum for the input power can be found between -5 and -10 dBm, corresponding to Fig. 2.15(b).

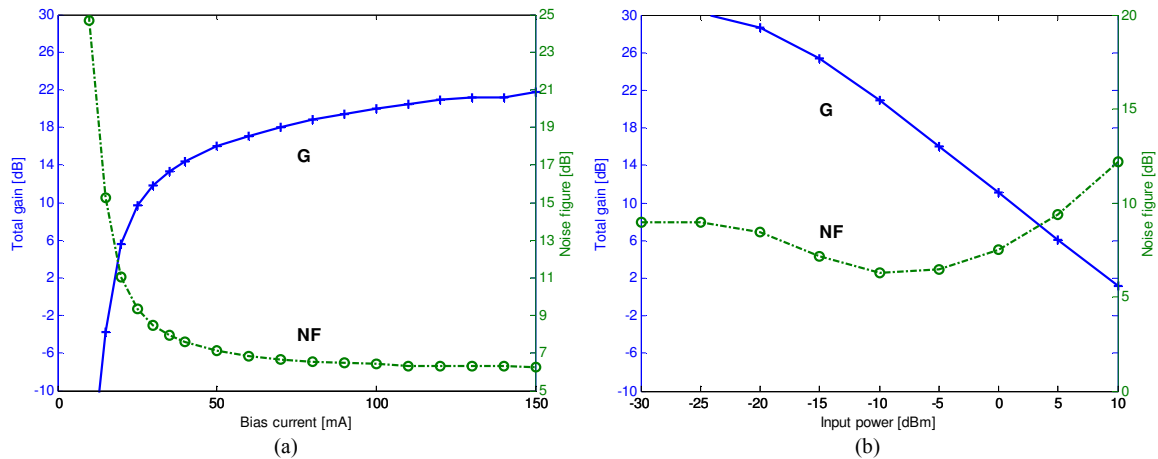


Fig. 2.15. Fiber-to-fiber gain and noise figure at 1550 nm for (a) an input of -10 dBm and (b) a bias current of 120 mA.

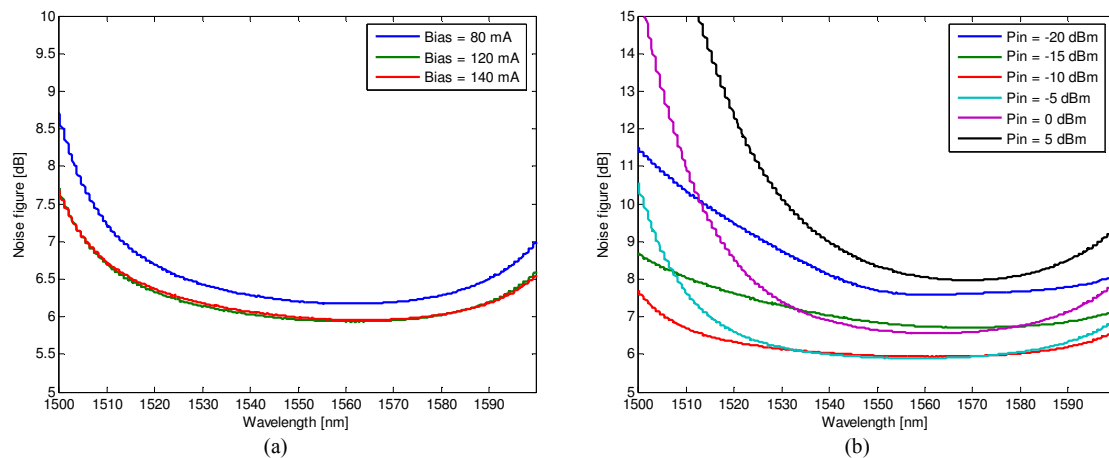


Fig. 2.16. Noise figure spectrum for (a) an input of -10 dBm and (b) a bias current of 120 mA.

Fig. 2.17 shows the noise figure contour several operation points that are defined by the bias current and the input power of the signal. Concerning the input power, two regions have to be excluded for operation to achieve optimum performance, as indicated by the dashed lines in the figure:

- If the input power of the signal is too low (below -20 dBm), the noise photon rate is quite high compared to the signal photon rate. The signal is then amplified with the small signal gain but does not reach a high output power level, and the noise contributes in a bigger ratio than if the signal would have output powers close to the saturation.
- An input signal with high input power cannot be amplified with high gain so that the amplifier is mostly adding noise. The area of operation for this scenario is located at input powers larger than 3 dBm for higher bias currents above 80 mA.

Between these two boundaries, a noise figure ~ 7.3 dB can be obtained for bias currents that are moderate or high to ensure operation well above the transparency threshold.

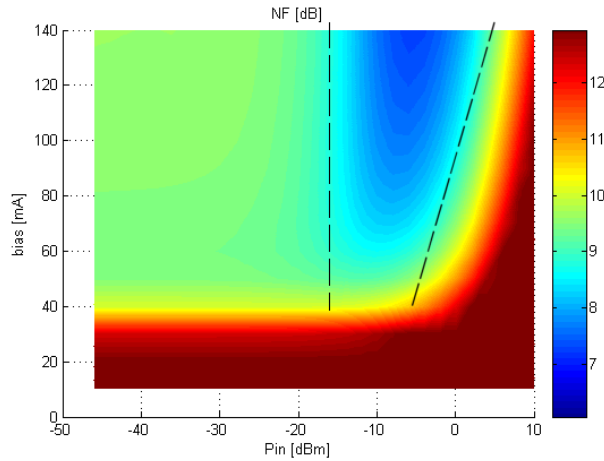


Fig. 2.17. Noise figure contour of a SOA as function of the bias current and optical input power.

Reflective SOA – Gain and Noise Figure

The gain and noise emission of a SOA is changed with a redesign of its back-facet towards a retro-reflector. The impact of this alternative design on gain and noise figure will be discussed briefly. For the analytical model, the reflectivity R_2 of the back facet was chosen with $1 - 5 \cdot 10^{-5}$, according to a high reflective dielectric coating. The output signals are then taken at the bidirectional front facet.

A moderate gain is expected to be obtained with a lower bias current due to the fact that the signal passes the active region twice due to the artificial reflection. On the other hand, the effect of gain saturation will therefore approach at lower values of input power. Fig. 2.18 and 2.19 show the gain saturation of the RSOA.

For an input as low as -25 dBm and a bias current of 40 mA near the transparency point, the gain of the RSOA is already 17.5 dB while it is 13 dB for the SOA. For the same (low) input power, a small signal gain of 22 dB can be already achieved for a bias current of 60 mA, which is ~ 15 mA lower than for the SOA.

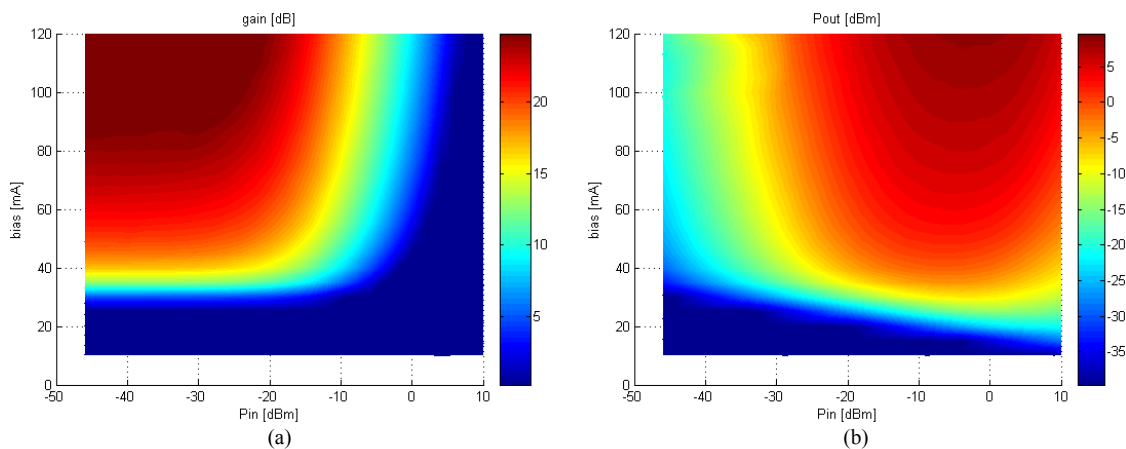


Fig. 2.18. (a) Gain and (b) output power of an RSOA as function of the bias current and optical input power.

Regarding the gain saturation at a moderate input power of -10 dBm, the gain drops to 18 dB for the SOA biased at a current of 100 mA and to 17 dB for the RSOA. For this bias current, a small signal gain of 26 dB can be obtained, which has its saturation point at an input power of -19.3 dBm or an output power of 3.7 dBm, respectively. The shallow dip in the gain of Fig. 2.19 that is present at higher bias currents and low input powers in the model is due to numerical effects in the calculation and has no physical reason. The curvature for high optical power values is due to the high carrier dependent loss coefficient.

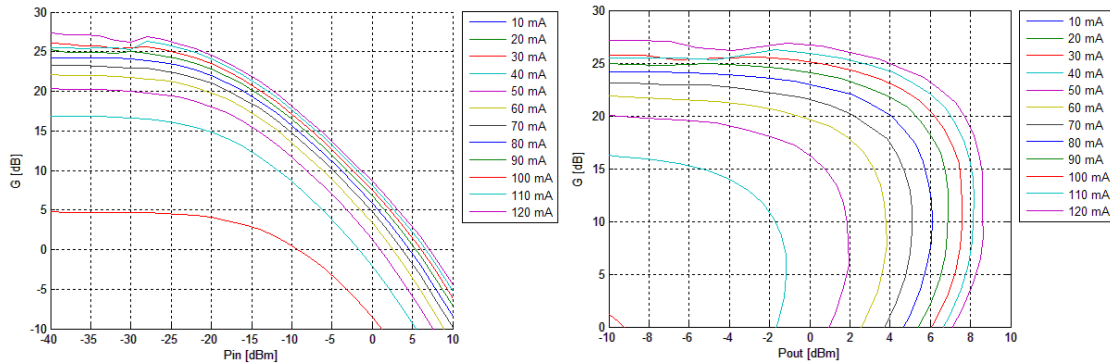


Fig. 2.19. Optical gain saturation for the RSOA at higher values of optical input power.

The RSOA has a higher noise figure due to its retro-reflective design. Fig. 2.20 shows the noise figure contour for different bias current and input power settings.

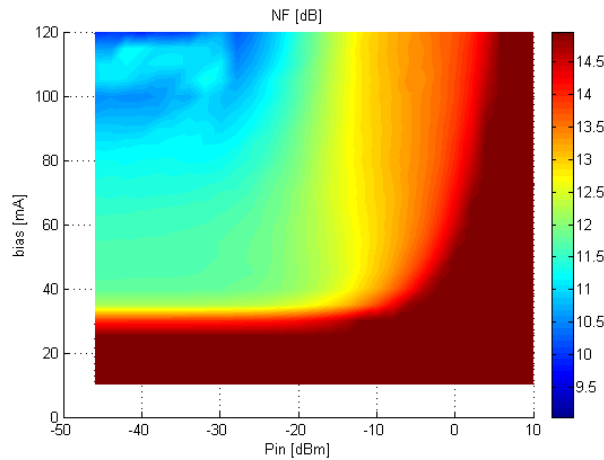


Fig. 2.20. Noise figure of a RSOA as function of the bias current and optical input power.

Compared to the SOA, the aforementioned optimum region indicated as the blue area in Fig. 2.17 does not appear in the model of the RSOA as the noise factor increases with raising input power due to the saturation onset where mostly noise photons are added while the signal power stays constant. The inhomogeneities in the optimum region in Fig. 2.20 are due to the same numerical effects that appeared when calculating the gain of the RSOA. For a low input power of -30 dBm and a bias current of 100 mA, the noise figure would be around 10.5 dB, neglecting those inhomogeneities mentioned. Compared to the optimum working point of the SOA, where a noise figure of 7.5 dB can be

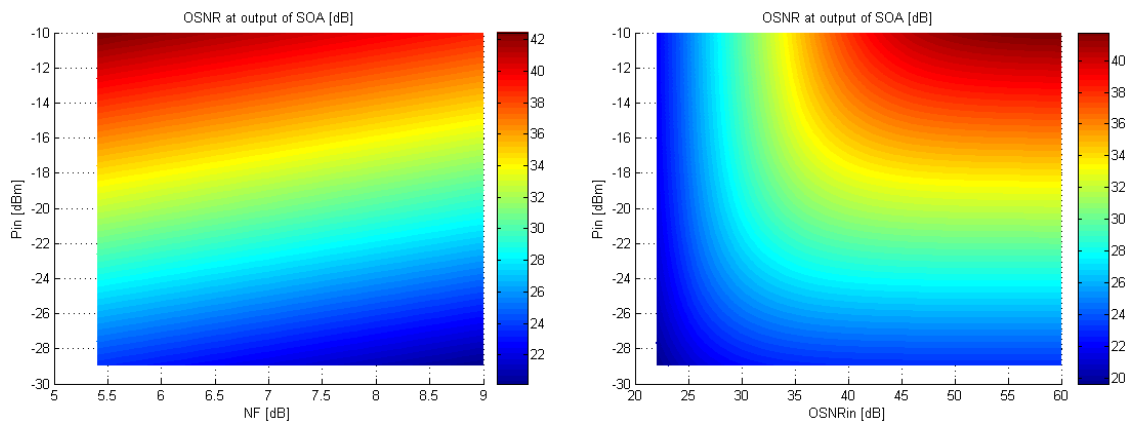
obtained for the same bias current but an input power of -5 dBm, the RSOA clearly performs worse.

Note. In transmission links it is important to have a measure for the signal degradation due to accumulated optical noise from intermediately placed optical amplifiers. The power ratio between signal and noise background is typically used for this reason. Since the optical noise is spectrally broad compared to the data channel, a reference bandwidth $\Delta\nu$ for the resolution of the noise is defined to relate just a portion of the ASE background to the signal. Commonly, this resolution bandwidth is chosen with 0.1 nm. This methodology of calculating the optical signal-to-noise ratio, short OSNR, allows to see the noise impact of different amplifiers in the network easily. A high OSNR degradation then means that the operating conditions of an amplifier, mostly related with its signal input, is not optimally chosen. In this way, faults in a complex optical network can be located easily. Alternatively, by measuring the OSNR with an optical spectrum analyzer, one can deduce the approximate noise figure of an amplifying element within the network.

The relation between the OSNR, the input power and the noise figure is given for a specific resolution bandwidth (e.g., for a bandwidth of 0.1 nm the accumulated ASE power spectral density is -58 dBm). According to [105], the relation between the noise figure and OSNR and the degradation due to an added amplifier are

$$NF_{dB} = P_{in,dB} - OSNR_{dB} - 10 \log(h\nu \Delta\nu) \quad \frac{1}{OSNR_{out}} = \frac{1}{OSNR_{in}} + \frac{NF \cdot h\nu \Delta\nu}{P_{in}}$$

A graphical interpretation of these expressions can be found in the figures below, which show the OSNR at the output of a SOA for different signal input powers, and in the second case, for different input OSNRs and a fixed noise figure of 6 dB.



2.3 Electro-Optical Modulation Bandwidth

Foremost the application of SOAs as low-cost intensity modulators has made this photonic device attractive for many applications. However, limitations are given by the electro-optical (e/o) response of the semiconductor [106], which will in turn prevent to reach high modulation data rates.

2.3.1 Electro-optical transfer function

The electro-optical response of the SOA depends on the chosen point of operation [107], for which stringent limitations for the applied modulation can be imposed. Next to the physical processes inside the semiconductor material that are related with the applied bias current and optical signal input of the SOA, also the packaging of the device has to be taken into account.

Physical design parameters for the differential gain coefficient as they have been mentioned in chapter II.2 and transport effects such as diffusion or tunneling [108,109] are not taken into account in the presented macroscopic model.

Analytical Model for the Semiconductor

According to equations 2.6 and 2.49, the SOA gain recovers with the time constant

$$\tau_e = A + Bn + Cn^2 = \frac{1}{\gamma} \quad \frac{\partial \gamma}{\partial n} = \frac{B + 2Cn}{\tau_e(n)} \quad (2.51)$$

and depends on the carrier density n . The exact composition is given by the non-radiative recombination rate A , the radiative recombination coefficient B and the Auger recombination coefficient C . Typical values for bulk components are around 200 ps.

The operation of the SOA follows the rate equation for the carrier density (equation 2.48), which can be simplified written either for carriers n^* or their density according to

$$\frac{\partial n^*}{\partial t} = \frac{I}{e} - R_{sp}^* - G^* P^* \quad \frac{\partial n}{\partial t} = \frac{I}{edWL} - R_{sp} - GP \quad (2.52)$$

In this version of the rate equation, the bias current I that is injected into the volume of the SOA leads to a gain G for a signal with photon number P^* or equivalent optical power P , respectively. The ASE build-up in the SOA waveguide, incorporated in equation 2.48, is neglected for the sake of simplicity.

The small signal steady state carrier density N_0 and the small signal gain coefficient g_0 can be retrieved with

$$N_0 = \frac{I\tau_e}{edWL} \quad g_0 = \Gamma a(N_0 - N_T) \quad (2.53)$$

where N_T is the carrier density that is necessary to achieve transparency, typically in the order of 0.9 to 1.1 $10^{24}/\text{m}^3$. This interpretation of the gain coefficient is also common for laser diodes, where a linear relation between gain and carrier density is given once the transparency point is reached. Although no temperature dependency is given in this model as it does not derive from the semiconductor design itself, an increasing temperature will cause a reduction in the gain coefficient a and an increased transparency carrier density N_T .

Considering the SOA to be linear, the signal gain G and the small signal gain G_0 are related with the material gain via

$$G = \exp(gL) \qquad G_0 = \exp(g_0L) \qquad (2.54)$$

Saturation for a higher optical input can be taken into account by a dependence on the signal power P , which is related to the saturation power P_{sat} [110].

$$G = \frac{G_0}{G_0 - (G_0 - 1) \exp\left(-\frac{P}{P_{sat}}\right)} \qquad P_{sat} = \frac{\hbar\omega dW}{a\Gamma\tau_e} \qquad (2.55)$$

The saturation power is determined by the waveguide cross-section and the optical frequency ω of the signal. With this interpretation of the gain, the travelling-wave equation for the optical signal, originally expressed by equations 2.24 and 2.25, becomes

$$\frac{\partial P^*}{\partial t} = (G^* - \gamma)P^* + R_{sp}^* \qquad (2.56)$$

The facet reflectivities are treated to be ideal, so that no counter-propagating signal is present inside the active waveguide. Note that the time dependence originates due to the treatment of the power in terms of photon flux. A transition from photon number P^* to optical power P and from carriers n^* to their density n can be made according to

$$P^* = \frac{n\epsilon_0 n_g}{2\hbar\omega} \int |E|^2 dV = \frac{n_1\epsilon_0 n_g}{2\hbar\omega} PL \qquad n^* = \int n dV \qquad (2.57)$$

where E is the optical field, n_1 is the refractive index of semiconductor material in the active waveguide that has a volume $V = dWL$, and n_g is the group refractive index, which has a value of ~ 4 .

Originating from this basic set of equations, the e/o response of the SOA can be investigated by small signal analysis. For this reason a small sinusoidal signal with angular frequency Ω is applied to the bias current, and the fluctuations on the carrier density and the output power are observed.

$$I = \bar{I} + \Delta I \qquad \Delta I \ll \bar{I} \qquad \rightarrow \qquad \begin{aligned} n &= \bar{n} + \Delta n \\ P &= \bar{P} + \Delta P \end{aligned} \qquad (2.58)$$

As the gain depends on the carrier density and on the optical power of the signal, it will be treated as

$$G(n, P) = \bar{G} + \frac{\partial G}{\partial n} \Delta n + \frac{\partial G}{\partial P} \Delta P \quad (2.59)$$

For the rate equation, the introduced change in the carrier density is then

$$\frac{\partial \Delta n}{\partial t} = -\gamma \Delta n - \bar{n} \frac{\partial \gamma}{\partial n} \Delta n - \bar{G} \Delta P - \bar{P} \frac{\partial G}{\partial P} \Delta P + \frac{\Delta I}{eV} \quad (2.60)$$

$$\text{with } \frac{\partial G}{\partial P} = -G \frac{G_0 - 1}{P_{sat}} \exp\left(-\frac{P}{P_{sat}}\right)$$

Further, by taking the sinusoidal modulation into account, the time-derivative can be related with a multiplication by $j\Omega$ so that

$$j\Omega \Delta n = \Delta n \left(-\gamma - \bar{n} \frac{\partial \gamma}{\partial n} \right) + \Delta P \left(-\bar{G} - \bar{P} \frac{\partial G}{\partial P} \right) + \frac{\Delta I}{eV} \quad (2.61)$$

$$\text{with } \Gamma_n = \gamma + \bar{n} \frac{\partial \gamma}{\partial n} \quad \text{and} \quad \bar{G} \gg \frac{\partial G}{\partial P} \bar{P}$$

Considering primarily deviations due to the bias current, this gives

$$(j\Omega + \Gamma_n) \Delta n = -\bar{G} \Delta P + \frac{\Delta I}{eV} \quad \rightarrow \quad \Delta n = \frac{\Delta I}{eV (j\Omega + \Gamma_n)} \quad (2.62)$$

For the optical power, the small signal approach ends up with

$$\frac{\partial \Delta P}{\partial t} = (G - \gamma) \Delta P + \Delta P \frac{\partial G}{\partial P} \bar{P} + \bar{P} \frac{\partial G}{\partial n} \Delta n + \frac{\partial R_{sp}}{\partial n} \Delta n \quad \bar{P} = -\frac{R_{sp}}{G - \gamma} \quad (2.63)$$

$$\text{whereby } \frac{\partial G}{\partial n} = \Gamma_a$$

With some considerations, the derivative can be expressed as

$$\begin{aligned} \Gamma_p &= \frac{R_{sp}}{\bar{P}} - \frac{\partial G}{\partial P} \bar{P} & \bar{P} \frac{\partial G}{\partial n} &\gg \frac{\partial R_{sp}}{\partial n} \\ j\Omega \Delta P &= -\Gamma_p \Delta P + \bar{P} \frac{\partial G}{\partial n} \Delta n & \Delta n &= \Delta P \frac{j\Omega + \Gamma_p}{\frac{\partial G}{\partial n} \bar{P}} \end{aligned} \quad (2.64)$$

which yields further a second order response

$$\Delta P = \bar{P} \frac{\partial G}{\partial n} \frac{\Delta I}{eV(j\Omega + \Gamma_n)(j\Omega + \Gamma_p)} = \bar{P} \frac{\partial G}{\partial n} \frac{\Delta I}{eV(\Omega_R + \Omega - j\Gamma_R)(\Omega_R - \Omega + j\Gamma_R)} \quad (2.65)$$

$$\Omega_R = \sqrt{\left(\bar{G} + \frac{\partial G}{\partial P} \bar{P}\right) \left(\frac{\partial G}{\partial n} \bar{P} + \frac{\partial R_{sp}}{\partial n}\right) - \frac{1}{4}(\Gamma_n - \Gamma_p)^2} \quad \Gamma_R = \frac{1}{2}(\Gamma_n + \Gamma_p)$$

Γ_R determines the damping factor of the transfer function of the e/o response, as can be seen later in the simulations. Re-expressing the carrier density according to this second order response gives

$$\Delta n = \frac{\Delta I(j\Omega + \Gamma_p)}{eV(\Omega_R + \Omega - j\Gamma_R)(\Omega_R - \Omega + j\Gamma_R)} = \frac{\Delta I(j\Omega + \Gamma_p)}{eV(\Omega_R^2 + \Gamma_R^2 + 2j\Omega\Gamma_R - \Omega^2)} \quad (2.66)$$

The e/o response can be found as the change of power for a certain change of current, and is determined by

$$\frac{\Delta P}{\Delta I} = \frac{\frac{\bar{P}}{eV} \frac{\partial G}{\partial n}}{(\Omega_R + \Omega - j\Gamma_R)(\Omega_R - \Omega + j\Gamma_R)} \quad \bar{G} = \exp\left[a\left(\frac{I\tau_e}{eV} - N_T\right)L\right] \quad (2.67)$$

This function shows a resonance peak that depends on the operation point of the SOA that is determined by the average values of bias current and input power. The resonance frequency follows the oscillation of a coupled population of electrons and photons: the energy shifts back and forth between being stored as photons or as excited carriers.

Electrical-electrical Response of Packaging Parasitics and Bonding Wires

The e/o response of the semiconductor is not the only limitation for modulation. In addition, the electrical interface of the bias electrode will introduce a natural low-pass transfer function for the electrical signal [111]. The exact filter function depends on the quality of the bonding interface. Typically, commercial SOA devices are not intended to be primarily used as intensity modulator so that the bonding interface inside the package is not optimized for high modulation bandwidths. Microwave losses occur during propagation, caused e.g. by the n-cladding and the substrate that act as lossy ground plane, an eventual insufficient gold thickness of the top contact or due to the forward conduction [112].

The electrical model for the packaged SOA, sketched in Fig. 2.21, consists of the chip itself with a low junction resistance R_j and the capacitance C_j of the SOA electrode, the bonding wire which introduces an inductive element L_p and the relatively large bonding pad that is characterized by its capacitance C_p . A small series resistance R_c accounts for the cladding region of the SOA.

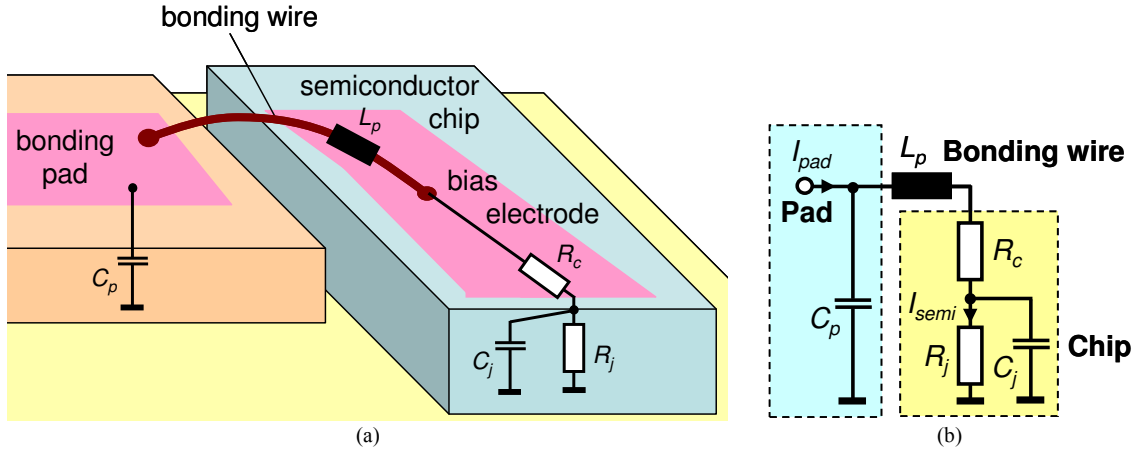


Fig. 2.21. (a) Electronic package of the SOA and (b) equivalent circuit model.

With a simple analysis, the e/e response, defined between the bias current of the semiconductor chip and the applied modulation current at the pad of the package, is obtained with

$$\frac{I_{semi}}{I_{pad}} = \frac{1}{1 - L_p C_p \Omega^2 + j\Omega C_j (R_c + R_j)} \quad (2.68)$$

A typical response of a commercial package was used for the simulation of the electrical package.

Overall electro-optical Response

The overall response of the SOA is a concatenation of both transfer functions, respecting limitations from the semiconductor chip and from the electrical interface.

$$\text{overall } e/o \text{ response} = \frac{I_{semi}}{I_{pad}} \frac{\Delta P}{\Delta I} \quad (2.69)$$

Dependence on Bias Current and Optical Input Power

To see the dependence on the bias point, the optical input power was fixed to -15 dBm, while the bias current was chosen with different values (Fig. 2.22 to 2.24). The relative response is thereby related to the response at $\Omega = 0$.

The e/e response of the bonding interface forms together with the resonance peak of the second-order e/o response of the SOA itself a plateau after a first low-pass roll-off (Fig. 2.24). Depending on the optical input power and the bias current, this plateau can reach higher e/o bandwidths (typically around 1.5 to 3 GHz), before the response shows again a strong roll-off due to the low-pass behavior of the e/o response.

If the resonance of the e/o response is strong enough, the plateau is located just a few Decibels below the begin of the first roll-off (which is typically around 150 to 800 MHz, depending on the way of packaging). As this difference would produce a ripple in the data pattern once the SOA is used as modulator, it is necessary to cut the first roll-off,

so that the overall e/o response corresponds to a first-order low-pass with a cut-off that coincides with the resonance of the e/o response of the SOA.

By increasing the bias current, the resonance peak of the e/o response is enhanced and shifted towards higher modulation frequencies. While there is no peak for bias currents just above the transparency point (Fig. 2.22), one is established at 1.4 and 2.2 GHz for currents of 100 and 150 mA, respectively (Fig. 2.23 and Fig. 2.24). The plateau of the overall transfer function, which is found after the first roll-off, is broadened for a higher resonance peak.

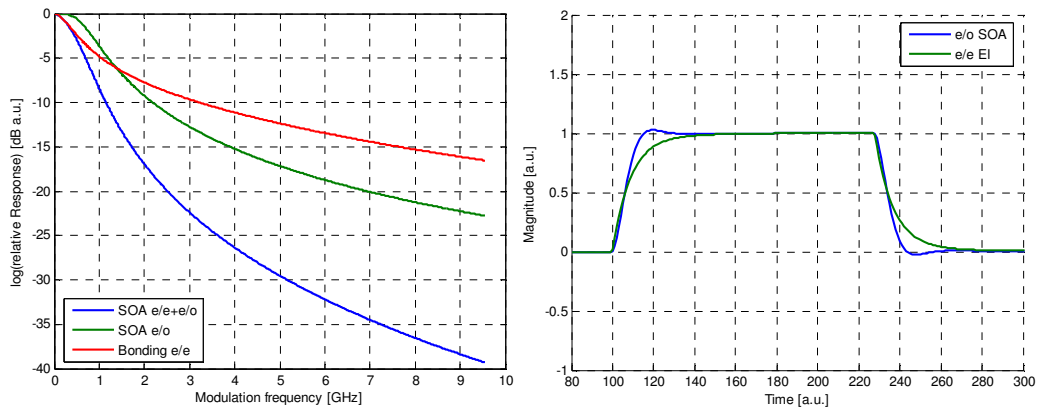


Fig. 2.22. Response and patterning for a bias of 50 mA and an input power of -15 dBm.

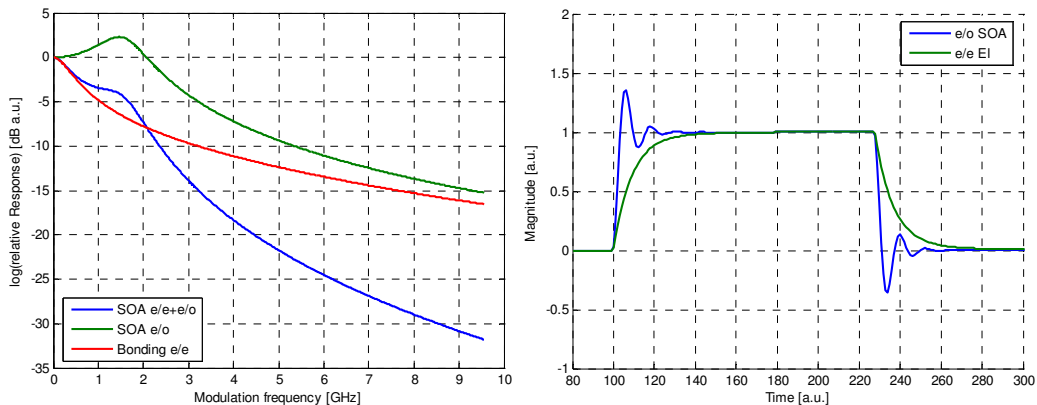


Fig. 2.23. Response and patterning for a bias of 100 mA and an input power of -15 dBm.

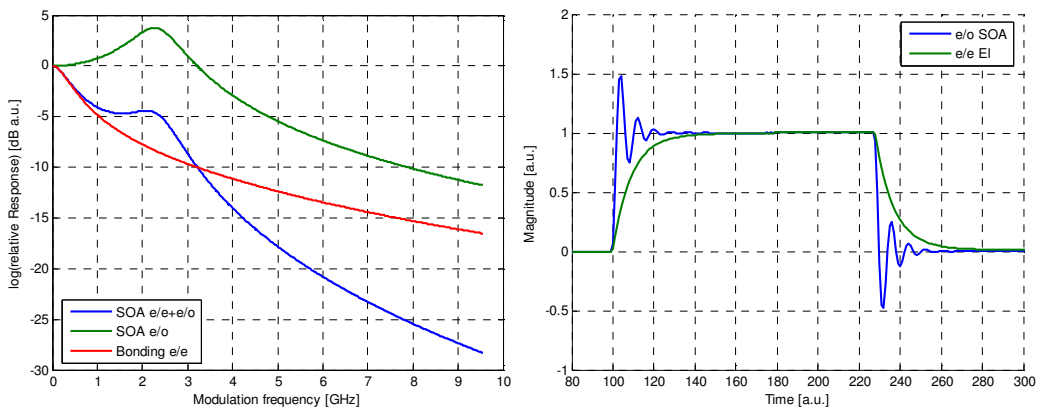


Fig. 2.24. Response and patterning for a bias of 150 mA and an input power of -15 dBm.

The influence of the optical input power is shown in Fig. 2.25 to 2.26 for a fixed bias current of 100 mA. A decrease in the optical input power leads to a reduced e/o response. With a high input power of -10 dBm, the resonance peak is located at 2.3 GHz while for -20 dBm it shifts downwards to just 0.9 GHz. However, it is still present due to the higher bias current chosen for operation, far off the transparency point.

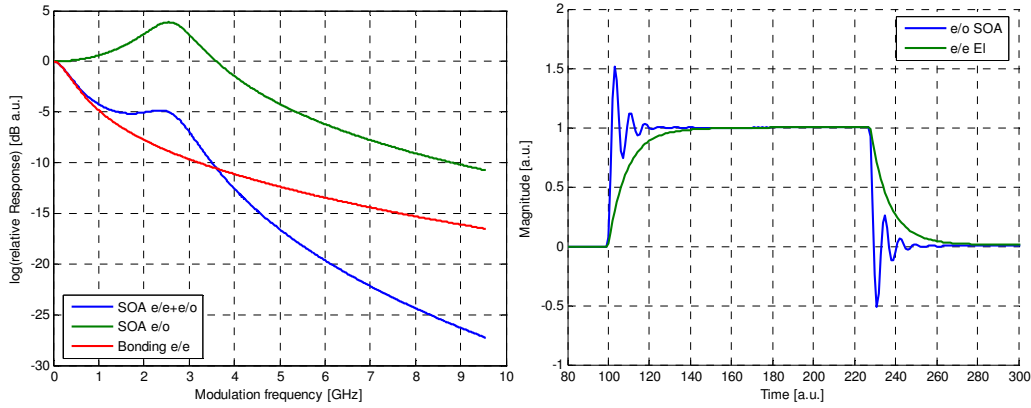


Fig. 2.25. Response and patterning for a bias of 100 mA and an input power of -10 dBm.

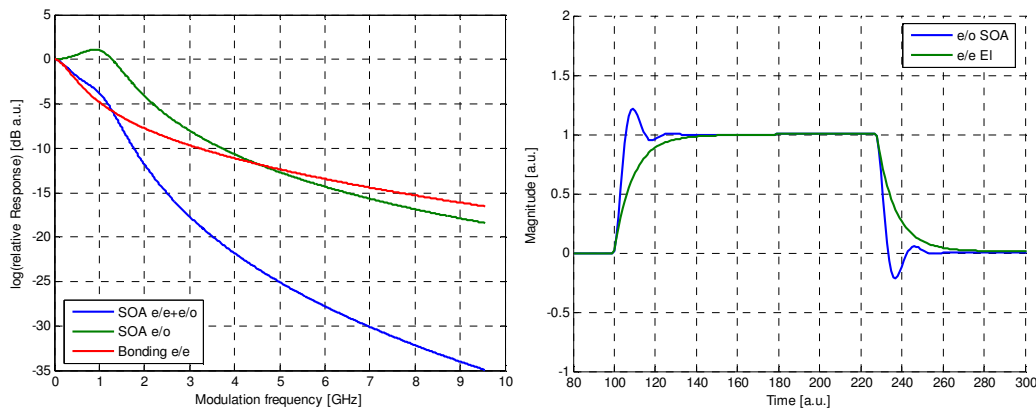


Fig. 2.26. Response and patterning for a bias of 100 mA and an input power of -20 dBm.

Note that the time response shown in Fig. 2.22 to 2.26 may not always correlate to the e/o response due to nonlinear effects of the SOA.

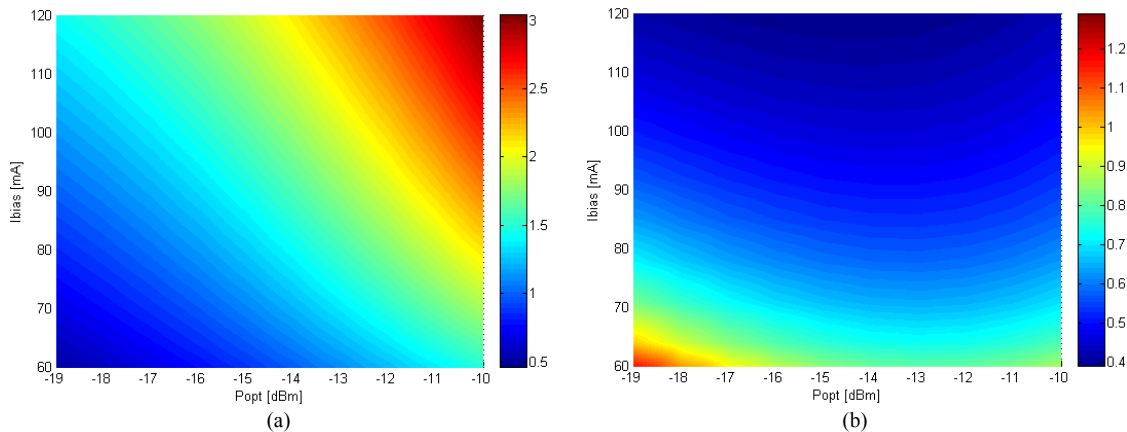
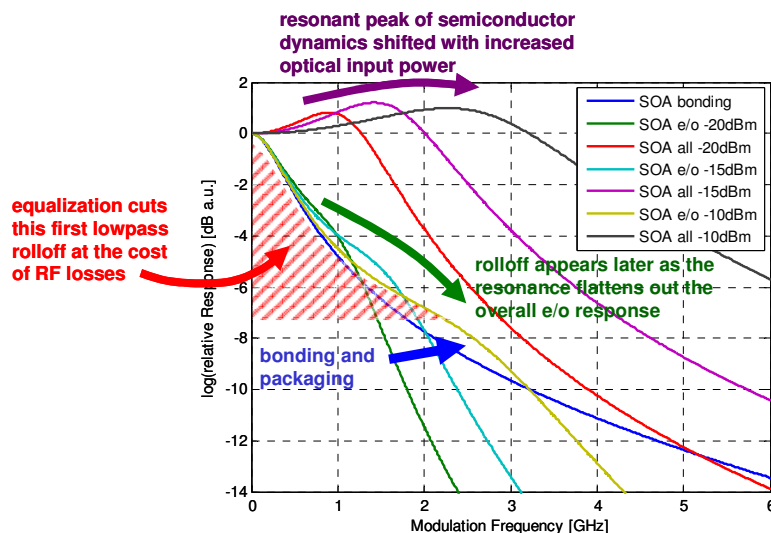


Fig. 2.27. (a) Resonance frequency of the e/o response and (b) its damping factor.

The resonant behavior of the e/o response is characterized in terms of resonance frequency and damping factor (defined as the ratio Γ_R/Ω_R), which both depend on the operation point and are therefore functions of optical input power and bias current (Fig. 2.27).

For a fixed resonance frequency, e.g. 1.5 GHz, the damping factor drifts for changes in the operation point. Comparing operation at -12 dBm and 74 mA with another bias point of -16 dBm and 105 mA, the damping factor decreases from 0.63 to just 0.46, leading to a stronger resonant behavior.

Note. The ripple in the envelope of the bit stream that is introduced due to the roll-off at low frequencies below the plateau can be flattened by a pre-equalization of the e/o optical response. As it is illustrated in the figure below, the response can be modified at the cost of some losses, in terms of an additional e/e-filter function that aims at cutting the disturbing roll-off. In this way, the overall e/o transfer function will approximately appear as first-order low-pass filter, with a cut-off that is shifted towards higher modulation bandwidth, according to the resonant peak of the semiconductor.



2.4 Patterning and Optical-Optical Transfer Function

On the contrary to an EDFA, transients at the bit level have to be taken into account for SOAs due to their much faster gain recovery that is primarily related with interband transitions. For the bit rates considered here, such transients do not only appear at the borders of a data packet as it is the case for EDFAs that are not stabilized for bursty data traffic, but at each edge inside the bit stream. Overshoots at the build-up of optical pulses and undershoots at their falling edges occur. The first kind of bit transients root in the unused gain before the bit and the finite speed of optical gain saturation once the pulse is established. A similar behavior is exploited at the falling edge, when the carrier

density is still depleted at the begin of the consecutive space after the pulse, which causes the low optical power to be amplified with less gain.

Due to these phenomena, the rails in the marks and spaces of the eye diagrams are pronounced and lead to a closing of the eye. Although they cannot be considered as noise source, these transients will cause degradation on the amplified signal and are therefore critical in transmission systems [113], especially when a cascade of SOAs is used along the overall communication link [114].

The intraband relaxation processes that determine the finite speed of the gain dynamics are depicted in Fig. 2.28. The stimulated emission leads to a fast depletion of carriers, which are partially recovered due to carrier heating and cooling [115], the latter resulting in carriers with energies that are below the average through simulated absorption. The slow process of carrier injection determines the overall recovery time but can be decreased with novel SOA designs such as quantum dot SOAs.

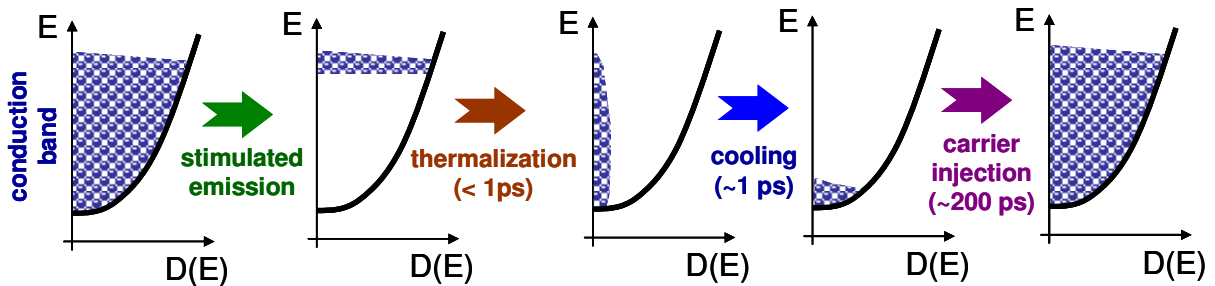


Fig. 2.28. Intraband relaxation processes behind the gain dynamics of the SOA.

It is difficult to assess the magnitude of distortion analytically due to the random nature of bit streams. Typical data streams are sequences that typically contain long sequences of consecutive marks and space bits. Though these blocks of similar bits appear with low probability, they are causing severe distortions due to the fact that low bit error probabilities are aimed for. From an experimental point of view, the distortions caused by these critical sequences of consecutive identical bits are not visible in the eye diagram – though in the bit error ratio – and therefore difficult to identify.

A simple characterization of the induced transients can be performed in terms of their relative values referenced to the eye opening for reference signals such as rectangular bit patterns. For the overshoot, a measure is given according to

$$\text{relative overshoot} = 10 \log \left(\frac{M_1 - P_1}{P_1 - P_0} \right) \text{dB} \quad (2.70)$$

where M_1 is the maximum output power that is reached during a pulse. The power levels P_1 and P_0 are the mean values for marks and spaces, respectively, corresponding to a transmitted mark or space bit.

The distortions in the bit pattern raise when the saturation regime is approached. The signal input power plays therefore an important role as can be seen in Fig. 2.29(a), which shows the results that were obtained with the analytical model and a rectangular input signal. The extinction ratio of the input signal was thereby fixed to 6 dB, meaning

that the space bits remain with some residual optical power. This results in a partial clamping for the carrier density and thus in a weak stabilization for the optical gain.

As it is obvious from Fig. 2.29(b), a random bit sequence is affected by transients with different magnitude, since sequences of consecutive mark bits allow the gain to build up to a high instantaneous value at the first following mark bit.

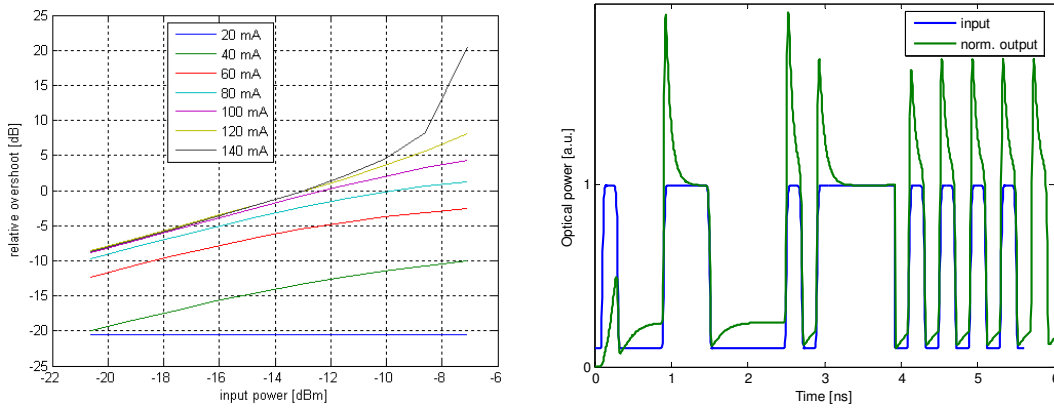


Fig. 2.29. (a) Relative overshoot on the amplified data signal as function of the input power for different bias currents. The extinction ratio of the input signal was 6 dB. (b) Distorted random bit pattern with over- and undershoots. The output signal is normalized in its steady state magnitude to the input signal.

Once transparency is achieved with an appropriate bias current, transients are observed. A compression of the relative overshoot is experienced when the bias current increases. For a bias current of 100 mA, the overshoot is twice as large as the eye for an input power of -8 dBm.

An analytical approach to assess these effects can be obtained by expressing the SOA gain in terms of an optical-optical (o/o) response. Although this does not directly allow to deduce the magnitude of the transients, the capability of a SOA to suppress optical noise – a beneficial effect that supports the seeding of an optical carrier as it will be discussed in chapter VI.2 – derives from this model.

Analytical Model for the Semiconductor

The modulation of the carrier density Δn solely due to a variation of the optical input signal ΔP_{in} is derived from the rate equation 2.52 with

$$\frac{\partial \Delta n}{\partial t} = -\frac{\Delta n}{\tau_e} - \frac{g \Delta P_{in}}{\tau_e P_{sat}} - \frac{\partial g}{\partial n} \frac{\bar{P}}{\tau_e P_{sat}} \Delta n \quad (2.71)$$

The recombination term R is here expressed in a way to exploit its characteristic effective carrier lifetime τ_e , according to equation 2.6, and the saturation power P_{sat} is given by equation 2.55.

Considering small signal analysis, the time derivatives can be easily solved, which leads to a low-pass expression for the modulation of the carrier density Δn that depends on an effective time constant τ_{eff} .

$$\Delta n = -\Delta P_{in} g v_g \frac{\tau_{eff}}{1 + j\Omega \tau_{eff}} \quad (2.72)$$

$$\tau_{eff} = \frac{1}{\tau_e} + \frac{\partial g}{\partial n} \frac{\bar{P}}{\tau_e P_{sat}} \quad \frac{1}{\tau_e} = \frac{\partial R}{\partial n}$$

This effective time constant τ_{eff} is determined by the mean optical power in the SOA and can be modified by one or more additional signals at different wavelengths. Note that the saturation power for this “holding” beam depends on the chosen wavelength.

Together with the travelling-wave equation 2.33, here neglecting the material loss coefficient α for the sake of simplicity so that

$$\frac{\partial P_k}{\partial z} = \Gamma a (n - N_T) P_k(z) \quad \leftrightarrow \quad \frac{\partial P_k}{\partial t} = \Gamma a v_g (n - N_T) P_k(t) \quad (2.73)$$

The index k denotes the different signals that are inserted into the SOA and v_g is the group velocity that spans a conjunction between the aforementioned interpretation of the travelling-wave equation and the one as photon flux. The differential gain coefficient a and the transparency carrier density N_T is considered to be the same for these signals. Treating the amplifier with length L as linear allows to predict the output power variation ΔP_{out} .

$$z = L: \quad \Delta P_{out} = \Delta P_{in} G + \bar{P}_{in} \frac{\partial g}{\partial n} L \Delta n \quad (2.74)$$

This leads with the retrieved modulation of the carrier density Δn to an expression for the o/o response. Looking at equation 2.72, it is obvious that the low-pass behavior of the carrier density modulation is subtracted, yielding a high-pass behavior for the o/o response.

$$\frac{\Delta P_{out}}{\Delta P_{in}} = G - \Gamma \frac{\partial g}{\partial n} L \bar{P}_{in} g v_g \frac{\tau_{eff}}{1 + j\Omega \tau_{eff}} \quad (2.75)$$

The high-pass behavior of the o/o response is pronounced for large optical confinements Γ , a large differential gain coefficient and high bias currents or input power values. For this reason short SOAs are preferred since they are typically designed for lower bias currents and have a smaller differential gain coefficient to reach the same SOA gain.

Dependence on Bias Current and Optical Input Power

The magnitude of the high-pass characteristic is shown in Fig. 2.30 as function of the bias current and optical input power. Once the saturation regime is approached as it is the case in Fig. 2.30(a) for an intermediate current of 60 mA at an already high input power of -10 dBm, the excursion at low frequencies raises to more than 4 dB.

The saturation effect can be obviously seen from Fig. 2.30(b), where the input power is varied. Despite the high bias current of 80 mA, low input levels of -15 dBm do not cause an excursion of more than 1 dB.

Fig. 2.31 summarizes a complete set of bias currents and input power values.

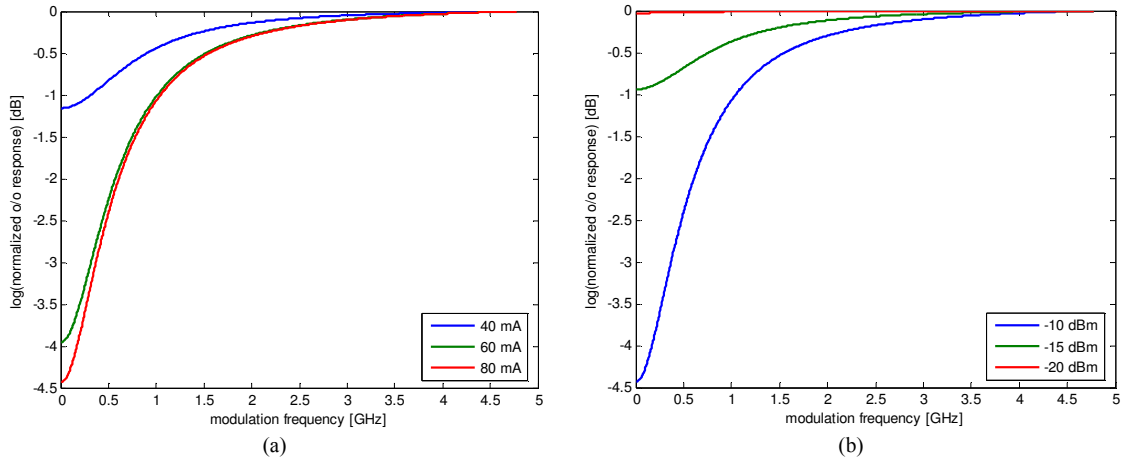


Fig. 2.30. Relative o/o response of a SOA for (a) an input power of -10 dBm and (b) a bias current of 80 mA.

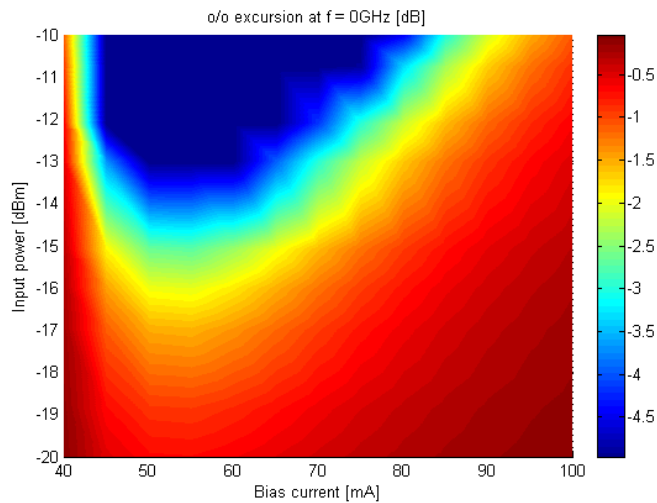


Fig. 2.31. Excursion of the o/o response at modulation frequency $\Omega = 0$, shown for different bias currents and input power values.

Although this saturation-induced filtering of low frequency components can be beneficial used to suppress low-frequency noise components such as it is often the case for increased relative intensity noise [116], the induced patterning for data signals with originally thin rails in the mark and space levels is often dominating [117]. These intrachannel distortions reduce significantly if constant envelope signals with appropriate modulation formats such as optical phase shift keying are used. The transients that occur are then negligible even for high optical input levels [118].

For amplitude shift keyed signals different approaches exist to mitigate these overshoots without applying additional holding beams, though they are introducing some complexity to the overall transmission system. A constant envelope input signal for the SOA that avoids a pattern-dependent carrier density can be obtained by a second inverted data channel. This method has been demonstrated with a second channel that is

located at an orthogonal state of light polarization [119] or at a second wavelength [120]. Alternatively, optical filters can be added to the system to suppress the induced transients, which has been demonstrated with birefringent fiber-loop mirrors [121] or integrated all-optical equalizers [122].

2.5 Chirp

The modulation of the injected bias current of a SOA does not only cause intensity modulation, but leads also to modulation of the optical frequency due to band filling effects. The introduced phase modulation for the signals that are originally intended to be purely intensity modulated, sketched in Fig. 2.32, can lead to problems as well as to beneficial aspects that will be discussed in later chapters.

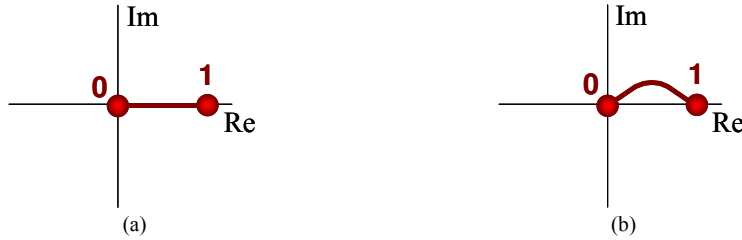


Fig. 2.32. Phasor diagram for (a) an unchirped and (b) a chirped transmitter.

The linewidth enhancement factor α quantifies this phenomenon via the refractive index n and the carrier density N [95].

$$\alpha = \frac{\frac{d \operatorname{Re}(n)}{dN}}{\frac{d \operatorname{Im}(n)}{dN}} \quad (2.76)$$

Typical values for the change of the real and imaginary components of the refractive index have been found for AlGaAs with $-11.3 \cdot 10^{-3}$ and $-1.82 \cdot 10^{-3}$ [123]. While the chirp parameter of early semiconductor lasers has been measured from 4 to 7 for $1.3 \mu\text{m}$ devices and around 6 in the $1.55 \mu\text{m}$ region, improvements have led to smaller values of ~ 2 for directly modulated laser diodes.

The definition of the chirp parameter is made according to the Kramers-Kronig relation [124] in which a modulation of the gain is always accompanied by a modulation of the refractive index. The latter is equivalent to a modulation of the optical phase and therefore also to a broadening of the optical spectrum. The coupling between optical gain and phase can be expressed as

$$\alpha = -\frac{4\pi}{\lambda} \frac{\frac{\partial n}{\partial N}}{\frac{\partial g}{\partial N}} = -\frac{4\pi}{\lambda} \frac{\frac{\partial n_{\text{eff}}}{\partial N}}{\frac{\partial \Gamma g_m}{\partial N}} \quad \alpha \propto \frac{1}{a} \quad (2.77)$$

where n_{eff} is the effective refractive index that is related with the modal gain Γg_m .

Since the denominator of equation 2.77 is proportional to the differential gain coefficient a as can be deduced from equation 2.53, the chirp parameter strongly depends on the wavelength as the differential gain coefficient does (Fig. 2.7). For this reason the chirp increases with longer wavelength [125], as will be experimentally assessed in chapter V.4.

The frequency variation $\Delta\nu$ and the change in the optical phase φ that is caused by chirping can be split into a transient and an adiabatic contribution [126], which are determined by

$$\Delta\nu(t) = -\frac{\alpha}{4\pi} \frac{1}{P} \frac{dP}{dt} + \kappa P \quad \varphi(t) = 2\pi \int_0^t \Delta\nu(t) dt \quad (2.78)$$

where κ is a constant that takes the geometry, the quantum efficiency and the photon energy into account.

Chirping during modulation introduces together with a dispersive transmission link penalties for the reception, especially for modulation with large extinction ratios [127]. A possibility to reduce this unwanted effect is to apply a holding beam that maintains the separation of the quasi-Fermi levels and prevents therefore chirping. On the other hand, benefit can be taken out of the introduced parasitic phase modulation as will be addressed in chapters IV and V.

2.6 Summary

The performance of operation of SOA and RSOA depends on the bias current and the optical input power, which define as pair the bias point. Different applications such as modulation or amplification will exploit different performance in terms of gain, noise figure, induced patterning or modulation bandwidth in different areas of operation, as it is summarized in Table 2.2.

SOA RSOA		optical input power		
		low $P_m < -15$ dBm	medium -15 dBm $< P_m < -5$ dBm	high $P_m > -5$ dBm
bias current	high	high gain and NF for very low input powers, good modulation ER for long devices, capable to modulate the optical phase	gain decreases due to saturation but low NF, good modulation bandwidth for short devices	low gain, NF increases with input power level, strong patterning, large modulation bandwidth for short devices
	medium	moderate gain, moderate-high NF, modulation bandwidth reduced	moderate gain and NF	low gain, higher NF, patterning appears, good modulation bandwidth for short devices
	low	quite low gain, higher NF, low modulation bandwidth	low gain, high NF, low modulation bandwidth	no gain, high NF

Table 2.2. Areas of operation for SOA and RSOA and its exploited performance for their application as light modulator.

Chapter III

A Practical Perspective of SOAs

The experimental operation of SOAs requires not only the careful preparation of the device, it demands also to identify problems with the help of pattern and eye diagram analysis or spectral measurements.

This chapter gives an overview about experimental procedures that go in parallel with the theoretical explanations made in chapter II, starting with a discussion of the physical design of different devices, continuing with a characterization of fundamental properties such as gain and noise emission to evolve later to basic applications such as intensity modulation, though handling already high data rates of 10 Gb/s.

3.1 Introduction

The semiconductor-based version of nowadays optical amplifiers are closely related with Fabry-Pérot laser diodes due to their similar structure. The difference can be found in the anti-reflection elements at the end facets that avoid the presence of typical longitudinal modes in the gain spectrum. Recent designs include anti-reflective coatings, tilted waveguides and window regions to eliminate the reflection of the end facet almost perfectly. This effectively prevents the amplifier from acting as a laser and thus ensures a spectrally flat optical gain over a wide region.

The SOA has a small size, which raises potentially the interest for photonic integrated circuits. Together with its electrically pumping scheme, it becomes less expensive than the EDFA and can be combined with other semiconductor-based devices such as modulators. Its reflective version, the RSOA, consists of a conventional SOA in combination with a rear facet mirror so that the amplified light wave is retro-reflected. The reflective design of the RSOA provides an increased gain due to the double pass of the light through the gain region. Alternatively, the length of the RSOA can be smaller for achieving the same gain magnitude. The performance as amplifier is still not comparable with the EDFA due to its higher noise and the lower gain besides the moderate polarization dependence and high nonlinearity with fast transient time.

However, an additional characteristic is the ability to modulate the incoming signal as reflective modulator, removing the need for a local light source. The SOA has found many applications in optical telecommunication next to the use as intensity or phase modulator [128-130] or more traditionally as gain element in long-haul [131] and access

networks [132]. Some of them are related with wavelength conversion [133-138], optical switching [139-144] signal regeneration [104] and all-optical signal processing [145].

3.2 Principal Amplifier Design

The SOA design originates from the one of a Fabry-Pérot laser diode, whereby anti-reflective coatings are attached to the facets to obtain a travelling-wave amplifier with a smooth optical gain spectrum. Fig. 3.1 shows a typical design for a SOA and an RSOA. The semiconductor chip holds a relative small area that is guiding the light and being pumped via the bias electrode, and eventually small passive sections close to the end facets that act as taper to increase the coupling efficiency from fiber to the chip and vice versa.

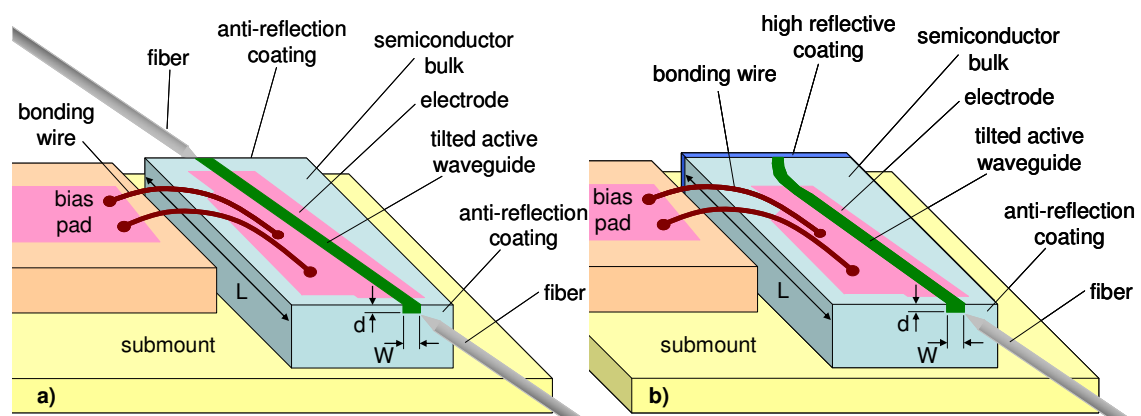


Fig. 3.1. Principal design of (a) a SOA and (b) a RSOA.

While there are two fiber-to-waveguide couplings necessary for the SOA, its reflective version requires only one coupling, which significantly reduces the packaging cost of the latter. However, it has to be noted that SOAs can easily exploit their advantages in photonic integrated circuits where no fiber coupling is required.

Additional lenses or tapered fibers such as in Fig. 3.2 can be used to enhance the efficiency of the fiber coupling since the waveguides are from smaller dimensions (mode size around $1.5 \mu\text{m}$) than the mode-field diameter of a single-mode fiber ($\sim 10 \mu\text{m}$). In addition, a tapered waveguide can be used inside the chip to reduce the large divergence (e.g. $35^\circ \times 27^\circ$) to smaller values (e.g. $17^\circ \times 17^\circ$), thus enhancing the coupling efficiency.

Several optical components used in the light path should be free of reflections and therefore covered with appropriate anti-reflections coatings to prevent the formation of an optical cavity that could lead to lasing effects. For typical small signal gain values provided by nowadays SOAs, the facet reflectivities have to be kept around 10^{-4} or lower for an acceptable ripple in the gain spectrum, and even lower for RSOAs. This can be attained by a tilted waveguide (around $7\text{-}10^\circ$ depending on the desired suppression for the reflection) so that the signal does not arrive perpendicular to the

front and rear facet of the semiconductor chip, and hence reflections are not guided due to an extent beyond the critical angle. What remains is the change in refractive index between semiconductor (~ 3.1) and air. This difference in the optical density can be overcome with anti-reflective coatings, which are provided by appropriate dielectric multi-layer systems.

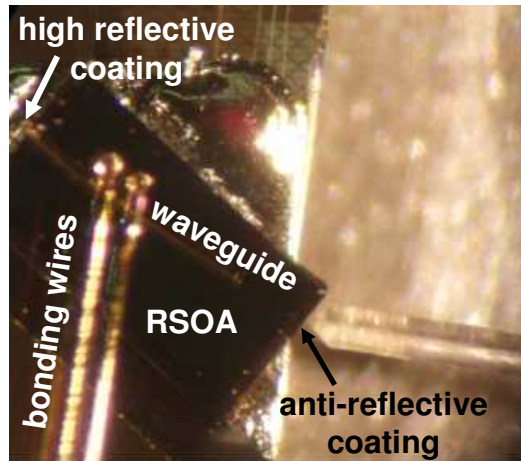


Fig. 3.2. RSOA with waveguide coupling comprising of a tapered fiber.

An electrode is attached to the top of the chip for pumping the amplifying waveguide. The electrode has to be as large as the active region to ensure a uniform injection of carriers. Considering a packaged device, the pump current is typically provided externally via the bias pad, which is connected to one of the pins of the package. The interconnection with the semiconductor chip is made via small bonding wires, which will determine together with the geometry of the bias pad and the electrode on the top of the semiconductor chip the electro-optical response for gain modulation, according to the previous chapter.

Here the RSOA benefits from the fact that its active waveguide is passed twice, which allows shorter designs for keeping the same gain magnitude. Due to the decreased device length and the therefore shorter electrode for the RSOA, the parasitic capacitance can be kept low and the modulation speeds are therefore not that limited as for the SOA. Since there is typically just one electrode present, the DC bias and the high frequency data signals are fed together via the electrical interface. An external bias-T with a sufficient low cut-off frequency is therefore necessary to split the DC bias and the data signals that are delivered for modulation or stem from detection of an incoming optical data signal. A too high cut-off for the low-frequency components of the data signal translates into transient distortions for bit sequences with consecutive digits and appears in the eye diagram as additional “noise” in both, the mark and the space rail.

Besides these conventional SOAs, devices with dual-electrode design exist and allow to perform not only intensity but also phase modulation, which can be also used to enhance the transmission performance of data signals via chirp control [146]. However, there is always a trade-off between performance improvement and cost, and hence, a

multi-electrode design is typically not the preferred choice due to the more complicated packaging.

Typical dimensions for a SOA that is used with intermediate gain values for small-signal amplification are a length L of 400-700 μm , a waveguide width W of 2 μm , and a waveguide thickness d of 1 μm . Nonlinear SOAs can be much longer, reaching up to values around 2 mm.

A packaged SOA device comes normally but not necessarily with a Peltier element and a thermistor that is included in the package, as discussed in the next section. Some products also have a photo diode included to monitor the output signal for the purpose of regulating the current and, in turn, the signal gain [147]. Angled connectors are used for the fiber pigtailed to avoid further reflections, although SOAs with an integrated isolator for booster applications exist too.

3.3 Packaged Devices and Chips-on-Carriers

SOAs and RSOAs can be ordered as bare chip, as chip-on-carrier or inside a butterfly package or a transistor outline (TO) can. While the first two options require to handle the electrical and optical interface in terms of electrical bondings and fiber alignment, a packaged version provides a plug & play solution for incorporating the amplifier directly into a test-bed. However, it should be noted that in the case of using the packaged SOA as intensity modulator, the electrical interface is not accessible for enhancing its electro-optical bandwidth so that the inherent modulation bandwidth depends on the quality of the bonding interface inside the package – which might be not always optimized for modulation purposes. On the contrary, devices that are shipped on a chip carrier allow to exploit the full capabilities in terms of the e/o modulation bandwidth.

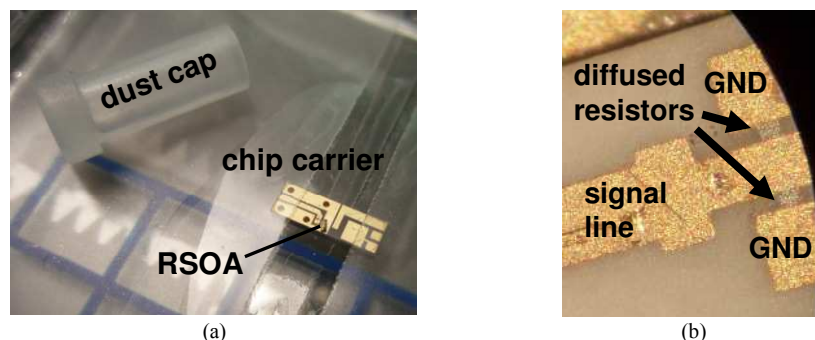


Fig. 3.3. (a) RSOA as chip-on-carrier with a dust cap of a fiber patch-cord next to it. (b) Example for a diffused resistor included on a chip carrier.

Fig. 3.3(a) shows a RSOA as chip-on-carrier version and Fig. 3.4 a possible electrical interface for it. The chip is hereby bonded to a micro-strip line, which leads to a coplanar interface on the edge of the carrier. It is then supposed to provide three electrical connections to a printed circuit board, where one of them supplies the signal for the RSOA and the other two constitute a ground connection besides the signal line.

The carrier is fixed to the support by a thermo-conductive glue to enable the thermo-element (TE), best in form of a Peltier element below the sub-mount of the carrier, to keep a constant temperature for the chip. For the case that the whole sub-mount has to be heated to cure the glue, care should be taken not to harm the electrical connection between the SOA chip and the carrier, which can be sensitive to high temperatures. A thermistor, usually with a negative temperature coefficient (NTC), should then be placed as close as possible to the carrier, e.g. with the help of some thermo-conductive but also isolating paste. The TE and the NTC are connected to a temperature controller (TEC) which provides the necessary control electronics.

Since the impedance of the SOA is much lower than the one of a 50 Ohm matched load as it is common for communication systems with high frequency electronics, impedance matching can be done by simply adding a series resistor with a value that corresponds to the mismatch (typically 39 to 42 Ohm). Important hereby is that this resistor does not introduce a parasitic capacitance or inductance since this will again limit the modulation bandwidth. Note that this matching resistor has to be placed as near as possible to the SOA chip. In some cases a diffused resistor is already added to the micro-strip line of the carrier, as shown in Fig. 3.3(b), so that no external resistor has to be added. The use of this resistor may indirectly cause heating of the chip due to the high currents that are typically needed for driving the SOA.

Modulation bandwidths for data transmission of up to 2.5 Gb/s have been achieved in this way [49] and rates up to 10 Gb/s with an additional passive electrical pre-distorting filter [15].

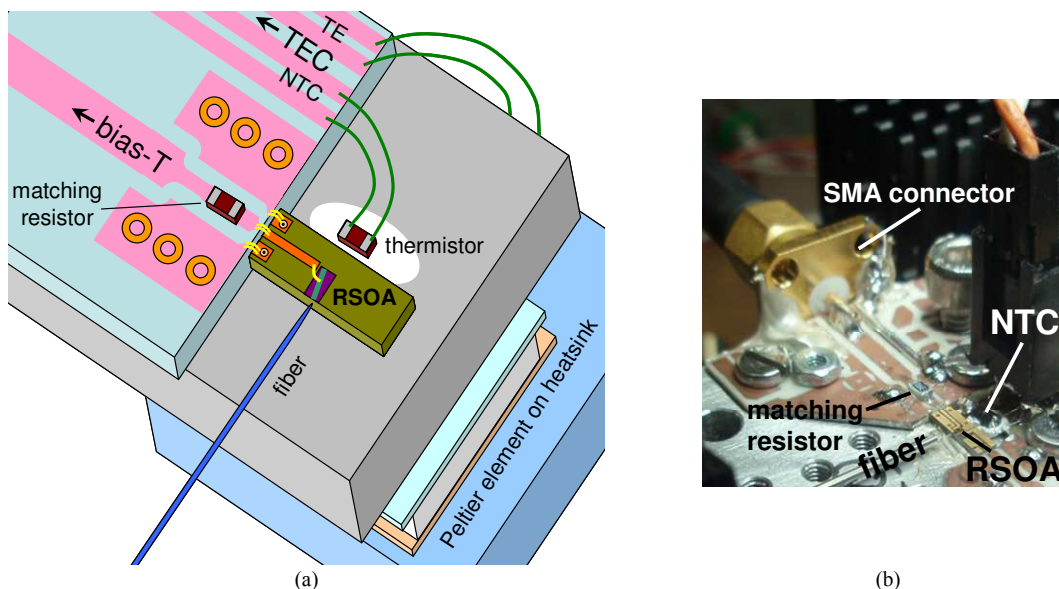


Fig. 3.4. Electrical and thermal interface for a RSOA shipped as chip-on-carrier, (a) scheme and (b) experimental realization.

It is recommended to proof the electrical interface in its electrical reflections to determine eventual problems when being interfaced with radio frequency (RF) amplifiers. Since the SOA has to be also supplied with a constant DC bias current, the bias-T that is included in the electrical interface, best directly in front of the matching

resistor, should be also present during this measurement. The bias-T is normally inserted between RF driver and matching resistor to keep the distance between matching resistor and SOA chip as small as possible. In this way an enhanced ripple in the electro-optical response is avoided.

Fig. 3.5 shows a typical measurement for electrical reflections that derive from the interface of a RSOA in chip-on-carrier version. By adding the matching resistor, the reflections decrease by 10 dB and allow to connect the RSOA with a RF driver. The high frequency ripple that is present in the curve that refers to the case with matching resistor stems from a residual mismatch.

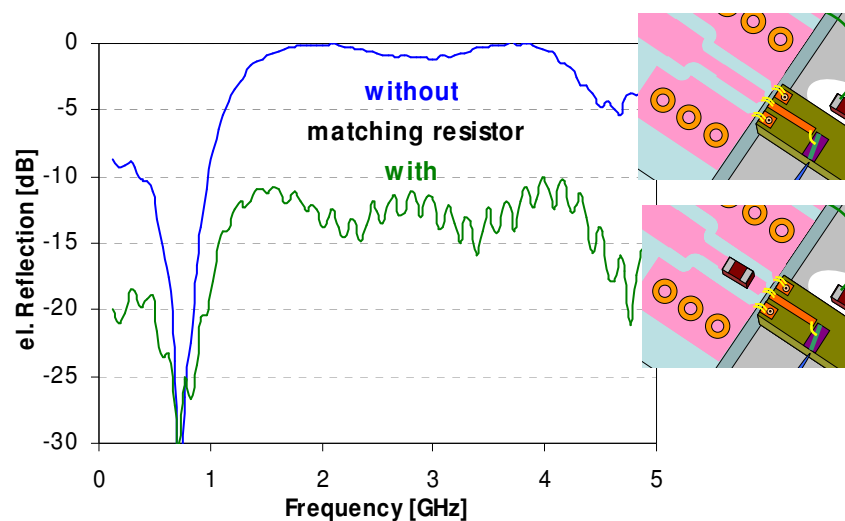


Fig. 3.5. Electrical reflection for a matched and mismatched RSOA interface.

Packaged devices can be integrated together with means of thermal cooling as it is typically the case for devices that come in a butterfly package (Fig. 3.6). Since the space is limited inside the TO-can (Fig. 3.7), which is intended to be used in gadgets where small form-factors that come at reduced cost are necessary, this type of package comes without TE and thermistor so that the temperature inside the TO-can may not be constant.

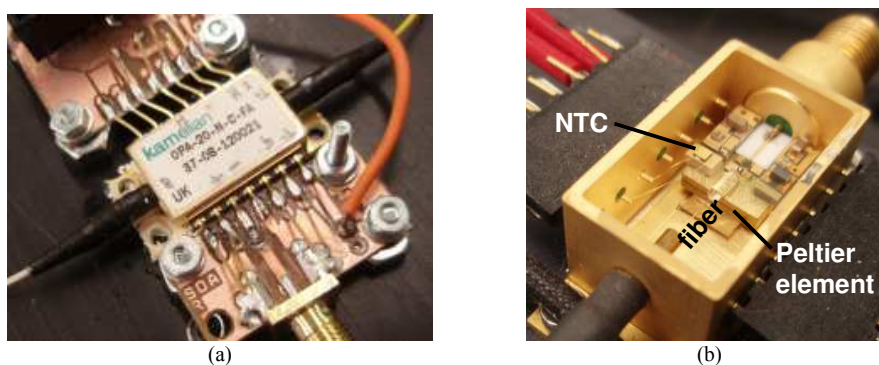


Fig. 3.6. (a) SOA in a butterfly package and (b) Peltier element and thermistor inside a butterfly with a subminiature-A connector.

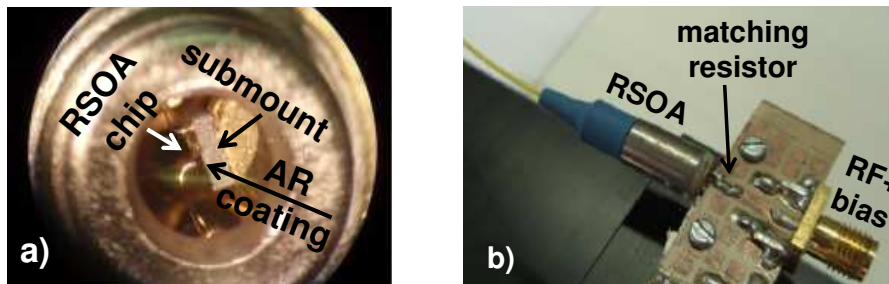


Fig. 3.7. Examples for TO-can RSOA devices: (a) without fiber-coupling, where the fiber comes from the view-plane, and (b) pigtailed version.

While temperature instabilities cause small deviations in frequency-related optical parameters like a shift in the gain ripple, the more critical impacts affect the small signal gain and the electro-optical bandwidth of the SOA, which may both decrease with increasing chip temperature.

The typical pinout of commercial SOAs that are shipped in a 14-pin butterfly package requires a connection between the TE (pins 1,14) and the thermistor (pins 2,5) with a TEC, and the anode and cathode SOA (pins 10,11) together with a probably present photo diode with a current controller, as it is sketched in Fig. 3.8. The whole butterfly package should then be mounted on a heatsink that can be a passive cooler in the simplest case.

Since there are several types of TO-cans with different number of pins, there is no common pin-out for this type of package. However, care should be also taken in the grounding of the outside can for improving the electro-optical bandwidth and the cooling.

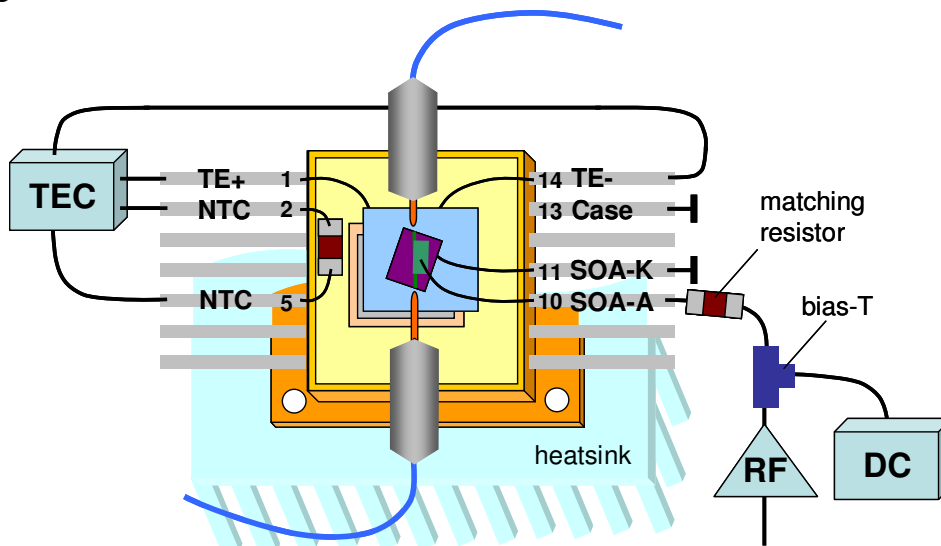


Fig. 3.8. Schematic representation for the operation of a butterfly-packaged SOA.

If the SOA is used as intensity modulator at high data rates, the pins of the butterfly package that lead to the SOA chip should be cut as short as possible to avoid an impedance mismatch due to an improper geometry.

3.4 Optical Properties and Characterization

Before the dynamic behavior of the RSOA is investigated, its static properties are characterized to determine not only the spectral operation range but also the best operation point in terms of biasing. This includes the measurement of the ASE spectrum and imperfections such as gain ripple and polarization dependent gain (PDG).

With respect to gain modulation, the gain/current relation is explored to obtain the exact operation regimes of the RSOA such as transparency and saturation region. The borders of these regimes will determine the bias settings and the swing of the modulation current. Finally, the dependence of the gain bandwidth and the noise figure on the input power level is analyzed.

Most of the measurements reported in the following sections have been carried out with a buried-ridge RSOA that has an efficient current injection and a small confinement factor of $\Gamma \sim 20\%$. The latter allows to provide a relative low noise figure and a large optical bandwidth [49]. The InGaAsP active zone of the RSOA that was mounted as chip-on-carrier was grown using molecular beam epitaxy and the low optical confinement was achieved by surrounding the gain layer with confinement layers of InGaAsP with a larger band gap.

3.4.1 ASE Spectrum and Gain Ripple

The gain ripple gives an idea about the reflection at the facets of the semiconductor chip. Fabry-Pérot modes appear in the spectrum due to feedback that is provided in terms of reflections at the in- and output of the travelling-wave SOA. A detailed analysis will be given in chapter V.2.

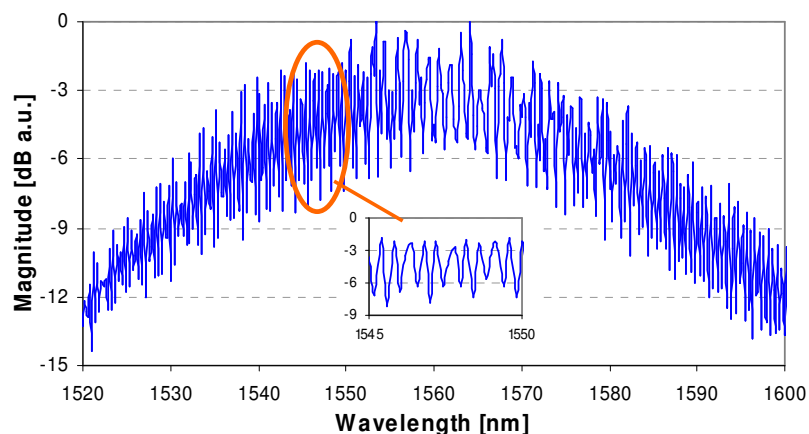


Fig. 3.9. ASE spectrum of an RSOA with high small signal gain. A reflection in the fiber pigtail causes a strong gain ripple.

The reflections that influence the gain spectrum may not only derive from the facet of the SOA but also from the optics of the fiber-to-chip coupling such as the fiber pigtail. The ripple is therefore sometimes not uniform. Fig. 3.9 shows a typical ASE spectrum for a RSOA with a high small signal gain of 26 dB, where a residual reflection from a

fiber pigtail was present. As can be seen, a return loss of about -40 dB can already cause serious degradations in an originally smooth ASE spectrum.

As will be shown later in chapters V.2 and V.3, an artificially introduced gain ripple can be, together with means of wavelength stabilization of the data signal, beneficially used for demodulation purposes.

3.4.2 Polarization Dependent Gain

The polarization dependence of the small signal gain can vary with the device, depending on its design. The origin of PDG is the light-heavy hole transition split, which translates to a different response of the TM / TE mode due to different confinement factors.

While for low PDG devices values of <1 dB can be reached, the gain can differ in more than 10 dB between the TE- and TM-mode for SOAs with high PDG.

3.4.3 Gain Saturation and Transparency Threshold

SOAs suffer from a limited optical output power and low saturation power values when being compared with other optical amplifiers. As it is usual for amplifiers, a certain amount of pump has to be provided to drive the SOA, whose waveguide introduces some loss, into a transparent state. An important measure for the saturation and transparency of a SOA is its gain-current relation.

As can be seen in Fig. 3.10, the G/I curve, which is shown for a low input of -20 dBm and a RSOA with a gain peak at 1565 nm, does not have a strict bend at the threshold region as it is the case for laser diodes. Note that in this and following measurements an optical spectrum analyzer was used, which allows to discriminate the signal from the noise background and thus avoids inaccuracies when working with small optical signals.

Three regions can be distinguished for the applied bias current: the threshold region where the RSOA becomes transparent and provides a small gain, the linear region where the differential gain dG/dI is constant, and the saturation region where the differential gain is not constant anymore and decreases with the applied bias current.

The transparency threshold current, defined for a gain of 0 dB, and the differential gain depend on the operating wavelength due to the material gain of the semiconductor chip that shows a spectral preference. For the application as intensity modulator, the RSOA current should be slightly above the threshold for the space bits while it should be as high as possible for the mark bits. Due to the spectral sensitivity of the transparency of the RSOA, the DC bias point has to be adjusted according to the operating wavelength to achieve an optimal extinction ratio (ER).

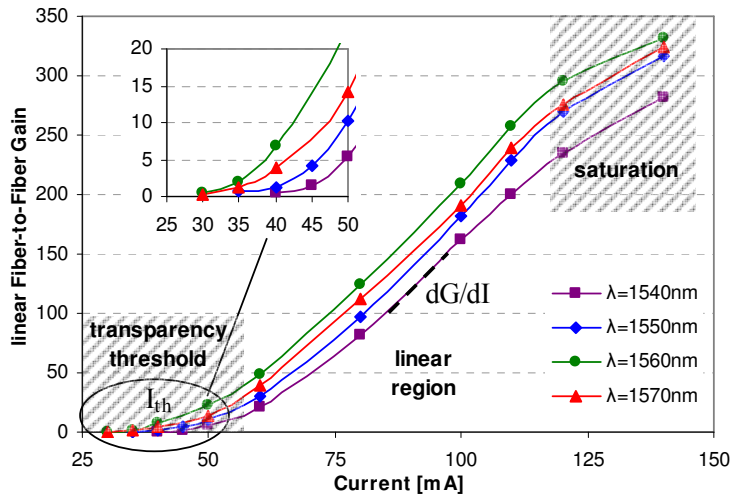


Fig. 3.10. Gain-current relation for a RSOA with an input power of -20 dBm.

3.4.4 Gain Spectrum and Gain Bandwidth

The spectral response of the gain depends on the spectra for the material gain and its loss and is seen as the average gain in the presence of a gain ripple. For the given RSOA, Fig. 3.11(a) shows the gain spectrum for different input power values and a fixed RSOA bias current of 100 mA.

The typical figure of merit for the spectral response of the gain is the small-signal gain bandwidth, which is typically measured within the wavelengths that correspond to a 3-dB compression, referenced to the peak gain. It is hereby important to recall that optical amplifiers suffer from saturation, which occurs for increased input power values. Considering an input of -15 dBm as small-signal operation, the 3-dB gain bandwidth is 64 nm. Looking at high input power values, the obtained gain vanishes rather quickly with increased input power, while the gain spectrum flattens and leads to larger gain bandwidths since there is still gain provided at the edges of the small-signal gain spectrum.

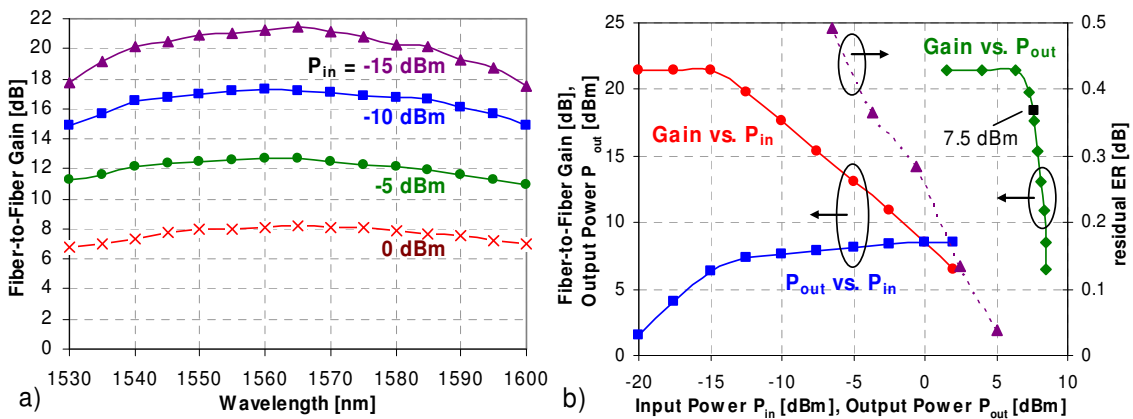


Fig. 3.11. (a) Gain spectrum for a bias current of 100 mA and (b) behavior in the saturation regime for a wavelength of 1550 nm.

The behavior of the RSOA in terms of saturation is presented in Fig. 3.11(b), where the gain is shown as function of the input and output power, respectively, for an operating wavelength of 1550 nm and a RSOA bias current of 100 mA.

The 3-dB penalty of the small-signal gain is reached with an input power of -11.5 dBm, which corresponds to an output power of 7.5 dBm. Note that this behavior can be advantageously used to erase fluctuations of the optical power in the input signals, e.g. when a data pattern is imprinted with not too high ER.

For the case that the inverse of the data rate is larger than the gain relaxation time, the RSOA is “fast” enough to follow the data pattern and the space bits can experience a higher gain than the mark bits. This mechanism of pattern suppression, which will also find application in chapters IV and VI.2, becomes interesting once the mark bits experience saturation, so that the difference in gain determines the reduction of the ER for the pattern. Fig. 3.11(b) shows an example where the input signal of the RSOA had an ER of 5 dB, which was reduced to below 0.5 dB when the average power of the input signal was above -6.5 dBm. However, it has to be noted that the noise figure is different for the residual mark and space bits, as will be discussed in the next section.

3.4.5 Noise Figure

SOAs have generally higher noise figures than fiber-based amplifiers. Typical values for the noise figure are 6 to 8 dB for SOAs and 8 to 10 dB for RSOAs. The exact performance depends on the design parameters of the semiconductor chip such as the confinement factor.

The impact of ASE noise generated by the SOA depends on the signal gain that is obtained when the signal passes the amplifier. Fig. 3.12 shows a typical dependence on the optical input power for the mentioned RSOA. According to the theoretical investigation in chapter II, two regions can be distinguished, showing a slight increase in the noise figure for too weak signals with power levels below -22 dBm, where the RSOA does not reach a high signal output due to a limited small signal gain while noise is added, and too high signal levels above -15 dBm, which drive the RSOA into saturation.

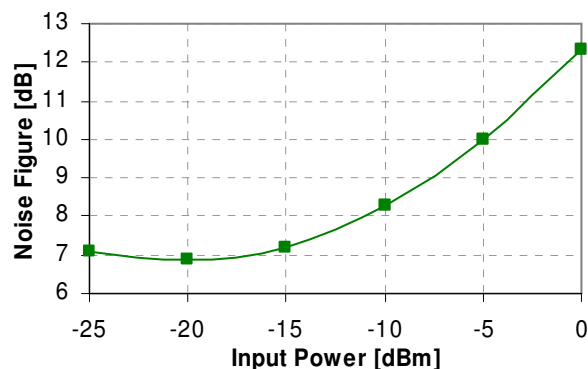


Fig. 3.12. Noise figure for a bias current of 100 mA and a wavelength of 1550 nm.

It is therefore not necessarily preferred to have a high input power values as it is the case for fiber-based optical amplifiers that are in contrary capable to handle stronger input signals when applying strong pumps due to their high saturation output power.

Note. Although SOAs offer capabilities for optical signal processing and intensity modulation, they are less competitive when being used as optical amplifier and compared with other fiber-based solutions such as EDFAs or Raman amplification. On the other hand, since the gain spectrum can be modified easily by changing the design of the semiconductor material, SOAs can offer their capabilities in spectral regions that cannot be covered by fiber-based amplifiers due to the lack of suitable dopands.

	(R)SOA	EDFA	Raman	
Gain	moderate, >20	high, >30	moderate, >20	dB
Response	wide, 1280-1650	narrow, 1530-1620	wide, 1280-1650	nm
Gain Bandwidth	wide, 60	moderate, 30-60	pump dependent	nm
Sat. Output Power	low, 15	high, 20	0.5 Pump	dBm
PDG	present, 0.5	insensitive, 0	insensitive, 0	dB
Noise Figure	high, 6-10	low, 5	low, 5	dB
Pump	<400 mA	25 dBm	>30 dBm	
Time Constant	0.2 ns	10 ms	fs	
Size	compact	bulky	bulky	
Gain Modulation	yes, up to 7 GHz	no	no	
Cost	low	medium	high	

3.5 SOAs in Applications as Intensity Modulators

Intensity modulation occurs by controlling the bias current of SOAs, which corresponds to the pump of the amplifier, and thus the gain. Since the dimensions of RSOAs are smaller, large electrodes as it is the case for SOAs and therefore large parasitic capacitances can be avoided. The reflective devices are therefore typically used as intensity modulators.

The figures of merit for this specific application of RSOAs are a large modulation bandwidth, as it is discussed in chapter II.3, and a high ER for the amplitude shift keying. Unfortunately, a natural trade-off between these two figures is given, since a high e/o bandwidth is typically reached only with a high bias current setting.

3.5.1 Operational Bias Point

The proper DC bias point is chosen in a way so that the electrical data signal, which is added via the bias-T, leads to a current slightly above the transparency threshold for the

spaces in the bit stream, and to a current which does not exceed the maximum rating of the SOA for the marks. In this way the ER of the output signal is maximized, which is desired for having a good sensitivity at the receiver, as it will be explained later in chapter IV.2.

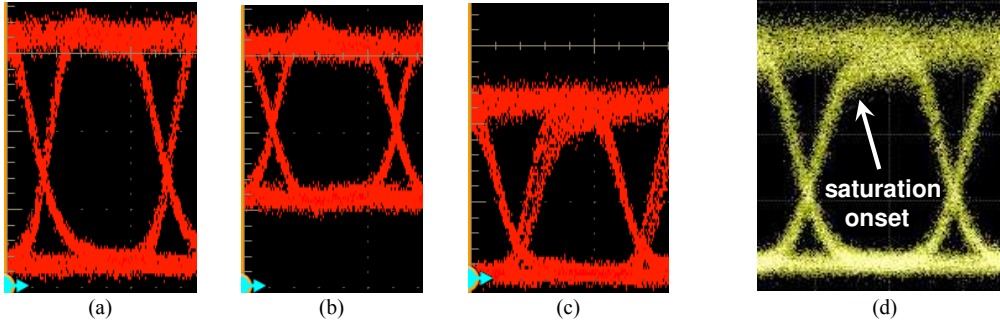


Fig. 3.13. Bias point setting via the eye diagram: (a) optimum bias, (b) too high bias, (c) too low bias. The blue arrow on the left of indicates the reference level. (d) Eye distortion due to the saturation onset.

However, when SOAs are used as modulators, the ER might not always be optimized since the transparency threshold is in general much smoother than for laser diodes. The optimum bias setting, shown in Fig. 3.13(a), corresponds then not only to a slightly asymmetrical eye diagram but has also a reduced ER that is nevertheless still above 6 dB for typical components. A too high DC bias is visible due to the strongly reduced ER and the reduced eye height due to saturation of the mark level, as can be seen in Fig. 3.13(b). On the other hand, if the bias is too low as in the case of Fig. 3.13(c), the eye is highly asymmetrical and problems in the rising edge appear due to the operation below the quasi-threshold level, though the ER would tend towards infinite.

Note that the bias current that corresponds to the marks in the bit stream has to be chosen according to the saturation characteristics of the SOA. If there is a strong gain saturation, it is visible in a broader rail in the mark level of the eye diagram as it is indicated in Fig. 3.13(d). This is due to the saturation onset that is passed when the current raises above the saturation knee of the gain-current relation.

Considering operation in the linear regime of the SOA, the optical output power P_{out} contains the modulation of the electrical signal with power p_{RF} that is imprinted on the continuous-wave optical input signal P_{in} according to

$$P_{out}(t) = P_{in} \left(G(I_{dc}) + \frac{dG}{dI} i_{pp}(t) \right) \quad i_{pp}(t) = 2\sqrt{2} \sqrt{\frac{p_{RF}[W]}{50\Omega}} \quad (3.1)$$

where I_{dc} is the DC bias current and i_{pp} the peak-to-peak modulation current that is applied to the SOA via a high frequency interface that is terminated for a 50 Ohm adaptation. Table 3.1 shows the conversion for recently used values.

Prf dBm	Prf mW	Up-p Vpp	Ip-p mApp	Prf dBm	Prf mW	Up-p Vpp	Ip-p mApp	Prf dBm	Prf mW	Up-p Vpp	Ip-p mApp
-30	0.001	0.02	0.4	-10	0.1	0.20	4.0	10	10	2.00	40.0
-29	0.001	0.02	0.4	-9	0.13	0.22	4.5	11	12.59	2.24	44.9
-28	0.002	0.03	0.5	-8	0.16	0.25	5.0	12	15.85	2.52	50.4
-27	0.002	0.03	0.6	-7	0.20	0.28	5.7	13	19.95	2.83	56.5
-26	0.003	0.03	0.6	-6	0.25	0.32	6.3	14	25.12	3.17	63.4
-25	0.003	0.04	0.7	-5	0.32	0.36	7.1	15	31.62	3.56	71.1
-24	0.004	0.04	0.8	-4	0.40	0.40	8.0	16	39.81	3.99	79.8
-23	0.005	0.04	0.9	-3	0.50	0.45	9.0	17	50.12	4.48	89.5
-22	0.006	0.05	1.0	-2	0.63	0.50	10.0	18	63.10	5.02	100.5
-21	0.008	0.06	1.1	-1	0.79	0.56	11.3	19	79.43	5.64	112.7
-20	0.010	0.06	1.3	0	1	0.63	12.6	20	100	6.32	126.5
-19	0.013	0.07	1.4	1	1.3	0.71	14.2	21	125.9	7.10	141.9
-18	0.016	0.08	1.6	2	1.6	0.80	15.9	22	158.5	7.96	159.2
-17	0.020	0.09	1.8	3	2.0	0.89	17.9	23	199.5	8.93	178.7
-16	0.025	0.10	2.0	4	2.5	1.00	20.0	24	251.2	10.02	200.5
-15	0.032	0.11	2.2	5	3.2	1.12	22.5	25	316.2	11.25	224.9
-14	0.040	0.13	2.5	6	4.0	1.26	25.2	26	398.1	12.62	252.4
-13	0.050	0.14	2.8	7	5.0	1.42	28.3	27	501.2	14.16	283.2
-12	0.063	0.16	3.2	8	6.3	1.59	31.8	28	631.0	15.89	317.7
-11	0.079	0.18	3.6	9	7.9	1.78	35.7	29	794.3	17.83	356.5
-10	0.100	0.20	4.0	10	10.0	2.00	40.0	30	1000.0	20.00	400.0

Table 3.1. Conversion between RF power and voltage / current swing for a load of 50 Ohms.

3.5.2 Electro-optical Response and Modulation Bandwidth

As discussed in chapter II.3, the bias current and the optical input power have strong impact on the modulation bandwidth. Fig. 3.14 presents typical responses for a commercial TO-can RSOA that is not necessarily intended to be used as modulator. This RSOA experiences a tilt in the roll-off of the electro-optical response when the input power is increased from -15 to -10 dBm so that the 3-dB modulation bandwidth is extended from 450 to ~750 MHz, which would be already sufficient high for the application as 1 Gb/s intensity modulator. The chosen bias current is less critical for this specific device as can be seen for an increase of 20 mA that leads to just a small improvement, which also comes at the cost of an increased gain for the space bits and therefore a reduced ER.

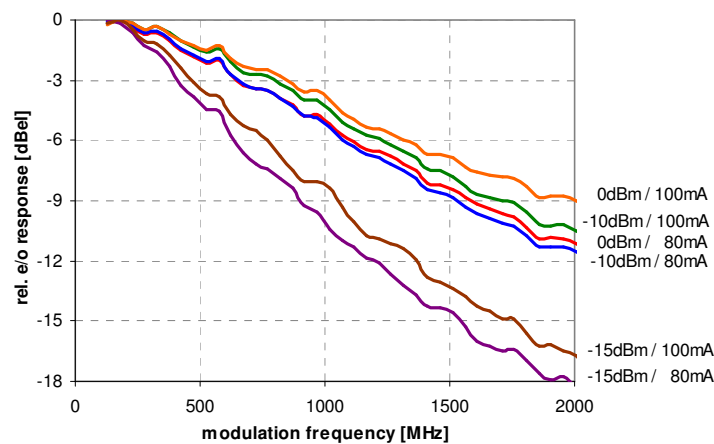


Fig. 3.14. Electro-optical response for a commercial low-cost RSOA in a TO-can package.

The modulation bandwidth of the chip-on-carrier device that was characterized in its gain and noise figure in the previous section is shown in Fig. 3.15. The better RF interface allows an electro-optical 3-dB bandwidth of 2.5 GHz for the RSOA, when the

input power and the bias current are -15 dBm of 100 mA, respectively. The sub-mount of the semiconductor chip prevented a continuous roll-off up to ~ 7.2 GHz. With the insertion of a passive equalizer that consists of resistors and capacitors in the RF path at the input of the RSOA, the bandwidth can be extended to 7.2, 7.1 and 6.9 GHz for input power values of -15, -20 and -25 dBm. Fig. 3.15(a) depicts the simulated transfer function of the equalized RSOA that derives from its measured, unequalized response and the transfer function of the RC-equalizer, while Fig. 3.15(b) shows experimental measurements before and after equalization. The electrical losses that were caused by this filter were ~ 6 dB.

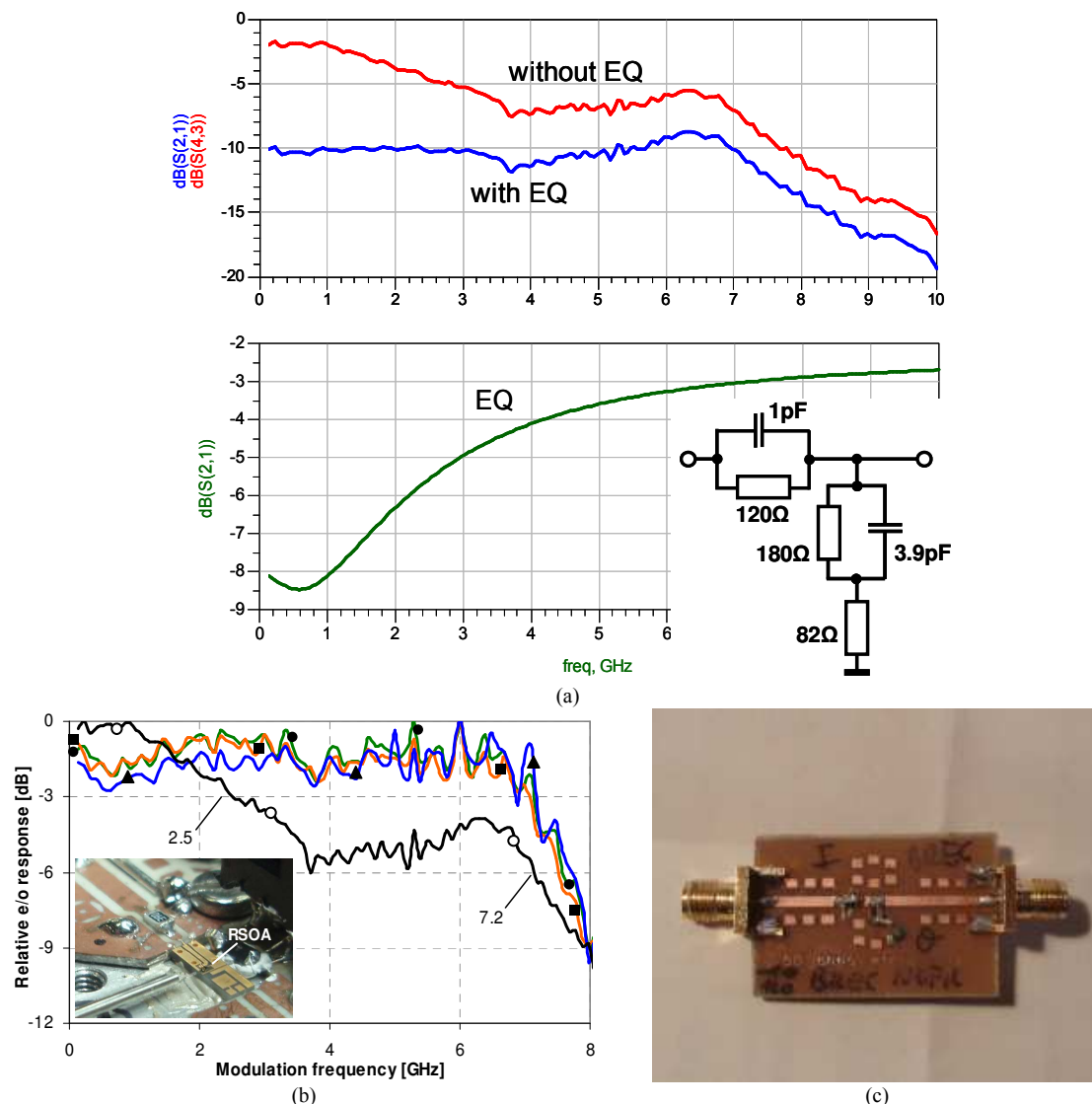


Fig. 3.15. (a) Simulated equalization through shown RC-circuit. (b) Electro-optical response of the RSOA without (o marker) and with passive RC-equalizer for a bias current of 100 mA. The ●, ■, ▲ markers indicate an RSOA input power of -15, -20 and -25 dBm, respectively. (c) Passive RC-circuit that was used for pre-distortion.

Note that the modulation bandwidth of this RSOA prototype is 5 to 10 times higher than the one of commercial devices. However, since the yield of RSOAs with high electro-optical bandwidth is always limited for a run of new devices and no specific equalizers

can be placed for particular devices in commercial products, the nominal bandwidths are typically rated lower in terms of a guaranteed value.

I_{bias}	$P_{\text{in}} = -15 \text{ dBm}$		$P_{\text{in}} = -20 \text{ dBm}$		$P_{\text{in}} = -25 \text{ dBm}$	
	$f_{e/o}$	ER	$f_{e/o}$	ER	$f_{e/o}$	ER
85 mA	6.8	7.1	6.7	7.8	6.4	8.1
100 mA	7.2	6.1	7.1	7.2	6.9	8.0
120 mA	7.4	4.4	7.3	6.3	7.3	7.6

Table 3.2. Electro-optical modulation bandwidth and ER of the RSOA. Values are shown in Decibels for the equalized RSOA at a wavelength of 1550 nm.

With a bias of 100 mA and a peak-to-peak modulation current of 100 mA_{pp} at a data rate of 10 Gb/s, ERs of >6 dB can be obtained at 1550 nm (Table 3.2), except for the case where the gain becomes saturated due to a high input power. A further increase of the ER is prohibited by the demand for a high bandwidth. The dependence of the ER on the bias point is given by the transparency current I_{th} and the differential gain coefficient dG/dI , which can be derived from the gain-current relation and depend on the operating wavelength (Fig. 3.10).

A simple PON setup, presented in Fig. 3.16(a), was used to evaluate the applicability of the RSOA device under conditions of a high loss budget (i.e. a low input power into the RSOA for a moderate launch). The PON was constituted by a dual-feeder standard single mode fiber (SMF) of 10 km length, and an attenuator (A_D) that emulates the loss of the power splitter that is typically placed in TDM- and hybrid PONs. Bidirectional transmission is supposed to take place on two different wavelengths as it is common for nowadays PON standards. Waveband splitters, here for separation of the C- and L-band, were therefore inserted at the OLT and the ONU. The launched power of the carrier at 1550.92 nm that is used as seed for upstream modulation at the ONU was fixed to 3 dBm at the OLT transmitter but could be in principle increased since Rayleigh backscattering is avoided with the dual-feeder configuration when no drop fiber is present at the same time.

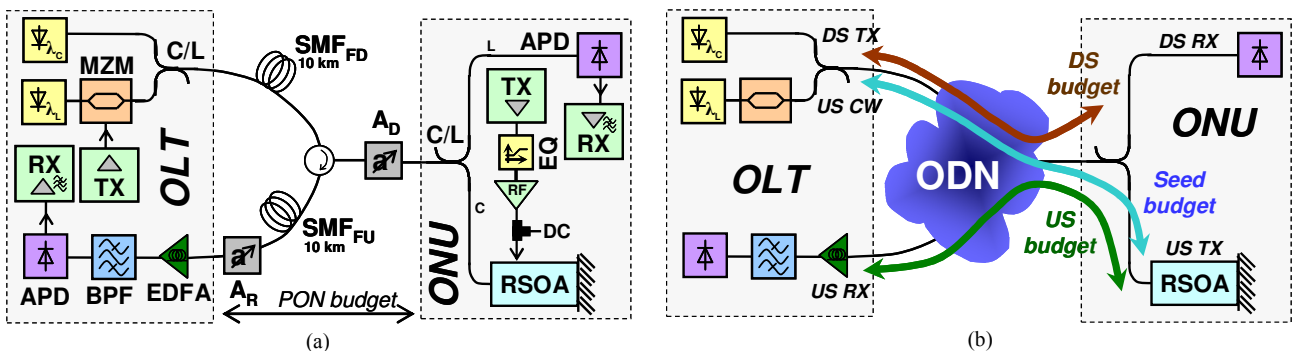


Fig. 3.16. (a) Experimental setup used for evaluating the applicability of the RSOA device in a dual-feeder fiber PON with high loss budget. (b) Definition of the loss budgets in case of the loop-back configuration with reflective, remotely seeded upstream modulator

The RSOA was biased at 100 mA and modulated at 10 Gb/s with 100 mA_{pp}, according to its characterization. The pseudo-random bit sequence (PRBS) for the upstream was

chosen with lengths of $2^{31}-1$ and also 2^7-1 to investigate the transmission performance of continuous data streams equivalent to GPON and EPON payloads. The OLT receiver comprised an EDFA with a noise figure of 4.7 dB, an optical band-pass filter (BPF) with a bandwidth of 100 GHz that was centered with respect to the upstream wavelength and an avalanche photo diode (APD). An attenuator (A_R) was placed for evaluating the sensitivity of the upstream reception. For the downstream transmission, a Mach-Zehnder modulator (MZM) with an ER >10 dB was used after a laser diode. The data was modulated on a carrier at 1590 nm with 10 Gb/s and the launched power from the OLT transmitter was 0 dBm.

The transmission performance for down- and upstream was evaluated in terms of bit error ratio (BER) measurements. This is a common practice that will be followed also in later experiments. The input power levels into the receivers of ONU and OLT are thereby varied with the help of attenuators (A_D , A_R) to evaluate the reception sensitivity for the two data streams at certain BER levels. As a figure of merit, the power margin is thereby defined as the difference between the delivered power at the receiver and the reception sensitivity. The available power is in turn given by the launched power at the down- and upstream transmitter, the loss budget of the PON and the amplification that is achieved in the fiber plant.

Two representative BER levels are typically considered: a BER of 10^{-10} that is supposed to be low enough to allow transmission without additional data encoding and proper operation of end-user applications, and a BER of 10^{-4} , which enables transmission in conjunction with a Reed-Solomon (255,239) forward error correction (FEC) [148,149] as it is proposed for GPON systems. This in turn allows to define a FEC gain as the difference between the sensitivities at the BER levels of 10^{-10} and 10^{-4} , which can be alternatively seen as an increase in the power margin for the case that FEC is incorporated in the electronics of the receiver.

Three loss budgets have to be distinguished for a bidirectional transmission in a PON with separate wavelengths for down- and upstream and a remotely seeded reflective modulator, as it is introduced in Fig. 3.16(b). Next to the transmission budgets across the optical distribution network (ODN) that are given by the launch conditions at the transmitters of the OLT and the ONU and the sensitivities of the ONU and OLT receivers, the seed conditions of the RSOA can cause limitations to the overall PON budget. The three chosen input seed power values of -15, -20 and -25 dBm of the RSOA limit together with the given launch for the upstream wavelength at the OLT the PON budgets to 18, 23 and 28 dB (Table 3.3). The mentioned seed power values lead to ONU output power levels of 3.9, 2.6 and -0.3 dBm, and the corresponding OSNR values after upstream modulation are 34.7, 31.1 and 26 dB at the ONU output.

The sensitivity for the downstream was -24.1 and -24.5 dBm at a BER of 10^{-10} for the back-to-back case and with feeder fiber (Fig. 3.17). A loss budget of 24.5 dB can be covered, and could be improved with a higher launch from the OLT. Alternatively, the incorporation of FEC would improve the sensitivity by ~3.5 dB.

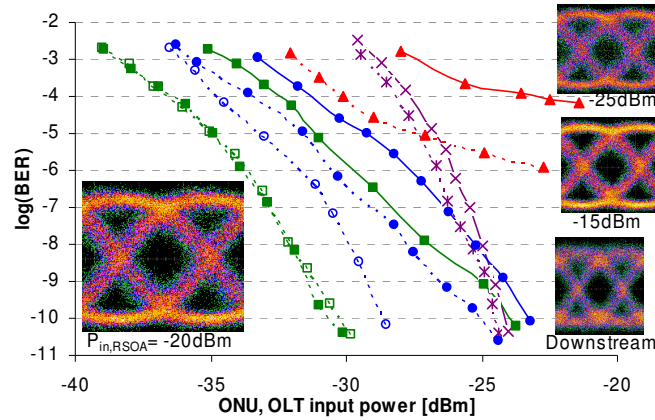


Fig. 3.17. BER measurements at 10 Gb/s for down- (\times markers) and upstream for the back-to-back case (dotted) and the presence of a feeder fiber (solid lines). Filled markers represent a PRBS of $2^{31}-1$ and hollow markers a PRBS 2^7-1 . The $\bullet, \blacksquare, \blacktriangle$ markers correspond to an RSOA seed of -15, -20 and -25 dBm, for which the insets show the eye diagrams for a present feeder fiber.

For the upstream in the back-to-back case, the best performance is given for an RSOA seed of -20 dBm, which is supported by two aspects; First, the OSNR degrades for lower seeds at the RSOA, whereby not only at the amplification at the RSOA is responsible but also at the optical OLT receiver due to the higher loss budget in the transmission path that sets the lower seed. This noise degradation leads to an error floor above a BER of 10^{-10} . Second, higher input power values for the RSOA induce transient distortions. The latter is visible in the patterning effects that translate to a penalty of 3.6 dB for the PRBS of length $2^{31}-1$, compared to a word length of 2^7-1 . This penalty vanishes for a seed as low as -20 dBm (Fig. 3.17). The sensitivities for upstream reception at a BER of 10^{-10} and a PRBS length of $2^{31}-1$ are -25 and -30.6 dBm for RSOA seed values of -15 and -20 dBm, respectively. Despite the good upstream sensitivity, the loss budget is here limited by the seeding conditions of the RSOA and therefore to 18 and 23 dB. Upstream reception is possible for an RSOA seed of -25 dBm with FEC, leading to a sensitivity of -30.1 dBm and therefore a budget of 28 dB would be compatible.

With the presence of the feeder fiber in the upstream transmission path, higher penalties than for the downstream are introduced. This stems from the higher chirp of the RSOA when compared to the negligible low one of the MZM. A multi-electrode RSOA design could be applied to reduce the influence of the chirp [146]. However, with the high gain of the RSOA the upstream loss budgets that can be covered are 27.2, 26.5 and 22.8 dB for a PRBS length of $2^{31}-1$. The budget is therefore still limited by the seed conditions for an RSOA input power of -15 and -20 dBm. The high FEC gain for the upstream could lead to a covered budget of 35 dB for an RSOA seed of -20 dBm.

The loss budget is therefore limited by the upstream due to the seeding conditions of the RSOA. However, with stronger transmitters at the OLT, incorporating also booster amplifiers, more balanced budgets reaching up to the GPON class B+ or the 10G-EPON class PR20 could be obtained.

$P_{in,RSOA}$ [dBm]	-15		-20		-25	
at BER:	10^{-10}	10^{-4}	10^{-10}	10^{-4}	10^{-10}	10^{-4}
$P_{out,RSOA}$ [dBm]	3.9		2.6		-0.3	
DS budget [dB]	24.1	27.6	24.1	27.6	24.1	27.6
Seed budget [dB]	18		23		28	
US budget [dB]	27.2	35.3	26.5	35	-	22.8

Table 3.3. Operational parameters and obtained loss budgets.

This experimentally proof stresses the maturity of RSOA devices for 10 Gb/s modulation in PONs with high loss budgets [15]. Modulation with higher data rates often requires to take benefit of the additional phase modulation that SOAs are introducing when their bias current and therefore the carrier density and in turn the refractive index inside the active waveguide are changed. These chirp-managed transmission schemes [150] also require means of phase-to-amplitude conversion elements such as detuned optical filters, which introduce significant additional losses (in the order of ~ 7 to 10 dB) at the receiver. Therefore, if the RSOA has a sufficiently high modulation bandwidth, not only a simpler OLT receiver design but also a more cost-efficient and less power consuming solution is given.

3.5.3 Optical Response and Patterning

As addressed in chapter II.4, the optical gain response is not completely flat for the signal spectrum so that especially lower spectral components are affected when the SOA is driven into saturation.

Fig. 3.18 shows the measured optical-optical response and the dependence of the low-frequency cut-off and the gain excursion on the bias conditions of the SOA.

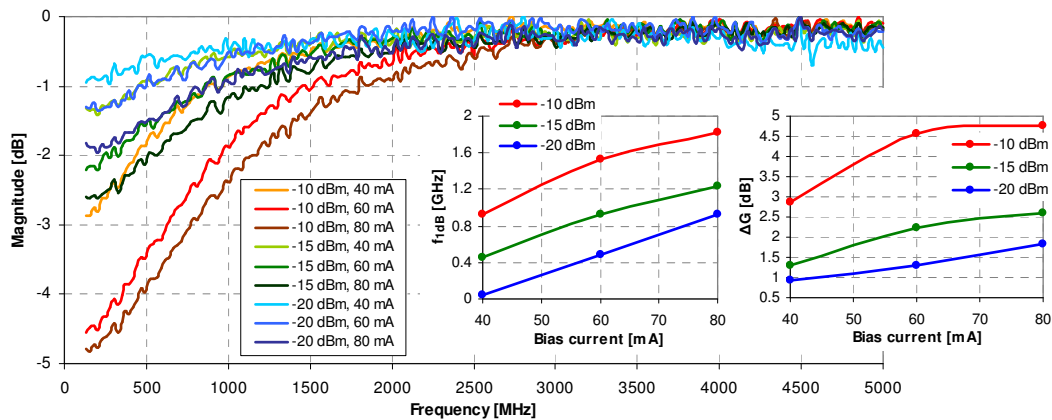


Fig. 3.18. Optical-optical response for different input power levels and bias currents. The insets show the cut-off frequency for the 1-dB deviation point (left) and the gain excursion at 300 MHz (right).

Transient distortions in the eye diagram can appear due to a non-uniform response and can be reduced by means of gain clamping or operation of the SOA in a more linear regime. The first approach cannot only be achieved via an additional holding beam but also by an ASE noise background. This might be interesting in transmission links where

the SOA is fed by a weak signal so that the ASE from the SOA is overcasting the applied ASE background for the purpose of gain clamping.

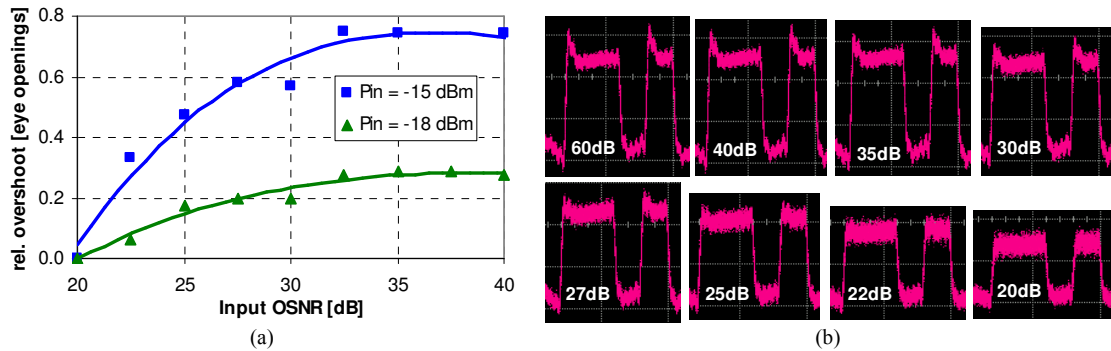


Fig. 3.19. (a) Relative overshoot in the mark level as function of the input OSNR of the SOA and (b) bit pattern for an input of -18 dBm for various OSNR values.

Fig. 3.19 shows the relative overshoot in the mark level of a bit stream, referenced to the eye opening, as function of the OSNR at the input of the SOA. With decreased OSNR, the overshoot is suppressed, however, at the cost of some eye closure.

3.6 Chirp

Modulating the SOA always results in chirping of the optical signal since the modulation of the bias current results in a carrier density variation and therefore in a modulation of the refractive index, leading also to phase modulation of the signal. The α -parameter determines the residual chirp after modulation and can be simply measured with a network analyzer [151]. The method is based on an investigation of the fiber transfer function for long link spans, which show dips in the response due to the interplay of chirp and fiber dispersion [152,153]. Alternatively, the chirp parameter of semiconductors could be also determined with an investigation of the optical output spectrum, by measuring the mode gain and wavelength shift of the spectral modes [154].

3.6.1 Measurement

The weak interplay between chirp and fiber requires large amounts of accumulated dispersion for the accurate measurement of the chirp parameter. Link spans of 100 km or more are typically needed. For this reason EDFAs and optical filters have been therefore inserted between the chirped transmitter and the receiver to account for the link losses but do not distort the results due to their transparent nature.

The response of the fiber span is shown in Fig. 3.20 for a DML and a RSOA, respectively. As can be seen, the first dip appears at significantly lower frequencies for the RSOA, proving that the chirp parameter of this device is larger. While the response of the DML was acquired at a wavelength of 1545 nm and a link span of 100 km, the response of the RSOA was obtained at a wavelength of 1532 nm and a link span of 125

km. The bias point of the RSOA was chosen with 120 mA and -8 dBm for this measurement. An important point is not to use predistorting electrical filters that have a strong roll-off in their transfer function at higher frequencies since the overall transfer function of the transmission system will show severe distortions.

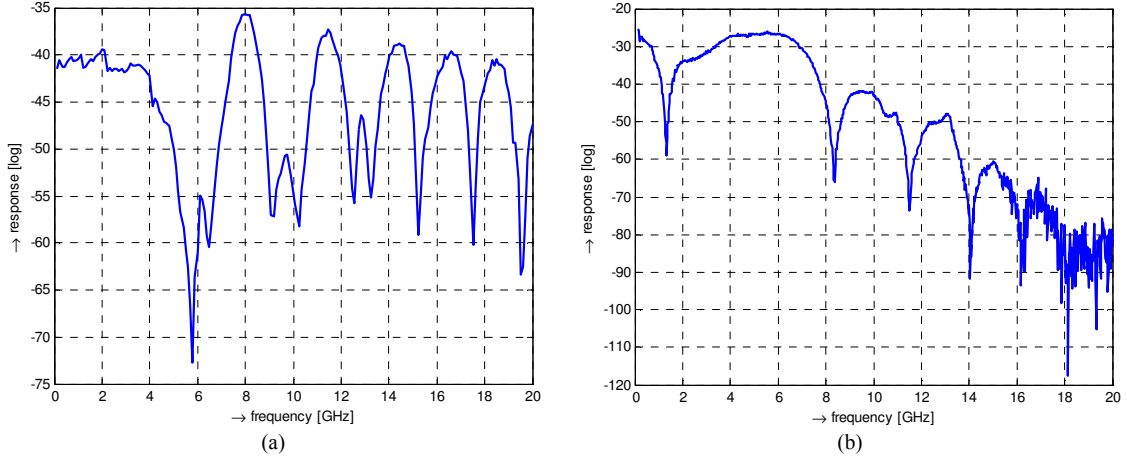


Fig. 3.20. Small-signal response of the fiber for (a) the DML and (b) the RSOA.

According to the frequency spacing of the dips in the fiber response, the dispersion of the fiber and the chirp parameter can be determined. The resonant frequency f_i of the dip with index i is related to the fiber length L , the dispersion D and the chirp parameter α via

$$f_i^2 L = \frac{c}{2D\lambda^2} \left(1 + 2i - \frac{2}{\pi} \arctan(\alpha) \right) = ki + d \quad (3.2)$$

This product of fiber length and the square of the resonant frequencies lead to a linear relation with the index of the dips, as can be seen in Fig. 3.21. This linear function is characterized by the constants k and d of equation 3.2, which are in turn determined by the dispersion of the fiber and the chirp parameter of the transmitter, respectively.

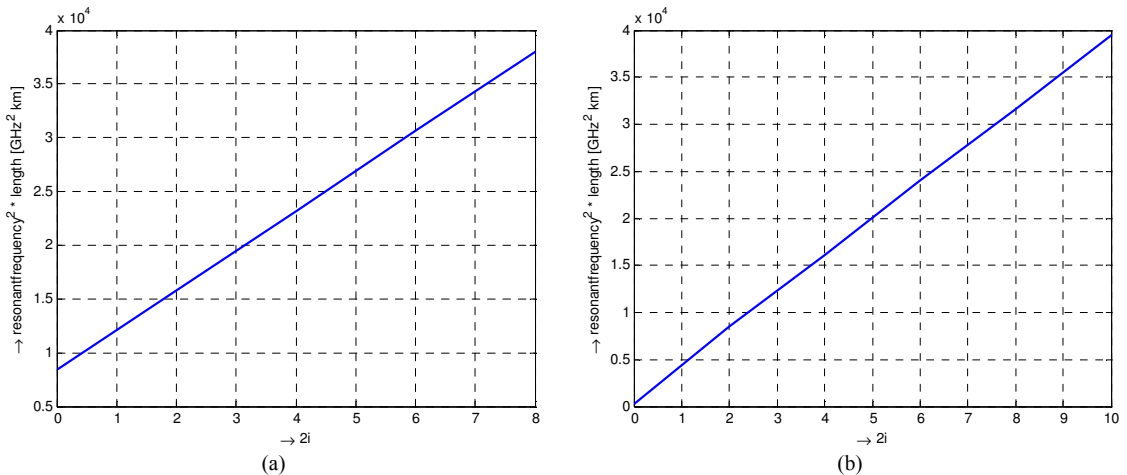


Fig. 3.21. Linear relation for the dips in the fiber response for (a) the DML and (b) the RSOA.

The extracted dispersion and chirp parameter are shown in Fig. 3.22 and 3.23,

respectively. The deviation in the dispersion gives an idea about the accuracy of the accompanying chirp measurement, e.g. the first point of the RSOA curve will have to be excluded for the averaging.

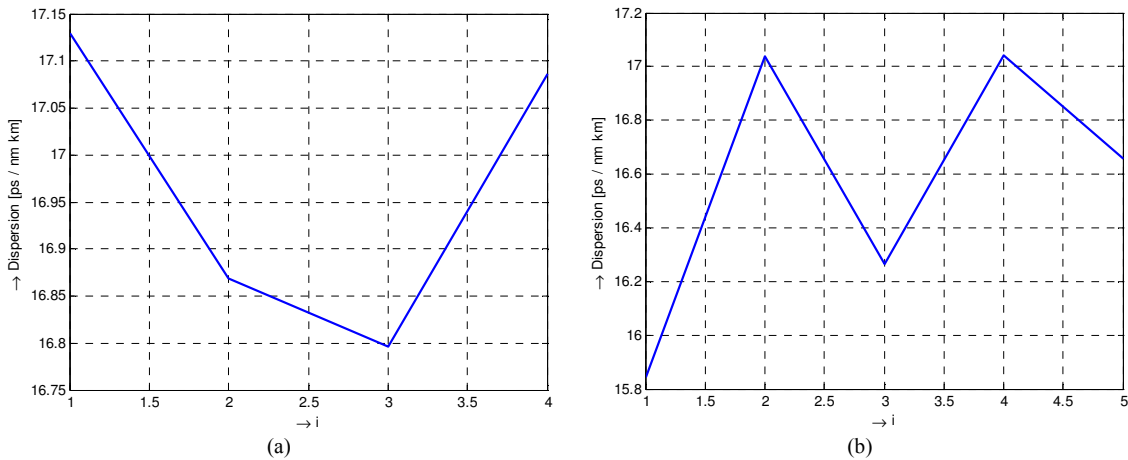


Fig. 3.22. Extracted dispersion coefficient of the fiber obtained via the interplay between chirp and dispersion for (a) the DML and (b) the RSOA.

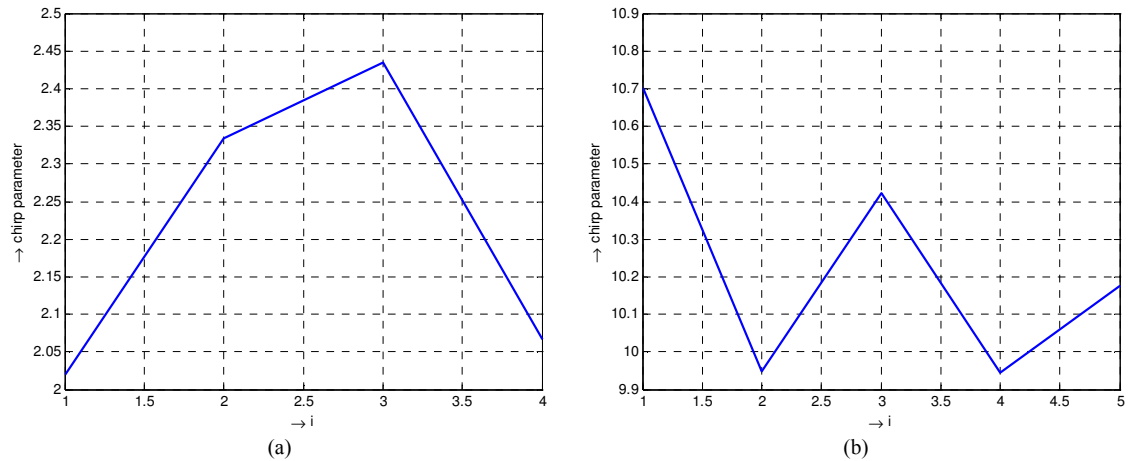


Fig. 3.23. Extracted chirp parameter for (a) the DML and (b) the RSOA.

The averaged chirp parameter of DML and RSOA can be found with 2.21 and 10.12.

3.6.2 Assistance for Transmission at Higher Data Rates

The behavior of the chirp that is induced during modulation can be advantageously used in conjunction with spectral processing [72]. Since the instantaneous optical frequency for the signals of SOA-based modulators raises during the onset of the modulation and lowers during its offset, the rising and falling edges of a bit pattern are subject to increased and decreased optical frequency (i.e. a decreased and increased instantaneous wavelength), respectively.

By including a narrowband optical filter with steep transmission edges (e.g. included at the optical receiver of the transmission system), this change in the optical frequency can be transferred into an amplitude change, though the spectral placement of the signal inside the filter transmission function will in general cause some insertion losses for the

pass through this pulse-reformatting optical filter. For the case that the filter is properly blue-shifted towards the signal, the rising bit edges experience less insertion loss while the falling edges experience additional loss according to the steep transmission function of the filter.

This means an increase in electro-optical bandwidth when being translated into the modulation capabilities of a SOA, as can be seen in Fig. 3.24 for a RSOA with a chirp of ~ 9 and an initially reduced modulation bandwidth of ~ 2.8 GHz after equalization of its electro-optical response with a passive predistorting filter.

The shift in the peak for the detuned optical filter (FD in Fig. 3.24) can be explained by the response for the phase modulation of a SOA, which has a resonance peak that is located at a higher frequency than for intensity modulation. Note that the electro-optical response with detuned filter would have to be equalized to cut the peak in the region from 0.5 to 3.5 GHz.

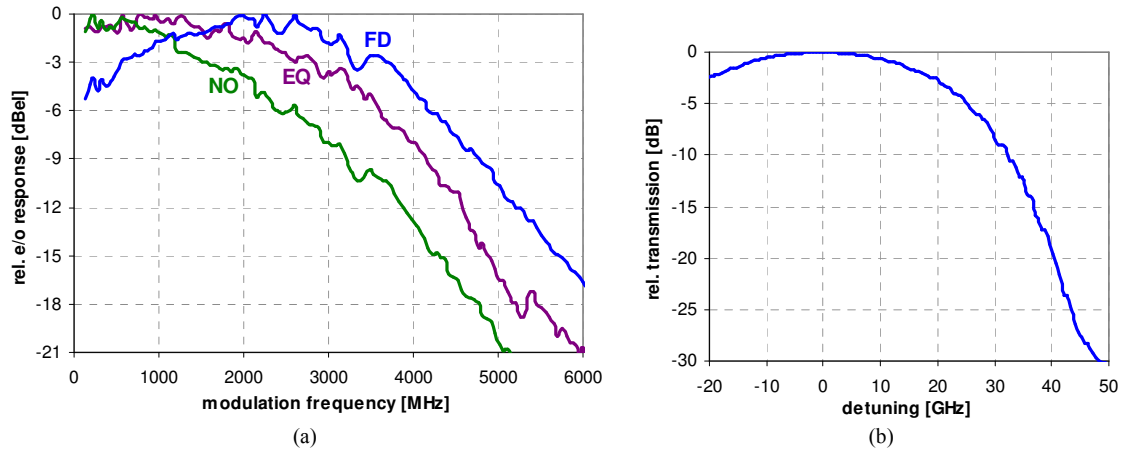


Fig. 3.24. (a) Electro-optical response of a low-bandwidth RSOA in normal operation (NO) with direct modulation, simple electronic equalization (EQ) of its intrinsic response and chirp-assisted modulation bandwidth enhancement in conjunction with a detuned optical filter (FD), whose relative transmission function that is referenced to its nominal insertion loss is shown in (b).

Finally, it shall be noted that the behavior of chirping depends on the type of transmitter. While LiNbO_3 -based Mach-Zehnder intensity modulators do not suffer from any chirping, so that the spectral width $\delta\lambda_M$ of the data signal at λ_{sig} corresponds to the accumulated width of both modulation sidebands, the spectral broadening for InP-based modulators differs.

DMLs for example show adiabatic and transient chirping, which result in two different spectral components for the mark and space bits at λ_1 and λ_0 , as indicated in Fig. 3.25. The difference in the peak power of these two spectral components corresponds to the ER due to data modulation. As it is obvious, this typically low ER can be enhanced by filtering the spectral tributary of the space bits at λ_0 [155]. Such chirp managed transmission with DMLs has been demonstrated up to 40 Gb/s [156].

On the contrary to DMLs, SOA-based modulators show mainly transient chirping, which leads to a broadening of the signal without significant displacement from its nominal wavelength λ_{sig} . The rising and falling edges in the bit pattern are lurking in the

lower and upper wavelength components of the signal spectrum, respectively. As mentioned earlier, this circumstance can be advantageously used to enhance the modulation speed (i.e. the rise and fall times for the bit slopes) by offset filtering of the data signal.

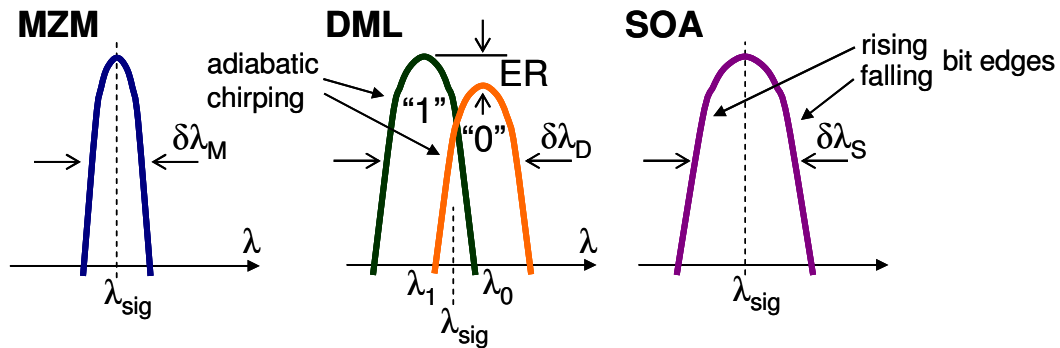


Fig. 3.25. Exemplified spectra for data signals modulated by MZM-, DML- and SOA-based transmitters. Adiabatic and transient chirping manifest themselves in spectral detuning and broadening.

Chapter IV

Full-Duplex ASK-Transmission on a Single Wavelength

The following chapter is devoted to cost-efficient bidirectional data transmission in extended reach PONs. Focus is given on strategies for the implementation of full-duplex data delivery by using foremost the simple ASK modulation format, which does not require photonic integrated demodulators or filters as discriminators. As a next step, chapter V will contrast the results presented in this chapter with possibilities to apply orthogonal modulation formats without increasing the complexity of the ONU significantly.

4.1 Introduction

It is not always acceptable to use two wavelengths for down- and upstream transmission, as it was presented in the previous chapter. Especially in PONs that require optical repeaters to overcome high loss budgets in the light path, the re-use of a single wavelength for full-duplex transmission guarantees low Capex since no extra amplifiers for a second optical carrier have to be used and the fiber plant can be shared among a higher number of users due to a higher spectral efficiency.

Additionally, the subsystems of the PON, which are determined in their design also by the chosen modulation format, will have significant impact on cost issues, especially if they require complexity at the ONU. ASK can provide a trade-off between the deployment of simple receivers and transmitters and the non-orthogonality between the bidirectional data streams, which will cause severe crosstalk and penalties of their transmission performance.

The different techniques that can achieve the goal of wavelength re-cycling are highlighted in their performance and induced complexity in the next sections, starting with an analytical estimation of the introduced penalties, followed by an evaluation of the intrinsic pattern suppression thanks to the gain saturation of a SOA and more advanced electrical and optical techniques for downstream cancellation.

Finally, additional aspects such as light backscattering in fibers and their impact on wavelength reuse are addressed.

4.2 Wavelength Reuse in Bidirectional Transmission

The basic idea of wavelength re-utilization is to recover a suitable optical carrier out of the downstream signal before upstream modulation takes place (Fig. 4.1). Since the downstream reception is subject of the ONU, this recovery of the upstream carrier cannot be performed before the signal reaches the ONU as the downstream information has to be kept till it is properly received. An exception would be a spectral displacement of the upstream carrier from the downstream wavelength so that both signals can be distinguished by a colorless splitter at the ONU, thus avoiding any complexity at the customer premises. However, such a wavelength conversion technique typically affords electrically powered components or strong pump signals for nonlinear effects in passive elements such as specialized fibers. For this reason such an approach of generation a second wavelength at the fully passive network nodes in the fiber plant of the PON is not considered here. Though wavelength conversion at the OLT itself would be possible, it is against the primary requirement of having just a single wavelength till the last optical amplifier on the way to the ONU.

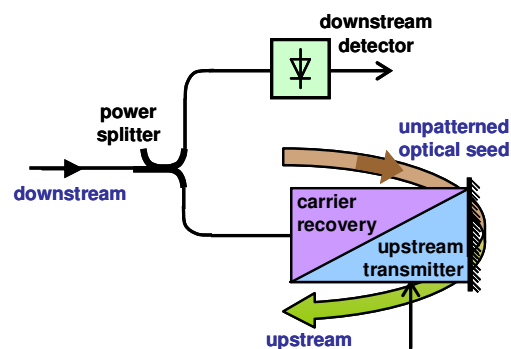


Fig. 4.1. Incorporation of a downstream cancellation technique at the ONU to recover an optical seed for the upstream transmission.

Naturally, the technique applied for carrier recovery will have some imperfections so that its efficiency becomes an important parameter. This efficiency is here referred to as the ability to suppress a present patterning in its modulation swing and therefore the carrier recovery is referred to as the downstream cancellation. The following sections will evaluate the efficiency of different cancellation techniques and analyze the intrinsic limitations.

Note that due to the full-duplex ASK transmission the downstream will be in general modulated with reduced modulation index (i.e. extinction). This can ease the recovery process for an optical upstream carrier. The optimum ER for the downstream will thereby depend on the efficiency of the cancellation technique and the performance of the downstream reception, which is affected negatively for reduced modulation indices.

Note also that the term “carrier recovery” does not necessarily translate to the formation of an unpatterned, smooth optical signal as it will be discussed in chapters IV.3-IV.5. An alternative approach is to obtain optical pulses as seed for the upstream

transmitter by using optical means of clock recovery. This approach also relaxes the requirements of the upstream modulator such as the electro-optical bandwidth and will be presented in chapter IV.6.

The efficiency of the cancellation will translate into residual patterning from the ASK downstream, which will cause crosstalk into the ASK upstream. This in turn will reduce the power margins for the transmission inside the PON or introduce error floors in the worst cases. For this reason the upstream transmission, which is typically performed at lower data rate than the downstream, can become the more critical data stream for the case of full-duplex transmission.

The penalties for the down- and upstream reception that are induced by a reduced ER or an imperfect downstream cancellation technique can be analytically evaluated as follows.

The downstream penalty ζ_{DS} is a consequence of the reduced eye opening. A given modulation index m , defined as

$$m = \frac{P_1 - P_0}{P_1} \quad (4.1)$$

and related to the ER_{DS} via

$$ER_{DS} = \frac{P_1}{P_0} \quad m = 1 - \frac{1}{ER_{DS}} \quad (4.2)$$

will lead to an optical downstream pattern p_{DS} in the form of

$$p_{DS}(t) = \frac{P_1}{ER_{DS}} + A_{DS} \cdot \pi_{DS}(t) \quad (4.3)$$

where π_{DS} is the logical downstream bit pattern comprising of logical 0- and 1-bits. The optical eye height that corresponds to the amplitude A_{DS} of the downstream is related to the average optical power via

$$A_{DS} = P_1 - P_0 = P_1 \left(1 - \frac{1}{ER_{DS}} \right) \quad (4.4)$$

$$A_{DS} = 2 \frac{ER_{DS} - 1}{ER_{DS} + 1} \bar{P} \quad \bar{P} = \frac{P_1 + P_0}{2} \quad (4.5)$$

The definition of the Q factor includes the averages of the detected photo currents I_1 and I_0 for the mark and space bit level, respectively, and their noise variances σ_1 and σ_0 caused by thermal, shot and Rayleigh beat noise. The photo currents I_i are related to the optical power levels P_i via the responsivity S of the photo detector, which is in turn determined by the quantum efficiency η of the detector.

$$Q = \frac{I_1 - I_0}{\sigma_1 + \sigma_0} \quad (4.6)$$

$$I_i = P_i S = P_i \frac{\eta e}{h\nu} \rightarrow Q = \frac{S A_{DS}}{\sigma_1 + \sigma_0} \quad (4.7)$$

In above equation, e stands for the elementary charge, h for the Planck constant and ν for the optical frequency of the incident signal.

The Q factor and the average optical power P_s that is required for the reception with this certain Q factor can be found with equations 4.5 and 4.7. Both are determined by ER_{DS} according to

$$Q = \frac{m}{2-m} \frac{I_1 + I_0}{\sigma_1 + \sigma_0} = \frac{1 - 1/ER_{DS}}{1 + 1/ER_{DS}} \frac{I_1 + I_0}{\sigma_1 + \sigma_0} \quad (4.8)$$

$$\bar{P}_s(ER_{DS}) = \frac{1 + 1/ER_{DS}}{1 - 1/ER_{DS}} \frac{Q(\sigma_1 + \sigma_0)}{2S} \quad (4.9)$$

The penalty ξ_{DS} for the downstream reception corresponds to the extra amount of optical power needed to obtain the same Q factor that would be given for an infinite ER_{DS} – which reflects the optimal case of downstream transmission. Its logarithmic value can be found with

$$\xi_{DS}(ER_{DS}) = 10 \log \left(\frac{\bar{P}_s(ER_{DS})}{\bar{P}_s(ER_{DS} \rightarrow \infty)} \right) = 10 \log \left(\frac{1 + 1/ER_{DS}}{1 - 1/ER_{DS}} \right) \quad (4.10)$$

In case of the transmission of an upstream bit pattern π_{US} , this present downstream modulation has to be taken into account as distortion. The upstream transmitter is assumed to be an intensity modulator with reduced modulation index, which is accounted by the limited ER_{US} . Although the extinction of the space bits could be infinite for the upstream, the practical realization of the low-cost modulator does typically not achieve a high ER_{US} . For this reason next-generation PON (NG-PON) standards define a minimum ER_{US} of 6 dB [39].

With simultaneous down- and upstream modulation the upstream pattern p_{US} becomes

$$p_{US}(t) = \left[\frac{P_1}{ER_{DS}} + A_{DS} \cdot \pi_{DS}(t) \right] \frac{1}{ER_{US}} + \left[\frac{P_1}{ER_{DS}} + A_{DS} \cdot \pi_{DS}(t) \right] \left(1 - \frac{1}{ER_{US}} \right) \pi_{US}(t) \quad (4.11)$$

according to the upstream bit pattern π_{US} . This upstream pattern is a multi-level intensity modulated signal. It is supposed that an additionally included downstream cancellation technique is able to reduce the amplitude A_{DS} of the downstream significantly to a portion $A_{DS,res}$.

This remaining magnitude of the downstream pattern will cause a distortion $I_{DS,res}$ for the upstream reception that depends on the electrical reception bandwidth B_{el} . The electrical spectrum Θ of the downstream and therefore the downstream data rate will have significant influence on the induced distortion.

$$\chi \propto I_{DS,res}(A_{DS,res}) = \int_{-B_{el}}^{B_{el}} \Theta(f) df \quad (4.12)$$

The remaining downstream pattern is treated as additional Gaussian noise contribution χ , which is an acceptable approximation [157].

Due to the relative high ER_{US} the noise contribution χ to the mark bits will dominate so that no extra contribution for the standard deviation σ_0 is included for the sake of simplicity. For the mark level the deviation σ_1 broadens to

$$\tilde{\sigma}_1 = \sqrt{\sigma_1^2 + \chi} \quad (4.13)$$

The required average input for the upstream reception differs from the ideal sensitivity $P_{s,ideal}$ by the term χ according to

$$\bar{P}_s(\chi) = \frac{Q(\sqrt{\sigma_1^2 + \chi} + \sigma_0)}{2S} \quad (4.14)$$

$$\bar{P}_{s,ideal} = \bar{P}_s(\chi = 0) = \frac{Q(\sigma_1 + \sigma_0)}{2S} \quad (4.15)$$

Expressing this difference in terms of a reception penalty ξ_{US} for the upstream transmission leads to

$$\xi_{US}(\chi) = 10 \log \left(\frac{\bar{P}_s(\chi)}{\bar{P}_s(\chi = 0)} \right) = 10 \log \left(\frac{\sqrt{\sigma_1^2 + \chi} + \sigma_0}{\sigma_1 + \sigma_0} \right) \quad (4.16)$$

and with the assumption that the contributions from thermal and shot noise are negligible, this penalty simplifies to

$$\sigma_1 \approx \sigma_0 = \sigma: \quad \xi_{US}(\chi) = 10 \log \left(\frac{1 + \sqrt{1 + \chi/\sigma^2}}{2} \right) \quad (4.17)$$

For the more realistic case of having a limited modulation index for the upstream transmitter, as discussed previously, the penalty ξ_{US} increases according to equation 4.10 to

$$\xi_{US}(\chi, ER_{US}) = 10 \log \left(\frac{1 + \frac{1}{ER_{US}} \frac{1 + \sqrt{1 + \chi/\sigma^2}}{2}}{1 - \frac{1}{ER_{US}}} \right) \quad (4.18)$$

The magnitude of the reception penalty ξ_{US} will depend not only on the chosen modulation index for the downstream, which translates to the additional noise contribution χ , but can also be subject of certain parameters that are related to the technique itself, such as the electro-optical modulation bandwidth of the upstream transmitter.

Fig. 4.2 shows the penalties as function of the ERs for down- and upstream and the unsuppressed downstream pattern. The downstream suffers from a penalty of 4.8 dB once its ER is reduced to 3 dB. For the upstream reception the penalty stays below 5 dB for a typical upstream ER of 6 dB if there is no significant downstream that causes crosstalk, but raises to values of 10 dB and more if the downstream data survives its cancellation.

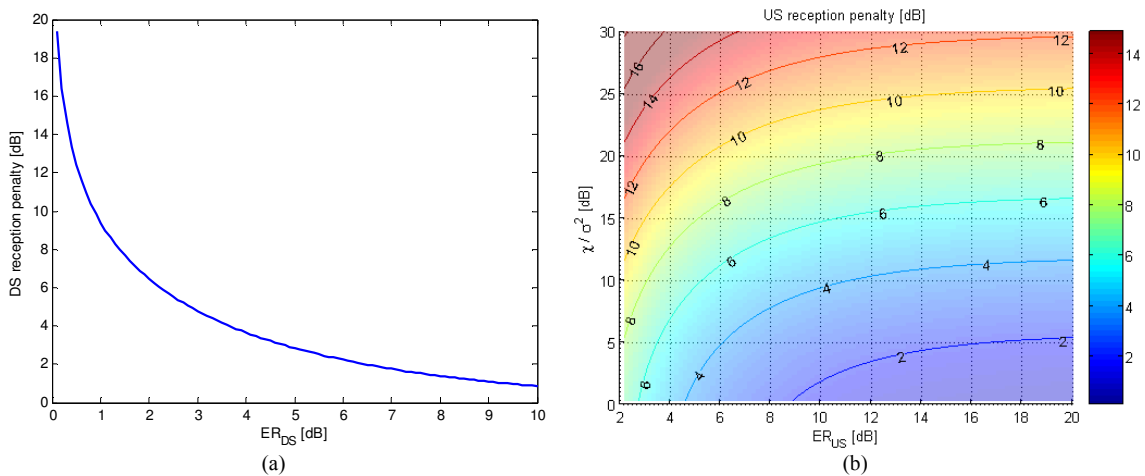


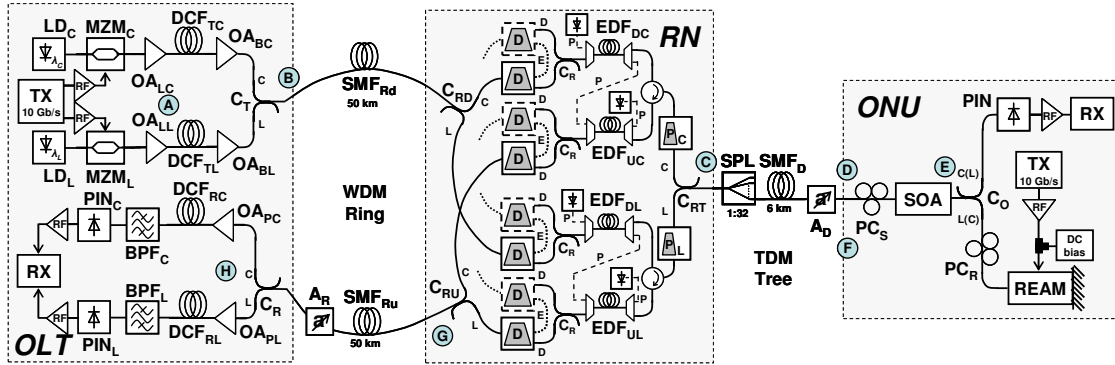
Fig. 4.2. (a) Downstream and (b) upstream penalty in reception sensitivity as function of the ER for the data stream and the remaining downstream pattern, respectively.

Full-duplex transmission with the simple ASK modulation format suffers therefore not only from crosstalk of the downstream information into the upstream channel, but requires to further adapt the downstream in its magnitude. For this reason a trade-off between the Q factors for down- and upstream reception has to be made.

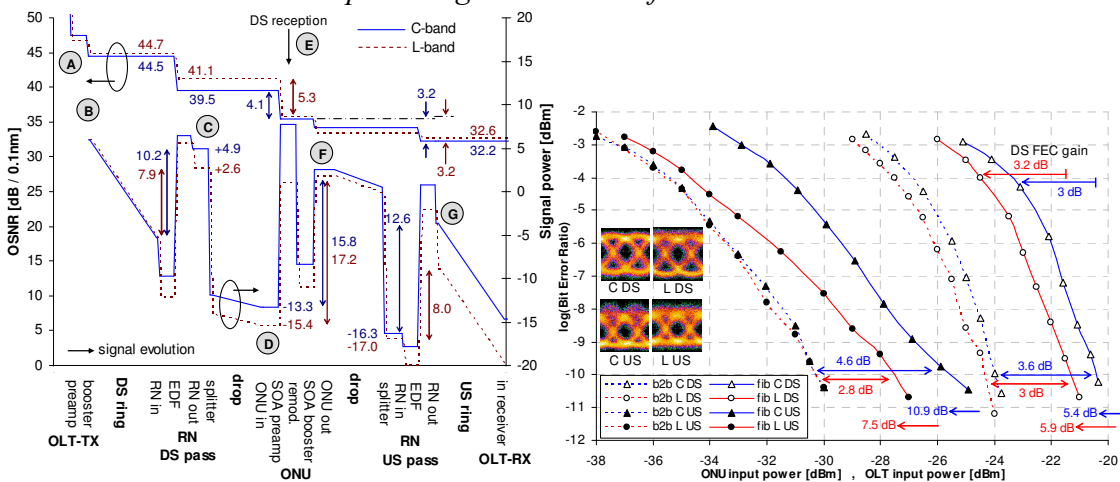
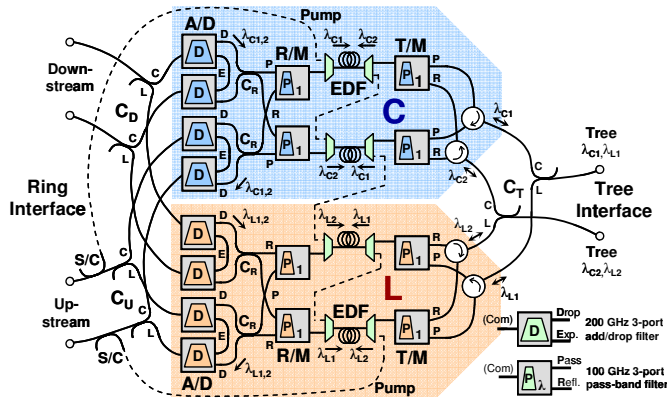
Note. All these aforementioned penalties can be avoided by a dual wavelength scheme that allocates the down- and upstream to two particular optical carriers in two different wavebands. The idea is then to split and combine these wavelengths with a red/blue waveband splitter, which is compatible with a colorless ONU design. At which extra cost this “ideal” transmission for down- and upstream is purchased, will be addressed briefly in the following case study [158].

A hybrid ring+tree PON with extended reach can achieve full-duplex operation by dedicating different wavebands (C and L or vice versa) for down- and upstream. In the presented case, two wavelengths at 1560.61 and 1586.2 nm were used for symmetrical transmission at 10 Gb/s. While the downstream is sent from the OLT together with an unmodulated carrier in the second waveband, the ONU takes advantage of this optical carrier to imprint its upstream information onto it without suffering from a

remodulation penalty. Colorless operation is guaranteed since the two signals can be split with a simple C/L separator. A combination of commercially available SOA and REAM constitutes the ONU.



Dispersion compensating fibers at the OLT and also optical amplification in the fiber plant are required due to the ring length of 50 km and the tree split of 1:32. In this scenario of having a hybrid PON this amplifier is nested in the remote node, which is responsible for dropping wavelengths from the ring to its trees. Due to the dual wavelength feed for the ONU the complexity of this network node, which has to be placed on several locations along the ring, raises significantly. The reason for this can be found in the gain spectrum of rare-earth doped fibers, which is limited in its gain bandwidth. This implies that just a reduced number of wavelengths can be amplified if the gain spectrum has to be divided into a red and a blue window, according to the chosen wavelength allocation. Two different Erbium-doped fibers dedicated to C- and L-band were included in the node to keep the original number of data channels.



With the proper power budget and a net gain of ~10 dB for the remote node, the transmission results show no problems in terms of high error floors for neither the C- nor the L-band wavelength. Power margins of 5 to 10 dB have been obtained for down-and upstream, whereby the downstream has been shown up to be more critical. With the covered wavelength range from 1530 to 1563 nm in the C- and 1570 to ~1600 nm in the

L-band in which sufficient gain can be provided for the given power margins, a PON with data transmission on 32 wavelengths in each waveband can be considered, serving with the use of a splitting ratio of 1:32 in the tree altogether 1024 users with a full-duplex data transmission of 10 Gb/s. Together with the nominal reach of 56 km for the PON, a capacity-length product of 17.9 Tb/s km is provided.

What is left is to assess possibilities to reduce the complexity of this PON, which will be addressed in this chapter in terms of employing downstream cancellation techniques for wavelength re-utilization during upstream transmission.

4.3 Gain Saturation of a SOA

The simplest technique for the desired downstream pattern suppression is to exploit the natural gain saturation effect of SOAs [Takesue06]. If a RSOA is used as upstream transmitter, this technique comes at zero cost and is therefore beneficial. However, gain saturation typically requires strong input signals. Alternatively, the RSOA could be designed with a low saturation output power. This in turn would also mean that the launched upstream signal is weak and would limit the optical loss budget for the upstream due to the reflective transmission scheme. Since high loss budgets are always present in PONs with extended reach and high customer density, the second approach with reduced saturation output power is not considered here. Instead, the limitations have been assessed with device parameters of commercial SOA elements that offer saturation output power values well above 0 dBm.

Experimental applications can be found in [130,159-160]. Although the gain saturation effect is not considered as cancellation technique for long reach PONs due to the in general low input power of the ONU, a downstream cancellation technique that is solely based on the optical gain saturation will be used in the later sections as reference for comparison of more advanced cancellation techniques.

4.3.1 Natural Suppression of Bit Patterns due to Gain Saturation

The fast gain recovery of SOAs enables the suppression of bit patterns with data rates that are used in typical access applications. Since the gain is quick enough to follow the downstream pattern, the mark and space bits experience a different gain, whereby the gain of the space bits is higher if the SOA is operated in its saturation. The ER at the output of the SOA element is then

$$ER_{out} = \frac{P_{1,out}}{P_{0,out}} = \frac{G_1 P_{1,in}}{G_0 P_{0,in}} \quad (4.19)$$

where $P_{i,out}$ and $P_{i,in}$ are the power levels for the different bit levels at the output and input of the SOA, respectively. According to equation 4.2 and 4.5, the input power levels can be expressed as

$$P_{1,in} = \frac{2ER}{ER+1} \bar{P}_{in} \quad P_{0,in} = \frac{2}{ER+1} \bar{P}_{in} \quad (4.20)$$

The gain G_i of the saturated SOA for the particular bit levels is determined by the constant output saturation power $P_{sat,out}$. Not only the signal but also the noise N_{in} at the input of the SOA will contribute to the saturation of the amplifier.

$$G_i = \frac{P_{sat,out}}{P_{in,i} + N_{in}} \quad P_{sat,out} = P_{i,out} + N_{out} \quad (4.21)$$

Although the noise levels for mark and space bits would be different due to the fast response of the SOA, the noise is treated here as an average value that experiences average gain. According to this, the noise power is derived from the average input signal power, to which it is related with the OSNR.

$$\bar{N}_{out} = \bar{G} \bar{N}_{in} \quad \bar{N}_{in} = \frac{\bar{P}_{in}}{OSNR} \quad (4.22)$$

With these assumptions, equation 4.19 now becomes

$$ER_{out} = \frac{2ER_{in} OSNR + (ER_{in} + 1) ER_{in}}{2ER_{in} OSNR + ER_{in} + 1} \quad (4.23)$$

and the ratio ε between the output and input ER of the downstream is given by

$$\varepsilon = \frac{ER_{out}}{ER_{in}} = \frac{2OSNR + ER_{in} + 1}{2ER_{in} OSNR + ER_{in} + 1} \quad (4.24)$$

The ratio ε is below unity for several values of the input ER and OSNR, and decreases strongly for higher ER_{in} , meaning a strong compression of the downstream bit pattern.

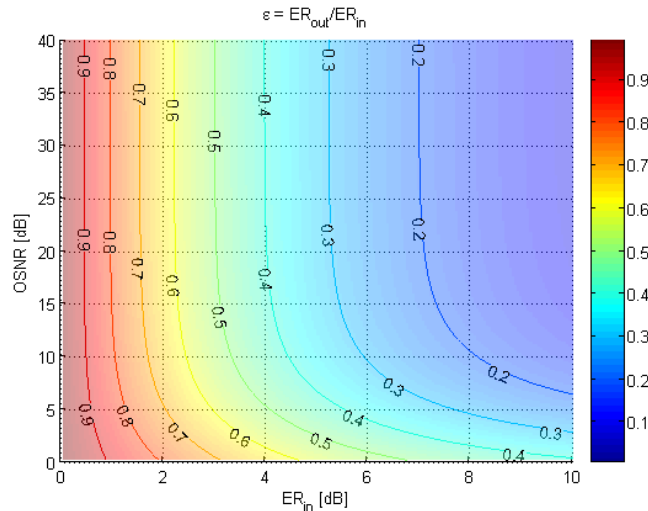


Fig. 4.3. Reduction of the ER of a bit pattern due to gain saturation in a SOA, shown as function of the initial ER and the OSNR.

As can be further seen in Fig. 4.3, the dependence on the input OSNR is quite weak for values of >20 dB. Such high OSNR levels are common for PONs with reflective ONUs, as will be confirmed later but can be already expected from the case study of the dual

wavelength feed that was presented previously in chapter IV.2, in which the delivered OSNR to the ONU was 40 dB.

Note that the induced compression of the modulation of a data stream in SOA elements has two aspects, which affect the data transmission not only positively:

- In the case of the downstream, the data pattern is partially erased in the SOA before it is remodulated with upstream, as it is desired. This supports the process of downstream cancellation in further more complex approaches in a positive way.
- For the upstream, which is of course also affected, a high ER, which can be provided with specific modulators such as EAMs and is typically in the order of up to 20 dB, will be worsened by passing a SOA that is used as common preamplifier and booster at the ONU.

An analytical investigation of the residual downstream ER, obtained via the static model for the SOA that was presented in chapter II.2, is shown in Fig. 4.4 for different input power values and bias currents of the SOA. A downstream ER of 6 dB was considered for the first case and an upstream with an ER of 20 dB for the second. These values are reasonable when considering an application where the downstream is modulated with reduced extinction to allow for remodulation with upstream, and the mentioned compression of an ideal upstream modulation with high ER.

A SOA bias current of 100 mA leads to a compression of the downstream to an ER of 3 dB once the input power for the marks in the data stream reaches a level of -12.5 dBm. The compression is pronounced for the case of the high upstream ER since the difference in the power levels for space and mark bits is bigger. For the same bias current, a reduction of 3 dB is already suffered at an input power of -15 dBm.

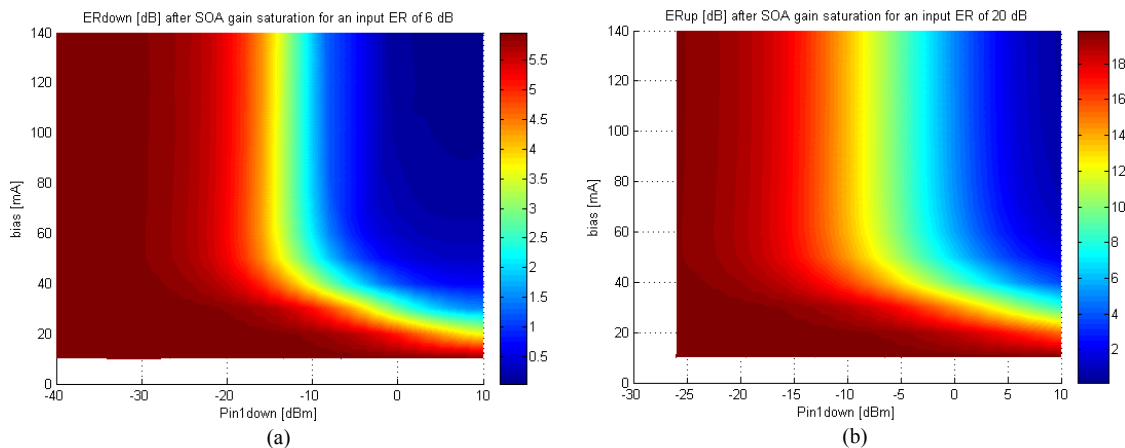


Fig. 4.4. Remaining extinction of a bit pattern after optical gain saturation in a SOA for different bias currents and input power values for the case of (a) the downstream with an ER of 6 dB and (b) the upstream with an ER of 20 dB.

In case of having a RSOA, Fig. 4.5 shows that a present pattern is removed earlier in terms of lower input power values. A bit stream with an initial ER of 6 dB loses 3 dB already at an input power of -15.7 dBm for the same bias current of 100 mA. This can

be an advantage for the case of downstream cancellation where only an RSOA is used and no EAM is present for upstream transmission.

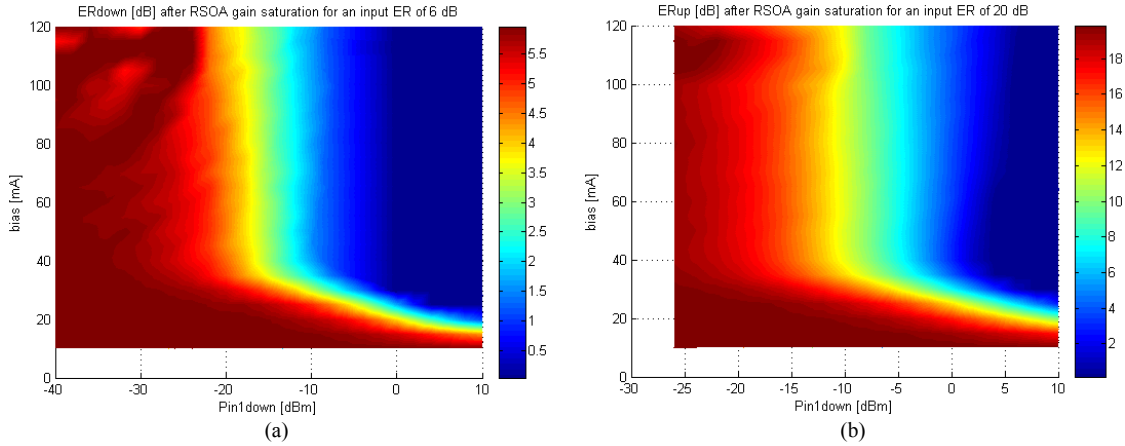
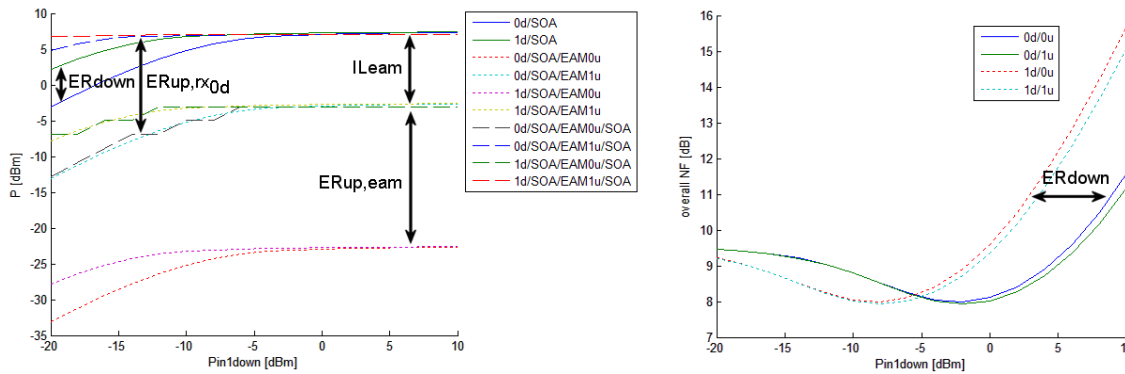


Fig. 4.5. Remaining extinction of a bit pattern after experiencing optical gain saturation in a RSOA for an initial ER of (a) 6 dB and (b) 20 dB.

Note. A cascade of SOA and REAM, where the SOA is used as preamplifier and booster while the EAM imprints the upstream data onto the optical carrier can be already seen as implementation in Fig. 4.1. In this case the SOA acts as carrier recovery by exploiting its gain saturation effect.

The different power levels along the transmission path are plotted in the figure below as function of different optical power in the mark bits for different bit combination of transmitted data in downstream ('0d', '1d') and upstream direction ('0u', '1u'). According to the reflective upstream transmitter, the SOA is passed twice and erases the downstream as well as part of the upstream pattern. The downstream ER is here chosen to be 6 dB and the SOA model previously introduced was used with a fixed bias current of 100 mA. The EAM was treated ideally but with an insertion loss (IL_{eam}) of 10 dB. The upstream $ER_{up,eam}$ was 20 dB.



It is obvious that after the first pass through the SOA, the downstream pattern is removed, which corresponds to the shrinking difference in power for the solid green and blue lines. As there is no kind of saturation in the EAM, the remodulated data (dotted lines) are shifted by either the insertion loss of the EAM for marks in the upstream data and also the extinction for the space bits. At the upstream receiver the extinction is kept for very low input power values, as it can be seen for the remaining extinction $ER_{up,rx0d}$ when a space bit was sent in the downstream. For an input power of

0 dBm not only the downstream ER is drastically removed but also the upstream (dashed curves) suffers from optical gain saturation and what remains from its initial ER of 20 dB are just 10.5 dB.

The overall noise figure for this cascade of SOA and REAM can be determined by the addition of the particular noise contributions according to Friis' formula,

$$NF_{overall} = NF_{go} + \frac{NF_{return} - 1}{G_{go}} \quad (4.25)$$

Taking the bidirectional pass through the SOA and the losses of the EAM into account, this formula has to be modified to include another stage with a gain that is related to the insertion loss and an appropriate noise figure that equals these losses via

$$G_{eam} = -IL_{eam} \quad NF_{eam} = IL_{eam} \quad (4.26)$$

$$NF_{overall} = NF_{go} + \frac{NF_{eam} - 1}{G_{go}} + \frac{NF_{return} - 1}{G_{go} G_{eam}} \quad (4.27)$$

The noise that is added to the downstream is the dominating one as this first pass through the amplifier sees the SOA as a front-end. The minimum in the noise figure of the SOA for a moderate input power level, which was also experienced in the analytical model in chapter II.2, is also pronounced in the overall noise figure (see figure above). Strong degradation takes especially place in the region where a strong downstream is received by the SOA. The shift in optical power between the dotted curves for a space bit in the downstream and the solid curves that correspond to a mark bit in the downstream arises from the simple fact that the axis is referenced to the power in the mark bits. For this reason the optimum point with minimal noise figure is achieved at a higher optical power level for the space bits since the downstream ER has to be subtracted from the shown curves to have the real value of optical power in the mark bits. Due to the statistical distribution of mark and space bits, the mean of both sets of curves for mark and space bits will have to be optimized.

According to the obtained residual downstream pattern, the optimum downstream ER for applications in optical access networks can be chosen.

4.3.2 Selection of the Optimum Modulation Index

The preferred condition for optimization of the downstream extinction ER_{DS} is given when the power margins for down- and upstream transmission are balanced and maximized. This can be expressed with

$$PB_{DS} - S_{DS} \Big|_{CR, ER_{DS} opt.} + PB_{US} \Big|_{CR opt.} - S_{US} \Big|_{CR, ER_{DS}, ER_{US} opt.} = \max \quad (4.28)$$

and

$$PB_{DS} - S_{DS} \Big|_{CR, ER_{DS} opt.} \stackrel{!}{=} PB_{US} \Big|_{CR opt.} - S_{US} \Big|_{CR, ER_{DS}, ER_{US} opt.} \quad (4.29)$$

where PB_{DS} and PB_{US} are the power budgets for downstream and upstream, respectively, and CR is the coupling ratio of the optical coupler that splits the signal at the ONU for downstream detection and upstream modulation according to Fig. 4.1. Before above conditions are explained, a discussion on the variables and parameters is given.

The power budgets are given by the amplification and the losses inside the access network. The power budget PB_{DS} for the downstream is defined as the input power levels into the ONU that can be reached according to the optical losses in the network. Accordingly, the power budget PB_{US} for the upstream corresponds to the input power level into the OLT in upstream direction. As the power budget represents an average power level, it is assumed that there is no strong dependence on the ER of the downstream and upstream around the point of optimization.

The power budget PB_{US} for the upstream depends also on the CR since it cannot be assumed that a consecutive amplifier in the ONU or in the overall network is operated in saturation so that a limiting function for the optical power flow is given somewhere inside the ONU or the network during upstream transmission.

The reception sensitivity S_{DS} for the downstream is defined as the input power level into the ONU that is required to have a certain defined BER for the downstream reception. A typical value for the BER that is also recommended for GPON is 10^{-10} , meaning 1 bit error in a data stream consisting of 10^{10} bits. The BER is defined as the ratio of bit errors detected in a bit stream with arbitrary data rate. Accordingly, the sensitivity S_{US} of the upstream is defined as the input power level into the OLT that is necessary to have a certain defined BER for the upstream reception. The BER used for defining the sensitivities for downstream and upstream reception do not have to be the same. It is generally possible to use error correcting codes such as FEC in one transmission direction, which then allows high quality transmission for a higher BER as mentioned in chapter III.5.

The sensitivity S_{DS} will depend on the CR and the ER_{DS} since these two parameters will define the ratio of coupled input power into the photo detector, which leads to a lower BER for higher input power (i.e. a higher CR).

The sensitivity S_{US} depends in general on the CR , the ER_{DS} and the ER_{US} . A higher CR leads now to a reduced optical power level towards the upstream modulator according to the definition of the ratio CR . The upstream modulator may include means of optical amplification and therefore a reduced OSNR results for a lower input power. Supposing that the optical downstream cancellation worsens for a higher ER_{DS} , an increasing ER_{DS} will lead to a higher amount of unsuppressed downstream patterning and therefore to a worse sensitivity S_{US} . Finally, the ER_{US} will define the eye opening for the upstream and accordingly a limited ER_{US} will cause a worse sensitivity S_{US} compared to the ideal case with an infinite ER_{US} .

The power margin for the downstream and the upstream is defined as the difference between the power budget and the sensitivity and is related to a certain BER as also the corresponding sensitivity is. Optimum selection of the ER_{DS} is given when the sum of the power margins for down- and upstream is maximized, leading to optimum

robustness against additional losses in the access network, whereby the power margins for down- and upstream are equal. In this optimal case, the loss budget that can be overcome is maximized.

The two conditions expressed in equations 4.28 and 4.29 lead to a set of optimized parameters for the CR , the ER_{DS} and the ER_{US} , which may in turn reflect physical parameters at corresponding subsystems and components of the OLT and the ONU. Examples are the bias points of the down- and upstream intensity modulators or design parameters for the optical coupler inside the ONU. The optimization is given for a certain architecture of the access network and the OLT and ONU design, and is generally not subject for adaptation during the operation of the network. However, considering a hybrid WDM/TDM network, the parameters of optimization may differ for the different TDM trees inside the network. Due to the demand of deploying identical ONUs across the whole network, the parameters of the latter have to be defined in terms of maxima and minima for its single sections such as the trunk or drop fiber length or tree split. The optimization has then to be made according to an average optimum performance for all ONUs of the network.

4.4 Electrical Feed-Forward Downstream Cancellation

An efficient suppression of the downstream pattern even for weak input power levels at the ONU can be provided with a scheme where the downstream is actively erased. The upstream modulator can exploit thereby its ability of gain or loss modulation.

4.4.1 Functional Scheme of Operation

The principle for the cancellation relies on the synchronized gain or loss modulation of the RSOA or REAM that is used as upstream modulator with the detected downstream data, as it is shown in Fig. 4.6. This technique is therefore based on signal manipulation in the electrical domain: the detected signal is fed forward to the remodulating device, which is assumed to be an intensity or loss modulator by its nature, to counteract the pattern that is present on the optical carrier. The level of the mark bits is brought to the lower one of the space bits or vice versa. A flat optical carrier suitable to embed the upstream is recreated from the optical downstream signal only if the time delay and the magnitude of the detected electrical downstream signal are adjusted according to the incident seed of the upstream modulator by electrical means. The upstream modulator is simultaneously used for its original purpose, namely the upstream transmission. First results of such an approach have been shown at low data rates [161-163].

The conditions of having matched magnitudes and path lengths for the electrical and optical downstream signal after detection and before entering the upstream modulator, respectively, can be satisfied with appropriate RF amplifiers and electrical as well as optical delay lines (DL). The latter is mandatory due to the accumulated delay in the

electrical feed-forward path. Typically a sensitive photo detector such as an APD will be used since low ONU input power values are desired and therefore not compatible anymore with simple PIN diodes.

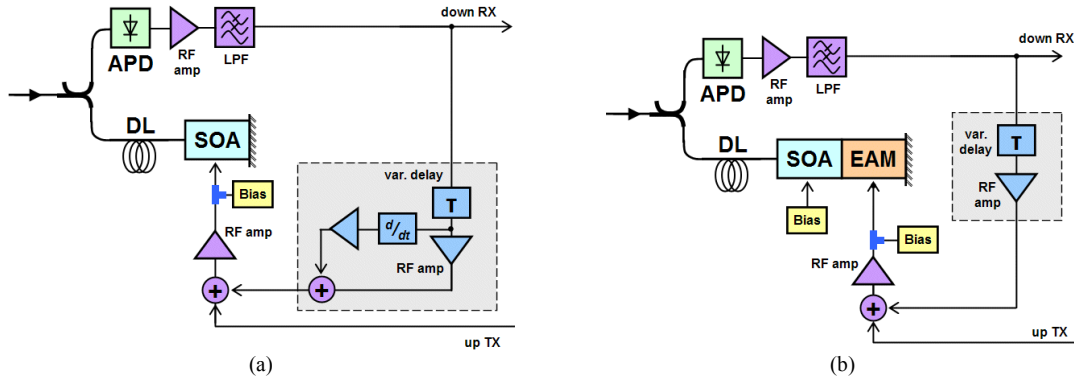


Fig. 4.6. Functional scheme for a downstream cancellation obtained via an electrical feed-forward approach with an ONU based on (a) a RSOA and (b) an integrated combination of SOA and REAM as upstream modulator.

The polarity of the feed-forward signal has to be chosen in accordance with the physical method on which the modulation in the SOA and the EAM relies upon. Since the SOA features gain modulation, an inverter for the detected downstream will be required to achieve the desired cancellation effect.

The limited electro-optical response of the RSOA can be partially compensated with an additional pre-equalization of the forwarded electrical downstream signal [161], which is symbolized by the derivative function in Fig. 4.6(a). This can be interesting for access networks with asymmetrical data rates for down- and upstream since the upstream transmitter is then typically designed to accommodate only for the lower upstream bit rate. However, for the purpose of cancellation the upstream modulator does not have to account for the whole downstream bandwidth since spectral parts of the downstream can be rejected with an electrical low-pass filter at the OLT receiver as will be discussed shortly.

Analytical Model

The method of feed-forward downstream suppression can be analytically expressed in the linear operation range of the SOA where the output power P_{out} follows the input signal P_{in} according to

$$P_{out} = P_{in} \frac{dG}{dI} (I_{bias} - I_{thres}) \quad (4.30)$$

considering I_{thres} as the quasi-threshold current of the SOA. Gain saturation effects that are compressing the downstream modulation are not considered here.

The bias current I_{bias} is composed by the modulation I_{mod} with the upstream signal π_{US} and the detected downstream signal π_{DS} that is fed forward with the magnitude I_{ff} to

the SOA. In addition, a DC bias I_{dc} is applied to compensate for the threshold in the gain-current relation.

$$I_{bias} = I_{ff} \bar{\pi}_{DS}(t) + I_{mod} \pi_{US}(t) + I_{dc} \quad (4.31)$$

The downstream signal that is obtained by the photo detector is thereby inverted according to the gain modulation of the SOA. With equation 4.3, the input power is patterned according to the downstream data and the output of the SOA follows accordingly with

$$P_{in} = P_0 [1 + (ER_{DS} - 1) \pi_{DS}(t)] \quad (4.32)$$

$$P_{out} = \pi_{US}(t) \left[P_0 \frac{dG}{dI} I_{mod} + P_0 \frac{dG}{dI} (I_{ff} \bar{\pi}_{DS}(t) + I_{mod} (ER_{DS} - 1) \pi_{DS}(t)) \right] + P_0 \frac{dG}{dI} (I_{dc} - I_{thres}) [(ER_{DS} - 1) \pi_{DS}(t) + 1] \quad (4.33)$$

Neglecting the issues for matching the optical and electrical path length, two considerations have to be fulfilled to erase the downstream pattern.

$$\begin{aligned} I_{dc} &= I_{thres} \\ I_{ff} &= (ER_{DS} - 1) I_{mod} \end{aligned} \quad (4.34)$$

With these the output power becomes

$$P_{out} = P_0 \frac{dG}{dI} I_{mod} \pi_{US}(t) \quad (4.35)$$

as it is intended for a SOA that is used as intensity modulator in its linear regime, with the difference that some optical power of the input signal is wasted.

The analytical expressions for the cancellation with the EAM follow a similar way, whereby the output power for the EAM is given by the differential loss coefficient da/dV according to

$$P_{out} = P_{in} \frac{da}{dV} (V_{knee} - V_{bias}) \quad (4.36)$$

where V_{knee} is the (negative) knee voltage from which onwards the EAM behaves as a linear loss element and V_{bias} is the (negative) bias voltage. The latter is composed by a DC voltage, the upstream modulation and the feed-forward signal for the cancellation.

The output signal of the EAM is then given by

$$P_{out} = \pi_{US}(t) \left[-P_0 \frac{da}{dV} V_{mod} - P_0 \frac{da}{dV} (V_{ff} \bar{\pi}_{DS}(t) + V_{mod} (ER_{DS} - 1) \pi_{DS}(t)) \right] + P_0 \frac{da}{dV} (V_{knee} - V_{dc}) [(ER_{DS} - 1) \pi_{DS}(t) + 1] \quad (4.37)$$

and the conditions for the downstream cancellation are

$$\begin{aligned} V_{dc} &= V_{knee} \\ V_{ff} &= (ER_{DS} - 1)V_{mod} \end{aligned} \quad (4.38)$$

so that the output signal is just determined by the upstream modulation π_{US} and free of any downstream patterning π_{DS} .

$$P_{out} = P_0 \frac{da}{dV}(-V_{mod}) \pi_{US}(t) \quad (4.39)$$

Linearity of the Upstream Transmitter

When multi-level intensity modulation signals are used for the downstream, the upstream transmitter has to be linear in a wide range of its electrical input. This can be a problem, especially for EAMs, since the transmission function of such modulators is highly nonlinear for low and high bias voltages. The typical transfer function of an EAM follows the applied bias voltage V_{bias} according to

$$T_{eam}(V_{bias}) = (1 - \varepsilon_{min}) \exp \left[- \left(\frac{V_{bias}}{V_a} \right)^\alpha \right] + \varepsilon_{min} \quad (4.40)$$

where ε_{min} is the minimum extinction and V_a and α are fitting parameters. A desired transmission function T_{eam} would follow a linear behavior for its input voltage V_{in} with

$$T_{eam}(V_{bias}) \propto \exp \left[- \left(\frac{V_{bias}}{V_a} \right)^\alpha \right] \stackrel{!}{=} kV_{in} + d \quad (4.41)$$

where k and d are the parameters for the linear relation between V_{in} and T_{eam} . A non-linear function is required at the input of the EAM to obtain this relation via a predistortion of the electrical driving signal. This desired function between input voltage V_{in} of the overall driving circuit and the bias voltage V_{bias} of the EAM can be derived with

$$V_{bias} = V_a \left[-\ln(kV_{in} + d) \right]^{1/\alpha} \quad (4.42)$$

The exact realization of this non-linear function that includes the natural logarithm is not further addressed here but could be in principle achieved with circuits that include diode or transistor elements. The diode current I_D is related to its voltage U_D according to

$$I_D = I_s \exp \left(\frac{U_D}{nU_T} \right) \quad U_T = \frac{kT}{e} \quad (4.43)$$

where I_s is the reverse diode current, n is the emission coefficient that is typical unity for low currents and U_T is the thermal voltage which is around 25 mV/K. A logarithmic relation is therefore given between the diode voltage and its current.

$$U_D = nU_T \ln\left(\frac{I_D}{I_s}\right) \quad (4.44)$$

An example of linearization is given in Fig. 4.7 for the case of having an EAM that fits to the parameters of $\epsilon_{min} = -20$ dB, $V_a = -1.1$ V and $\alpha = 2$. In this case, the term inside the exponential function in equation 4.40 is squared, so that a square root function is required for linearization. This non-linear function has been already demonstrated as integrated electronic element [164].

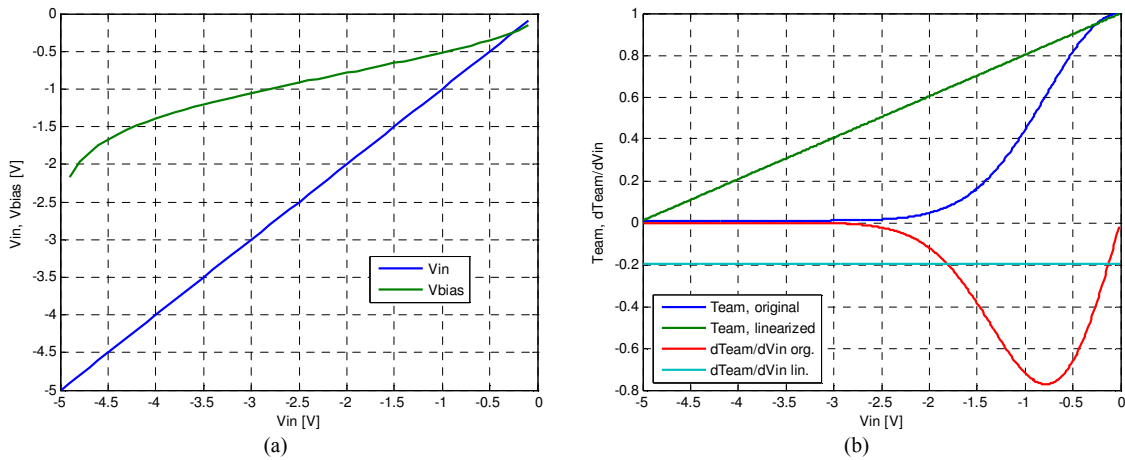


Fig. 4.7. Linearization of an EAM with the help of a nonlinear function. (a) transfer function for the applied voltage due to the included nonlinear function in front of the EAM and (b) the linear net transfer function.

As can be seen, the original transfer function in Fig. 4.7(b) becomes perfectly linear so that a constant slope dT_{eam}/dV_{in} is obtained. This in turn allows to use the EAM with analog signals or discrete multi-level intensity modulation.

Reduced Modulation Bandwidth of the Upstream Transmitter

Typical low-cost modulators suffer from limitations in their electro-optical bandwidth. The derivative filter in Fig. 4.6(a) in the feed-forward path can give emphasis to the high bit rate transients of the downstream, which is crucial for asymmetrical data rates when the modulating device at the ONU is designed for the lower upstream data rate. The cancellation current i_{ff} is then a composition of the detected downstream i_{DS} according to

$$i_{ff}(t + \Delta\tau) = -G_{ff} \left(i_{DS}(t) + \kappa \frac{\partial i_{DS}(t)}{\partial t} \right) \quad (4.45)$$

$$I_{ff}(j\omega) = -G_{ff} I_{DS}(j\omega) (1 + j\omega\kappa) e^{j\omega\Delta\tau}$$

where the gain G_{ff} of the feed-forward path and its delay $\Delta\tau$ are adjusted to the power level and ER of the downstream as well as to the electrical and optical path length, respectively. The magnitude κ of the derivative is chosen according to the gain relaxation time of the SOA. In this way, the transients caused due to the gain dynamics of the upstream transmitter are not further pronounced once the cutoff frequency of the derivative filter is kept low enough.

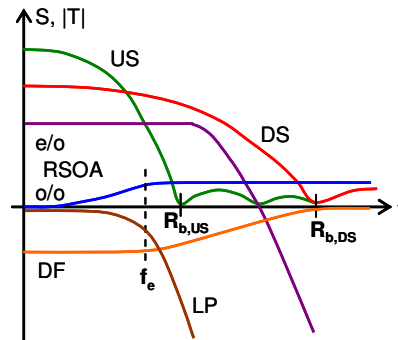


Fig. 4.8. Spectra for down- and upstream for the case of asymmetrical data rates and the functions for the derivative filter (DF), the low-pass filter at the upstream receiver and SOA-related responses.

Fig. 4.8 shows conceptually the spectra of down- and upstream, whereby the downstream data rate $R_{b,DS}$ is twice the upstream data rate $R_{b,US}$, as it can be the case for GPON deployment with asymmetrical 2.5/1.25 Gb/s transmission. In addition, several transfer functions for the subsystems in the ONU and the electrical OLT receiver are depicted. The low pass filter (LP) at the OLT receiver has a bandwidth that is adjusted to the upstream data rate. The electro-optical response of the RSOA is suitable for modulation up to the upstream data rate $R_{b,US}$ but has a strong roll-off for higher modulation frequencies. Emphasis on the suppression of the faster downstream transients can be given by a passive derivative filter (DF) that has in principle a high-pass response and allows a slightly improved cancellation around the upstream data rate $R_{b,US}$, where the low-pass filter at the OLT receiver has still some transmission for spectral components of the downstream.

4.4.2 Principal Proof of Concept

The feasibility of the feed-forward carrier recovery scheme was proven for two scenarios that differ in the desired upstream data rate. The downstream was transmitted at a data rate of 10 Gb/s in each case. While the RSOA-based ONU is intended to operate at 2.5 Gb/s, its substitution by a SOA/REAM at the ONU is expected to provide an upstream with 10 Gb/s.

The first ONU design with RSOA will suffer from an imperfect suppression of the downstream due to the mismatch in the bit rates for down- and upstream. On the contrary, the ONU that features a SOA/REAM can provide an ideal cancellation with its EAM section. However, residual distortions may arise in the recovered optical carrier

due to the finite gain recovery time of the SOA. These distortions cannot be suppressed by the cancellation technique since they are not present in the detected downstream signal and a prediction by means of electrical filtering is not easily accessible due to the bit memory that the filter would require. Additional crosstalk due to cross gain modulation between the incident – by the downstream patterned – seed and the outgoing upstream in the common SOA can be avoided by an integrated SOA/REAM solution since its optical length is much shorter than the length of a bit.

Sensitivity to Errors in the Adjustment of the Cancellation Circuit

The recovery of an optical carrier itself with the RSOA-based ONU is shown in Fig. 4.9 for the case of a downstream signal that comprises Super-Gaussian pulses [165] with a bit envelope

$$P(t) = P_0 + P_1 \left(1 - \frac{1}{ER}\right) \exp \left[- \left(5 \left(\frac{t}{T_b} - \frac{1}{2} \right) \right)^{2F} \right] \quad (4.46)$$

where T_b is the bit period and F the pulse format, which was chosen with $F = 5$. The ER of the signal was 10 dB.

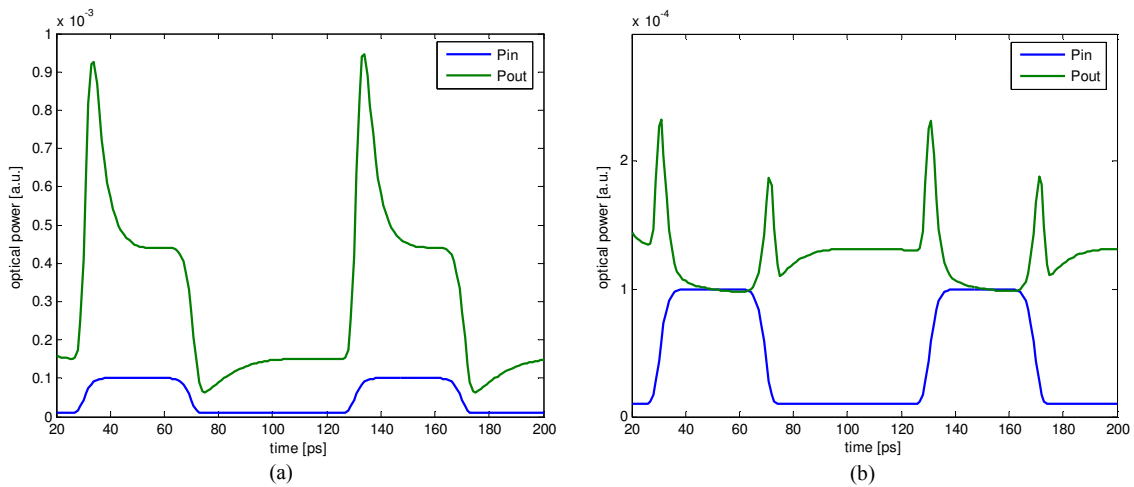


Fig. 4.9. Optical carrier recovery from an input signal that contains Super-Gaussian pulses and an ER of 10 dB, (a) without and (b) with cancellation.

Fig. 4.10 shows qualitatively the error of the feed-forward cancellation technique if the two parameters for the feed magnitudes of the direct signal and its derivative are changed. The error ρ is defined as the square of the deviation from the average power value of the recovered carrier, integrated over a full bit period.

$$\rho = \int_0^{T_b} (P(t) - \bar{P})^2 dt \quad (4.47)$$

Note that without any cancellation the performance worsens significantly.

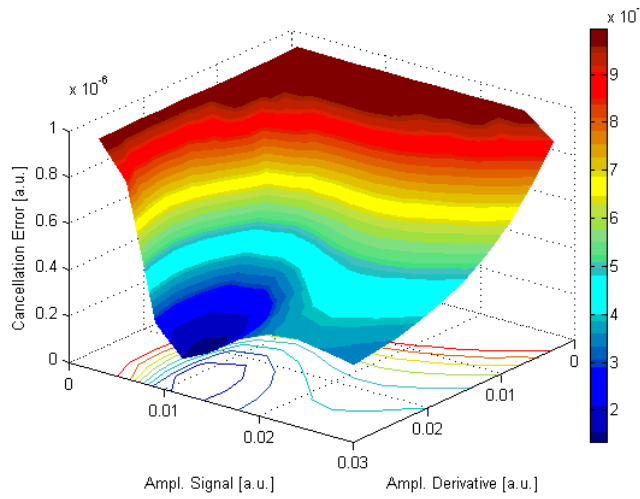


Fig. 4.10. Dependence of the cancellation efficiency on the feed-forward parameters of direct signal feed and derivative signal feed.

Impact due to a Limited Electro-Optical Response of the RSOA

A limited e/o modulation response of the SOA will induce distortions for the downstream cancellation. Considering solely carrier recovery without upstream modulation (i.e. no modulation current is applied in equation 4.31), the output signal of the SOA becomes

$$p_{out}(t) = G(I_{dc}) \frac{2\bar{P}}{ER+1} \left[1 + (ER-1) (\pi_{DS}(t) + (h_{eo} * \bar{\pi}_{DS})(t)) \right] \quad (4.48)$$

where h_{eo} is the impulse response due to the finite e/o modulation bandwidth.

The quality of the recovered carrier will therefore depend on the mismatch between the o/o bandwidth for the amplification of the optically present downstream signal and the e/o modulation bandwidth of the counter-injected electrical downstream signal. For the following simulations no optical gain saturation has been taken into account for the reflective upstream modulator.

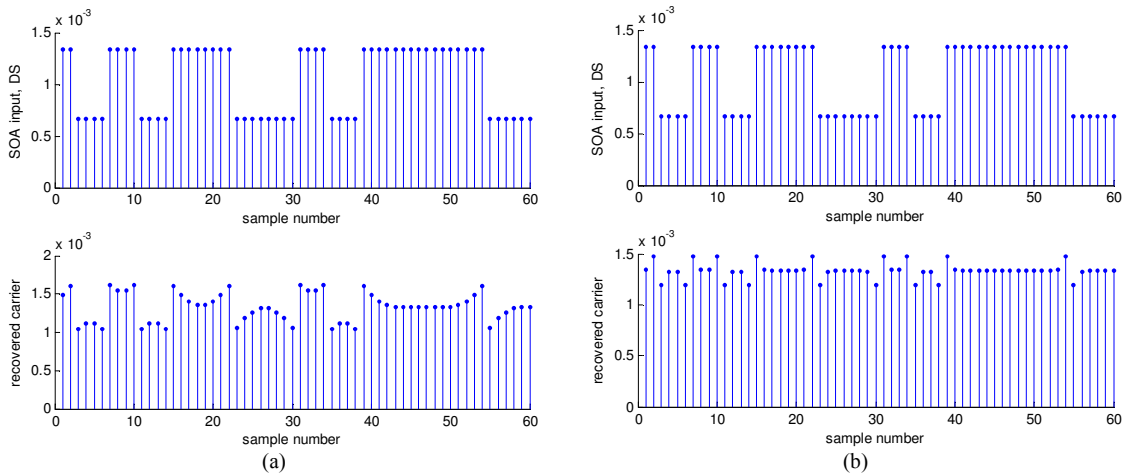


Fig. 4.11. Recovered optical carrier after downstream cancellation for an incident data signal with an ER of 3 dB and an electro-optical modulation bandwidth of (a) $0.25 R_{b,DS}$ and (b) $0.75 R_{b,DS}$ for the upstream transmitter.

Fig. 4.11 shows the recovered optical carrier after suppression of a downstream with an ER of 3 dB in the case of having a strong e/o bandwidth limitation of $0.25 R_{b,DS}$ and also for an acceptable modulation bandwidth of $0.75 R_{b,DS}$. As can be seen, though the latter is supposed to be enough not to suffer from severe penalties in upstream transmission, there are still some residual distortions in the recovered optical carrier, which lead to a residual ER of 1 dB when being referenced as peak-to-peak value.

The distortions that reside in the optical carrier are causing a broad mark rail in the eye diagram. Fig. 4.12(a) to (d) show these enhanced rails for the case of having the same downstream and upstream data rate but different modulation bandwidths of the reflective transmitter. The upstream was imprinted on the recovered carrier with an ER of 10 dB.

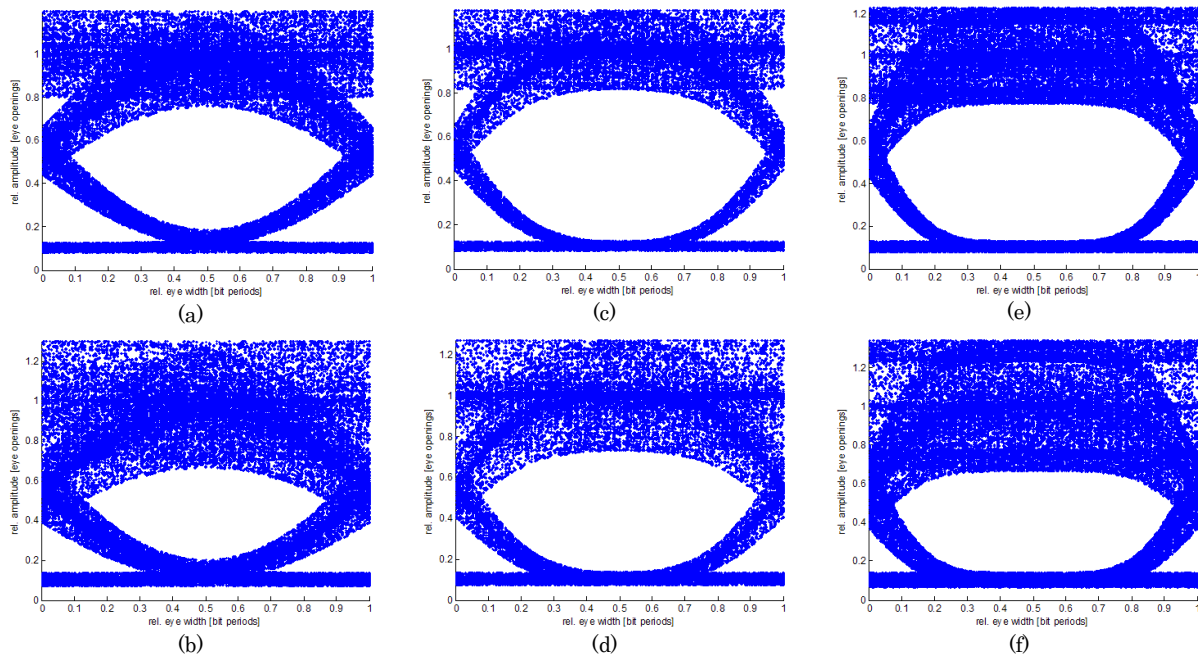


Fig. 4.12. Upstream eye diagram for the case of having a bandwidth-limited downstream cancellation. (a) Downstream ER of 3 dB and e/o bandwidth of $0.5 R_{b,DS}$, (b) 6 dB and $0.5 R_{b,DS}$, (c) 3 dB and $0.75 R_{b,DS}$, and (d) 6 dB and $0.75 R_{b,DS}$. (e),(f) Eye diagrams for the case of having a downstream with much higher data rate than the upstream, $R_{b,DS} = 4 R_{b,US}$. The downstream ER was (e) 3 dB and (f) 6 dB. The outer extents of the rails are pronounced.

Although the distortions are clearly visible, the outer extents of the mark rail are less pronounced than the average mark level – similar to ASE noise. This indicates that the transients caused by the imperfect cancellation are from spurious nature.

Fig. 4.12(e) and (f) show the case of having a downstream data rate that is four times the one of the upstream, as it is the case in full-duplex 10/2.5 Gb/s transmission. Compared to Fig. 4.12(a) to (d), the rails are slightly broadened but also denser, indicating a stronger effective distortion.

An extreme case of pronounced extents in the mark rails is shown in Fig. 4.13, which shows – for the sake of completeness – the case of a downstream with ER of 6 dB without applied cancellation.

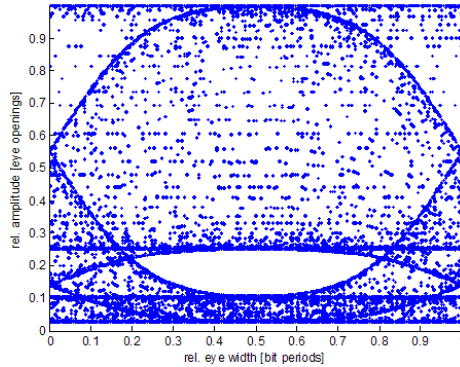


Fig. 4.13. Upstream eye diagram without downstream cancellation and an ER of 6 dB for the downstream. The modulation bandwidth is $0.75 R_{b,DS}$.

Residual Distortions and Effective Noise Figure

The degradation that originates from either unsuppressed downstream or induced over- and undershoots in the bit pattern influences the upstream reception as it affects the eye opening. It can be considered according to

$$\frac{\text{signal}}{\text{noise}} = \frac{S/ER_{DS,res} - \int_0^{T_b} \xi(t) dt}{N_{ASE}} \quad (4.49)$$

where S is the signal power and $ER_{DS,res}$ is the linear residual ER of the downstream that leads to a reduced power level for the marks of the upstream. ξ is a function that includes the impact of eye closure due to several transients induced by the SOA. The upstream ER is considered to be large enough to have a negligible average power level in the space bits.

According to this representation the distortions can be also treated in terms of an effective noise figure. The ASE noise causes deviations σ_1 and σ_0 at the mark and space levels of the bit stream. The eye opening is reduced due to reasons mentioned and given by the minimum and maximum rail levels P_{1min} and P_{0max} for the mark and space bits, respectively. The effective Q factor can be then expressed as

$$Q_{eff} = \frac{P_{1min} - P_{0max}}{\sigma_1 + \sigma_0} \quad (4.50)$$

The relation between the OSNR and the effective Q factor depends on the optical and electrical reception bandwidth according to

$$Q_{eff} = \frac{2OSNR\sqrt{B_o/B_e}}{1 + \sqrt{1 + 4OSNR}} \quad OSNR = \frac{Q_{eff}}{\sqrt{B_o/B_e}} \left(1 + \frac{Q_{eff}}{\sqrt{B_o/B_e}} \right) \quad (4.51)$$

It is assumed that the optical ASE noise is dominating over the electrical thermal noise. The optical bandwidth B_o was chosen with 0.1 nm and the electrical bandwidth B_e

according to the data rate of the upstream. Furthermore, the OSNR is related to the noise figure via

$$OSNR = \frac{P_{in}}{NF \cdot h\nu \Delta\nu} \quad NF_{dB} = P_{in,dB} - OSNR_{dB} - 10 \log(h\nu \Delta\nu) \quad (4.52)$$

where $\Delta\nu$ corresponds to the optical resolution bandwidth.

The effective noise figure NF_{eff} of the downstream cancellation was analyzed with a dynamic analytical model according to chapter II.2 and an additional simulation in a state-of-the-art tool such as VPI transmission maker.

A downstream signal with a fixed ER of 6 dB was used for the evaluation. A reasonable electro-optical bandwidth for the RSOA was emulated with an electrical interface that holds an electrical Bessel filter with a 3-dB bandwidth of 2 GHz. The bias current was composed by a DC level of 75 mA and a peak-to-peak RF current of 90 mA_{pp}.

For the SOA/REAM-based ONU the intrinsic loss of the EAM was 10 dB while the upstream ER was 20 dB. The SOA section was biased at a current of 100 mA. Detection of the upstream signal took place after filtering the optical ASE noise with a 100 GHz broad optical band-pass filter and the detected electrical signal with an electrical Bessel filter matched to intensity modulation and the nominal upstream bit rate of 10 Gb/s, thus having a bandwidth of 7.5 GHz.

Three different scenarios have been analyzed. Next to the case where no downstream is present, meaning an ER of 0 dB for it, the case without and with downstream cancellation were investigated for a present downstream pattern.

The effective Q factor of the RSOA-based cancellation seems to be lower for the simulation than for the model at low input power values. This derives from the difference in the noise figure where also the static investigation showed a difference for low input power. On the contrary, for high input power values it favors a better Q parameter due to the fact that the noise figure for the model raises earlier when approaching higher input power values.

The downstream cancellation leads to effective noise figures of 21.1 dB for the model and 25.5 dB for the simulation, considering an input power of -15 dBm (Fig. 4.14(b)). If there is no cancellation present the effective noise figure raises slightly to 21.8 dB according to the model and 26.9 dB for the simulation.

Agreement between model and simulation can be found for the effective OSNR of the SOA/REAM-based cancellation in a wide range of input powers. Just for very low input power there is a deviation that may have its origin in the different behavior regarding the transients that are more pronounced in the simulation for such low power values. The effective noise figure is 13.3 dB for the model and 15.6 dB for the simulation for an input power of -15 dBm and the case of applying means of downstream cancellation (Fig. 4.14(d)). If there would be no cancellation, the effective noise figure would raise to 17.2 dB for the model and 19 dB for the simulation.

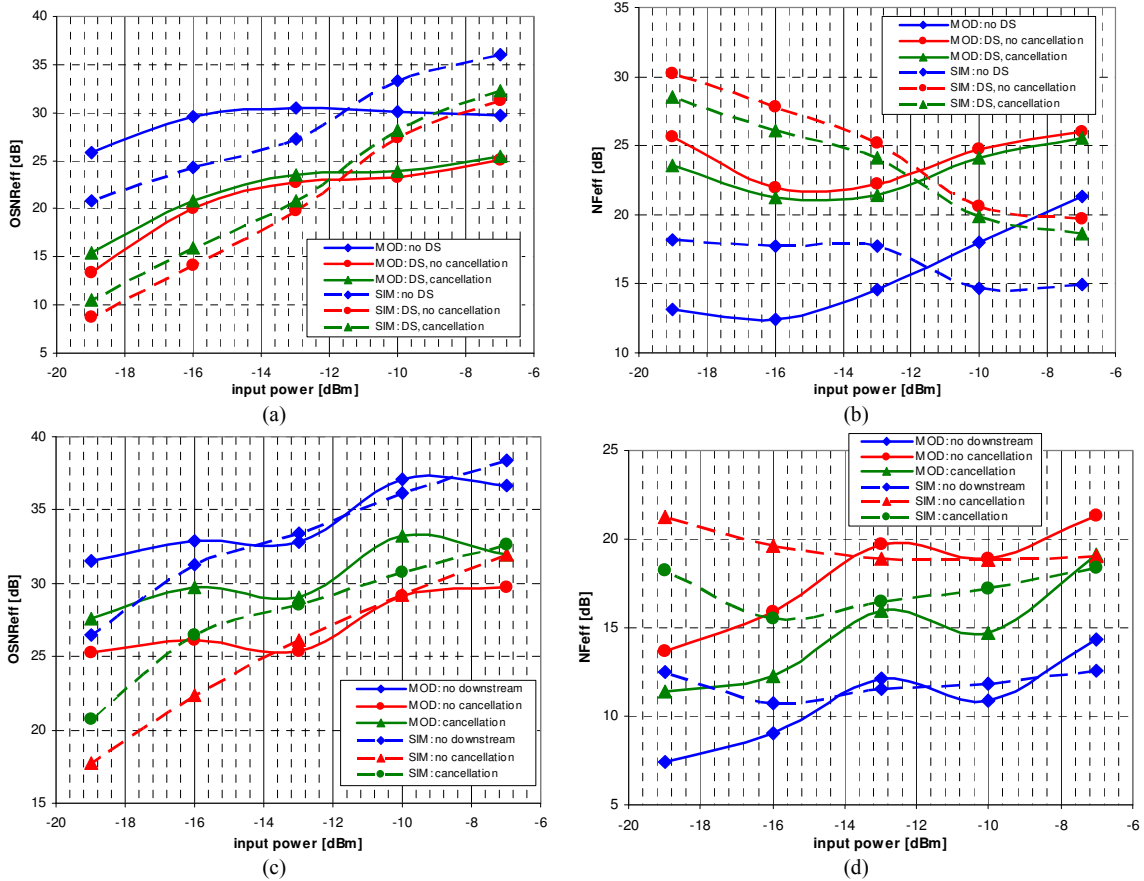


Fig. 4.14. (a),(c) Effective OSNR and (b),(d) effective noise figure obtained by model (solid lines) and simulation (dashed lines) for (a),(b) a RSOA and (c),(d) a SOA/REAM as upstream modulator at the ONU.

The increase of the effective noise figure strongly depends on the cancellation technique. Especially for the SOA/REAM based ONU, the difference between the case with and without the cancellation is large, mostly due to the perfect operation of the EAM that does not suffer from a limitation in the required electro-optical bandwidth. If the downstream is switched on, the effective noise figure increases by ~ 7.5 dB for an input power of -13 dBm but can be reduced to an increase of 4 to 5 dB with cancellation (Fig. 4.15(a)).

The limited bandwidth of the RSOA leads to a compression of this difference. For the same optical input power the effective noise figure increases by the same value of ~ 7.5 dB applying downstream data. A part of the penalty can be reduced with the help of the cancellation so that the effective noise figure is increased by ~ 6.5 dB (Fig. 4.15(b)). This rather small improvement compared to the ONU with SOA+REAM is directly related to the performance of nowadays commercially available devices and it is expected to achieve better results in future. Due to the higher net gain of the RSOA a stronger dependence on the optical input power is given since the gain saturation removes the pattern more efficiently for higher input power values.

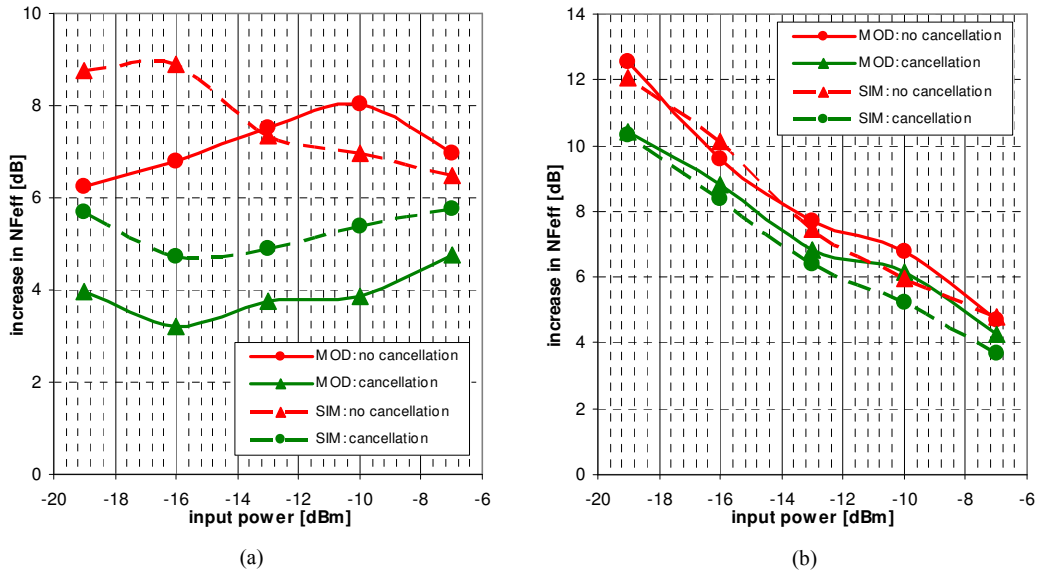


Fig. 4.15. Relative increase of the effective noise figure, referenced to the case of remote carrier modulation with the absence of downstream data, for having (a) a SOA/REAM and (b) a RSOA as reflective modulator at the ONU.

4.4.3 Optimum Reception Bandwidth for the Upstream

Although it is in principle possible to counteract the downstream signal at the ONU by its counter-injection, the feed-forward approach is practically limited by the low electro-optical bandwidth that nowadays RSOAs are suffering from.

The filter at the electrical OLT receiver has to be therefore adjusted to reject the remaining spectral components of the downstream. Although this is in principle no further problem, penalties can arise when the modulation bandwidth of the RSOA approaches values that are below the required bandwidth for the desired upstream data rate. In this case a trade-off between residual downstream pattern and cut in the upstream spectrum has to be made when designing the electrical low-pass filter at the OLT receiver.

An evaluation of the optimum bandwidth for this filter at the electrical OLT receiver can be made based on four different scenarios that are summarized as follows.

- *US only*: an unmodulated optical carrier is sent to the ONU and remodulated by the RSOA with upstream at a data rate of 2.5 Gb/s
- *US + DS*: the optical carrier sent from the OLT is modulated with a 10 Gb/s downstream that has an ER of 3 dB
- *US + DS + bandwidth limited cancellation*: in addition to the upstream, a feed-forward cancellation is applied to reduce the impact of the downstream in the upstream bit pattern. The electrical interface was emulated by a 4th order Bessel filter with a bandwidth of 2 GHz and therefore the overall electro-optical response that is given by the RSOA is limited by the response of the bonding interface between package and semiconductor.

These four cases were assessed with an analytical model. The delivered OSNR at the OLT receiver was 32 dB according to an input of -15 dBm at the RSOA and a nominal RSOA noise figure of 11 dB. An EDFA with a noise figure of 3.5 dB was chosen as preamplifier and provides a gain of 20 dB. The ASE was then filtered with a 100 GHz optical band-pass filter and the signal was detected with an APD that had a multiplication $M=6$, an ideal conversion efficiency and a thermal noise density of $28.8 \text{ pA}/(\text{Hz})^{1/2}$. A noiseless electrical amplifier with a gain of 20 dB was placed in front of the electrical receiver, which contains the electrical low-pass filter that is subject to optimization.

A PRBS was assumed for the down- and the upstream and hence the spectrum S_{PRBS} of the data streams is determined by the *sinc* function according to

$$S_{PRBS}(f) \propto \text{sinc}^2(\pi fT) \quad (4.53)$$

In a conventional receiver the electrical reception filter would be expected to be wide enough not to cut the upstream data signal and narrow enough to reject the optical noise that is detected after the optical band-pass filter as well as beat noise contributions. On the other hand, the residual downstream will be the dominating source of distortion and the optimal bandwidth will be therefore less than 75% of the upstream data rate $R_{b,US}$ that would be typically chosen for intensity modulated data signals.

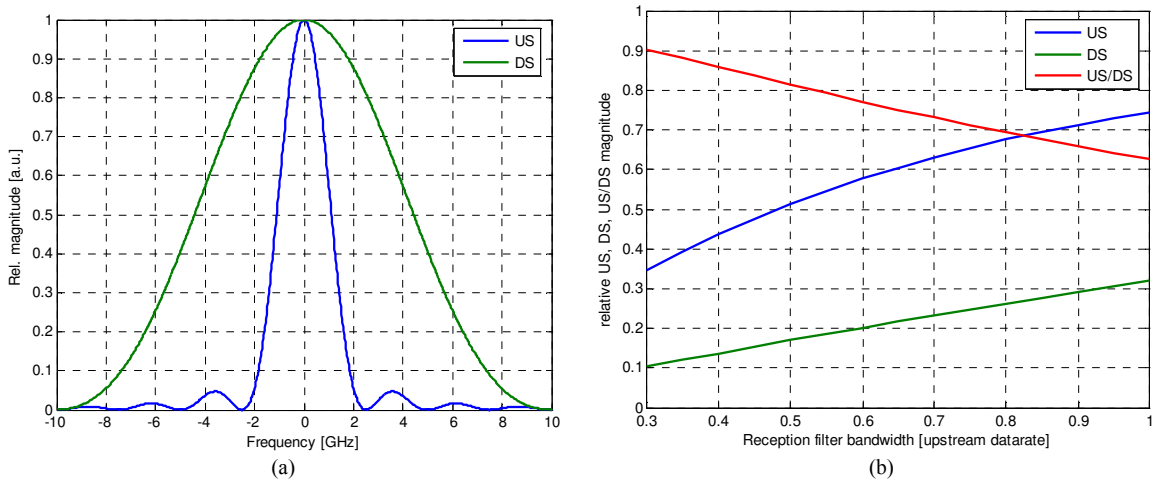


Fig. 4.16. (a) Spectra of upstream (US) and downstream (DS), both treated as PRBS, and (b) relative up- and downstream magnitude when their spectra are cut with a Bessel filter at the electrical OLT receiver as well as the ratio between the data streams.

Fig. 4.16(b) shows the magnitude of the received signal components for different reception filter bandwidths. While the ratio between up- and downstream decreases with a spectrally wider filter and leads to a reduced suppression of the residual downstream, the upstream signal is cut too much if the filter bandwidth is chosen too narrow.

For plain upstream modulation without downstream data the optimal reception filter bandwidth is $0.75 R_{b,US}$ and coincides with the value that can be found in literature (Fig. 4.17(a)). The penalty for narrower bandwidths is stronger than for wider ones since a

cut in the signal spectrum affects the BER worse than a slightly increased noise contribution.

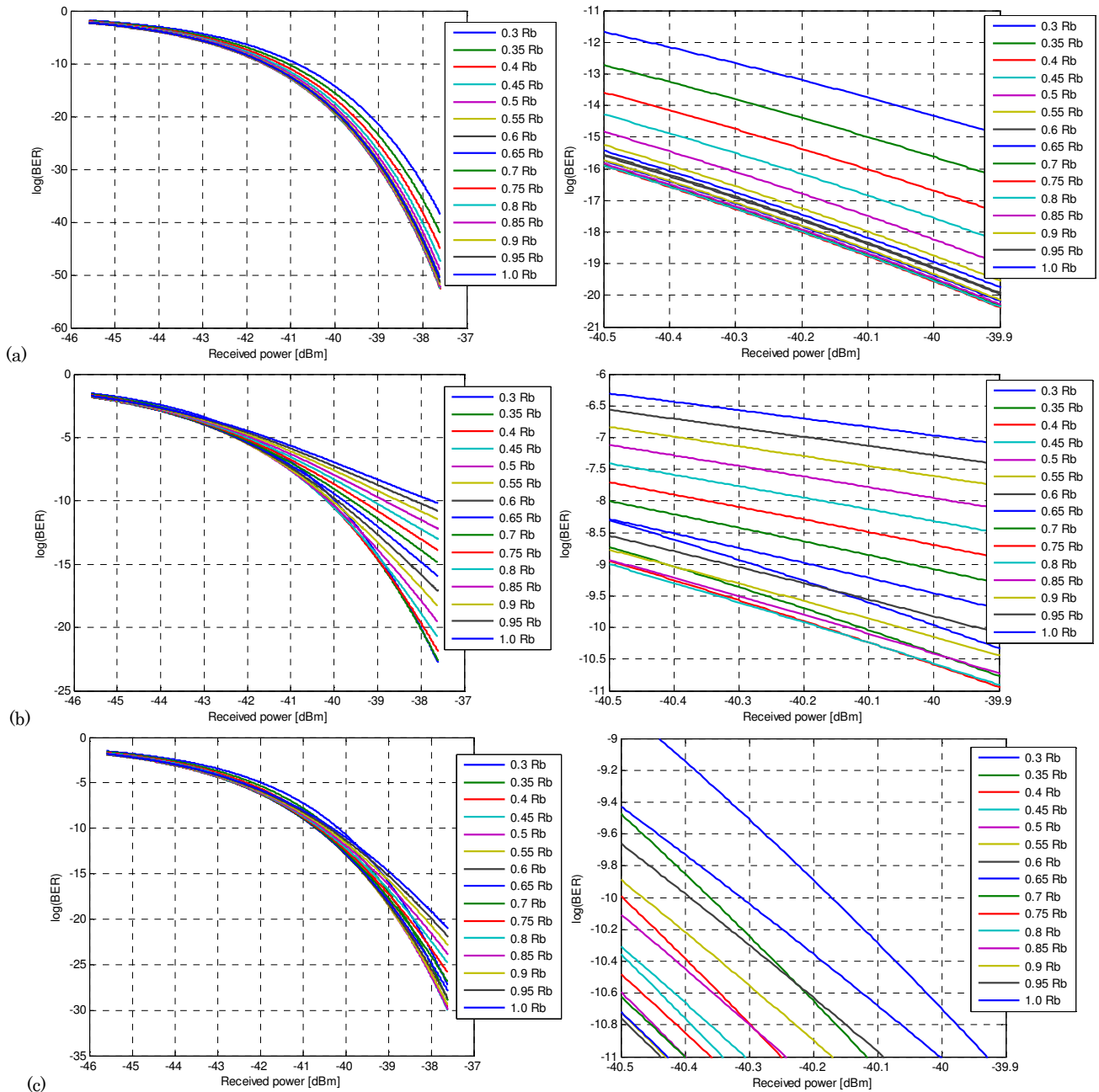


Fig. 4.17. BER vs. input power into the optical OLT receiver for (a) transmission of only upstream data, (b) an unsuppressed downstream with an initial ER of 3 dB and (c) the case of downstream cancellation.

If a downstream is present but not cancelled (Fig. 4.17(b)), the optimal filter bandwidth is shifted to a lower value of $0.4 \dots 0.5 R_{b,US}$. Although the upstream signal is cut slightly, the downstream is suppressed even more and due to that a net benefit is obtained. However, the overall BER performance is naturally worse.

An additional downstream cancellation reduces the residual downstream pattern in the upstream so that the optimal filter bandwidth is $0.55 \dots 0.6 R_{b,US}$ and therefore located between the two previously mentioned cases (Fig. 4.17(c)). The BER performance is

improved towards the original scenario of imprinting data on an unmodulated optical carrier.

The chosen scenarios show that the optimal reception filter bandwidth shifts to lower values for the case of an unsuppressed downstream, as can be seen in Fig. 4.18(a). This proves that an unsuppressed downstream dominates the reception penalty when being compared to a cut in the upstream signal spectrum.

The penalty in sensitivity, shown in Fig. 4.18(b), increases much stronger for unnecessary wide filter bandwidths when a downstream is present, reflecting that the residual downstream pattern is dominating the BER over other noise contributions.

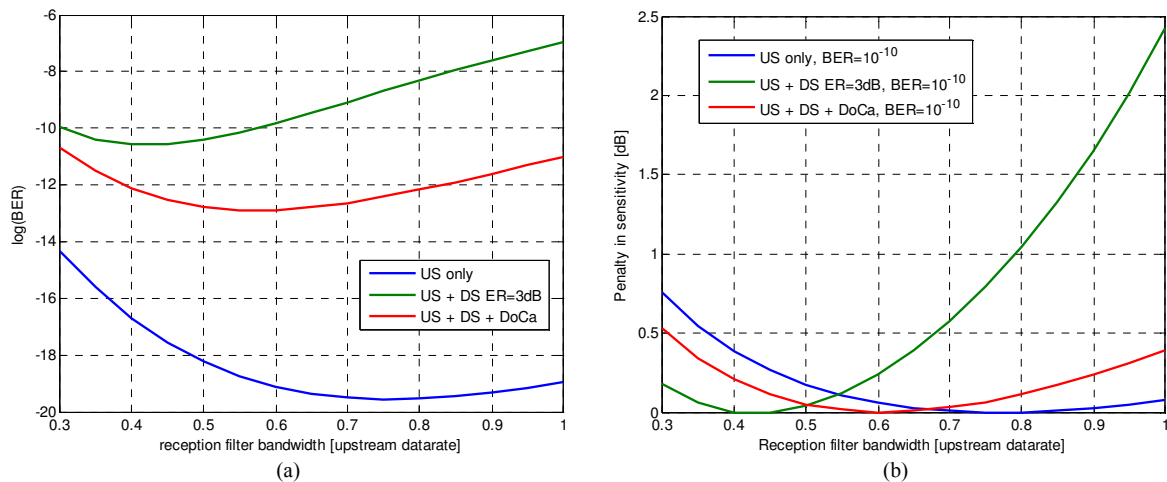


Fig. 4.18. (a) BER for an input power of -40 dBm into the optical receiver at the OLT, and (b) penalty in sensitivity for plain upstream transmission, without and with cancelled downstream data, at a BER level of 10^{-10} and referenced to the sensitivity of the optimal reception filter bandwidth.

4.4.4 Experimental Validation

Before the feed-forward cancellation technique is applied to a PON, its back-to-back performance is assessed for a RSOA- and also for a REAM-based ONU [166]. The feasibility in WDM- and WDM/TDM-PONs with extended loss budget is proven for bit rates up to symmetrical 10 Gb/s.

Back-to-Back Performance

According to the feed-forward carrier recovery, a coupler (C_O) splits the detection and the remodulation branch inside the ONU, whereby the latter holds a fiber delay line (FDL) to cope for the slower propagation of the electronic cancellation signal that originates at the APD (Fig. 4.19). As there is no information about the power margins and the sensitivities of down- and upstream so far, the coupling ratio was chosen to be 50/50. The APD at the ONU had a sensitivity of better than -27 dBm and an electrical filter matched to the downstream was placed in front of the electrical receiver of the ONU.

The cancellation circuit consists of an electrical delay ($\Delta\tau$) for fine tuning of the path lengths, a derivative filter (DF) as described earlier and RF amplifiers. A passive star combiner was taken to add the upstream to the cancellation signal.

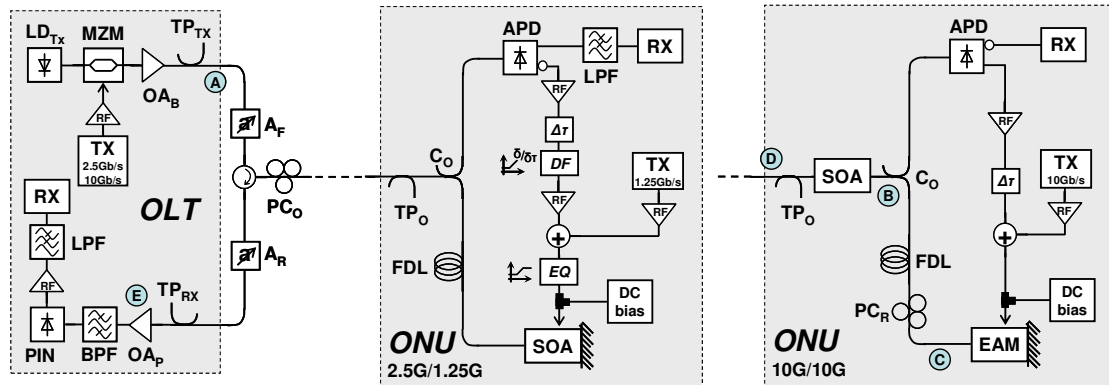


Fig. 4.19. Proof-of-concept setup for the feed-forward downstream cancellation in a RSOA- and a REAM-based ONU, exploiting gain and loss modulation to flatten the optical seed of the upstream modulator.

The RSOA used was packaged in an uncooled TO-can and its electro-optical response had a 3 dB bandwidth of 0.8 GHz for the chosen bias point for operation. The electro-optical bandwidth was extended to ~ 1.2 GHz with the help of a passive RLC-network that acts as equalizer (EQ), at the cost of RF losses (Fig. 4.20). The RSOA that is nominally rated for 1 Gb/s is therefore suitable for 2.5/1.25 Gb/s transmission.

The noise figure was 9 dB and the small signal gain was 21.7 dB with an optical 3-dB gain bandwidth of 54 nm that is centered at 1550 nm. An upstream ER of 8 dB was achieved and is limited by the requirement of keeping the RSOA transparent during the space bits. Since the electro-optical bandwidth is less critical after equalization, the upstream ER is not compromised as in chapter III.5.

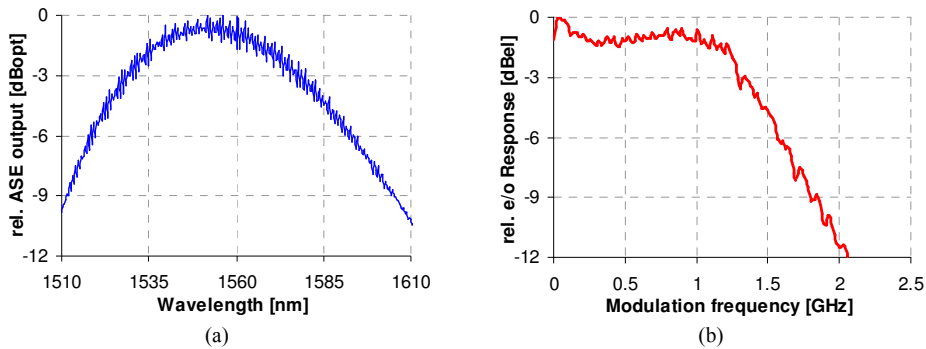


Fig. 4.20. (a) ASE spectrum and (b) electro-optical response of the equalized RSOA.

A REAM replaces the RSOA in case of a higher symmetrical data rate of 10 Gb/s as it offers a larger electro-optical bandwidth. The intrinsic optical losses of 16 dB restrict to use this device solely without optical amplifier since the ONU would then provide a too low output power to cover a typical power budget of a PON. The missing gain is provided by a SOA at the ONU input which not only compensates for the losses of the REAM but also acts as preamplifier for the downstream – though no optical filter can be placed for ASE rejection to retain a colorless ONU design.

For the REAM-based ONU the SOA at its input had a small signal gain of 21 dB. The bias of the REAM was $-1.8V$, while the modulation was $3.5V_{pp}$, leading to an upstream ER of 13 dB. No cross-gain modulation between down- and upstream was observed in the common SOA thanks to high intrinsic losses of the REAM.

For an input power of -14 dBm at this ONU the power levels and OSNR levels are: 3 dBm and 46 dB after the OLT booster (point A in Fig. 4.19), -1.5 dBm and 38.8 dB after amplification with the SOA (B), -20.5 dBm after remodulation with the REAM (C) and -12.1 dBm and 27.7 dB after being boosted by the SOA (D). The ONU had a net gain of 1.9 dB.

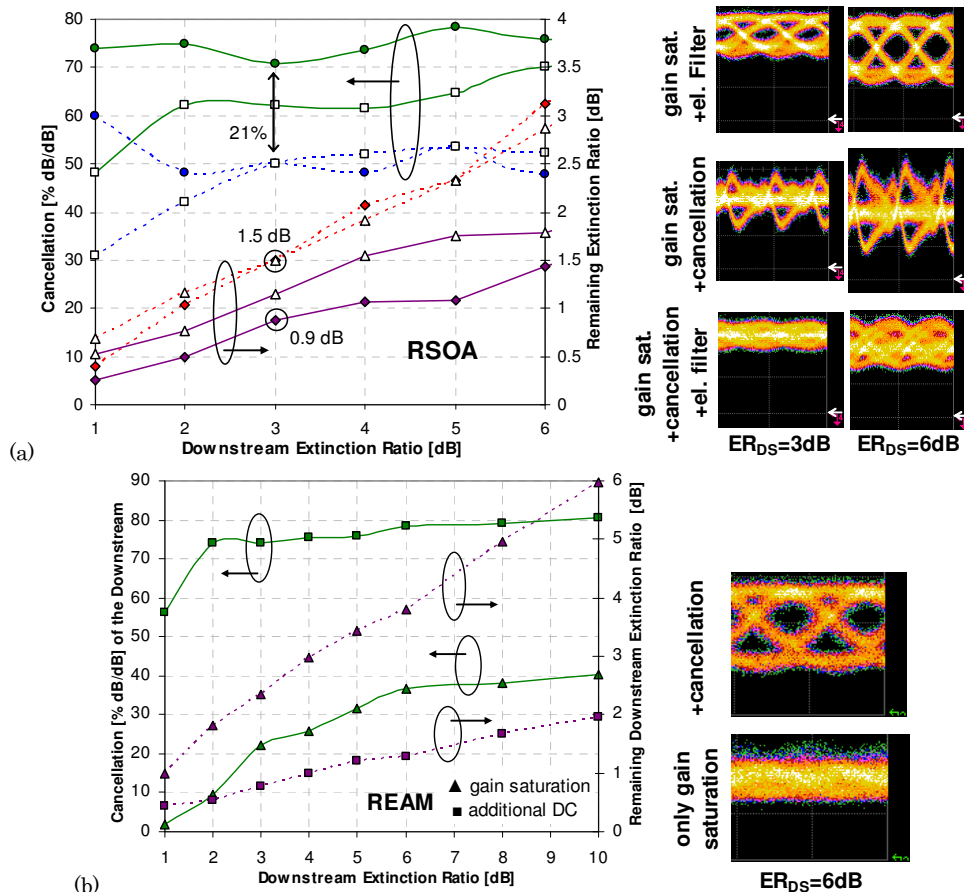


Fig. 4.21. Cancellation efficiency and remaining downstream for after carrier recovery using (a) a RSOA (dashed lines correspond to optical gain saturation, solid lines to an additional cancellation, hollow markers indicate the absence of the electrical filter at the OLT receiver while filled markers represent its presence) and (b) a REAM for the purpose of downstream cancellation.

The remodulation quality is proven in terms of carrier recovery and BER measurements. For this reason the downstream ER was not fixed but varied by setting the bias point and modulation swing of the MZM. The operating wavelength was set to 1551.32 nm for the RSOA-based ONU and to 1560.61 nm for the REAM-based ONU since the latter is intended to be used in the L-band. The launched power at the OLT was fixed to 3 dBm. The ONU and OLT input levels were varied with attenuators (A_F , A_R) to obtain BER measurements, while the ONU input was fixed to -14 dBm for the upstream measurements.

The efficiency of the natural optical gain saturation and an additional feed-forward cancellation (marked as ‘DC’) to counteract a downstream is presented in Fig. 4.21 for an ONU input power of -14 dBm. The cancellation efficiency is here defined as the reduction of the ER in reference to its initial value. With the RSOA as remodulator, an electrical filter with a bandwidth of 1.25 GHz was additionally placed after the upstream detector in some of the shown cases, while there was no upstream modulation itself. The efficiency increases by 21% for an ER of 3 dB, where the remaining ER is 1.5 dB with the gain saturation effect and 0.9 dB with additional feed-forward cancellation. For the REAM-based ONU the efficiency increases by 42% for an ER of 6 dB when employing electrical means of cancellation, meaning a decrease in the remaining ER from 3.8 dB to 1.3 dB. The efficiency is constant for both ONUs at high downstream ERs, while for lower ones distortions due to the overshoot of the SOA cause a reduction. This is explained by the fact that these transients are then already in the order of magnitude of the unsuppressed downstream and have influence on the calculation of the cancellation efficiency.

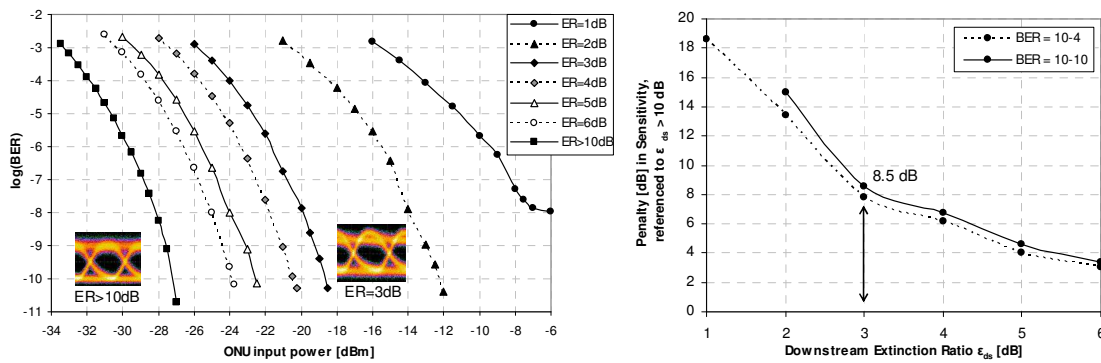


Fig. 4.22. Downstream BER measurements for the RSOA-based ONU and its penalty in sensitivity.

The downstream BER measurements for the RSOA-based ONU are shown in Fig. 4.22. ERs larger than 2 dB are reasonable considering a BER of 10^{-10} and typical PON power budgets. A BER floor above 10^{-10} appears for an ER of 1 dB, while FEC allows also an ER of 2 dB to reach an acceptable sensitivity of -18.4 dBm.

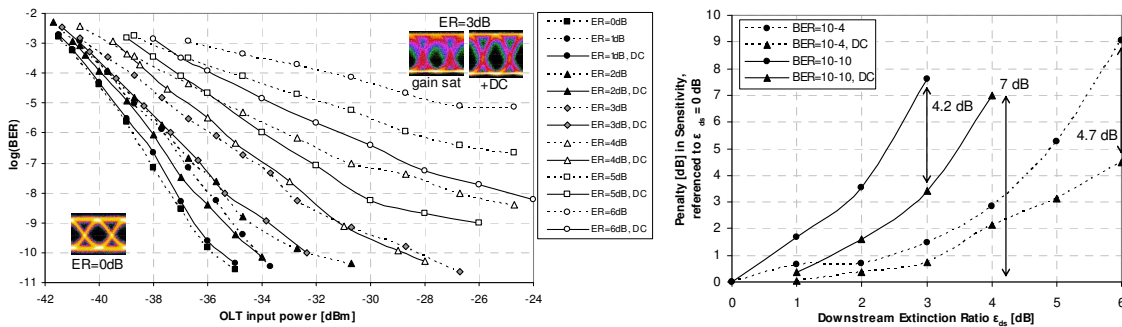


Fig. 4.23. Upstream BER measurements for the RSOA-based ONU and its penalty in sensitivity.

For the upstream a BER of 10^{-10} was obtained for ERs of 3 dB and less without downstream suppression and also for 4 dB with cancellation (Fig. 4.23). The penalty

referenced to the case without downstream is then 7 dB. At an ER of 3 dB the penalty decreases by 4.2 dB when using the cancellation. The FEC threshold can be reached even with an ER of 6 dB. For this ER the sensitivity increases by 4.7 dB once feed-forward cancellation is used.

For the REAM-based ONU reasonable ERs for the downstream (Fig. 4.24) are 3 dB or larger (Fig. 4.30). Operation at the FEC threshold does not give a significant advantage.

The operating range for the upstream at a BER of 10^{-10} can be extended from an ER of 1.5 dB to 3 dB when employing the cancellation (Fig. 4.25). The sensitivity is then just -10.5 dBm due to the low net gain of the ONU, giving a penalty of 4.2 dB. At the FEC level the ER can be extended from 4.5 dB to at least 6 dB.

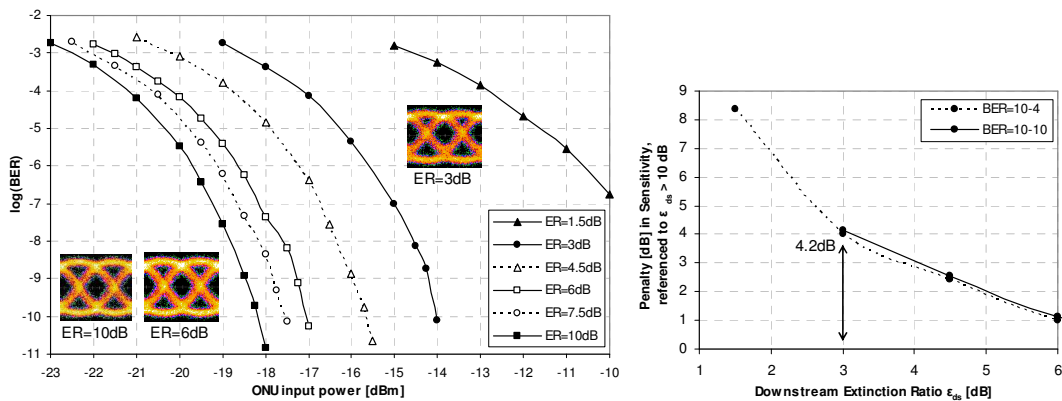


Fig. 4.24. Downstream BER measurements for the REAM-based ONU and its penalty in sensitivity.

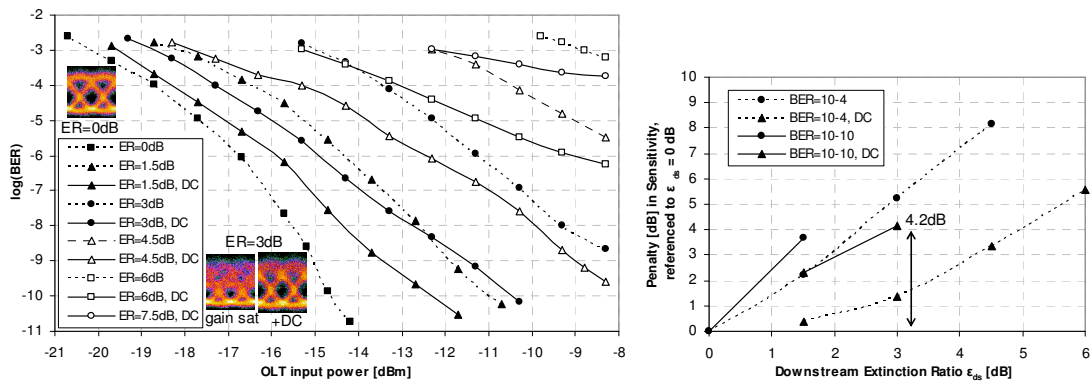


Fig. 4.25. Upstream BER measurements for the REAM-based ONU and its penalty in sensitivity.

In continuation to this experimental proof-of-concept that shows the extension of compatible downstream ERs, the application of the RSOA-based ONU with its high net gain is addressed for long reach PONs with extended loss budget and the feasibility for an EAM-based ONU in a simpler WDM-PON is proven.

Long Reach PON with GPON-compatible 2.5/1.25 Gb/s ONU

The presented RSOA-based ONU was further embedded in a hybrid PON with 100 km reach and 1:32 split in the trees [167]. This scenario corresponds to an extended GPON

access network but utilizes just a single wavelength for full-duplex data transmission. The degradation of the OSNR, which is caused by accumulation of noise along the light path when reamplification takes place, may limit the transmission performance in addition to the unsuppressed downstream pattern.

The architecture of the PON is from ring+tree type (Fig. 4.26) and has a 100 km long double fiber ring to keep Rayleigh backscattering (RB) effects to just a relative short bidirectional segment of 10 km length at the tree. Single wavelengths are dropped from the ring at the remote node (RN) where also remote amplification is applied to cope for the advanced loss budget. The amplification stages in the RN have been pumped locally with two laser diodes of each 20 dBm power at 1480 nm for the sake of simplicity.

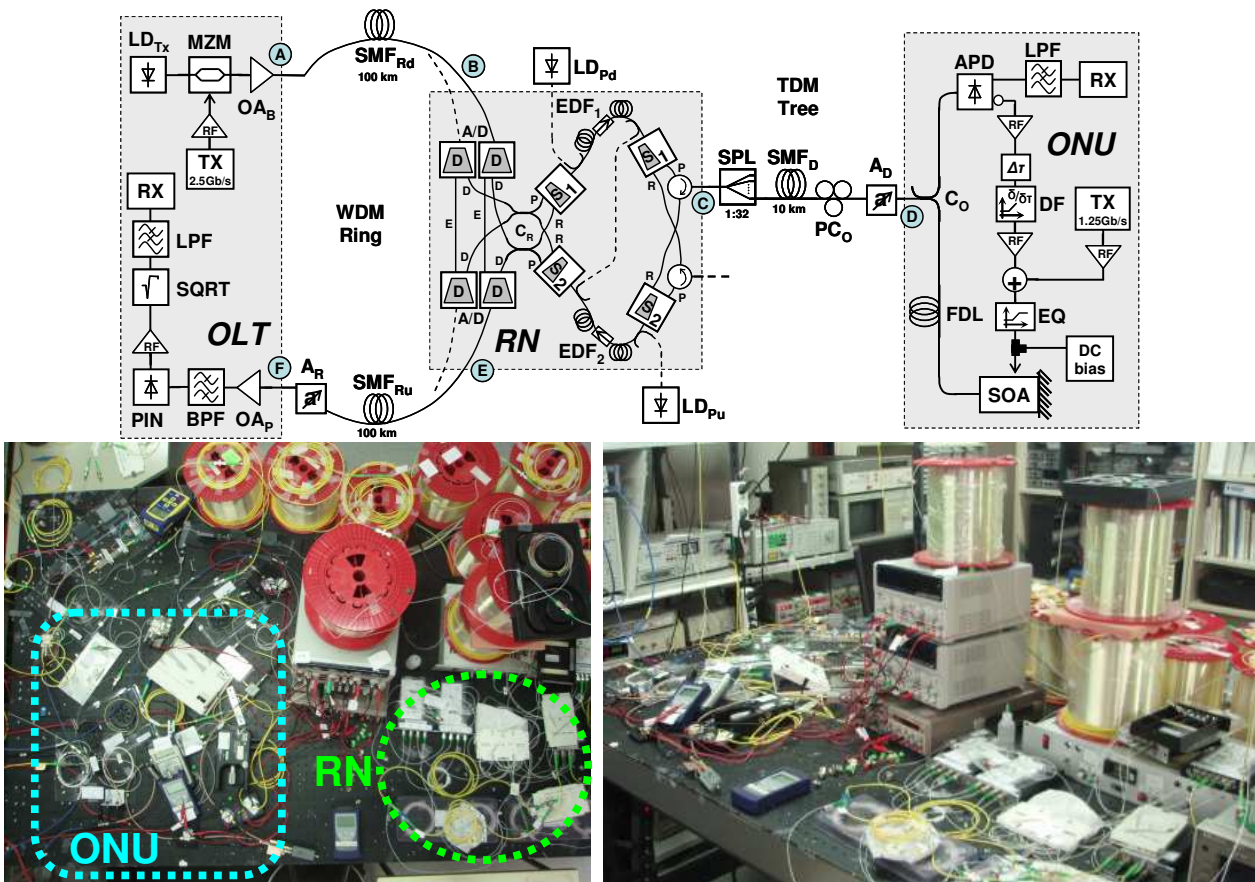


Fig. 4.26. Experimental setup for a long reach PON employing remote amplification and downstream cancellation techniques at ONU and OLT.

In detail, the RN that will be also used in a later experiment in a slightly simplified version comprises two 15m long HE980 EDFs for both, the downstream and the upstream branch. An isolator was placed between them to avoid amplified reflections and lasing due to the high gain. For the drop and insertion of the signals into the ring, 200 GHz thin film add/drop filters (A/D) were used together with a 50/50 resiliency coupler (C_R). This ring interface of the RN caused 4.5 dB of insertion loss. At the tree interface, 100 GHz thin film filters are used together with circulators to filter the ASE noise from the downstream amplification stage and also from the ONU while the bidirectional data traffic from the tree is split into the unidirectional paths for amplification. This output stage of the RN has another 1.5 dB of insertion loss.

An additional non-linear square root (SQRT) function at the OLT receiver works as a soft limiter [164], expanding the upstream and compressing the remaining downstream. Due to the limiting behavior of the electrical SQRT at the OLT receiver the transients induced by the gain dynamics of the RSOA are reduced in their magnitude.

Note. The SQRT function is an alternative though not that efficient approach to counteract the degrading downstream pattern. Its nonlinearity provides a mean of electrical suppression in terms of compressing the mark level of a received signal while the space level is expanded. The downstream is therefore compressed and the upstream is not harmed if the space level is close to the dark level of the detector, meaning a high upstream ER. A more detailed analysis of the SQRT behavior is as follows.

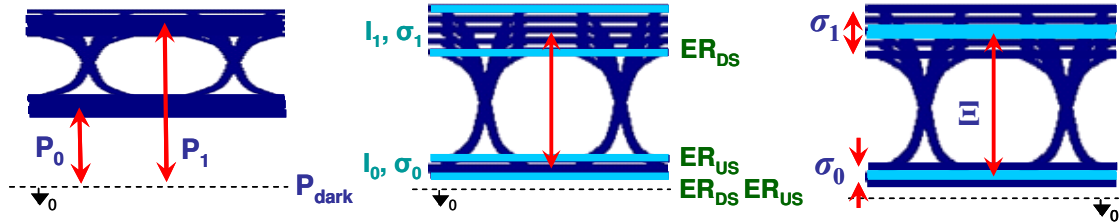
Having only downstream according to equations 4.3 and 4.7, the detected photo current $i_{det,DS}$ is

$$i_{det,DS} = S \left(\frac{P_1}{ER_{DS}} + A_{DS} \cdot \pi_{DS}(t) \right) \quad ER_{DS} = \frac{P_1 - P_{dark}}{P_0 - P_{dark}} \quad (4.54)$$

while for a combined case of concurrent down- and upstream transmission the detected current i_{det} is given by

$$i_{det} = S \left[\left[\frac{P_1}{ER_{DS}} + A_{DS} \cdot s_{DS}(t) \right] \frac{1}{ER_{US}} + \left[\frac{P_1}{ER_{DS}} + A_{DS} \cdot \pi_{DS}(t) \right] \left(1 - \frac{1}{ER_{US}} \right) \pi_{US}(t) \right] \quad (4.55)$$

and depends on both modulation indices for down- and upstream.



There are four possible cases for the detected current levels, defined by the bit combinations of down- and upstream. Considering an upstream ER that is larger than the downstream ER, the received eye will have a mark level that is much broader than the space level. The detected photo currents without and with SQRT for the possible combinations are the following, considering that $I_1 = S P_1$.

$$\bullet \quad \pi_{DS} = 1, \pi_{US} = 1: i_{det} = I_1 \quad i_{det,SQRT} = \sqrt{I_1} \quad (4.56)$$

$$\bullet \quad \pi_{DS} = 0, \pi_{US} = 1: i_{det} = \frac{I_1}{ER_{DS}} \quad i_{det,SQRT} = \frac{\sqrt{I_1}}{\sqrt{ER_{DS}}} \quad (4.57)$$

$$\bullet \quad \pi_{DS} = 1, \pi_{US} = 0: i_{det} = \frac{I_1}{ER_{US}} \quad i_{det,SQRT} = \frac{\sqrt{I_1}}{\sqrt{ER_{US}}} \quad (4.58)$$

$$\bullet \quad \pi_{DS} = 0, \pi_{US} = 0: i_{det} = \frac{I_1}{ER_{DS}ER_{US}} \quad i_{det,SQRT} = \frac{\sqrt{I_1}}{\sqrt{ER_{DS}ER_{US}}} \quad (4.59)$$

Looking at the eye diagram, the width of the mark and space level, σ_1 and σ_0 , and the eye height Ξ , defined as the difference between the average mark and space level, are

$$\sigma_1 = I_1 \left(1 - \frac{1}{ER_{DS}} \right) \quad \sigma_{1,SQRT} = \sqrt{I_1} \left(1 - \frac{1}{\sqrt{ER_{DS}}} \right) \quad (4.60)$$

$$\sigma_0 = I_1 \left(\frac{1}{ER_{US}} - \frac{1}{ER_{US}ER_{DS}} \right) \quad \sigma_{0,SQRT} = \sqrt{I_1} \left(\frac{1}{\sqrt{ER_{US}}} - \frac{1}{\sqrt{ER_{US}ER_{DS}}} \right) \quad (4.61)$$

$$\Xi = \bar{I}_1 - \bar{I}_0 = \frac{I_1}{2} \left[\left(1 + \frac{1}{ER_{DS}} \right) - \left(\frac{1}{ER_{US}} + \frac{1}{ER_{US}ER_{DS}} \right) \right] \quad (4.62)$$

$$\Xi_{SQRT} = \frac{\sqrt{I_1}}{2} \left[\left(1 + \frac{1}{\sqrt{ER_{DS}}} \right) - \left(\frac{1}{\sqrt{ER_{US}}} + \frac{1}{\sqrt{ER_{US}ER_{DS}}} \right) \right]$$

As a figure of merit for the BER improvement, the Q factors for the case without and with SQRT are compared, according to the definition in equation 4.6. In this way, it is obtained that

$$Q = \frac{1}{2} \frac{ER_{DS}ER_{US} + ER_{US} - ER_{DS} - 1}{ER_{DS}ER_{US} - ER_{US} + ER_{DS} - 1} \quad (4.63)$$

$$Q_{SQRT} = \frac{1}{2} \frac{\sqrt{ER_{DS}ER_{US}} + \sqrt{ER_{US}} - \sqrt{ER_{DS}} - 1}{\sqrt{ER_{DS}ER_{US}} - \sqrt{ER_{US}} + \sqrt{ER_{DS}} - 1}$$

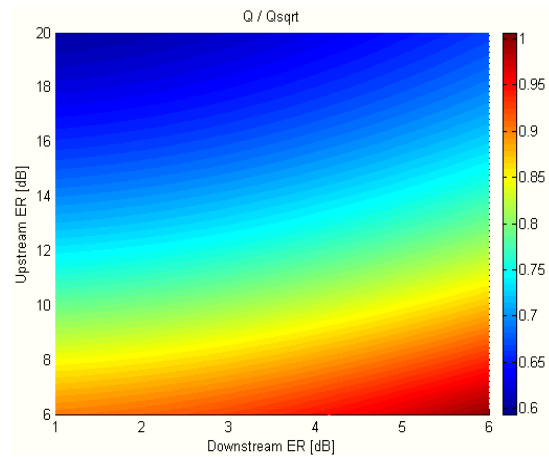
and further

$$Q = \frac{1}{2} \frac{(ER_{DS} + 1)(ER_{US} - 1)}{(ER_{DS} - 1)(ER_{US} + 1)} \quad Q_{SQRT} = \frac{1}{2} \frac{(\sqrt{ER_{DS}} + 1)(\sqrt{ER_{US}} - 1)}{(\sqrt{ER_{DS}} - 1)(\sqrt{ER_{US}} + 1)} \quad (4.64)$$

The improvement is now defined as the relation between the Q factor without and with SQRT according to

$$\psi = \frac{Q}{Q_{SQRT}} = \frac{(ER_{DS} + 1)(\sqrt{ER_{DS}} - 1)(ER_{US} - 1)(\sqrt{ER_{US}} + 1)}{(ER_{DS} - 1)(\sqrt{ER_{DS}} + 1)(ER_{US} + 1)(\sqrt{ER_{US}} - 1)} \quad (4.65)$$

The improvement ψ is below unity for all ERs for down- and upstream. It approaches unity for a low upstream ER when the downstream ER is high at the same time. This can be understood in terms of compression and expansion of the nonlinear SQRT function: although the high downstream ER is compressed, the low upstream ER means a broad space level in the eye, which is expanded to an even broader band and thus leading to just a negligible improvement.



In a long reach PON with cascaded optical amplification it is always useful to look at the signal evolution along the light path (Fig. 4.27) to determine eventual degrading problems. For a downstream ER of 3 dB the signal power levels and OSNRs, measured with a resolution bandwidth of 0.1 nm, were: 3 dBm and 47.2 dB after the OLT booster (A), -18.8 dBm after passing the downstream ring at the input of the RN (B), 7.7 dBm and 30.2 dB after amplification in the RN when launched into the tree (C). In the drop, a splitter of 1:8 and 1:4 as well as the drop SMF causes a low ONU input signal of -14 dBm (D). The further power levels and OSNRs were -6.5 dBm and 26.9 dB at the ONU output (D), meaning a net gain of 7.5 dB for the ONU, -27.6 dBm after the return across the high tree loss to the RN (C), -0.6 dBm and 23 dB when injected into the upstream ring (E), and -22.3 dBm when reaching the OLT after passing the upstream ring (F). The OSNR was 21 dB after the preamplification at the optical OLT receiver which consisted of an EDFA that was pumped at 980 nm. The PIN diode used for photo detection at the OLT had a sensitivity of -18.5 dBm.

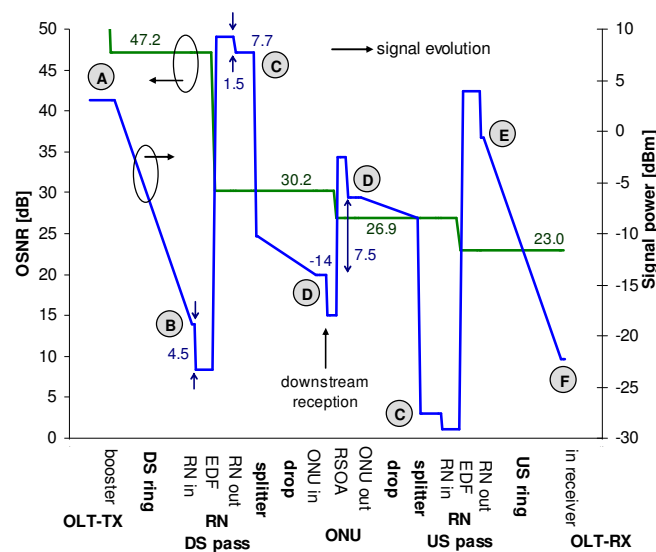


Fig. 4.27. Evolution of signal power level and OSNR along the PON.

The high optical losses in the different segments of ring and tree, situated between the different amplification stages, lead to a rapid OSNR degradation along the PON. The high initial OSNR degrades by 17 dB at the downstream drop amplification of the RN. Despite the higher noise figure of the RSOA, the OSNR degradation of 3.3 dB is lower compared to the upstream amplification in the RN, which causes 3.9 dB of degradation, showing that the ONU net gain is slightly too low.

The Optical Signal-to-RB-Ratio (OSRR) at the drop fiber is determined by the high split in the tree and the net gain of the ONU. Since both of them are from high value, it is more probable that the downstream becomes affected before the upstream does. For the given conditions the OSRR was as high as 27 dB for the down- and 37 dB for the upstream. Therefore no strong RB penalty is expected for both data stream.

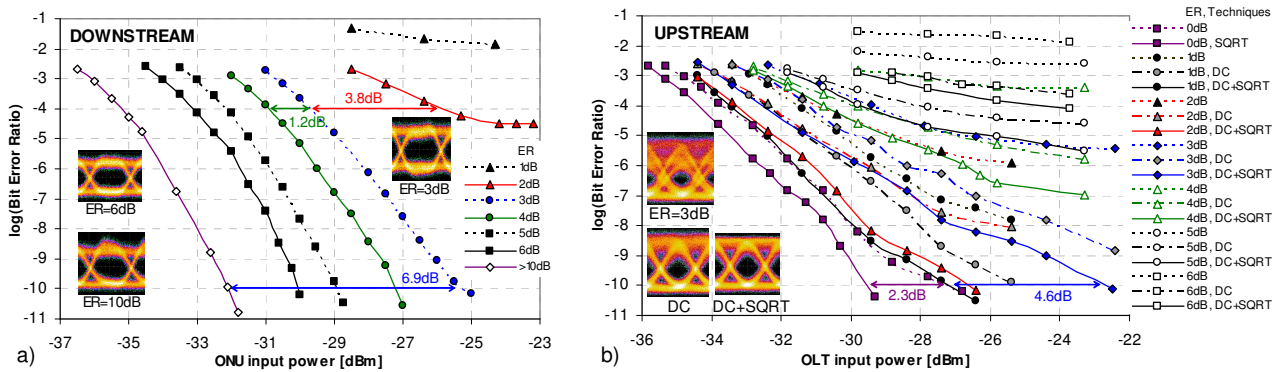


Fig. 4.28. BER measurements in the long reach PON for (a) the downstream and (b) the upstream for different downstream ERs.

The optimum ER for the downstream is defined for the most balanced power margins for the down- and upstream reception and can be found with an evaluation of the transmission performance which is shown in Fig. 4.28(a) and (b) for the down- and upstream, respectively.

A BER of 10^{-10} can be obtained for the downstream without problems for ERs of 3 dB or more. This proves that the power budget of the PON does not limit downstream transmission as the margin is 11.2 dB for the minimum required ER of 3 dB at this low BER level. An error floor is present at lower ERs due to the interplay of ASE and eye opening: an ER of 2 dB allows to reach only the FEC limit where the FEC gain is 4.5 dB. The penalty referenced to the case of having a separate wavelength for the downstream, which can be modulated with an ER as high as possible, is 6.9 dB for an ER of 3 dB at a BER of 10^{-10} . A slight variation around this operating point of having an ER of 3 dB shows a different behavior: while for the FEC level the penalty decreases by 1.2 dB once the ER is increased to 4 dB, it increases by 3.8 dB when the ER is reduced to 2 dB.

The BER measurements for the upstream show that a BER of 10^{-10} can be obtained for an ER of 3 dB when using both, feed-forward cancellation and square root equalization. Even for an ER of 6 dB the FEC threshold can be then reached. This is a quite big improvement compared to the cases where no means of downstream cancellation are employed: the best possible BER for an ER of 3 dB is then already

above 10^{-6} and for an ER of 6 dB there is a BER floor at 10^{-2} . Without any cancellation technique a BER of 10^{-10} is inaccessible except for the case where no downstream is present.

The SQRT enhances the transmission for low BERs as the disturbing RSOA induced overshoot is reduced by the SQRT and the electrical low-pass filter. In addition, strong optical noise is present in the PON due to the low received OSNR. An equal distribution of overshoot and noise contributions in the eye due to the expansion of the space level and the compression of the mark level leads to a more symmetrical eye with improved Q factor, giving a better BER at low values. This is evident for the pure upstream modulation where no downstream was present on the optical carrier: the improvement given by the SQRT for a low BER is advanced by 1.6 dB compared to the FEC level, reflecting the reduction of noise and overshoot in the mark level. The added SQRT allows for a BER lower than 10^{-10} with a downstream ER up to 3 dB, while without the SQRT it is not possible to access that low BER unless the downstream is switched off. In this case, the SQRT improves the sensitivity by 2.3 dB.

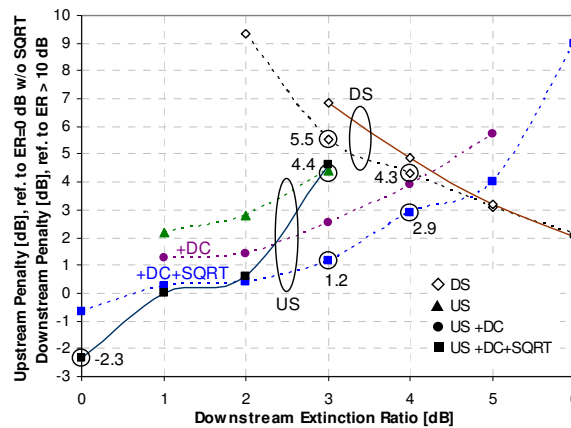


Fig. 4.29. Penalties in sensitivity for down- (hollow markers) and upstream (filled markers), referenced to an ER >10 dB and 0 dB, respectively. Solid lines correspond to a BER level of 10^{-10} , while dashed lines indicate reception at the FEC threshold. The \blacktriangle , \bullet , \blacksquare markers stand for unsupported transmission, feed-forward downstream cancellation (DC) and additional SQRT equalization.

Looking at the penalties (Fig. 4.29) where for the upstream the case of remodulating a plain optical carrier without having an additional SQRT at the OLT receiver is taken as the reference, it can be seen that incorporation of FEC is a very interesting option though it is related with extra but also shared cost. At its higher BER threshold the improvement when including both techniques, feed-forward cancellation and SQRT, grows with the ER and enables operation up to an ER of 5 dB. The unsupported transmission is not possible beyond an ER of 3 dB at the FEC level. The penalty is kept low by the SQRT for ERs up to 3 dB where it is just 1.2 dB and the difference to the case where only the feed-forward cancellation is present is about 1 to 1.5 dB and is independent of the ER.

Fig. 4.30 summarizes the FEC gain and the power margins for down- and upstream. The FEC gain for the downstream is quite flat compared to the upstream and has values

around 3.5 dB unless the eye becomes small so that a BER floor just below 10^{-10} is caused. The higher penalties for the upstream transmission at low BER given by the RSOA-induced transients and also by remaining downstream lead to a higher FEC gain when compared to the downstream transmission. In the back-to-back case where a BER of 10^{-10} can be obtained also for higher ERs due to the missing noise accumulation, the FEC gain rises from 4.5 dB at an ER of 1 dB up to 11.2 dB for an ER of 5 dB, when both techniques are applied for cancellation. If the SQRT is discarded, the BER floors rise and so does the FEC gain. This behavior is even more pronounced if also the feed-forward cancellation is not applied. In the PON the FEC gain shows the same steep rise with the ER but is shifted to higher values due to the enhanced error floors for low BERs. Without cancellation techniques the FEC gain for pure upstream modulation is 6.5 dB.

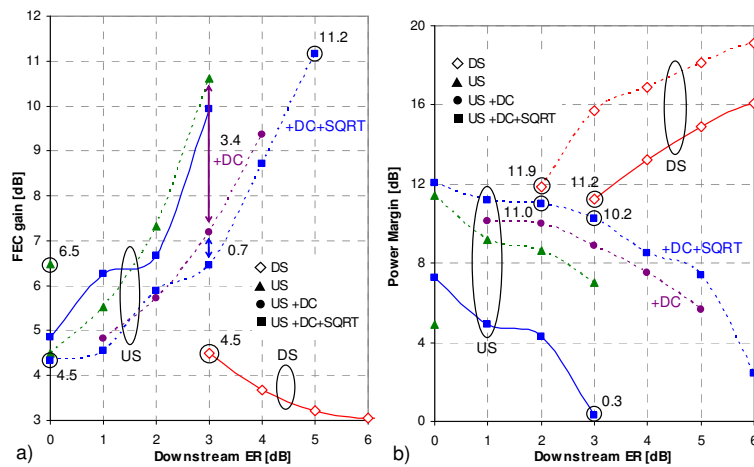


Fig. 4.30. (a) FEC gain for down- and upstream, where dashed lines indicate the back-to-back case, solid lines the case of the PON, hollow markers stand for the downstream (DS) and filled markers for the upstream (US), for which the $\blacktriangle, \bullet, \blacksquare$ markers indicate unsupported transmission, feed-forward downstream cancellation (DC) and additional SQRT equalization, respectively. (b) Power margins for down- and upstream. Solid lines indicate a BER of 10^{-10} , while dashed lines show results with FEC.

The power margins for the PON, shown in Fig. 4.30(b), partially reflect the differences in the FEC gain. Without any FEC applied the only compatible ER is 3 dB. The downstream has then a margin of 11.2 dB while only 0.3 dB are left for the upstream. The upstream margin can be increased to 10.2 dB when incorporating FEC at the upstream receiver and the ER of 3 dB stays the optimum. Both margins are then balanced and differ in only 1 dB. If FEC is also applied at the downstream receiver, the optimum ER is shifted to 2 dB, leading to margins of 11.9 and 11 dB for down- and upstream. However, this small increase of less than 1 dB at an already relative high margin comes at the significant additional cost of applying FEC at each ONU in the PON. The available margin of more than 10 dB for both, down- and upstream can be used to increase the reach of the PON or splitting ratio of the tree further.

Higher data rates with symmetrical transmission can be achieved with an EAM-based cancellation, which was tested in a WDM-PON with reduced link loss due to the limited net gain of the ONU.

Symmetrical 10 Gb/s WDM-PON with SOA/REAM-based ONU

The feed-forward approach works also for higher data rates and reflective modulators with appropriate modulation bandwidth, such as EAMs. Combined with a SOA section [168], such modulators can be an attractive low-cost solution for access since they have been proven to operate up to high temperatures without being thermally penalized [169]; While the working wavelength range for a temperature of 20°C was 80 nm within a 2 dB penalty in reception, it can be still maintained with 30 nm for a temperature of 70°C while a shift to longer wavelengths is introduced due to the band gap variation of the semiconductor material.

A typical response of such a SOA/REAM is shown in Fig. 4.31. While the EAM section allows high extinction of the incident light of up to more than 20 dB, the SOA compensates for the intrinsic EAM losses. The low net gain is caused by the waveguide-to-chip coupling that could be further improved by a tapered waveguide near the chip facet.

The operation point of the SOA/REAM was chosen with a SOA bias current of 160 mA and an EAM bias of -2V. The modulation voltage was 4 V_{pp}. Both, the DC bias and the drive voltage of the data signal could be lowered for the EAM at the cost of the upstream ER. In this way the modulator becomes more energy efficient since low drive voltages around 1 V_{pp} can already lead to an ER of 10 dB for the upstream signal, even at high data rates of 100 Gb/s [170].

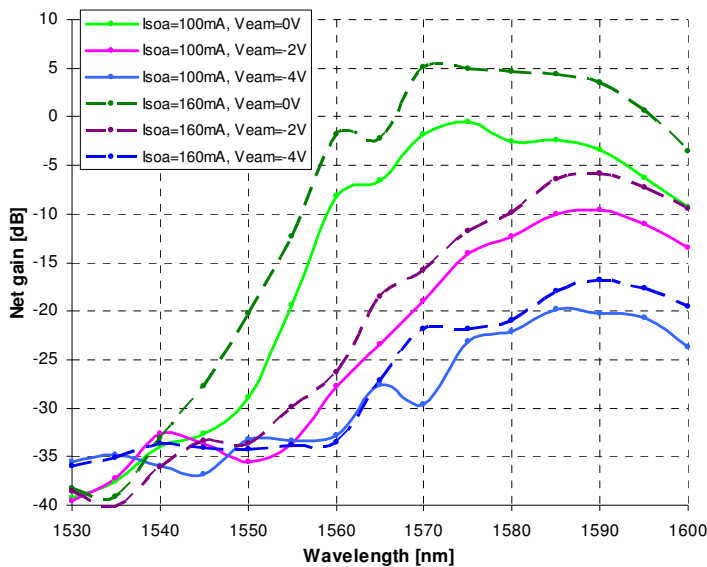


Fig. 4.31. Spectral net gain of a SOA/REAM for different bias points and the SOA/REAM device.

Fig. 4.32 shows a SOA/REAM-based ONU in a WDM-PON that is operated for full-duplex 10 Gb/s transmission. According to the WDM principle a continuous data stream

was transmitted from the OLT with a PRBS of length $2^{31}-1$ and remodulated with upstream data while the downstream pattern is erased at the same time. A DCF is required due to the positive chirp of the EAM that degrades the optical signal in conjunction with anomalous chromatic dispersion. Although a high negative EAM bias and operation close to the excitonic peak would cause a negative chirp, these conditions are typically not feasible due to the high insertion loss and the limitation in the operating wavelength range. Alternatively, the SOA could be modulated with the same data signal to convert the positive chirp of the EAM into a negative one [171].

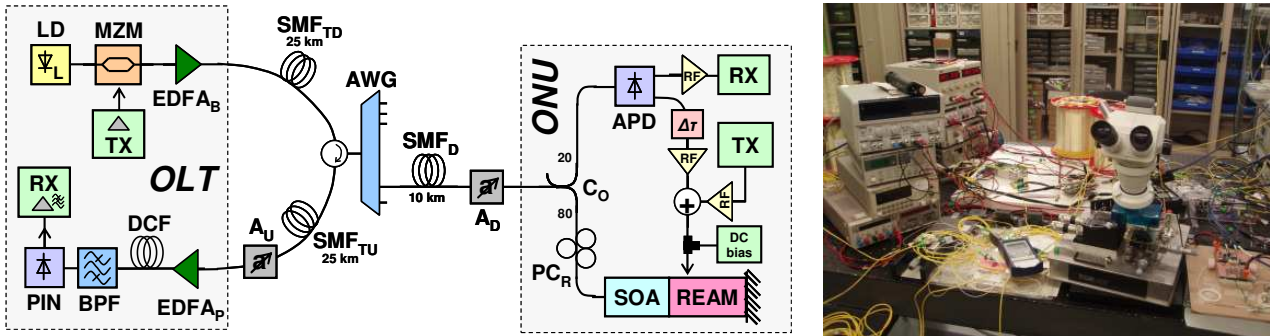


Fig. 4.32. WDM-PON with SOA/REAM-based ONUs for full-duplex 10 Gb/s transmission and wavelength reuse.

The transmission results are shown in Fig. 4.33 and reflect similar performance as in the previous section. Note that the reception sensitivity of the downstream could be improved by changing the splitting ratio of the power splitter (C_0) inside the ONU, which is here chosen with 20/80 and favors clearly the remodulation branch.

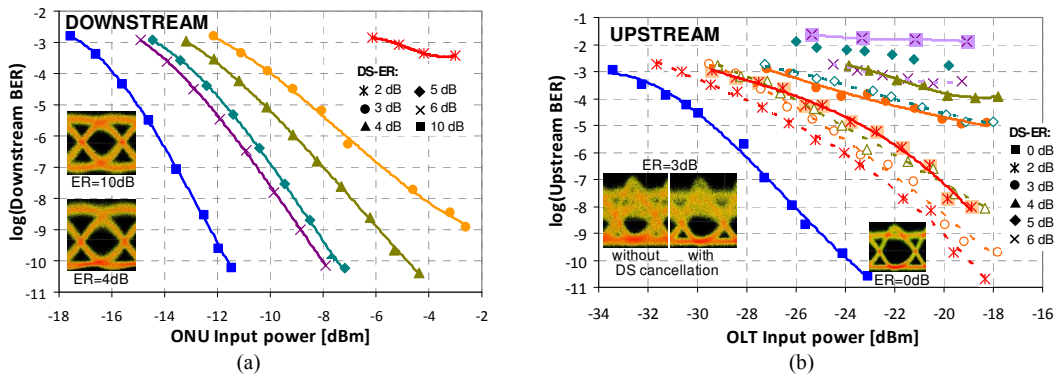


Fig. 4.33. Transmission performance for (a) the downstream and (b) the upstream.

A combination of both, high symmetrical data rates and a high net gain for the ONU would be the key for cost-efficient deployment of the proposed downstream suppression technique in hybrid PONs with extended reach. For this reason a third and last experimental evaluation is presented, aiming at increased data rates while keeping a RSOA-based design.

Symmetrical Extended Reach WDM/TDM-PON with RSOA-based ONU

The architecture of the hybrid PON [172], shown in Fig. 4.34, is based on a WDM ring that is used to deliver signals via the RNs to the TDM trees and is an extended version of the first PON study. The ring acts thereby as metro distribution network, to transfer data streams on different wavelengths to single local access networks, by providing a resiliency mechanism at the same time. The trees that are connected to the metro ring then distribute the traffic locally among a bunch of 16 users each, or other optical network terminals that aggregate low-bandwidth traffic.

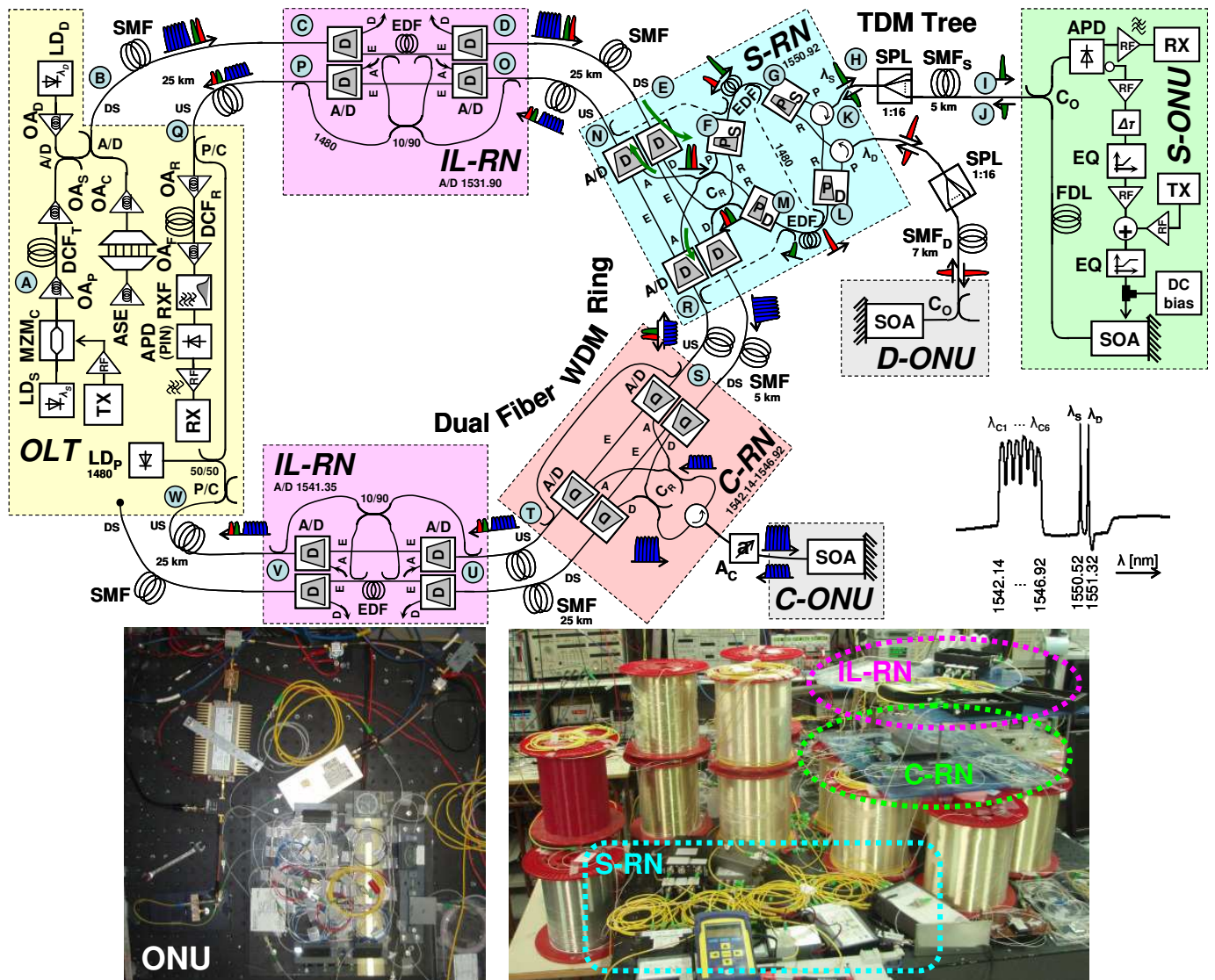


Fig. 4.34. PON architecture based on dual-fiber WDM ring for down- (DS) and upstream (US) and a bidirectional power splitting tree. The metro/access network contains RNs with inline- and drop-amplification, remotely pumped from the OLT. The inset shows the wavelength allocation for the data and the comb signals, which is also repeated inside the setup to indicate the presence and absence of particular wavelengths at different locations.

The network comprises three different types of RNs, which are primarily intended to provide add/drop functionality and signal amplification. Next to the signal-RNs (S-RN), inserted in the ring to drop specific wavelengths to their connected trees, two inline-

RNs (IL-RN) are distributed along the ring to re-amplify the data signals that are passed to the S-RNs. Finally, an extra RN has been inserted to include the influence of multi-wavelength transmission into account. Since this is implemented by transmitting a comb of dummy signals together with the data signals instead of adding a series of S-RNs, this third RN is referred to as the comb-RN (C-RN). These three kinds of RNs, located at the dual-ring of 100 km and carrying down- and upstream signals separately, the OLT, and the ONUs that are connected to the different RNs, will be now discussed in detail. Note that a high capacity is not in focus and that the PON was kept as simple as possible with a minimum number of RNs for demonstrating the transmission performance of the chosen modulation format.

At the interconnection between the ring and the trees, the S-RN corresponds to the one that was previously discussed with the difference that just a single EDF is used per amplification stage. The RN provides the possibility to drop and add the signals to both ring directions, which ensures that even if a ring segment on the East side of the S-RN is interrupted, communication can still be established via the West side, or vice versa. The applied wavelength allocation scheme of dropping two wavelengths in each S-RN is mainly motivated by the bidirectional signal amplification in the EDF-based stages. The two tree signals (λ_S, λ_D), which are intended for data transmission to the two connected trees, are thereby fed into the amplifiers in a way so that the counter-propagating continuous-mode downstream signal from the other tree stabilizes the gain of the burst-mode upstream traffic [173]. At the same time, RB is avoided since the down- and upstream signal of the same wavelength are amplified in different EDF stages. Separation and combination of the tree signals inside the S-RN are done via 100 GHz filters (P_S, P_D) and circulators. In this work, the pump is dropped by two WDM couplers connected to the East and West upstream ports of the RN.

The downstream is imprinted at the OLT on the carrier at $\lambda_S = 1550.52$ nm via a MZM with variable ER. The carrier of the second tree at $\lambda_D = 1551.32$ nm was left unmodulated. A DCF with a dispersion of -1362 ps/nm was used for the modulated downstream signal at λ_S and also at the upstream receiver to compensate for pulse broadening along the SMF spans. A dual-stage booster configuration is thereby used to keep the OSNR high [16]. Each of the 8 carriers ($\lambda_S, \lambda_D, \lambda_{C1} \dots \lambda_{C6}$) was injected with 3 dBm into the downstream ring. The two optical signals at 1480 nm, which are used to supply the RNs with the required pump for their EDF-based amplification stages, were each launched into both directions of the upstream ring with a power of 28.5 dBm, in order to provide also some Raman gain for the upstream. For a larger number of RNs along the ring, which is not considered in this work, the transmitted pump would have to be increased to account for the pass-through losses and the dropped pumps at each of the RNs.

The ONU corresponds to the one used in the first PON study and differs in the TO-can RSOA for which an improved model regarding its modulation bandwidth, though with less optical gain, was used. The limitation given by the low intrinsic electro-optical

bandwidth of the RSOA is overcome by optical offset filtering at the OLT receiver [72]. The phase modulation that is introduced by the chirp of the RSOA is thereby converted into supportive amplitude modulation when the reception filter (RXF) at the OLT is properly blue-shifted. In addition, the response of the RSOA was equalized with a passive RLC-filter. This kind of electronic equalization was designed according to the detuned 100 GHz RXF filter in front of the APD at the OLT receiver. With a chirp parameter of 7.7 and a filter detuning of 16 GHz the response was extended from 1.6 to 5.8 GHz for an optical input power of -17 dBm (Fig. 4.35). Though the obtained bandwidth is not high enough, penalized transmission at 10 Gb/s should be possible at least at the FEC level without additional cost deriving from adaptive electronic equalization at the electrical OLT receiver.

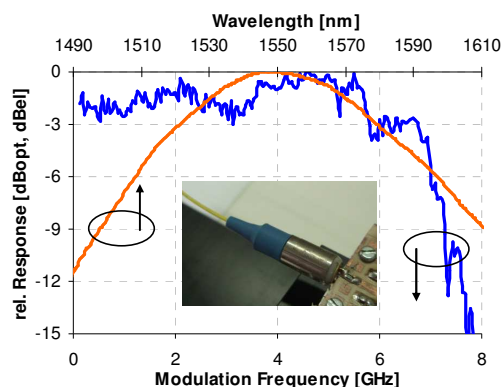


Fig. 4.35. Electro-optical response and small signal gain spectrum of the ONU transmitter, which is based on a TO-can RSOA. Values are given for the operating conditions inside the PON.

An upstream ER of 6.4 dB was reached and is compromised by the need for a high RSOA bias current to enhance the electro-optical bandwidth of the RSOA. The gain spectrum of the RSOA was centered at 1550 nm, had a 3 dB bandwidth of 58 nm and a small signal gain of 13 dB. The noise figure was 9.3 dB for the given bias point.

To assess the influence of gain transients in the remote amplification stages inside the S-RN on the transmission performance, additional burst-mode measurements have been performed according to a GPON-compatible 125 μ s frame with a duty cycle of 1:4, meaning a packet length and gating for the RSOA of 31.5 μ s. Since no burst-mode APD receiver was available, a PIN diode was placed as photo detector of the OLT receiver.

Next to the S-ONU, which provides transmission at the wavelength λ_S , a dummy-ONU (D-ONU) was added for the second tree that is also emerging from the S-RN. The D-ONU emulates a simple version of the S-ONU and operates at the second tree wavelength λ_D . Although no modulation is applied to the RSOA inside the D-ONU, this methodology is acceptable since the gain relaxation time of the EDFs is much larger than the inverse of the data rates used so that the gain of the EDF does not vary at the bit level. Therefore, the gain stabilization that is achieved inside the EDF due to the second wavelength λ_D stays the same as long as its optical power level matches the one of a potential modulated carrier at λ_D .

Besides the drop amplification in the S-RNs, the IL-RNs are designed not only to drop wavelengths as a S-RN does but also to provide additional inline amplification along the downstream ring via a short piece of EDF. The required pump is dropped by a fixed ratio of 10% from the pump that is propagating through the upstream ring, which delivers the carrier at 1480 nm that is used for pumping several RNs along the ring. These IL-RNs are placed on half the way (after 25 km) towards the farthest S-RN in normal PON operation.

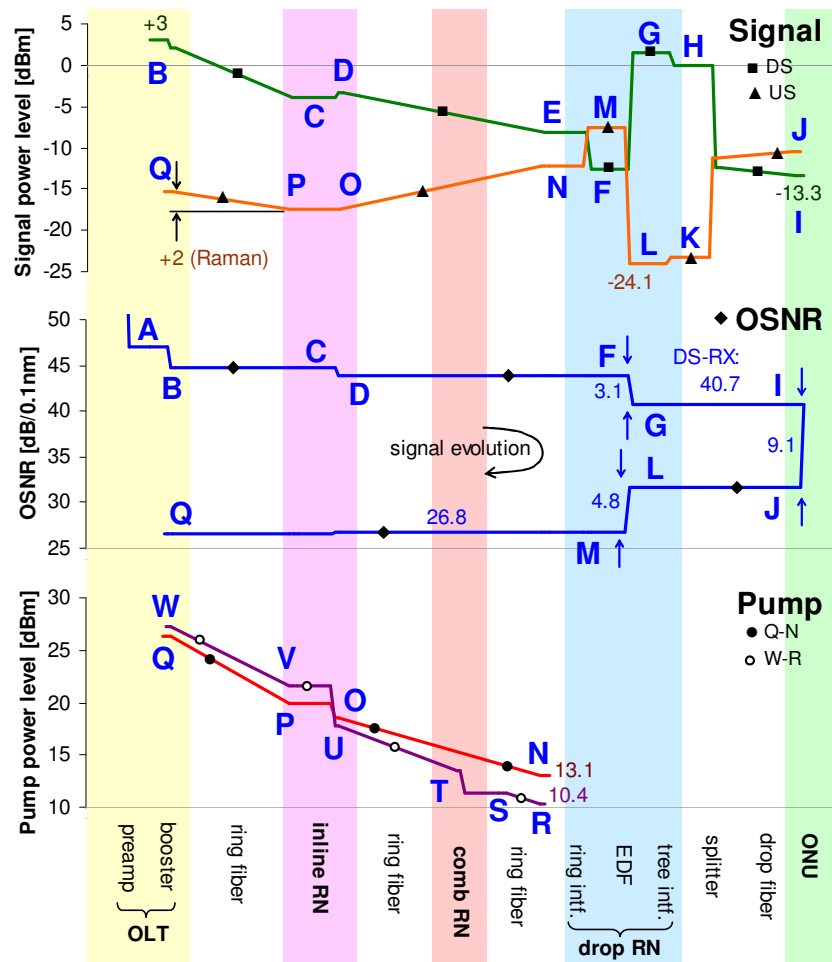


Fig. 4.36. Evolution of signal, pump and OSNR along the PON. Strong dynamics appear only at the power splitter of the tree.

Due to the remote pumping scheme via the upstream ring, the signals benefit from Raman gain when passing from the ONU to the OLT. A comb of six wavelengths ($\lambda_{C1} \dots \lambda_{C6}$), sliced out of amplified spontaneous emission and containing an equivalent power as a tree signal so that $P_{\lambda_{C1}} = P_{\lambda_S} = P_{\lambda_D}$ for each of its wavelengths, was fed together with the tree signals to cope with a potential Raman pump depletion in a real scenario. For this latter reason the comb was dropped at the C-RN, forwarded to the reflective comb-ONU (C-ONU) and inserted into the upstream ring with an equivalent power level as the tree signals that are dropped at the S-RN. This emulates a multiple wavelength drop from the downstream ring and insertion into the upstream ring at the same time, and takes pump depletion and a reduced inline amplification in the IL-RNs into account. The C-ONU is thereby kept as simple as possible and contains a

RSOA that is solely used as amplifier, whose input power was adjusted by an attenuator (A_C) to accommodate for the required power level that is inserted into the upstream ring. The incorporation of the C-RN into the PON is mainly motivated by a simple but realistic setup which takes several transmission-related impairments into account to guarantee an accurate evaluation of the chosen modulation format.

The power levels for the pumps and the data signal (λ_S) along the PON are illustrated together with its OSNR in Fig. 4.36. As the 8 downstream signals pass the IL-RN (C-D), they experience a net gain of 0.5 dB while the insertion losses of this RN are compensated. The drop losses at the S-RN (E-F) are 4.5 dB and the OSNR degrades in the drop amplifier (F-G) by 3.1 dB and keeps a level of 40.7 dB. The tree interface loss (G-H) of 1.4 dB in the RN and mainly the high splitting loss of ~ 12.3 dB in the tree (H-I) cause an input power in the ONU (I) as low as -13.3 dBm. This leads together with the 50/50 coupler at the ONU to a strong OSNR degradation of 9.1 dB to 31.6 dB at the output of the ONU, which is also pronounced due to the high noise figure of the RSOA. The low net gain (I-J) of 2.9 dB at the ONU, limited by the commercial low-gain RSOA, provides also a low input of -24.1 dBm into the upstream amplifier (L-M) in the S-RN. The OSNR is therefore further degraded by 4.8 dB and settles at 26.8 dB. For a higher ONU net gain this degradation could be significantly reduced. Although there is no visible Raman gain for the upstream signal on the pass through the first traversed ring spool (N-O) on the way to the OLT, the loss of the second ring spool (P-Q) is compensated and the signal experiences an additional gain of 2 dB.

There has been no strong pump depletion observed for the upstream Raman amplification (P-Q) since the injected signal is quite low with -16.5 dBm per wavelength. The pump arrives with 13.1 and 10.4 dBm at the S-RN (N, R), which is strong enough for the low-doped HE980 EDFs used inside the RN [8]. The difference in the pump values derives from the pass through the C-RN (T-S) and the additional short fiber spool (S-R) for the second pump. The average kilometric loss experienced by the pump sent at 1480 nm via the SMF was 0.229 dB/km. For the case of having multiple RNs connected to the ring, the required pump will increase according to the pass-through losses for signal and pump, as described earlier, and due to the dropped pump power levels for the feed of the EDFs.

The downstream BER, presented in Fig. 4.37(a), is shown for 5 Gb/s with a PRBS of length of $2^{31}-1$ and for 10 Gb/s with a PRBS length 2^7-1 . The FEC gain for a downstream ER of 3 dB at these data rates is 6.3 and 5.5 dB, respectively. The power margins can be therefore raised to 8.5 and 5.9 dB. The penalty in sensitivity, which arises due to a reduced downstream ER when compared to an ER >10 dB, is then 6.7 and 6.5 dB for the FEC level, as it is also shown in Fig. 4.38(a). Note that if the ER is chosen with <2 dB for the downstream signal, no transmission can be established, even when incorporating FEC. On the other hand, once the ER is increased to 5 dB, which is the optimum ER with FEC for a data rate of 5 Gb/s as will be proven shortly, this penalty is reduced to 4.2 dB and allows a margin of 11 dB.

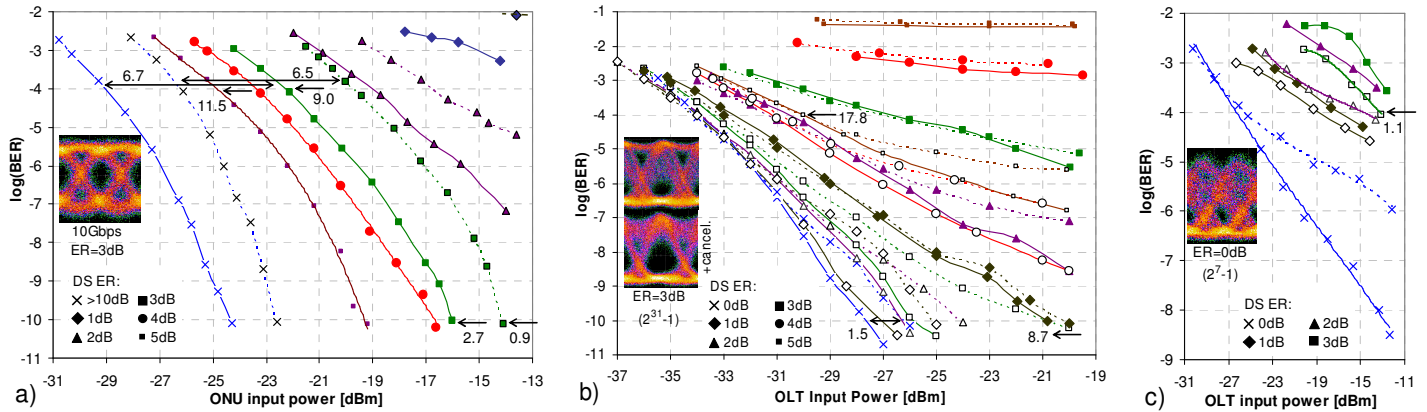


Fig. 4.37. BER measurements for (a) the downstream (solid curves: 5 Gb/s, PRBS $2^{31}-1$, dashed curves: 10 Gb/s, PRBS 2^7-1), (b) the upstream at 5 Gb/s (solid curves: PRBS 2^7-1 , dashed curves: $2^{31}-1$, filled markers: no cancellation, blank markers: cancellation) and (c) the upstream at 10 Gb/s. Single ended arrows indicate the obtained power margins for the reception.

For the case that the feed-forward downstream cancellation is applied, continuous-mode upstream transmission at 5 Gb/s can be provided for a low BER of 10^{-10} up to a downstream ER of 3 dB, as can be seen in Fig. 4.37(b). The penalty that is introduced by the remaining unsuppressed downstream is then 1.7 dB for a PRBS length of 2^7-1 as presented in Fig. 4.38(b) and increases to 5.3 dB for a PRBS $2^{31}-1$. This penalty is attributed to RSOA-induced patterning. The dependence on the PRBS is reduced at the FEC level, where the difference is <0.6 dB. When incorporating FEC, the reception penalty can be kept <1 dB for ERs up to 3 dB, and raises to ~ 4.1 dB for an ER as high as 5 dB.

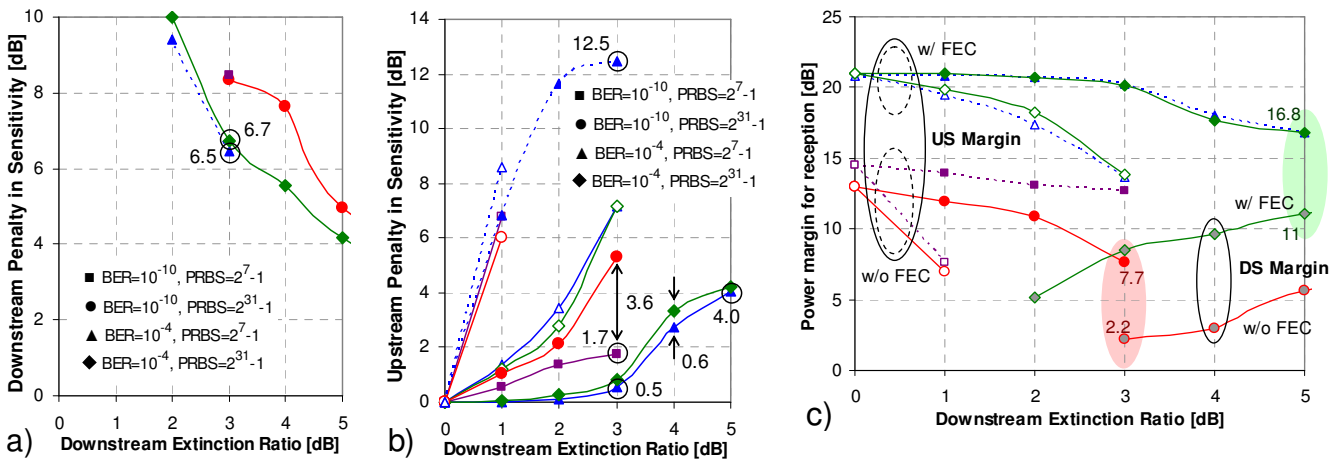


Fig. 4.38. Penalties in sensitivity for (a) down- and (b) upstream, referenced to a downstream ER of >10 dB and 0 dB, respectively. For the downstream, the penalties are only shown for ERs where an upstream can be provided. Solid curves indicate a data rate of 5 Gb/s, while dashed curves correspond to a data rate of 10 Gb/s. Blank and filled markers refer to an operation without and with downstream cancellation. (c) Power margins for down- and upstream. Dashed and solid curves correspond to a PRBS length of 2^7-1 and $2^{31}-1$, respectively, while filled and blank markers indicate the presence and absence of the downstream cancellation.

Without cancellation, the downstream ER is limited to 3 dB for the use of FEC, whereby the crosstalk from the downstream pattern into the upstream already causes a

penalty of 7.2 dB. A BER of 10^{-10} can only be reached with a low ER of 1 dB, where the upstream transmission suffers already from a penalty of 8.7 dB at a PRBS of length 2^7-1 , proving again the need for a downstream suppression technique.

The upstream power margins obtained for a downstream ER of 3 dB and a data rate of 5 Gb/s are 12.7 and 7.7 dB at a BER of 10^{-10} and a word length of 2^7-1 and $2^{31}-1$, respectively. This ER is compatible for full-duplex transmission without FEC (red shaded area in Fig. 4.39). At the FEC level, the margins are 20.2 dB for both PRBS lengths, resulting in a FEC gain of 7.5 and 12.5 dB. Note that this high margin at the FEC level is not given for the optimum downstream ER (and is therefore not reported in Table 4.1). Instead, an ER of 5 dB would be favored with FEC (green shaded area in Fig. 4.39), since the margins are more balanced: while the upstream margin is still 16.8 dB, the downstream margin is increased to 10.5 dB, and therefore 2.5 dB higher than for an ER of 3 dB.

US data rate at BER:	5 Gb/s		10 Gb/s	
	10^{-10}	10^{-4}	10^{-10}	10^{-4}
optimum ER [dB]	3	5	-	3
DS margin [dB]	2.2	11	0.4	5.9
US margin [dB]	12.7 (7.7)	16.8 (16.8)	- (-)	0.1 (-)

Table 4.1. Optimum downstream ER and corresponding power margins for the case of a present downstream cancellation. Values for the upstream margin are shown for a PRBS 2^7-1 , and in brackets for a PRBS $2^{31}-1$.

The patterning induced by the RSOA due to its carrier recovery dynamics is also visible for pure upstream modulation with continuous-wave light injection, where the sensitivity degrades by 1.5 dB between word lengths of 2^7-1 and $2^{31}-1$.

The burst-mode measurements, presented in Fig. 4.39 for a PRBS length of $2^{31}-1$ and an applied downstream cancellation, confirm that there is no significant penalty introduced by the remotely pumped EDF stages in the S-RN. The overshoot of the gain transient, measured between begin and end of the data packet, has been found with 0.55 dB. Compared to the continuous-mode transmission the burst-mode penalty is ~ 1 dB for downstream ERs of 0, 3 and 5 dB. While the reception sensitivity is decreased by 6 dB compared to the APD-based OLT receiver due to the use of a less sensitive PIN diode, the error floors that arise for present downstream stay at the same BER level and are not further degraded due to the burst-mode traffic.

For an increased upstream data rate of 10 Gb/s only a word length of 2^7-1 leads to continuous-mode upstream reception at the FEC level as it can be seen in Fig. 4.37(c). This limitation for the upstream is also pronounced by the insufficient electro-optical bandwidth of the RSOA, which now affects not only the upstream modulation but also the downstream suppression. Without cancellation, only a downstream ER of 1 dB leads to a compatible situation for full-duplex data transmission while the ER can be extended to 3 dB applying cancellation. However, a large penalty of 12.5 dB is experienced in this case and leaves a margin of just 0.1 dB.

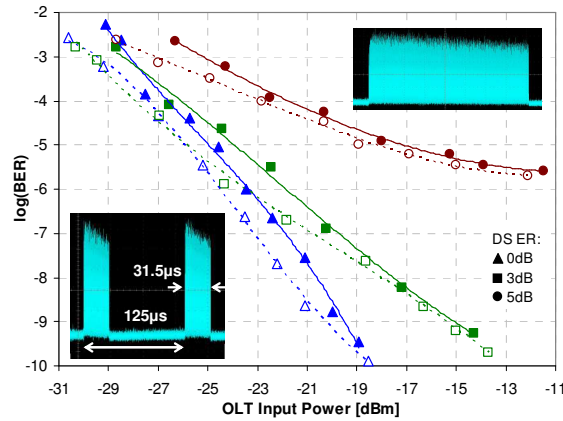


Fig. 4.39. Burst- (solid curves) and continuous-mode (dashed) upstream BER measurements. The insets show the data packets at the OLT receiver.

Although the feed-forward downstream cancellation technique has been proven to be feasible for RSOA-based ONUs at data rates of 5 Gb/s that are also targeted for NG-PON standards, severe penalties exist for higher data rates due to the limited electro-optical modulation bandwidth of commercial devices. All-optical downstream suppression techniques that are not bound to electro-optical schemes will perform therefore much better, as will be analytically and experimentally validated in the next section.

4.5 All-Optical Downstream Cancellation by Carrier Recovery

The efficiency of this electro-optical feed-forward cancellation technique depends strongly on the modulation bandwidth on the upstream transmitter, and so does the reception sensitivity for the upstream. Unfortunately, commercial low-cost devices are far from providing a sufficient large bandwidth for 10 Gb/s upstream transmission, while access standards are already targeting this relative high data rate.

As a solution for the required cancellation procedure, an optically assisted technique can offer a more data rate independent performance as it is often the case for all-optical subsystems (e.g. the gain of a SOA does not depend on the data rate of the signal for access applications up to 10 Gb/s and quantum dot SOAs can extend the data rate of the amplified signal up to 40 Gb/s).

In this section the optical memory effect of a passive optical resonator is exploited to recover an optical carrier out of the downstream signal. This not only provides a better efficiency for the cancellation, as will be proven, but also a greener solution since the electro-optical upstream modulator has to be driven by just the upstream data signal.

4.5.1 Principal Scheme

The design of the all-optical downstream suppression, sketched in Fig. 4.40(b), relies on the use of a passive optical resonator that is placed at the ONU and tuned at the carrier

wavelength [174]. Acting as a spectrally periodic filter, the optical resonator partially recovers the carrier wavelength and effectively suppresses the modulation within the downstream signal. An optical filter with a periodic frequency transfer function such as a Fabry-Pérot filter (FPF) is used to provide its functionality as optical memory element and at the same time maintains colorless operation due to the spectral periodicity of the filter. A following SOA element that can be part of the upstream transmitter further compresses remaining transients.

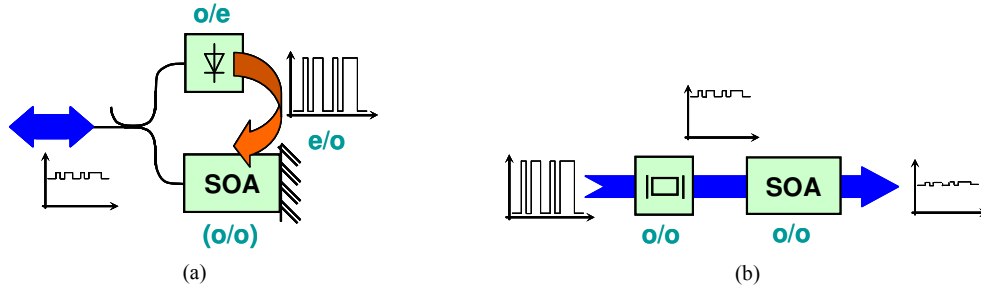


Fig. 4.40. (a) Traditional electro-optical feed-forward cancellation and (b) all-optical downstream suppression technique.

4.5.2 Analytical Model

In the time domain, the cavity effect leads to a smoothing of the signal envelope. A present non-return to zero (NRZ) bit pattern can be suppressed since light from mark bits is filling up the space bits for an appropriate design of the filter. The output field E_{out} is related to the input field E_{in} via the reflectivity R of the FPF facets and the round trip time T_{rtt} of the signal inside the cavity, taking multiple reflections and the transmission of the filter into account.

$$E_{out}(t) = (1 - R) \sum_{k=0}^{\infty} E_{in}(t - kT_{rtt}) R^k \quad (4.66)$$

The input signal is defined by the downstream pattern π_{DS} and the pulse shape A of the NRZ pulses that are transmitted at the optical frequency ω with a certain bit duration T_b .

$$E_{in}(t) = \sum_{n=-\infty}^{\infty} \pi_{DS}(n) A(t - nT_b) e^{j\omega t} \quad (4.67)$$

The bits of the downstream are considered to be chirped Super-Gaussian pulses similar to equation 4.46.

$$P(t) = P_0 + P_1 \left(1 - \frac{1}{ER_{in}} \right) \exp \left[-\frac{1}{2} (1 - j\alpha) \left(\frac{t}{T_b} \right)^{2F} \right] \quad (4.68)$$

In the frequency domain, the optical carrier recovery scheme translates to the filtering of the optical carrier while the modulation information is rejected.

$$E_{out}(f) = H(f) E_{in}(f) \quad (4.69)$$

The complex filter function H for the FPF is defined as

$$H(f) = \frac{1-R}{1-R e^{j2\pi f/FSR}} \quad (4.70)$$

where FSR is the free spectral range of the filter. The response for the magnitude and the phase are then

$$|H(f)| = \frac{1-R}{\sqrt{(1-R)^2 + 4R \sin^2\left(\frac{\pi f}{FSR}\right)}} \quad (4.71)$$

$$\arg(H(f)) = \arctan\left(\frac{R \sin\left(\frac{2\pi f}{FSR}\right)}{1-R \cos\left(\frac{2\pi f}{FSR}\right)}\right)$$

and the FSR is defined by the optical length of a full circulation inside FPF, which depends on its geometrical length L and its refractive index n . For the desired application as carrier recovery the FSR should be matched with a multiple M of the inverse round trip time for the reason of bit synchronization.

$$FSR = \frac{c}{2nL} = \frac{M}{T_{rt}} \quad (4.72)$$

The relation between the reflectivity and the filter finesse F , which is a typical design parameter for resonators, is given according to

$$F = \frac{\pi\sqrt{R}}{1-R} \quad R = -\frac{\pi}{2F} + \sqrt{\left(\frac{\pi}{2F}\right)^2 + 1} \quad (4.73)$$

The decay of light inside the FPF is given by the bandwidth $\delta\nu$ of the FPF

$$\tau = \frac{1}{2\pi\delta\nu} = \frac{nLF}{\pi c} = \frac{nL\sqrt{R}}{c(1-R)} \approx \frac{nL}{c(1-R)} \quad \delta\nu = \frac{FSR}{F} \quad (4.74)$$

considering high values for the reflectivity close to unity. The number N of bits that fit inside this decay time τ (referenced to $1/e$) can be retrieved with

$$N = \frac{\tau}{T_b} = \frac{1}{2FSR(1-R)T_b} \quad (4.75)$$

Since the round trip time and the data rate B of the data signal are matched, N becomes (for the case $M = 1$)

$$B = \frac{FSR}{M} : \quad N = \frac{F}{2\pi M\sqrt{R}} \approx \frac{F}{2\pi M} \quad (4.76)$$

considering equation 4.73 and again high values for the reflectivity.

However, what matters is the decay during the maximum number of consecutive identical space bits in a given data stream. The exponential decay of optical power P_{out} towards the residual power during the space bits follows the function

$$P_{out}(t) = \Delta P \exp\left(-\frac{t}{\tau}\right) + \frac{P_{max}}{ER_{in}} \quad \Delta P = \bar{P}_{avg} - \frac{P_{max}}{ER_{in}} \quad (4.77)$$

the maximum swing in optical power ΔP due to a block of consecutive identical bits in the downstream with extinction ratio ER_{in} is determined by average optical power P_{avg} at the FPF output and the power level that is present during the space bits.

The average power itself depends on the maximum transmission T_{max} of the FPF and the average input power, while the power during the space bits is related with the ER and the maximum power P_{max} that is present at the output of the FPF. This power follows the mark bits of the downstream signal and the transmission of the filter.

$$\bar{P}_{avg} = \bar{P}_{in} T_{max} \quad P_{max} = 2\bar{P}_{in} \frac{ER_{in}}{ER_{in} + 1} T_{max} \quad (4.78)$$

The maximum transmission of the FPF can be retrieved with

$$T_{max} = \frac{(1-R_1)(1-R_2)\alpha}{(1-\sqrt{R_1 R_2} \alpha)^2} \quad (4.79)$$

where α is the cavity loss. For a PRBS of length 2^z-1 and a data rate R_b , the radix z determines the number of consecutive identical bits. The worst case of having z space bits at an arbitrary point of time t_0 leads to the maximum decay of

$$P\left(t_0 + \frac{z}{R_b}\right) = \Delta P \exp\left(-\frac{z}{\tau R_b}\right) + \frac{P_{max}}{ER_{in}} \quad (4.80)$$

The caused fluctuation in the output power, which are characterized by their ER_{out} , are then

$$ER_{out} = \frac{P_{max}}{P\left(t_0 + \frac{z}{R_b}\right)} = ER_{in} \frac{1}{1 + \frac{1}{2}(ER_{in} - 1) \exp\left(-\frac{z}{\tau R_b}\right)} \quad (4.81)$$

However, the maximum power level P_{max} will never be reached due to the finite filling of the cavity with light. The maximum power level that will be reached with a consecutive number of z mark bits that appear at time point t_1 is

$$P_{max,z}\left(t_1 + \frac{z}{R_b}\right) = P_{max} - \Delta P_1 \exp\left(-\frac{z}{\tau R_b}\right) \quad \Delta P_1 = P_{max} - \bar{P}_{avg} \quad (4.82)$$

and therefore the effective residual ER_{out} expressed by the physical design parameters of the FPF is

$$ER_{out} = \frac{P_{\max,z} \left(t_1 + z/R_b \right)}{P \left(t_0 + z/R_b \right)} = ER_{in} \frac{1 - \frac{1}{2ER_{in}} (ER_{in} - 1) \exp \left(-z\pi c / nLFR_b \right)}{1 + \frac{1}{2} (ER_{in} - 1) \exp \left(-z\pi c / nLFR_b \right)} \quad (4.83)$$

The finite filling speed for consecutive number of mark bits will not only cause a reduction in the output ER but also an additional filtering loss that increases the net transmission loss of the filter.

Note that ER_{out} in equation 4.83 corresponds to a peak value for the remaining downstream ER, which is only given for the worst case of having z consecutive identical bits that appear with a probability of 2^{-z} inside the PRBS [175]. An average ER_{out} value for the PRBS does not make sense, since the worst-case ER_{out} has to be taken into account. This is the case where a few errors can be introduced, causing error floors at low BER levels, as will be discussed shortly in course of an experimental validation.

Further, the passive resonating circuit will be subject to temperature fluctuations δT due to the temperature sensitivity of the device parameters. The resonance frequency will be affected due to variations in the refractive index and the cavity length by a shift δf that is normalized to the FSR.

$$\delta f = \frac{f}{B} \left(\frac{1}{L} \frac{dL}{dT} + \frac{1}{n} \frac{dn}{dT} \right) \delta T \quad (4.84)$$

Typical values are $10^{-5}/^{\circ}\text{C}$ for $(dL/dT)/L$ and $5 \cdot 10^{-7}/^{\circ}\text{C}$ for $(dn/dT)/n$ [176].

4.5.3 Simulation

The carrier recovery with FPF-assisted downstream cancellation is expected to provide relative low residual patterning even with high initial downstream ER. For a first assessment of this technique, a FPF with a finesse of 40 that is matched in its FSR to a 10 Gb/s data signal and a consecutive SOA whose input power was -13 dBm is used for simulation. The analytical SOA model from chapter II was applied for this reason. The downstream pulses were not chirped.

Fig. 4.41 shows the output of the FPF for a downstream constituted by a PRBS of length 2^7-1 with infinite ER. A residual power level is already visible over the duration of the whole data signal and the spectral components of the data signal have been mostly suppressed. However, severe patterning exists but can be further reduced by the consecutive SOA (Fig. 4.42).

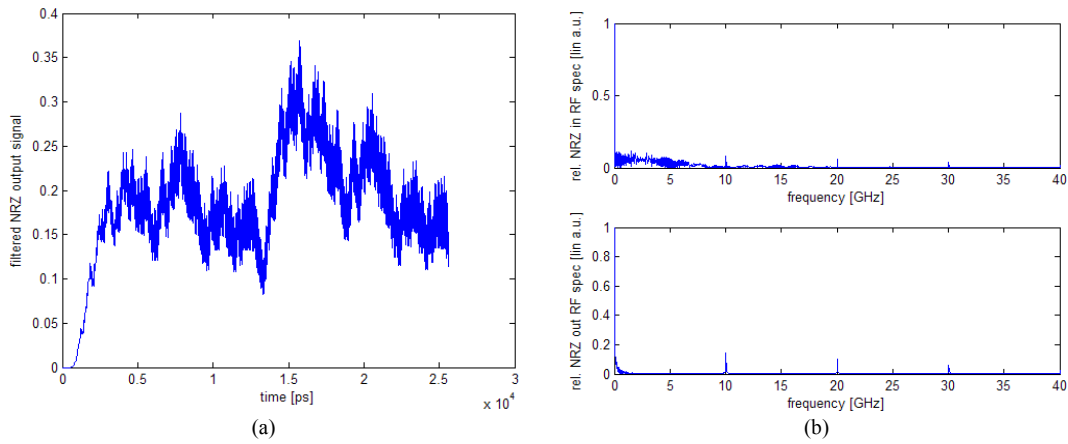


Fig. 4.41. FPF-assisted carrier recovery with a downstream of infinite ER as input signal. (a) FPF output and (b) signal spectrum before and after the FPF.

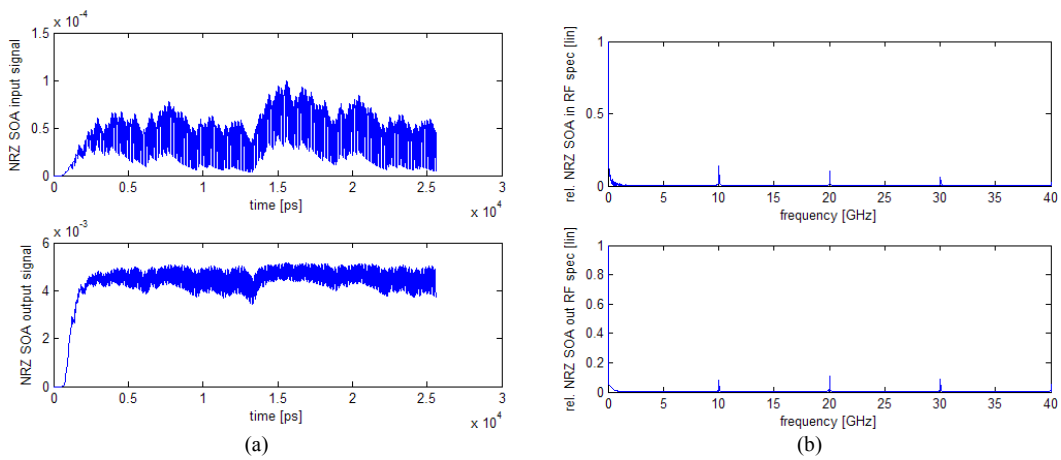


Fig. 4.42. Improvement due to a SOA after the FPF. (a) SOA in- and output signal and (b) their spectra.

Just by an increase of the filter finesse to 100, the residual patterning is reduced in its swing (Fig. 4.43). The RF spectrum of the SOA output shows then mainly a strong DC component.

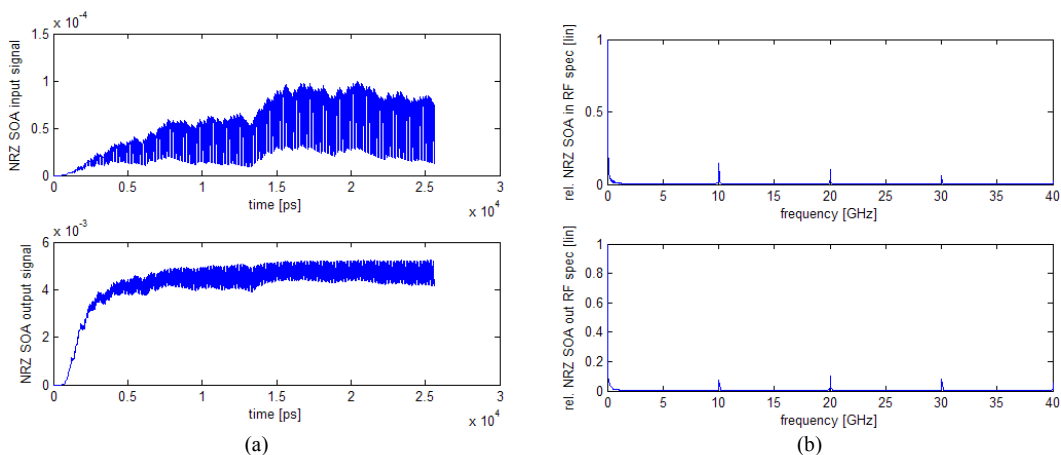


Fig. 4.43. Improvement due to an increased filter finesse. (a) SOA in- and output signal and (b) their spectra.

In a practical implementation a lowered downstream ER will not introduce a significant penalty as long as it stays in the range of 6 dB or higher. The residual downstream ER at

the output of the FPF before the SOA is shown in Fig. 4.44 for a finesse of 100 and different initial downstream ERs and PRBS lengths.

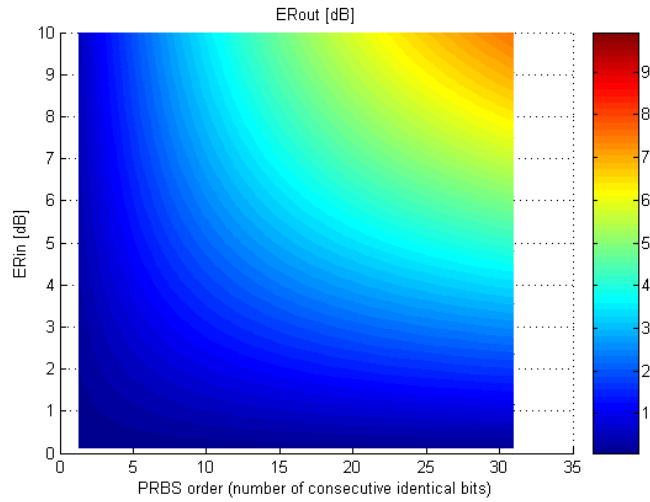


Fig. 4.44. Residual ER after the FPF-assisted carrier recovery as function of the downstream (input) ER and the PRBS length.

The eye diagrams for the upstream that reuses the recovered carrier after the FPF (without SOA) as optical seed are shown in Fig. 4.45 for full-duplex 10 Gb/s transmission with an ideal upstream transmitter. The downstream ER was chosen with 3 and 6 dB and the filter finesse was 100.

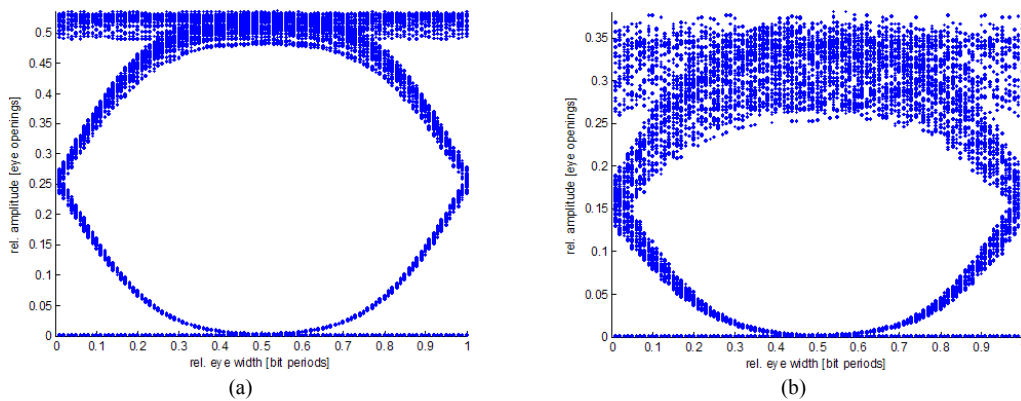


Fig. 4.45. Upstream eye diagrams for remodulation at the FPF output. The downstream ER was (a) 3 dB and (b) 6 dB.

As can be seen when comparing with the previous results, the mark rail stays relative thin for this relative low ER. The impact of a consecutive SOA is shown in Fig. 4.46 for a high downstream ER of 9 dB. While for the case without SOA the upstream eye in Fig. 4.46(a) shows a remaining downstream ER of 2.1 dB due to the transients at the output of the FPF that are also visible in the recovered carrier in Fig. 4.46(b), an additional SOA shows significant improvement; The recovered carrier is further smoothed as it is obvious from Fig. 4.46(d) so that the residual downstream in the upstream transmission is reduced to an ER of 0.8 dB as it is visible from Fig. 4.46(c).

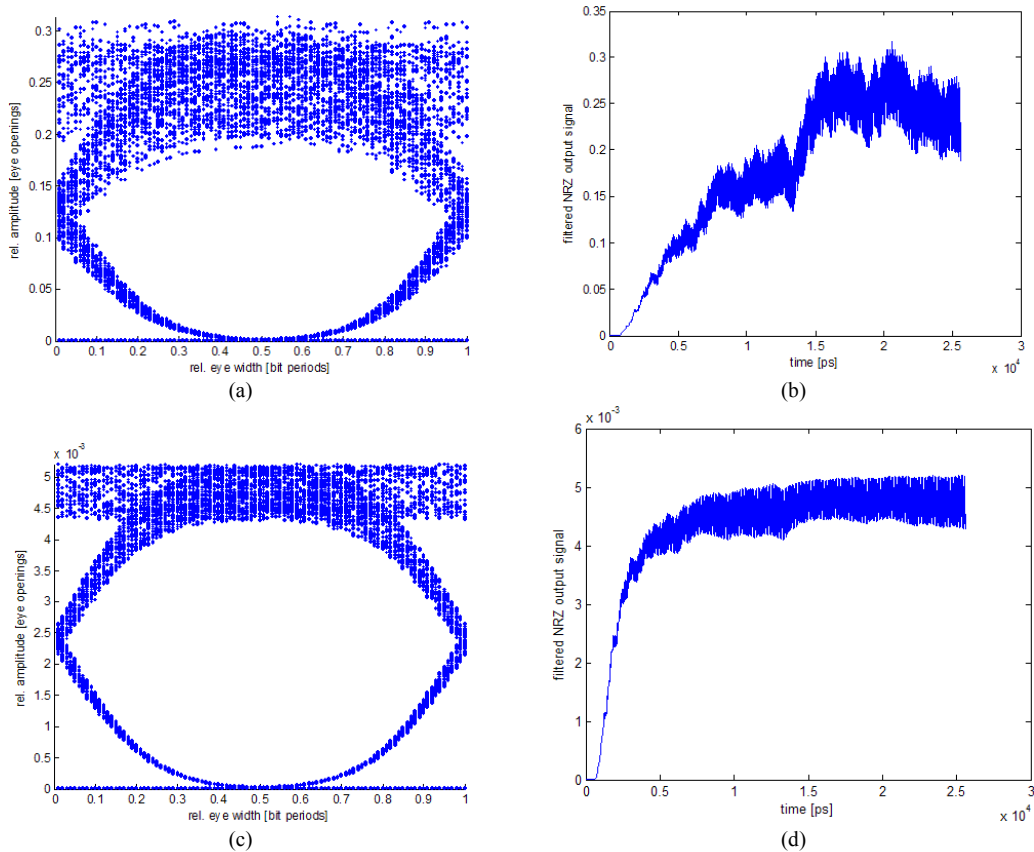


Fig. 4.46. Upstream eye diagrams (a),(c) and recovered optical carrier (b),(d) for a downstream ER of 9 dB. The use of a SOA after the FPF (c),(d) improves the transmission quality for the upstream significantly.

4.5.4 Experimental Validation

The FPF-assisted downstream cancellation was experimentally proven in its ability to erase a high data rate 10 Gb/s downstream signal while remodulating with a lower data rate 2.5 Gb/s upstream and further analyzed in its ability to extend the loss budget for full-duplex 10 Gb/s transmission in WDM- and hybrid PONs.

Proof of Principle

The suppression of an incident data pattern, which translates into the aforementioned cancellation efficiency, was investigated as a first figure of merit. A FPF with a FSR of 10 GHz and a finesse of 40 was placed in front of a RSOA, which will later play the role of the reflective upstream modulator as illustrated in Fig. 4.47(a).

The FPF was a fiber-based device with integrated piezo-based stabilization circuit for maintaining the comb transfer function. The FPF was aligned with the downstream to obtain optimal suppression. The FPF is aligned with respect to the incident data signal by fine-tuning of its spectral transmission function inside the FSR rather than over the full operating wavelength range. The FPF transmission is in principle designed to match with the downstream wavelength grid. While the FPF might be aligned with most of the

downstream channels, wavelength drifts of the downstream laser diodes may require a fine tuning at some of the branches of the WDM network.

The residual polarization sensitivity afforded controllers to optimize the response. However, this can be avoided with an integrated design where the FPF is replaced by e.g. non-reflective and polarization-insensitive ring resonators [177].

For comparison, a standard ONU without FPF was also implemented. In this alternative ONU, the optical gain saturation of the RSOA is solely used as natural compression of the downstream. The same TO-can RSOA as in the experiment with the hybrid PON and feed-forward cancellation was used but in this first proof-of-concept without equalizer so that its intrinsic modulation response – good enough for 2.5 Gb/s transmission as can be seen in Fig. 4.47(b) – is exploited. The optical input power at the ONU was fixed with -10 dBm.

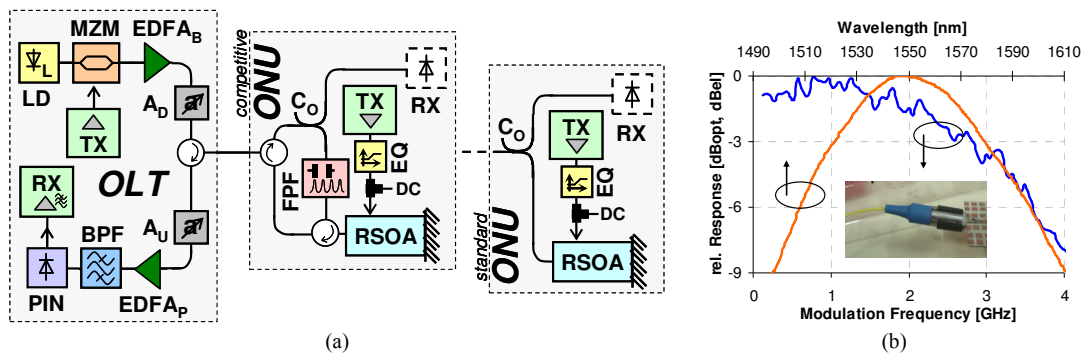


Fig. 4.47. (a) Experimental setup for the evaluation of the proposed all-optical carrier recovery technique at the FPF-assisted ONU, which is supported by an optical filter with controlled spectral periodicity. (b) Optical gain spectrum and electro-optical response of the RSOA for an input power of -10 dBm.

The cancellation efficiency, shown in Fig. 4.48(a), is defined as in chapter IV.4.4 between the ONU input and the RSOA output signal. For a standard ONU design without FPF, the gain saturation effect of the RSOA leads to a natural suppression of the present pattern with an efficiency of $\sim 50\%$. For a downstream ER of 3 dB the pattern remains with an ER of 1.5 dB and causes severe crosstalk into the upstream.

When the FPF is used inside the ONU, the downstream is further suppressed and is left at the recovered optical carrier with only 0.2 dB for this ER, corresponding to a cancellation of 93%. For higher ERs the PRBS length starts to affect the signal cancellation due to the large number of consecutive zeros and the limited memory effect of the filter for a given finesse value. This can be observed for ERs > 6 dB where a PRBS of length $2^{31}-1$, indicated by the solid lines in Fig. 4.48(a), suffers from a slightly reduced cancellation efficiency when compared to a short PRBS of length 2^7-1 (dashed lines). However, this reduction is small with $< 3\%$ and proves that this technique is suitable for GPON systems. With a higher finesse of the FPF, which effectively translates to a stronger filter memory effect, this sensitivity to the word length can be reduced. Compared to the gain saturation of the RSOA, the suppression of the downstream can be maintained even for high ERs of 6 and 9 dB, for which the remaining ER for a PRBS of length $2^{31}-1$ is as small as 0.4 and 1 dB, respectively. Fig.

4.48(b) shows the recovered optical carriers at the output of the FPF-assisted ONU for an initial downstream ER of 9 dB and a short and long PRBS of length 2^7-1 and $2^{31}-1$, respectively. The FPF had 2 dB insertion loss, whereas an additional loss between 0.3 and 1 dB for ERs from 3 to 9 dB was induced due to the filtering function of the FPF as it was commented earlier.

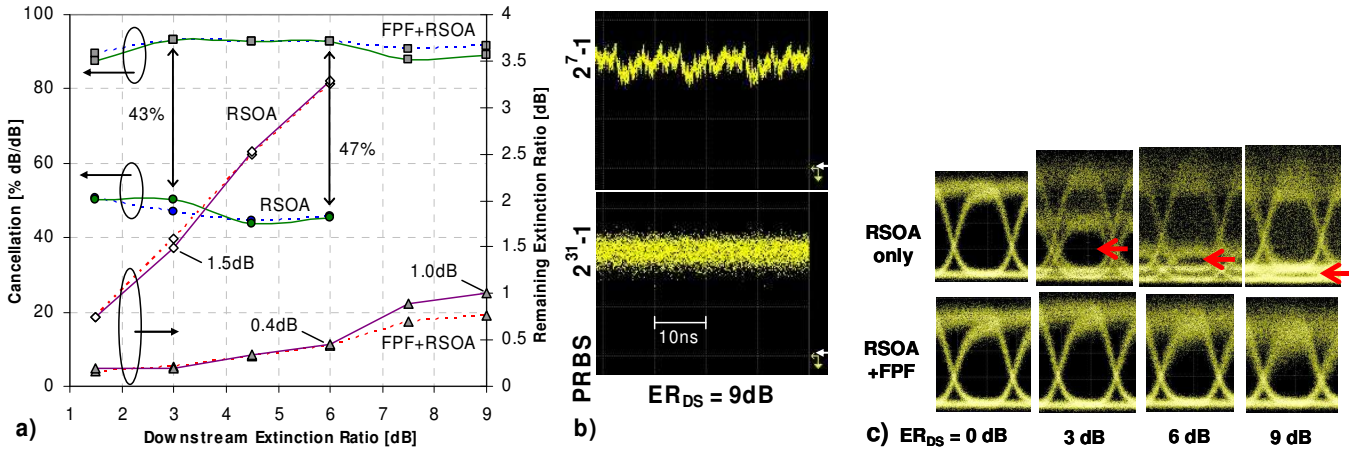


Fig. 4.48. (a) Cancellation efficiency and remaining ER as function of the downstream ER. Solid and dashed lines correspond to a PRBS of length $2^{31}-1$ and 2^7-1 , respectively. Values are mentioned for the long PRBS. (b) Recovered optical carrier at the output of the FPF-assisted ONU for a downstream ER of 9 dB. The arrows on the right indicate the reference level of the PIN detector. (c) Upstream eye diagrams for both ONU designs and different downstream ERs.

The impact of the cancellation efficiency on the upstream transmission was assessed with BER measurements. The standard ONU already suffers from an upstream reception penalty of 4 dB for a downstream ER of 3 dB and word lengths of 2^7-1 and $2^{31}-1$ at a BER of 10^{-10} and 10^{-4} , respectively. The error floors that arise for the longer PRBS are caused by gain dynamics of the RSOA. As can be seen in Fig. 4.49(a) no transmission can be established with an ER of 6 dB, not even with FEC.

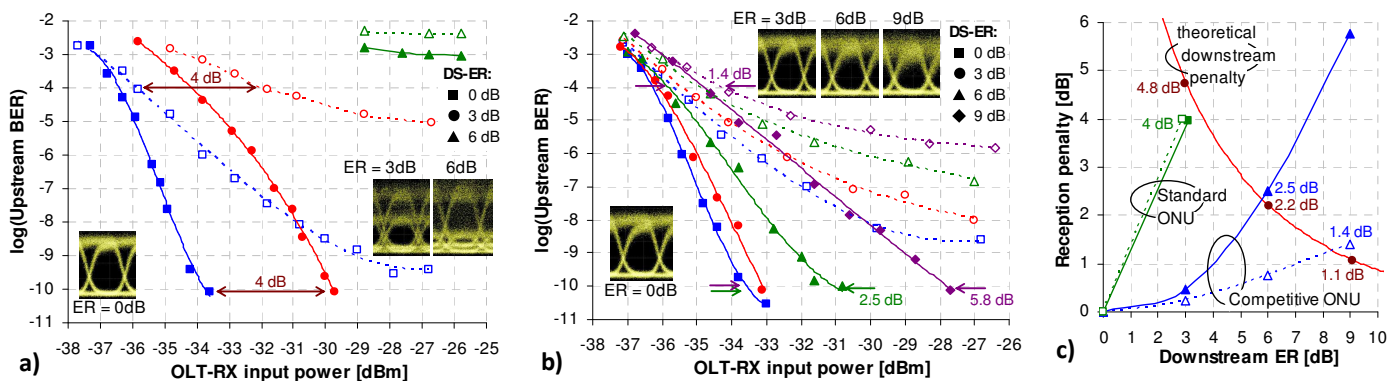


Fig. 4.49. Upstream BER for (a) the standard ONU and (b) the FPF-assisted ONU. Solid lines and dashed lines represent a PRBS of length 2^7-1 and $2^{31}-1$, respectively. The insets show the eye diagrams for different downstream ERs and a PRBS length of $2^{31}-1$. (c) Penalty curves for upstream and downstream reception, referenced to a downstream ER of 0 and ∞ dB, respectively. Filled and blank markers represent a PRBS of length 2^7-1 and $2^{31}-1$.

On the contrary, the FPF-assisted ONU allows to operate at large downstream ERs of 6 and even 9 dB, for which the penalties are 2.5 and 5.8 dB for a short PRBS at a BER of

10^{-10} and 0.8 and 1.4 dB for the long PRBS and FEC (Fig. 4.49(b)). A small penalty of 0.2 dB is given for the downstream-less case when compared to the standard ONU, which is attributed to the additional loss and OSNR degradation that is caused by the FPF and the circulators. This difference in the performance of the two ONU designs is also obvious from the upstream eye diagrams, which are presented in Fig. 4.48(c).

The reception penalties for up- and downstream are shown in Fig. 4.49(c), whereby the reference is given for a downstream ER of 0 and ∞ dB, respectively. For the standard ONU, an ER of 3 dB would already lead to penalties > 4 dB for both data streams since upstream transmission is prohibited for larger ERs. The penalties for the FPF-assisted ONU are much smaller as the downstream reception benefits from the robustness against crosstalk at larger ERs. While for an ER of 6 dB the penalties are 2.2 and 2.5 dB for down- and upstream reception without FEC, penalties < 1.5 dB can be achieved at an ER of 9 dB with FEC.

Performance Investigation

To validate the performance of the all-optical carrier recovery and investigate its operating range, a further experimental characterization regarding the PRBS length and filter bandwidth of the FPF was carried out. For this investigation that considers the upstream reception penalty as the figure of merit, the RSOA at the ONU in Fig. 4.47(a) was replaced by a combination of MZM and EDFA, to avoid additional patterning effects in the upstream modulator [117,118]. The driving conditions of the MZM and the EDFA input power and gain were adjusted to provide the same upstream ER, net ONU gain and OSNR at the ONU output. Note that for this following study the receiver at the OLT was replaced by a PIN diode since no detuned optical filter is required to achieve upstream transmission at 10 Gb/s thanks to the large inherent modulation bandwidth of the MZM, and hence no optical losses are introduced by the optical band-pass filter at the optical upstream receiver.

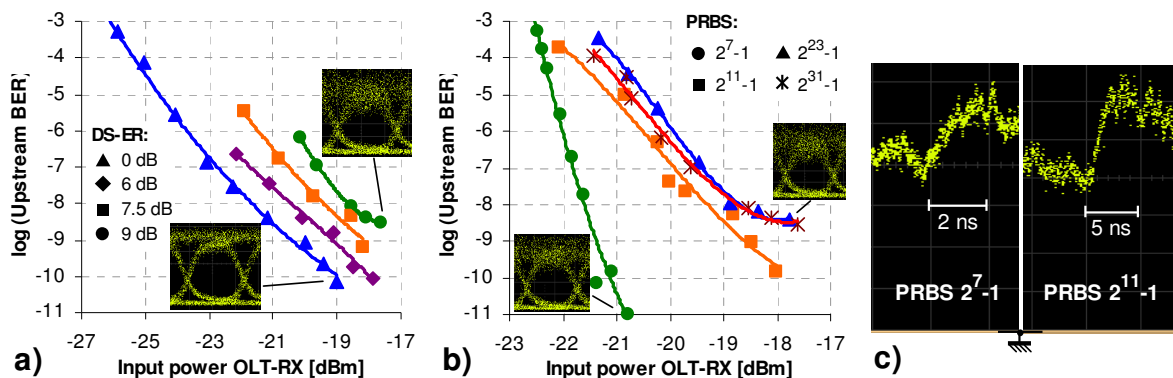


Fig. 4.50. Upstream BER for (a) a PRBS $2^{31}-1$ and different downstream ERs, and (b) a fixed downstream ER and different PRBS lengths. (c) Recovered optical carrier after the FPF for the case of experiencing the largest number of consecutive identical mark bits inside the PRBS.

Fig. 4.50(a) shows the upstream reception performance for the long PRBS length of $2^{31}-1$ at the down- and upstream data pattern. Compared to the previously studied case

with a PRBS 2^7-1 , the optical memory effect by the FPF is not strong enough anymore to prevent amplitude fluctuations in the recovered optical carrier and, consequently, the longer sequence of consecutive identical bits causes an error floor slightly above 10^{-9} in case of a downstream ER of 9 dB. As it is also obvious from equation 4.83, the BER performance could be improved by choosing either a higher finesse F or, in case that this is not possible for some reason as in the presented experimental case where no FPF with higher finesse was available, a lower downstream ER; The swing in the amplitude fluctuations is reduced once the downstream ER is, and for an ERs of 7.5 dB a BER level of 10^{-9} can be obtained, leaving just a penalty of 2.3 dB compared to the remodulation of an optical carrier without present downstream pattern. Note that this reduction of the ER leads to a theoretical increase in the reception penalty for the downstream of 0.46 dB.

The dependence of the upstream performance on the PRBS length for a fixed downstream ER of 9 dB is presented in Fig. 4.50(b). As it is obvious, error floors appear for longer PRBS lengths of $2^{23}-1$ and $2^{31}-1$. Fig. 4.50(c) shows the residual pattern of a downstream with an ER of 9 dB for consecutive identical mark bits in case of the two PRBS lengths of 2^7-1 and $2^{11}-1$. The latter causes a slightly higher swing in the amplitude fluctuations of the recovered optical carrier.

Fig. 4.51(a) shows the measured upstream reception sensitivity at a BER of 10^{-9} for various downstream ERs and PRBS lengths. For low and intermediate values of the downstream ERs, there is no significant penalty for a long PRBS since the finesse of the chosen FPF is sufficiently high to prevent error floors from raising above this reference BER level. Once the downstream ER increases to 7.5 dB and above, penalties are introduced for longer PRBS lengths and even prevent reaching error-free operation for data pattern with lengths of $2^{23}-1$ or longer in case of a high downstream ER of 9 dB.

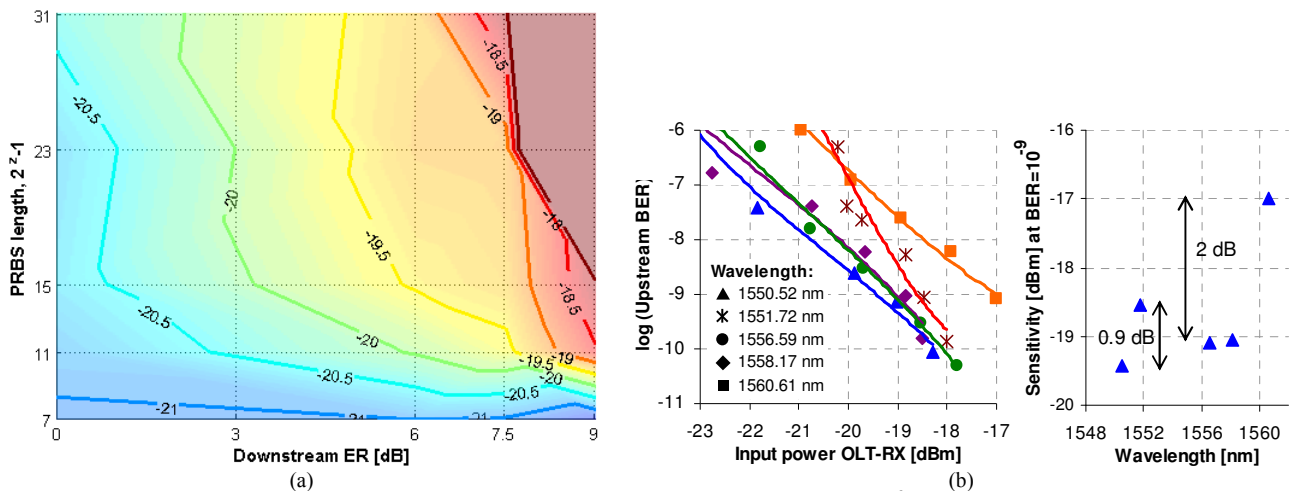


Fig. 4.51. (a) Upstream reception sensitivity for a BER of 10^{-9} as function of the downstream ER and the PRBS length. The dark area on the top right indicates a BER floor above 10^{-9} . (b) Upstream BER for different downstream wavelengths and the corresponding reception sensitivity spectrum for a BER of 10^{-9} .

Being a component with a spectrally periodical transfer function, the FPF obviously provides a wavelength-agnostic solution that is compatible to WDM-based transmission

systems. To demonstrate colorless operation of the all-optical downstream cancellation, upstream measurements have been performed for a downstream ER of 9 dB, a filter bandwidth of 0.21 GHz and a PRBS $2^{11}-1$ for different wavelengths. As can be seen in Fig. 4.51(b), the reception sensitivity at a BER level of 10^{-9} differs by just 0.9 dB. The larger reception penalty of ~ 2 dB for the wavelength at 1560.61 nm is attributed to the roll-off of the C-band EDFA gain profile, which was already located at this upper border downstream wavelength.

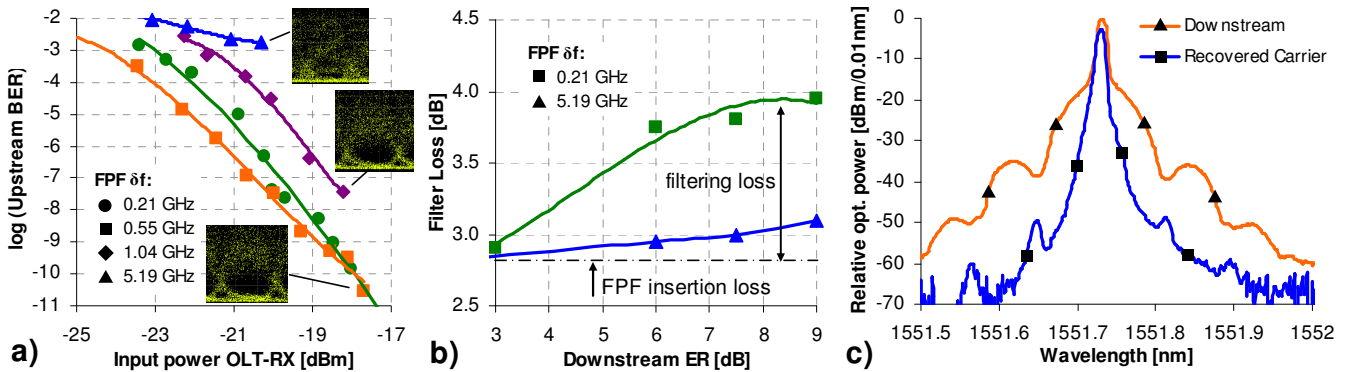


Fig. 4.52. (a) Upstream BER for a PRBS $2^{11}-1$ and a downstream ER of 9 dB for different FPF bandwidths, (b) the FPF loss and (c) the signal spectra for the incident downstream and the recovered carrier, whose optical power levels are referenced to the one of the optical carrier wavelength at 1551.72 nm of the downstream.

The previously discussed effect of the finesse, which is related to a certain filter bandwidth δf , is addressed in Fig. 4.52(a) that shows the upstream performance for a downstream ER of 9 dB. Since the highest finesse of available FPFs was 47, results are shown for a PRBS $2^{11}-1$ and the finesse is gradually reduced to investigate the impact on the error performance.

The reception sensitivity of the original FPF with $\delta f = 0.21$ GHz can be still kept with a slightly wider bandwidth of 0.55 GHz. However, with a further increase of the bandwidth, power penalties and error floors are introduced, since the effect of downstream cancellation is lost. As a result, a filter bandwidth of approximately half the data rate already prevents to reach the FEC level.

Note that the downstream cancellation effect with a spectrally narrow filter is bound to optical losses since the modulation information of the incident light signal is rejected on its way to the upstream modulator. These losses are presented in Fig. 4.52(b) for the two extreme cases of $\delta f = 0.21$ and 5.19 GHz. Although the filtering loss of the more appropriate narrow filter bandwidth is increased for higher modulation indices, this extra loss of 1.2 dB for a downstream ER of 9 dB is relatively small compared to the unavoidable FPF insertion loss that is experienced when passing an unmodulated optical carrier. The spectra of the incident downstream signal and the recovered optical carrier are presented in Fig. 4.52(c), where the rejection of the optical sidebands can be seen.

Symmetrical 10 Gb/s WDM-PON with RSOA-based ONU

Both ONUs were embedded in a WDM-PON for further evaluation (Fig. 4.53), comprising a dual feeder and a drop SMF with 25 and 6 km of length. A detuned BPF was used as for the feed-forward cancellation to achieve 10 Gb/s operation with the RSOA and DCFs at the OLT cope for dispersive effects in the transmission. The ratio of the optical coupler (C_0) inside the ONU was chosen with 10/90 to favor the upstream branch with a higher optical power, thus preventing OSNR degradation during remodulation.

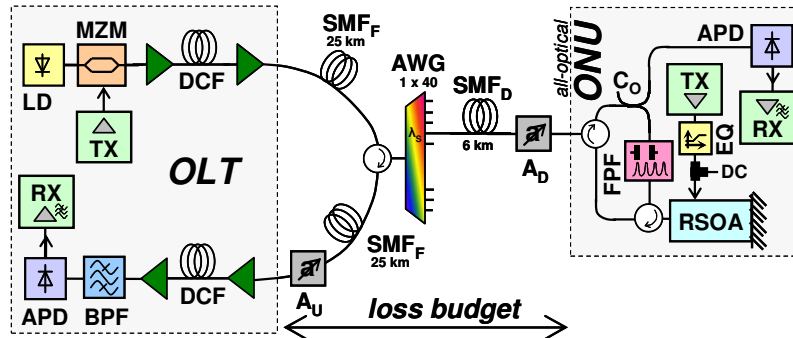


Fig. 4.53. WDM-PON with single wavelength reuse, assisted by an optical downstream cancellation.

The downstream was launched with 6 dBm from the OLT. The OSNR was 46.8 dB for an ER of 3 dB after the OLT booster and 40 dB after remodulation with the RSOA at the ONU, whose net gain is limited to 5.8 dB due to the low small signal gain of the RSOA. The OSRR was >29 dB for down- and upstream and thus no degradation is expected to arise from the drop fiber due to RB.

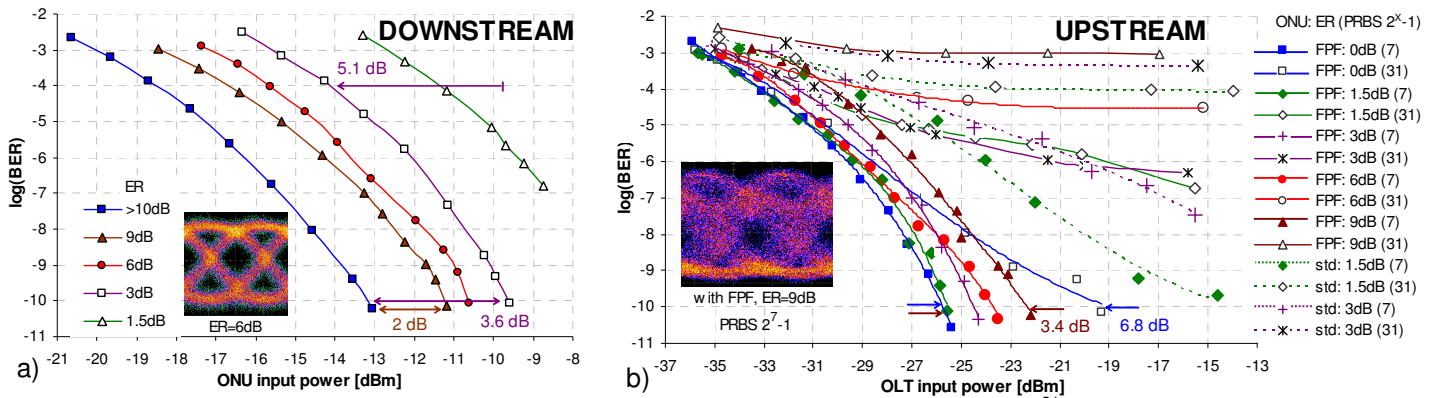


Fig. 4.54. BER measurements for (a) the downstream with a PRBS $2^{31}-1$ and (b) the upstream, for downstream ERs reaching from 0 to 9 dB. For the latter, solid lines indicate the ONU with all-optical downstream cancellation (FPF), while dotted lines belong to the standard (std) ONU; filled markers correspond to a PRBS 2^7-1 , hollow markers to a PRBS $2^{31}-1$.

The downstream BER performance for the standard ONU, which is not included in Fig. 4.54(a) for sake of brevity, benefits by the missing circulator loss; However, ERs larger than 3 dB are not compatible with upstream modulation for this ONU as it is obvious from Fig. 4.54(b).

On the contrary, the FPF-assisted ONU allows downstream ERs up to 6 dB for upstream transmission at the FEC level and a PRBS of $2^{31}-1$. With an ER of 9 dB there is a penalty of only 3.4 dB at a BER of 10^{-10} for a PRBS of 2^7-1 when compared to the downstream-less case. The penalty suffered from a long PRBS of $2^{31}-1$ is already 6.8 dB at a BER of 10^{-10} without downstream pattern. As can be seen from the measurements with the standard ONU, this dependence on the PRBS is not caused by the FPF but due to patterning effects in the RSOA.

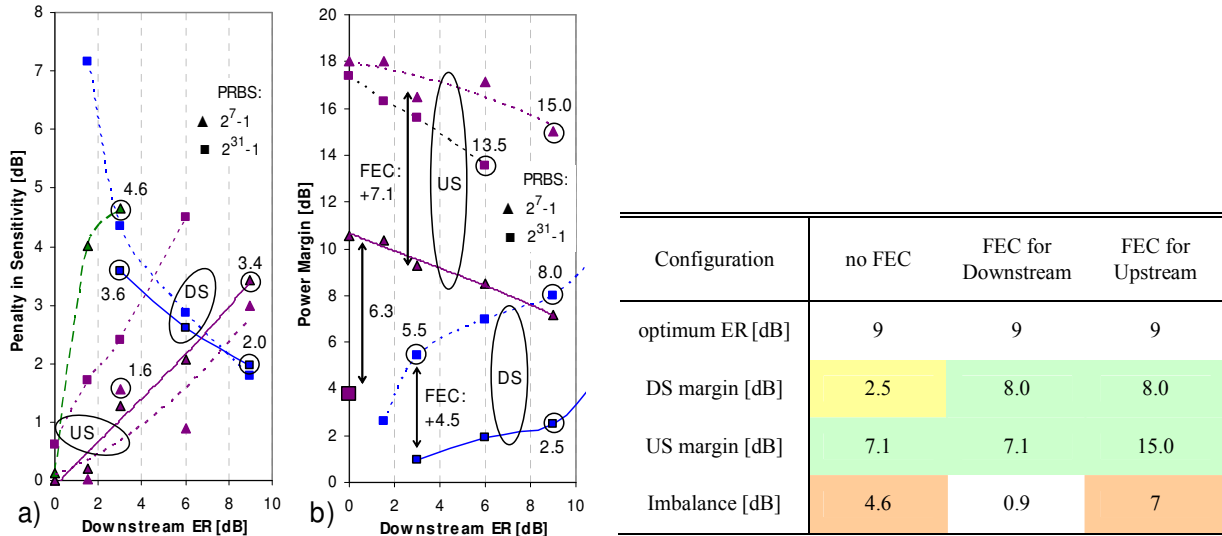


Fig. 4.55. (a) Penalties in sensitivity, referenced to an ER of >10 dB for the downstream and to an ER of 0 dB with a PRBS of 2^7-1 for the upstream, (b) power margins for the ONU with the FPF (solid lines: BER of 10^{-10} , dotted lines: BER of 10^{-4} , dashed lines: standard ONU, BER of 10^{-4}). (c) Optimum downstream ER and corresponding power margins. The imbalance in the margins is defined as the absolute difference between the down- and upstream margins.

The penalties in the sensitivity are shown in Fig. 4.55(a). The standard ONU suffers from a strong penalty once the ERs is increased, causing already 4.6 dB at an ER of 3 dB for the short PRBS while the FPF-assisted ONU is penalized with just 1.6 dB. For an ER of 9 dB the penalty for the same PRBS is 2 and 3.4 dB for down- and upstream, respectively. This results in an extended and optimized power margin at this ER as can be seen in Fig. 4.55(b). Once FEC is included in the more critical downstream reception, the margins are balanced with a higher ER of 9 dB to 8 and 7.2 dB for down- and upstream, leading to maximum PON budgets of 21.5 and 20.7 dB. These margins are already feasible for WDM-PONs. Note, however, that due to the loopback configuration of the WDM-PON the seed budget of the RSOA has to be taken into account as well. In this case, the loss budget would be limited to 13.5 dB due to the chosen downstream launch and ONU input power that was compromised to a high value by the low-gain RSOA. However, loopback configurations with high-gain RSOAs able to operate at optical power levels as low as -20 dBm have been already demonstrated in chapter III.5.

Compared to a typically chosen ER of 3 dB as for the electrical feed-forward cancellation approach, with margins of 5.5 and 9.3 dB, additional improvement

regarding the balanced margin is achieved with the higher optimal ER of 9 dB thanks to a significant reduction of the downstream reception penalty. If FEC is also used for the upstream, its margin raises to 15 dB at an ER of 9 dB, leaving the downstream margin of 8 dB as the limiting factor. Note that the downstream margin could be alternatively optimized by changing the splitting ratio of the coupler C_0 inside the ONU.

The all-optical carrier recovery approximates therefore the performance of ideal orthogonal modulation formats that benefit from the intrinsically small remodulation penalty of frequency or phase modulated downstream signals, however, without utilizing complex modulators at the OLT. What is left is the experimental validation in a hybrid PON with extended reach and loss budget.

Symmetrical 10 Gb/s Extended Reach WDM/TDM-PON with RSOA-based ONU

The FPF-assisted ONU was further integrated in the same hybrid ring+tree PON presented in chapter IV.4.4 (Fig. 4.34) to test its applicability to long reach and OSNR degradation.

The signal evolution for a downstream ER of 6 dB is as follows. As the eight signals that are launched from the OLT pass the IL-RN (C-D), they experience a small gain of 0.3 dB while the insertion losses of this RN are compensated. The drop losses at the S-RN (E-F) are 5.1 dB and the OSNR degrades in the drop amplifier (F-G) by 2.9 dB and keeps a level of 40.2 dB. However, the tree interface loss (G-H) of 1.4 dB in the RN and mainly the high splitting loss in the tree (H-I) cause an ONU input power (I) of -12.7 dBm. This leads together with the insertion and filtering loss of the FPF at the ONU and the high noise figure of the RSOA to a strong OSNR degradation of 10.4 dB to 29.8 dB. The net gain (I-J) of 6.7 dB at the ONU, which is limited by the low-gain RSOA, provides a low input of -23.7 dBm into the upstream amplifier (L-M) in the S-RN. However, the OSNR is just degraded by 0.1 dB due to the dominating ASE background that is already present. Although there is no visible Raman gain on the pass through the first traversed upstream ring spool (N-O), the loss of the second 25 km ring spool (P-Q) is compensated as the signal traverses and the upstream experiences an additional gain of 1.7 dB.

Also in this case no strong pump depletion was visible for the upstream Raman amplification (P-Q) since the injected signal is low with -12.9 dBm. The pump arrives with 11.8 and 8.9 dBm at the S-RN (N, R).

Low BER values of 10^{-10} can be obtained for the downstream with ERs of 6 dB or larger (Fig. 4.56(a)), whereby the penalty compared to an ER > 10 dB is already 4.8 dB for an ER of 6 dB, leaving a power margin of 0.1 dB. With the incorporation of FEC this margin is extended to 6 dB. Also an ER of 3 dB is acceptable with FEC; however, the margin is then reduced to 1.7 dB.

For the FPF-assisted ONU and a word length of 2^7-1 , ERs up to 6 dB allow upstream transmission at a BER of 10^{-10} , for which a penalty of just 2 dB is introduced compared

to the downstream-less case. The margin is then already as high as 7 dB and can be increased to 18.1 dB with FEC. On the contrary, there was no transmission possible with the standard ONU at a BER of 10^{-10} once a downstream signal was present, not even with an ER of just 1 dB (Fig. 4.56(b)).

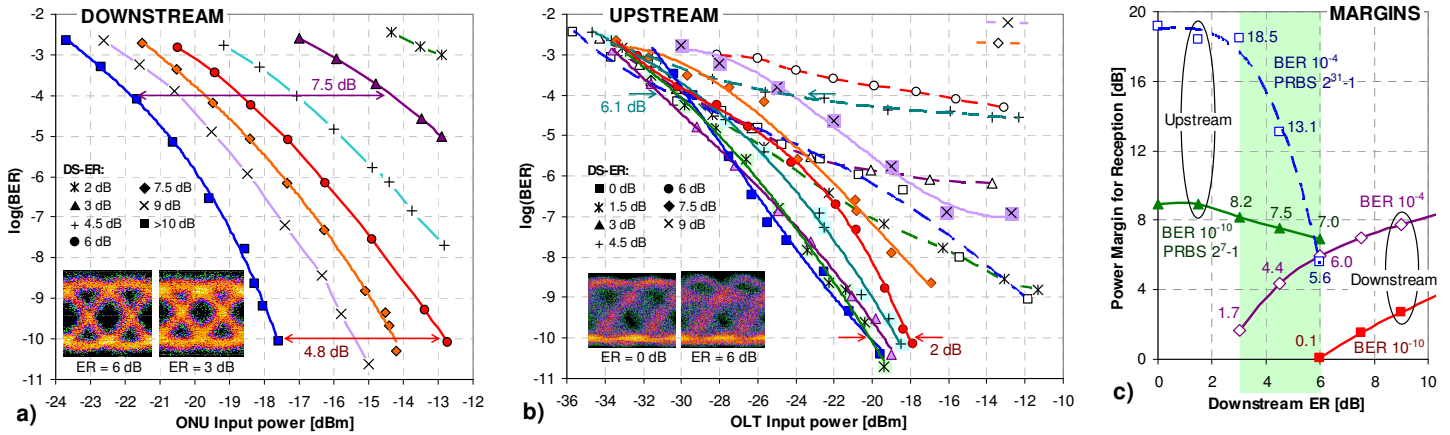


Fig. 4.56. BER measurements at 10 Gb/s for the FPF-assisted ONU. (a) Downstream, (b) upstream (solid curves: PRBS 2^7-1 , dashed: PRBS $2^{31}-1$), and (c) power margins for down- and upstream for different PRBS lengths and BER levels (blank markers: 10^{-4} , filled: 10^{-10}).

For a word length of $2^{31}-1$ error floors appear due to patterning in the RSOA and require the use of FEC. At this BER level, ERs of up to 3 dB show a negligible penalty of < 2 dB with the FPF-assisted ONU, while it raises to 6.1 and >10 dB for an ER of 4.5 and 6 dB, respectively. It was not possible to reach the FEC threshold for ERs > 3 dB with the standard ONU.

Compatible downstream ERs for full-duplex transmission are indicated by the shaded area in Fig. 4.56(c). The optimum ER that leads to balanced margins for down- and upstream can be found with 6 dB regardless of the upstream PRBS length. While for a short upstream PRBS the margin is limited to 6 dB by the downstream, a long upstream PRBS causes a margin of 5.6 dB that is then limited by the upstream.

By applying the all-optical downstream cancellation, the transmission performance in the hybrid ring+tree PON can be significantly improved. The all-optical downstream cancellation outperforms the more traditional feed-forward approach by keeping the crosstalk penalties from remaining downstream patterning lower than 2 dB, even for downstream ERs of 6 dB. As already presented in chapter IV.4.4, the feed-forward cancellation already requires the mandatory use of FEC at this data rate of 10 Gb/s and cannot provide any large margin for the upstream transmission.

4.5.5 Possibilities for Photonic Integration

The all-optical downstream cancellation does not necessarily require a FPF. Each comb generating filter can substitute the FPF as long as the free spectral range and finesse are chosen in a way to achieve optimal performance.

A suitable photonic structure for integration is a ring resonator [178], which can be also cascaded to obtain a wider range of FSR values while keeping the dimensions small [179]. Tunability can be provided via thermal heaters that are included together with the waveguide [180].

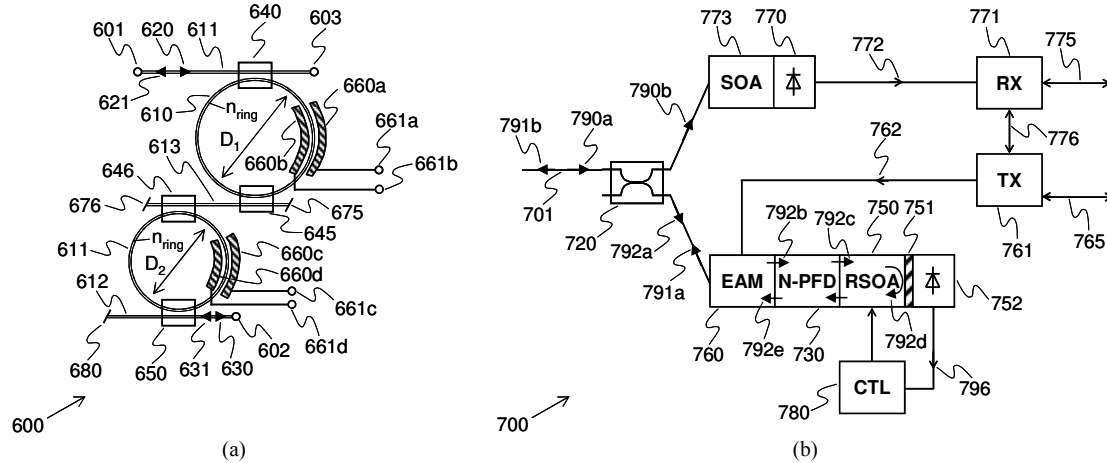


Fig. 4.57. Photonic integration of the all-optical downstream cancellation.

The ring resonator can be thereby placed after the upstream modulator (Fig. 4.57) to avoid the circulators used in the previously reported experiments. In this way the passive resonating circuit removes the downstream signal that is first modulated by the upstream modulator. Afterwards, a SOA element reflects the recovered carrier back to the upstream modulator that can now imprint the data towards the OLT.

4.6 All-Optical Downstream Cancellation with Pulse Shaping

Another kind of all-optical carrier recovery can be constituted by an optical clock recovery unit, though the term “carrier recovery” might then be misleading. The optical clock that is obtained from the downstream signal acts then as the seed for the upstream modulator.

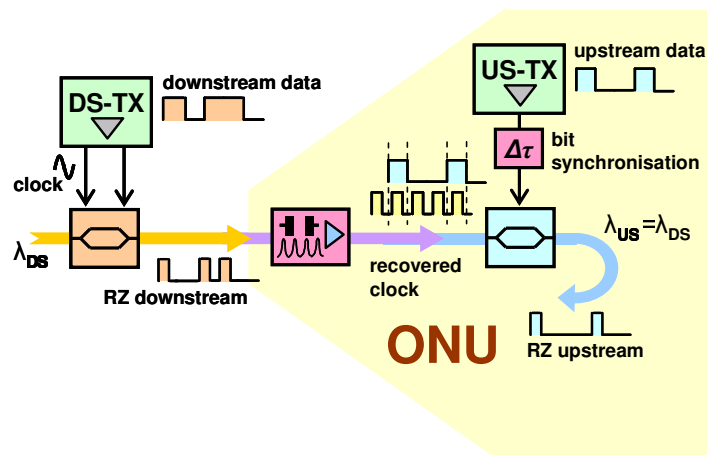


Fig. 4.58. Principal scheme of the optically assisted downstream cancellation with pulse shaping for the optical seed of the upstream modulator.

The advantage of such an approach is obvious; first, a clock recovery circuit provides inherently the pulse shaping for the upstream, so that the quality of the data transmission is less dependent from the modulation bandwidth of the low-cost upstream modulator. Besides, the downstream is typically modulated with high ER to support the clock recovery. This would favor the downstream reception since a penalty due to a reduced modulation index is avoided.

Though these aspects seem to be apparently strong arguments for this method of wavelength reuse, the practical implementation is bound to some complexity. The clock recovery process relies on the synchronized circulation of optical pulses inside a matched cavity, which leads to a filling of spaces in the bit stream with optical pulses. In the alternative representation in the frequency domain, the clock component that can be found at multiples of the data rate is extracted by a spectrally periodic filter with high finesse, similar as for the all-optical carrier recovery technique. To provide a clock component, pulse carving is applied at the transmitter, which leads to a return-to-zero (RZ) modulation for the downstream. Further, to reuse the optical clock efficiently at the ONU, symmetrical data rates should be chosen for down- and upstream since otherwise a single bit in the upstream is composed by multiple pulses.

The capability of the clock recovery to provide a suitable seed for the upstream modulator can be investigated similarly as in chapter IV.5.2, by choosing the RZ pulse envelope $A(t)$ for the downstream.

$$A(t) = \exp\left(-\frac{1+jC}{2} \frac{t^2}{T_b^2}\right) \quad (4.85)$$

4.6.1 Simulation

As for the all-optical carrier recovery, the residual amplitude modulation of the recovered clock is considered as the figure of merit.

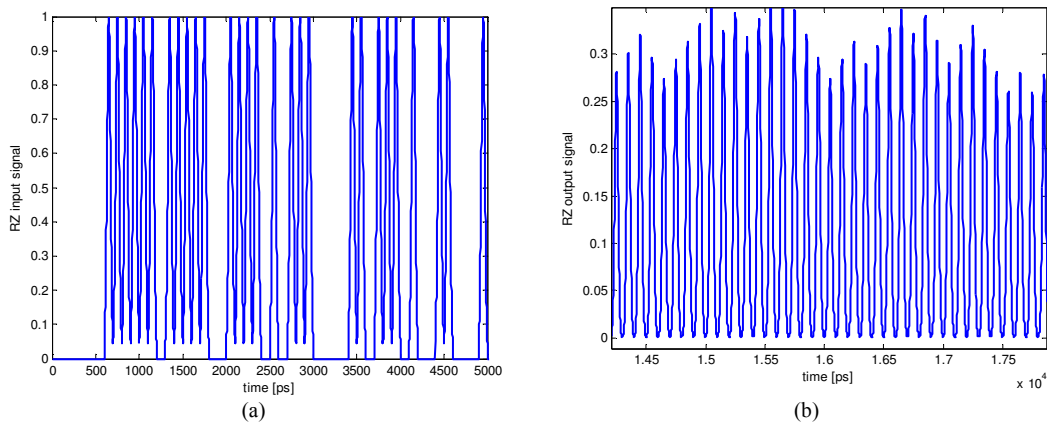


Fig. 4.59. Incident RZ downstream signal at the FPF and (b) recovered optical clock at the FPF output.

Fig. 4.59(a) shows the incident RZ downstream at the FPF input, whose FSR was matched with the downstream data rate and whose finesse was set to 40. Thanks to its optical memory effect, the spaces in the bit stream are filled with optical light, though the envelope of the optical clock stream, presented in Fig. 4.59(b) and 4.60(a), is patterned. The filtering effect of the optical cavity is obvious from the electrical spectrum in Fig. 4.60(b), which shows the suppression of the data modulation while the clock harmonics are left.

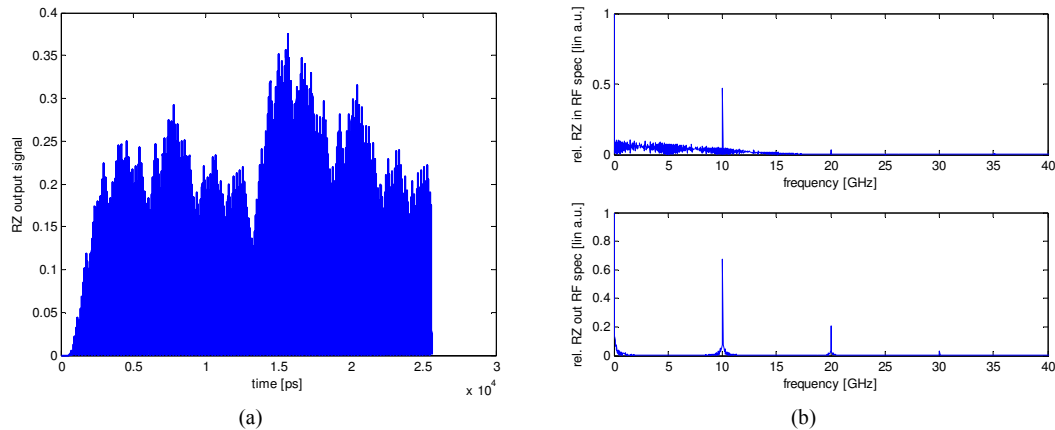


Fig. 4.60. Recovered optical clock for a FPF with a finesse of 40. (a) FPF output signal and (b) the spectra at the FPF in- (top) and output (bottom).

A reduction of the residual intensity fluctuations can be obtained with a subsequently used SOA. Fig. 4.61 shows the beneficial exploitation of the gain saturation effect for an input power of -13 dBm. As can be seen, the intensity modulation of the optical clock is reduced significantly.

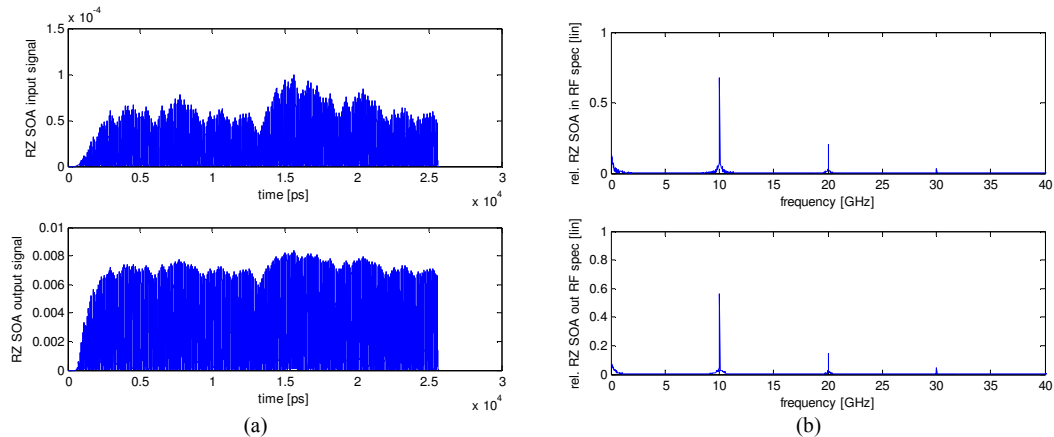


Fig. 4.61. Improvement of the optical clock by reducing the intensity modulation in its envelope with the help of a saturated SOA. (a) SOA in- and output signal and (b) their spectra.

The relative large patterning after the FPF can be reduced by increasing the finesse of the filter. Fig. 4.62 shows the output of the FPF and the SOA for a finesse of 100, which reduces the patterning significantly once the cavity of the FPF is filled with light.

The low amplitude variations of the generated optical pulses demonstrate the feasibility of the clock remodulation method.

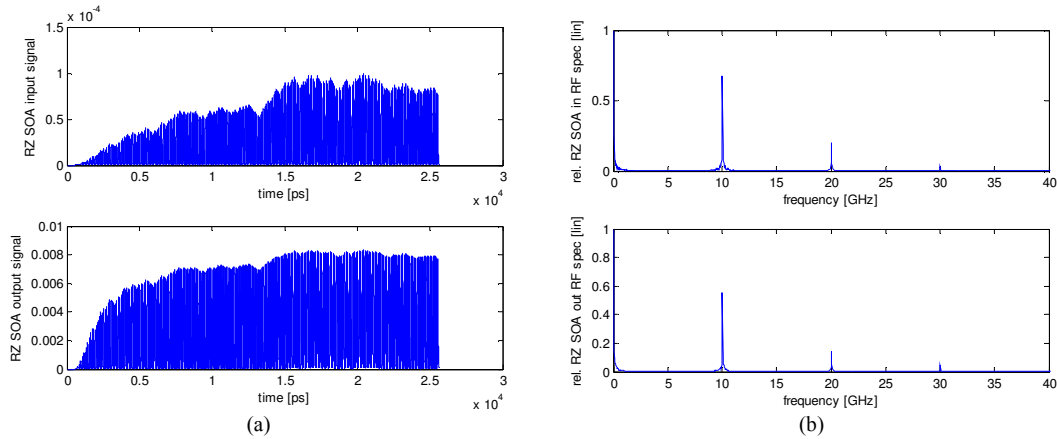


Fig. 4.62. FPF and SOA output for a finesse of 100. Signals in (a) the time- and (b) the frequency domain.

4.6.2 Experimental Validation

A principal proof of the optical clock remodulation method was carried out in a simple WDM-PON, presented in Fig. 4.63. The RZ downstream was generated at a wavelength of 1556.55 nm with an EAM as pulse carver and synchronized data modulation at 10 Gb/s with a MZM. The downstream ER was optimized and > 13 dB.

At the ONU, the downstream is first split by a 50/50 coupler (C_0) for being detected and remodulated. A combination of low-gain EDFA and 10 Gb/s PIN diode was used as detector since no APD was available.

The clock recovery is constituted by a FPF with a FSR of 10.2278 GHz and a finesse of 40, and an inline SOA. The downstream data rate was matched to the exact value of the FSR to optimize the performance of the clock recovery. On top of this, an EDFA with a low small signal gain of 10 dB was added in front of the SOA since the gain of the latter prevented to reach the saturation regime of the amplifier. With this combination of amplifiers, sufficient suppression of the residual amplitude modulation after the FPF is provided. In a real deployment, the SOA would have to be redesigned to meet the requirements. A MZM imprints then the upstream data at 10 Gb/s synchronized to the recovered clock pulses with the help of a delay line ($\Delta\tau$).

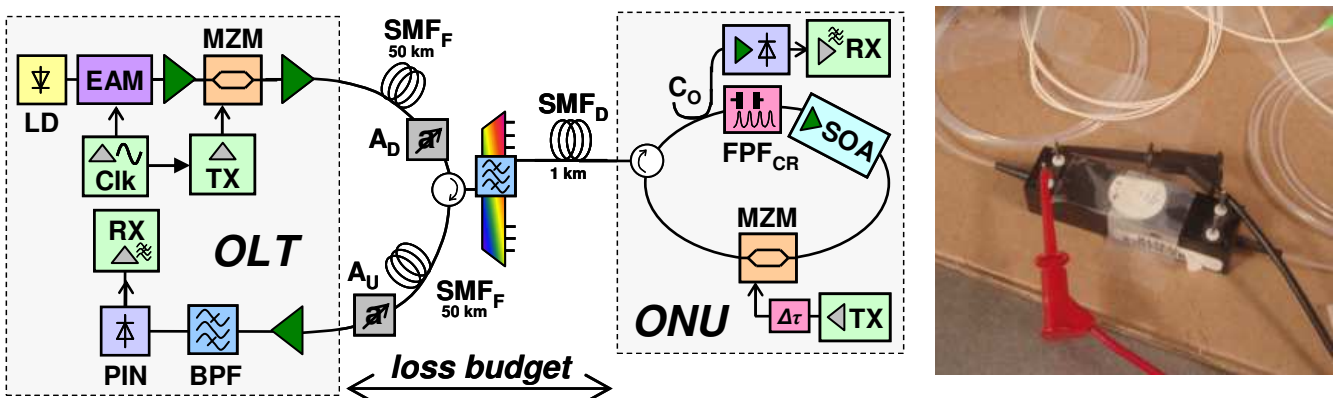


Fig. 4.63. Experimental setup with wavelength reuse by means of optical clock remodulation and fiber-based FPF device.

The loss budget of the optical distribution network was fixed to 20 dB with the attenuators A_D and A_U . The downstream was launched with 10 dBm, resulting in an ONU input power of -10 dBm. At the input of the EDFA that supports the SOA at the clock recovery subsystem of the ONU, the signal arrives with a power as low as -22 dBm. The OSNR values for a resolution bandwidth of 0.1 nm are 41.5 dB after the OLT transmitter and 29.4 dB at the ONU output and the upstream was launched with a power of -0.5 dBm from the ONU.

The ability of the clock recovery unit at the ONU to provide a suitable optical seed for the upstream modulator [181] was assessed in terms of the residual amplitude modulation, for which the peak ER of the recovered clock was taken as a figure of merit. The corresponding eye diagrams for the recovered optical clock are shown in Fig. 4.64.

In back-to-back conditions without fiber span, the space bits in the bit streams are filled with optical pulses by the FPF, however, with stronger residual intensity fluctuations. Peak ERs of 6.5 and 6.8 dB can be found after the FPF for a PRBS 2^7-1 and $2^{31}-1$, respectively. This initially large remaining patterning is strongly reduced by the saturated SOA, whose output signal shows just small amplitude fluctuations with peak ERs of 1.7 and 1.9 dB.

The inclusion of a 50 km long fiber span between OLT and ONU penalizes the performance of the clock recovery, since the downstream signal is affected by chromatic dispersion. This leads to increased peak ERs, which are then 2.2 and 3.2 dB after the SOA.

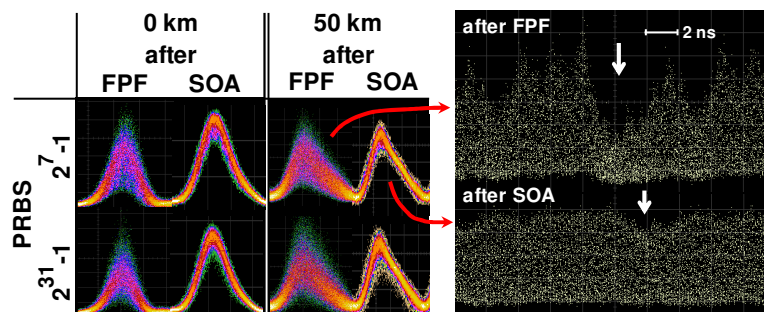


Fig. 4.64. Eye diagrams and trace of the recovered downstream clock. The arrows in the traces indicate the bit sequence with largest number of consecutive space bits within the PRBS.

In case of the upstream, the transmission performance was first evaluated in a back-to-back scenario without downstream modulation, meaning a continuous-wave feed for the ONU and a NRZ upstream. Subsequently, the downstream modulation was switched on and the RZ upstream that is imprinted on the recovered clock is characterized for different downstream PRBS lengths.

Fig. 4.65(a) shows the BER measurements for the NRZ upstream and continuous-wave seed of the upstream transmitter, while Fig. 4.65(b) shows the performance for the RZ upstream that is modulated on the recovered downstream clock.

For both cases there is no strong penalty when increasing the PRBS length of the downstream. A penalty of 1.1 dB remains for the RZ upstream, which is attributed to

the patterning effects of the clock recovery which are not fully suppressed by the saturation of the SOA. However, these patterning effects could be also reduced by increasing the finesse of the FPF.

Note that the apparently improved sensitivity of the RZ upstream compared to its NRZ counterpart is caused by the duty cycle of the RZ signal that turns into a power conversion penalty of 5.6 dB. With this, there is a reasonable reception penalty of ~ 3.4 dB at a BER of 10^{-10} between the two cases of having an ideal optical seed for the upstream modulator and the recovered optical clock of the downstream. However, this penalty has to be seen as a compromise for having a downstream signal with infinite ER and, consequently, no reception penalty due to a reduced modulation index.

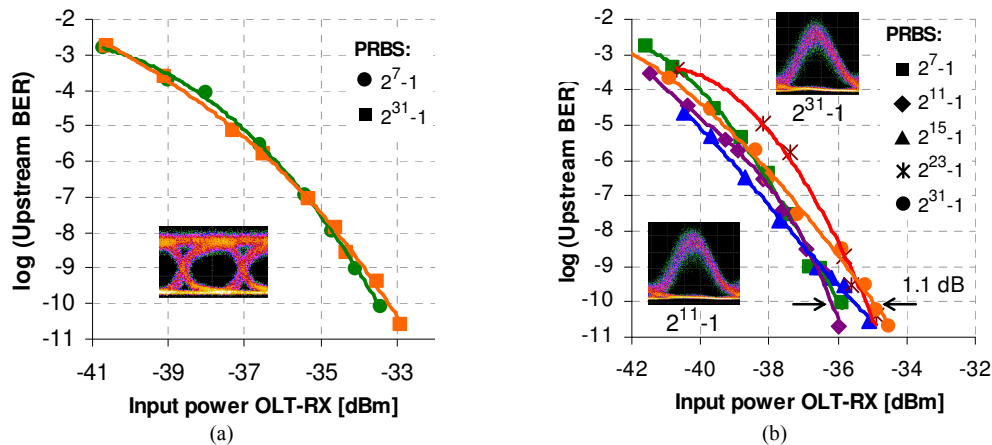


Fig. 4.65. Upstream back-to-back BER measurements for (a) continuous-wave light seed and NRZ modulation, (b) concurrent RZ downstream transmission and remodulation of its recovered optical clock.

The transmission performance over a fiber-based light path is shown in Fig. 4.66 for representative PRBS lengths.

The BER measurements of the RZ downstream are presented in Fig. 4.66(a). A fiber length of 25 km causes a reception penalty of ~ 5 dB due to dispersive effects; however, a BER of 10^{-10} can be still obtained. A high loss budget of 35 dB, found as the difference between the downstream launch and the reception sensitivity referenced to the ONU input, is compatible and exceeds the nominal budget of 20 dB since the reception penalty due to a reduced ER is fortunately avoided for the downstream. When the length of the transmission link is further increased to 50 km, there is still penalized reception possible at the FEC level, suffering from a penalty of ~ 9 dB compared to the back-to-back case.

For the RZ upstream that uses the downstream with dispersion-induced pulse broadening as seed for the optical clock recovery, dispersive effects are pronounced due to the bidirectional transmission link. As can be seen in Fig. 4.66(b) where also results of Fig. 4.65(b) are partially added for comparison with the back-to-back case, the PRBS penalty increases. This stems from the degraded clock signal and causes already an error floor for a long PRBS of $2^{31}-1$ in conjunction with a 25 km long span. For shorter PRBS lengths of 2^7-1 and $2^{11}-1$, the reception penalties at a low BER of 10^{-10} compared to the back-to-back case are 5 and 9 dB, respectively. The loss budget for the PRBS $2^{11}-1$ is

then 28.3 dB and clearly above the nominal PON budget of 20 dB. As it is the case for the downstream, upstream reception can be obtained at the FEC level at a 50 km reach. However, the compatible loss budget is strongly reduced by more than 10 dB, proving the need for dispersion compensation.

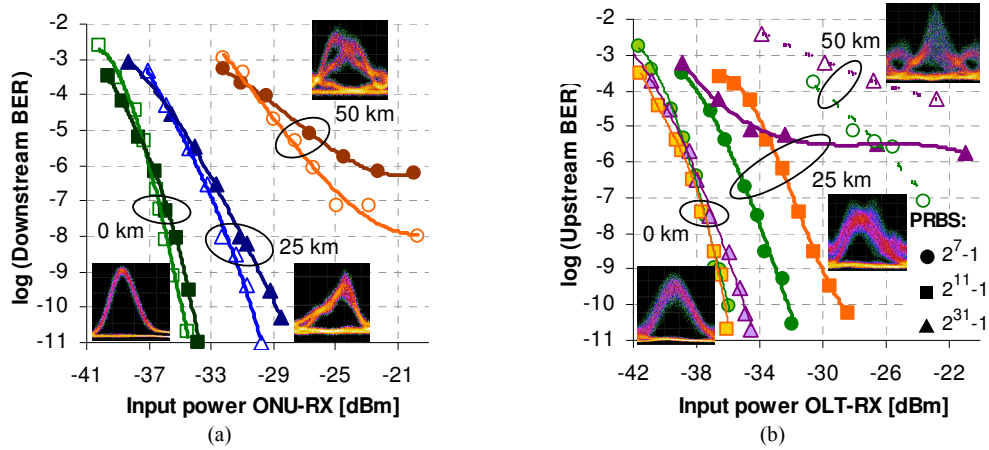


Fig. 4.66. BER performance for transmission over fiber spans in case of (a) the downstream (filled and hollow markers indicate a PRBS $2^{31}-1$ and 2^7-1 , respectively), and (b) the upstream.

Finally, the clock remodulation method was evaluated for different downstream wavelengths. Fig. 4.67 shows the upstream sensitivity spectrum for the back-to-back case and a downstream PRBS of $2^{11}-1$. Since the sensitivity differs by just 1.5 dB among all the chosen optical carrier frequencies, it is obvious that colorless operation can be guaranteed.

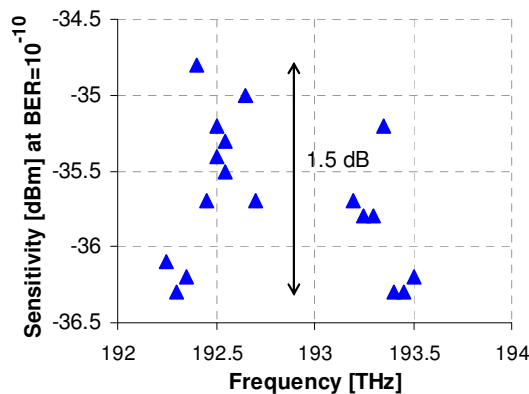


Fig. 4.67. Sensitivity spectrum for the back-to-back upstream reception.

4.7 Additional Aspects for Wavelength Reuse

Wavelength reuse for full-duplex data transmission on a single, bidirectionally used fiber span requires not only a method for data erasure. Further more, RB might limit the transmission performance in case that the light path is subject to high loss dynamics: for the case that signals with strong power levels are transmitted over fiber spans while weak, counter-propagating signals are received at the same time, Rayleigh scattering in the transmission medium can impose limits for the optical transmission system [182].

Such high differences in the power levels are given for highly shared network infrastructures, since the high number customers introduces high optical losses with the insertion of WDM multiplexers [18] and power splitters for TDM [19]. In a hybrid PON that typically consists of a WDM trunk and a TDM tree section, the downstream signal in the feeder fiber typically causes severe RB, while the upstream signal transmitted by the reflective modulator at the ONU is in turn responsible for RB into the downstream at the drop fiber span to which the ONU is connected [183].

Different means for the mitigation of RB have been earlier investigated, such as line coding combined with high-pass filtering [184,185], dithering of the optical seeding signal [186], phase modulation of the upstream data signal and additional optical offset filtering [187-189], most of them aiming at reducing the spectral overlap between the upstream signal and the degrading back-reflected downstream light. Although these approaches allow to operate a PON with a lower OSRR between the upstream signal and its backscattered optical seed, their efficiency is limited since the spectra of the two counter-propagating signals are only partially displaced. On the contrary, wavelength shifting at the ONU allows to spectrally re-locate the upstream next to the downstream, so that the RB caused in the feeder fiber can be filtered at the upstream receiver and thus in principle fully suppressed. However, such techniques typically require complex elements at the cost-sensitive ONU such as bulky modulators and are therefore often not feasible from a techno-economical point of view.

4.7.1 Wavelength Shifting due to Clock Tone Extraction

The all-optical clock remodulation technique presented just previously in chapter IV.6 can be also used for the purpose of wavelength shifting.

The clock recovery at the ONU cannot only be used for remodulation purposes. Given the fact that it can recover an initially suppressed harmonic of the RZ downstream signal, it allows – together with the extraction of the same clock harmonic after the clock recovery process – to immunize the upstream data transmission against RB from the downstream. The advantage can be found in the simplicity: in addition to the remodulation scheme presented in chapter IV.6, just passive optical filtering is applied to obtain the desired wavelength shift for the upstream signal.

The approach is illustrated in Fig. 4.68. The RZ downstream signal is passed to a narrowband notch-filter to remove one of its clock harmonics. Due to that, the RB that derives at the bidirectional fiber link does not contain any spectral component at this suppressed RZ clock tone. Consequently, if the upstream signal is transmitted at exactly this frequency, no RB degradation arises. To generate the optical upstream carrier at the desired wavelength, an all-optical clock recovery is used together with a narrow optical passband filter so that just a single optical carrier remains at the input of the upstream modulator. Depending at which clock harmonic the upstream is modulated, a wavelength shift of up to a multiple of the downstream rate R_{DS} is provided. At the

upstream receiver, the RB contribution that is now out-of-band with the data signal can be simply filtered with another optical band-pass filter that is centered in respect to the upstream signal.

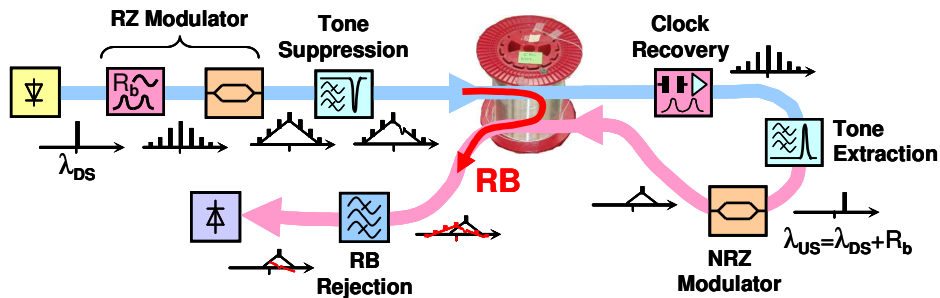


Fig. 4.68. Schematic representation of the wavelength shifting scheme, based on passive optical filtering.

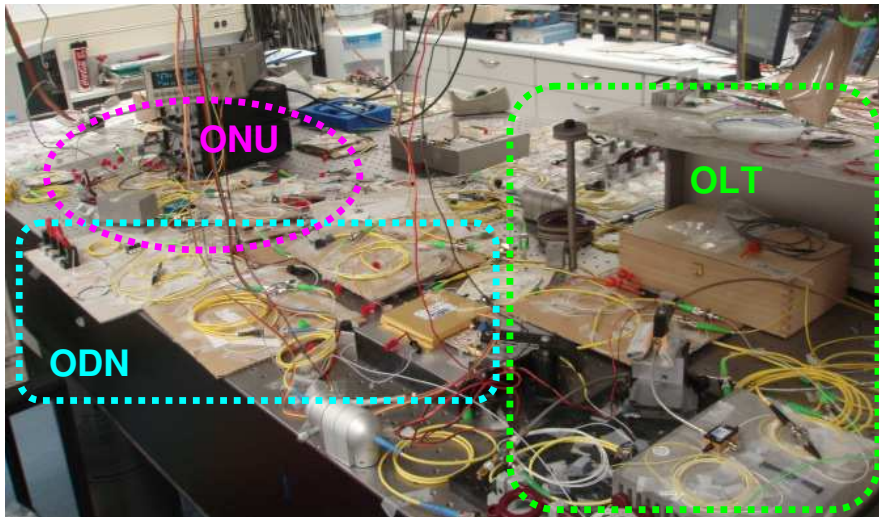
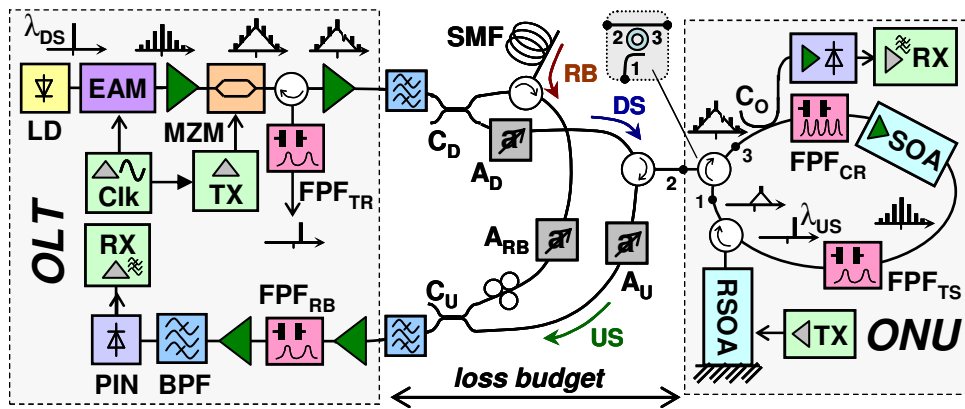


Fig. 4.69. Experimental proof-of-concept setup for the wavelength shifting method supported by clock recovery and selective optical filtering.

The concept was evaluated for a PON-like scenario, shown in Fig. 4.69, and the case of having asymmetrical data rates of 10 and 1 Gb/s in down- and upstream direction, respectively.

Several optical filters for clock recovery and narrow-band filtering were constituted by FPFs. For the RZ tone rejection at the OLT transmitter and the tone extraction after the clock recovery at the ONU, FPFs with bandwidth of 0.55 and 0.29 GHz were

chosen. The clock recovery is identical with the one used in chapter IV.6. At the OLT receiver, a 5 GHz broad FPF was included inside a dual-stage Erbium-doped fiber preamplifier to filter the RB.

The RB was generated at a 25 km long SMF span, whose backscattered light was added to the upstream signal. The attenuators A_D and A_U were fixed to a loss budget of 20 dB between OLT and ONU, meaning with the downstream launch of 10 dBm from the OLT transmitter an ONU input of -10 dBm. The third attenuator A_{RB} was used to adjust the upstream OSRR. Two 3 nm broad band-pass filters were included in the distribution network to emulate the multiplexer of WDM-PONs.

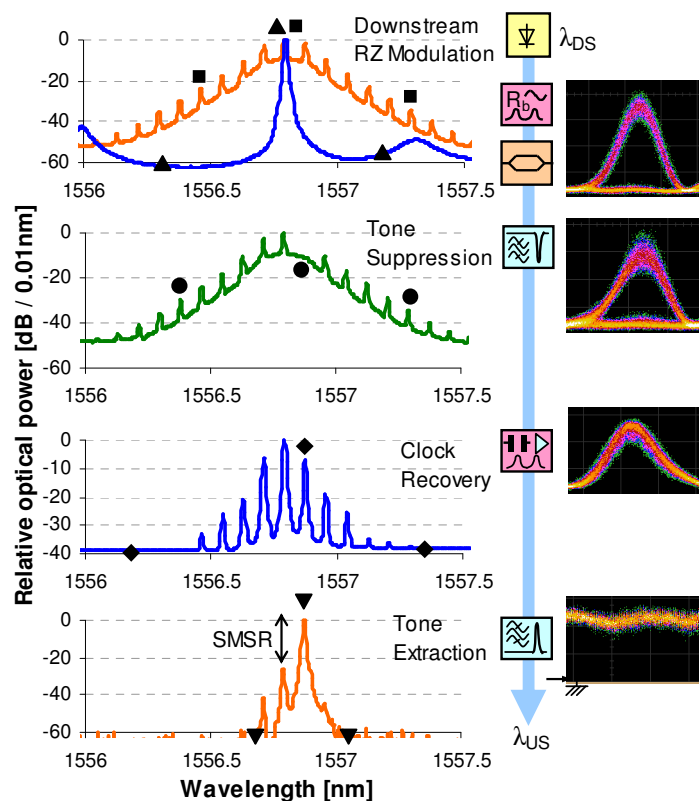


Fig. 4.70. Optical spectra illustrating the evolution of the RZ downstream towards a shifted upstream signal and the corresponding eye diagrams.

A 50/50 coupler (C_0) at the ONU splits the incident downstream for the purpose of remodulation and detection. For the latter, a combination of PIN diode and transimpedance amplifier was used. The high-gain RSOA with low electro-optical bandwidth of chapter IV.4.4 constituted the upstream transmitter and was fed by a PRBS of length $2^{31}-1$. With the upstream launch of 2.5 dBm, the net gain of the ONU is 12.5 dB.

Note that in case of an inline SOA, the circulator at the bidirectional port of the RSOA can be removed, while the second circulator at the ONU input could be replaced by a ring resonator as shown in Fig. 4.69, having its drop port connected to the upstream transmitter (i.e. RSOA) while its express port relays the downstream to the clock recovery. In this way, an ONU design suitable for photonic integration can be obtained.

The spectral evolution of the downstream is presented in Fig. 4.70, where the optical power is normalized to the strongest spectral component. The downstream carrier (\blacktriangle) was located at a wavelength of 1556.8 nm and shows solely the side-modes of the distributed feedback laser diode. After RZ modulation (\blacksquare) with a PRBS 2^7-1 and clock tone suppression with the FPF (\bullet), the +1 harmonic is rejected with more than 13 dB. This value can be increased with non-reflective filters such as ring resonators. The suppressed harmonic is again established after the clock recovery at the ONU (\blacklozenge). Besides the obtained wavelength shift of R_{DS} in respect to the optical downstream carrier, the SMSR after the tone extraction FPF (\blacktriangledown) is already in the range of 25 dB. Note that the separation between the strongest side peak, which derives from the downstream carrier at λ_{DS} , corresponds to the downstream rate R_{DS} and is wider than the FPF bandwidth at the OLT receiver, so that this SMSR is further improved before upstream detection.

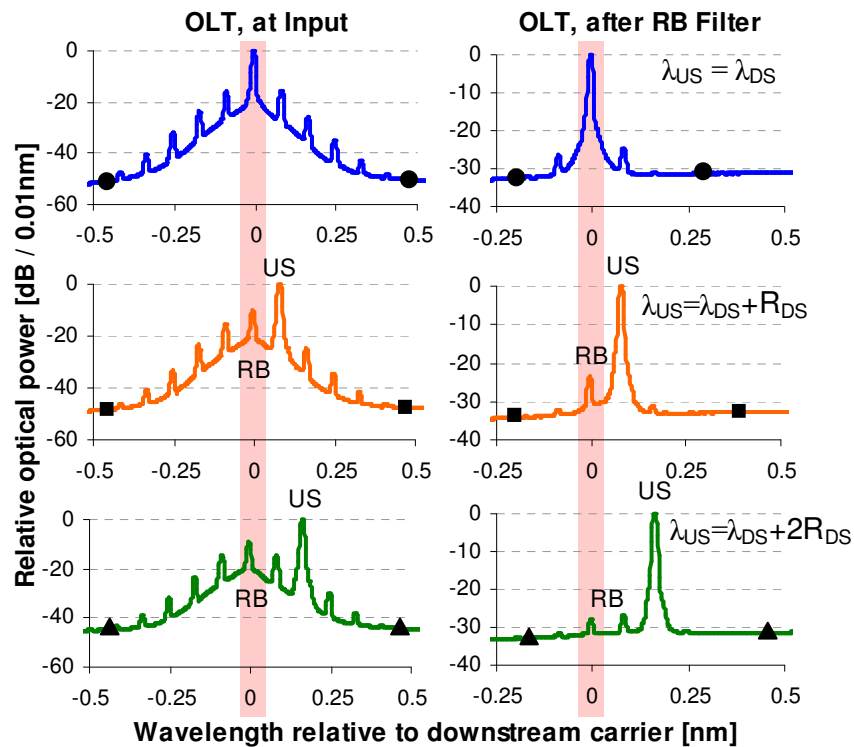


Fig. 4.71. Impact of the RB filter at the OLT receiver on upstream signals with different wavelength shifts corresponding to the downstream carrier wavelength, the +1 and +2 harmonic.

This is obvious from the spectra in Fig. 4.71, showing the received upstream signals after RB addition at the OLT input and after the FPF that selects the upstream. Though the SMSR is high for the upstream without wavelength shift (\bullet), there is significant in-band RB noise. On the contrary, for the shifted upstream, no in-band RB contribution exists thanks to the suppression of the clock harmonic at the OLT transmitter. For the upstream that is located at the +1 (\blacksquare) and +2 harmonics (\blacktriangle), the SMSR is thus determining the reception performance. As can be seen, this SMSR is in the range of 25 dB.

The high SMSR stems from the sufficient suppression of the other clock harmonics by the FPF during extraction of the upstream carrier. Fig. 4.72(a) shows the obtained SMSR and the caused filtering loss of the carrier extraction process, that latter referenced to the extraction of the downstream carrier. It is obvious that the filtering of farther harmonics, e.g. the spectral +3 or -3 clock component, is subject to increased loss. The tilt in the filtering loss towards lower values for the positive harmonics is attributed to the chirp of the SOA of the clock recovery.

As can be deduced from the eye insets in Fig. 4.70, there is no strong distortion in the downstream once the +1 harmonic is suppressed, while it is even less for rejecting higher-order harmonics that carry less power. The recovered upstream carrier at the initially rejected harmonic does not show significant patterning from the clock recovery process. Note that for a longer downstream PRBS the finesse of the FPF used at the clock recovery has to be increased accordingly.

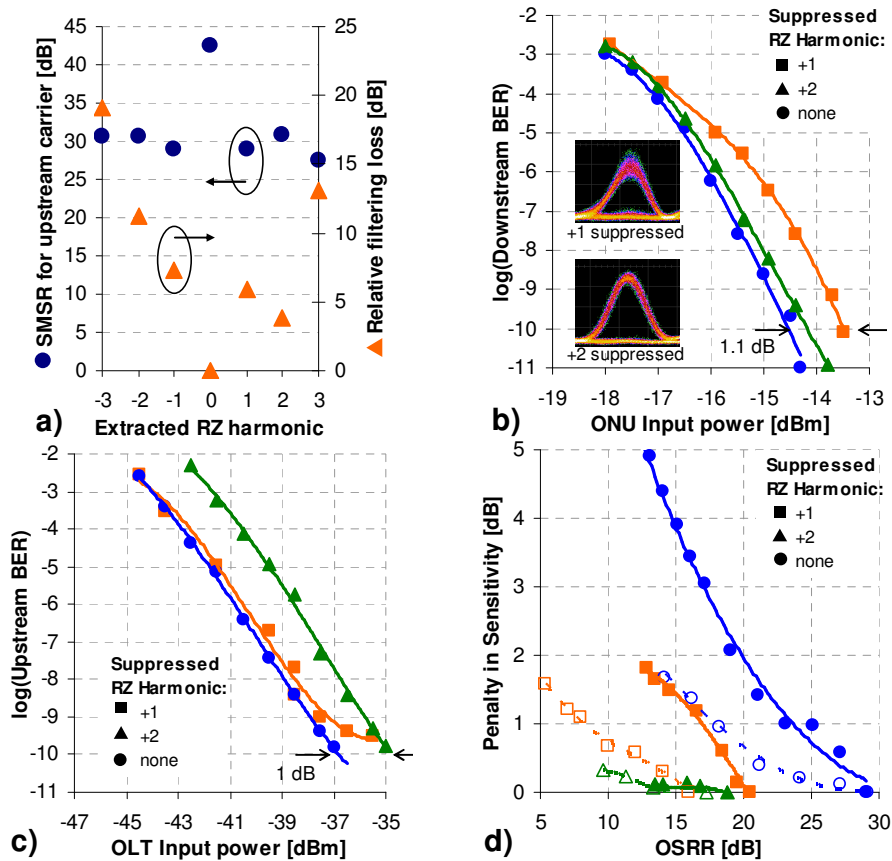


Fig. 4.72. (a) Obtained SMSR and filtering loss after upstream carrier extraction at the ONU and BER performance for (b) the RZ downstream with tone suppression, and (c) the upstream at the recovered harmonic. (d) Penalty in sensitivity as function of the OSRR for the received upstream. Filled markers indicate a low BER of 10^{-9} , while hollow markers correspond to a higher BER level of 10^{-4} .

The transmission performance for both data streams is presented in Fig. 4.72(b) to Fig. 4.72(d). While for the suppression of the +1 harmonic of the RZ downstream a penalty of 1.1 dB arises at a BER of 10^{-10} compared to the RZ downstream containing all initial

clock tones (Fig. 4.72(b)), this penalty reduces to <0.5 dB for rejecting the +2 harmonic. A power margin of 3.8 dB was found, considering the targeted loss budget of 20 dB.

In case of the upstream reception without added RB, shown in Fig. 4.72(c), the penalty that is attributed to the filtering loss of the wavelength shifting technique at the ONU is 1 dB for a BER of 10^{-10} and the worse case of extracting the +2 tone as optical upstream carrier. This proves that with a reasonable amount of optical amplification inside the ONU, the inherent filtering losses of this scheme can be overcome without being penalized. A budget of >38 dB is compatible for the upstream.

When adding the RB deriving from the downstream, the beneficial effect of wavelength shifting is obvious and dominates over the rather small unfavorable impact of the filtering loss at the ONU. Fig. 4.72(d) shows the extra amount of optical power that is required to obtain a certain BER level when degrading the upstream OSRR. While the original, without tone suppression remodulated RZ downstream is penalized quickly and already at high OSRR values, the shifted upstream signals show higher robustness against RB noise. Especially the upstream that is transmitted at the +2 harmonic of the downstream does not show strong penalties, which remain <0.5 dB even for a low OSRR of ~10 dB.

With a 1-dB reception penalty as reference, the compatible minimum OSRR values for a low (high) BER level of 10^{-9} (10^{-4}) are 23.5 (17.7) dB without wavelength shifting, 18.7 (8.2) dB for a shifted upstream at the +1 harmonic and <13 (<9.5) dB for a shifted upstream at the +2 harmonic.

Since the transmission performance is improved at both shifted upstream signals compared to the simple remodulation of the incoming RZ downstream, an access network configuration where different users are bundled is thinkable. While these users share a common high data rate downstream signal as in a TDM scheme, their upstream signals can be allocated to different RZ clock harmonics. This would allow a mix between WDM and TDM, or the introduction of an UDWDM approach in upstream direction.

4.7.2 Wavelength Generation due to Four-Wave Mixing

A farther spectral displacement of the upstream carrier, far outside of the downstream signal band, can be obtained by four-wave mixing (FWM) in SOA elements at the ONU [190]. In this case, a wavelength generation takes place, however, without providing an optical carrier signal at the targeted upstream wavelength before. For this reason there is also no RB contribution present in the feeding light path.

The WDM trunk section of hybrid PONs can be used for overlaying a bunch of tree-like TDM-PONs with the help of a single WDM multiplexer such as an AWG or, alternatively, it can be deployed as a ring as in Fig. 4.34. Due to the high splitting ratios in the trees of the PON that is sketched in Fig. 4.73(a), the downstream has to be

launched from the RNs with high optical power to reach the ONUs with sufficient remaining power. Considering a limited net gain of the reflective ONU, the upstream arrives in general weak at the feeder fiber and, consequently, the OSRR falls to a level where no upstream transmission can be established due to severe RB beat noise – as discussed initially in this chapter.

By alternating the filtering scheme of the RN of Fig. 4.34 in terms of an additional centered band-pass filter, as will be explained shortly, a four channel allocation can be provided. This in turn is suitable to a FWM scheme with two (inner) pumps and two (outer) FWM products, the latter referred to as the satellites in the following sections.

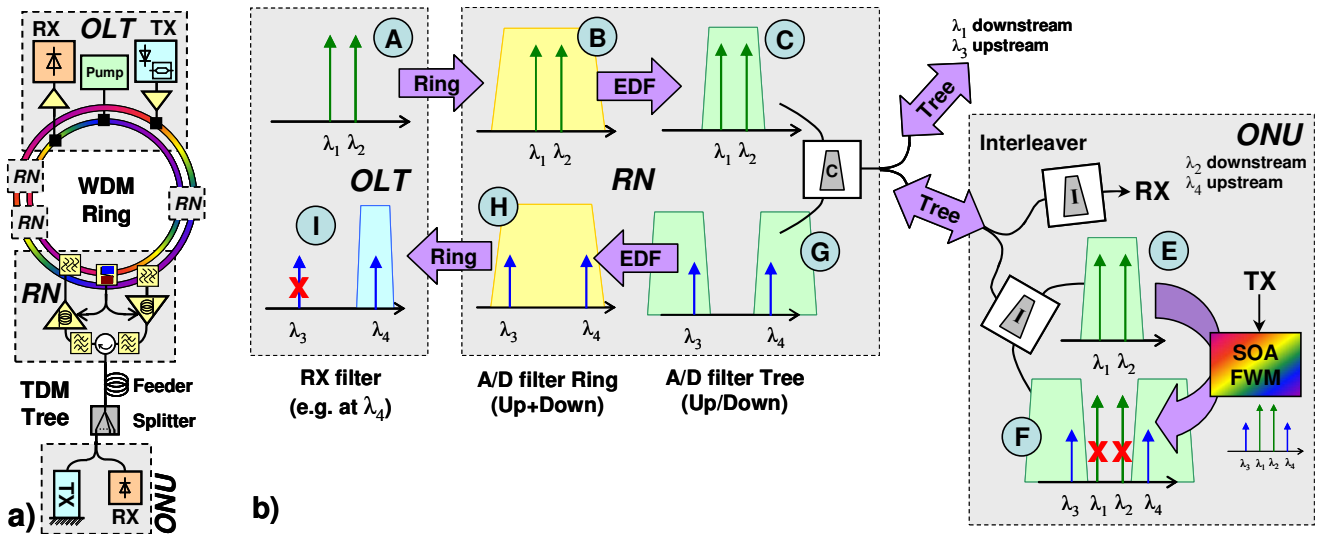


Fig. 4.73. (a) Hybrid ring+tree PON architecture and (b) functional scheme of the PON. Two downstream signals are fed as pumps to each tree. The filters in the RN and the interleavers in the ONU are chosen to suppress unwanted spectral components for downstream detection and for upstream transmission, after exploiting the FWM process at the ONU. The SOA element at the ONU can be re-used as upstream modulator.

The pumping and transmission scheme is illustrated in Fig. 4.73(b) and shows the specific filtering used in the RN and the ONU. The two required pumps for the FWM process are sent at the wavelengths (λ_1 , λ_2) from the transmitter of the OLT via the ring to the RN, where they are dropped as downstream signals, amplified and fed to the trees. Instead of releasing just a single wavelength to the tree as in the conventional PON [8,172], both signals are fed to both trees. Therefore, a 50/50 coupler is added in front of the two trees. Since the downstream wavelengths are spectrally located close together on neighboring channels of the ITU grid due to their common A/D filter at the ring [8], no broad wavelength shift is asked for the FWM process. This in turn implies a reasonable efficiency for the generation of the satellite wavelengths (at λ_3 and λ_4) [138]. The exact downstream wavelengths are chosen so that both downstream and the satellites (i.e. upstream) signals fit with the passband of the A/D filters (see point B and H in Fig. 4.73(b)) of the RN.

At the ONU, the pumps are directed with an interleaver to a SOA-based element, in which the FWM and also the upstream modulation takes place. The two satellite wavelengths (λ_3 , λ_4) that carry the upstream data pass the interleaver on the return to the

ONU output, while the remaining pump signals (λ_1, λ_2) are now rejected. In the same way the centered A/D filter that is used as interleaver at the RN not only directs the modulated satellites towards the upstream EDF amplifier, but suppresses the pump wavelengths further. In a real deployment a multiplexing element would be required at the tree interface of the RN to combine the two different upstream satellites (λ_3, λ_4) from both trees. For simplicity, the 50/50 coupler was kept in lieu of this multiplexer and accounts for a similar insertion loss. After being inserted to the ring and arriving at the OLT, the upstream signal (e.g. λ_4) of the targeted tree is filtered, while other side channels are suppressed.

In front of the downstream receiver at the ONU, another interleaver would have to be inserted to split the two downstream signals from both trees. Besides, this interleaver beneficially rejects Rayleigh backscattering from the upstream signals into the downstream detector. It has to be noted that interleavers apparently maintain a colorless solution for the ONU, which is also suitable for photonic integration, e.g. by utilizing Mach-Zehnder structures or ring resonators, which can be designed as tunable filter element [180].

The efficiency of the FWM process was experimentally assessed for different pump wavelength spacing and its sensitivity to input power variations in a proof-of-concept setup that is shown in Fig. 4.74(a).

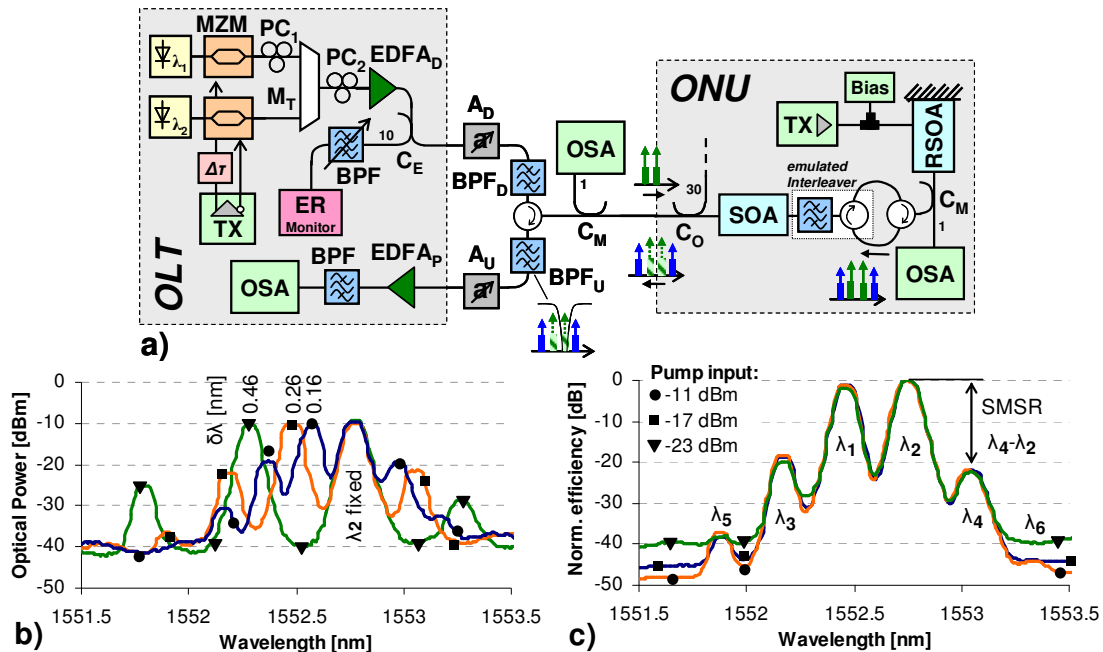


Fig. 4.74. (a) Experimental setup for evaluating the FWM efficiency of the proposed ONU. Spectra after the RSOA for (b) different pump spacing $\delta\lambda$ and (c) different pump power levels at the ONU input.

Two wavelengths at $\lambda_1 = 1552.46$ nm and $\lambda_2 = 1552.72$ nm were modulated independently by MZMs at a data rate of 10 Gb/s, using a PRBS with a length of $2^{31}-1$ to emulate a GPON payload. For simplicity, the same pattern generator was used for both signals, with a delay ($\Delta\tau$) applied in one electrical path to decorrelate the two driving signals. A booster amplifier (EDFA_D) was placed after the multiplexer (M_T) to

ensure a launch of 6 dBm per wavelength, as it will be later the case in the PON. A 10/90 coupler (C_E) and a tunable band-pass filter (BPF) were placed to monitor the ER of each downstream wavelength. The ER was set to 3 dB as good compromise for the utilization of a single wavelength for down- and upstream transmission.

Due to variation of the pump spacing $\delta\lambda = \lambda_2 - \lambda_1$ between the two downstream wavelengths, which is achieved by altering the first pump wavelength at λ_1 while keeping λ_2 constant, no fixed narrowband filter can be used to emulate the RN. Instead, a 8 nm broad band-pass filter (BPF_D) was placed to reject the ASE of the booster amplifier at the OLT. The input power of the ONU was set with a variable attenuator (A_D) to investigate the FWM efficiency also in terms of delivered pump power.

The ONU comprised of a 30/70 splitter (C_O) to split the incoming signal for downstream detection and upstream transmission, a SOA that is used as preamplifier and booster, an interleaver that was emulated by a similar broad ASE filter and a circulator, and a RSOA from chapter III.5 acts as upstream modulator and FWM element. With the SOA biased at 160 mA, a high small signal gain > 23 dB can be achieved without noticeable cross-patterning effects between the outgoing upstream signal and the incoming pumps. The noise figures of SOA and RSOA were 6.4 and 12.5 dB, whereby the latter is increased due to operation in the saturation regime of the RSOA. At this point of operation the optical 1-dB bandwidth of the RSOA gain spectrum is increased to 58 nm, having a center wavelength at 1565 nm. The RSOA was include in the ONU without electrical equalizer as its modulation bandwidth is sufficient large for upstream transmission at 2.5 Gb/s, for which a PRBS of length $2^{31}-1$ was used. The downstream remained with just an ER < 0.5 dB thanks to the gain saturation effect at the RSOA. Instead of the RSOA, an inline EAM could be used in principle, best in combination with a preceding SOA in form of an integrated SOA/REAM. This would avoid the circulator that is not suitable for photonic integration so far.

The upstream path at the RN consisted of a band-pass filter (BPF_U) that combines broad ASE filtering and rejection of the second pump wavelength λ_2 , as sketched in Fig. 4.74(a). This is required to emulate the realistic rejection of the two pump wavelengths in a realistic RN that is designed for a certain spacing $\delta\lambda$. The optical OLT receiver comprised an EDF-based preamplifier ($EDFA_p$) and a tunable ASE rejection filter with a 3-dB bandwidth of 50 GHz, adjusted to the upstream wavelength λ_4 . A variable attenuator (A_U) emulates the typical link losses of the PON in the range of 20 dB. The spectra at certain points in the setup were monitored with optical spectrum analyzers (OSA) by inserting 1/99 power splitters (C_M) for monitoring.

The polarization state of the first pump was aligned to the second pump after the corresponding MZM with a polarization controller (PC_1) to optimize the FWM efficiency. Note that for an integrated transmitter such as in [191] this polarization controller could be avoided. Since the fiber transform of the polarization state is the same for closely spaced wavelengths [192], there was no degradation visible even when

a long fiber span was placed between OLT transmitter and ONU as it was the case in the PON setup that is shown in the next section.

For the satellite that is created at λ_4 , the signal power at the RSOA output is shown in Fig. 4.75(a) for different values of the pump spacing $\delta\lambda$. The input power for each of the pumps was fixed to -17 dBm for these measurements. The FWM process becomes more efficient for narrower spacing $\delta\lambda$, where it benefits by ~ 9 dB when $\delta\lambda$ is reduced from 0.46 to 0.16 nm, as it is also visible in the spectra of Fig. 4.74(b). As $\delta\lambda$ reduces, the side mode suppression ratio (SMSR), defined between the upstream wavelength and the neighboring peaks as indicated in Fig. 4.74(c), improves thanks to the increased FWM efficiency. The SMSR of Fig. 4.75(a) which was measured at the RSOA output, where no interleaver is used so far to suppress the pumps, improves with additional filtering on the return to the OLT receiver. Note that a compromise is given by the availability of filter material that is supposed to have sharp filter edges, so that crosstalk from the close pumps remains in the upstream signals. As can be seen in Fig. 4.75(a), the SMSR at the OLT receiver improves due to this reason for large $\delta\lambda$. Besides, a narrower pump spacing requires also to reject further FWM products, which raise closely to the upstream signals as additional ghosts at λ_5 and λ_6 and cause additional crosstalk. The SMSR towards these ghost wavelengths has been found with 13.3 dB for $\delta\lambda = 0.16$ nm and indicates that the filtering scheme in a PON has to take these additional ghosts into account as well.

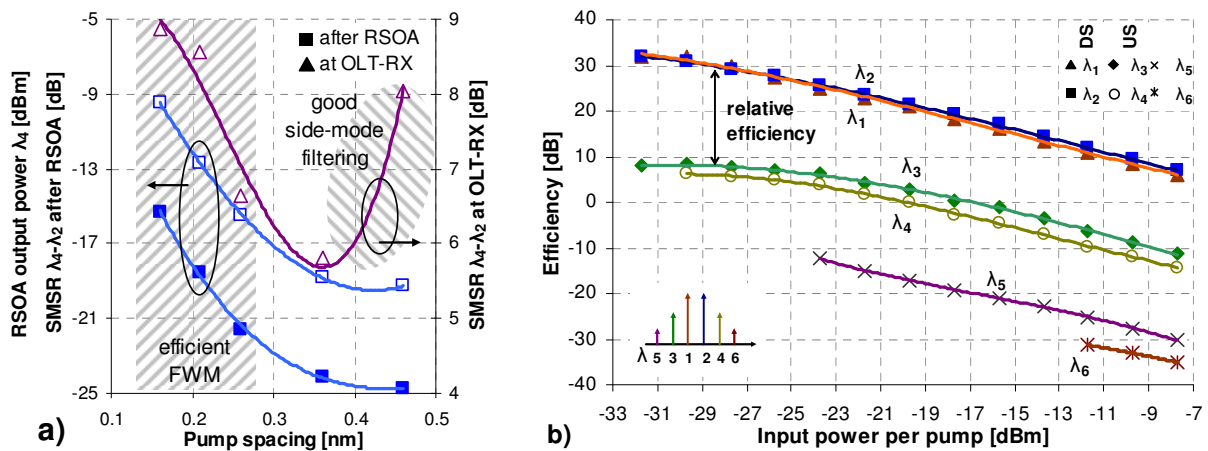


Fig. 4.75. (a) FWM output (filled marker) as function of the pump spacing $\delta\lambda$ for the satellite at λ_4 , including its SMSR (hollow markers) towards the pump at λ_2 . (b) FWM efficiency as function of the pump power at the ONU input. While λ_1 and λ_2 carry the downstream signals, λ_3 and λ_4 are dedicated to the upstream.

The pump spacing was chosen with 0.26 nm for all further measurements and is compatible with commercially available filter equipment with steep slopes. In addition, this spacing is a good compromise to avoid a significant penalty for the downstream reception deriving from cross-phase modulation of the two pump signals at the fiber spans [193,194]. The SMSR between λ_4 and λ_6 (λ_3 and λ_5) was then 15.2 (16.4) dB at the OLT receiver. Nevertheless, these values are expected to improve for a PON due to additional filtering at the ring interface of the RN.

The efficiency itself, defined as the ratio between a certain RSOA output signal at a pump, satellite or ghost wavelength and the ONU input power at a pump wavelength (λ_2), is shown in Fig. 4.75(b) for different ONU pump input power values. According to this definition the small signal net gain for the input (pump) signals can be found with their own efficiency and is mainly limited by the saturation output power of the RSOA. For an input signal of -17 dBm the net gain is as high as 18 dB and thus plays an important role for the suppression of the downstream signal that is present on the pumps.

For the FWM products at λ_3 and λ_4 , which constitute the upstream carriers, the efficiency for this pump input power is given with 0 and -3.3 dB, respectively. This proves that after the modulator a sufficient upstream signal is available, which is further boosted by the SOA at the output of the ONU. A difference of ~6 dB has been found for the additional ghosts at λ_5 and λ_6 , which raise above the ASE floor for higher pump input levels. For the desired pump input at the ONU around -17 dBm the relative efficiency, defined as the difference between the efficiency at λ_2 and the surrounding wavelengths, is quite constant, as it can be also deduced from Fig. 4.74(c).

When altering the polarization state of the multiplexed signals (PC_2), no decrease in the FWM efficiency was visible. This proves not only the polarization insensitive operation of the wavelength conversion when having co-polarized pumps, but also the low polarization dependent gain of the SOA-based elements at the ONU.

The architecture of the long-reach PON is shown in Fig. 4.76 and comprises of a long ring section with more than 50 km and a tree that holds a feeder fiber whose length was varied from 0 to 17 km. A 1:32 power splitter (SPL) was placed between feeder and ONU. DCFs were included in the OLT to account for pulse broadening along the SMF spans. The dispersion of the DCFs for down- and upstream were -1365 and -671 ps/nm, respectively.

Thin film A/D filters at the ring interface of the RN, centered at 1552.61 nm with a 3-dB bandwidth of 150 GHz, select two neighboring wavelengths (λ_1 , λ_2) as the downstream signals. Two 50/50 couplers (C_R) were incorporated to accommodate for resiliency in the dual fiber ring, whereas the full ring was not implemented for simplicity. The signals are then amplified by 15 m of HE980 EDF, locally pumped by a laser diode (LD) at 1480 nm with a power of 19 dBm for the sake of simplicity.

A 100 GHz A/D filter (F_R), centered at the same wavelength as the A/D filters at the ring, then feeds the signals into the tree. Several filters rejected the adjacent channels outside their pass-band with >25 dB. A 50/50 coupler (C_T) is placed at the output of the RN to feed both trees, as it was discussed earlier. A possible design for the tree interface of the RN that allows to combine upstream signals from both trees is shown in Fig. 4.76 (inset “dual tree upstream”). It doubles the A/D filter F_R and uses a Red/Blue waveband splitter (R/B) inside the spectral window of the ring A/D filters to combine the two different satellites (λ_3 , λ_4). Nevertheless, for a later comparison with a standard PON that does not utilize FWM in the ONU, the interleaver and 50/50 coupler were replaced

by a circulator and an ASE rejection filter, as it is indicated in Fig. 4.76 (inset “standard RN”).

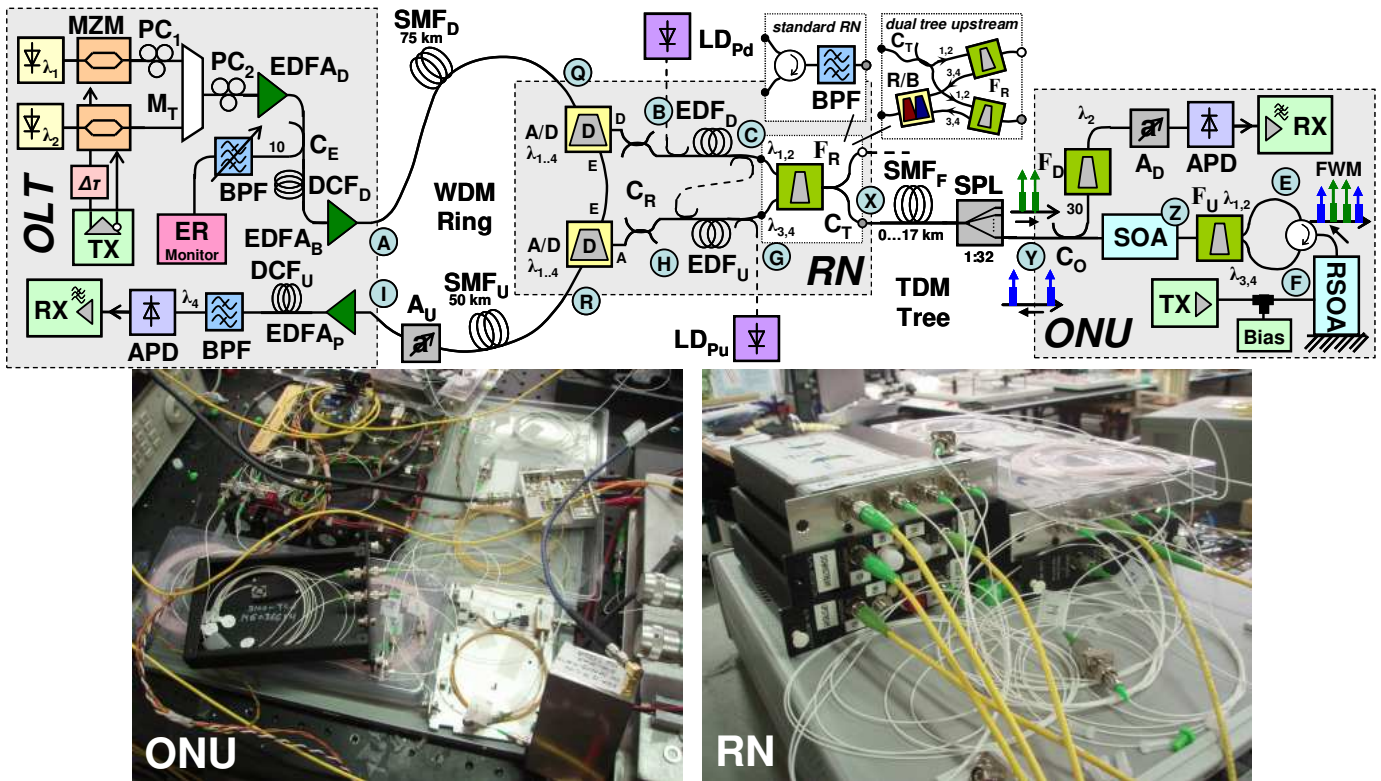


Fig. 4.76. Experimental setup for a hybrid PON whose ONUs include means of wavelength shifting, assisted by FWM in SOA elements.

The interleaver (F_U) at the ONU, which directs the incoming (pump) signals at λ_1 and λ_2 towards the RSOA and further selects the upstream (satellite) wavelengths at λ_3 and λ_4 for upstream transmission, was emulated with a similar A/D filter as it is used at the tree interface of the RN (F_R). The filter function plays an important role since the background noise at the upstream wavelengths (λ_3 , λ_4) is suppressed after pre-amplification with the SOA. This in turn ensures that the OSNR after the FWM process in the RSOA, typically being a limiting factor for wavelength conversion [195,196], does not suffer from an already present strong ASE background. The interleaver (F_D) that is used to filter the appropriate tree signal (λ_2) for the downstream detection was emulated by a fixed band-pass filter with a 3-dB bandwidth of 50 GHz.

With the chosen spacing $\delta\lambda = 0.26$ nm, the net ONU gain, defined between the incident pump at λ_2 and outgoing satellite signal at λ_4 , was 20.4 dB for this ONU configuration. A standard ONU, containing only the RSOA without preceding SOA, interleaver and circulator, was also implemented and experimentally evaluated for comparison.

The A/D filter F_R at the tree interface of the RN now routes the satellites (λ_3 , λ_4) to the upstream EDF amplifier, which had a slightly shorter length of 12 m thanks to the good sensitivity of the optical OLT receiver. It shall be noted that this A/D filter at the tree interface of the RN does not have to provide a spectral periodical transfer function like an interleaver has, since the RN does not have to be colorless. Although this RN

has an overall relative complex design, it is kept passive and does not cause operating expenditures.

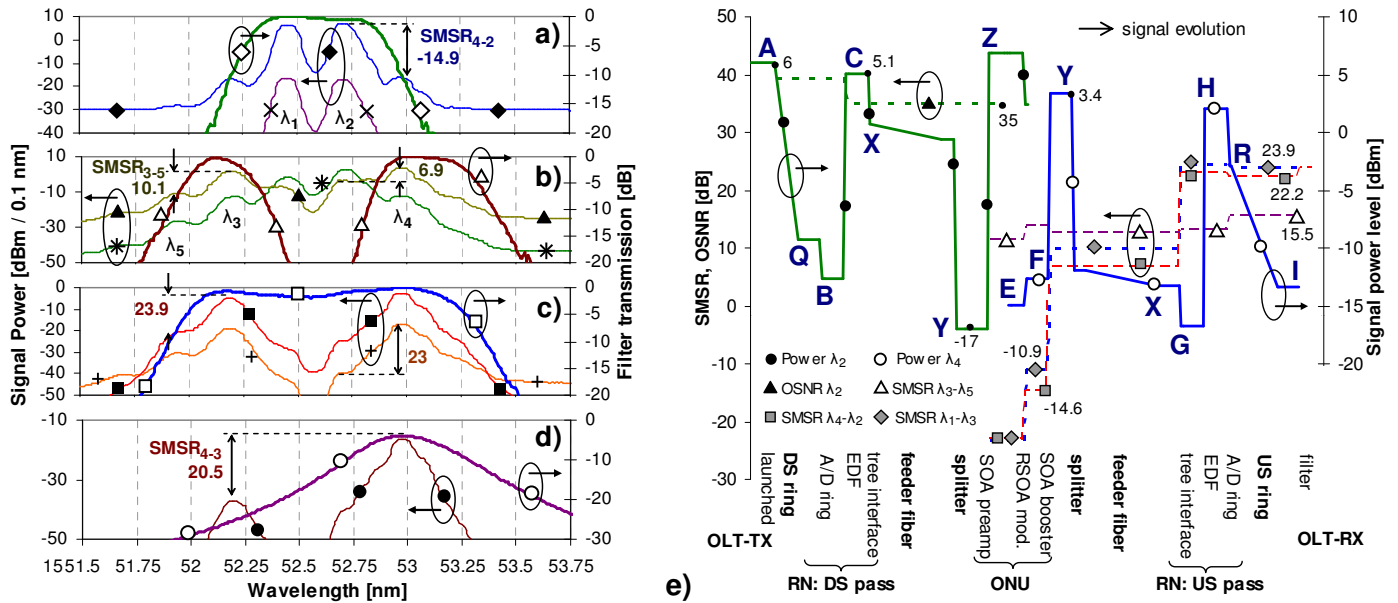


Fig. 4.77. Signal spectra and filter transmission functions: a) at the ONU input (\times), after SOA pre-amplification (filled \blacklozenge) and pump window of interleaver FU for λ_1 and λ_2 (hollow \diamond); (b) after RSOA modulation ($*$), upstream ghost window of the interleaver for λ_3 and λ_4 (hollow \triangle) and after SOA booster (filled \blacktriangle); (c) after RN tree interface FR ($+$), ring A/D filter transmission (hollow \square) and after injection into the ring (filled \blacksquare); (d) transmission of the reception filter (BPF) at the OLT (hollow \circ) and filtered upstream at λ_4 (filled \bullet). (e) Signal power levels, OSNR and SMSR along the PON.

The process of shifting can be seen in the optical spectra (Fig. 4.77(a-d)), where also the transmission windows of several filters are included. A quantitative representation for the evolution of these signals along the PON is shown in Fig. 4.77(e) for a feeder with 6 km, including the OSNR of the pump signal at λ_2 and the SMSR for the two upstream wavelengths at λ_3 and λ_4 in respect to their neighboring wavelengths at λ_1 , λ_5 and λ_2 .

After being transmitted across ring and tree, the pumps arrive with a power of -17 dBm and an OSNR of 30.5 dB at the input at the ONU. The upstream OSNR was 28.1 dB after modulation with the RSOA and 27.4 dB after the upstream amplification in the RN. Although for the satellites at λ_3 and λ_4 several SMSR towards the pumps are below -10 dB after upstream modulation with the RSOA (Fig. 4.77(b)), the rejection of the pump wavelengths on the return pass through the interleaver of the ONU and through the tree interface of the RN ensures a high SMSR of >23 dB (Fig. 4.77(c)). While there was no ghost established at λ_6 above the ASE floor for the given conditions, the spurious signal at λ_5 arrived at the OLT receiver with a SMSR of 15.5 dB towards the upstream at λ_3 and is therefore not negligible when compared with the remaining pumps. For the case of upstream transmission with the satellite at λ_4 , the rejection of the second upstream signal (λ_3) at the OLT receiver was > 20 dB (Fig. 4.77(d)).

No crosstalk arises for the upstream transmission due to undesired FWM along the single-mode fiber spans: while for the given downstream power levels after the OLT

transmitter and the RN no significant FWM products are generated at λ_3 and λ_4 but also rejected by the filters at the tree interface (F_R) and after the SOA (F_U), the backscattered light of these FWM components at the feeder fiber is too weak to cause distortions.

Regarding the transmission performance, the FWM-assisted ONU provides 2.5 Gb/s upstream transmission up to a feeder length of 17 km, by receiving a 10 Gb/s downstream signal for feeder spans up to 6 km at the same time when using FEC. For a compatible 6 km feeder length, the power margins are 11 and 27.5 dB for down- and upstream, respectively, for a splitting ratio of 30/70 at the ONU (C_O) and could be balanced by changing this ratio.

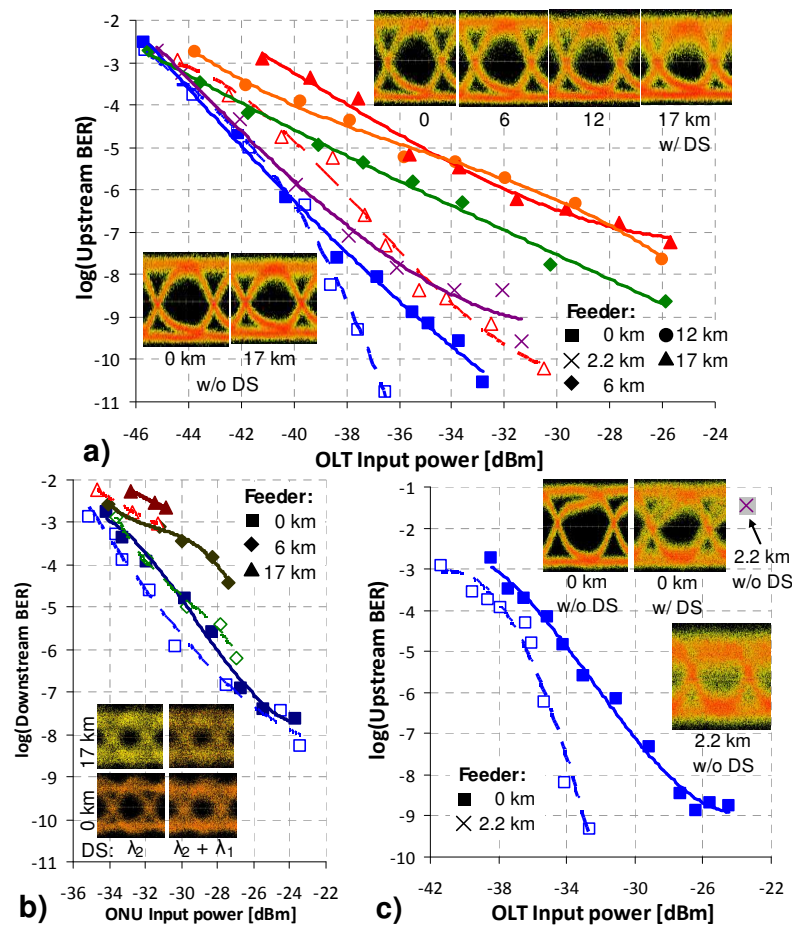


Fig. 4.78. BER measurements for the ONU assisted by FWM: (a) upstream for the case of present (solid lines, "w/") and absent (dashed lines, "w/o") downstream modulation, and (b) downstream for the case of transmitting two pumps at λ_1 and λ_2 (solid lines) and just one pump at λ_2 (dashed lines); (c) Upstream transmission with the standard ONU, comprising just a RSOA (dashed line and \times marker: no downstream, solid line: present downstream).

The upstream BER, shown in Fig. 4.78(a), was measured for the satellite at λ_4 . Transmission at λ_3 was obtained with a similar BER performance. The absence of downstream allows upstream reception at a BER level of 10^{-10} , regardless of the feeder length. However, the crosstalk that derives from unsuppressed downstream into the upstream signal leads already to a penalty of 3.7 dB for the back-to-back case without feeder fiber. Note that the downstream is solely suppressed by the optical gain

saturation of the SOA elements and could be further suppressed by additional means that were described earlier in chapter IV.

The reception penalties for having feeder lengths of 2.2, 6, 12 and 17 km (corresponding to an OSRR of 19.1, 16.7, 14 and 12.3 dB) are 0.2, 1.3, 3.2 and 5.6 dB at the FEC level. This proves that the PON is able to operate with low OSRR values thanks to the shifted upstream signal at λ_4 , which has become more insensitive to RB of the downstream at λ_2 , as it is also evident from the eye diagrams (Fig. 4.78(a)). It shall be recalled that the OSRR definition made here refers to the backscattered light of the optical seed that is found at another wavelength than the upstream signal. Although this backscattered light is consequently out-of-band at the upstream receiver, this definition is kept to ease the relation between the power levels for counter-propagating signals in the feeder when changing particular network parameters such as the feeder length.

The downstream reception, which is not in the main focus but nevertheless proven for the feasibility of the proposed scheme, was measured at λ_2 and is shown in Fig. 4.78(b). The reception suffers from a limited power budget for long tree fiber lengths and the crosstalk that derives from the finite suppression of the second downstream signal at λ_1 with the filter F_D . However, the FEC threshold can be reached for a feeder of up to 6 km length and longer tree spans are expected to be compatible either by changing the splitting ratio of the power splitter C_O or by replacing the band-pass filter that had an insertion loss of ~ 4 dB by a more appropriate filter with smaller losses and steeper filter edges. Note that RB of the remaining downstream pumps that are emitted in upstream direction towards the feeder fiber does not cause a degradation due to the high splitter loss that is located between the ONU and feeder. Consequently, the OSRR for the downstream is >40 dB for the given conditions, even for the longest feeder lengths considered in this work.

Upstream transmission with the standard ONU, comprising just a RSOA, is strongly penalized by RB. Despite no downstream is sent, a feeder of just 2.2 km makes any upstream transmission impossible (see eye diagram in Fig. 4.78(c)) since the minimum BER is $>10^{-2}$. In the back-to-back case without feeder fiber nor downstream, reception is possible at a BER of 10^{-10} , which proves that the loss budget is compatible with the chosen ONU design that contains just a single reflective SOA element. However, with a present downstream signal, the RSOA does not provide the same suppression of the downstream pattern as the combination of SOA and RSOA does. This difference is obvious when comparing the back-to-back upstream eye diagrams and leads already to an error floor above 10^{-10} for the standard ONU despite the absence of RB.

For a realistic deployment of this technique, the complexity would have to be significantly reduced by means of photonics integration.

Chapter V

Orthogonal and Advanced Modulation Formats for Access

The advantages of orthogonal modulation formats for full-duplex transmission on a single wavelength – as it was presented in chapter IV for the simpler ASK format – will be discussed. Commonly used semiconductor components such as integrated SOA/REAM devices are shown to be capable of being beneficially operated for colorless demodulation and detection of FSK signals, as well as for more advanced modulation formats such as quadrature amplitude modulation (QAM).

5.1 Introduction

Some of the problems that arise in optical telecommunications can be typically solved by modification of the applied modulation format. In the field of optical access, wavelength reuse can be simplified if an appropriate modulation strategy is found for the simultaneous transmission of down- and upstream. However, the complexity that is introduced by orthogonal modulation formats comes often at increased cost and compromises their successful integration. For this reason cheap and integrated solutions have to be provided to invade the access segment.

Moreover, the introduction of advanced modulation formats [197,198] can be beneficial in terms of enabling high data rates. Since orthogonality is also a hot topic in this case, similar cost-effective solutions have to be found, avoiding extra or bulky devices as they are common in the subsystems of transport networks.

5.2 Integrated FSK Demodulator and Detector for FSK/ASK

Demodulation of a FSK downstream would require an optical filter at the ONU [199], which is not in line with a wavelength-agnostic design. Colorless demodulation of FSK signals can be practically performed by a photo detector and a preceding optical filter with a comb-like transmission function and a controlled spectral periodicity. Such a comb filter can be obtained with a travelling-wave SOA that is left without anti-

reflection (AR) coating on its facets, which leads to a wavelength-specific gain ripple with interference fringes according to a Fabry-Pérot spectrum.

Besides, a highly negative biased EAM can offer its capability as detector with large electro-optical bandwidth. Both together, SOA and EAM, enables then a single SOA/REAM chip to work as an integrated colorless FSK demodulator and detector [200] once the incident signal is adjusted to the comb (or vice versa), as will be explained shortly.

5.2.1 Gain Ripple of a SOA

Considering a simple gain model as in equation 2.53, the spectral dependency of the parabolic gain curve can be included with

$$g_0(\lambda) = \Gamma \left[a(N_0 - N_T) - a_\lambda(\lambda - \lambda_c) \right] \quad (5.1)$$

where a_λ is a gain constant that describes the spectral roll-off of the gain and λ_c is the peak wavelength at the center of the gain curve. The gain is reduced to half its value for a deviation of half the 3-dB gain bandwidth $\delta\lambda$.

$$\lambda = \lambda_c - \frac{\delta\lambda}{2} : \quad g_0(\lambda) = \frac{1}{2} g_0(\lambda_c) \quad (5.2)$$

With this condition the 3-dB gain bandwidth can be obtained as

$$\delta\lambda = 2 \sqrt{\frac{a(N_0 - N_T)}{2a_\lambda}} \quad (5.3)$$

If the FSR of the gain ripple is much smaller than the 3-dB gain bandwidth, which is typically the case for the geometrical dimensions used in nowadays devices, the contrast Ψ in the gain ripple of a SOA can be found from equations 2.40 and 2.41, considering a flat gain between the resonant and anti-resonant frequency.

$$\Psi = \frac{G_{res}}{G_{ares}} = \left[\frac{1 + \sqrt{R_1 R_2 G_s}}{1 - \sqrt{R_1 R_2 G_s}} \right]^2 \quad (5.4)$$

For a single-pass gain of 20 dB and a gain ripple of not more than 1 dB, the reflections at the SOA facets have to be 10^{-3} or less. Since the reflectivity R_2 corresponds to a high reflective coating in case of the RSOA, the reflection caused at the input facet has to be 10^{-6} and therefore much lower compared to a SOA.

In a similar manner the ripple of a SOA/REAM with a single facet with reflectivity R can be found. The EAM section of a SOA/REAM chip will not alter only the geometrical length and thus the FSR but will also introduce losses L_{eam} to the cavity. These losses are compensated by the gain G_{soa} of the SOA. The transfer function of the SOA/REAM is defined as P_{det}/P_{in} due to its functionality as detector, where P_{det} is the

optical power that is detected by the EAM section inside the folded active Fabry-Pérot cavity and P_{in} is the input power of the SOA/REAM.

$$\frac{P_{det}}{P_{in}} = \frac{1}{1-R} \frac{(1-R)^2 G_{soa} L_{eam}}{(1+R G_{soa} L_{eam})^2 + 4R G_{soa} L_{eam} \sin^2\left(\frac{\omega}{FSR}\right)} \quad (5.5)$$

The free spectral range is given by the lengths and refractive indices of the SOA and EAM sections and the passive waveguide. The EAM has to be operated in drop-and-continue mode [201] to achieve operation as comb-generating element. This ensures that part of the signal is passed back as feedback signal to the SOA.

5.2.2 Demodulation of FSK Signals

The capability as FSK demodulator was assessed in a simulation, for which a FSR of 125 GHz and a refractive index of 3.17 were chosen for the SOA/REAM and a frequency deviation of 10 GHz for the FSK downstream signal. According to equations 4.72 and 4.73, these values lead to a cavity length of 0.38 mm and a facet reflectivity of 0.76. This proves not only the feasibility for the chip design, it shows also that for the desired data rate of 10 Gb/s there will be no patterning inside the cavity since the bit period is much larger than the round trip time.

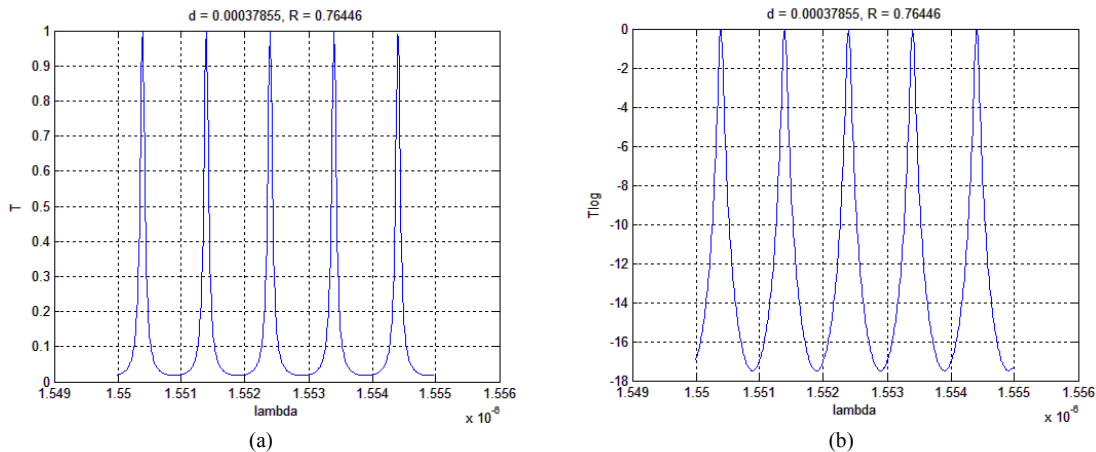


Fig. 5.1. Comb-like Fabry-Pérot spectrum of the SOA/REAM cavity in (a) linear and (b) logarithmic scale.

The design parameters can be optimized to minimize the influence of dispersive effects on the transmission performance of FSK signals with large frequency deviation. However, some parameters such as the FSR will be in general fixed by the physical design of the SOA/REAM chip. For the given chips the FSR was 0.6 nm, which is larger than required but still suitable for colorless operation within the ITU WDM grid specification. In addition, the gain of the SOA cannot be chosen with its largest value to avoid lasing of the SOA/REAM chip for high residual reflectivities and therefore the achieved sensitivity of the FSK demodulator will be limited.

The influence of the chosen frequency deviation F_{Δ} , the reflectivity R at the SOA/REAM facet and the splitting between TE- and TM-mode on the FSK demodulation will be analyzed in the following sections in terms of obtained ER for the demodulated ASK signal after FSK-to-ASK conversion. The parameters for each of the investigated scenarios are thereby the shift of the comb from its center position, e.g. caused by temperature drifts or fluctuations of the incident optical power level, and the different response to the TE- and the TM-mode, which is covered by the power distribution α between these modes that is in turn defined by the angle θ .

$$\alpha = \sin^2(\theta) \qquad \theta = \angle(TE, TM) \qquad (5.6)$$

In addition to the obtained ER after FSK demodulation the normalized gain inside the cavity, which gives a figure of merit for the reception sensitivity of the integrated FSK demodulator and detector, is evaluated. Finally, the special case of having a semiconductor-to-air transition at the SOA/REAM facet is investigated.

The aim is to find a working point with a targeted ER of 5 dB and the possibility of achieving gain with the SOA. The latter is mainly limited by higher values of the facet reflectivity R . Furthermore it has to be stressed that there should be no signal emitted into upstream direction to avoid the use of an isolator, thus preferring lower values for the reflectivity.

Dependence on the Finesse

The dependence on the facet reflectivity, which translates to the finesse of the cavity, was assessed for a fixed frequency deviation of 10 GHz and a polarization dependent loss (PDL) of 1 dB between the TE and the TM mode.

Higher values for reflectivity show not only a deeper contrast in the filter function, they also suffer from less tolerance against shifts between the TE and TM filter slopes regarding the achievable gain. The tolerance in the ER is acceptable thanks to a high finesse, as long as the polarization state is not solely the worse. This can be explained as there is no crosstalk given anymore once the shift exceeds some initial value.

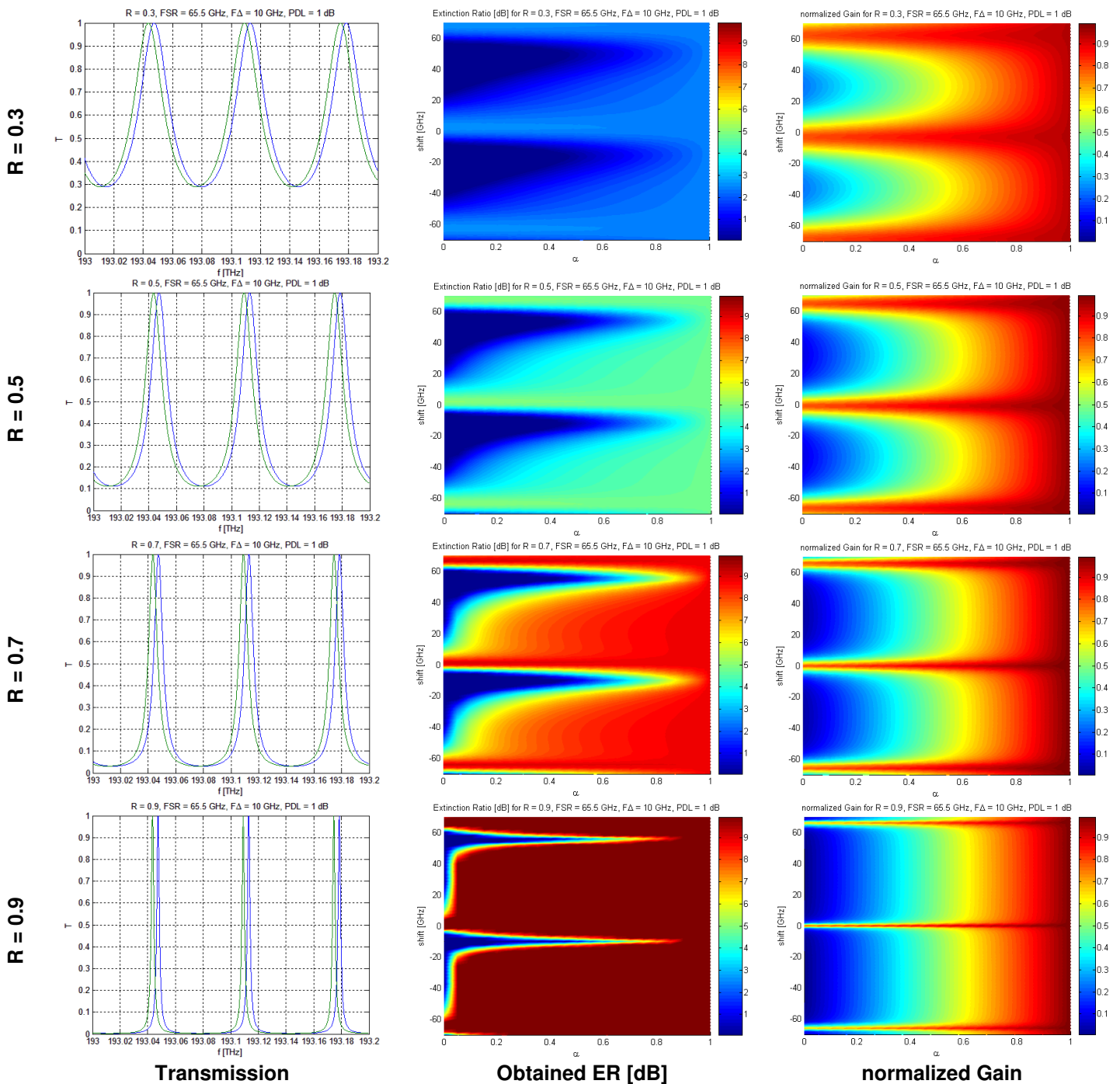


Fig. 5.2. FSK demodulation for different values of the facet reflectivity.

Dependence on the Polarization Dependent Loss

The reflectivity was fixed to 0.7 and the frequency deviation was 10 GHz for the following scenario.

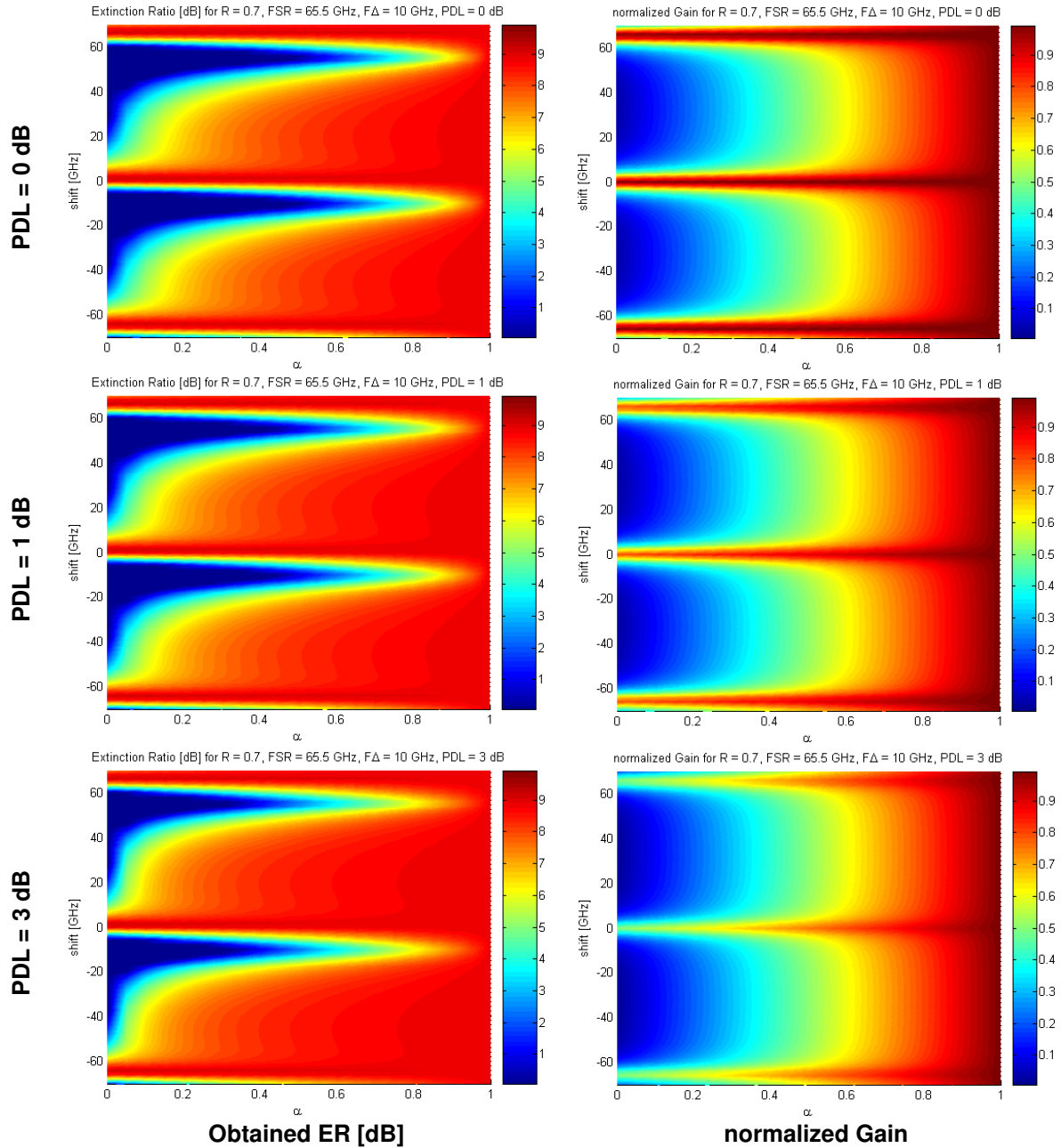


Fig. 5.4. FSK demodulation for different values of polarization dependent loss inside the SOA/REAM cavity.

An increased PDL shows that the crosstalk is a little bit reduced and the safe operating area is slightly extended for high PDL. On the other hand, the gain decreases drastically once a worse polarization state is experienced, according to the expected polarization dependent gain.

Semiconductor-to-Air Interface

The transition from semiconductor to air leads with the given refractive indices to a reflectivity parameter of 0.3 if no AR coating is applied to the SOA/REAM facet after being cleaved perpendicular to the propagation direction of the incident light. This case is further analyzed for a fixed PDL of 1 dB in its sensitivity to the frequency deviation of the incident FSK downstream signal.

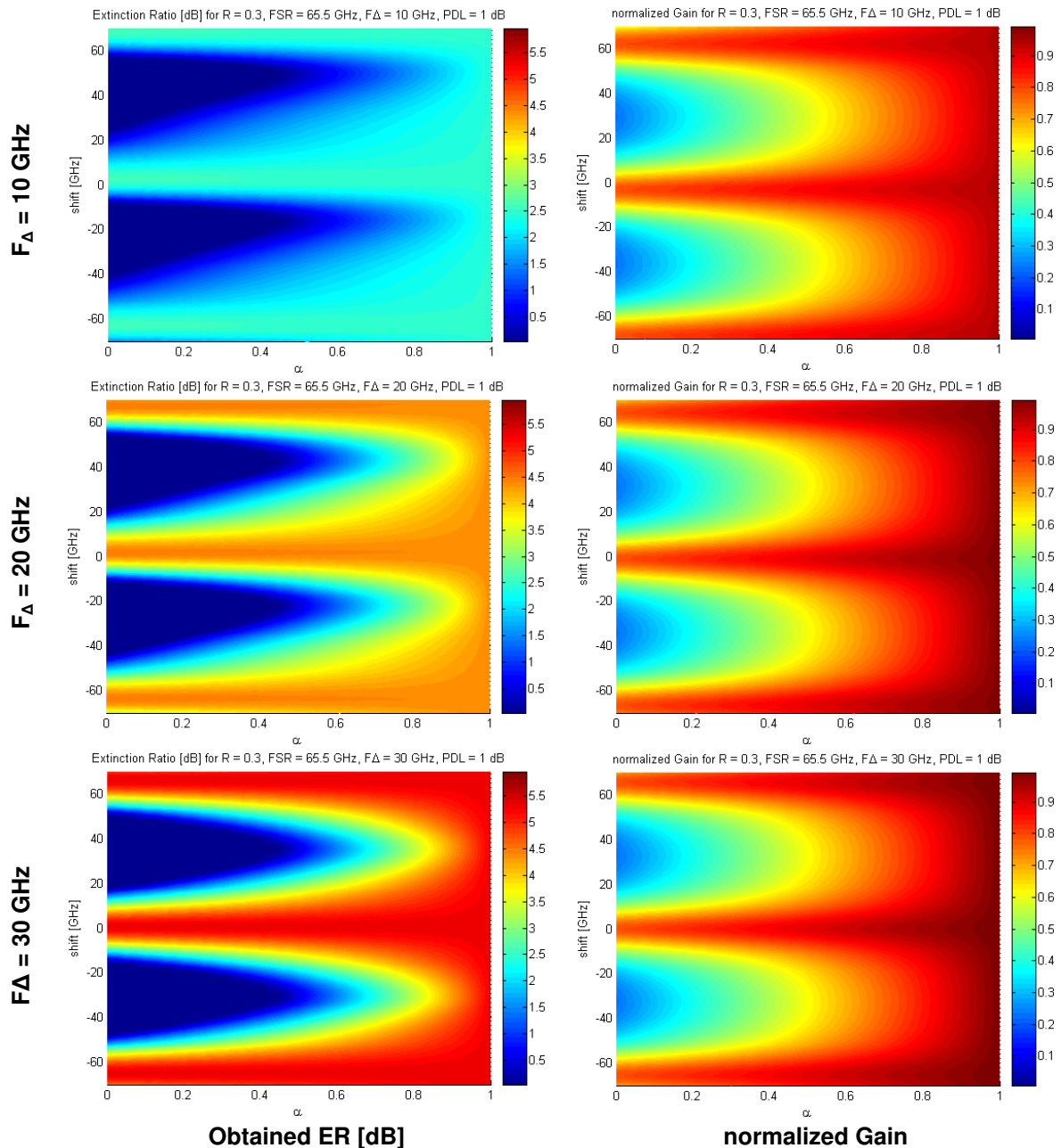


Fig. 5.5. FSK demodulation for a semiconductor-to-air transition at the SOA/REAM facet.

A good ER of the detected signal can be reached for a frequency deviation between 20 and 30 GHz, whereby still some gain can be achieved inside the cavity, leading to improved detection sensitivity.

Conclusion

Table 5.1 summarizes the influence of the design parameters on the FSK-to-ASK demodulation performance, which is characterized by the obtained ER of the detected downstream signal.

A desired ER of 5 dB for the demodulation can be reached just with cleaved chip samples that do not incorporate any specialized reflective coating. Although the frequency deviation has to be higher in a case with reduced reflectivity ($R = 0.3$) and penalties may derive from that fact, a low-cost solution could be provided.

Furthermore, for the case of higher reflectivities and steep edges in the transmission function of the comb filter, a possible shift can be steered back in a limited range by means of temperature tuning (to cover low frequency drifts) or bias current adjustment (to face drifts with faster behavior), as will be shown shortly.

It should also be noted that designs with higher reflectivity can limit the applicability due to crosstalk in the upstream, since parts of the incident downstream are reflected back into upstream direction when no isolator is used.

ER		Frequency Deviation F_{Δ}			
		low	medium	high	
Reflectivity R	low	ER is too low	3 to 5 dB, sensitive to TE/TM-splitting and input polarization state	slightly above 5 dB, insensitive to splitting for small drift between TE and TM	low upstream penetration
	medium	ER is about 5 dB and sensitive to splitting	around 6 to 7 dB	8 dB, becomes sensitive to splitting	
	high	ER > 5 dB can be achieved	10 dB can be maintained also in case of splitting, problems only in the worst case	>> 10 dB, sensitive to splitting at optimum but stays above 10 dB, also sensitive to polarization state	high upstream crosstalk

Table 5.1. Sensitivity of the FSK-to-ASK demodulation on different design parameters of the SOA/REAM cavity and the downstream signal.

The safe operating area for a SOA/REAM chip with a reflectivity of 0.5 and a FSK downstream signal with a frequency deviation of 30 GHz is shown in Fig. 5.6, where the influence of the polarization sensitivity and drifts of the comb function can be observed.

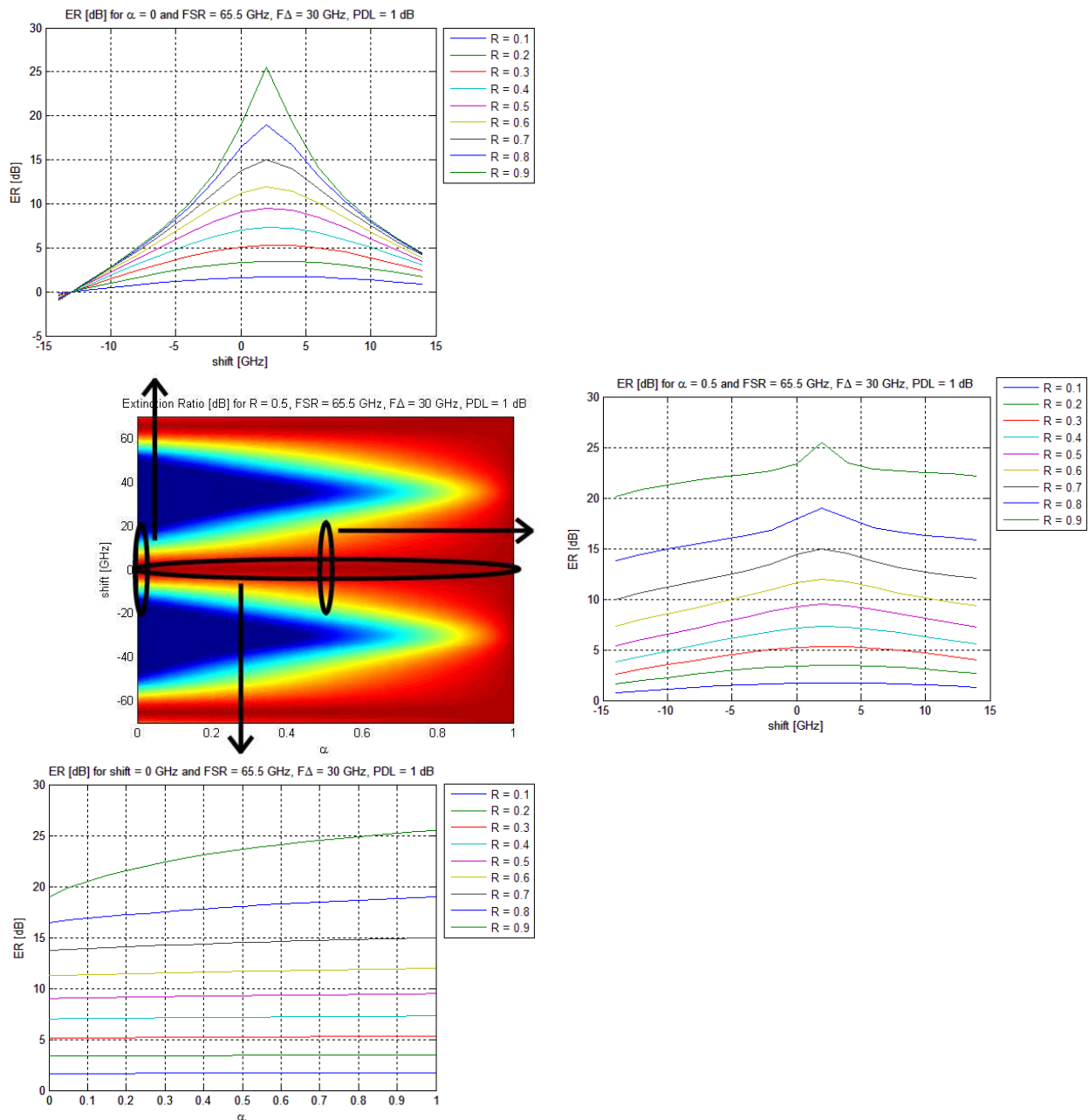


Fig. 5.6. Safe operating area for a SOA/REAM chip with a reflectivity of 0.5 and a FSK downstream with a frequency deviation of 30 GHz.

5.2.3 Experimental Validation

The functionality of the proposed optical FSK receiver, which is sketched in Fig. 5.7(a), was proven experimentally with an integrated SOA/REAM chip [200]. The input facet of the waveguide that leads to the SOA section of this chip was cleaved without angle and aligned to a tapered fiber that is used as fiber pigtail. A chip length of 610 μm and the difference in the refractive index between the semiconductor material and the air leads to a FSR of 0.6 nm and a finesse of 6.3 for typical operation points, as shown in Fig. 5.7(b).

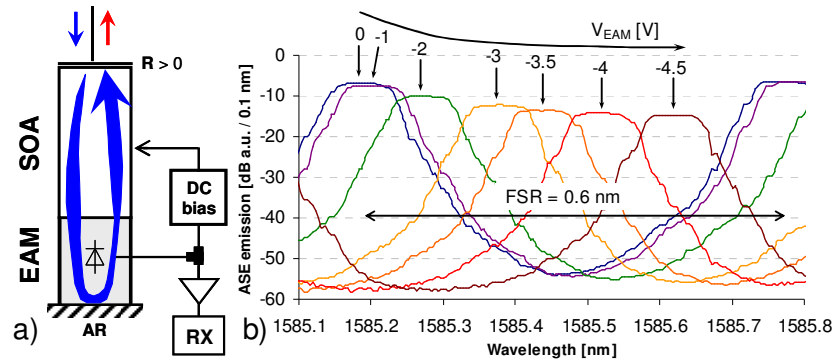


Fig. 5.7. (a) Scheme of the integrated colorless FSK demodulator and detector and (b) the obtained comb-like ASE spectrum for an EAM bias voltage from 0 to -4.5 V, a SOA bias current of 100 mA and a temperature of 22°C.

A spectral shift of the comb derives from variations in the carrier density, which are in turn caused by changes in the input signal power, the SOA and EAM bias and the temperature. This can be seen in the ASE spectrum in Fig. 5.7(b) for a variation of the EAM bias voltage. Fig. 5.8 shows the induced shifts around a certain operation point when different parameters are slightly changed. The relative shifts are thereby related to small perturbations in the altered parameter around the point of operation and the peak centers of the plots are defined for 24°C, 100 mA and -4 V, respectively. The operation point itself is given by the temperature and the SOA and EAM bias.

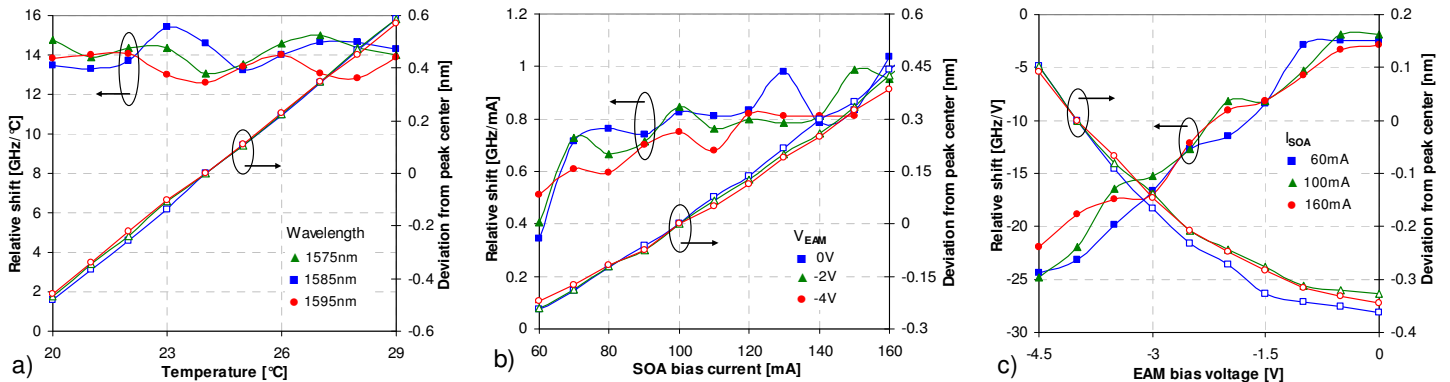


Fig. 5.8. Induced shifts for the comb measured at 1586 nm for (a) a variation of the temperature for a SOA bias of 100 mA and an EAM bias of -4 V, (b) a variation of the SOA bias at a temperature of 22°C and (c) a variation of the EAM bias at a temperature of 22°C.

The shifts can be advantageously used to align the comb to the incident data signal. As can be seen in Fig. 5.8(a), the shift with temperature is ~ 14 GHz/°C regardless of the operation point. Variations of the SOA bias, shown in Fig. 5.8(b), lead to a shift in the order of 0.8 GHz/mA at a bias current of 100 mA, which slightly depends on the operation point. The shift is not linear anymore for a change in the EAM bias due to the electro-refractive nature of its origin. It strongly depends on the bias point of the EAM as can be seen in Fig. 5.8(c) and varies from -2.5 to -25 GHz/V. The tunability of the comb that is achieved via small deviations in the SOA and EAM bias can also be used to compensate small temperature drifts.

Two complementary ASK modulated signals were used to evaluate the performance of the FSK downstream detection. The detected signal was thereby centered at one of the peaks of the comb while another, separated from the first by the spacing $\delta\lambda$ corresponding to the frequency deviation of continuous-phase FSK signals, is located between two peaks and determines the crosstalk distortion for the detection. The constant signal power of this FSK signal provides a possibility for ASK remodulation to embed upstream data onto the incident downstream.

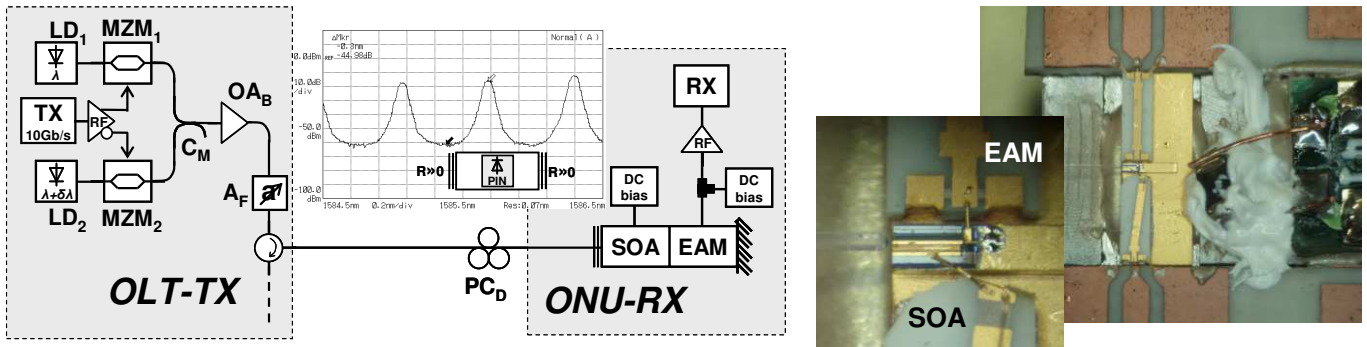


Fig. 5.9. Experimental setup for the proof of FSK downstream detection. The inset shows the equivalent functional scheme of the FSK detector and the measured ASE spectrum of the SOA/REAM with a scale of 10 dB/div and 0.2 nm/div.

The FSK modulator (Fig. 5.9) is based on two differentially driven MZMs and provides an ER of ~ 13 dB for each of the two ASK signals. No transients were observed at the bit edges after passing the 50/50 coupler (C_M) that combines the ASK signals. The remaining ER of the FSK signal was < 0.5 dB and indicates a good approximation for a constant power for the downstream. Although this OLT transmitter may not be a cost-effective solution and does not provide a continuous-phase FSK signal, it is suitable for the proof of concept of the proposed ONU.

The FSK detector was characterized in terms of FSK-to-ASK conversion penalty and colorless operation. The optimum bias point for REAM and SOA, operated at a temperature of 22°C , were found with -4.1V and 80 mA , respectively. The latter was kept low to avoid lasing effects that would appear due to the cleaved chip facet.

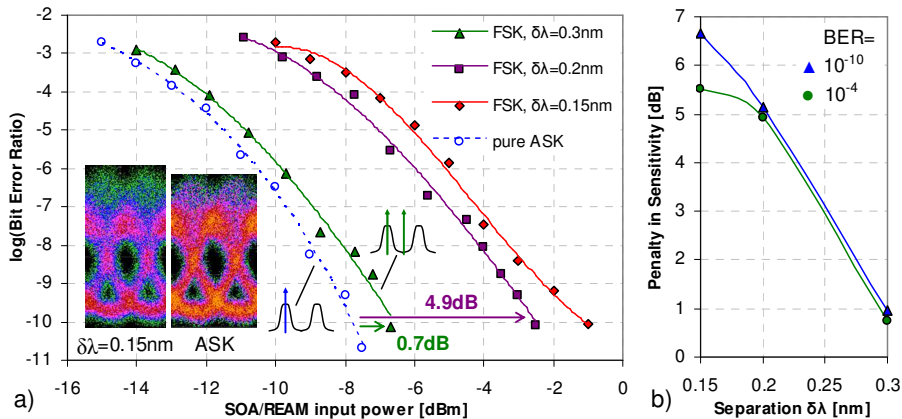


Fig. 5.10. BER curves and penalty for FSK demodulation when creating a constant signal power downstream signal.

The influence of the spacing $\delta\lambda$ on the FSK detection is shown in Fig. 5.10. For the pure ASK downstream, consisting of a single signal from laser diode LD₁ that is aligned to a peak of the comb as sketched in the inset in Fig. 5.10, a sensitivity of -7.7 dBm is obtained at a BER of 10^{-10} for a 10 Gb/s signal with a PRBS of length $2^{31}-1$. For a FSK signal and the optimum case with $\delta\lambda = \text{FSR}/2 = 0.3$ nm, meaning a placement of the second carrier between two peaks, the penalty that is suffered from applying a constant downstream signal power by adding the second ASK signal is ~ 1 dB. This low FSK-to-ASK demodulation penalty confirms a good contrast in the comb spectrum, which is sufficiently high to provide a FSK-to-ASK converted signal with a high enough ER. The penalty increases up to 6.7 dB for a smaller separation of $\delta\lambda = 0.15$ nm = FSR/4. This high penalty is attributed to the low finesse of the FSK detector. For the implementation in a PON with deployed fiber a trade-off would have to be made between the reception penalty that derives from a reduced contrast due to a closer spacing $\delta\lambda$ and the dispersion penalty that grows with larger spectral widths (i.e. wider spacings $\delta\lambda$) of the FSK downstream. Alternatively a redesign of the chip could lead to a reduced FSR and therefore to a smaller required spacing $\delta\lambda$.

Since an EAM is used as signal detector and the SOA section of the chip is used for establishing a cavity, an additional preamplifier would be required at the ONU to increase the sensitivity further. However, considering full-duplex upstream transmission this additional optical amplifier, which might be a SOA, can be reused for boosting the upstream signal as will be shown later.

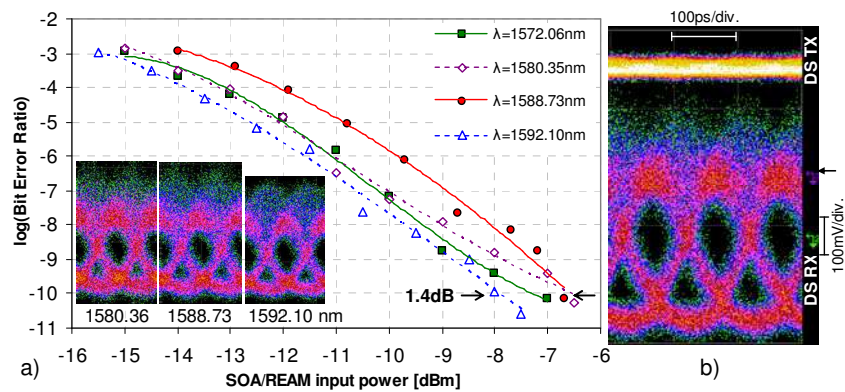


Fig. 5.11. (a) BER curves showing the colorless FSK demodulation. (b) Eye diagrams for the transmitted (DS TX) and detected (DS RX) downstream after the OLT transmitter and after demodulation, for a wavelength of 1572.06 nm, with an ER of the DS TX of 0.35 dB (the reference is indicated by the arrow).

Fig. 5.11 shows the proof for a colorless operation of $\delta\lambda = 0.3$ nm for different operating wavelengths in a range from 1572 to 1592 nm. The sensitivity at a low BER of 10^{-10} is quite independent of the operating wavelength and deviates by 1.4 dB. Since the gain spectrum of the SOA/REAM, which was designed for the L-band, had a roll-off in its gain around 1595nm, longer wavelengths were not evaluated.

The FSK detector was included into an ONU with a REAM and a SOA for the fundamental proof in a WDM-PON (Fig. 5.12) with a symmetrical data rate of 10 Gb/s [202]. This allows to remodulate the constant power signal with ASK upstream data and

to enhance the sensitivity. Reflections due to the cleaved facet of the chip were avoided by an isolator. The operating wavelength was 1585.36 nm and a deviation of $\delta\lambda = 0.3$ nm was set while focus was given on a back-to-back evaluation to avoid dispersive effects.

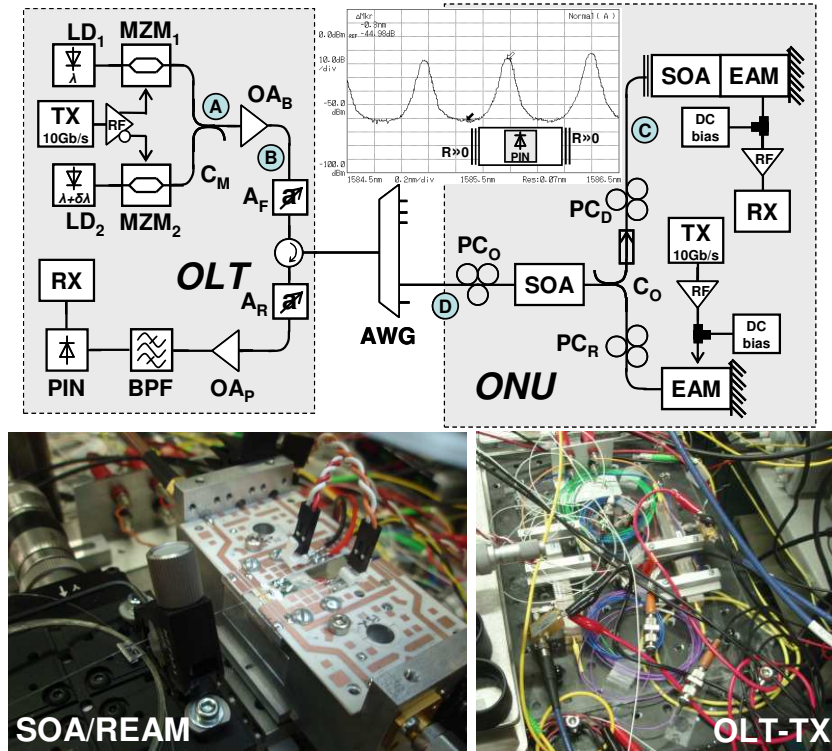


Fig. 5.12. WDM-PON with FSK downstream and ASK upstream.

The REAM at the ONU provided a high upstream ER of more than 13 dB. Its intrinsic loss of 11 dB assures that the down- and upstream do not pattern themselves due to cross gain modulation in the SOA: no patterning effect was observed for the downstream that will in turn not affect the upstream due to its constant envelope.

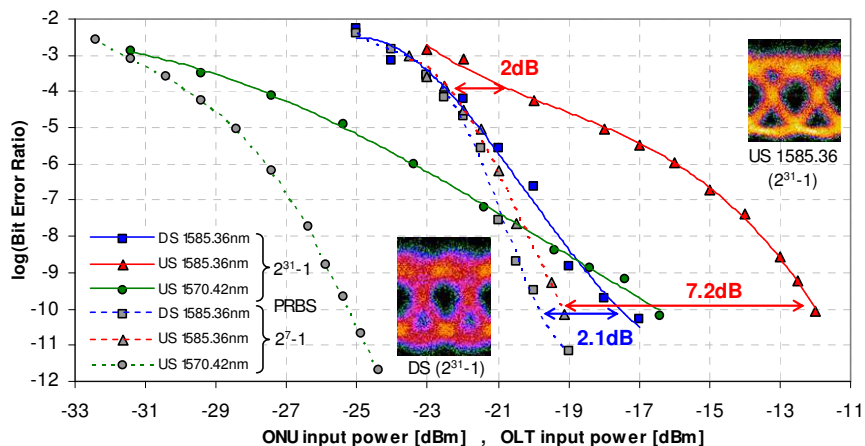


Fig. 5.13. Back-to-back BER measurements for an ONU in a WDM-PON with symmetrical FSK/ASK 10 Gb/s.

For the downstream reception a sensitivity of -17.5 dBm was reached for a BER of 10^{-10} and a PRBS of $2^{31}-1$ (Fig. 5.13). A PRBS of 2^7-1 has a 2.1 dB better sensitivity due to the reduced overshoot induced by the SOA. The ONU input power was fixed to -14.9

dBm for the upstream measurement so that an error-free downstream is guaranteed. The power levels and OSNRs are then -7.7 dBm and 53 dB after the FSK modulator (A), 4.4 dBm and 44 dB after the OLT booster (B), -5 dBm and 36 dB in the detection branch (C), -11 dBm and 25.5 dB after being boosted (D), resulting in a ONU net gain of 3.9 dB. Since the L-band EDFAs and the common C-band SOA (which had still gain in the L-band) were more efficient for shorter wavelengths, results are also shown for 1570 nm (Fig. 5.13). A stronger dependence on the PRBS length was observed for the upstream due to the high ER of its bit pattern. The sensitivity for a BER of 10^{-10} (10^{-4}) was -12 (-20.4) dBm for 1585.36 nm and a PRBS of $2^{31}-1$, while for a PRBS of 2^7-1 it is -19.2 (-22.4) dBm, leading to a penalty of 7.2 (2) dB. For a wavelength of 1570.42 nm the sensitivity for a BER of 10^{-10} is increased by 4.6 dB in case of the long PRBS.

5.2.4 Possibilities for Photonic Integration

A suitable approach for photonic integration of the evaluated FSK receiver is shown in Fig. 5.14, where several required components such as the SOA, EAM and facets are located on a single waveguide. The alignment to the incident signal can be obtained by the SOA and EAM bias or – for the case of having larger drifts – by an additional phase shifter. An external but closely packaged electronic control circuit can simply take the detection efficiency as a figure of merit to steer the comb to its optimal position.

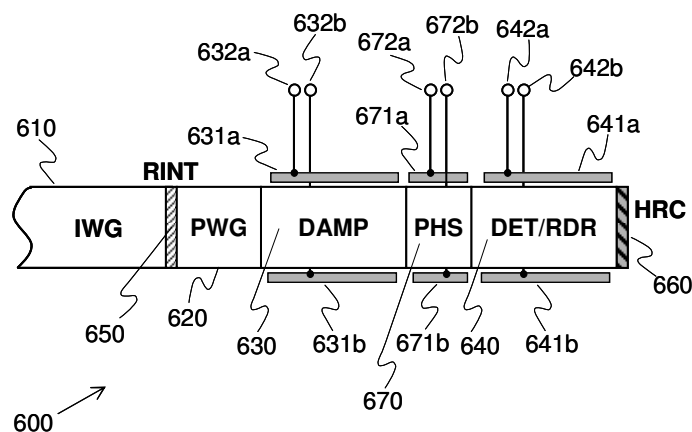


Fig. 5.14. Photonic integration of the colorless FSK demodulator and detector.

In contrary to the ONU shown in Fig. 5.12, the whole ONU could be integrated on a single photonic chip that includes also the remodulator for upstream transmission. The isolator can be avoided by minimizing the reflections from the comb-generating facet (RINT in Fig. 5.14) and by choosing the splitting ratio of the power splitter inside the ONU (C_O in Fig. 5.12) in a way so that the remodulation branch is favored. The reflections from the downstream signal at the FSK detector that interfere with the upstream signal are then weakened since the incident light that is reflected back in upstream direction has to pass the splitter twice while the upstream faces just a small loss when it passes this coupler.

Orthogonal modulation formats cannot only avoid crosstalk in bidirectional transmission, they can also be advantageously used to increase the transmission capacity.

5.3 Advanced Downstream Data Rates with FSK+ASK/ASK

The continuous and rapid evolution of multi-media services will soon demand higher data rates for access networks. Besides the use of traditional downstream detectors such as PIN or APDs for ASK downstream signals with a data rate of 10 Gb/s, upstream operation at 10 Gb/s can be provided with low-cost devices such as the RSOA or the SOA/REAM as it was demonstrated in earlier chapters. The cost limitations of the components that constitute the ONU are playing an important role for a further increase of the data rates since they prevent the use of advantageous, though more complex modulation formats that are based on phase shift keying [61] or OFDM [73]. While these formats are usually compromised by the required expensive delay interferometers or energy-hungry digital signal processing, FSK can be alternatively used as orthogonal modulation format with respect to ASK. In this way a single wavelength can carry twice the data without introducing elements at the receiver that have to be designed for a larger opto-electrical bandwidth.

However, the optical filter that acts as FSK-to-ASK demodulator introduces wavelength-specific elements in the ONU if the downstream carries FSK modulation. As it was demonstrated in the previous section, an artificial SOA gain ripple can be used as comb filter to face this design issue. Instead of a SOA/REAM also a RSOA is able to provide this spectrally periodic filter function for colorless demodulation of a FSK+ASK data signal [203]. In addition, the RSOA can then also be re-used for upstream modulation.

5.3.1 Colorless ASK+FSK Demodulation

The design of the proposed ONU is shown together with the experimental setup for a back-to-back proof in Fig. 5.14. While the ASK downstream is received with an APD, the demodulated FSK signal is detected with a PIN diode. The signal for the APD is split off with a 50/50 coupler (C_D) and an isolator was placed in front of the PIN diode to avoid lasing effects from the RSOA due to back-reflections from the photo detector. The RSOA, whose gain ripple is aligned in its spectral transmission function to the incident downstream signal as will be discussed later, performs the FSK-to-ASK conversion and is also used in half-duplex operation for upstream transmission. At the same time the natural gain saturation of the RSOA is used to suppress the ASK component of the FSK+ASK downstream signal, which causes severe crosstalk to the FSK detection.

With this ONU design the upstream transmitter is advantageously used as FSK demodulator and provides a solution to double the downstream data rate by simply adding a second photo detector at the ONU. Alternatively, a second RSOA could be placed at the ONU to separate the functionalities of FSK demodulation and upstream transmission, thus allowing full-duplex operation. However, half-duplex operation at twice the data rate makes sense considering the delivery of large data contents such as for video-on-demand, where mostly downstream transmission is preferred at a given time and bandwidth partitioning will be useful.

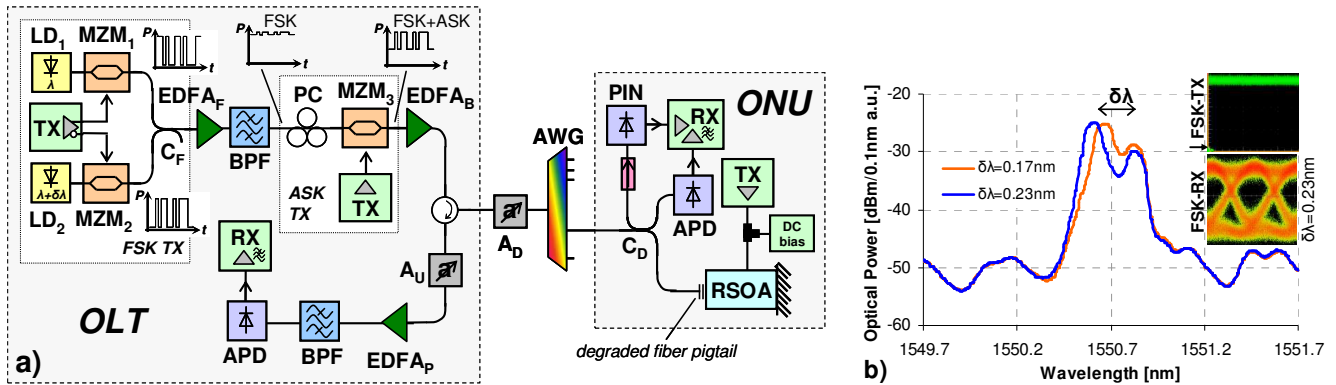


Fig. 5.14. (a) Experimental setup and (b) spectra at the input of the FSK PIN detector for different spacings $\delta\lambda$. The arrow in the inset of the pure FSK downstream (FSK-TX) indicates the reference level of the detector.

The same RSOA as in chapter III.5 was used at the ONU. Since an anti-reflection coating was applied to the input facet of the RSOA, the gain ripple was formed via the fiber-pigtail. In this way controlled reflections towards the active RSOA waveguide were caused. The gain ripple in the transmission function was 6.4 dB for a bias of 100 mA and a wavelength around 1550 nm. A free spectral range of 0.46 nm is given. This transmission function suits for a comb filter with sufficient contrast for a FSK-to-ASK conversion. The shift of the comb was measured with ~ 65 GHz/ $^{\circ}$ C and was proven to be independent of the RSOA operation point, as can be seen in Fig. 5.15.

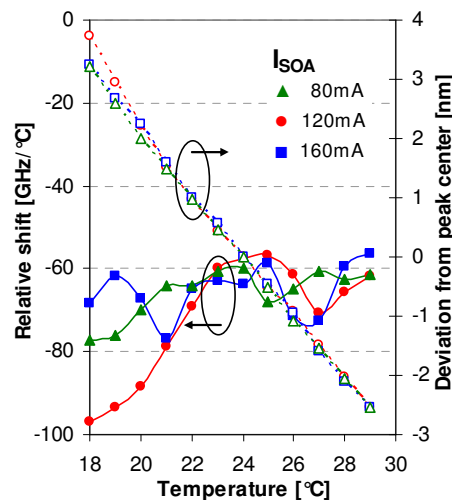


Fig. 5.15. Temperature-induced shift of the RSOA transmission comb. The peak center is defined for a temperature of 24°C.

Note that the ASE noise of the RSOA has impact on the FSK downstream detection since no optical rejection filter can be placed before the PIN diode when a colourless ONU design has to be retained. To assess this degradation, an optical carrier at 1550.63 nm is consecutively modulated with FSK and ASK data at the OLT, similar as in the previous section. While the two wavelengths (λ and $\lambda+\delta\lambda$) are differentially modulated and show a negligible ER of 0.26 dB for the FSK signal at the input of the ASK modulator (see inset in Fig. 5.14(b)), the latter imprints its data with a reduced ER in the range from 2 to 4 dB. The output power of the second booster amplifier was fixed to 3 dBm for the FSK+ASK downstream signal and the OSNR after the booster was 39.9 dB. An AWG was inserted between OLT and ONU to account for the multiplexing device that is typically used as signal distributing element in WDM access networks.

5.3.2 ASK+FSK / ASK Transmission Performance

Fig. 5.16 shows the BER measurements for the downstream for FSK and ASK detection at 10 Gb/s and a PRBS of length $2^{31}-1$. The FSK-to-ASK conversion penalty has been found with 2.4 dB at a BER of 10^{-10} for the case that the second ASK carrier is placed exactly between two peaks of the comb, meaning a frequency spacing $\delta\lambda = 0.23$ nm. For smaller spacings of 0.2 and 0.17 nm the reception penalty increases by 0.3 and 2.2 dB due to the reduced suppression of the second carrier, which can be also observed in Fig. 5.14(b). No strong dependence on the PRBS length has been experienced. The difference in the sensitivity for the detection of an ASK signal was improved by less than 0.2 dB at a BER of 10^{-10} for a PRBS of length 2^7-1 .

Pure FSK reception without ASK modulation in the downstream is possible with a sensitivity of -17 dBm at a BER of 10^{-10} and -22.4 dBm with FEC. The presence of ASK modulation at the downstream causes crosstalk for the FSK reception and introduces penalties of 2.1 and 5 dB at the FEC level for ASK-ERs of 2 and 3 dB, respectively. FSK reception can not be obtained anymore for an ER of 4 dB.

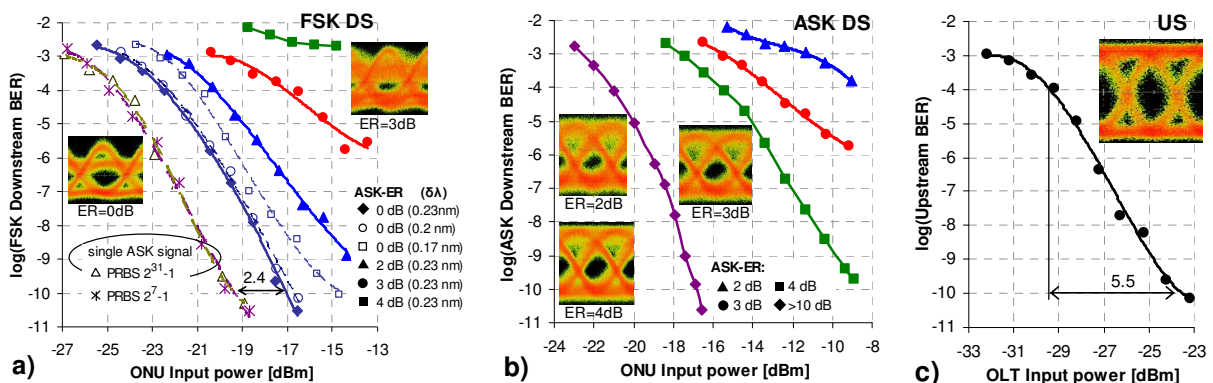


Fig. 5.16. BER measurements for (a) the FSK downstream tributary, (b) the ASK downstream tributary and (c) the ASK upstream.

The ASK reception is affected by the reduced ER and is compromised with the FSK reception performance. A sensitivity of -16.7 dBm is obtained at a BER of 10^{-10} for an

ASK-ER of >10 dB. The penalties due to a reduced ER are 4.5 and 7.5 dB at the FEC level for ASK-ERs of 4 and 3 dB, respectively. The FEC threshold cannot be reached anymore with an ER of 2 dB. A possible solution to increase the ER can be the use of ASK downstream cancellation techniques at the FSK-to-ASK conversion as they have been presented in chapter IV.

These would allow an additional full-duplex 10 Gb/s ASK/ASK operation mode with a single RSOA at the ONU. A flexible ONU configuration can then be obtained, allowing to switch between a full-duplex transmission with symmetrical data rate to an application-adapted high downstream data rate, without doubling the RSOA component as mentioned earlier. Another method for flexible bandwidth allocation will be presented in chapter VII.

The optimum ASK-ER is given by balanced BER performances for the FSK and the ASK reception and depends on the optical loss budget of the access network. Fig. 5.17(a) presents the minimum achievable BER for simultaneous detection of the FSK and ASK downstream tributary for different loss budgets. The optimum ASK-ER shifts to larger values with increasing budget to favor the more critical ASK reception. However, the introduced crosstalk into the FSK channel increases the BER to above the FEC threshold for large budgets such as 23 dB.

For the given downstream launch of 3 dBm at the OLT transmitter a budget of ~ 17.5 dB allows transmission at a BER level of 10^{-4} for an optimum ASK-ER of 3.5 dB, as can be seen in Fig. 5.17(b). The downstream BER limit is thereby defined as the worst BER of ASK and FSK detection. In case of a stronger FEC [204] that allows a BER of 10^{-3} at the cost of some more overhead, the budget can be increased to 20 dB for an ER of 3.7 dB. Since the upstream transmission does not limit the loss budget, as will be shown shortly, higher values for the loss budget can be obtained with a stronger downstream launch.

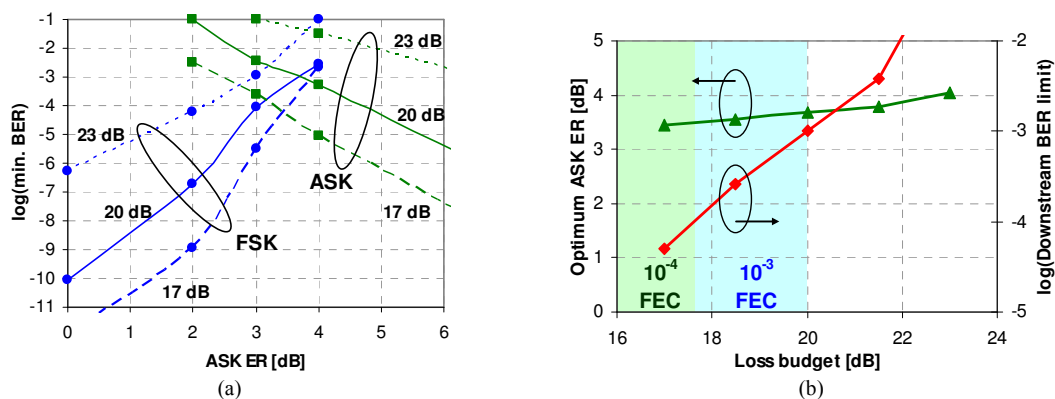


Fig. 5.17. (a) Minimum BER for simultaneous detection of the FSK and ASK downstream tributaries for different loss budgets and (b) optimum ASK-ER and the achieved downstream BER as function of the loss budget.

The input power into the ONU was fixed to -15 dBm for the upstream measurement. A BER of 10^{-3} , which is suitable for a strong FEC, can then be obtained for both, the ASK and the FSK downstream tributary. The OSNR after modulation was 31.4 dB.

A reception sensitivity of -23.7 dBm was obtained for the 10 Gb/s upstream at a BER of 10^{-10} , while another 5.5 dB of sensitivity can be gained with additional FEC (Fig. 5.16(c)). Together with the launch of -1.4 dBm from the ONU, a loss budget of 27.8 dB can be covered for the upstream, showing that the downstream reception is more critical in terms of link losses.

By reusing already existing components at the ONU for additional functionality such as demodulation, extra value can be provided to the customer premises equipment without introducing extra cost.

Besides the use of advanced modulation formats for the downstream, they can be also cost-effectively applied in upstream direction if the intrinsic properties of low-cost semiconductor-based modulators are fully exploited.

5.4 QAM with Integrated InP-based Modulators

The inherent phase modulation of SOAs can be alternatively used to construct advance modulation formats. Especially in its saturation regime the SOA provides mainly phase modulation without introducing significant patterning in the intensity of the amplified optical signal [205,206]. This is also related with the fact that a SOA can transfer intensity noise into phase noise in its deep saturation regime [207]. QAM can be then applied to the optical signal together with an EAM, so that information is simultaneously encoded in the amplitude and the optical phase [208]. Although such modulation formats are common for traditional but bulky modulators such as nested Mach-Zehnder structures, devices from small form factors that provide additional optical amplification are required for a successful infiltration of the access networks. Integrated SOA/REAM components provide that possibility, as will be demonstrated in this section.

5.4.1 SOA as Phase Modulator

Changes in the refractive index of the active region in a SOA, caused by modulation of the carrier density of the active waveguide, will affect the phase velocity of the optical wave and therefore the instantaneous optical frequency, as it was addressed in chapter II.5. The deviation from an equilibrium carrier density may stem from either a data pattern with sufficient high ER in the optical signal or from modulating the SOA bias current.

Originating from equations 2.52, 2.53 and 2.55, the rate equation for the carrier density N for having i input signals can be found with

$$\frac{\partial N}{\partial t} = -\frac{N - N_0}{\tau_e} - \sum_i \frac{(N - N_{0,i}) P_i}{\tau_e P_{sat,i}} \quad (5.7)$$

where N_0 is the carrier density in equilibrium.

Input signals which carry data will lead to a change in the refractive index of the SOA, depending if they experience loss or gain condition. For the case of loss the carrier concentration will increase, which leads to a decrease of the refractive index. Gain will decrease the carrier concentration and increase the refractive index. The point of operation for the data signal can be set by either the wavelength, the injected optical power of an eventually present holding beam or by the bias current. In case of a variation in the power of the optical input signal, the carrier density changes for the amount ΔN that is determined by the saturation power P_{sat} .

With an effective lifetime that has been shortened due to a holding beam on another wavelength or a sufficient strong noise background, the saturation energy for the optical input signal will be increased and therefore the effect on a carrier density change due to an optical input signal will vanish.

The optical phase φ inside the SOA with length L for its waveguide is given by the chirp parameter α (equation 2.77). There will be in general a dependence on the wavelength and the actual carrier density. For a change in the carriers from an initial density N_0 towards N , the change in the optical phase is

$$\varphi(N, \lambda) = \varphi(N_0, \lambda) - \frac{L}{2} \int_{N_0}^N \alpha(N, \lambda) \frac{\partial \Gamma g_m(N, \lambda)}{\partial N} dN \quad (5.8)$$

With the definition of the chirp parameter and consideration of small changes in the carrier density, this expression can be simplified and expressed by the refractive index n_0 of the waveguide, which varies according to this change in the carrier density.

$$\varphi = \left[n_0 + \Gamma(N - N_0) \frac{dn}{dN} \right] \frac{2\pi}{\lambda} L \quad (5.9)$$

The resulting phase change $\Delta\varphi$ can be then simply obtained by knowledge of the change of refractive index n_{eh} per carrier pair via

$$\Delta\varphi = \Gamma \Delta N n_{eh} \frac{2\pi}{\lambda} L \quad (5.10)$$

e.g., for the GaInAsP semiconductor compound, $n_{eh} = 2 \cdot 10^{-20} \text{ cm}^3$ which causes a change in the carrier population in the order of $\Delta N = 10^{17} \text{ cm}^{-3}$. This in turn leads to a variation of the refractive index of $\sim 10^{-3}$ and thus to a phase shift of π for a 500 μm long SOA operated at a wavelength in the 1.5 μm region.

5.4.2 Experimental Validation

The chirp parameter $\alpha(N, \lambda)$ that is related with the capability of modulating the optical phase was measured for the SOA and the EAM of a L-band SOA/REAM according to the previously in chapter III.6 introduced method [151] and is shown in Fig. 5.18. The

optical input power and its optical frequency, and the SOA bias were varied to assess the dependence of the chirp on the wavelength and carrier density.

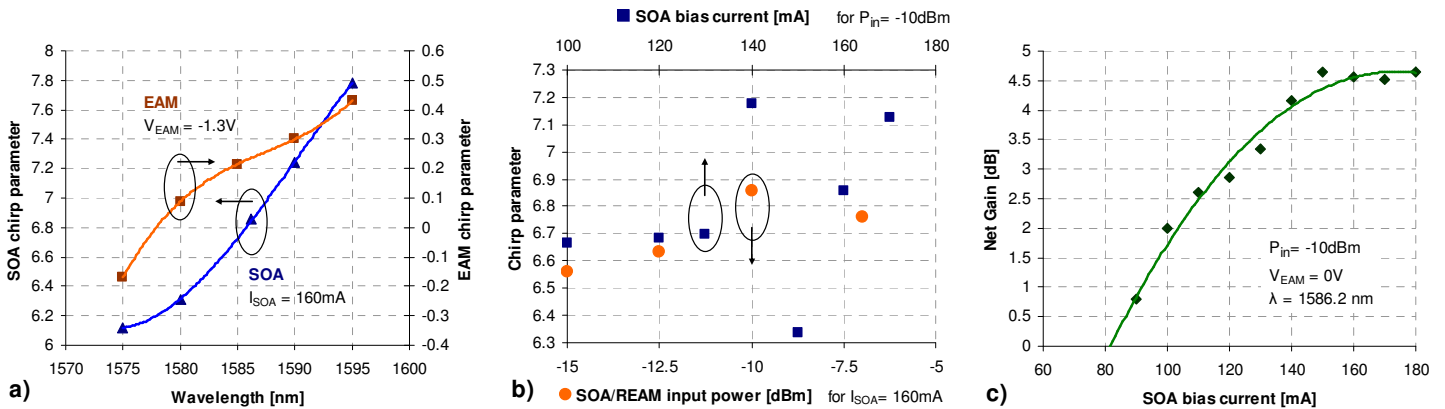


Fig. 5.18. Characterization of the SOA/REAM. (a) Spectral dependence of the chirp parameter for SOA and EAM, (b) sensitivity of the SOA chirp to input power variations and (c) gain saturation of the SOA.

The spectral dependence is given due to the differential gain coefficient, which leads an enhanced chirp for longer wavelengths. The chirp parameter of the SOA raises from 6.12 at 1575 nm up to 7.78 at 1595 nm while for the EAM values from -0.17 to 0.43 are obtained for this wavelength range. The chirp of the SOA, which is used as phase modulator, is quite independent of the optical input power of the SOA/REAM chip and the bias current of the SOA section, as can be seen in Fig. 5.18(b).

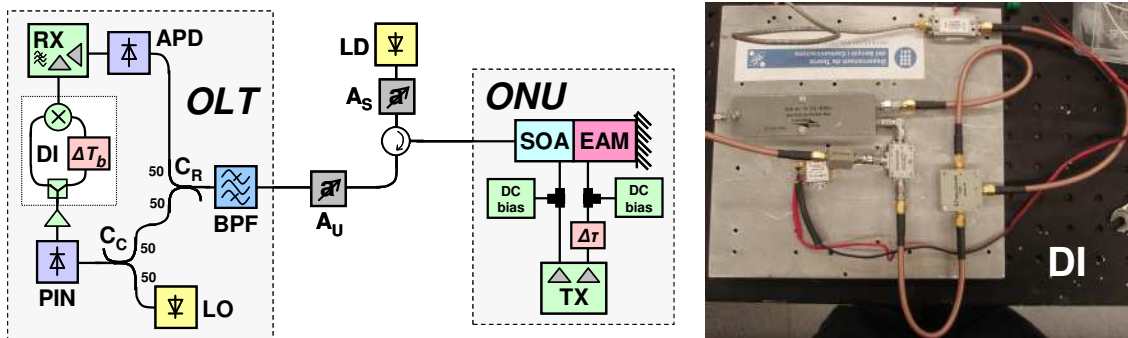


Fig. 5.19. Experimental setup for the proof of QAM modulation with a SOA/REAM.

The proof-of-concept for the QAM modulation is experimentally evaluated with the setup shown in Fig. 5.19. An optical carrier at 1586.2 nm is locally distributed by a laser diode and the input power into the SOA/REAM at the ONU is adjusted to -10 dBm.

While reception of the ASK signal at the OLT was carried out with an APD, coherent detection including an electrical delay interferometer (DI) was used for PSK-to-ASK conversion. Both receivers were fed by a 50/50 coupler (C_R) while a second 50/50 coupler (C_C) is included for the mixing with the local oscillator (LO). After heterodyne detection the modulation information is recovered in the DI and the RF data signal is down-converted to the baseband. Although this configuration of the OLT receiver is not cost-efficient, it is suitable for the proof of the concept.

Both, the SOA and EAM section were modulated at a data rate of 1 Gb/s with a PRBS of length 2^7-1 , without synchronizing the data streams of both modulated sections.

The low data rate and the short word length are chosen due to the low modulation bandwidth of the SOA and also to ensure that no additional patterning is introduced by its gain dynamics.

The SOA and EAM were biased at 160 mA and -1.3 V for QAM modulation, and modulated with 40 mA_{pp} and 2.4 V_{pp}, respectively. With the given gain-current relation of the SOA, this means operation in its saturation regime and introduces just a small intensity modulation with an ER of ~0.7 dB, as it is obvious from Fig. 5.18(c). On the contrary, the ER of the ASK signal generated by the EAM had an ER of 5 dB, which has been found as the best trade-off between ASK reception and crosstalk introduced into the PSK data channel.

The transmission at a single data channel, either ASK or PSK, was assessed additionally for comparison. Accordingly, the SOA or EAM, respectively, was then biased at a constant level without modulation: for the bias of the EAM this means a level of 0 V for pure PSK modulation and -2 V to achieve an ASK signal with an ER > 13 dB when applying a modulation of 4 V_{pp}.

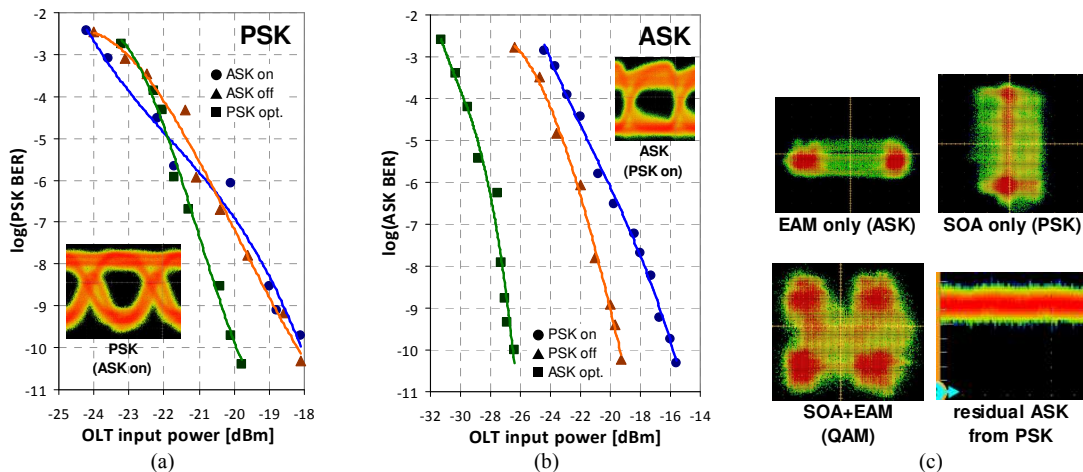


Fig. 5.20. Reception of (a) the PSK and (b) the ASK tributary of the QAM. (c) Constellation diagrams and residual ASK due to the PSK modulation.

The BER measurements for the PSK and the ASK tributary of the QAM signal are presented in Fig. 5.20. For the desired QAM operation, meaning the EAM biased at -1.3 V, the degradation in reception sensitivity for a present ASK modulation is <0.5 dB. The sensitivity at a BER of 10^{-10} improves by 1.8 dB for pure PSK modulation, which is attributed to the increased OSNR that benefits from the EAM bias of 0 V.

The ASK channel shows a stronger sensibility to crosstalk from the PSK channel. With bias conditions according to QAM transmission, the ASK reception suffers from a penalty of 3.3 dB at a BER of 10^{-10} once the PSK channel is used in addition, though the residual intensity modulation from the PSK channel had a relative low ER of just 0.8 dB. This penalty is attributed to the distortions that derive from the residual intensity modulation of the SOA section. With an optimum EAM bias of -2 V for pure ASK modulation with high ER, the reception sensitivity was improved by further 7.1 dB.

The constellations for pure ASK and PSK modulation as well as for the QAM are shown in Fig. 5.20(c).

Chapter VI

Seeding Techniques

This chapter discusses the beneficial recycling of ASE noise that is unavoidable when working with SOAs. By providing feedback to the amplifier, the noise emission can be shaped towards useful optical carriers. The seeding techniques behind such approaches are discussed and evaluated for applications in optical access networks.

6.1 Introduction

Active semiconductor devices such as SOAs are often not exploited in their full functionality. A more unconventional application – that is less chaotic as it sounds – is the use of a SOA element as self-oscillating laser. This allows to establish an optical carrier at an arbitrary wavelength inside the ASE spectrum of the SOA by providing a wavelength-selective feedback with a filtering element close or far from the amplifying medium. In this way a colorless ONU containing a RSOA as upstream modulator can be “tuned” to its desired upstream wavelength, which is intended to be established via controlled lasing. Though the quality of the obtained optical carrier will be degraded, it is not necessarily from bad quality as will be proven in chapter VI.2.

Simultaneous lasing and signal amplification at two remote wavelengths is another aspect that leads not only to advantageous spectral shaping of the ASE background but makes also sense for SOAs with wide gain spectra, since they are then also able to seed a pump that can be used for a remote EDF-based amplification stage. The feasibility of such an approach will be discussed in chapter VI.3, together with an evaluation of different scenarios for the deployment in PONs with high loss budget.

6.2 Self-Seeded Upstream Transmission

PONs become cost-effective when ONUs with colorless design are deployed. Mostly reflective modulators have attracted research and commercial products based on RSOAs or derivatives already exist [5]. In the simplest case or when crosstalk between down- and upstream has to be avoided, it is required to distribute a pair of wavelengths from the central office to each of the wavelength-agnostic customer premises equipment for the transmission of downstream data and modulation of the second wavelength with the

upstream [48]. Alternatively, an optical carrier can be generated via a seed loop between the colorless ONUs and the RN, the latter holding the multiplexing device of the WDM-PON or other wavelength-specific devices. Since the RN is typically placed much closer to the ONUs than to the OLT of the network operator, transmission losses are avoided at the trunk segment of the PON and arise only at the last link span in the drop segment. While the use of spectrally sliced ASE to seed the RSOA is well studied [209], the technique of reusing the RSOA of the ONU to obtain an optical carrier for upstream transmission has been shown to nearly cover the loss budgets of WDM-PONs without additional means of amplification [210]. The applicability of this self-seeding approach to a fully passive hybrid ring+tree PON as it is sketched in Fig. 6.1 will be proven in this section, showing that a seed loop can be established despite the high loss budget of the tree section with the help of the high gain of the RSOA at the ONU. The self-seeded upstream transmission at 2.5 Gb/s simplifies the PON architecture as it avoids the distribution of an optical carrier from the OLT which in turn simplifies the metro ring segment in addition.

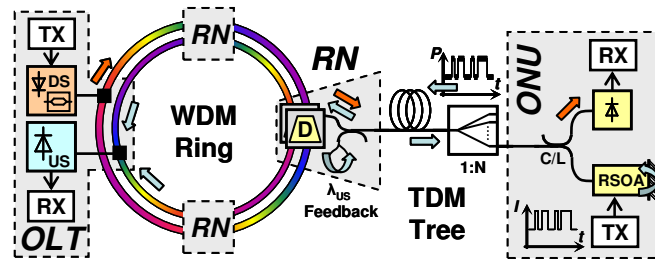


Fig. 6.1. Architecture for a self-seeded hybrid PON from ring+tree type. A seed loop exists between the RN and the ONU transmitter.

6.2.1 PON Architecture and Seed Loop Design

In case of a hybrid WDM/TDM-PON that has short reach trees connected to a long reach resilient single-fiber ring [211], the RNs that are located along the ring are responsible for dropping and adding wavelengths for down- and upstream transmission towards and from the tree, as sketched in Fig. 6.1. In the shown scenario, full-duplex transmission is established by using two wavelengths in the C- and L-band for up- and downstream, respectively.

The seed-loop that is spanned over the ONUs and the RN can also benefit from remote amplification which is typically used between the ring- and the tree-interface of the RNs. Fig. 6.2 shows the experimental setup, in which a fiber Bragg grating (FBG), centered at 1550.97 nm with a full-width half-maximum bandwidth of 0.41 nm, was placed after the tree-interface of the RN to reflect noise that derives from the RSOA back towards the tree. The choice of the bandwidth is a trade-off between the dispersion sensitivity of broad optical signals and the reduced feedback for narrowly sliced ASE, which prevents the seed of an optical carrier for the case of an additional high loss inside the seed loop. Since the signal that comes from the ONUs contains also the upstream data, a 90/10 power splitter (C_S) before the FBG feeds a small portion of the

signal towards an EDF-based amplification stage that leads to the ring section of the PON. In addition, another amplification stage is placed directly before the FBG to overcome a part of the splitting loss in the drop segment. Both amplifiers in the RN contained 15 m of HE980 and were remotely pumped from the OLT. No self-oscillations have been experienced in the bidirectionally operated low-doped EDF in front of the FBG.

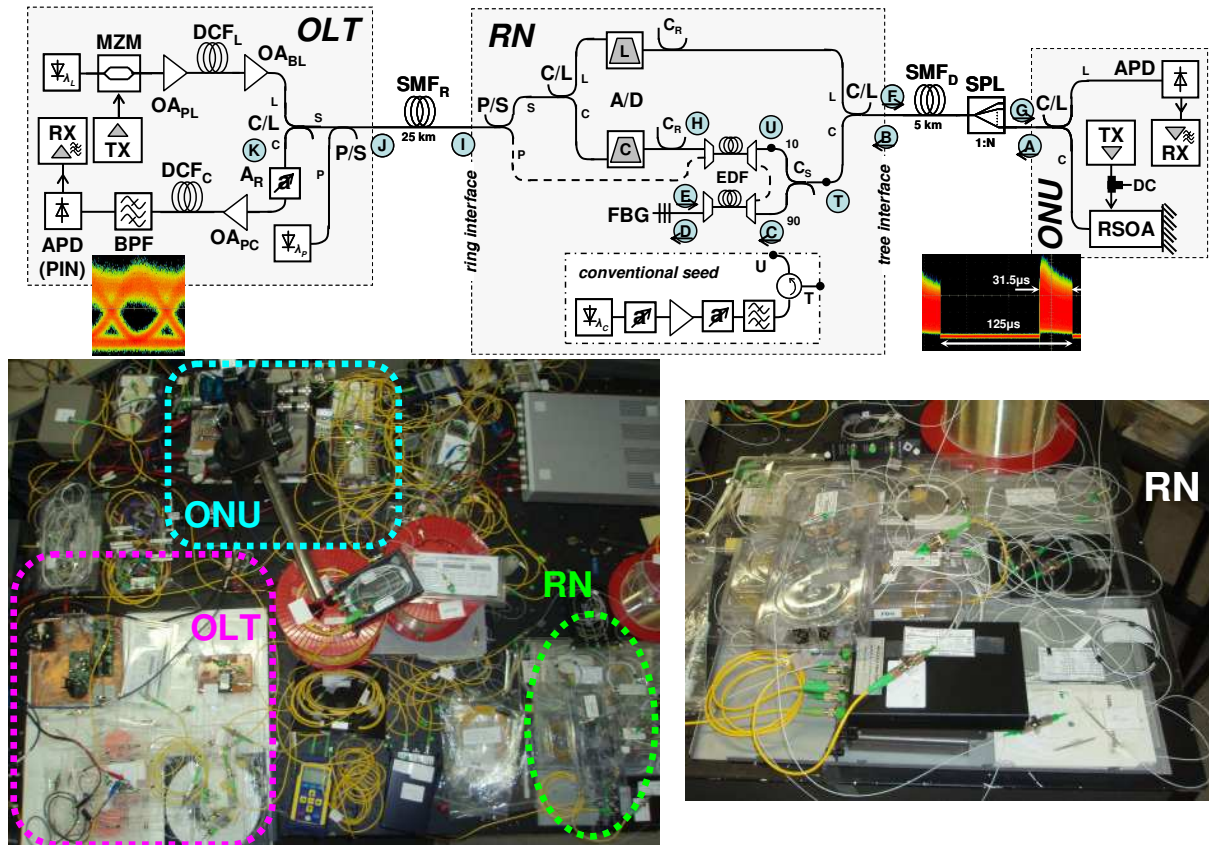


Fig. 6.2. Experimental setup for the PON. Besides the carrier that is obtained with the seed loop which is spanned via the RN, the ONU is for comparison seeded with the seed loop which is spanned via the RN, the ONU is for comparison seeded with an optical carrier, emitted by an optical source in the RN. The insets show a burst-mode upstream data packet and its eye.

The drop segment comprised of a SMF of 5 km length and a power splitter whose ratio was varied to investigate the impact of the splitting loss.

In the ONU, an APD detects the downstream while a RSOA is used for generating an optical carrier which is in addition modulated. The same RSOA as in chapter III.5 was used.

At the RN, the upstream is added via thin-film filters to the ring in the same manner as the downstream is dropped. 50/50 couplers (C_R) were added for resiliency purposes to feed and receive the signals from both ring directions [212]. Waveband splitters (C/L) for the C- and the L-band are added at the ring- and tree-interface of the RN, the OLT and the ONU.

The RN is connected to the OLT via a SMF span of 25 km, corresponding to the farthest RN in a 50 km ring in normal operation, or to the farthest RN in a 25 km ring in

resiliency. The pump for the remote amplification stages in the RN was transmitted at 1480 nm and multiplexed from the data signals by additional pump/signal splitters (P/S). Since the downstream, transmitted on an optical carrier at 1586.2 nm, will benefit from Raman amplification at the ring and an APD with a high sensitivity of -27 dBm is used at the ONU for reception, no extra amplification stage was placed at the RN for boosting the downstream towards the tree.

A MZM at the OLT imprints the downstream at 10 Gb/s with a PRBS of length $2^{31}-1$ with high ER. A DCF with a dispersion of -671 ps/nm was used in the OLT transmitter and receiver.

For comparison with the conventional approach, where an optical carrier is sent from the OLT to seed the RSOA, the FBG in the RN was replaced together with its amplification stage by a light source. This configuration with an electrically powered RN is necessary if a double-fiber ring has to be avoided since RB prevents any upstream transmission when having a single-fiber ring, as will be proven later. The competitive seed source, shown in the box inside the RN of Fig. 6.2, adapts itself to the splitting ratio in the tree and emits a signal that is strong enough so that the input power level of the ONU is fixed to -15 dBm while the OSNR for this signal is kept at 40 dB, which is a typical value for this location inside the PON.

6.2.2 Characterization of ONU and Upstream Carrier

A self-seeding technique with high optical loss between the RSOA and the reflective wavelength selector demands the RSOA to have not only a high saturation power level but also to erase the upstream pattern that was previously imprinted when the back-reflected signal from the RN arrives at the RSOA. This ensures that the actual upstream is free of any residual patterning, which would lead to a penalty in the reception of the actual transmitted data, herein referred to as cross-patterning. This crosstalk would have similar impact as the remaining downstream in chapter IV.

The same RSOA as in chapter III.5 was used. Its optical gain spectrum is shown in Fig. 6.3(a) for a bias current of 110 mA and different input power values. Stronger saturation occurs once the input power level is increased, leading not only to a reduced gain but also to a wider optical gain bandwidth. While for an input of -15 dBm the 3-dB bandwidth is 64 nm, it widens to more than 70 nm for higher input power values due to saturation in the spectral region around the peak gain wavelength. This dependence is shown in Fig. 6.3(b) for the 1-dB gain bandwidth, which is extended from 35 to above 50 nm once saturation is caused. Besides, the presence of saturation not only reduces the gain while flattening its spectrum, it also affects the noise figure of the RSOA. Although it is only 7.2 dB for an operating wavelength of 1550 nm and an input of -15 dBm at the border of the saturation regime, it increases to more than 12 dB for an input of 0 dBm.

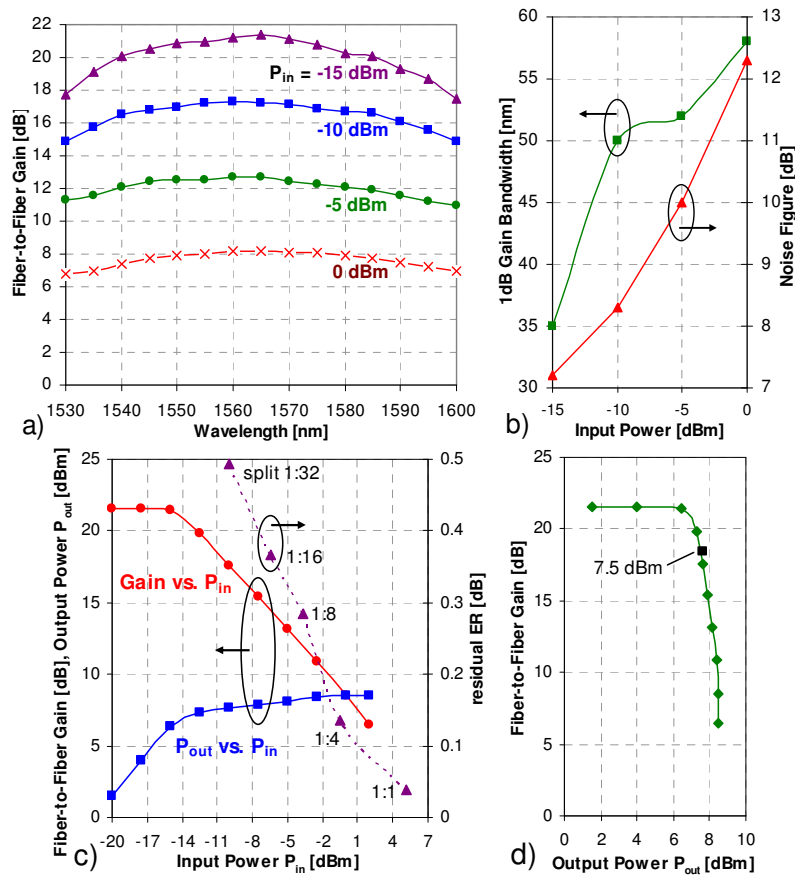


Fig. 6.3. Characterization of the RSOA gain: (a) spectra for a bias current of 110 mA, (b) 1-dB bandwidth of the gain spectrum and noise figure at 1550 nm, both for different input power values, and (c),(d) gain saturation and its relation with the residual cross-patterning for the seeding process of the upstream carrier for different splitting ratios in the tree.

No means of equalization have to be applied to guarantee 2.5 Gb/s operation thanks to the inherent large electro-optical bandwidth of the RSOA. Fig. 6.4 shows the dependence of the transmitter bandwidth of the ONU for different RSOA input power values and bias currents that were later used in the self-seeded and the conventional PON. The 3-dB bandwidth is found between 2.8 and 2.9 GHz for several operation points and does not strongly vary with the bias currents and the input power values of the RSOA that are considered for its application inside the PON.

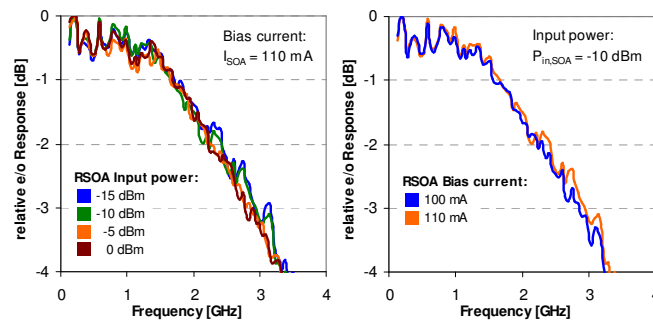


Fig. 6.4. Relative electro-optical bandwidth of the RSOA for different operation points that are given according to the application in the self-seeded and the conventional PON.

The RSOA was modulated with a current of 100 mA_{pp} at a data rate of 2.5 Gb/s and a PRBS of length $2^{31}-1$, leading to an ER of 5 dB. Although this ER is sub-optimal regarding the transmission performance, it is found to be the best operation point for the self-seeded PON due to the compromise of having either a wide eye opening or low residual cross-patterning. This ensures a higher optical power level during the space bits, which reduces in turn the patterning onto the mark bits when the seeded carrier is reflected back to the RSOA and modulated with the actual upstream data.

The capability of the ONU to suppress a data pattern on the incoming signal is presented in Fig. 6.3(c), which shows the relation between gain saturation and residual ER for an operating wavelength of 1550 nm and an input ER of 5 dB in the case of modulating the RSOA with upstream data when the self-seeding technique is used for generating an optical carrier to feed the RSOA. With the given saturation output power of 7.5 dBm the residual output ER can be kept below 0.5 dB for a splitting ratio of 1:32, meaning, together with the EDFA at the RN, a RSOA input power level of -6.5 dBm. The residual pattern decreases for lower splitting ratios since the mark level of the pattern experiences a stronger gain saturation than the space level. Note that due to the gain relaxation time of the EDFs, which is much larger than the inverse of the bit rate, no suppression of the pattern is supported. Without strong cross-patterning, upstream transmission is found to be possible with some penalty for higher splitting ratios.

In addition to the continuous-mode measurements the feasibility of burst-mode operation was assessed for a GPON-compatible 125 μ s frame with a duty cycle of 1:4. It is possible to establish a seed for data packets generated by the burst-mode upstream transmitter. However, the gain dynamics of the EDF introduce an overshoot, as can be seen in the insets of Fig. 6.2, which is also visible as broadened mark level in the eye diagram of Fig. 6.2. This gain transient could be further decreased by an appropriate all-optically gain-clamped design of the EDF stage [213]. The burst-mode reception at the OLT was carried out with a PIN diode instead of the APD since no DC-coupled APD receiver was available.

6.2.3 Signal Evolution

The signal evolution along the self-seeded and the conventional PON is shown for different splitting ratios in Fig. 6.5(a) and (b), respectively.

Due to the reflective nature of the RN towards the ONU, two light paths have to be distinguished for the self-seeded PON: the seed loop (A-G) and the upstream transmission path (U, H-K). Looking at the bidirectional seed loop, the splitting loss at the tree determines several power levels. Thanks to the EDF that is placed before the FBG, the strong launched signal (F) from the RN towards the ONU ensures high power values of 5.1, -0.6, -3.7, -6.5 and -10 dBm into the RSOA (G) for splitting ratios of 1:1, 1:4, 1:8, 1:16 and 1:32, respectively. Strong cross-patterning effects are thus avoided as it was shown in Fig. 6.3(c).

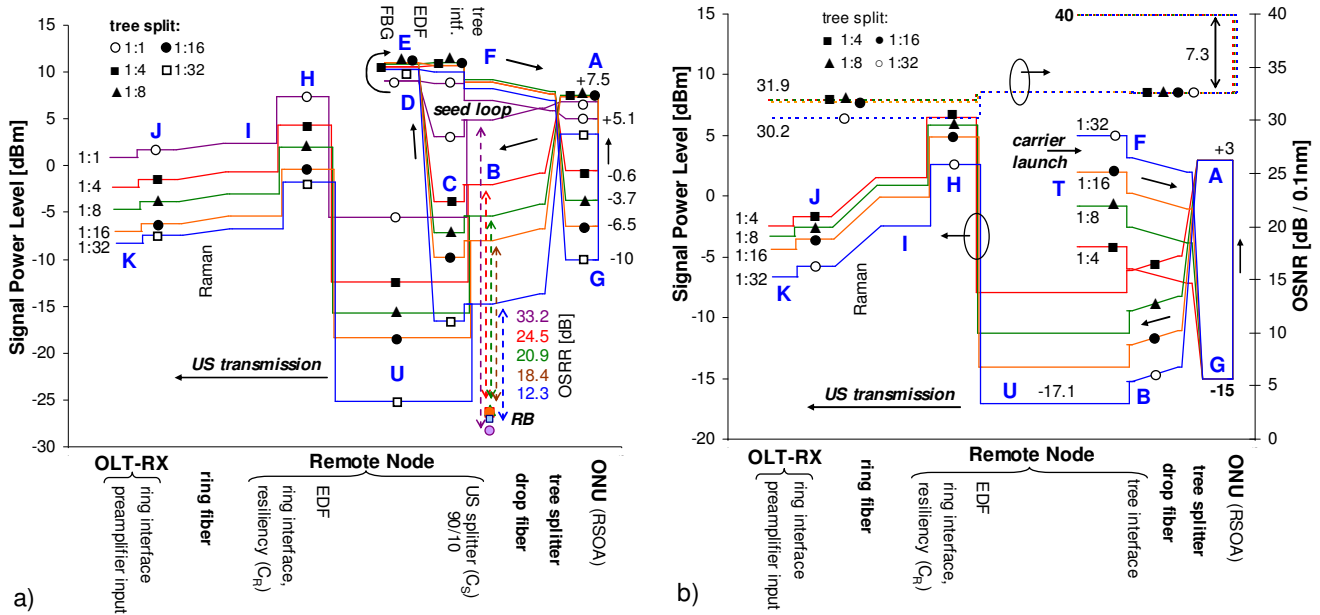


Fig. 6.5. Signal evolution for (a) the self-seeded PON and (b) the conventional PON with additional light source for the RSOA seed.

With the given launch from the RN and the ONU, determined by the saturation levels of the EDF and the RSOA, the RB that is caused by the drop fiber degrades the OSRR to <20 dB for a split of 1:16 and higher, as shown in Fig. 6.5(a). Although this would cause severe degradation in a conventional PON [182], the incoherent nature of the seeding signal leads to an upstream that is more tolerant to RB, similar as for a frequency dithering technique [186].

With the high RSOA saturation output power of 7.5 dBm (A), the signal arrives at the upstream amplifier of the RN (U) with a power level higher than -20 dBm after passing the 90/10 coupler (C_S), even for a split of 1:16. This ensures not only a low noise accumulation in the following EDF stage, but allows also to favor the seed loop in terms of a low insertion loss for the coupler C_S , which is passed bidirectionally.

After experiencing an EDF gain of 18 dB and suffering from 5 dB of losses in the ring-interface while being injected into the ring, the upstream signal reaches the OLT with just small losses of 0.8 dB along the ring fiber thanks to the Raman gain of 4.3 dB that is provided by the pump which was transmitted at 1480 nm with a power of 26 dBm.

While missed gain in the upstream amplification stage will cause a reduced power budget for the upstream signal, gain variations in the EDF of the seed loop can cause increased cross-patterning effects and are therefore more critical for the upstream transmission.

The spectra of the seeded upstream signals are shown in Fig. 6.6 for a tree splitting ratio of 1:8. The signals are defined in their center wavelength by the reflectivity of the FBG. The exact spectral shape of the upstream is determined by the gain peak of the RSOA and its gain ripple, which is caused by the pigtail of the fiber-end used for chip-to-fiber coupling and was measured to be <3 dB. Due to the chirp of the RSOA, which is

enhanced in the saturation regime, the upstream establishes towards the longer wavelengths inside the spectral window that is defined by the FBG [214]. The side-modes of the grating, which are more than 15 dB below the peak reflectivity, do not cause any additional seed wavelengths as they provide a too low feedback towards the RSOA.

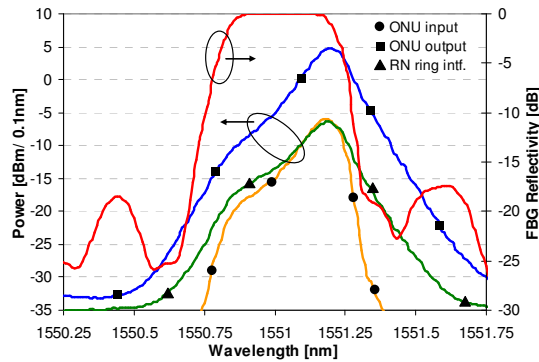


Fig. 6.6. Reflectivity of the FBG and spectra for the signals at the ONU port and the upstream after passing the EDF stage in the RN when being injected into the ring, shown for a split of 1:8 in the tree.

The downstream, not included in Fig. 6.5(a) for the ease of reading, was launched with 6 dBm and an OSNR of 42 dB from the OLT. The signal experiences Raman gain as the upstream does and is injected despite the passive nature of the signal light path in the RN with -0.4 dBm into the tree.

The given loss budget allows for a maximum ONU input power of -14.4 dBm for a splitting ratio of 1:16, which will determine the margin of the downstream. The remote amplification of the upstream in the RN guarantees for input power values of 0.9, -2.3, -4.7, -7 and -8.2 dBm at the optical OLT receiver in the case of splitting ratios of 1:1, 1:4, 1:8, 1:16 and 1:32, respectively.

Fig. 6.5(b) shows the signal power levels and the OSNR for the conventional PON, which provides an optical carrier by an additional light source for the upstream transmission, placed at the tree-interface (F) of the RN. Due to the unrealistic scenario of having an upstream EDFA in the RN and a pure WDM-PON with a tree split of 1:1 at the same time, this case was not considered for the conventional PON.

With the input power of -15 dBm into the ONU (G), an output power of 3 dBm (A) is obtained with the slightly lower RSOA bias and the OSNR is maintained at 32.7 dB. Thanks to the RSOA, which can operate at such low input power values, the influence of the RB is acceptable even for high splitting ratios. However, since the input power of the upstream amplification stage depends on the splitting ratio, a further OSNR degradation is caused. Especially for the high split of 1:32, the input level of -17.1 dBm causes an additional degradation of 1.4 dB compared to a lower splitting ratio.

With the reduced pump of 23 dBm, which is strong enough to pump just the upstream EDF stage, and a present downstream signal as in the case of the self-seeded PON, the Raman gain at the ring fiber is lower with 1.7 dB, leading to a net loss of 3.4

dB at the fiber segment. The upstream arrives therefore with levels of -2.5, -3.3, -4.4 and -6.5 dBm at the OLT receiver for a tree split of 1:4, 1:8, 1:16 and 1:32, respectively.

6.2.4 Relative Intensity Noise

The relative intensity noise (RIN) is the spectrum of the intensity fluctuations relative to the mean steady-state intensity and provides information on the frequency content of the fluctuations. It is an important measure for the noise emission of light sources, giving also information about limitations in the transmission performance, e.g. in terms of BER floors.

For an evaluation of the introduced error floors, the RIN is attributed to the mark level in the received bit stream, which was transmitted from an imperfect ASK transmitter that emits a bit stream with an average power level and a finite ER (equation 4.20). The Q factor for an ideal noise-less receiver with an electrical bandwidth B_{el} is found according to

$$\begin{aligned} I_1 &= 2\bar{I} \frac{ER}{ER+1} & I_0 &= 2\bar{I} \frac{1}{ER+1} \\ \sigma_1^2 &= I_1^2 RIN B_{el} & \sigma_0^2 &= 0 \end{aligned} \quad (6.1)$$

with

$$Q = \frac{I_1 - I_0}{\sigma_1 + \sigma_0} = \frac{2\bar{I} \frac{ER-1}{ER+1}}{\sqrt{\left(2\bar{I} \frac{ER}{ER+1}\right)^2 RIN B_{el}}} = \frac{1 - \frac{1}{ER}}{\sqrt{RIN B_{el}}} \quad (6.2)$$

The RIN of a signal and its average value are defined as

$$RIN = \frac{\overline{\tilde{P}(t)^2}}{\overline{P(t)^2}} \quad \overline{RIN} = \frac{1}{0.75R_b} \int_0^{0.75R_b} RIN(f) df \quad (6.3)$$

where R_b is the data rate of the intensity modulated signal.

Since the RIN is measured for an optical signal, the electrical power levels that are acquired with an electrical spectrum analyzer can be used directly due to the square-law for optical detection. The optical signal power P_{sig} is related to the photo current I_{det} and the electrical RF power P_{rf} via

$$P_{rf,el} \propto I_{det,el}^2 = \left(\frac{\eta e}{hf} P_{sig,opt}\right)^2 \quad (6.4)$$

where η is the quantum efficiency for detection, determining the sensitivity of the photo detector, e the elementary charge, h the Planck constant and f the optical frequency of the incident light.

The RIN can be then derived as

$$RIN = \frac{\overline{\tilde{P}_{sig,opt}(t)^2}}{\overline{\tilde{P}_{sig,opt}(t)^2}} = \frac{\overline{\tilde{P}_{rf,el}}}{\overline{\tilde{P}_{rf,el}}} = \frac{\overline{\tilde{S}_{rf,el} \delta f}}{\overline{\tilde{P}_{rf,el}}} \quad (6.5)$$

where S is the measured spectral density and δf the resolution bandwidth of the electrical spectrum analyzer.

For light sources the RIN directly relates to the SNR with

$$SNR = 1 \left/ \int_{f_0}^{f_1} RIN(f) df \right. \quad (6.6)$$

where f_0 and f_1 are the electrical cut-off frequencies for the receiver, e.g. 0.1 and 10 GHz for 10 Gb/s applications.

Especially for sources that are built out of fiber ring lasers or mode-locked lasers, increased RIN at low frequencies, deriving mostly from mode partition noise [116] [215], can cause serious degradation of the received SNR and the data reception [216]. A possible source for RIN in distributed feed-back laser diodes can be the residual reflections at the chip facets, which convert the intrinsic phase noise into intensity noise [217].

A quantitative evaluation of induced BER floors is given in Fig. 6.7(a) for different receiver bandwidths and an ER of 5 dB.

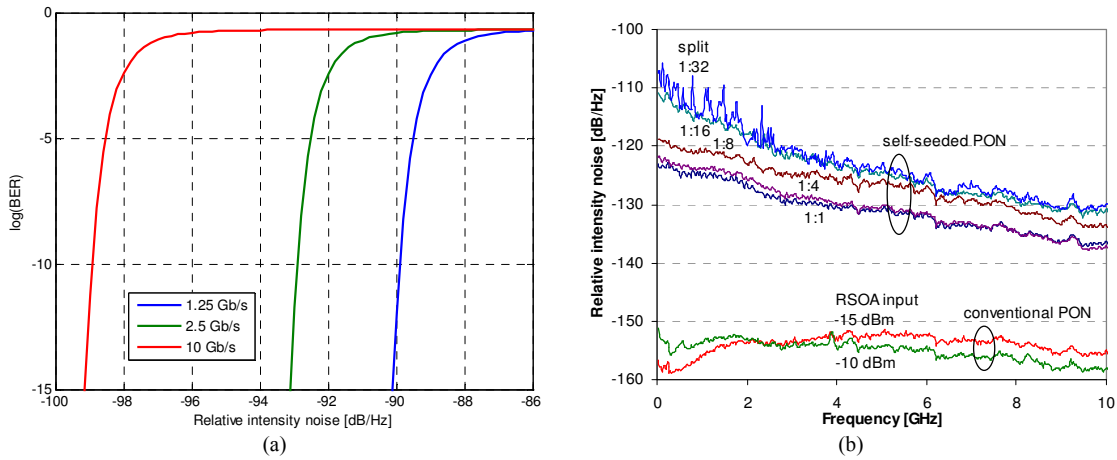


Fig. 6.7. (a) BER floors for ASK data signals deriving from RIN of the optical source and (b) RIN measurements for the unmodulated upstream carrier of the self-seeded and the conventional PON, taken at the input of the upstream amplification stage of the RN after passing the 90/10 splitter.

The RIN of the optical upstream carrier in the proposed PON was analyzed at point U in Fig. 6.2, corresponding to the input of the upstream amplifier. The self-seeded PON suffers from a higher noise impact due to the incoherent nature of the carrier, which was constituted by the sliced and reamplified spontaneous emission of the RSOA. The RIN increases with the splitting ratio and is in average -114 dB/Hz for a split of 1:16 (Fig. 6.7(b)). The conventional PON, which benefits from the low-noise injection into the RSOA, provides an optical carrier with a RIN of less than -150 dB/Hz.

6.2.5 Transmission Performance

For the downstream the sensitivity for reception is -24.5 dBm at a BER of 10^{-10} and a splitting ratio of 1:32 (Fig. 6.8(a)). When the DCF is removed at the OLT transmitter, a penalty of 2.4 dB is suffered. This penalty is acceptable thanks to the low chirp of the MZM and still ensures a margin of 7.7 dB, which is high enough for PON applications.

The continuous-mode upstream of the self-seeded PON experiences BER floors above 10^{-10} (Fig. 6.8(b)), however, these floors are well below the FEC threshold. The obtained reception sensitivities lead to margins that are >20 dB for several splitting ratios, except for the case of having a 1:32 split, where RB and the enhanced cross-patterning prevent to reach the FEC level. By replacing the drop fiber with its equivalent attenuation, the BER floor can be lowered to less than 10^{-4} due to the absence of RB.

Since low splitting ratios lead to a higher input power into the RSOA, patterning effects due to the gain dynamics of the RSOA become enhanced. While for a split of 1:1 a BER floor appears at 10^{-7} for a PRBS length of $2^{31}-1$, a shorter PRBS of 2^7-1 allows for transmission at a BER level of 10^{-10} .

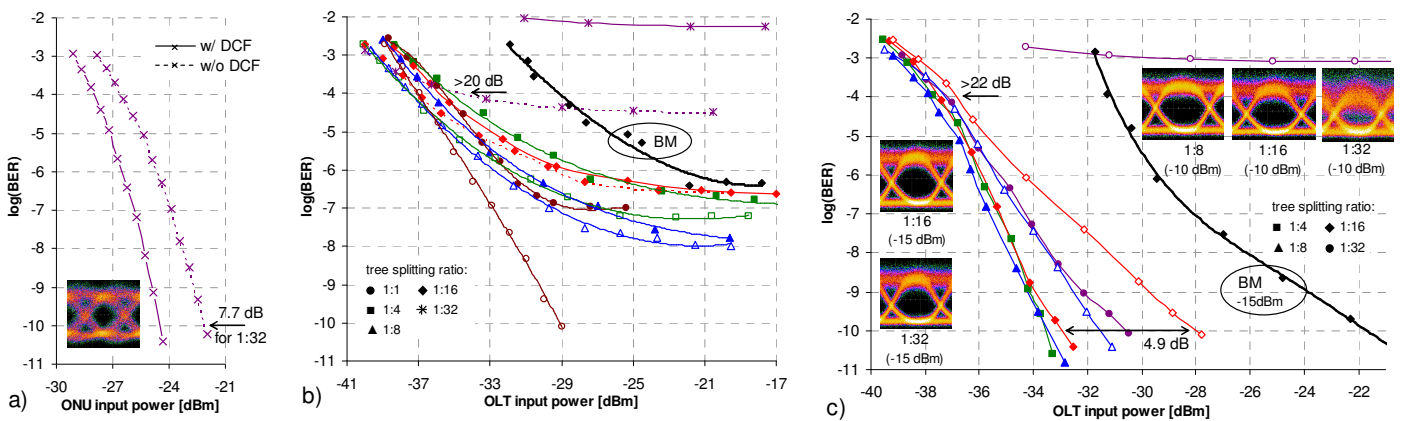


Fig. 6.8. BER measurements for (a) the down- and (b) the upstream of the self-seeded PON, and (c) the conventional PON seeded by an additional light source. For the self-seeded PON, measurements are taken with a PRBS of length $2^{31}-1$ (filled) and 2^7-1 (hollow markers). Dotted lines indicate the replacement of the drop fiber with its equivalent attenuation. For the conventional PON, the RSOA input power was -15 dBm (filled) and -10 dBm (hollow markers). Thick lines for the upstream measurements correspond to burst-mode (BM) measurements at a tree split of 1:16 and PIN receiver at the OLT.

The burst-mode transmission, which was assessed for a tree split of 1:16 and a PRBS of length $2^{31}-1$, experiences a similar BER floor as the continuous-mode upstream (see BM curve in Fig. 6.8(b)). The shift in sensitivity of ~ 7 dB at the FEC level is explained by the less sensitive PIN receiver that was used at the OLT instead of the APD.

Several error floors that appear for the self-seeded PON are summarized in Fig. 6.9 for continuous-mode traffic. While for higher splitting ratios RB and cross-patterning raise the floors, the RSOA-induced distortions prevent to reach a low BER for long word

lengths. For a PRBS of length $2^{31}-1$, a split of 1:8 in the tree results in the lowest achievable BER of $\sim 10^{-8}$. The effects that cause the floors are also evident when looking at the eye diagrams, which are presented in Fig. 6.10. Especially for the high split of 1:32 the eye becomes closed due to RB at the self-seeded PON, while for the conventional PON there is just an increased noise level in the marks due to the slightly lower OSNR and OSRR.

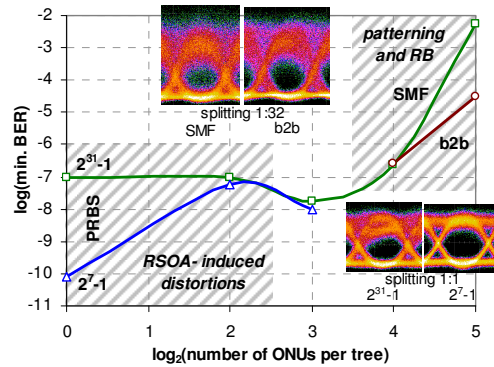


Fig. 6.9. Error floors for the self-seeded PON due to RSOA-induced distortions, cross-patterning and RB. Measurements are in principle taken with a PRBS of length $2^{31}-1$ and present drop fiber (■ markers). For further investigation, the PRBS length was lowered to 2^7-1 (▲ markers) and the drop fiber was replaced by its equivalent attenuation (● markers).

The conventional PON benefits from the optical carrier that was injected from the RN towards the ONU and allows a BER of 10^{-10} for the upstream, as can be seen in Fig. 6.8(c). The RSOA was operated at a slightly lower bias of 100 mA to increase the ER of the upstream signal to 6.3 dB, leading to an increased eye opening when compared to the self-seeded PON. The electro-optical bandwidth did not degrade due to this reduction in the RSOA bias current (Fig. 6.4).

Note that for the case of having the optical seed source of the conventional PON at the OLT, by keeping the single-fiber architecture at the same time, no upstream transmission is possible due to the strong RB that is caused by the seed light and backscattered into the upstream signal at the ring segment (see eye diagram labelled with “seed light from OLT” in Fig. 6.10).

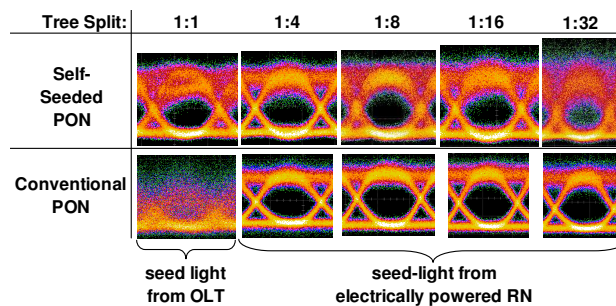


Fig. 6.10. Eye diagrams for the self-seeded and the conventional PON for different splitting ratios in the tree. RB in the single-fiber ring demands an electrically powered RN for the conventional PON.

When compared to the self-seeded PON, the margin for continuous-mode data is increased by just 2 dB at the FEC threshold, proving the feasibility of the self-seeded approach. Thanks to the capability of the RSOA to work with low input power values

around -15 dBm, the OSRR is high enough not to cause degradation in the upstream transmission, as can be seen in the corresponding eye insets in Fig. 6.8(c).

For comparison the BER measurements are also shown for an ONU input power of -10 dBm, which is still a few Decibels below the input power levels that are used in the self-seeded PON. The vulnerability of the conventional PON to RB is then visible in the penalty for splitting ratios of 1:8 and above when compared to the measurements with an ONU input of -15 dBm. Although for a split of 1:8 an acceptable penalty of ~2 dB is introduced, which is small compared to the large margin that can be provided for the reception, it raises to 4.9 dB for a split of 1:16 and makes any transmission impossible for a split of 1:32, as it is also the case for the self-seeded PON.

In burst-mode transmission with an input of -15 dBm at the ONU and a tree split of 1:16, a BER of 10^{-10} can be reached although a penalty of ~11 dB is suffered due to the less sensitive PIN diode (Fig. 6.8(c)).

The dependence of the upstream transmission in both PON architectures on dispersive effects is presented in Fig. 6.11, which shows a comparison for continuous-mode data and a tree split of 1:16 in the case of present and absent dispersion compensation.

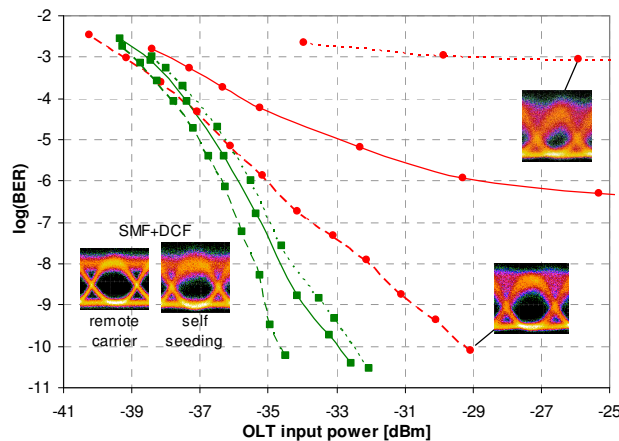


Fig. 6.11. Vulnerability of the self-seeded and the conventional PON with a tree split of 1:16 to dispersion in the light path. The \bullet , \blacksquare markers correspond to the self-seeded and the conventional PON, respectively. Solid lines indicate the presence of the DCF, dotted lines its absence and dashed lines the back-to-back case with fibers and DCF replaced by their attenuation.

The conventional PON suffers from a penalty of 0.5 dB when the DCF is removed and an accumulated dispersion of ~530 ps/nm is faced. It has to be noted that the dispersion of the DCF was not matched to the ring and drop fiber spans due to the unavailability of a suitable DCF length, leaving a residual dispersion of around -140 ps/nm. However, since a DCF spool cannot adapt to the conditions for all ONUs that are connected to the PON due to their different reach from the OLT, this corresponds to a realistic case of having a fixed dispersion compensation with some residual pulse broadening. For the case of replacing all fibers and the DCF with their equivalent attenuation, the sensitivity increases by 1.6 dB and a substantial margin of 30.2 dB guarantees error-free upstream transmission.

On the contrary, the self-seeded PON shows a much stronger sensibility to dispersion due to the broad spectrum of the upstream and the RIN increase that is induced by chromatic dispersion [214]. While for a present DCF a BER floor below 10^{-6} exists, the absence of the DCF causes a BER floor around 10^{-3} . On the other hand, when the residual dispersion that is given also with the presence of the DCF is removed by replacing fiber spools with their attenuation, the self-seeded PON allows upstream transmission with a BER of 10^{-10} and a sensitivity of -29.2 dBm, leading to a margin of 22.2 dB and therefore 8 dB less compared to the conventional PON.

6.2.6 Comparison between Self-Seeded and Conventional PON

Although error floors are present for the transmission with a self-seeded optical carrier, the incorporation of FEC that is supposed for NG-PON standards makes this technique feasible. For a practical implementation, the feedback, defined as the ratio between the received and the transmitted power at the ONU, should not be lower than -14 dB. This can be derived from the BER performance (Fig. 6.9) for the case of having a 1:16 tree split and the signal power levels in Fig. 6.5(a).

Regarding the vulnerability to RB, note that due to the self-seeding approach only a single ring has to be deployed compared to an approach where a carrier is sent from the OLT and modulated remotely at the ONU, such as in [212]. Alternatively, an electrically fed RN needs to be employed for the case of a conventional PON in this study, which does not maintain the fully passive nature of the PON.

Besides, laser diodes and multiplexing components can be discarded from the OLT transmitter while some wavelength selective devices have to be added at the RN, whose complexity increases slightly. The sensitivity to dispersion requires the use of dispersion compensation at the OLT receiver for the self-seeded approach; However, a foreseeable increase in the upstream data rate to 10 Gb/s for RSOA-based ONUs makes an adaptive dispersion compensation an indispensable element of the upstream receiver. Although self-seeding avoids the amplification stage that would be necessary for boosting the unmodulated upstream carrier that is sent by the OLT, the additional amplifier that is used to overcome the losses of the splitting to obtain an optical carrier requires for approximately the same amount of optical pump.

A reduction of the net loss for high split in the tree with the help of distributed amplification inside the splitting stage, by removing the additional EDF amplifier in the RN at the same time, could solve the problems of RB and residual cross-patterning. This technique will be presented in the next section.

6.3 Seeding of an EDF Pump for Transparent Power Splitting

Hybrid PONs with TDM stages often suffer from the high concentrated optical loss in the tree that is given by the unavoidable power splitter. In this section, a method to partially reduce this splitting loss is introduced. The ASE of an optical amplifier at the customer premises is thereby reshaped and reused as a natural pump source for an EDF inside the TDM signal distribution elements of an access network. This increases the number of served customers and supports the transmission in terms of reduced OSNR and OSRR requirements at no extra cost, just by recycling optical noise.

6.3.1 Noise-Pumped Extender Box

The required pump for a concentrated fiber amplifier that is inserted in the light path can be either transmitted from the OLT or the ONU. While the first option suffers from the high transmission losses for the pump on the long way towards the EDF, a scheme, where the ONUs provide a pump towards the amplification stage, is advantageous. One possibility to add pumping capabilities to the ONU relies on the incorporation of optical sources for the pump waveband of the EDF [218]. Although this might be seen to be in agreement with a colorless ONU design and retains the possibility for its mass deployment, this method is inefficient when considering the extra cost and power consumption of the light sources.

Alternatively, a SOA can fulfill the task of pump generation while it is also used as amplifier for a weak data signal. This functionality as dual-waveband amplifier can be established by laying a seed loop over the SOA and parts of the fiber plant, as it is illustrated in Fig. 6.12 for a typical ONU and PON configuration as it was used previously in chapter IV.

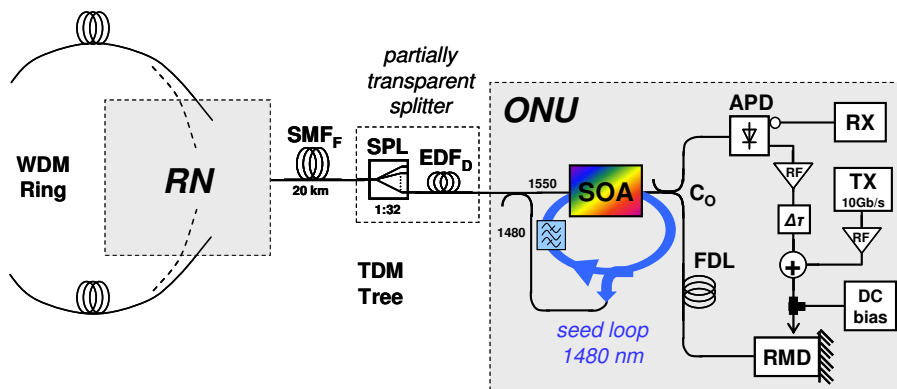


Fig. 6.12. An additional pump is provided from the ONU when reusing the ASE of the inline SOA.

A SOA in the ONU operates as preamplifier/booster in the C-band for data transmission but seeds also a pump signal in the 1480 nm band simultaneously. As long as the seeding process does not prevent the concurrent amplification of the weak data signal, a

beneficial effect of recycling the ASE can be obtained. This in turn allows a more efficient use of energy, without dismissing the previous functionality of the SOA.

The ONU is extended by a seed loop around this SOA to generate the EDF pump. Integration of this loop can be made via WDM couplers with low insertion loss for these two wavebands. In a first simple scheme, a band-pass filter ensures that the seeded wavelengths are well defined and do not hop over the broad ASE peak of the SOA, which is expected to provide gain in the C-band as well as in a wavelength range that is used for the pump of the EDF. In addition, a high saturation output power capable to deliver enough power to reach gain in the EDF is required. The EDF has to provide a high pump conversion efficiency in addition, as it is the case for a HE980 EDF.

The shared SOA gain medium for down-, upstream and pump has advantages and disadvantages. Although some gain will be missed by the data signals, the relative strong pump will allow gain clamping for the SOA and in turn reduce the induced transients that derive from the gain saturation dynamics. The ASE output of the SOA will be spectrally re-shaped towards a wavelength range far from the data signal thanks to the wavelength selective filtering inside the seed loop. The noise photons that are coupled into the weak data signals will be therefore kept inside the seed loop and not pass along the light path of the data signal.

Note that the location of the EDF inside the power splitter may not be the optimal one in Fig. 6.12. Much more interesting can be a dual-stage splitter with intermediate EDF since the optical loss between the different amplification stages in ONU, RN and power splitter is then more distributed as it is the amplification itself (similar as Raman amplification). Before the different possibilities of optimization and seed loop designs are discussed, some considerations about the physical design of the SOA are made.

Design Considerations for the SOA

The SOA gain has to cover not only the wavelength range of the employed data signals but also the pump waveband. It should be additionally tailored in its spectral response to optimize the efficiency for the pump wavelength. The semiconductor material can be adapted for this reason by means of band gap engineering [91] to optimize the SOA for a certain wavelength range. This includes a to shift the gain peak to the nominal pump wavelength for the EDF, as it was discussed in chapter II.2.1 and more specifically shown in Fig. 6.13(a).

The seeded pump at 1480 nm leads to population of the excited energy state of the EDF, which in turn provides amplification due to the stimulated emission process in a wide spectral (data signal) range that covers the 1550 nm band. Several discretely spaced energy bands for the EDF exist and are suitable for the amplification process, as for example the commonly used $^4I_{13/2}$ band that fits to a pump of 1480 nm (Fig. 6.13(b)). This pump wavelength has been found to be attractive since it can be transmitted along

fiber spans without suffering from severe transmission losses due to the low material loss of commonly deployed fibers in the third telecommunication window.

The efficiency of the amplification process in the EDF is determined by the overlap between the density of states inside these energy bands and the absorption and emission spectra $\alpha(\nu)$ and $\varepsilon(\nu)$ of the EDF, which are illustrated in Fig. 6.13(c).

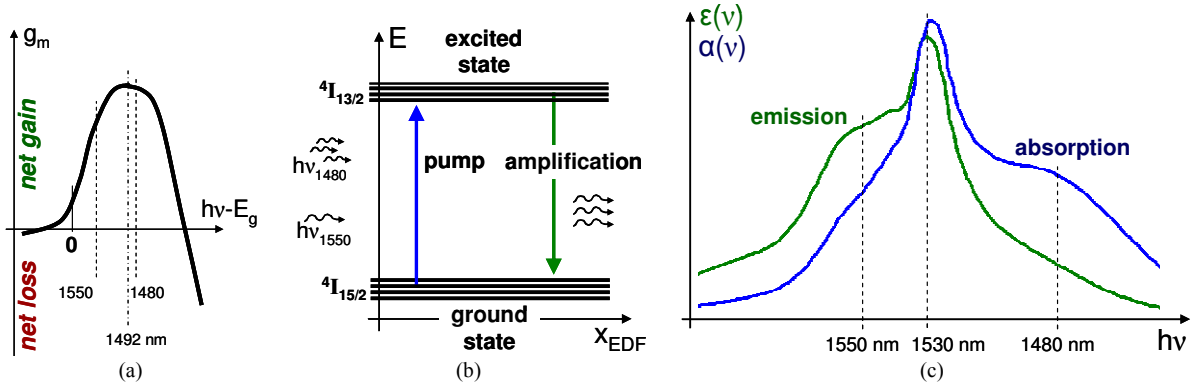


Fig. 6.13. (a) Adapted SOA gain spectrum, (b) energy states of the EDF and (c) its absorption and emission spectra.

Although rare-earth doped fibers can be modified in their absorption and emission spectra, such processes require complicated means of fiber processing. What matters is therefore the simpler accessible design of the SOA that is used for pump generation. This engineering step has to aim at reducing the electrical pump of the SOA to stay energy efficient.

The pumping of the semiconductor material of the SOA with electrical carriers is – from a macroscopic point of view – reflected in the carrier rate equation. It is considered that the carriers distribute themselves in the energy bands rapidly.

$$\frac{dN}{dt} = \frac{I}{eV} - R(N) - \frac{\Gamma}{dW} \left[\sum_{k=1}^M g_m(\nu_k, N) \Psi_k \right] \quad (6.7)$$

In this form of the rate equation, M signals are supposed to be amplified in the SOA (e.g. $M = 2$, with optical frequencies ν_1 and ν_2 corresponding to 1480 nm for the seeded pump and 1550 nm for the simultaneously present data signal). Ψ_k is the photon rate of the corresponding signal according to its optical power.

It is necessary that the material gain is adjusted to the pump wavelength to establish an EDF pump effectively:

- A strong pump with a high output power is required, meaning a high photon rate Ψ_p for the pump.
- The signal itself is supposed to arrive weak and, more important, it does not necessarily have to be “blown up” to a high output power (thus the photon rate Ψ_s will be moderate), considering distributed means of amplification along the light path and highly sensitive receivers at the end-nodes.

- The high photon rate for the pump can be only reached in a power-efficient way if the material gain $g_m(\nu_P)$ is high, and therefore the semiconductor should be tailored in an appropriate way.
- For this case the required bias current for the SOA, which gives a macroscopic figure of merit for the energy efficiency of the pumping scheme, can be minimized.

Besides the spectral gain adjustment of the SOA, the seed loop can be optimized too.

Seed Loop Design and ASE Shaping

Different scenarios are possible in terms of ONU connectivity and pump multiplexing. The tree can be first of all loaded with just a single ONU since it cannot be guaranteed that customers will leave their ONU connected to the optical access network. These free and *individual* ONUs cannot be considered to contribute a pump if they are left inactive. On the other hand, cases where the user does not necessarily have access to the ONU are feasible such as it is the case in multiple dwelling units with shared optical access and collection of low-bandwidth traffic. The latter type of ONUs can be seen as *bounded* to the tree and are able to seed a pump also when they are inactive.

The seed loop itself can be adapted to these scenarios but can be in principle from one of two types: a local, *concentrated* seed loop whose ASE filter that determines the seed wavelength is placed locally at the ONU, or a distributed, *giant* seed loop that is transparent for the ONU in terms of an external ASE filter in the fiber plant. Both kinds of seed loops are depicted in Fig. 6.14.

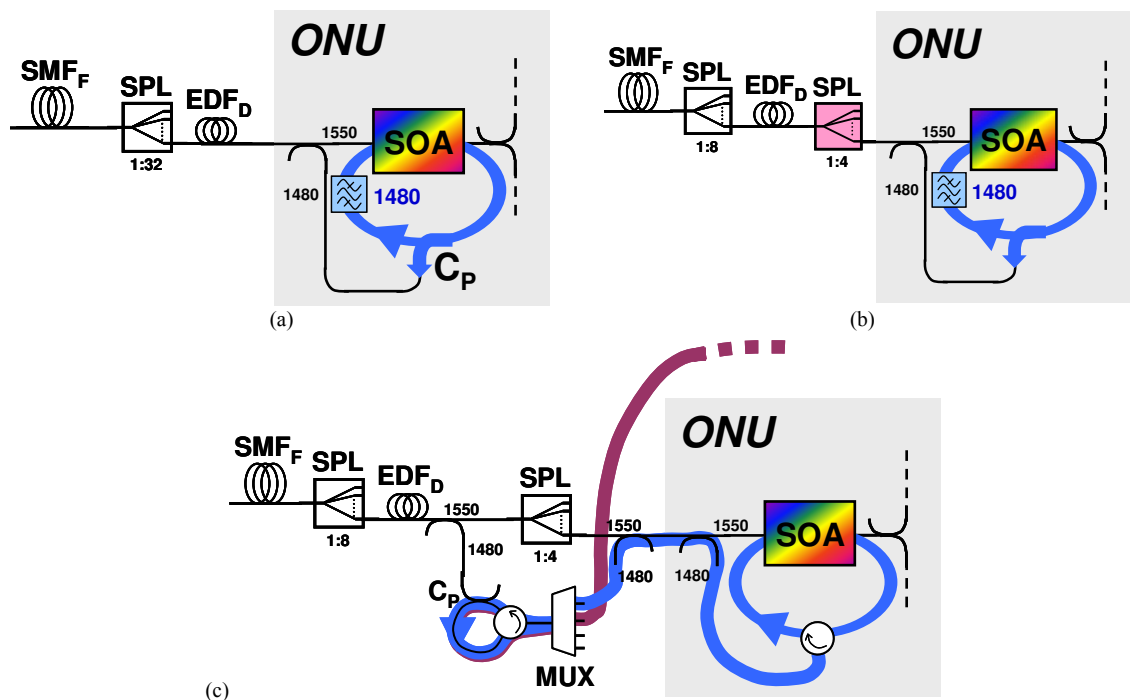


Fig. 6.14. Concentrated seed loop design with (a) an EDF at the bidirectional port of the ONU and (b) an EDF inside a dual-stage splitter. (c) Giant seed loop with pump multiplexing.

The concentrated seed loop suffers from the disadvantage that the EDF has to be placed between power splitter and ONU since otherwise high saturation output power levels are required for the SOA due to the attenuation that the pump experiences when passing the second splitter stage (shaded box in Fig. 6.14(b)) towards the EDF.

On the contrary, the giant seed loop with its external ASE filter can provide additional pump multiplexing while the seeded pump can be bypassed through the second splitting stage thanks to the multiplexing capability of the loop that is achieved by using different ASE filters in the fiber plant. This allows to achieve high pump power values even with moderate saturation power levels of the SOA and keeps a colorless ONU design. As it is obvious from Fig. 6.14(c), this advantage is obtained at the cost of some losses such as the insertion loss of the pump multiplexer or the loss of the redirecting circulator that acts as loop mirror.

The granularity of the seeded pumps is not only limited by the need for a sufficiently strong ASE feedback towards the SOA (i.e. a spectrally broad feedback) but depends also on the network design of the tree segment. Considering the case that the EDF is placed inside the power splitter to reduce its net splitting loss, the number of ONUs that are bundled in a single seed loop is determined by the split M of the second splitting stage. In a simple topology where half of the ONUs are used for forward pumping of the EDF and the other half for backward pumping, the number of required pump wavelengths is hence $M/2$.

A summary of possible scenarios is given in Table 6.1. Focus will be given on the giant seed loop during the later evaluation due to its higher efficiency.

		Nature of the ONU	
		Free (Individual)	Bounded (Collector)
Seed Loop Design	Concentrated	efficiency drops quickly with loss between ONU and EDF, e.g. given by the second stage of a tree splitter that is divided into two parts	pumps cannot be combined due to preserving a colorless ONU design, therefore still vulnerable to splitting stages before the EDF
	Giant	gain is determined by the seeding capability of a single ONU, therefore the seed loop efficiency matters, splitting stage between ONU and EDF possible	very high gain possible by bundling pump wavelengths, even with separated splitter stages

Table 6.1. Possible scenarios for applying an ASE-powered extender box regarding ONU connectivity and seed loop design.

Regardless of the exact seed loop design the ASE is shaped with the 1480/1550 waveband splitters that are used to insert the seed loop. An example for the spectral re-allocation of the ASE noise with a filter at 1480 nm is shown in Fig. 6.15 for a SOA

with an ASE spectrum that is centered at 1492 nm. Next to the emission of a strong and spectrally broad pump between 1480 and 1490 nm, the ASE background in the C-band is suppressed due to the shared carrier reservoir in the SOA. Note that the peak in the ASE spectrum at the peak wavelength stems from residual reflections that already caused lasing for high bias currents. The dip in the shaped ASE at 1500 nm is caused by the guard window of the 1480/1550 splitter.

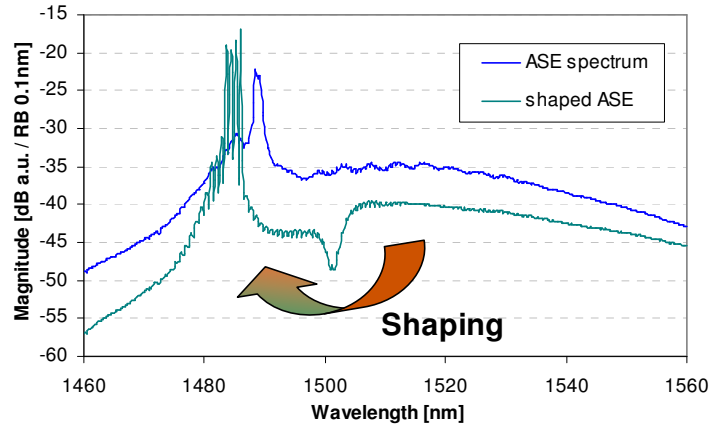


Fig. 6.15. ASE shaping due to the introduction of a concentrated seed loop.

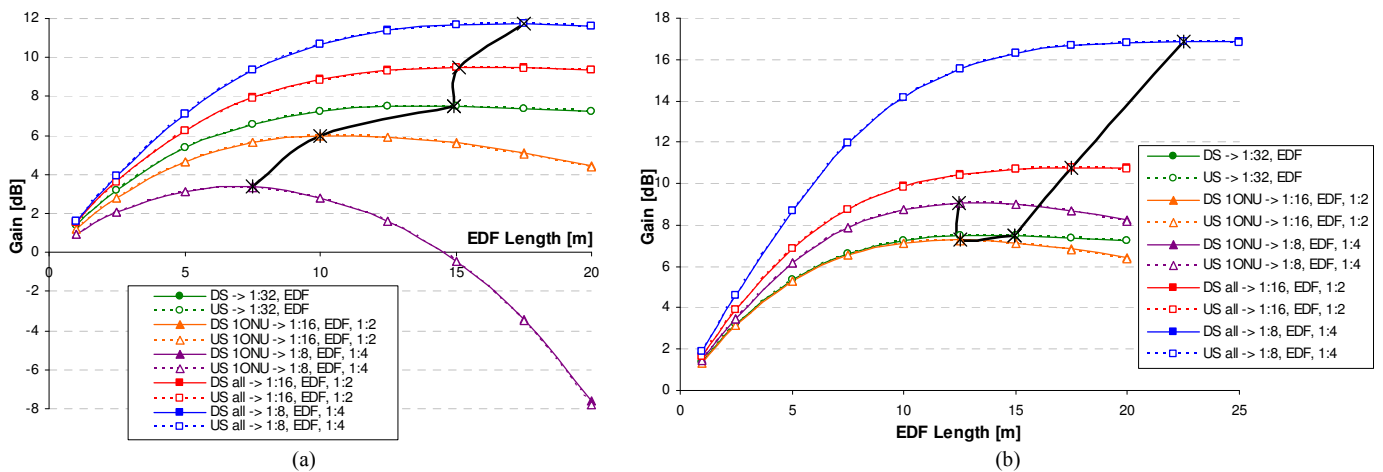


Fig. 6.16. Obtained EDF gain as function for the EDF length for down- (DS) and upstream (US), shown for different combinations of loss distribution inside the dual-stage power splitter. (a) Concentrated seed loop where pump and signal are both attenuated on the way to the EDF and (b) giant seed loop where the pump is fed-through to the EDF across the second splitting stage. The tree is either full with ONUs (labeled “all”) or only one ONU is connected (labeled “1ONU”). The black lines indicate the optimum EDF length.

Optimum EDF Length

Depending on the strength of the seeded pump, the EDF length will have to be optimized. A simulation has been carried out to illustrate the impact of an EDF length mismatch. The SOA at the ONU had its ASE spectrum centered at 1492 nm and a small signal gain and noise figure of 23.3 dB and 6.4 dB at 1550 nm. The saturation output power at 1530 nm was 12 dBm and a pump power of 8 dBm can be obtained at 1480

nm at the output of the simple concentrated seed loop, where the 90% port of a 10/90 coupler (C_P in Fig. 6.14(a)) is used to extract the pump. In the case of the giant seed loop the considered pump wavelengths were 1460, 1470, 1480 and 1490 nm.

Different combinations of splitting ratios in the first and second splitting stage were analyzed. Fig. 6.16 shows that although an optimum EDF length exists, the gain does not change strongly for moderate variations of the EDF length for most of the cases. The gain for down- and upstream is identical since the stronger signal clamps and therefore sets the gain in the EDF.

Rayleigh Backscattering and Noise Accumulation across the Tree

A power splitter with lower loss leads to decreased launched power from the RN at the root of the tree towards the ONU and also to a higher input power of the upstream into the RN. Therefore, the critical degradation in the OSRR due to the combination of feeder fiber and splitter, where the fiber comes before the splitter and is fed at the same time with a higher optical power, can be faced too. The partially transparent splitter will relate a stronger upstream to the RB caused by the downstream, which is now also weaker compared to the original scenario with lossy power splitter.

The OSRR can be assessed according to the conditions in the tree, as they are sketched in Fig. 6.17(a). The important parameters are the launched downstream power Λ and the RB coefficient Δ of the feeder fiber, which determine the amount of backscattered light ζ , the loss Φ of the feeder and loss Σ of the splitter as well as the reduction χ in its loss due to the gain provided by the EDF. The required input power J will assure a (fixed) output power O at the ONU.

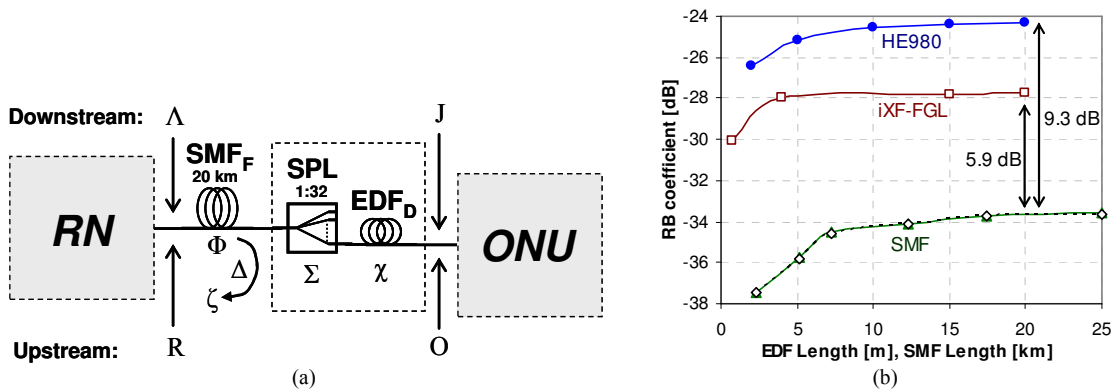


Fig. 6.17. (a) Scheme of the tree segment in the PON where RB is caused and (b) RB coefficient of EDF and SMF as function of its length.

The upstream arrives at the RN with a power level R and a certain OSRR, which is derived via

$$\begin{aligned}
 J &= \Lambda - \Phi - (\Sigma - \chi) \\
 \zeta &= \Lambda + \Delta \\
 R &= O - (\Sigma - \chi) - \Phi \\
 OSRR &= R - \zeta
 \end{aligned}
 \tag{6.8}$$

Considering a 20 km long feeder fiber with 4.5 dB loss and a RB coefficient of -33.6 dB, a 1:32 power splitter with 16 dB loss and a required input power of -15 dB at the ONU that provides an output level of 0 dBm, the OSRR without EDF gain is 17.6 dB. This low OSRR can penalize upstream transmission if no additional techniques for the mitigation of RB are applied.

The reduction in the effective splitter loss gained by the pumped EDF at its output port will affect the OSRR doubled due to the bidirectional tree segment: while the launched downstream can be reduced according to the lowered insertion loss of the splitter for keeping the same input power of the ONU, the upstream arrives stronger at the feeder fiber where significant RB is produced in the initial scenario. For this reason a moderate to low EDF gain of 10 dB will already boost the OSRR to a high value of 37.6 dB. Note that in this simple model no EDF saturation is taken into account and no RB from the EDF is considered, neither in the upstream nor in the downstream direction.

The latter RB effect in the EDF is pronounced compared to SMF and might therefore impose a serious limit. Considering a HE980 EDF, the RB coefficient increases with the EDF length and saturates at a length around 15 m to a value below -17 dB (Fig. 6.17(b)). To assess the impact of this effect in a more accurate way, a simulation for both RB impacts was carried out whose results are shown in Fig. 6.18(a) for the two proposed seed loop designs and different scenarios of loss distribution for the power splitter.

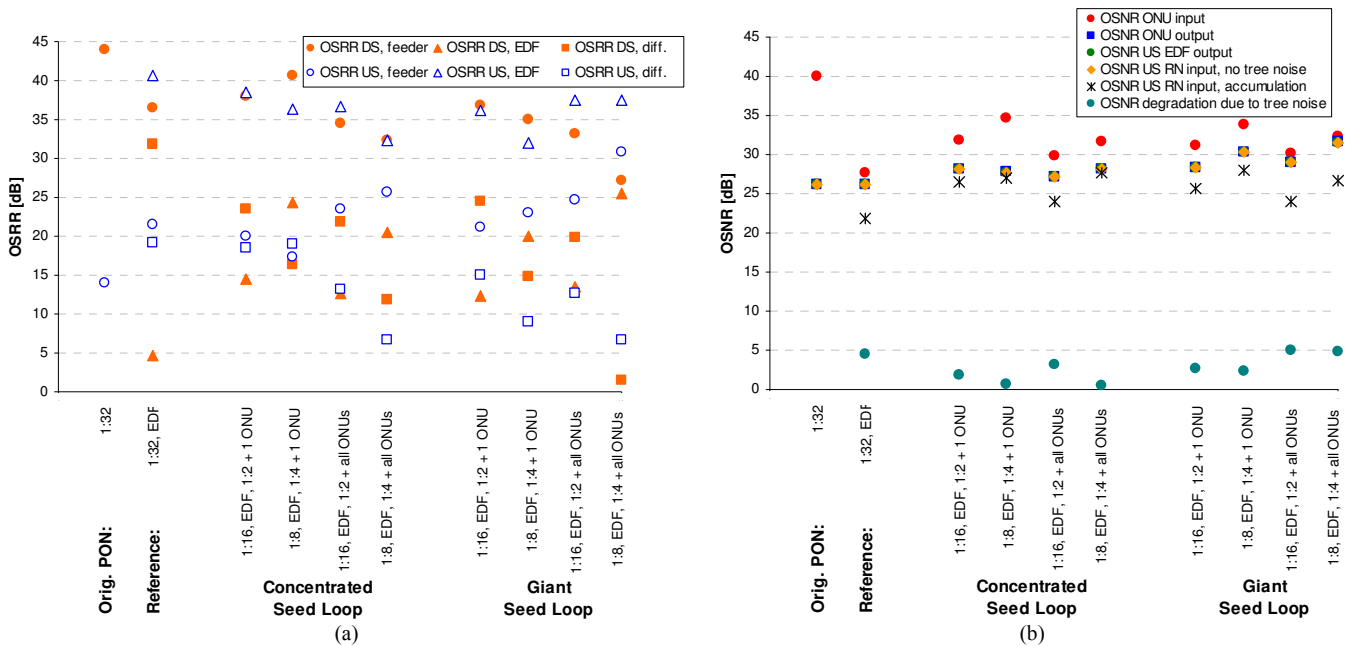


Fig. 6.18. (a) OSRRs for down- and upstream due to RB caused by the feeder fiber and the EDF. (b) OSNR degradation when only the active ONU is present at the tree for different scenarios.

The feeder fiber and the EDF have different impacts on down- and upstream due to their location in the tree segment. RB in the EDF determines the OSRR of the downstream while the feeder fiber does for the upstream. The OSRR difference in Fig. 6.18(a) is defined as the difference between the OSRR of the dominating and the weak source of RB and becomes smaller once the ratios of the two splitting stages are equalized. The

critical RB contribution has been found to be the one into the downstream direction, which derives from the relatively strong upstream signal due to the lower split in the second splitter stage. By increasing the splitting ratio in the second splitter stage, the OSRR can be improved while the upstream is not effectively affected by RB.

The particular noise contributions from the EDFs inside the power splitter accumulate across the whole tree. Since N EDFs are required for the case of having a split of $1:N$ at the first splitting stage, the accumulation worsens if the EDF is placed closer towards the ONU. Even for the scenario where an EDF is placed between power splitter and ONU, as it is sketched in Fig. 6.19, the requirement of receiving downstream (i.e. a pump has to be provided by each ONU to feed the EDF) leads to the worst case although the ONUs are not considered to be bounded to the tree. However, the worst case has to be considered so that 32 ONUs will contribute with ASE noise at their corresponding EDFs.

The noise that is caused by the inactive ONUs will be added to the upstream of the active ONU with a magnitude close to the one of a single EDF. Therefore, to assess the impact of ASE accumulation, all the EDFs of the inactive ONUs can be virtually replaced by a single EDF and a single inactive ONU while the power splitter is substituted by a coupler with a splitting ratio of $1/32:31/32$.

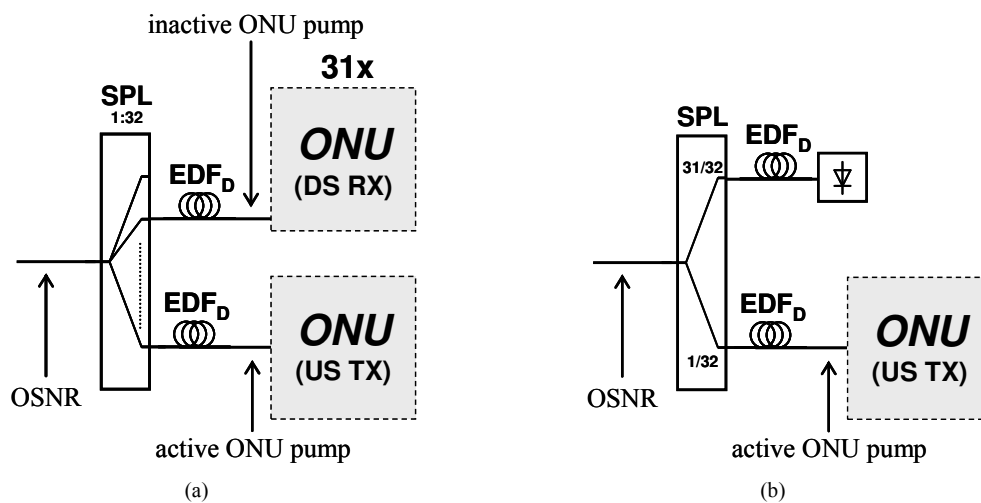


Fig. 6.19. Inactive ONUs lead to a decreased OSNR due to noise accumulation. (a) Initial 1:32 split configuration and (b) equivalent model for the tree.

The threshold for accumulation for which an OSNR degradation takes place after the upstream passes the TDM power splitter will be reached according to three conditions:

- *Splitting Ratio of First Splitter Stage*
The first splitting stage will determine the number of EDFs per tree and therefore the amount of accumulated ASE noise.
- *Delivered Downstream OSNR*
Noise accumulation takes effectively place if the noise that is added has an approximately equal of higher level than the noise that is already present in the

upstream signal. If the noise degradation of the down- or upstream signal along the light path is already high so that in turn the OSNR is that low that the accumulation from all the inactive branches of the tree will not have a significant effect on the overall OSNR. Note that the noise generated by the inactive tree branches does not depend on the downstream OSNR.

- *Noise Shaping Efficiency*

The input noise level of the EDF in the spectral region of the C-band will depend on the spectral shaping obtained in the SOA of the ONU. For the case that noise power is taken away from the C-band due to the seeding process, the ASE emitted by the EDF itself will be dominant and lead to the lowest bound of generated noise in the EDFs for the inactive tree branches, where no upstream transmission is actually taking place due to the TDM scheme.

An evaluation of the OSNR levels along the tree can be seen in Fig. 6.18(b). The OSNR for the downstream after amplification in the RN was considered to be already degraded to 40 dB and the noise figure of the SOA inside the ONU was chosen with 8 dB.

It can be seen that the degradation due to noise accumulation is quite low and does not deviate strongly from the original PON scenario where no EDF is present at all (26.1 dB). An important parameter is the location of the EDF. If the tree is divided into more balanced sections with splitting stages of equally distributed insertion loss, the OSNR can be improved.

6.3.2 Experimental Proof of Concept

The giant seed loop scenario where four ONUs are seeding the EDF that is placed between a 1:8 and 1:4 splitter stage was considered to further evaluate the performance of the transparent power splitting experimentally [219]. This PON, shown in Fig. 6.20, is referred to as the *modified PON* and will be compared with the *standard PON*, which has a tree that consists of the same feeder fiber connected to a 1:32 splitter.

The ASE in the pump waveband is shaped into a specific range with the WDM multiplexer (M_1 , M_2) at the fiber plant to keep the ONU colorless. This allows to combine the pumps of a few ONUs for a single EDF, in this case two 1460/1480 combiners allow for four pumps at the EDF. With the losses in the loop and the feedback to the SOA that is provided by 20/80 couplers (C_{S1} , C_{S2}), a pump of 5.5 dBm per ONU is obtained at the EDF input, shaped at 1480 and 1460 nm. A 15m long HE980 EDF with good pump conversion efficiency was inserted between a 1:8 and 1:4 splitting stage. Two ONUs were seeding at 1480 and 1460 nm while two laser diodes, with their output power adjusted to the obtained seed power, were emulating the two other ONUs at the 1:4 splitting stage.

As the SOAs in the ONUs that are not transmitting any upstream data are active, noise accumulates across the tree. A coupler (C_A) was therefore added with an ASE source, adjusted to the corresponding ASE of all other ONUs across the tree.

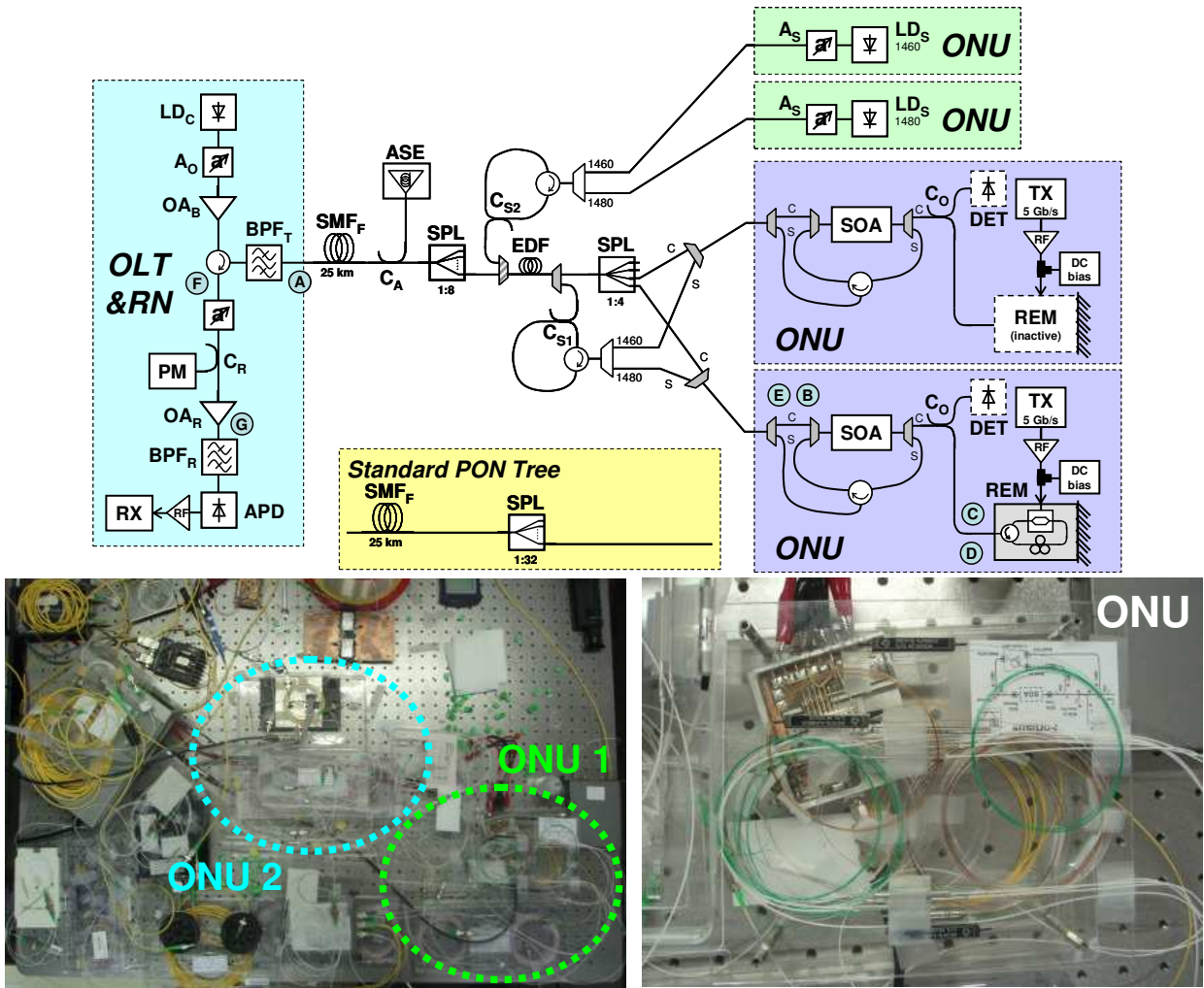


Fig. 6.20. Experimental setup for a giant seed loop with four ONUs.

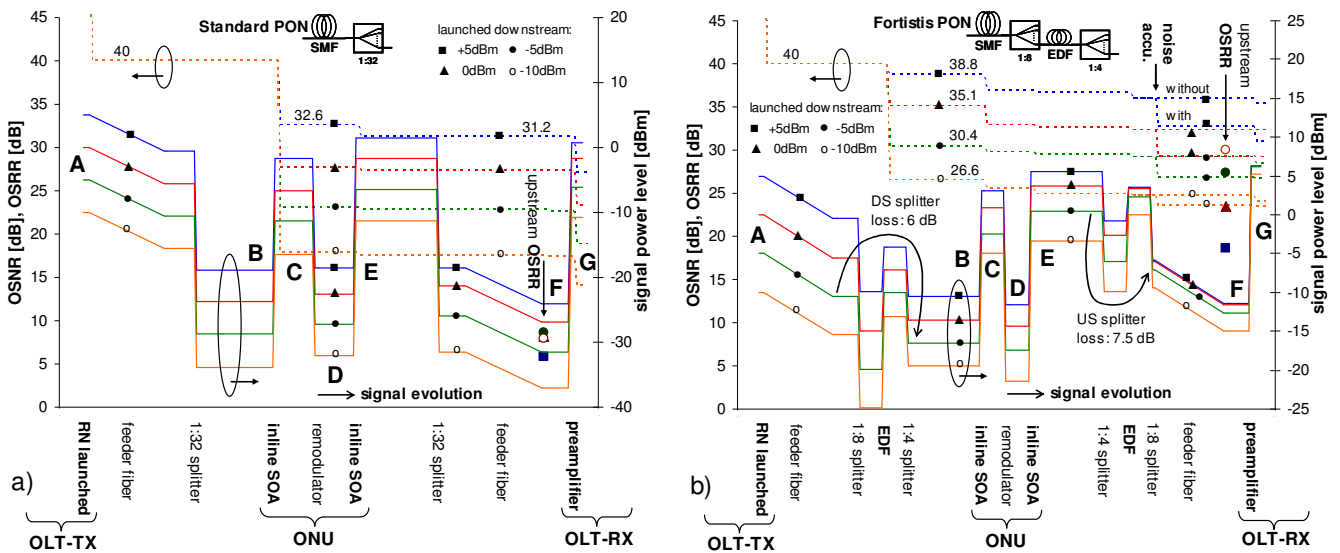


Fig. 6.21. Signal power (solid) and OSNR (dashed) for (a) the standard PON and (b) the modified PON for the case with and without noise accumulation across the tree. The latter shows reduced dynamics due to the distributed amplification scheme, and raises the OSNR and OSRR.

The tree segment was fed from the RN with the downstream, having a variable launch power P_{RN} but a fixed OSNR of 40 dB. For comparison a standard PON with the same feeder SMF of 25 km and a 1:32 splitter was also evaluated. At the ONU a remodulator consisting of a MZM was used after a 50/50 coupler (C_O). No downstream modulation was present on the optical carrier at 1552.52nm to avoid additional errors deriving from an unsuppressed pattern. The upstream was modulated at 5 Gb/s with a PRBS of length $2^{31}-1$. The receiver of the OLT comprised of an EDFA and an APD. Several optical band-pass filters for ASE rejection had a bandwidth of 100 GHz.

The standard PON suffers from strong power dynamics (Fig. 6.21(a)) due to the high splitter loss. A launched power of 0 dBm is necessary to keep the OSNR higher than 25 dB after the first SOA pass. The OSRR is <10 dB with present feeder fiber, making any transmission impossible (Fig. 6.22(a)). Even for the back-to-back case for which the fiber was replaced by attenuation, the budget is too high to maintain transmission for a decreased launch without additional amplification in the tree.

The modified PON has a smoothed signal evolution (Fig. 6.21(b)) due to the distributed amplification scheme. The splitter loss is reduced from the theoretical value of 15 dB (in practice it will be ~ 16 dB due to excess loss) to 6 and 7.5 dB for down- and upstream when a power of -5 dBm is launched from the RN. The OSNR is then 30.4 dB at the downstream reception, while it is 29.3 and 26.8 dB for the upstream without and with ASE accumulation at the tree. The OSRR can be maintained as high as 18.6 dB for a launched power of 5 dBm and is bigger than 23 dB for 0 dBm or less. A trade-off exists for the launched power regarding the OSNR and OSRR: the OSNR can be kept high with a strong downstream, however, the OSRR decreases due to saturation effects in the amplifiers along the upstream path. For a lower launch the OSRR is improved at the cost of the OSNR. Transmission in the modified PON is also possible with present feeder fiber (Fig. 6.22(b)).

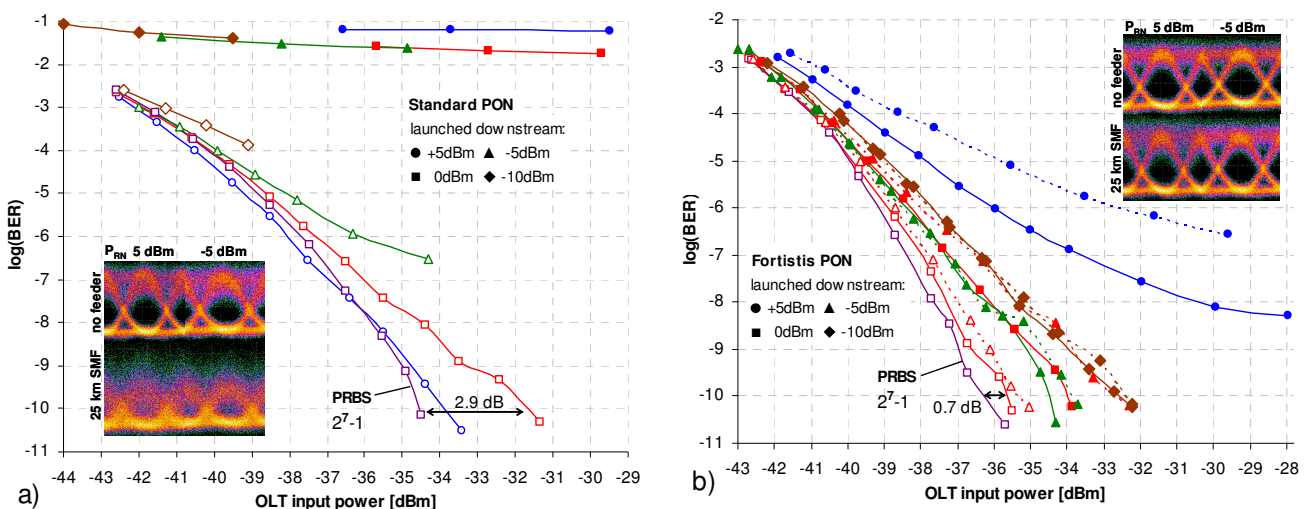


Fig. 6.22. BER measurements for (a) the standard PON and (b) the modified PON. For the ease of reading, some curves are not shown. Measurements are taken for the case without (solid) and with (dashed lines) ASE accumulation, in the back-to-back (hollow) case and with feeder fiber (filled markers). Several curves correspond to a PRBS of length $2^{31}-1$ if not otherwise mentioned.

The penalty in sensitivity for a BER of 10^{-10} , referenced to the back-to-back case with optimum launch, is shown in Fig. 6.23. The optimum levels were 5 dBm for the back-to-back cases due to the high OSNR and the absence of RB, and -5 dBm for the modified PON with feeder fiber, having a penalty of 1.6 dB and additional 0.6 dB caused by ASE accumulation across the tree. A BER floor is only present for the highest launch of 5 dBm. The downstream OSRR has been found to be >20 dB for a launched power of -5 dBm and is therefore the lower one compared to the upstream OSRR after balancing.

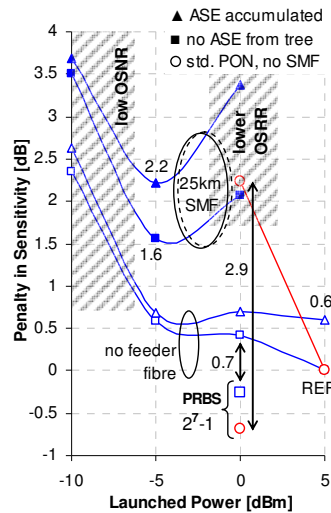


Fig. 6.23. Penalties for a BER of 10^{-10} , referenced to the optimum launch in the back-to-back case.

Thanks to the seed loop the carrier density in the SOA is clamped. The patterning penalty between a PRBS of length 2^7-1 and $2^{31}-1$, deriving from the transient distortions introduced by the gain dynamics of the SOA, is reduced to 0.7 dB for a launch of 0 dBm and is therefore much lower when compared to the 2.9 dB of the standard PON.

The overall benefit from the partially transparent power splitter is summarized in Table 6.2.

With the assumed conditions between OLT and RN, having an OSNR of 40 dB and an optimum launch of -5 dBm, power margins of 8 and 21.2 dB for down- and upstream can be reached. These margins can be further increased by remote amplification in the RN, providing margins above 23 dB when a gain of 15 dB is assumed in the RN [7]. This would correspond to a ring reach of 50 km and an additional split of 1:16, forming with 32 wavelengths a PON that can serve 16.3k customers.

The feasibility of this self-pumped approach will be now proven in three different PON architectures. The widespread usage of SOAs enables thereby the proposed technique to be deployed in a variety of ONU designs with downstream receivers that contain a SOA as preamplifier in ONUs with externally modulated lasers (EML) or with transmitters that are based on a combination of SOA and REAM or solely on RSOAs. For the last case, the seed loop will have to be modified as sketched in Fig. 6.24.

		Criteria / Figures of Merit		
		RB, OSRR	OSNR	Others
Scenario	Standard PON	<p>OSRR < 10 dB for $P_{RN} = 5$ dBm: OSRR = 5.9 dB</p> <p>FEC threshold cannot be reached for a 25 km feeder fiber</p>	<p>for highest launched power of 5 dBm: OSNR = 31.2 dB</p> <p>strong degradation for lower launched power, 27.4 dB for $P_{RN} = 0$ dBm 22.7 dB for $P_{RN} = -5$ dBm</p>	<p>patterning due to long PRBS given in the SOA, penalty of 2.9 dB between lengths $2^{31}-1$ and 2^7-1</p> <p>high launched power of 5 dBm from the RN to keep the OSNR high requires a strong pump to be transmitted from the OLT to the RN</p>
	Modified PON	<p>OSRR > 18 dB for $P_{RN} = 0$ dBm: OSRR = 23.5 dB improvement > 17 dB</p> <p>for launched power levels of 0 dBm and below, a BER of 10^{-10} can be reached with a penalty < 3 dB</p>	<p>high without noise accumulation: 36 dB for $P_{RN} = 5$ dBm 32.3 dB for $P_{RN} = 0$ dBm 29.2 dB for $P_{RN} = -5$ dBm</p> <p>degradation due to noise accumulation: 3.3 dB for $P_{RN} = 5$ dBm 3dB for $P_{RN} = 0$ dBm 2.4 for $P_{RN} = -5$ dBm</p>	<p>patterning in the SOA reduced due to gain clamping with the seed loop, penalty reduced to 0.7 dB</p> <p>launched power can be in the range of 0 to -5 dBm, therefore pump reduction for drop amplification is expected</p>

Table 6.2. Performance evaluation for the standard and the modified PON, the latter featuring partially transparent power splitting.

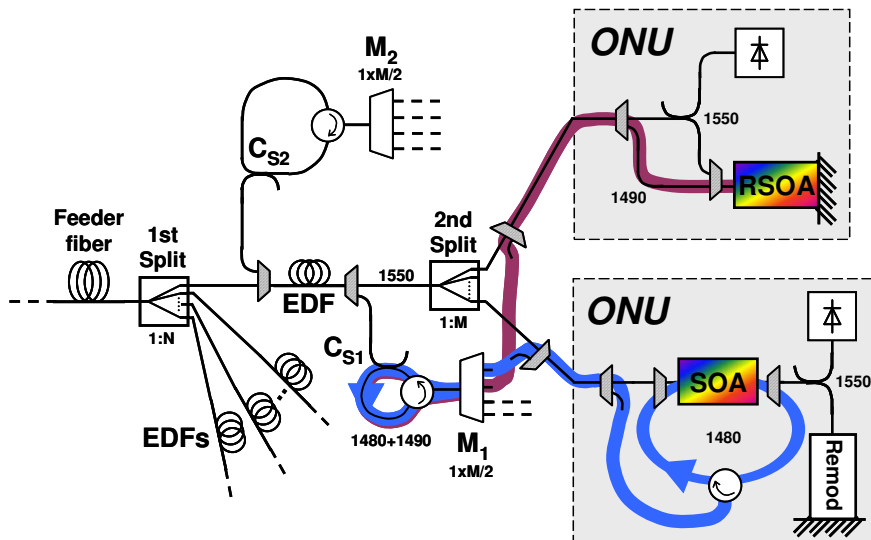


Fig. 6.24. Scheme of the optically noise-powered extender box, placed between the two tree splitting stages with split 1:N and 1:M. The seeding mechanism can rely on a SOA or a RSOA inside the ONU.

6.3.3 Scenario 1: Reflective ONU based on SOA and REAM

The transmission performance of a self-pumped PON was first assessed with an ONU implementation that contains a transmitter that is based on a SOA and a REAM [220]. Focus is given only on the upstream transmission although full-duplex transmission could be easily obtained by adding a downstream signal on a separate wavelength in another waveband.

The experimental setup of the hybrid PON, shown in Fig. 6.25, corresponds to a tree-like architecture in which a 1x40 AWG with a channel spacing of 100 GHz is preceding a dual-stage power splitter with an overall split of $N \times M = 32$. This dense PON is therefore capable of serving more than 1200 customers. In addition a dual SMF trunk of 25 km length is placed between the OLT and the AWG, and the tree splitter is connected to the AWG via a 10 km long feeder SMF. RB effects are therefore considered for the TDM segment after the AWG.

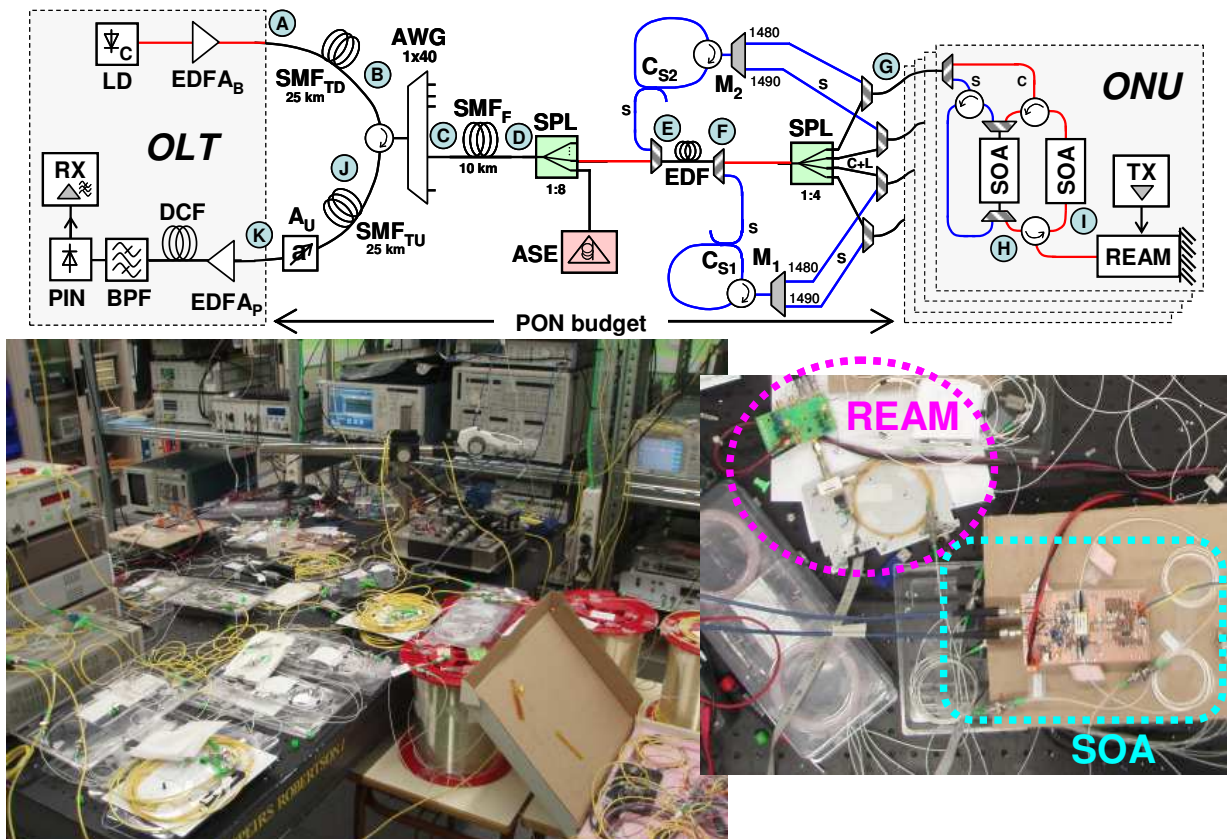


Fig. 6.25. PON architecture with dual-stage power splitter including an intermediate EDF amplifier, pumped via the ASE output of the SOA+REAM based ONU.

An unmodulated optical carrier at 1559.6 nm is transmitted from the OLT towards the ONU, where the upstream data is continuously imprinted via the REAM, using a data rate of 10 Gb/s and a PRBS with length $2^{31}-1$. Upstream reception at the OLT occurs with a PIN diode that is placed after an EDFA preamplifier with a noise figure of 4.7 dB and a 200 GHz band-pass filter. A DCF with a dispersion of -671 ps/nm compensates

for the pulse broadening along several fiber spans, which is pronounced due to the chirp of the REAM.

Since the REAM is subject to high intrinsic losses of ~ 16 dB, SOAs are placed at the ONU to act as preamplifier and booster. Since a single integrated SOA+REAM device with high saturation output power was not available, this configuration with a dual SOA was chosen to avoid cross-gain modulation between the outgoing REAM signal and the incident unmodulated optical carrier.

The preamplifier-SOA is not only intended to level the received optical carrier but also to seed the EDF pump in the 1480 nm waveband. The giant seed loop is spanned as explained previously and contains a 1x2 pump multiplexer for the 1480 and the 1490 nm wavelength. These spectral pump windows are compatible with the 15 m long HE980 EDF, which was inserted between the 1:8 and 1:4 splitting stage. Due to a limited availability of components, the EDF pumps of the three other ONUs that contribute to the overall pump seed were emulated by laser diodes that were set to the obtained pump power values of the shaped ASE from the other three ONUs.

The spectra of the seeded pumps for both channels are shown in Fig. 6.26(a) for the case that a single ONU is seeding in one of these channels. The spectra are thereby located at the maximum overlap between the ASE spectrum of the SOA, which has a maximum at 1492 nm, and the transmission of the pump channels. A shift of the nominal pump wavelengths is therefore given. Besides, the pump spectrum is tilted towards longer wavelengths due to the chirp of the SOA [214].

The shared SOA gain medium for the shaped ASE and the upstream carrier lead to a reduction of the EDF pump once the power of the upstream carrier increases. However, for reasonable input values below -12 dBm for the carrier, there is no significant reduction for the pump, as can be seen in Fig. 6.26(b). Power values of 6.4 and 5.9 dBm can be obtained in the 1480 and 1490 nm channel, respectively.

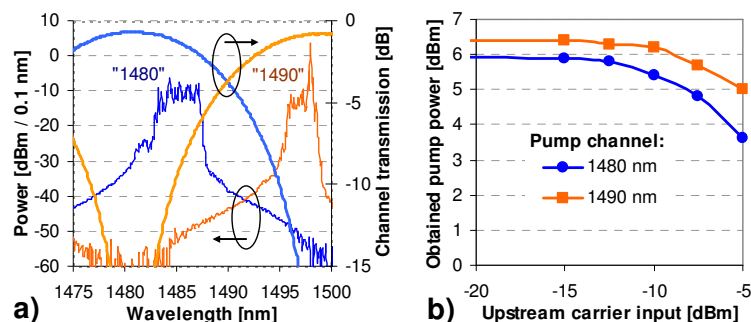


Fig. 6.26. (a) Spectra of the injected EDF pumps that can be obtained in one of the channels by a single ONU and (b) delivered pump power for different power values of the received upstream carrier.

For these pumps, the EDF provides a gain of 8.9 and 10 dB for the unmodulated carrier and the modulated upstream signal, and reduces the net splitting loss of the 1:32 splitter to just 6.6 and 5.5 dB, respectively.

The evolution of the power levels for down- and upstream is shown in Fig. 6.27 together with the OSNRs for the upstream. Three different power levels of $P_{TX} = 4, 7$

and 10 dBm have been considered for the launched upstream carrier (A). For a launch of 7 dBm the power levels and OSNRs are -8.2 dBm and 53.3 dB at the input of the power splitter (D) and -14.8 dBm and 33.2 dB at its output (G) when reaching the ONU. While a stronger launch of 10 dBm does not benefit from additional output power at the EDF, the OSNR of a weaker launch of 4 dBm is additionally degraded. The strong OSNR degradation to 23.1 dB for a launch of 7 dBm at the booster SOA (I-G) is caused by the high intrinsic loss of the REAM (H-I) that was 16.8 dB. However, the net gain of the ONU (G-H-I-G) is 8.1 dB. On the return path, the signal reaches the power splitter (G) with -6.7 dBm and the feeder fiber (D) with -12 dBm and an OSNR of 22.1 dB, already considering the noise accumulation from other EDFs. The signal arrives with -26.3 dBm at the OLT receiver and sets the available power for upstream reception. For a weak launch of 4 dBm not only the received power is lower with -30 dBm, but also the OSNR is reduced to 19.2 dB.

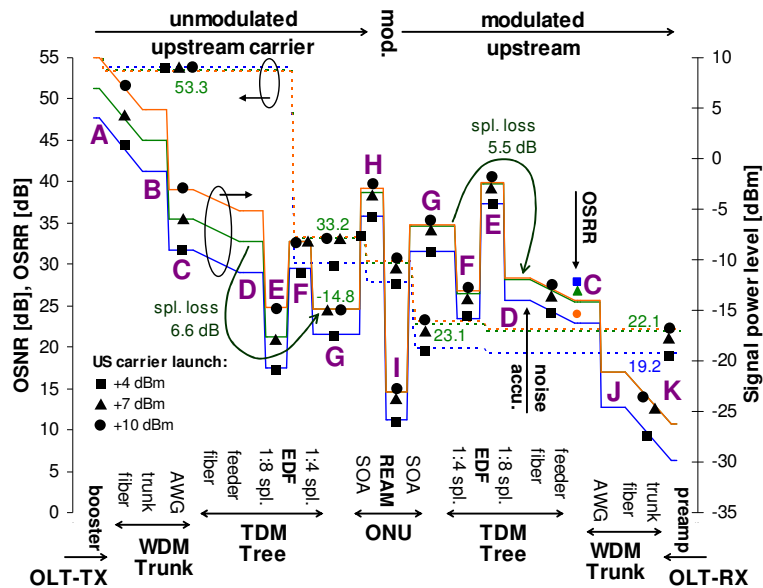


Fig. 6.27. Signal evolution for three different launches of the upstream carrier.

The OSRR at the feeder fiber (C) is 26.8 and 24 dB for a launch of 7 and 10 dBm, respectively. The OSRR contribution from the EDF was 28.7 dB and therefore not dominant due to the high loss of the first splitter (i.e. the low EDF input power).

The high loss budget of the PON restricts to reach low BER values of 10^{-10} for launched upstream carriers of 4 and 10 dBm. This is caused by error floors which derive from the low OSNR and the RB in the feeder fiber, respectively. However, for the optimum launch of 7 dBm a BER of 10^{-10} can be reached. The power margin is then 1 dB and could be increased to 7.7 dB with the incorporation of FEC.

Note that if the EDF-based extender box inside the splitter is removed, the high loss budget prevents data transmission due to a low received upstream signal power level below -40 dBm and/or a low OSNR and OSRR, even at the FEC level.

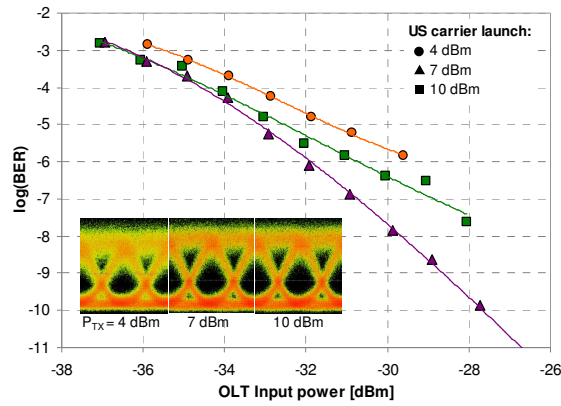


Fig. 6.28. BER measurements for different upstream carrier launches.

6.3.4 Scenario 2: ONU based on Gated EML

In the second case study the reflective transmitter of the ONU is replaced by a laser diode that was integrated together with an EAM [21]. Especially for high splitting ratios such an approach is common [20,221]. Together with a booster SOA this allows to launch a powerful upstream signal from the ONU, which does not suffer from OSNR degradation due to modulation of an already noisy optical carrier as in the previous scenario. However, a degradation can be given for high splitting ratios if the pass-through loss of the SOA is not high enough in its off-state since residual power from the EMLs across the tree will then cause crosstalk [222].

The investigation aims at achieving high splitting ratios by investigating the best combination between the first split N and the second split M at the tree segment. The PON is therefore reduced to a TDM tree without WDM segment (Fig. 6.29).

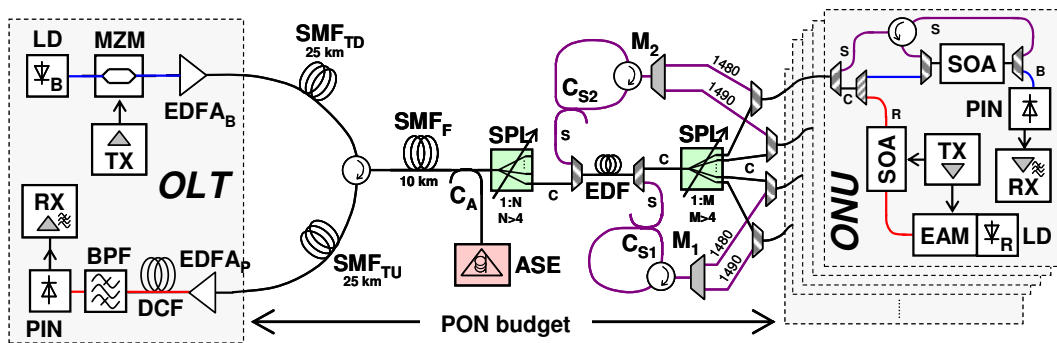


Fig. 6.29. Self-pumped PON with an ONU transmitter based on a gated EML.

The 10 Gb/s downstream is provided at 1531.9 nm via a MZM while the 10 Gb/s burst-mode upstream was transmitted at 1548.22 nm with a GPON-compatible 125 μ s frame and a duty cycle of 1:4. A PRBS of length $2^{31}-1$ was chosen for both data streams. Separation of down- and upstream is therefore possible with red/blue splitters inside the C-band. The same OLT receiver and the same EDF as in the previous scenario were used.

Since the booster-SOA at the ONU is intended to be gated for burst-mode transmission, it is not possible to reuse it for seeding a pump. Instead, the ONU receiver

is implemented by a combination of SOA+PIN diode that substitutes the typically used APD. The SOA had a noise figure of 8.9 dB, and the optical reception bandwidth for the PIN diode was 20 nm. The seed loop is spanned in a similar way over the ONU while at the second splitting stage just four ONUs are connected. The obtained pumps at 1480 and 1490 nm are similar to the ones reported previously. With power levels for the received downstream below -15 dBm, there is also no significant degradation for the pump seed due to the shared SOA gain medium, as can be seen in Fig. 6.30.

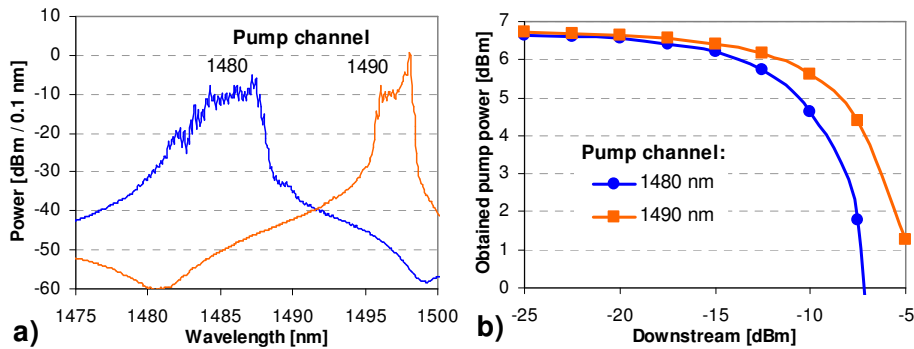


Fig. 6.30. (a) Seeded pumps injected into the EDF and (b) impact of the received downstream on the pump power.

The obtained EDF gain is shown in Fig. 6.31 for different split combinations. Since the upstream arrives strong at the EDF for a low second split M , it sets the saturation point and clamps the gain, which is also low in this case. The gain of the weaker downstream is then quite independent of the first split N . Just for the case that the first split N is very low and the second split M is high at the same time, the downstream has significant influence on the upstream gain. Note that the upstream gain is slightly higher due to the burst-mode transmission and the resulting EDF gain transients since the chosen packet length of 31.5 μ s is small enough to still have some excess gain of ~ 0.5 dB at the end of the packet (Fig. 6.32) while no severe asymmetries have been observed in the eye. There was no visible patterning of the continuous-mode downstream due to the bursty upstream traffic.

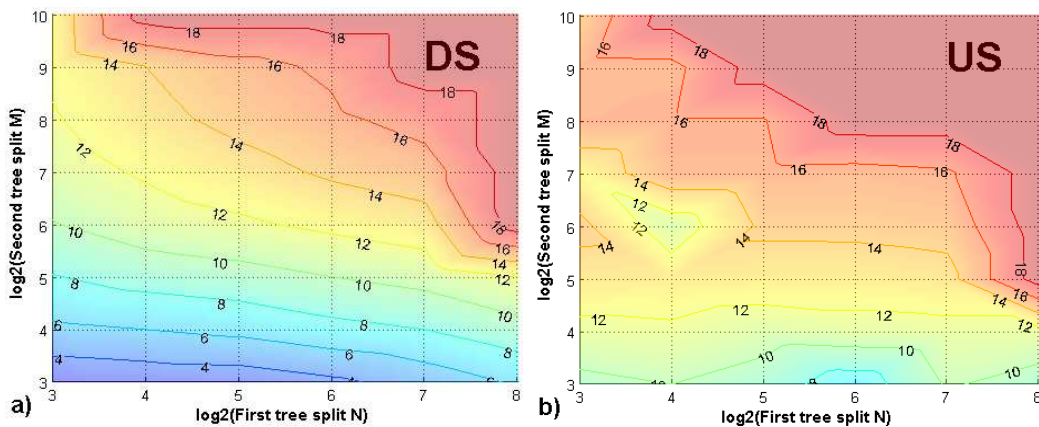


Fig. 6.31. EDF gain provided for (a) the downstream at 1531.9 nm and (b) the upstream at 1548.22 nm. The values for the iso-gain curves are shown in Decibels.

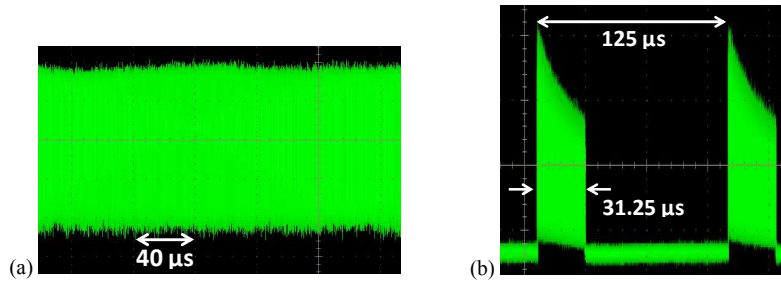


Fig. 6.32. (a) Continuous-mode downstream and (b) burst-mode upstream signal for a split combination of $N \times M = 16 \times 64$.

For the BER contour measurements, the two splitting ratios $1:M$ and $1:N$ were emulated with variable attenuators, whereby a excess loss of 0.5 dB for each splitting stage was considered. The splitting loss for each attenuator was independently increased in steps of 3 dB (i.e. a doubling the splitting ratio). An important measure to explain the BER is the OSNR, which is shown in Fig. 6.33(b) and 6.33(d) for the upstream.

The downstream BER, presented in Fig. 6.33(a), shows a strong tilt in its iso-BER curves. This is caused by the OSNR degradation in the EDF between the splitting stages. For a certain split N (e.g. 32) the second split M does not cause additional penalties unless it reaches higher values (e.g. 128), meaning a further OSNR degradation due to the SOA in ONU receiver. An overall 1:4k split is possible for a downstream BER of 10^{-10} for $N \times M = 16 \times 256$. Preferring higher second splits, a PON split of 1:2k is possible for a series of split combinations. The total split can be extended to 1:8k ($N \times M = 16 \times 512, 32 \times 256, 64 \times 128$) with FEC.

The iso-BER curves of the burst-mode upstream without noise accumulation across the tree are following the iso-split of the PON if there is no ASE accumulation at the first splitting stage (Fig. 6.33(c)). This can be explained by the quite constant upstream gain which is independent of the first split N , leading in turn to a low upstream OSNR for a high total split regardless of the split combination $N \times M$ (Fig. 6.33(b)). BER values of 10^{-10} can be obtained for a total split of 1:4k, preferring equal splits. The total split can be raised to 1:8k for additional FEC.

Including the influence of ASE accumulation, the OSNR worsens for higher first splits N so that a split $M > N$ is preferred (Fig. 6.33(d)). This means not only less employed EDFAs in the fiber plant but leads to a more distributed amplification scheme at the same time. The iso-BER curves for the upstream, shown in Fig. 6.33(e), follow this OSNR degradation and are shifted towards a reduced total split. Nevertheless, reception at a BER of 10^{-10} can be obtained for an overall split of 1:1k for not too high first splits ($N \times M = 8 \times 128, 16 \times 64, 32 \times 32, 64 \times 16$), while a total split of 1:4k can be achieved with the help of FEC, preferably for higher second splits ($N \times M = 8 \times 512, 16 \times 256, 32 \times 128, 64 \times 64$).

The continuous-mode upstream performs slightly worse compared to its burst-mode operation. Fig. 6.33(f) shows the continuous-mode BER contour for the case of noise accumulation. The difference is obvious for iso-split combinations with low second split M since then the upstream arrives strong at the EDF and experiences an enhanced gain transient due to saturation of the EDF. Total splits of 1:1k are then limited to a much

smaller set of compatible split combinations ($N \times M = 8 \times 128, 16 \times 64$), while FEC can still provide overall splits up to 1:4k ($N \times M = 8 \times 512, 16 \times 256, 32 \times 128$). The reason for this difference is the build-up of EDF gain during the idle time when no data packet is present in the TDM frame. In a realistic network, packets from other ONUs would fill up these unused time slots so that the overshoots are not experienced in the same way and a behavior interpolated between the results of Fig. 6.33(e-f) would be expected.

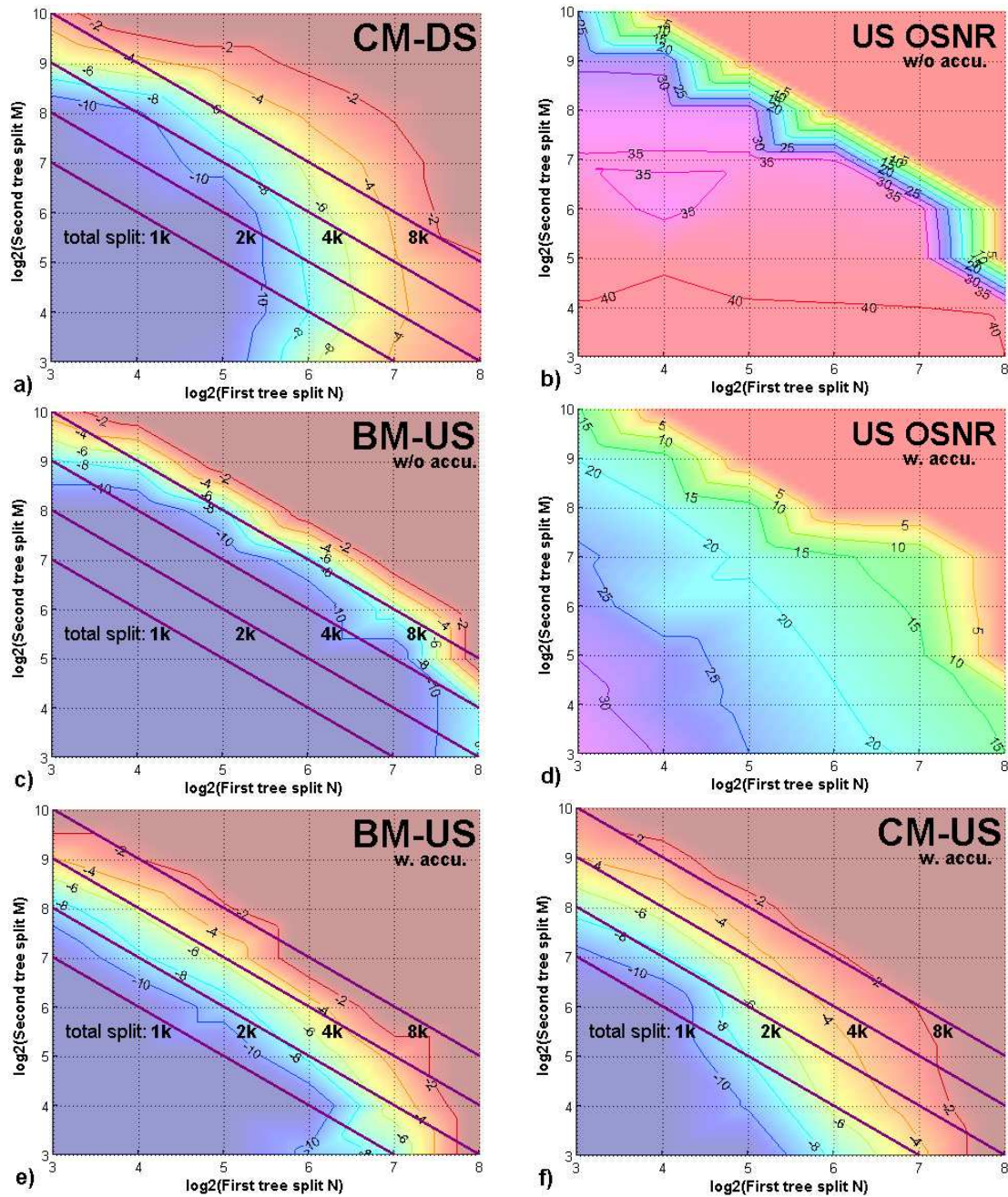


Fig. 6.33. BER and OSNR contours for different splitting ratios M and N . (a) Continuous-mode (CM) downstream BER, (b) upstream OSNR without noise accumulation, (c) burst-mode (BM) upstream BER without noise accumulation, (d) upstream OSNR with noise accumulation, (e) burst-mode upstream BER with noise accumulation and (f) continuous-mode upstream BER with noise accumulation.

N \ M	8	16	32	64	128	256	512
8	US	US	US	US FEC			
16	US	US	US	US	US FEC		
32	US	US	US	US FEC	US FEC	DS	
64	US	US	US FEC	US FEC			
128	US	US FEC	US FEC	DS			
256	US FEC	US FEC	DS				
512	US FEC	DS					

Table 6.3. Compatible splitting ratios respecting noise accumulation. The green, orange and blue colour represent transmission without upstream FEC, with upstream FEC and the case of solely downstream reception.

Considering full-duplex transmission, the maximum split is limited by the upstream reception, allowing a PON split of 1:1k at a BER of 10^{-10} ($N \times M = 8 \times 128, 16 \times 64, 32 \times 32$) and 1:4k with FEC ($N \times M = 8 \times 512, 16 \times 256, 32 \times 128, 64 \times 64$). Although these high splits limit the guaranteed bandwidth per user, it shows that a high customer density of PONs is not restricted by the split, making such PONs attractive for very short reaches with increased data rates.

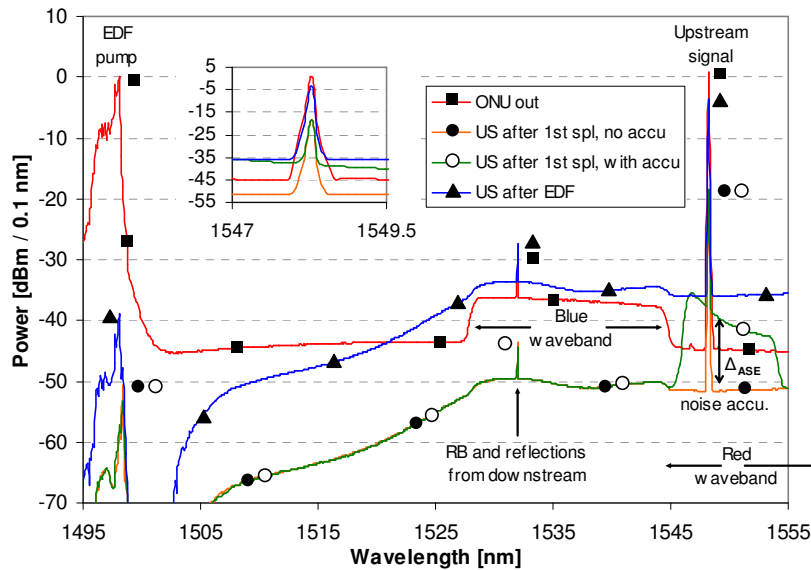


Fig. 6.34. Spectra of the upstream signals along the PON. The power level of the upstream data signal corresponds to its burst-mode duty cycle of 1:4.

The particular case of $N \times M = 16 \times 64$ is chosen among the error-free iso-split configurations to avoid strong noise accumulation and further analyzed in its power margins. This PON has a loss budget of 39.5 dB, which is far beyond the GPON class C++ or 10G PON Extended Class.

Fig. 6.34 presents the spectra in upstream direction at different locations inside the PON for this split combination. The signal at the ONU output consists of the EDF pump and the burst-mode upstream. The background at the (blue) downstream waveband is

caused by the C-band ASE emission of the SOA, while the artifacts at the downstream wavelength stem from an amplified reflection in the ONU and later, on the way to the OLT, also from RB. The noise accumulation, marked as Δ_{ASE} , causes an OSNR degradation of ~ 12 dB for the upstream.

For the downstream (Fig. 6.35(a)) no degradation has been experienced due to the bidirectional amplification of the continuous down- and the burst-mode upstream in the common EDF at the tree splitter. The difference of ~ 0.1 dB in the sensitivity at a low BER of 10^{-10} proves an unpatterned and therefore flat envelope of the downstream as it is also obvious from Fig. 6.32(a). The power margin at this BER is 3.4 dB and could be increased to 7.8 dB with FEC.

The upstream that was measured in continuous- and in burst-mode is shown in Fig. 6.35(b). Without noise accumulation at the first splitting stage the burst-mode transmission benefits from the gain overshoots of the EDF and has a 1.7 dB better sensitivity at a BER of 10^{-10} when compared to a continuous data stream. When noise accumulation is taken into account an error floor appears in continuous mode while a BER of 10^{-10} can still be reached in burst-mode, though a penalty of 2.1 dB is suffered. The power margin is then 5.4 dB and can be increased to 11.6 dB with FEC.

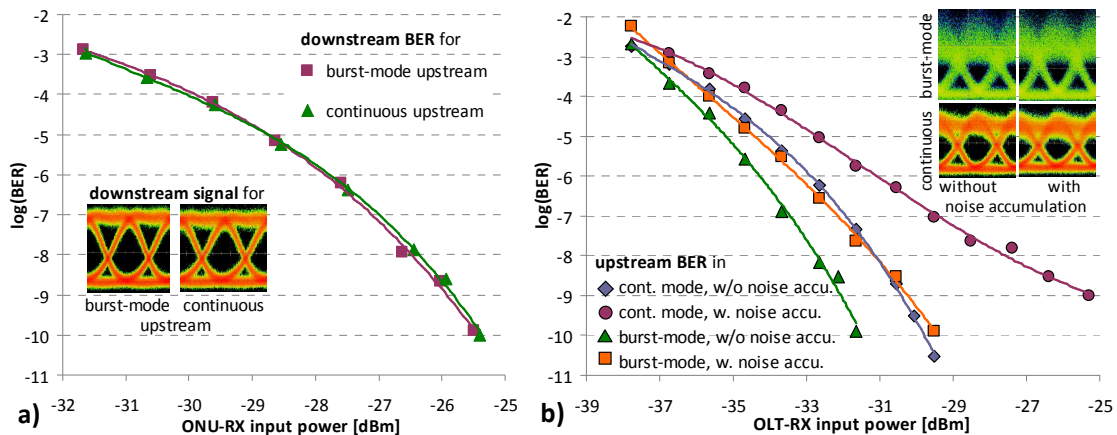


Fig. 6.35. (a) Down- and (b) upstream BER measurements for a PON with a split of 16x64.

Finally, the pump delivery for a realistic deployment scenario with a split $M \gg 4$ will be assessed. This means that just a small percentage of ONUs of Fig. 6.29 is required to provide the EDF pump for the overall number of M ONUs connected to this second splitting stage. If the ONUs are bounded by their operational aspect and not disconnected from the tree, arbitrary ONUs can be used to generate this pump. On the contrary, if ONUs are not supposed to be permanently part of the access network since it is left to the customer to decide its connectivity, the seed loop has to be slightly modified. Unfortunately, the simplest approach of employing a pump multiplexer with $M/2$ seed channels fails since the sliced ASE that is provided as feedback to the SOA is not strong enough for narrow pump channels. This is obvious when looking at the analytical requirement for the establishment of the pump that can be derived from the common lasing condition. The gain G of the SOA, which depends on the downstream power level P_{DS} has to be large enough to compensate not only for the accumulated seed

loop losses L_{SL} during the round-trip of the ASE but also for the slicing losses ξ in the pump multiplexer, where most of the ASE emission of the SOA is rejected during the lasing onset. For a certain pump at wavelength λ_p , this seeding condition is

$$\xi \frac{G(\lambda_p, P_{DS})}{L_{SL}} > 1 \quad \xi < 2 \frac{\delta\Lambda}{\delta A} \quad (6.8)$$

The slicing losses are thereby determined as the ratio between the channel width $\delta\Lambda$ of the pump multiplexer and the typically much larger 3-dB bandwidth δA of the ASE spectrum of the SOA that falls in a suitable pump wavelength range. The factor 2 is included to account the reduced ASE emission at the 3-dB border of the emission spectrum. Since the SOA at the ONU receiver had a small signal gain of >22 dB and an ASE bandwidth δA of 38 nm, the pump channels that were 10 nm broad could be reduced to multiplex at least 4 pump wavelengths. This would in turn not only provide a stronger pump to the EDF but allow also placing additional drop losses between the second splitter stage and the ONU.

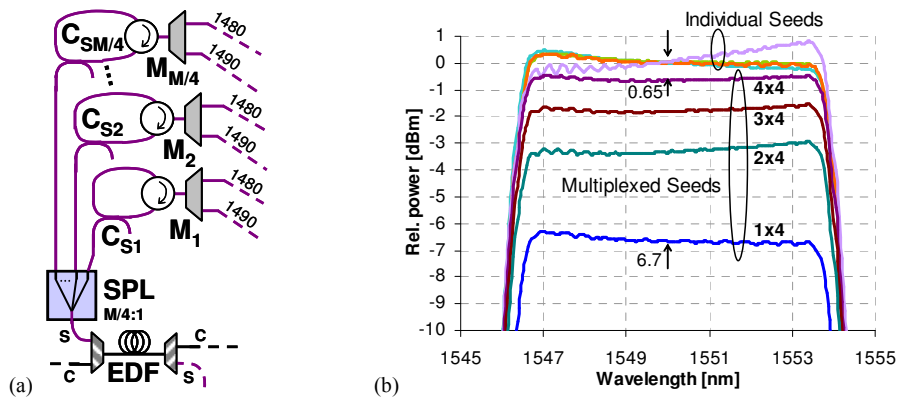


Fig. 6.36. (a) Resilient pump multiplexing in the loopback of the seed loop head-end and (b) multiplexed pump seed for the resilient combination of 4 seed loops and an arbitrary seed wavelength of 1550 nm.

The alternative solution aims at the incorporation of a resiliency mechanism as it is sketched in Fig. 6.36(a). The ONUs are thereby arranged in quadruples, each of them forming a separate seed loops at both sides of the EDF. The multiplexed pumps of these loops can then be combined with $M/4 \times 1$ splitters thanks to the incoherent nature of ASE noise. It is then possible to generate a powerful pump even when a bunch of ONUs is disconnected from the tree.

Fig. 6.36(b) shows the multiplexing of 4 seeds that have been obtained with EDF-based amplifiers for the proof of this concept since there were not enough SOAs available for establishing these seeds at 1480 nm. The individual seeds from the 4 different loops have the same magnitude at their center wavelength of 1550 nm. The relative power is further defined at this center wavelength. As can be seen, a loss of 6.7 dB is experienced when passing a single seed through the 4×1 splitter that acts as resiliency coupler to combine the particular seeds. By adding the three other seeds, the combined seed shows a power loss of just 0.65 dB, which corresponds to the excess loss of the 4×1 splitter – as it was also experienced by the single seed considering the

theoretical splitting loss of 6 dB. The excess loss would have to be further minimized to avoid deficiency for the pump due to the introduction of the resiliency mechanism [223].

With a power margin Π between the obtained multiplexed pump seed and the required EDF pump for sufficient amplification, and an excess loss ε for the resiliency coupler, the maximum allowed number μ of disconnected ONUs at the second splitting stage with split M is determined by

$$\mu = M \left(1 - 10^{-\frac{\Pi - \varepsilon}{10}} \right) \quad \mu \ll M \quad (6.9)$$

where Π and ε are given in Decibels. For a second split $M = 64$, a margin of 1 dB and an excess loss 0.5 dB, correct operation can be guaranteed for a drop of up to 7 ONUs.

6.3.5 Scenario 3: ONU based on a RSOA

In the third and last case study the ONU transmitter is reduced to a single RSOA, which is advantageously used for data signal remodulation and EDF pump generation [24].

The PON architecture, shown in Fig. 6.37, corresponds to the one that was also used in the first scenario but with a swapped splitting ratio N and M for the first and second splitter, respectively. This is motivated by the expected lower pump output from the ONU, requiring a larger number of pump wavelengths and therefore a higher splitting ratio in the second stage. Down- and upstream are continuously modulated at 10 Gb/s on a single wavelength in the L-band. The OLT receiver was slightly altered by using an APD instead of the PIN diode.

The downstream, whose ER is reduced, is split by a 50/50 coupler (C_0) at the ONU and remodulated by the RSOA that is identical with the one characterized in chapter III.5. The gain spectrum of this RSOA provides not only the possibility to amplify a L-band data signal but also to seed a pump at 1540 nm. This in turn is compatible with e.g. a 50 m long C-band HE980 EDF amplifier that can offer also amplification over a wide wavelength range in the L-band when being pumped around 1540 nm [224]. The shaped ASE in the C-band is bypassed around the C_0 splitter with C/L waveband couplers not to suffer from additional loss in the seed loop. For a practical implementation with burst-mode traffic a switchable loss-element (S_0), which could be also implemented by a cheap attenuator, would have to be inserted in the ONU at the data signal path between the C_0 coupler and the RSOA. Otherwise all inactive ONUs would also amplify and reflect the incident downstream signal towards the tree, causing severe crosstalk for the upstream signal of the active ONU.

The 1x4 multiplexers M_1 and M_2 in the optical distribution network had a bandwidth of 200 GHz for each of the four channels that were located at 1538.19, 1539.77, 1541.35 and 1542.94 nm (Fig. 6.38(a)). The obtained pump levels were 4.5, 4.7, 5.0 and 5.1 dBm for a RSOA bias of 200 mA (inactive ONU), and 2.2, 2.7, 3.1, and 3.3 dBm for

a bias of 120 mA that is used for data modulation. The RSOA gain for the data signal at 1585 nm was 22.5 dB for an input power of -20 dBm, while a pump was seeded in addition.

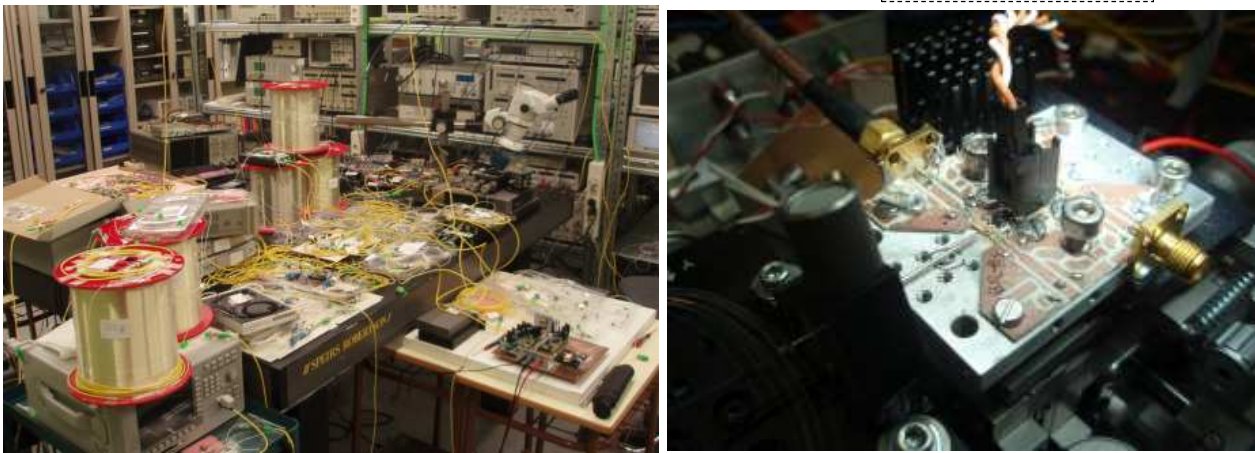
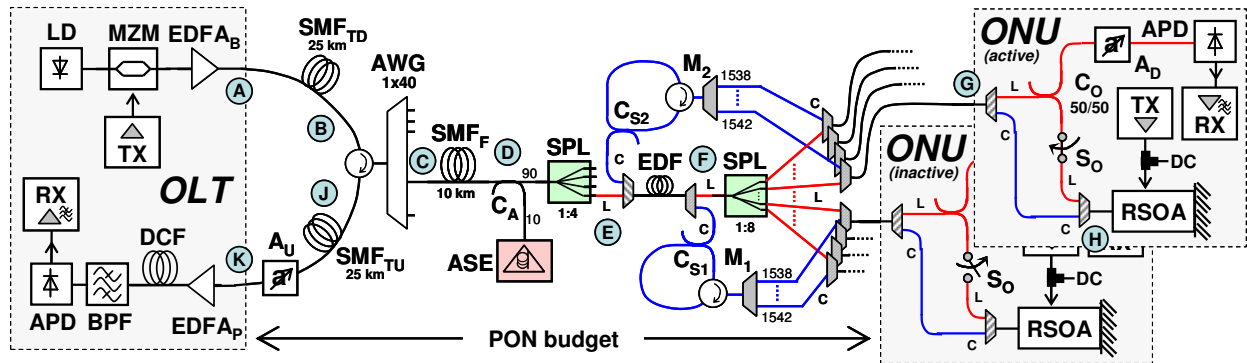


Fig. 6.37. Self-pumped PON with RSOA-based ONUs and wavelength reuse. The L-band data signals are amplified by an EDF that is pumped in the C-band.

Fig. 6.38(b) shows the obtained EDF gain at 1585 nm and the OSNR for the case of unidirectional amplification. Different signal and pump power levels were measured at different pump wavelengths. For a pump power in the range of the multiplexed pump seeds, a gain of ~10 dB quite independent of the pump wavelength can be achieved. The obtained OSNR values correspond to a noise figure of ~6 dB.

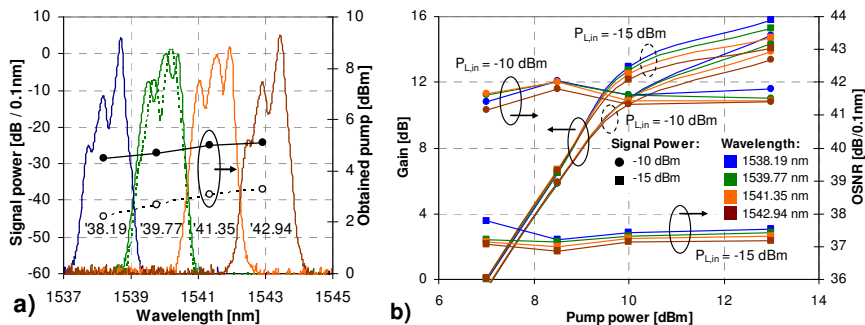


Fig. 6.38. (a) Seeded pumps (the solid line represents inactive ONUs while the dashed line indicates active ONUs regarding the TDM-based upstream transmission) and (b) EDF gain at 1585 nm and OSNR for unidirectional amplification.

With the reduction of the net 1:32 splitting loss from 15.8 dB to just 5 dB, the self-pumped PON allows full-duplex transmission even with reflective ONUs based on RSOAs. The gain provided by the EDF stage inside the power splitter is evident in the evolution for the power level and the OSNR of the data signal (Fig. 6.39). The self-pumped PON significantly benefits over the standard PON (concentrated 1:32 splitter without EDF and no C/L splitters in the fiber plant and the ONU) that suffers from a low input power into the ONU. This causes not only a severe OSNR degradation during remodulation with the RSOA but also a low OSRR for the upstream at the feeder fiber. Only with an increase in the launched power from the OLT transmitter to 10 dBm a reasonable signal of -22.7 dBm reaches the ONU receiver. However, the upstream OSRR is kept as low as 14.3 dB.

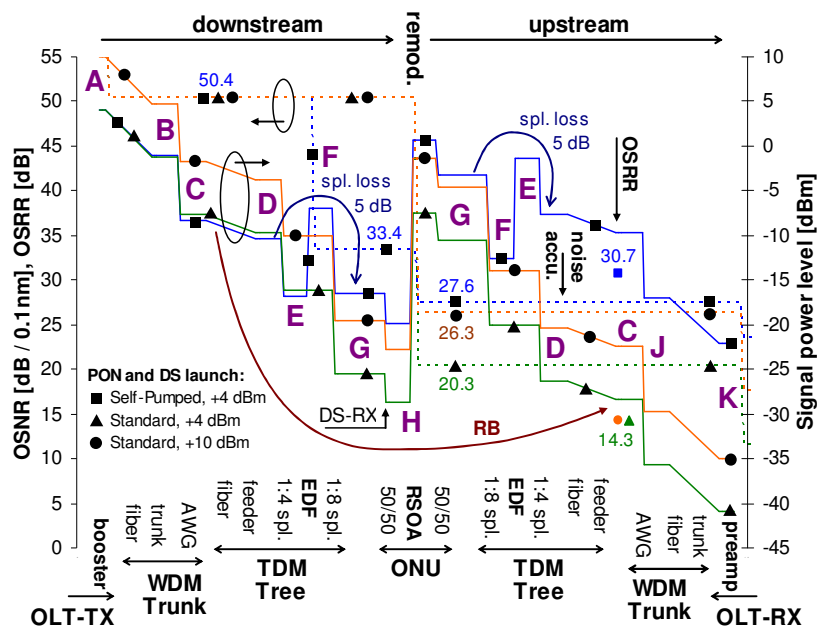


Fig. 6.39. Signal evolution for the self-pumped and the standard PON.

On the contrary, the self-pumped PON provides a strong downstream to the ONU and guarantees also a high OSRR of 30.7 dB (including RB in the EDF) while the upstream reaches the OLT with a power of -22.1 dBm and an OSNR of 27.6 dB. Note that although the downstream OSNR is 33.4 dB, the reception suffers from the fact that no ASE filter was used after the EDF, not to further increase the complexity of the optical distribution network.

Noise accumulation is negligible as it is obvious from Fig. 6.40 where the RSOA noise overcasts the noise of a single EDF stage substantially so that after the accumulation the difference in the ASE background, marked as Δ_{ASE} , is larger than 6 dB.

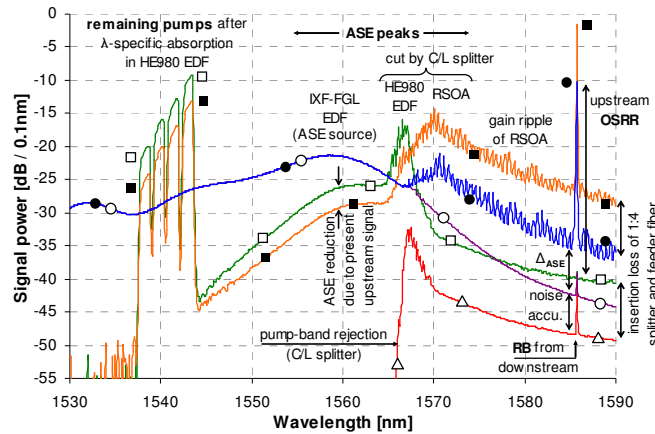


Fig. 6.40. Upstream spectra after amplification with a single EDF stage (■) and after the feeder fiber without (▲) and with noise accumulation (●). Blank markers indicate inactive ONU while filled markers correspond to active ONUs.

The BER measurements are shown in Fig. 6.41 and the corresponding penalties and power margins are presented in Fig. 6.42. The downstream is constrained by the unfiltered ASE background of the EDF though a sensitivity of -22.8 dBm at a BER of 10^{-10} can be still provided with standard APD receiver for a data rate of 10 Gb/s and an ER > 10 dB. For an ER of 3 dB an expected penalty of 5.4 dB is suffered over an ER of >10 dB at the FEC level, leaving a power margin of 1.4 dB.

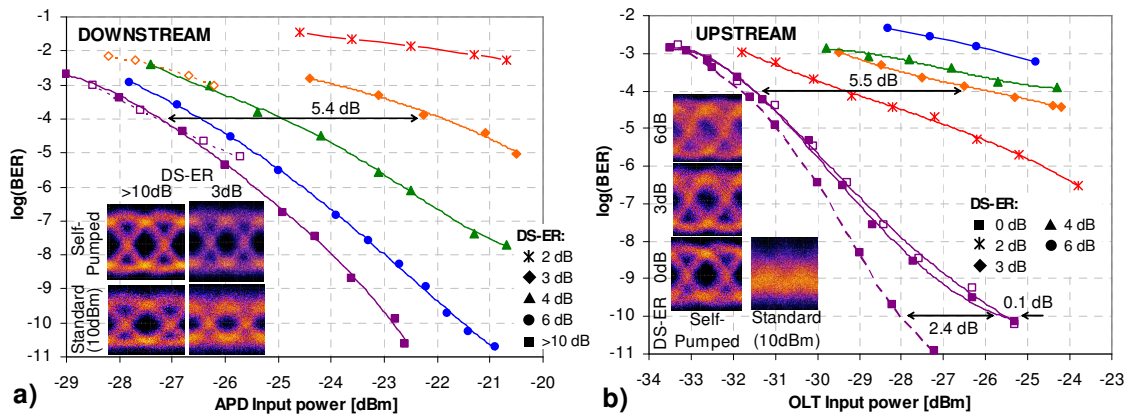


Fig. 6.41. BER measurements for (a) the downstream (solid lines: self-pumped PON, dashed lines: standard PON) and (b) the upstream (solid lines: PRBS length $2^{31}-1$, dashed lines: PRBS length 2^7-1 , filled markers indicate a present feeder fiber and hollow markers the case where the feeder fiber is replaced by equivalent attenuation).

The upstream of the self-pumped PON suffers from error floors that are introduced from the present downstream pattern, which is only suppressed by the optical gain saturation effect of the RSOA. Better performance could be achieved by incorporating additional downstream cancellation techniques as discussed in chapter IV. However, transmission is possible with FEC, having a penalty of 5.5 dB over the downstream-less case and a margin of 2.2 dB. The replacement of the feeder fiber with equivalent attenuation did not enhance the upstream performance – even at low BERs, – proving that the downstream crosstalk is the dominant impairment and more critical than RB.

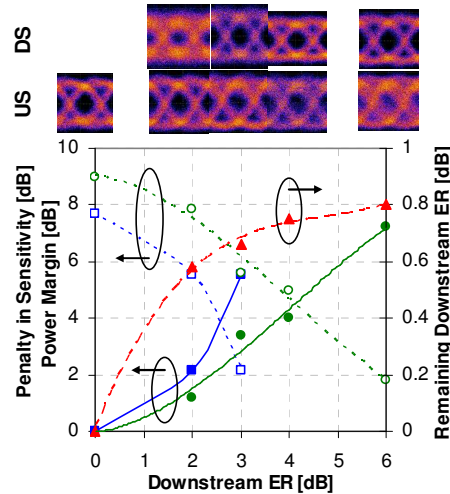


Fig. 6.42. Penalties (solid lines) and power margins (dashed lines) for the upstream transmission and remaining downstream ER. The \bullet and \blacksquare marker corresponds to a FEC threshold of 10^{-3} and 10^{-4} , respectively. The penalties for downstream (DS) and upstream (US) are referenced to downstream ERs of >10 and 0 dB.

The demonstrated PON allows to serve >1000 customers with full-duplex transmission at 10 Gb/s over loss budgets equivalent to the GPON class C or NG-PON class PR30, considering the signal launch from OLT and ONU and the reception sensitivities for down- and upstream, the seeding condition of the RSOA and the nominal power splitter loss.

6.3.6 Comparison with Other Amplification Schemes

The energy efficiency of the proposed ASE-powered extender box can be assessed with a simple approach similar to [13] or [26]. Comparing the additional required power at the ONU to seed the EDF pump, the difference to a standard ONU design is mainly found in the continuous gating of a SOA that is originally intended to be switched in burst-mode (scenarios 1 and 3). However, looking at the power-hungry 10 Gb/s electronics at the ONU that are used for higher layer functionalities and also the modulator driver for the high frequency data signals, this continuous SOA bias contributes just a small part of ~ 0.3 W when compared to a typical overall ONU power of 5 W [26]. Note that this contribution depends strongly on the SOA design since an overlap between the SOA gain spectrum and the pump wavelength of the EDF is required to achieve optimum energy efficiency. The semiconductor material should be therefore optimized by means of band structure engineering [91].

Considering alternative amplification schemes that deliver a pump from the OLT [8,30], or schemes where electrically-powered extender boxes or protocol terminators are located inside the fiber plant [5,225-226], the high power consumption that is needed for these added subsystems requires extra power supplies and environmental conditioning and contribute therefore with some overhead [26]. Utilizing commercial equipment that is shared among 32 users per tree, these amplification schemes

contribute with ~ 1 to 4 W/user, depending on the exact realization, and eventually raise the capital and operating expenditures due to the need for cabinets and environmental conditioning in the field.

Especially the use of electronics at remote network nodes, applied to perform network protocol translation [5], shows up with a high additional power requirement of 4 W/user. A strong reduction of this additional amount of energy consumption to just 1 W/user can be obtained by keeping the data in the optical domain, just performing optical amplification with local electrical supply [225]. However, the required pump laser diodes and their thermal conditioning prevent to reach lower power consumptions.

On the contrary, remote pumping techniques allow to centralize electrically powered equipment [8]. Considering strong commercial pumps, the required extra power per user can be found about 0.4 W for the previously presented network architectures and is therefore comparable with the proposed technique. However, it shall be noted that a remote pumping scheme from the OLT has to overcome the transmission losses once the reach of the network is extended and requires stronger pumps in such a case. Although the use of pump laser diodes at the customer premises [218] would provide a more effective pumping scheme, it is inefficient in terms of energy consumption since an extra energy overhead is introduced due to the build-up of the inversion in the pump laser diode and also due to its extra thermal cooling for the case of a discrete ONU design. This has direct impact on the energy consumption per user, which raises to additional 1.6 W since no share among multiple network customers is given.

Chapter VII

ONU Designs Supporting Higher Layer Functionality

Designs for the customer premises that ease higher layer functionalities can be beneficial. This chapter presents a method that allows multi-operability and dynamic bandwidth allocation (DBA) thanks to an ONU design that does not have a fixed but swappable detection and remodulation branch.

7.1 Introduction

Optical access solutions are not only a collection of techniques to support basic data transmission. With the widespread deployment of multimedia services new requirements for the access networks arise. Advanced functionalities to steer the burst-like delivery of huge data contents become necessary to guarantee a smooth data transmission for all users of the shared network. The mechanisms used to do so are often found at the MAC layer or even higher. Porting this added value to the physical layer can be beneficial if no significant cost and performance limitations arise.

7.2 Multi-Operability and Dynamic Bandwidth Allocation

The bursty nature of data traffic and the time-varying data rates of down- and upstream can impose a limit for the data throughput on the application layer. The content delivery of video for example favors either highly asymmetrical data rates in case of broadcasting or symmetrical rates for peer-to-peer streaming [227]. Consequently, advanced functionalities for steering the burst-like delivery of huge data contents become necessary to guarantee a smooth data transmission for all users of the shared network. The mechanisms used to do so are often found at the higher layers. Alternatively, providing this added functionality at the physical layer can be, as we will show in this paper, beneficial if no significant cost and performance limitations arise. Although approaches for dynamic bandwidth partitioning already exist, they mostly rely on a fixed physical design for the ONU and guarantee provisioning in course of the delivered data rates in time division multiplexed networks, where the data rate per

network segment is shared among a bunch of users [19]. Similarly, such an allocation scheme is also possible for dense WDM-PONs with a reduced set of optical transmitters [228].

On top of this, regulator bodies ask for unbundling and multi-operability, where services are delivered by two or more operators that share the same infrastructure [229]. This extension can be also made at the physical layer if the fiber plant itself is not amenable to unbundling, by dedicating separate wavelengths for the operators – presuming a balanced number of customers to stay efficient. The selection of the preferred operator is then in principle possible by inserting an optical filter at the ONU, however, this may not be seen as transparent enough for the user.

7.2.1 Principal Scheme

The key to transfer basic functionality from the higher to the physical layer is a symmetrical ONU design that employs a device which is capable to perform two functions (Fig. 7.1): detection of the downstream and remodulation of an optical carrier with upstream data. In both branches of the ONU, each one dedicated to one of two wavelengths as in [230], a reflective modulator performs the desired task of either detection or modulation. These basic functionalities have been particularly demonstrated for RSOA and SOA/REAM devices [201,231]. A tandem-configuration of such components inside the ONU permits advanced dual-operability and dynamic bandwidth partitioning functionalities in broadband access networks, as it will be now explained.

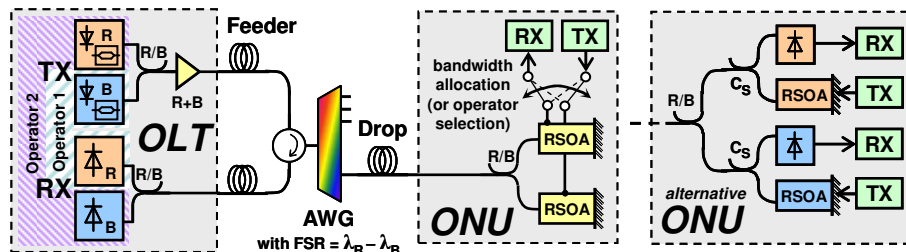


Fig. 7.1. Dual-operated PON with dynamic bandwidth partitioning. A pair of wavelengths is fed via the free spectral range property of the AWG towards the ONU that is designed with identical detector and remodulator. The alternative ONU, which duplicates its receivers and transmitters, is shown on the right.

Dual-Operability

According to the first aspect, namely the dual-operability of the access network, the two delivered wavelengths for each ONU are assigned to the two operators potentially sharing the PON infrastructure. The allocation of the optical carriers, illustrated in Fig. 7.2, is chosen so that the downstream of these operators is transmitted in the red and the blue waveband. Since a red/blue filter (R/B) acts as the separator of the detection and modulation branch inside the ONU, the two downstream signals of the particular service

operators will arrive at the different reflective modulators. Depending on which of them is biased for detection, it is possible to select the operator (i.e. the appropriate wavelength) by electrical means.

Subsequently, we specify the upstream operation. Since each ONU is fed by two wavelengths but just a single downstream, the wavelength that is assigned to the second operator that is actually not chosen for downstream transmission can be left unmodulated. At the ONU, this optical seed at the opposite waveband than the received downstream carrier, arrives at the second reflective modulator that can be operated as upstream transmitter. Accordingly, the receivers at the OLT for both operators will have the reverse wavelength allocation than the OLT transmitters. Thus, a maximum use of the available optical spectrum is obtained, as optical carriers non-operative for the downstream are used for the upstream and dual-operability does not imply halving the optical carrier availability of the WDM-PON.

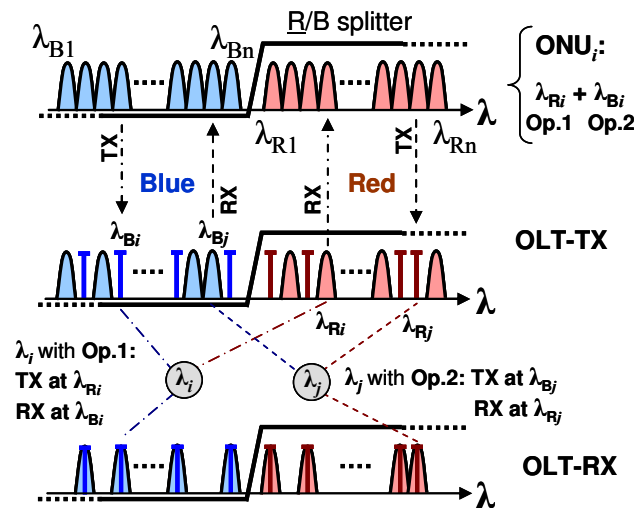


Fig. 7.2. Wavelength allocation to support dual-operability and dynamic bandwidth partitioning for n different ONUs fed by the wavelengths $\lambda_{R1} + \lambda_{B1}$ to $\lambda_{Rn} + \lambda_{Bn}$.

An example for this scheme follows. In case of ONU i that would receive the i -th pair of wavelengths at λ_{Bi} and λ_{Ri} , the user has chosen operator 1 corresponding to Fig. 7.2. As shown in Fig. 7.3(a), the inactive wavelength allocated to operator (e.g. λ_{Bi} in the blue waveband) is transmitted unmodulated at the OLT transmitter to allow the user to imprint it with upstream towards operator 1, which awaits this signal (at λ_{Bi}) at the OLT receiver.

Service operators can be now switched electrically by simply choosing the appropriate bias current of the reflective modulator while reversing the direction of the RF amplifier. In this way the dedication between down- and upstream branch (i.e. the wavebands for the reflective modulator) is swapped and operator 2 is selected, as it is sketched in Fig. 7.3(d).

An alternative approach would be a duplication of photo detector and reflective modulator at the ONU, where also a power splitter (C_S) would have to be placed in each

wavelength branch as it is illustrated in Fig. 7.1 as “alternative ONU”. This raises not only the cost but introduces also additional losses.

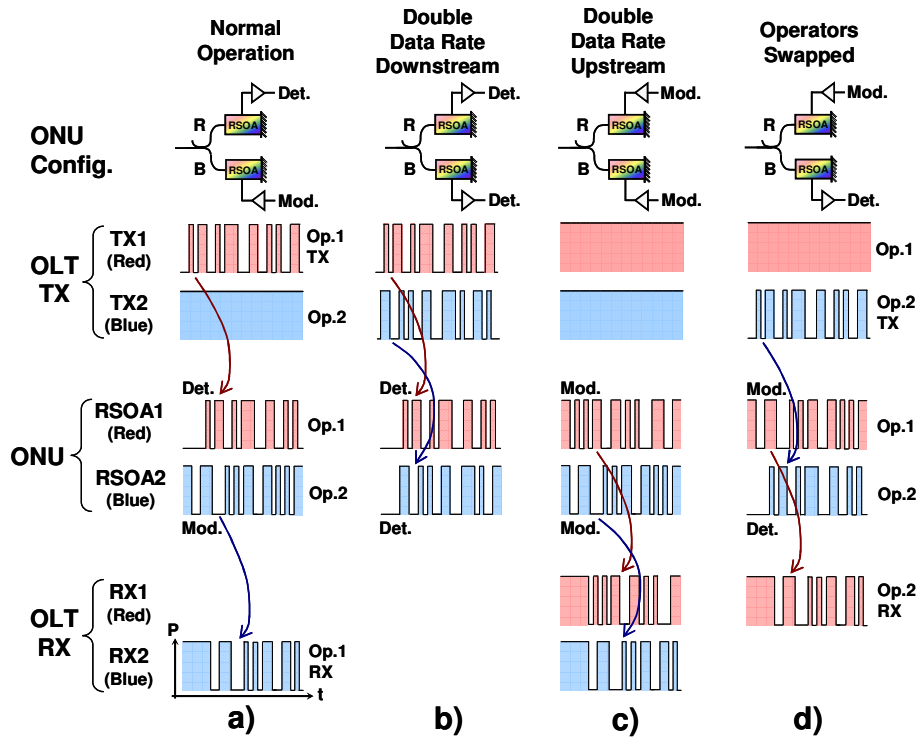


Fig. 7.3. Different modes of operation for the ONU regarding dynamic bandwidth allocation or a switch of the service operators.

Dynamic Bandwidth Allocation

Once the detector can be operated as remodulator, or vice versa, a configuration with two detectors or two remodulators is also feasible, allowing for fast and flexible electrical switching among down-/upstream transmission configurations from $0R_b/2R_b$ to $2R_b/0R_b$, where R_b is the nominal data rate for the data streams.

In the case of normal operation, corresponding to Fig. 7.3(a), the blue wavelength is remodulated at the ONU for upstream transmission. The detection and modulation bandwidth of the reflective modulators at the ONU will be in principle designed according to this data rate so that no upgrade path regarding a higher data rate per wavelength is provided. Alternatively to this normal operation mode, both wavelengths can be used for downstream detection (Fig. 7.3(b)) and upstream transmission (Fig. 7.3(c)), respectively. It is worth to note that each of the reflective modulators can be also operated in half-duplex transmission, allowing a variable upstream (or downstream) data rate between $0 R_b$ and $2 R_b$ (i.e. from 0 to 20 Gb/s for the case that $R_b = 10$ Gb/s). In such a case there is still downstream (or upstream) operation except for the extreme cases of operating the ONU with twice the nominal data rate.

This second aspect of varying the data rate in down- and upstream transmission can be advantageously used for the purpose of dynamic bandwidth partitioning. The

switching between the rates of both data streams can be in principle performed rapidly, so that the data transmission can adapt itself to the actual bandwidth demands of the end-user application.

7.2.2 Considerations for the Modulation Bandwidth

The modulation bandwidth of SOAs depends typically on the current density in the active waveguide region and the optical input power. Fig. 7.4(a) and 7.4(b) show the obtained electro-optical response for the transistor-outline packaged RSOA that was used in this work. While for bias currents around the transparency threshold just a low electro-optical bandwidth is guaranteed, values of 1.3 to 1.4 GHz can be obtained for typical bias currents (Fig. 7.4(a)). The dependence on the optical input power is less pronounced for the used RSOA. For input power values from -7.5 to -15 dBm, the electro-optical bandwidth stays around 1.4 GHz for the chosen modulation bias current of 70 mA (Fig. 7.4(b)). Transmission at higher data rates of 5 and 10 Gb/s has been demonstrated in conjunction with passive equalization [15,232]. The biasing condition for the RSOA current is then determined by a trade-off between a large modulation bandwidth and a high upstream ER.

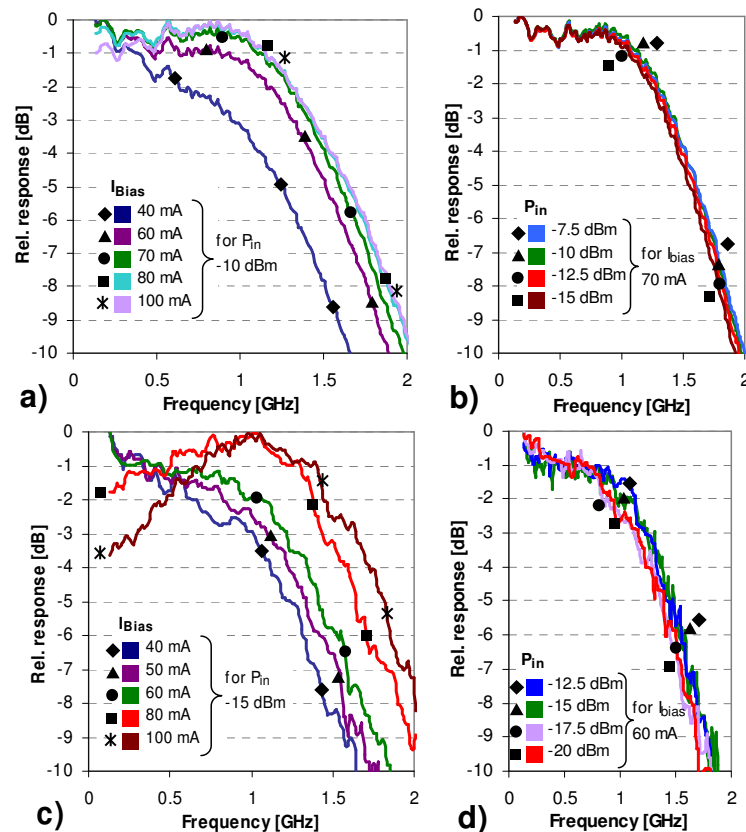


Fig. 7.4. (a), (b) Measured electro-optical modulation bandwidth and (c), (d) opto-electrical detection bandwidth of the RSOA for different bias current settings and input power levels.

In the case of the more rarely found application of a RSOA as detector, the detection bandwidth B is limited by the carrier lifetime τ_e . For a strong signal and negligible noise influence it can be found with

$$B = \frac{1}{2\pi\tau_e} \quad \tau_e = \frac{1}{L} \int_0^L \left(\frac{dR(N)}{dN} + \frac{\Gamma}{Wd} \frac{dg_m(z, N)}{dN} \Psi(z) \right)^{-1} dz \quad (7.1)$$

where L is the length of the SOA and z the coordinate inside the active waveguide in propagation direction. R is the recombination term that is determined by a series of recombination coefficients and depends on the carrier density N . Γ and Wd are the confinement factor and the cross-section area of the active waveguide, respectively, g_m is the material gain coefficient that depends indirectly on the bias current, and Ψ is the photon flux due to an incident data signal. A more detailed analysis on the detection performance of a SOA can be found in [233].

Fig. 7.4(c) and 7.4(d) present the detection bandwidth of the used RSOA for different conditions of input power and bias current. Similar as for the case of modulation, the detection bandwidth shifts to higher values with higher values for the injected bias current (Fig. 7.4(c)) and the photon density (Fig. 7.4(d)) inside the active waveguide – as it is also obvious from equation 7.1. The figure of merits that lead to the choice of the operational bias point are a high detection bandwidth and a high responsivity, the latter defined as the relation between the swing in the optical power of the input signal and the induced change in the bias current. Although a high bias current would guarantee a high detection bandwidth, the responsivity decreases when entering the saturation regime of the RSOA; Since the signal and the spontaneous noise emission share the same carrier reservoir, a present modulation in the optical input signal will cause a reduced swing in the detected photo current when compared to operation in the more linear regime [234].

In contrast to bandwidth-limited devices such as RSOAs, EAMs offer a much higher modulation and detection bandwidth. Although this kind of modulators are still bound to carrier dynamics and are therefore slower than interferometric electro-optical devices, the short device length and, consequently, the low capacitance has allowed to achieve electro-optical bandwidths of >50 GHz [170], especially with travelling-wave devices. Access applications with data rates of 10 Gb/s can easily take advantage of these well developed components without adding significant cost or bulky elements to the ONU [235].

7.2.3 Applicability to Access Networks

The feasibility of the proposed concept was assessed in terms of detection sensitivity and bandwidth requirements for the reflective modulators at the ONU. While the first will determine the compatible loss budget of the PON, the latter will have impact on the cost of the ONU. Two different kinds of reflective modulators were considered in this

work: a RSOA and a SOA/REAM, which are suitable for low and high data rate transmission at 2.5 Gb/s and up to $10\text{ Gb/s}</math>, respectively.$

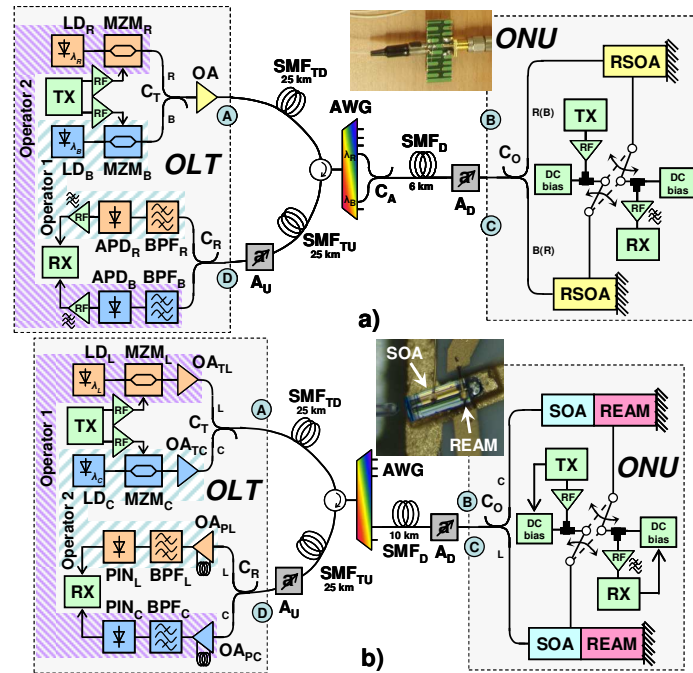


Fig. 7.5. Experimental WDM-PON setup with (a) RSOA- and (b) SOA/REAM-based ONU for the proof of the dual-operability and dynamic bandwidth allocation scheme.

RSOA as reflective modulator

In a first step, the RSOA-based ONU was included in the WDM-PON shown in Fig. 7.5(a). The wavelength pair for the ONU consisted of optical carriers in the C-band at 1546.12 nm (R) and 1535.82 nm (B), which were modulated with MZMs with high ER. Though the OLT implementation looks costly at first glance, integrated transmitters have been already demonstrated [191]. The wavelengths were then combined with a R/B coupler (C_T) that was centered at 1544 nm . A red and a blue wavelength are then recombined at each drop segment with a R/B coupler (C_A), which could be simplified with an AWG that has a specific FSR.

The RSOAs correspond to the high gain devices with a low electro-optical bandwidth of 1.2 GHz as they have been used in chapter IV.4.4. The optimum bias for the detection of the 1.25 Gb/s downstream with the RSOA was found with $\sim 60\text{ mA}$. Transmission was also analyzed for a data rate of 2.5 Gb/s in the back-to-back case, in which several fibers were replaced by their equivalent attenuation.

The signal levels and OSNRs for the red (blue) wavelength were 6 (6) dBm and 44 (42.7) dB when launched with the OLT booster (A in Fig. 7.4(a)), -8.1 (-8.7) dBm at the ONU input (B), 3.2 (1.6) dBm and 38.3 (37.8) dB after remodulation (C) and -12.9 (-14.9) dBm at the input of the OLT receiver (D). This means a net gain of 11.3 (10.3) dB for the ONU. Degradation from RB at the drop fiber span did not cause any degradation due to the carrier distributed scheme for the upstream transmission thanks

to the high gain of the RSOA: the OSRR was >40 dB. On the other hand, a high ONU net gain can cause severe RB of the amplified reflected downstream into the incident downstream signal. However, it was proven that the OSRR was >25 dB so that no significant performance degradation derives.

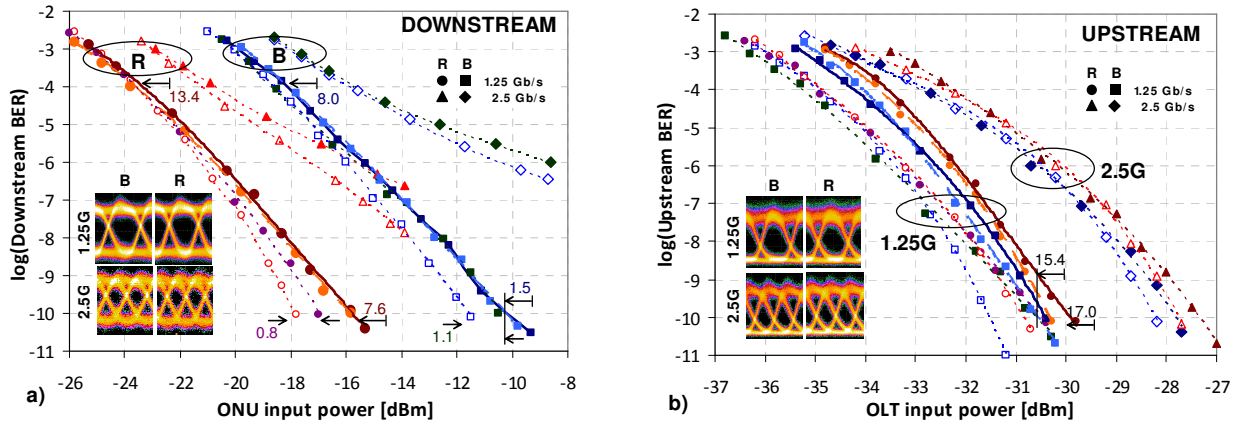


Fig. 7.6. BER measurements for (a) down- and (b) upstream. Dotted curves indicate the back-to-back case, dashed curves the presence of a feeder but no drop fiber and solid curves indicate present feeder and drop fibers. Hollow markers show results for a PRBS of length 2^7-1 while filled markers represent a PRBS of length $2^{31}-1$. Single ended arrows indicate power margins for the reception according to the delivered optical power.

The sensitivity for the downstream in the back-to-back case for the R-(B-)wavelength is -17.8 (-11.6) dBm at a BER of 10^{-10} and a PRBS of length 2^7-1 (Fig. 7.6(a)). This is reasonable for WDM-PONs and shows that the detection capability of RSOAs is sufficient good. A penalty of 0.8 (1.1) dB is given for a long PRBS of length $2^{31}-1$. When the feeder and drop segments are composed by fiber, a penalty of 0.1 (0.2) dB is introduced, showing that bidirectional transmission is not critical. The difference in the sensitivities between the red and blue band is caused by the different rejection of the opposite waveband in the R/B splitter. The crosstalk of the red into the blue wavelength was -23.4 dB and 15 dB lower for the opposite case.

The input power of the ONU was fixed to the one given by the budget in the PON for the upstream measurements (Fig. 7.6(b)). The penalty in the back-to-back case between the two PRBS lengths is 0.4 (0.9) dB at a BER of 10^{-10} . The difference in sensitivity between the red and the blue wavelength is reduced due to the additional band-pass filter used at the OLT receiver since crosstalk is then prevented. When transmitting through the fiber, the penalty over the back-to-back case is 0.4 (0.2) dB. The power margin for the downstream is 7.6 (1.5) dB and 17 (15.4) dB for the upstream.

Operation at 2.5 Gb/s suffers from reduced efficiency and an error floor in the downstream reception. However, transmission is possible at the FEC level with a penalty of 2.9 (2.9) dB for the downstream, while the upstream suffers from 3.1 (2.8) dB at a BER of 10^{-10} .

The compatible optical loss budget for the PON with a nominal data rate of 1.25 Gb/s is limited by the downstream reception to 21.7 (16.2) dB without FEC and to 29.5

(24.2) dB with FEC. It shall be recalled that the penalty for the blue wavelength could be easily avoided by an R/B filter with better rejection at the ONU.

SOA/REAM as reflective modulator

Higher data rates can be achieved when the RSOAs in the ONU are replaced by suitable modulators with higher electro-optical bandwidth for modulation and also for detection. A good candidate is the SOA/REAM whose EAM section can be used as fast PIN diode [201]. The burst-mode operation of such an ONU for downstream detection and upstream transmission at 10 Gb/s was proven in a similar WDM-PON configuration (Fig. 7.5(b)) as it was used in the previous section.

The two wavelengths were here located in the C- and L-band at 1560.61 and 1592.95 nm due to the gain spectrum of the SOA/REAM (see Fig. 4.31). The spacing between these optical carriers fits to the FSR of the AWG that was 32.5 nm. A burst-mode transmitter at the OLT and the ONU was generating a 125 μ s GPON-compatible frame (with a 60 ns preamble for the case of the downstream) and duty cycles of 1:4, 1:2 and 1:1 (i.e. continuous-mode) to further proof the DBA concept. A DCF with a dispersion of -671 ps/nm was included in the OLT receiver to reduce the interplay of the EAM chirp with the SMF.

Since there was only one chip available, the reception and transmission was not performed concurrently. However, no crosstalk into the channel of the other waveband has been observed when emulating the upstream signal with a laser diode at the ONU.

For downstream detection the SOA section was gated with a bias current of 120 mA according to the chosen duty cycle of the transmitted burst-mode downstream, while the EAM section was biased at -1.8 V (-4.2 V) at the C-(L-)band wavelength. The C-band EAM bias was lower due to the closer detuning from the absorption edge.

For upstream transmission the EAM section was biased at -1.1 V (-1.6 V) and modulated with 2 V_{pp} (3 V_{pp}), respectively, while the SOA was gated as mentioned for the reception. The L-band wavelength was changed to 1585.36 nm for the upstream for a better alignment with available L-band filters at the optical OLT receiver. Upstream ERs of 9.3 and 8.1 dB were obtained for the C- and L-band wavelength at the output of the ONU.

The signal levels and OSNRs for the C-(L-)band wavelength were then 7 (7) dBm and 42.3 (43.1) dB after the OLT booster (A in Fig. 7.5(b)) and -4.2 (-4.6) dBm at the ONU input (B). The ONU input was fixed to -7 dBm for the upstream measurements so that an error-free downstream reception can be guaranteed as will be shown shortly. The further power levels and OSNRs are -2.0 (-0.5) dBm and 36.6 (39.3) dB after remodulation at the ONU output (C) and -13.6 (-12.5) dBm at the input of the OLT receiver (D).

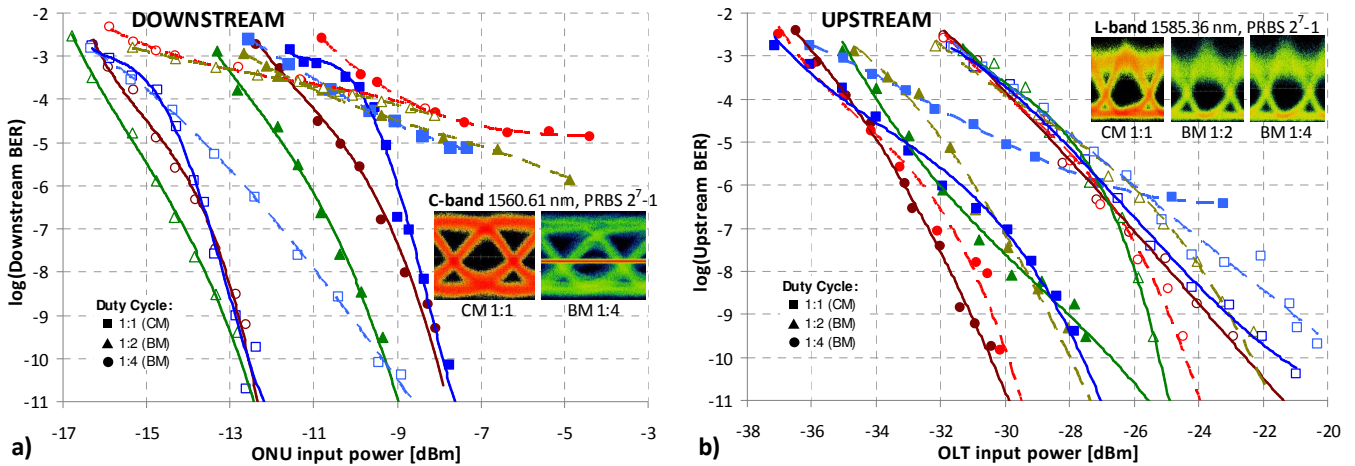


Fig. 7.7. BER measurements at 10 Gb/s for (a) downstream and (b) upstream in the C-band (filled markers) and the L-band (blank markers). Solid and dashed lines represent a PRBS of length 2^7-1 and $2^{31}-1$, respectively. The horizontal line in the burst-mode eye diagram of the downstream stems from the AC-coupled off-level.

The downstream in the L-band benefits from the improved L-band response of the SOA/REAM chips by ~ 3.5 dB when compared to the C-band transmission (Fig. 7.7(a)). The latter reaches sensitivities below -7.5 dBm for a PRBS of length 2^7-1 at a BER of 10^{-10} or a PRBS of length $2^{31}-1$ at the FEC threshold. Note that the 60 ns long preamble of the downstream, shown in Fig. 7.8(a) and excluded from the BER, is distorted due to the AC-coupling of the electronic receiver at the ONU.

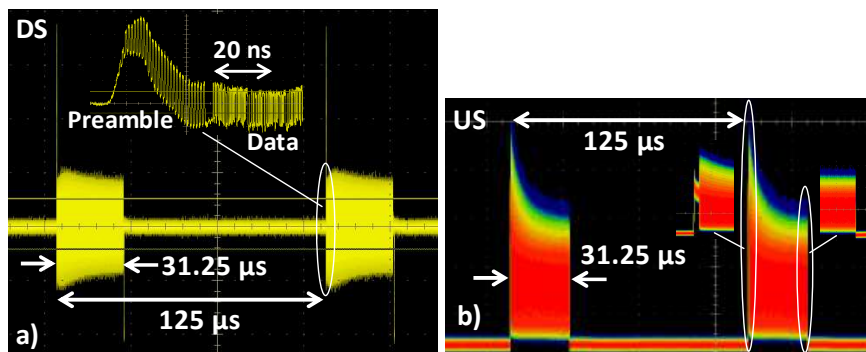


Fig. 7.8. Burst-Mode traffic with a duty cycle of 1:4 for (a) the downstream and (b) the upstream.

The C-band benefits from a 3 to 5 dB better reception sensitivity for the upstream since the used C-band HE980 EDF at the OLT preamplifier provides a higher gain than the L-band iXF-FGL EDF. Sensitivities below -22 dBm were obtained for the L-band at a BER of 10^{-10} while reception at a BER of 10^{-4} is possible with sensitivities below -29 dBm (Fig. 7.7(b)). Since the burst-mode traffic experiences excess gain in the EDF (which was operated without gain stabilization) as shown in Fig. 7.8(b), its sensitivity is slightly improved compared to the continuous-mode upstream, similar as in chapter VI.3.4. Compared to the downstream reception, no strong differences between the different PRBS lengths have been observed compared to the case of downstream reception, since the incident unmodulated optical carrier is partially clamping the carrier density inside the SOA.

Similar as for the RSOA-based ONU, the loss budget of the PON is limited by the downstream reception to 16 (16.5) dB for the C-(L-)band wavelength but can be in principle increased with a better fiber-to-waveguide coupling, e.g. with the help of an integrated mode size converter.

The validation of 10 Gb/s down- and upstream operation in burst-mode shows the feasibility of bandwidth partitioning up to 20 Gb/s, mainly supported by a substitution of the conventional photo diode -based receiver by a more functional integratable photonic device while still keeping a small form factor.

As a final comment, note that the Fabry-Pérot type SOA/REAM of chapter V.2 could be also used as tunable selector for different operators, which are operating the same PON at closely spaced wavelengths.

Chapter VIII

Conclusions

Different techniques for optical access have been discussed in the previous chapters, covering a wide range of topics such as electro-optical modulation, wavelength reuse for full-duplex transmission with simple customer premises equipment, seeding techniques for the creation of supportive optical signals and the possibility of porting higher layer functionality to the physical layer.

What remains is to draw a set of rules for energy- and cost-efficient subsystem design for next-generation photonic access with outstanding transmission performance. Before an outlook for the future is given, a short technical conclusion is made.

8.1 Technical Conclusion

Simple devices such as the RSOAs, which provide first of all a low-cost solution with small form factor, have been shown to be capable for direct 10 Gb/s modulation just by applying a passive pre-distorting electrical filter. At the same time, RSOAs offer also a significant amount of optical amplification with small-signal gain values of more than 20 dB for low optical seeds of -20 dBm and are therefore suitable for optical access networks with higher loss budgets in the GPON class B+ range – but at 10 Gb/s operation.

A further extension of the data rate can be obtained with integrated devices that are constituted by a SOA- and an EAM-section. Though the net gain of such devices is lower and the compatible loss budget is reduced, the driving requirements tend towards a greener solution due to the higher modulation efficiency of the EAM and the absence of the electrical pre-distortion losses thanks to the flat electro-optical EAM response beyond 10 GHz. The aspect of generating simultaneously phase and amplitude modulation can provide an upgrade path for the future, allowing not only to increase the data rate but can be also used to introduce aspects such as multi-operability, dynamic bandwidth allocation or in-band packet labeling. Some of these aspects can be further supported by the capability of the SOA/REAM to work as integrated, pre-amplified detector, whereas this functionality can be further extended for the reception of frequency modulated signals with an appropriate design of the device.

From a more integrating view on photonic subsystems that are incorporating these basic electro-optical building blocks, especially the inclusion of spectrally periodic

filters has shown the feasibility for full-duplex operation, in compatibility with WDM networks and high loss budgets. These optical filters give support for energy-efficient all-optical pattern erasure at high data rates at 10 Gb/s, thus enabling bidirectional transmission on a single wavelength using solely the amplitude modulation format for both, the down- and upstream direction. Though the downstream modulation is introduced on the optical carrier with an ER of 9 dB, the upstream transmission quality is good enough to leave just a small penalty after optical carrier recovery at the ONU, while complex modulators for phase- or frequency modulation are avoided at the downstream transmitter. Further, the downstream can be recycled by an all-optical clock recovery to obtain “ideal” optical pulses as seed for the upstream modulator, which is in principle bound to low electro-optical modulation bandwidths.

At the same time, the all-optical photonic circuits that have been shown to comprise mostly passive, resonating filter structures in combination with SOA elements can be applied for RB mitigation. The wavelength shift obtained by means of RZ clock tone recreation or FWM at the ONU has been proven to guarantee full-duplex transmission at fiber-based links with strong RB.

A last but not unimportant aspect when including SOA-based elements in the ONU is the recycling of the natural noise emission to generate optical signals with the help of seed loops. This not only allows to generate optical carriers for the self-seeded transmission of data signals and avoids the use of light sources for remote seeding of the reflective customer premises equipment, but provides also a way for generating pump signals for doped fiber amplifiers. Even with a limited output power per ONU, significant pump powers can be obtained by means of controlled noise slicing and multiplexing. As demonstrated, the splitting loss of optical power splitters can be reduced, e.g. from 15 to just 5 dB, leading to a smoother signal evolution along the optical network in terms of smaller concentrated losses between the particular amplification stages. This in turn allows to work with high splitting losses in tree-like access networks with splitting ratios of 1:1000 and higher, by reducing transmission impairments such as RB and noise accumulation at the same time.

8.2 Outlook for the Future

Looking closer at the investigation presented in the previous chapters, there are several ideas and thoughts hidden between the lines, which can be further developed.

Especially the generation of a QAM with an integrated SOA/EAM device can be a good driver for novel techniques in photonic networks, where different applications can rely on. Next to the dedication of the different tributaries for particular services or labeling purposes, this modulation technique can be also implemented as booster for the delivered data. Even with low modulation rates this can provide an interesting upgrade for photonic networks with spectrally closely spaced channels, such as UDWDM networks in conjunction with coherent detection.

As already partially included in the previous thought, photonic integration will guarantee not only a more cost-efficient solution but will also improve the performance of the proposed techniques presented in the previous chapters. A good example for key elements in conjunction with several electro-optical devices will be the incorporation of ring resonators as spectrally periodic filtering devices or highly non-linear waveguides for optical signal processing.

Finally, the efficient reuse of light of several active elements will be an important aspect for next-generation photonic subsystems. This is not only related to the minimization of losses but also to the beneficial use of noise emission. With an efficient seeding technique, this can result in distributed pump delivery in self-amplified passive networks with remote EDF-based amplification stages at, and this is the best argument of this approach, no extra cost.

As conclusion of the conclusion shall be mentioned that photonic integration is indispensable as next evolutionary step but will, when applied cleverly, allow to provide extra functionality and not just basic transmission of the physical layer – taking also advantage of what nature inherently provides, and if it is just another device impairment.

A. List of Acronyms

A	A/D	Add / Drop <i>Filter</i>
	AON	Active Optical Network
	APD	Avalanche Photo Diode
	AR	Anti-Reflection
	ASE	Amplified Spontaneous Emission
	ASK	Amplitude Shift Keying
	AWG	Arrayed Waveguide Grating
B	BER	Bit Error Ratio
	BM	Burst Mode
	BPF	Band-Pass Filter
C	C/L	C- / L- <i>Waveband</i>
	Capex	Capital Expenditures
	CM	Continuous Mode
	CO	Central Office
D	DBA	Dynamic Bandwidth Allocation
	DC	Directed Current
	DCF	Dispersion Compensating Fiber
	DF	Derivative Filter
	DI	Delay Interferometer
	DL	Delay Line
	DML	Directly Modulated Laser
	DPSK	Differential PSK
	DS	Downstream
E	e/o	electro/optical
	EAM	Electro-Absorption Modulator
	EDC	Electronic Dispersion Compensation
	EDF	Erbium-Doped Fiber
	EDFA	EDF Amplifier
	EML	Externally Modulated Laser
	EPON	Ethernet PON
	EQ	Equalizer
	ER	Extinction Ratio

F	FBG	Fiber Bragg Grating
	FDL	Fiber Delay Line
	FEC	Forward Error Correction
	FPF	Fabry-Pérot Filter
	FP-LD	Fabry-Pérot - Laser Diode
	FSK	Frequency Shift Keying
	FSR	Free Spectral Range
	FTTX	Fiber-to-the-X
	FWM	Four-Wave Mixing
G	GPON	Gigabit PON
I	IEEE	Institute of Electrical and Electronics Engineers
	IM/DD	Intensity Modulation / Direct Detection
	IRZ	Inverse RZ
	ITU	International Telecommunication Unit
L	LD	Laser Diode
	LO	Local Oscillator
	LPF	Low-Pass Filter
M	MAC	Medium Access Control
	MUX	Multiplexer
	MZM	Mach-Zehnder Modulator
N	NG-PON	Next-Generation PON
	NRZ	Non-Return to Zero
	NTC	Negative Temperature Coefficient
O	o/o	optical/optical
	OA	Optical Amplifier
	ODN	Optical Distribution Network
	OFDM	Orthogonal Frequency Division Multiplexing
	OLT	Optical Line Terminal
	ONU	Optical Network Unit
	OOK	On-Off Keying
	Opex	Operating Expenditures
	OSA	Optical Spectrum Analyzer
	OSNR	Optical SNR
OSRR	Optical Signal-to-RB Ratio	
P	P/S	Pump / Signal <i>Splitter</i>
	P2P	Point-to-Point
	PC	Polarization Controller
	PDG	Polarization Dependent Gain
	PDL	Polarization Dependent Loss
	PIN	Positive Intrinsic Negative
	PM	Phase Modulator <i>or</i> Polarization Multiplexing
	POF	Plastic Optical Fiber
	PON	Passive Optical Network
	PRBS	Pseudo-Random Bit Sequence
	PSK	Phase Shift Keying
		QAM

R	RB	Rayleigh Backscattering
	R/B	Red / Blue <i>Splitter</i>
	REAM	Reflective EAM
	RF	Radio Frequency
	RIN	Relative Intensity Noise
	RLC	Resistor-Inductor-Capacitor
	RN	Remote Node
	RoF	Radio-Over-Fiber
	RSOA	Reflective SOA
	RX	Receiver
	RXF	Reception Filter
	RZ	Return-to-Zero
S	SCM	Sub-Carrier Multiplexing
	SMF	Standard single Mode Fiber
	SMSR	Side-Mode Suppression Ratio
	SNR	Signal-to-Noise Ratio
	SOA	Semiconductor Optical Amplifier
	SPL	Splitter
	SQRT	Square Root
T	TDM	Time Division Multiplexing
	TE	Transversal Electrical <i>or</i> thermo-element
	TEC	Temperature Controller
	TM	Transversal Magnetical
	TO	Transistor Outline
	TX	Transmitter
U	UDWDM	Ultra-Dense WDM
	US	Upstream
V	VCSEL	Vertical Cavity Surface Emitting Laser
	VDSL	Very high speed Digital Subscriber Line
	VSR	Very Short Reach
W	WDM	Wavelength Division Multiplexing

B. List of Symbols

	<i>Chapter(s)</i>	
α	material loss coefficient	2
	chirp parameter	2, 3, 4, 5
	EAM fitting parameter	4
	loss of filter cavity	4
	TE/TM power splitting factor	5
a	quadratic coefficient for band-gap energy	2
	differential (EAM) loss coefficient	4
	differential (SOA) gain constant	2, 5
a_λ	optical gain constant for spectral roll-off	5
A, A_{nrad}	linear non-radiative recombination coefficient	2
δA	optical bandwidth of ASE spectrum	6
A_{rad}	linear radiative recombination coefficient	2
A_{DS}	optical downstream amplitude	4
$A_{DS,res}$	residual optical downstream amplitude	4
β	signal propagation coefficient	2
b	quadratic coefficient for band-gap energy	2
B	filter bandwidth	4
	bandwidth	7
B, B_{rad}	bimolecular radiative recombination coefficient	2
B_{nrad}	bimolecular non-radiative recombination coefficient	2
B_e, B_{el}	electrical bandwidth	4, 6
B_o	optical bandwidth	4
γ	the inverse of the carrier lifetime	2
Γ	confinement factor	2, 5, 6, 7
Γ_R	damping factor of modulation response	2
c	speed of light	2, 3, 4
	quadratic coefficient for band-gap energy	2
C_j	capacitance of SOA electrode	2
C_p	capacitance of bonding pad	2
C, C_{aug}	Auger recombination coefficient	2
CR	coupling ratio	4

d	(waveguide) thickness	2, 6, 7
Δ	RB coefficient of fiber	6
D	density of states in energy bands	2
	dispersion	3
D_{leak}	leakage recombination coefficient	2
ε	ratio between output and input extinction ratio	4
	excess loss	6
ε_0	absolute permittivity	2
ε_{min}	minimum power extinction for EAM	4
e	elementary charge	2, 4, 6
E	energy	2
	electrical field	2
E_a	bottom of conductance band	2
E_b	top of valence band	2
E_{fc}	quasi-Fermi level of conductance band	2
E_{fv}	quasi-Fermi level of valence band	2
E_g	band-gap energy	2
ΔE_g	band-gap shrinkage due to injected carriers	2
E_{g0}	band-gap energy without injected carriers	2
E_{in}	input field amplitude	2, 4
E_{out}	output field amplitude	2, 4
ER	extinction ratio	4, 6
ER_{DS}	downstream extinction ratio	4
$ER_{DS,res}$	residual downstream extinction ratio	4
ER_{in}	input extinction ratio	4
ER_{out}	output extinction ratio	4
ER_{US}	upstream extinction ratio	4
f	Fermi-Dirac distribution	2
	(optical or electrical) frequency	4, 6
δf	frequency shift	4
	electrical resolution bandwidth	6
f_0	lower electrical cut-off frequency	6
f_1	upper electrical cut-off frequency	6
f_c	Fermi-Dirac distribution of conductance band	2
f_i	resonance frequency	3
f_v	Fermi-Dirac distribution of valence band	2
F	electrical field distribution	2
	pulse format	4
	finesse	4
	fiber loss	6
FSR	free spectral range	4, 5

g	signal gain coefficient	2
g_0	small signal gain coefficient	2, 5
g_m	material gain coefficient	2, 5, 6, 7
g_m	gain coefficient of material gain	2
g_m	absorption coefficient of material gain	2
G	(optical) gain	2, 3, 4
G_0	small signal gain	2
	gain at space bit level	4
G_1	gain at mark bit level	4
G_{ares}	gain at resonance dip	2, 5
G_{bw}	(optical) backward gain	2
G_{ff}	(electrical) gain in feed-forward cancellation path	4
G_{res}	gain at resonance peak	2, 5
G_s	single pass gain	2, 5
G_{soa}	gain of SOA section	5
η	quantum efficiency for photo detection	4, 6
η_{in}	fiber coupling efficiency at input facet	2
η_{out}	fiber coupling efficiency at output facet	2
h	Planck constant	2, 4, 6
h_{eo}	electro-optical impulse response	4
H	field transfer function of filter	4
θ	arbitrary angle	5
Θ	electrical spectrum	4
i_{det}, I_{det}	detected electrical current	4, 6
i_{DS}	detected electrical downstream current	4
i_{ff}, I_{ff}	electrical feed-forward cancellation current	4
i_{pp}	peak-to-peak modulation current	3
I	electrical (injection) current	2, 4, 6
ΔI	small-signal modulation of electrical current	2
I_0	electrical (photo) current at space bit level	4, 6
I_1	electrical (photo) current at mark bit level	4, 6
I_{bias}	electrical bias current	4
I_D	electrical diode current	4
I_{dc}	DC bias current	3, 4
$I_{DS,res}$	electrical (photo) current due to residual downstream	4
I_{mod}	electrical modulation current	4
I_{pad}	injected current through bonding pad	2
I_s	reverse electrical diode current	4
I_{semi}	injected current in semiconductor	2
I_{thres}	electrical threshold current for transparency	4
IL	insertion loss	4
J	required input power at ONU	6
κ	arbitrary magnitude	4

k	Boltzmann constant	2, 4
K	noise normalization factor	2
K_0	carrier-independent absorption loss coefficient	2
K_1	carrier-dependent absorption loss coefficient	2
K_g	band-gap shrinkage coefficient	2
λ	wavelength	5
$\delta\lambda$	(optical) bandwidth	5
λ_c	center wavelength of gain peak	5
λ_P	pump wavelength	6
Λ	launched power at OLT	6
$\delta\Lambda$	channel bandwidth of optical filter	6
L	(waveguide, fiber, geometrical) length	2, 3, 4, 5, 7
L_{eam}	loss of EAM section	5
L_p	inductance of bonding wire	2
L_{SL}	seed loop losses	6
μ	maximum number of disconnected network units	6
m	modulation index	4
m_e	effective mass of an electron in the conduction band	2
m_{hh}	effective mass of a heavy hole in the valence band	2
m_{lh}	effective mass of a light hole in the valence band	2
M	tree split	6
M_1	maximum optical power inside an arbitrary pulse	2
ν	optical frequency	2, 4, 6
$\delta\nu$	optical filter bandwidth	4
$\Delta\nu$	optical bandwidth	2
	instantaneous chirp	2
	optical resolution bandwidth	2, 4
ν_{ares}	antiresonant optical frequency	2
ν_c	optical cut-off frequency	2
$\Delta\nu_c$	offset for optical cut-off frequency	2
$\Delta\nu_m$	mode spacing	2
ν_{res}	resonant optical frequency	2
n	density of electrons	2
	refractive index	2, 4, 5
	emission constant of diode	4
n^*	carrier number	2
Δn	small-signal modulation of carrier density	2
n_0	initial refractive index	5
n_1	refractive index of active region	2
n_2	refractive index of cladding material	2
n_{eff}	effective refractive index	2
n_{eh}	refractive index change per carrier pair	5
n_{eq}	equivalent refractive index	2
n_{eq0}	equivalent refractive index without carrier injection	2

n_g	group refractive index	2
N	carrier density	2, 5, 6, 7
	optical noise output power	2
ΔN	change in carrier density	5
N_0	carrier density at equilibrium	2, 5
N_{ASE}	ASE power	2
N_{in}	input optical noise power level	4
$N_{res,out}$	optical noise output power at resonant frequency	2
N_T	transparency carrier density	2, 5
NF	noise figure	2, 4
O	output power at ONU	6
$OSNR$	optical signal-to-noise ratio	2, 4
$OSRR$	optical signal-to-RB ratio	6
π_{DS}	logical downstream bit pattern	4
π_{US}	logical upstream bit pattern	4
Π	power margin	6
p	density of holes	2
p_{RF}, P_{rf}	radio frequency power	3, 6
P, P_{sig}	optical (signal) power, photon rate	2, 4, 5, 6
P^*	photon number	2
ΔP	small-signal modulation of optical power	2
	excursion in optical power	4
P_0	(average) optical power at space bit level	4
$P_{0,in}$	input optical power level at space bit level	4
$P_{0,out}$	output optical power level at space bit level	4
P_{0max}	maximum level in space rail	4
P_1	(average) optical power at mark bit level	4
$P_{1,in}$	input optical power level at mark bit level	4
$P_{1,out}$	output optical power level at mark bit level	4
P_{1min}	minimum level in mark rail	4
P_{avg}	average optical power level	4
P_{det}	detected power	5
P_{DS}	power of downstream signal	6
P_{in}	optical input power	2, 3, 4
P_{max}	maximum optical power level	4
P_{out}	optical output power	2, 3, 4
P_s	reception sensitivity	4
$P_{s,ideal}$	ideal reception sensitivity	4
$P_{sat,out}$	saturation output power	4
P_{sat}	saturation power	2, 5
PB_{DS}	power budget for downstream	4
PB_{US}	power budget for upstream	4
Q	quality factor	4, 6
Q_{eff}	effective quality factor	4

ρ	error magnitude	4
r_1	front facet field reflectivity	2
r_2	rear facet field reflectivity	2
R	recombination (facet) reflectivity received power at OLT	2, 6, 7 4, 5 6
R_1	front facet power reflectivity	2, 5
R_2	rear facet power reflectivity	2, 5
R_b	data rate	4, 6
R_c	resistance of cladding region of SOA	2
R_j	junction resistance of SOA	2
R_{nrad}	non-radiative carrier recombination rate	2
R_{rad}	radiative carrier recombination rate	2
R_{sp}	spontaneously emitted noise	2
RIN	relative intensity noise	6
σ_0	electrical noise variance at space bit level	4, 6
σ_1	electrical noise variance at mark bit level	4, 6
σ_{ASE}	spectral noise output power	2
σ_{in}	spectral density of optical noise input	2
σ_N	spectral density of optical noise photon rate	2
Σ	splitter loss	6
S	signal power responsivity of photo detector spectral density (in electrical domain)	2 4 4, 6
S_{DS}	reception sensitivity in downstream direction	4
S_{US}	reception sensitivity in upstream direction	4
SNR	signal-to-noise ratio	6
τ	decay time	4
$\Delta\tau$	time delay	4
τ_e	carrier lifetime	2, 5, 7
τ_{eff}	effective time constant	2
t	time	2, 4, 5, 6
t_0, t_1	arbitrary point of time	4
T	optical gain spectrum temperature	2 4
δT	temperature fluctuation	4
T_0	mean lifetime for coherent interaction of electrons	2
T_b	bit period	4
T_{eam}	EAM transfer function	4
T_{max}	maximum filter transmission	4
T_{rtt}	round trip time	4
U_D	electrical diode voltage	4

U_T	thermal voltage of diode	4
v_g	group velocity	2
V	electrical voltage	4
	volume	2, 6
V_a	EAM fitting parameter	4
V_{bias}	electrical bias voltage	4
V_{ff}	electrical feed-forward cancellation voltage	4
V_{in}	electrical input voltage	4
V_{knee}	electrical EAM knee voltage	4
V_{mod}	electrical modulation voltage	4
ω	electrical angular frequency	4
	optical angular frequency	2, 5
Ω	angular electrical modulation frequency	2
Ω_R	resonance angular frequency of modulation response	2
w, W	(waveguide) width	2, 6, 7
x	coordinate in space	2
ξ	transient-induced eye closure	2
	ASE slicing loss	6
ξ_{DS}	penalty for downstream reception	4
ξ_{US}	penalty for upstream reception	4
Ξ	electrical eye opening	4
y	molar fraction	2
	coordinate in space	2
φ	single-pass phase shift	2
	optical phase	2, 5
$\Delta\varphi$	optical phase change	5
Φ	fiber loss	6
χ	noise contribution due to residual downstream	4
	loss reduction	6
ψ	quality factor improvement	4
Ψ	photon rate, flux	2, 7
	gain ripple contrast	5
z	coordinate in space	2, 7
	PRBS radix	4
ζ	amount of backscattered light	6

C. Research Publications

C.1 Patents

- 1) *Method and devices for bidirectional optical point-to-multipoint link using an optical power splitter with reduced splitting loss (Método y dispositivos para transmisión bidireccional óptica punto-a-multipunto usando un divisor de señal óptica con pérdidas de inserción reducidas)*, B. Schrenk, F. Bonada, J.A. Lazaro, and J. Prat, P200902415
- 2) *Method and device for bidirectional optical link reusing a single wavelength for upstream transmission by suppression of downstream modulation*, B. Schrenk, E. Kehayas, P. Bakopoulos, J.A. Lazaro, J. Prat, and C. Kazmierski, EP10382063.5
- 3) *Method and apparatus for bidirectional optical link using a single optical carrier and colorless demodulation and detection of optical frequency shift keyed data*, B. Schrenk, J.A. Lazaro, J. Prat, and C. Kazmierski, US12/707,991
- 4) *Method and Apparatus for bidirectional optical link using a simple integrated and wavelength-agnostic semiconductor device for simultaneous phase and amplitude shift keyed data transmission (Método y aparato para enlace óptico bidireccional con modulación simultánea de amplitud y fase mediante un dispositivo de semiconductor integrado y agnóstico a la longitud de onda)*, B. Schrenk, J.A. Lazaro, P. Bakopoulos, C. Kazmierski, and J. Prat, *submitted*

C.2 Book Contributions

- 1) J. Prat, F. Neri, P. Chanclou, T. Koonen, S.D. Walker, B. Schrenk, *et al.*, “*Next-Generation FTTH Passive Optical Networks: Research Towards Unlimited Bandwidth Access*”, ISBN-10: 1402084692, ISBN-13: 978-1402084690, 1st edition July 2008, Springer.

C.3 Publications in International, Peer-Reviewed Journals

- 1) B. Schrenk, G. de Valicourt, J.A. Lazaro, R. Brenot, J. Prat, “*Rayleigh Scattering Tolerant PON Assisted by Four-Wave Mixing in SOA-based ONUs*”, IEEE/OSA J. Lightwave Technol., vol. 28, pp. 3364-3371, Dec. 2010.

- 2) B. Schrenk, F. Bonada, J.A. Lazaro, J. Prat, “*Remotely Pumped Long-Reach Hybrid PON with Wavelength Reuse in RSOA-based ONUs*”, IEEE/OSA J. Lightwave Technol., vol. 29, pp. 635-641, Mar. 2011.
- 3) B. Schrenk, J.A. Lazaro, C. Kazmierski, and J. Prat, “*Colorless FSK Demodulation and Detection With Integrated Fabry-Pérot Type SOA/REAM*”, IEEE Photonics Technol. Lett., vol. 22, pp. 1002-1004, Jul. 2010.
- 4) B. Schrenk, F. Bonada, J. Bauwelinck, J. Prat, and J.A. Lazaro, “*Energy-Efficient Optical Access Networks Supported by a Noise-Powered Extender Box*”, IEEE J. Sel. Topics in Quantum Electron., *accepted for publication*
- 5) B. Schrenk, G. de Valicourt, M. Omella, J.A. Lazaro, R. Brenot, and J. Prat, “*Direct 10 Gb/s Modulation of a Single-Section RSOA in PONs with High Optical Budget*”, IEEE Photonics Technol. Lett., vol. 22, pp. 392-394, Mar. 2010.
- 6) B. Schrenk, S. Chatzi, F. Bonada, J.A. Lazaro, I. Tomkos, and J. Prat, “*Dual Waveband Remote Node for Extended Reach Full-Duplex 10Gb/s Hybrid PONs*”, IEEE/OSA J. Lightwave Technol., vol. 28, pp. 1503-1509, May 2010.
- 7) A. Agmon, B. Schrenk, J. Prat, and M. Nazarathy, “*Polarization Beamforming PON Doubling Bidirectional Throughput*”, IEEE J. Lightwave Technol., vol. 28, pp. 2579-2585, Sept. 2010.
- 8) M. Omella, I. Papagiannakis, B. Schrenk, D. Klionidis, J.A. Lazaro, A.N. Birbas, J. Kikidis, J. Prat, and I. Tomkos “*10 Gb/s full-duplex bidirectional transmission with RSOA-based ONU using detuned optical filtering and decision feedback equalization*”, OSA Optics Expr., Vol. 17, pp. 5008-5013, Mar. 2009.

C.4 Publications in Scientific Congresses

- 1) B. Schrenk, G. de Valicourt, J.A. Lazaro, and J. Prat, “*Colourless FSK+ASK/ASK Operation for 20/10 Gbps Access Networks with Simple Reflective User Terminals*”, in Proc. OFC’11, JWA79, Los Angeles (CA), United States, Mar. 2011.
- 2) B. Schrenk, J.M. Fabrega, C. Kazmierski, J.A. Lazaro, and J. Prat, “*SOA/REAM as Vector Modulator for QAM Upstream*”, in Proc. OFC’11, OThK1, Los Angeles (CA), United States, Mar. 2011.
- 3) F. Bonada, B. Schrenk, J.M. Fabrega, M. Forzati, P.J. Rigole, and J. Prat, “*All-Optical Intra-PON Data Routing Between ONUs with a MG-Y Tunable Laser as 2.5 Gbps Burst-Mode Transmitter*”, in Proc. OFC’11, JWA74, Los Angeles (CA), United States, Mar. 2011.

- 4) B. Schrenk, C. Stamatiadis, I. Lazarou, A. Maziotis., G. de Valicourt, J.A. Lazaro, J. Prat, and Hercules Avramopoulos, "On an ONU for Full-Duplex 10.5 Gbps/ λ with Shared Delay Interferometer for Format Conversion and Chirp Filtering", in Proc. OFC'11, OThB7, Los Angeles (CA), United States, Mar. 2011.
- 5) J. Bauwelinck, B. Schrenk, C. Kazmierski, J.A. Lazaro, J. Prat, and X.Z. Qiu, "Multi-Operability and Dynamic Bandwidth Allocation in PONs with Electrically Reconfigurable SOA/REAM-Based ONUs", in Proc. ECOC'10, Th.10.B.4, Torino, Italy, Sept. 2010.
- 6) B. Schrenk, G. de Valicourt, F. Bonada, J.A. Lazaro, R. Brenot, and J. Prat, "Self-Pumped Dense ($40\lambda \times 32$ split) PON with Extended 30 dB Loss Budget and ONUs Comprising a Single 10 Gb/s RSOA", in Proc. ECOC'10, Tu.3.B.3, Torino, Italy, Sept. 2010.
- 7) J. Bauwelinck, B. Schrenk, F. Bonada, B. Baekelandt, J.A. Lazaro, P. Chanclou, J. Prat, and X.Z. Qiu, "Full-Duplex 10 Gb/s Transmission in Ultra-Dense PONs With Tree Splits $>1:1k$ and Noise-Powered Extender Box", in Proc. ECOC'10, Tu.5.B.4, Torino, Italy, Sept. 2010.
- 8) B. Schrenk, J. Bauwelinck, M. Omella, E. Kehayas, P. Bakopoulos, A. Maziotis, C. Kazmierski, D. Klonidis, X.Z. Qiu, J. Prat, I. Tomkos, H. Avramopoulos and J.A. Lazaro, "User-Terminal Subsystems of Next-Generation Access Networks: Trends and Challenges", in Proc. OSA Advanced Photonics Congress / ANIC, AWA4, Karlsruhe, Germany, Jun. 2010.
- 9) J. Bauwelinck, C. Antony, F. Bonada, A. Caballero, S. Chatzi, A.M. Clarke, L.N. Costa, M. Forzati, J.A. Lazaro, A. Maziotis, M. Mestre, I.T. Monroy, P. Ossieur, V. Polo, J. Prat, X.Z. Qiu, P.J. Rigole, B. Schrenk, R. Soila, A. Teixeira, I. Tomkos, P.D. Townsend, X. Yin, and H. Avramopoulos, "Optical Line Terminal and Remote Node Sub-Systems of Next-Generation Access Networks", in Proc. OSA Advanced Photonics Congress / ANIC, AWA5, Karlsruhe (Germany), Jun. 2010.
- 10) B. Schrenk, J.A. Lazaro, V. Polo, and J. Prat, "Multi-Operability in WDM-PONs with Electrically Reconfigurable RSOA-Based Optical Network Units", in Proc. OSA Advanced Photonics Congress / ANIC, ATuB4, Karlsruhe, Germany, Jun. 2010.
- 11) B. Schrenk, F. Bonada, J.A. Lazaro, and J. Prat, "Fortistis: Split Extension in Dense Passive Optical Networks by Inline Amplification with Remote ASE-Shaped Pump Delivery via Colorless Optical Network Units", in Proc. OFC'10, San Diego (CA), United States, Mar. 2010, JThA33.
- 12) B. Schrenk, J.A. Lazaro, and J. Prat, "Wavelength Conversion Towards Rayleigh Backscattering Tolerant PONs via Four-Wave Mixing in SOA-based ONUs", in Proc. OFC'10, OThG4, San Diego (CA), United States, Mar. 2010.

- 13) E. Kehayas, B. Schrenk, P. Bakopoulos, J.A. Lazaro, A. Maziotis, J. Prat, and H. Avramopoulos, "All-Optical Carrier Recovery with Periodic Optical Filtering for Wavelength Reuse in RSOA-based Colorless Optical Network Units in Full-Duplex 10Gbps WDM-PONs", in Proc. OFC'10, OWG4, San Diego (CA), United States, Mar. 2010.
- 14) B. Schrenk, F. Bonada, M. Omella, J.A. Lazaro, and J. Prat, "Enhanced Transmission in Long Reach WDM/TDM Passive Optical Networks by Means of Multiple Downstream Cancellation Techniques", in Proc. ECOC'09, We.8.5.4, Vienna, Austria, Sept. 2009.
- 15) B. Schrenk, J.A. Lazaro, C. Kazmierski, and J. Prat, "Colourless FSK/ASK Optical Network Unit Based on a Fabry P erot Type SOA/REAM for Symmetrical 10 Gb/s WDM-PONs", in Proc. ECOC'09, We.7.5.6, Vienna, Austria, Sept. 2009.
- 16) B. Schrenk, S. Chatzi, F. Bonada, J.A. Lazaro, D. Klondis, I. Tomkos, and J. Prat, "C+L Band Remote Node for Amplification in Extended Reach Full-Duplex 10Gb/s WDM/TDM Passive Optical Networks", in Proc. ECOC'09, We.P6.19, Vienna, Austria, Sept. 2009.
- 17) F. Bonada, B. Schrenk, J.A. Lazaro, V. Polo, P. Chanclou, and J. Prat, "Gain Transient Mitigation in Remote Erbium Doped Fibre Amplifiers by Burst Packet Carving at the ONU for Extended Power Budget PONs", in Proc. ECOC'09, We.P6.24, Vienna, Austria, Sept. 2009.
- 18) B. Schrenk, J.A. Lazaro, and J. Prat, "Employing Feed-Forward Downstream Cancellation in Optical Network Units for 2.5G/1.25G RSOA-based and 10G/10G REAM-based Passive Optical Networks for Efficient Wavelength Reuse", in Proc. ICTON'09, Th.B3.4, Ponta Delgada, Portugal, Jun. 2009.
- 19) A. Agmon, B. Schrenk, J. Prat, and M. Nazarathy, "Polarization Beamforming MIMO-based PON: 20 Gb/s Transmission over a 10 Gb/s System with Dynamic Power Allocation and ~1.8 dB Improved Reach", in Proc. OFC'09, OTuB7, San Diego (CA), United States, Mar. 2009.
- 20) M. Omella, I. Papagiannakis, B. Schrenk, D. Klondis, A.N. Birbas J. Kikidis, J. Prat, and I. Tomkos, "Full-Duplex Bidirectional Transmission at 10 Gbps in WDM PONs with RSOA-based ONU using Offset Optical Filtering and Electronic Equalization", in Proc. OFC'09, San Diego (CA), United States, OThA7, Mar. 2009.
- 21) V. Polo, B. Schrenk, F. Bonada, J.A. Lazaro, and J. Prat, "Reduction of Rayleigh Backscattering and Reflection Effects in WDM-PONs by Optical Frequency Dithering", in Proc. ECOC'08, vol. 5, pp. 173-174, Brussels, Belgium, Sept. 2008.
- 22) M. Omella, V. Polo, J.A. Lazaro, B. Schrenk, and J. Prat, "10 Gb/s RSOA Transmission by Direct Duobinary Modulation", in Proc. ECOC'08, vol. 2, pp. 121-122, Brussels, Belgium, Sept. 2008.
- 23) B. Schrenk, M. Omella, J.A. Lazaro, and J. Prat, "Remote Wavelength Generation for Upstream Transmission in Time and Wavelength Division Multiplexed Passive Optical Networks with C- and L-Band Utilization", in Proc. ICTON'08, vol. 4, pp. 174-177, Athens, Greece, Jun. 2007.

C.5 Submitted Publications

Book contributions

"Handbook of Experimental Fiber-Optic Systems for Telecommunications", to be submitted within the EU FP7 Euro-Fos NoE

Publications in International, Peer-Reviewed Journals

- B. Schrenk, P. Bakopoulos, E. Kehayas, A. Maziotis, J.A. Lazaro, H. Avramopoulos, and J. Prat, "*Comparison of Carrier Recovery Techniques for Access Networks with Simple ASK Modulation*", submitted to *IEEE/OSA J. Opt. Comm. and Netw.*
- J.M. Fabrega, B. Schrenk, F. Bonada, J.A. Lazaro, M. Forzati, P.J. Rigole, and J. Prat, "*Modulated Grating Y-Structure Tunable Laser for λ -Routed Networks and Optical Access*", submitted to *IEEE J. Sel. Topics in Quantum Electron.*
- B. Schrenk, J. Bauwelinck, F. Bonada, J.A. Lazaro, X.Z. Qiu, P. Chanclou, and J. Prat, "*Dense Passive Amplified PON Architecture with >1:1000 Split and Distributed Pump*", submitted to *IEEE/OSA J. Lightwave Technol.*
- B. Schrenk, J. Bauwelinck, J.A. Lazaro, C. Kazmierski, X.Z. Qiu, and J. Prat, "*Dual-Operability and Bandwidth Partitioning Enabling ONU by Tandem-Modulator*", submitted to *IEEE/OSA J. Opt. Comm. and Netw.*

D. Bibliography

- [1] O. Gerstel, "Optical Networking: A Practical Perspective", *IEEE Hot Interconnects*, Aug. 2000.
- [2] P. P. Iannone and K. C. Reichmann, "Strategic and Tactical Uses for Extended PON", in *Proc. OFC'08*, Workshop Presentation, Feb. 2008.
- [3] R. P. Davey *et al.*, "DWDM Reach Extension of a GPON to 135 km", *IEEE/OSA J. Lightwave Technol.*, vol. 24, pp. 29-31, Jan. 2006.
- [4] M. Maier and M. Herzog, "STARGATE: The Next Evolutionary Step toward Unleashing the Potential of WDM EPONs", *IEEE Comm. Mag.*, vol. 45, pp. 50-56, May 2007.
- [5] J.H. Lee *et al.*, "First Commercial Deployment of a Colorless Gigabit WDM/TDM Hybrid PON System Using Remote Protocol Terminator", *IEEE/OSA J. Lightwave Technol.*, vol. 28, pp. 344-351, Feb. 2010.
- [6] F.T. An *et al.*, "SUCCESS: A Next-Generation Hybrid WDM/TDM Optical Access Network Architecture," *IEEE/OSA J. Lightwave Technol.*, vol. 22, pp. 2557-2569, Nov. 2004.
- [7] J.M. Oh, S.G. Koo, D. Lee, and S.J. Park, "Enhancement of the Performance of a Reflective SOA-Based Hybrid WDM/TDM PON System With a Remotely Pumped Erbium-Doped Fiber Amplifier", *IEEE/OSA J. Lightwave Technol.*, vol. 26, pp. 144-149, Jan. 2008.
- [8] J.A. Lazaro, C. Bock, V. Polo, R.I. Martinez, and J. Prat, "Remotely amplified combined ring-tree dense access network architecture using reflective RSOA-based ONU", *OSA J. of Optical Netw.*, vol. 6, pp. 801-807, Jun. 2007.
- [9] C. Martin, "Realization of a SuperPON Demonstrator", in *Proc. NOC'97*, Antwerp, Belgium, pp. 188-193, Jun. 1997.
- [10] M. O. van Deventer *et al.*, "Architecture for 100 km 2048 split bidirectional SuperPONs from ACTS-PLANET", *Proc. SPIE*, vol. 2919, pp. 245-251, Nov. 1996.
- [11] D.P. Shea and J.E. Mitchell, "A 10 Gb/s 1024-Way Split 100-km Long Reach Optical Access Network", *IEEE/OSA J. Lightwave Technol.*, vol. 25, pp. 685-693, Mar. 2007.
- [12] K.-I. Suzuki, Y. Fukada, D. Nettet, and R. Davey, "Amplified gigabit PON systems", *OSA J. Optical Netw.*, vol. 6, pp. 422-433, May 2007.
- [13] A. Lovric, and S. Aleksic, "Power Efficiency of Extended Reach 10G-EPON and TDM/WDM PON", in *Proc. OFC'10*, NMC4, San Diego (CA), United States, Mar. 2010.

- [14] R.D. Feldman, E.E. Harstead, S. Jiang, T.H. Wood, and M. Zirngibl, "An Evaluation of Architectures Incorporating Wavelength Division Multiplexing for Broad-Band Fiber Access", *IEEE/OSA J. Lightwave Technol.*, vol. 16, pp. 1546-1559, Sept. 1998.
- [15] B. Schrenk, G. de Valicourt, M. Omella, J.A. Lazaro, R. Brenot, and J. Prat, "Direct 10 Gb/s Modulation of a Single-Section RSOA in PONs with High Optical Budget", *IEEE Photonics Technol. Lett.*, vol. 22, pp. 392-394, Mar. 2010.
- [16] Y. Sun, J.L. Zyskind and A.K. Srivastava, "Average inversion level, modeling, and physics of erbium-doped fiber amplifiers", *IEEE J. Sel. Topics Quantum Electron.*, vol. 3, pp. 991-1007, Aug. 1997.
- [17] R.E. Neuhauser *et al.*, "New remote pump scheme enabling high-capacity (3.2 Tb/s) unrepeaters C + L band transmission over 220 km", in *Proc. OFC'02*, TuR2, Anaheim (CA), United States, Mar. 2002.
- [18] A. Banerjee *et al.*, "Wavelength-division-multiplexed passive optical network (WDM-PON) technologies for broadband access: a review", *OSA J. Optical Netw.*, vol. 4, pp. 737-758, 2005.
- [19] J.R. Stern, J.W. Balance, D.W. Faulkner, S. Hornung, D. Payne and K. Oakley, "Passive optical local networks for telephony applications and beyond", *IEE Electron. Lett.*, vol. 23, pp.1255-1256, 1987.
- [20] I. Van de Voorde, C.M. Martin, J. Vandewege, and X.Z. Qiu, "The superPON demonstrator: an exploration of possible evolution paths for optical access networks", *IEEE Comm. Mag.*, vol. 38, pp. 74-82, Feb. 2000.
- [21] J. Bauwelinck *et al.*, "Full-Duplex 10 Gb/s Transmission in Ultra-Dense PONs With Tree Splits >1:1k and Noise-Powered Extender Box", in *Proc. ECOC'10*, Tu.5.B.4, Torino, Italy, Sept. 2010.
- [22] J. Bauwelinck, B. Schrenk, C. Kazmierski, J.A. Lazaro, J. Prat, and X.Z. Qiu, "Multi-Operability and Dynamic Bandwidth Allocation in PONs with Electrically Reconfigurable SOA/REAM-Based ONUs", in *Proc. ECOC'10*, Th.10.B.4, Torino, Italy, Sept. 2010.
- [23] C. Antony *et al.*, "Demonstration of a Carrier Distributed, 8192-Split Hybrid DWDM-TDMA PON over 124km Field-Installed Fibers", in *Proc. OFC'10*, PDPD8, San Diego (CA), United States, Mar. 2010.
- [24] B. Schrenk, G. de Valicourt, F. Bonada, J.A. Lazaro, R. Brenot, and J. Prat, "Self-Pumped Dense (40λ×32 split) PON with Extended 30 dB Loss Budget and ONUs Comprising a Single 10 Gb/s RSOA", in *Proc. ECOC'10*, Tu.3.B.3, Torino, Italy, Sept. 2010.
- [25] H. Rohde, S. Smolorz, E. Gottwald, and K. Kloppe "Next Generation Optical Access: 1 Gbit/s for Everyone", in *Proc. ECOC'09*, Th.10.5.5, Vienna, Austria, Sept. 2009.
- [26] J. Baliga, R. Ayre, W.V. Sorin, K. Hinton, and R.S. Tucker, "Energy Consumption in Access Networks", in *Proc. OFC'08*, OThT6, San Diego (CA), United States, Feb. 2008.
- [27] J. Armstrong, "OFDM for Optical Communications", *IEEE/OSA J. Lightwave Technol.*, vol. 27, pp. 189-204, Feb. 2009.

- [28] A. Barbieri, G. Colavolpe, T. Foggi, E. Forestieri, and G. Prati, "OFDM versus Single-Carrier Transmission for 100 Gbps Optical Communication," *IEEE/OSA J. Lightwave Technol.*, vol. 28, pp. 2537-2551, Sept. 2010.
- [29] L.G. Kazovsky, W. Shaw, D. Gutierrez, N. Cheng, and S. Wong, "Next-Generation Optical Access Networks", *IEEE/OSA J. Lightwave Technol.*, vol. 25, pp. 3428-3442, Nov. 2007.
- [30] R. Kjaer, I. T. Monroy, L. K. Oxenløwe, P. Jeppesen, and B. Palsdottir, "Bi-directional 120 km Long-reach PON Link Based on Distributed Raman Amplification", in *Proc. LEOS'06*, WEE3, Montreal, Canada, Oct. 2006.
- [31] K. Takada, M. Abe, T. Shibata, and K. Okamoto, "1-GHz-Spaced 16-Channel Arrayed-Waveguide Grating for a Wavelength Reference Standard in DWDM Network Systems", *IEEE/OSA J. Lightwave Technol.*, vol. 20, pp. 822-825, May 2002.
- [32] W. Jiang, K. Okamoto, F.M. Soares, F. Olsson, S. Lourdudoss, and S.J.B. Yoo, "5 GHz Channel Spacing InP-Based 32-Channel Arrayed-Waveguide Grating", in *Proc. OFC'09*, OWO2, San Diego (CA), United States, Mar. 2009.
- [33] J.J. Lepley, M.P. Thakur, I. Tsalamanis, C. Bock, C. Arellano, J. Prat, S.D. Walker, "VDSL Transmission over a Fibre Extended Access Network", *OSA J. Optical Netw.*, vol. 4, pp. 517-523, 2005.
- [34] J. Buus, and E.J. Murphy, "Tunable lasers in optical networks", *IEEE/OSA J. Lightwave Technol.*, vol. 24, pp. 5-11, Jan. 2006.
- [35] M. Mestre *et al.*, "Tuning Characteristics and Switching Speed of a Modulated Grating Y Structure Laser for Wavelength Routed PONs", in *Proc. ANIC'10*, AthC2, Karlsruhe, Germany, Jun. 2010.
- [36] C. Bock, J.M. Fabrega, and J. Prat, "Ultra-Dense WDM PON based on Homodyne Detection and Local Oscillator Reuse for Upstream Transmission", in *Proc. ECOC'06*, We3.P.168, Cannes, France, Sept. 2006.
- [37] IEEE 802.3ah, EPON standard, 2004.
- [38] Gigabit-Capable Passive Optical Networks (G-PON): Physical Media Dependent (PMD) layer specification, ITU-T Recommendation G.984.2, 2003.
- [39] IEEE 802.3av, 10G-EPON standard, 2009.
- [40] 10-Gigabit capable passive optical networks (XG-PON), ITU-T Recommendation G.987, 2010.
- [41] S.M. Lee, S.G. Mun, M.H. Kim, and C.H. Lee, "Demonstration of a Long-Reach DWDM-PON for Consolidation of Metro and Access Networks", *IEEE/OSA J. Lightwave Technol.*, vol. 25, pp. 271-277, Jan. 2007.
- [42] C.J. Chang-Hasnain, "Tunable VCSEL", *IEEE J. Sel. Topics Quantum Electron.*, vol. 6, pp. 978-987, Nov. 2006.

- [43] G.R. Lin *et al.*, “Long-Cavity Fabry–Perot Laser Amplifier Transmitter With Enhanced Injection-Locking Bandwidth for WDM-PON Application”, *IEEE/OSA J. Lightwave Technol.*, vol. 28, pp. 2925-2932, Oct. 2010.
- [44] J.H. Lee *et al.*, “First Commercial Service of a Colorless Gigabit WDM/TDM Hybrid PON System”, in *Proc. OFC’09*, PDPD9, San Diego (CA), United States, Mar. 2009.
- [45] S.J. Park, C.H. Lee, K.T. Jeong, H.J. Park, J.G. Ahn, and K.H. Song, “Fiber-to-the-Home Services Based on Wavelength-Division-Multiplexing Passive Optical Network”, *IEEE/OSA J. Lightwave Technol.*, vol. 22, pp. 2582-2591, Nov. 2004.
- [46] T.B. Gibbon, K. Prince, C. Neumeyr, E. Rönneberg, M. Ortsiefer and I. Tafur, “10 Gb/s 1550 nm VCSEL transmission over 23.6 km Single Mode Fiber with no Dispersion Compensation and no Injection Locking for WDM PONs”, in *Proc. OFC’10*, JThA30, San Diego (CA), United States, Mar. 2010.
- [47] R.G. Walker, “High-speed III-V Semiconductor Intensity Modulators”, *IEEE J. Quantum Electron.*, vol. 27, pp. 654-667, Mar. 1991.
- [48] G. Talli and P. D. Townsend, “Hybrid DWDM-TDM Long-Reach PON for Next-Generation Optical Access”, *IEEE/OSA J. Lightwave Technol.*, vol. 24, pp. 2827-2834, July 2006.
- [49] G. de Valicourt *et al.*, “High Gain (30 dB) and High Saturation Power (11 dBm) RSOA Devices as Colorless ONU Sources in Long-Reach Hybrid WDM/TDM-PON Architecture”, *IEEE Photonics Technol. Lett.*, vol. 22, pp. 191-193, Feb. 2010.
- [50] A. Garreau *et al.*, “10Gbit/s Amplified Reflective Electroabsorption Modulator for Colorless Access Networks”, in *Proc. IPRM’06*, Tu.A2.3, pp. 168-170, Princeton, United States, May 2006.
- [51] O. Leclerc *et al.*, “Polarisation-independent InP push-pull Mach-Zehnder modulator for 20 Gbit/s soliton regeneration”, *IEE Electron. Lett.*, vol. 34, pp. 1011-1013, May 1998.
- [52] M.J.R. Heck, H.W. Chen, A.W. Fang, B.R. Koch, D. Liang, H. Park, M.N. Sysak, and J.E. Bowers, “Hybrid Silicon Photonics for Optical Interconnects”, *IEEE J. Sel. Topics Quantum Electron.*, DOI 10.1109 / JSTQE.2010.2051798 (forthcoming)
- [53] P.J. Winzer, “Modulation and multiplexing in optical communication systems”, *IEEE LEOS News*, pp. 4-10, Feb. 2009.
- [54] B. Schrenk *et al.*, “User-Terminal Subsystems of Next-Generation Access Networks: Trends and Challenges”, in *Proc. OSA Advanced Photonics Congress / ANIC’10*, AWA4, Karlsruhe, Germany, Jun. 2010.
- [55] F. Payoux, P. Chanclou, M. Moignard, and R. Brenot, “Gigabit Optical Access using WDM PON based on Spectrum Slicing and Reflective SOA”, in *Proc. ECOC’05*, We.3.3.5, Glasgow, Scotland, Sept. 2005.
- [56] W. Lee *et al.*, “Bidirectional WDM-PON Based on Gain-Saturated Reflective Semiconductor Optical Amplifiers”, *IEEE Photonics Technol. Lett.*, vol. 17, pp. 2460-2462, Nov. 2005.

- [57] T.Y. Kim, and S.K. Han, "Reflective SOA-Based Bidirectional WDM-PON Sharing Optical Source for Up/Downlink Data and Broadcasting Transmission", *IEEE Photonics Technol. Lett.*, vol. 18, pp. 2350-2352, Nov. 2006.
- [58] M. Attygalle, T. Anderson, D. Hewitt, and A. Nirmalathas, "WDM Passive Optical Network With Subcarrier Transmission and Baseband Detection Scheme for Laser-Free Optical Network Units", *IEEE Photonics Technol. Lett.*, vol. 18, pp. 1279-1281, Jun. 2006.
- [59] Z. Xu, Y.J. Wen, W.D. Zhong, M. Attygalle, X.F. Cheng, Y. Wang, and C. Lu, "Carrier-Reuse WDM-PON Using a Shared Delay Interferometer for Separating Carriers and Subcarriers", *IEEE Photonics Technol. Lett.*, vol. 19, pp. 837-839, Jun. 2007.
- [60] J.M. Fabrega, E.T. Lopez, J.A. Lazaro, M. Zuhdi, and J. Prat, "Demonstration of a full duplex PON featuring 2.5 Gbps Sub Carrier Multiplexing downstream and 1.25 Gbps upstream with colourless ONU and simple optics", in *Proc. ECOC'08*, We.1.F.6, Brussels, Belgium, Sept. 2008.
- [61] N. Genay, P. Chanclou, T. Duong, N. Brochier, and E. Pincemin, "Bidirectional WDM/TDM-PON access networks integrating downstream 10 Gbit/s DPSK and upstream 2.5 Gbit/s OOK on the same wavelength", in *Proc. ECOC'06*, Th.3.6.6, Cannes, France, Sept. 2006.
- [62] N. Calabretta, M. Presi, R. Proietti, G. Contestabile, and E. Ciaramella, "A Bidirectional WDM/TDM-PON Using DPSK Downstream Signals and a Narrowband AWG", *IEEE Photonics Technol. Lett.*, vol. 19, pp. 1227-1229, Aug. 2007.
- [63] H.S. Kim, B.S. Choi, K.S. Kim, D.C. Kim, O.K. Kwon, and D.K. Oh, "Improvement of modulation bandwidth in multisection RSOA for colorless WDM-PON", *OSA Optics Expr.*, vol. 17, pp. 16372-16378, Sept. 2009.
- [64] Y. Zhang, N. Deng, C.K. Chan, and L.K. Chen, "A Multicast WDM-PON Architecture Using DPSK/NRZ Orthogonal Modulation", *IEEE Photonics Technol. Lett.*, vol. 20, pp. 1479-1481, Sept. 2008.
- [65] C.W. Chow, "Wavelength Remodulation Using DPSK Down-and-Upstream With High Extinction Ratio for 10-Gb/s DWDM-Passive Optical Networks", *IEEE Photonics Technol. Lett.*, vol. 20, pp. 12-14, Jan. 2008.
- [66] I. Tafur *et al.*, "Monolithically integrated reflective SOA-EA carrier re-modulator for broadband access nodes." *OSA Optics Expr.*, vol. 14, pp. 8060-8064, Sept. 2006.
- [67] E.K. MacHale *et al.*, "Extended-Reach PON Employing 10 Gb/s Integrated Reflective EAM-SOA", in *Proc. ECOC'08*, Th.2.F.1, Brussels, Belgium, Sept. 2008.
- [68] M. Omella, V. Polo, J. Lazaro, B. Schrenk, and J. Prat, "RSOA Transmission by Direct Duobinary Modulation", in *Proc. ECOC'08*, Tu.3.E.4, Brussels, Belgium, Sept. 2008.
- [69] K.Y. Cho, Y. Takushima, and Y.C. Chung, "Demonstration of 11-Gb/s, 20-km Reach WDM PON using Directly-Modulated RSOA with 4-ary PAM Signal", in *Proc. OFC'10*, OWG1, San Diego (CA), United States, Mar. 2010.

- [70] K.Y. Cho, Y. Takushima, and Y. C. Chung, "10-Gb/s Operation of RSOA for WDM PON", *IEEE Photonics Technol. Lett.*, vol. 20, pp. 1533-1535, Sept. 2008.
- [71] I. Papagiannakis *et al.*, "Investigation of 10-Gb/s RSOA-Based Upstream Transmission in WDM-PONs Utilizing Optical Filtering and Electronic Equalization", *IEEE Photonics Technol. Lett.*, vol. 20, pp. 2168-2170, Dec. 2008.
- [72] J. Leuthold *et al.*, "All-Optical Wavelength Conversion Using a Pulse Reformatting Optical Filter", *IEEE/OSA J. Lightwave Technol.*, vol. 22, pp. 186-192, 2004.
- [73] T. Duong, N. Genay, P. Chanclou, B. Charbonnier, A. Pizzinat, and R. Brenot "Experimental demonstration of 10 Gbit/s upstream transmission by remote modulation of 1 GHz RSOA using Adaptively Modulated Optical OFDM for WDM-PON single fibre architecture", in *Proc. ECOC'08*, Th.3.F.1, Brussels, Belgium, Sept. 2008.
- [74] D. Qian, J. Hu, P.N. Ji, T. Wang, "10.8-Gb/s OFDMA-PON Transmission Performance Study", in *Proc. OFC'09*, NME6, San Diego (CA), United States, Mar. 2009.
- [75] C. Milion *et al.*, "High Bit Rate Transmission for NG-PON by Direct Modulation of DFB Laser using Discrete Multi-Tone", in *Proc. ECOC'09*, We.7.5.4, Vienna, Austria, Sept. 2009.
- [76] D. Qian, T. Kwok, N. Cvijetic, J. Hu, and T. Wang, "41.25 Gb/s Real-Time OFDM Receiver for Variable Rate WDM-OFDMA-PON Transmission", in *Proc. OFC'10*, PDPD9, San Diego (CA), United States, Mar. 2010.
- [77] D. Hillerkuss *et al.*, "Single Source Optical OFDM Transmitter and Optical FFT Receiver Demonstrated at Line Rates of 5.4 and 10.8 Tbit/s", in *Proc. OFC'10*, PDPC1, San Diego (CA), United States, Mar. 2010.
- [78] K. Ennsner, S. Taccheo, T. Rogowski, and J. Shmulovich, "Efficient Erbium-doped waveguide amplifier insensitive to power fluctuations", *OSA Optics Expr.*, vol. 14, pp. 10307-10312, Oct. 2006.
- [79] M.J. O'Mahony, "Semiconductor Laser Optical Amplifiers for Use in Future Fiber Systems", *IEEE/OSA J. Lightwave Technol.*, vol. 6, pp. 531-544, Apr. 1988.
- [80] Y. Kim, H. Jang, Y. Kim, J. Lee, D. Jang, and J. Jeong, "Transmission performance of 10-Gb/s 1550-nm transmitters using semiconductor optical amplifiers as booster amplifiers", *IEEE/OSA J. Lightwave Technol.*, vol. 21, pp. 476-481, Feb. 2003.
- [81] P.W. Juodawlkis, J.J. Plant, W. Loh, L.J. Missaggia, K.E. Jensen, and F.J. O'Donnell, "Packaged 1.5- μm Quantum-Well SOA With 0.8-W Output Power and 5.5-dB Noise Figure", *IEEE Photonics Technol. Lett.*, vol. 21, pp. 1208-1210, Sept. 2009.
- [82] J. Jennen, H. deWaardt, and G. Acket, "Modeling and performance analysis of WDM transmission links employing semiconductor optical amplifiers", *IEEE/OSA J. Lightwave Technol.*, vol. 19, pp. 1116-1124, Aug. 2001.
- [83] B. Mikkelsen, C. G. Jorgensen, N. Jensen, T. Durhuus, K. E. Stubkjaer, P. Doussiere, and B. Fernier, "High-performance semiconductor optical preamplifier receiver at 10 Gb/s", *IEEE Photonics Technol. Lett.*, vol. 5, pp. 1096-1097, Sept. 1993.

- [84] H. Steinberg, "The Use of a Laser Amplifier in a Laser Communication System", *Proc. IEEE*, vol. 51, p. 943, 1963.
- [85] N. Chinone, K. Saito, R. Ito, K. Aiki, and N. Shige, "Highly efficient GaAlAs buried heterostructure lasers with buried optical guide", *AIP Appl. Phys. Lett.*, vol. 35, pp. 513-516, Oct. 1979.
- [86] Y. Yamamoto, "Characteristics of AlGaAs Fabry-Perot Cavity Type Laser Amplifiers", *IEEE J. Quantum Electron.*, vol. 16, pp. 1047-1052, Oct. 1980.
- [87] T. Saitoh, T. Mukhai, and O. Mikami, "Theoretical Analysis and Fabrication of Antireflection Coatings on Laser-Diode Facets", *IEEE/OSA J. Lightwave Technol.*, vol. 3, pp. 288-293, Apr. 1985.
- [88] I.W. Marshall, M.J. O'Mahony, and P.D. Constantine, "Optical System with Two Packaged 1.5 μm Semiconductor Laser Amplifier Repeaters", *IEE Electron. Lett.*, vol. 22, pp. 253-255, Feb. 1986.
- [89] R. Yu *et al.*, "Ultrahigh speed performance of a quantum well laser at cryogenic temperatures", *AIP Appl. Phys. Lett.*, vol. 65, pp. 528-530, Aug. 1994.
- [90] H. Nishimoto, M. Yamaguchi, I. Mito, and K. Kobayashi, "High-Frequency Response for DFB LD due to a Wavelength Detuning Effect", *IEEE/OSA J. Lightwave Technol.*, vol. 5, pp. 1399-1402, Oct. 1987.
- [91] I. Vurgaftman, J.R. Meyer, and L.R. Ram-Mohan, "Band parameters for III-V compound semiconductors and their alloys", *AIP J. Appl. Phys.*, vol. 89, pp. 5815-5875, Jun. 2001.
- [92] W.B. Joyce and R.W. Dixon, "Analytic approximations for the Fermi energy of an ideal Fermi gas", *AIP Appl. Phys. Lett.*, vol. 31, pp. 354-356, Sept. 1977.
- [93] M.J. Connelly, "Semiconductor Optical Amplifiers", Boston, *Kluwer*, 2002.
- [94] A. Yariv, "Optical Electronics", New York, *HWR International*, 1985.
- [95] C.H. Henry, "Theory of the Linewidth of Semiconductor Lasers", *IEEE J. Quantum Electron.*, vol. 18, pp. 259-264, Feb. 1982.
- [96] N.G. Nilsson, "Empirical approximations for the Fermi energy of a semiconductor with parabolic bands", *AIP Appl. Phys. Lett.*, vol. 33, pp. 653-654, 1978.
- [97] N.K. Dutta, "Calculated absorption, emission, and gain in $\text{In}_{0.72}\text{Ga}_{0.28}\text{As}_{0.6}\text{P}_{0.4}$ ", *AIP J. Appl. Phys.*, vol. 51, pp. 6095-6100, Dec. 1980.
- [98] B.R. Bennett, R.A. Soref, and J.A. del Alamo, "Carrier-induced change in refractive index of InP, GaAs and InGaAsP", *IEEE J. Quantum Electron.*, vol. 26, pp. 113-122, 1990.
- [99] M.Z. Iqbal, K.B. Ma, C.E. Zah, T.P. Lee, and N.K. Cheung, "Effects of Gain Ripples in Semiconductor Optical Amplifiers on Very High Speed Lightwave Systems", *IEEE Photonics Technol. Lett.*, vol. 2, pp. 48-50, Jan. 1990.

- [100] I.D. Henning, M.J. Adams, and J.V. Collins, "Performance predictions from a new optical amplifier model", *IEEE J. Quantum Electron.*, vol. 21, pp. 609-613, Jun. 1985.
- [101] J.C. Simon, P. Doussiere, L. Pophillat, and B. Fernier, "Gain and noise characteristics of a 1.5 μm near-travelling-wave semiconductor laser amplifier", *IEE Electron. Lett.*, vol. 25, pp. 434-436, 1989.
- [102] R. Olshansky, C.A. Su, J. Manning, and W. Powazinik, "Measurement of radiative and nonradiative recombination rates in InGaAsP and AlGaAs light sources", *IEEE J. Quantum Electron.*, vol. 20, pp. 838-854, 1984.
- [103] M. Kot and K. Zdansky, "Measurement of radiative and nonradiative recombination rate in InGaAsP-InP LED's", *IEEE J. Quantum Electron.*, vol. 28, pp. 1746-1750, 1992.
- [104] T. Akiyama *et al.*, "Nonlinear Gain Dynamics in Quantum-Dot Optical Amplifiers and Its Application to Optical Communication Devices", *IEEE J. Quantum Electron.*, vol. 37, pp. 1059-1065, Aug. 2001.
- [105] E. Desurvire, D. Bayart, B. Desthieux, and S. Bigo, "Erbium-Doped Fiber Amplifiers: Device and System Developments", *Wiley*, 2002.
- [106] K.Y. Lau, and A. Yariv, "Ultra-High Speed Semiconductor Lasers", *IEEE J. Quantum Electron.*, vol. 21, pp. 121-138, Feb. 1985.
- [107] K. Petermann, "Laser Diode Modulation and Noise," Dordrecht, *Kluwer*, 1988.
- [108] R. Nagarajan, R.P. Mirin, T.E. Reynolds, and J.E. Bowers, "Effect of the Confinement-Layer Composition on the Internal Quantum Efficiency and Modulation Response of Quantum-Well Lasers", *IEEE Photonics Technol. Lett.*, vol. 4, pp. 832-834, Aug. 1992.
- [109] M. Ishikawa, T. Fukushima, R. Nagarajan, and J.E. Bowers, "Temperature dependence of damping in high-speed quantum-well lasers", *AIP Appl. Phys. Lett.*, vol. 61, pp. 396-398, Jul. 1992.
- [110] G.P. Agrawal, N.A. Olsson, "Self-Phase Modulation and Spectral Broadening of Optical Pulses in Semiconductor Laser Amplifiers", *IEEE J. Quantum Electron.*, vol. 25, pp. 2297-2306, Nov. 1989
- [111] J.E. Bowers, "High speed semiconductor laser design and performance", *Solid-State Electronics*, vol. 30, pp. 1-11, Jan. 1987.
- [112] D.A. Tauber, R. Spickermann, R. Nagarajan, T. Reynolds, A.L. Holmes, and J.E. Bowers, "Inherent bandwidth limits in semiconductor lasers due to distributed microwave effects", *AIP Appl. Phys. Lett.*, vol. 64, pp. 1610-1612, Mar. 1994.
- [113] A. Elrefaie, and C. Lin, "Performance Degradations of Multigigabit-per-Second NRZ/RZ Lightwave Systems Due to Gain Saturation in Traveling-Wave Semiconductor Optical Amplifiers", *IEEE Photonics Technol. Lett.*, vol. 1, pp. 300-302, Oct. 1989.
- [114] H. Tomofuji, H. Nishimoto, T. Horimatsu, T. Minami, and T. Touge, "Cumulative Waveform Distortion in Cascaded Optical Amplifier Repeaters for Multigigabit IM/DD Systems", *IEEE Photonics Technol. Lett.*, vol. 2, pp. 756-758, Oct. 1990.

- [115] J. Mark, and J. Mork, "Subpicosecond gain dynamics in InGaAsP optical amplifiers: Experiment and theory", *AIP Appl. Phys. Lett.*, vol. 61, pp. 2281-2283, Nov. 1992.
- [116] K. Sato, and H. Toba, "Reduction of Mode Partition Noise by Using Semiconductor Optical Amplifiers", *IEEE J. Sel. Topics in Quantum Electron.*, vol. 7, pp. 328-333, Mar. 2001.
- [117] K. Inoue, "Waveform distortion in a gain-saturated semiconductor optical amplifier for NRZ and Manchester formats," *IEE Proc. Optoelectron.*, vol. 144, pp. 443-437, Dec. 1997.
- [118] X. Wei, Y. Su, X. Liu, J. Leuthold, and S. Chandrasekhar, "10-Gb/s RZ-DPSK Transmitter Using a Saturated SOA as a Power Booster and Limiting Amplifier", *IEEE Photonics Technol. Lett.*, vol. 16, pp. 1582-1584, Jun. 2004.
- [119] A.K. Srivastave *et al.*, "A Polarization Multiplexing Technique to Mitigate WDM Crosstalk in SOAs", *IEEE Photonics Technol. Lett.*, vol. 12, pp.1415-1416, Oct. 2000.
- [120] H.K. Kim and S. Chandrasekhar, "Reduction of Cross-Gain Modulation in the Semiconductor Optical Amplifier by Using Wavelength Modulated Signal", *IEEE Photonics Technol. Lett.*, vol. 12, pp. 1412-1414, Oct. 2000.
- [121] K.E. Zoiros, C. O'Riordan, and M.J. Connelly, "Semiconductor Optical Amplifier Pattern Effect Suppression Using a Birefringent Fiber Loop", *IEEE Photonics Technol. Lett.*, vol. 22, pp. 221-223, Feb. 2010.
- [122] A. Bhardwaj, C.R. Doerr, S. Chandrasekhar, and L.W. Stulz, "Reduction of Nonlinear Distortion From a Semiconductor Optical Amplifier Using an Optical Equalizer", *IEEE Photonics Technol. Lett.*, vol. 16, pp. 921-923, Mar. 2004.
- [123] M. Osinski and J. Buus, "Linewidth Broadening Factor in Semiconductor Lasers – An Overview", *IEEE J. Quantum Electron.*, vol. 23, pp. 9-28, Jan. 1987.
- [124] R. de L. Kronig, "On the theory of the dispersion of X-rays", *OSA J. Opt. Soc. Am.*, vol. 12, pp. 547-557, Jun. 1926.
- [125] L.D. Westbrook, "Dispersion of Linewidth-Broadening Factor in 1.5 μ m Laser Diodes", *IEE Electron. Lett.*, vol. 21, pp. 1018-1019, Oct. 1985.
- [126] T.L. Koch and R.A. Linke, "Effect of nonlinear gain reduction on semiconductor laser wavelength chirping", *AIP Appl. Phys. Lett.*, vol. 48, pp. 613-615, Mar. 1986.
- [127] P.J. Corvini and T.L. Koch, "Computer Simulation of High-Bit-Rate Optical Fiber Transmission Using Single-Frequency Lasers", *IEEE/OSA J. Lightwave Technol.*, vol. 5, pp. 1591-1595, Nov. 1987.
- [128] T.N. Nielsen *et al.*, "Cancellation Of Inherent AM In Semiconductor Optical Amplifier Phase Modulators", *IEE Electronic Lett.*, vol. 28, pp. 235-236, 1992.
- [129] J.-M. Kang, S.-K. Han, "A novel hybrid WDM/SCM-PON sharing wavelength for up- and down-link using reflective semiconductor optical amplifier", *IEEE Photonics Technol. Lett.*, vol. 18, pp. 502-504, 2006.

- [130] H. Takesue, and T. Sugie, "Wavelength Channel Data Rewriter Using Semiconductor Optical Saturator/Modulator", *IEEE/OSA J. Lightwave Technol.*, vol. 24, pp. 2347-2354, Jun. 2006.
- [131] J.J. Reid *et al.*, "An international field trial at 1.3 μm using an 800 km cascade of semiconductor optical amplifiers", in *Proc. ECOC'98*, pp. 567-568, Madrid, Spain, Sept. 1998.
- [132] F. Saliou *et al.*, "Class B+ GPON extended to 44dB while maintaining 15dB optical budget difference", in *Proc. ECOC'08*, We.P6.10, Brussel, Belgium, Sept. 2008.
- [133] L.H. Spiekman *et al.*, "All-Optical Mach-Zehnder Wavelength Converter with Monolithically Integrated DFB Probe Source", *IEEE Photonics Technol. Lett.*, vol. 9, pp. 1349-1351, 1997.
- [134] D.D. Marcenac, "Bandwidth enhancement of wavelength conversion via cross-gain modulation by semiconductor optical amplifier cascade", *IEE Electron. Lett.*, vol. 31, pp. 1442-1443, 1995.
- [135] G. Hunziker *et al.*, "Folded-Path Self-Pumped Wavelength Converter Based on Four-Wave Mixing in a Semiconductor Optical Amplifier", *IEEE Photonics Technol. Lett.*, vol. 9, pp. 1352-1355, 1997.
- [136] A. Mecozzi, "Small-Signal Theory of Wavelength Converters Based on Cross-Gain Modulation in Semiconductor Optical Amplifiers", *IEEE Photonics Technol. Lett.*, vol. 8, pp. 1471-1473, 1996.
- [137] H.Y. Yu *et al.*, "Improved Transmission of Chirped Signals from Semiconductor Optical Devices by Pulse Reshaping Using a Fiber Bragg Grating Filter", *IEEE/OSA J. Lightwave Technol.*, vol. 17, pp. 898-903, 1999.
- [138] A. Mecozzi *et al.*, "Four-wave mixing in travelling-wave semiconductor optical amplifiers", *IEEE J. Quantum Electron.*, vol. 3, pp. 689-699, 1995.
- [139] K.E. Stubkjaer, "Semiconductor Optical Amplifier-Based All-Optical Gates for High-Speed Optical Processing", *IEEE J. Sel. Topics in Quantum Electron.*, vol. 6, pp. 1428-1435, 2000.
- [140] R. Fan *et al.*, "Hybrid Optical Switch Using Passive Polymer Waveguides and Semiconductor Optical Amplifiers", *IEEE/OSA J. Lightwave Technol.*, vol. 18, pp. 546-554, 2000.
- [141] H. Ishii *et al.*, "Zero Insertion Loss Operations in Monolithically Integrated WDM Channel Selectors", *IEEE Photonics Technol. Lett.*, vol. 11, pp. 242-245, 1999.
- [142] R. Hemenway *et al.*, "Optical-packet-switched interconnect for supercomputer applications", *OSA J. Optical Netw.*, vol. 3, pp. 900-913, 2004.
- [143] B. Glance *et al.*, "Applications of the Integrated Waveguide Grating Router", *IEEE/OSA J. Lightwave Technol.*, vol. 12, pp. 957-962, 1994.
- [144] R.P. Luijten, and R. Grzybowski, "The OSMOSIS Optical Packet Switch for Supercomputers", in *Proc. OFC'09*, OTuF3, San Diego (CA), United States, Mar. 2009.

- [145] E. Kehayas *et al.*, “All-Optical Network Subsystems Using Integrated SOA-Based Optical Gates and Flip-Flops for Label-Swapped Networks”, *IEEE Photonics Technol. Lett.*, vol. 18, pp. 1750-1752, 2006.
- [146] G. de Valicourt *et al.*, “Chirp Reduction in Directly Modulated Multi-Electrode RSOA Devices in Passive Optical Networks”, *IEEE Photonics Technol. Lett.*, vol. 22, pp. 1425-1427, Oct. 2010.
- [147] D.C. Kim *et al.*, “Experimental Comparison between Front-Side and Rear-Side Signal-Monitoring in RSOA Transistor Outline Can Modules with Monitor-Photodiode and Thermoelectric Cooler”, *IEEE Photonics Technol. Lett.*, vol. 22, pp. 1527-1529, Oct. 2010.
- [148] I. S. Reed and G. Solomon, “Polynomial codes over certain finite fields”, *SIAM J. Appl. Math.*, vol. 8, pp. 300-304, Jun. 1960.
- [149] S. Yamamoto, H. Takahira, and M. Tanaka, “5Gbit/s optical transmission terminal equipment using forward error correcting code and optical amplifier”, *IEE Electron. Lett.*, vol. 30, pp. 254-255, Feb. 1994.
- [150] I. Papagiannakis *et al.*, “Design Characteristics for a Full-Duplex IM/IM Bidirectional Transmission at 10 Gb/s Using Low Bandwidth RSOA”, *IEEE/OSA J. Lightwave Technol.*, vol. 28, pp. 1094-1101, Apr. 2010.
- [151] F. Devaux, Y. Sorel, and J. F. Kerdiles “Simple Measurement of Fiber Dispersion and of Chirp Parameter of Intensity Modulated Light Emitter”, *IEEE/OSA J. Lightwave Technol.*, vol. 11, pp. 1937-1940, Dec. 1993.
- [152] R.C. Srinivasan, and J.C. Cartledge, “On Using Fiber Transfer Functions to Characterize Laser Chirp and Fiber Dispersion”, *IEEE Photonics Technol. Lett.*, vol. 7, pp. 1327-1329, Nov. 1995.
- [153] F. Ramos, and J. Marti, “Frequency Transfer Function of Dispersive and Nonlinear Single-Mode Optical Fibers in Microwave Optical Systems”, *IEEE Photonics Technol. Lett.*, vol. 12, pp. 549-551, May 2000.
- [154] I.D. Henning, and J.V. Collins, “Measurement of the Semiconductor Laser Linewidth Broadening Factor”, *IEE Electron. Lett.*, vol. 19, pp. 927-929, Oct. 1983.
- [155] Y. Matsui *et al.*, “Chirp-Managed Directly Modulated Laser (CML)”, *IEEE Photonics Technol. Lett.*, vol. 18, pp. 385-387, Jan. 2006.
- [156] J. Yu *et al.*, “Applications of 40-Gb/s chirp-managed laser in access and metro networks”, *IEEE/OSA J. Lightwave. Technol.*, vol. 27, pp. 253-265, Feb. 2009.
- [157] S.D. Personick *et al.*, “A Detailed Comparison of Four Approaches to the Calculation of the Sensitivity of Optical Fiber System Receivers”, *IEEE Trans. on Communication*, vol. 25, pp. 541-548, May 1977.
- [158] B. Schrenk, S. Chatzi, F. Bonada, J.A. Lazaro, I. Tomkos, and J. Prat, “Dual Waveband Remote Node for Extended Reach Full-Duplex 10Gb/s Hybrid PONs”, *IEEE/OSA J. Lightwave Technol.*, vol. 28, pp. 1503-1509, May 2010.

- [159] J.J. Koponen, and M.J. Söderlund, "A duplex WDM passive optical network with 1:16 power split using reflective SOA remodulator at ONU", in *Proc. OFC'04*, MF99, Los Angeles, United States, Feb. 2004.
- [160] F. Payoux, P. Chanclou, T. Soret, N. Genay, and R. Brenot, "Demonstration of a RSOA-based Wavelength Remodulation Scheme in 1.25 Gbit/s Bidirectional Hybrid WDM-TDM PON", in *Proc. OFC'06*, OTuC4, Anaheim (CA), United States, Mar. 2006.
- [161] E. Conforti, C.M. Gallep, S.H. Ho, A.C. Bordonalli, and S.M. Kang, "Carrier Reuse With Gain Compression and Feed-Forward Semiconductor Optical Amplifiers", *IEEE Trans. Microwave Theory and Techn.*, vol. 50, pp. 77-81, 2002.
- [162] W. Lee *et al.*, "Optical Transceiver employing an RSOA with Feed-Forward Current Injection", in *Proc. OFC'07*, OTuH1, Anaheim (CA), United States, Mar. 2007.
- [163] J.H. Yu, N. Kim, and B.W. Kim, "Remodulation schemes with reflective SOA for colorless DWDM PON", *OSA J. Optical Netw.*, vol. 6, pp. 1041-1054, Aug. 2007.
- [164] J. Prat *et al.*, "Electronic Equalization of Photodetection by Means of an SQRT Module", in *Proc. ICTON'07*, We.C3.6, Rome, Italy, 2007.
- [165] D. Anderson, and M. Lisak, "Propagation characteristics of frequency-chirped super-Gaussian optical pulses", *OSA Optics Lett.*, vol. 11, pp. 569-571, Sept. 1986.
- [166] B. Schrenk, J.A. Lazaro, and J. Prat, "Employing Feed-Forward Downstream Cancellation in Optical Network Units for 2.5G/1.25G RSOA-based and 10G/10G REAM-based Passive Optical Networks for Efficient Wavelength Reuse", in *Proc. ICTON'09*, Th.B3.4, Ponta Delgada, Portugal, Jun. 2009.
- [167] B. Schrenk *et al.*, "Enhanced Transmission in Long Reach WDM/TDM Passive Optical Networks by Means of Multiple Downstream Cancellation Techniques", in *Proc. ECOC'09*, We.8.5.4, Vienna, Austria, Sept. 2009.
- [168] N. Dupuis *et al.*, "10-Gb/s AlGaInAs Colorless Remote Amplified Modulator by Selective Area Growth for Wavelength Agnostic Networks", *IEEE Photonics Technol. Lett.*, vol. 20, pp. 1808-1810, Nov. 2008.
- [169] N. Dupuis *et al.*, "10 Gbit/s Semi-Insulating Buried Heterostructure Loss-less Reflective Amplified Modulator for Wavelength Agnostic Networks", in *Proc. OFC'08*, OThC2, San Diego (CA), United States, Feb. 2008.
- [170] C. Kazmierski *et al.*, "100 Gb/s Operation of an AlGaInAs Semi-Insulating Buried Heterojunction EML", in *Proc. OFC'09*, OThT7, San Diego (CA), United States, Mar. 2009.
- [171] T. Watanabe, N. Sakaida, H. Yasaka, F. Kano, and M. Koga, "Transmission Performance of Chirp-Controlled Signal by Using Semiconductor Optical Amplifier", *IEEE/OSA J. Lightwave Technol.*, vol. 18, pp. 1069-1076, Aug. 2000.
- [172] B. Schrenk, F. Bonada, J.A. Lazaro, and J. Prat, "Remotely Pumped Long-Reach Hybrid PON with Wavelength Reuse in RSOA-based ONUs", *IEEE/OSA J. Lightwave Technol.*, vol. 29, pp. 635-641, Mar. 2011.

- [173] F. Bonada *et al.*, “Remotely Pumped Erbium Doped Fibre Bidirectional Amplifier for Gain Transient Mitigation”, in *Proc. ICTON’09*, Tu.D5.4, Ponta Delgada, Portugal, Jun. 2009.
- [174] D. Apostolopoulos, E. Kehayas, L. Stampoulidis, P. Bakopoulos, and H. Avramopoulos, “All-Optical Contention Resolution in Space and Wavelength Domain with Ultra-Fast Packet Envelope Detection and Integrated Optical Gates”, in *Proc. ECOC’06*, We.1.4.2, Cannes, France, Sept. 2006.
- [175] I. Glover, and P. Grant, “Digital Communications”, Essex, *Prentice Hall*, 1998.
- [176] G.B. Hocker, “Fiber-optic sensing of pressure and temperature”, *OSA Appl. Opt.*, vol. 18, pp. 1445-1448, May 1979.
- [177] M. Geng, L. Jia, L. Zhang, L. Yang, Y. Liu, and F. Li, “Polarization-independent micro-ring resonator on silicon-on-insulator”, in *Proc. INEC’08*, pp. 624-626, Shanghai, China, Mar. 2008.
- [178] O. Schwelb, “Transmission, Group Delay, and Dispersion in Single-Ring Optical Resonators and Add/Drop Filters – A Tutorial Overview”, *IEEE/OSA J. Lightwave Technol.*, vol. 22, pp. 1380-1394, May 2004.
- [179] D.G. Rabus, M. Hamacher, U. Troppenz, and H. Heidrich, “Optical Filters Based on Ring Resonators With Integrated Semiconductor Optical Amplifiers in GaInAsP–InP”, *IEEE J. Sel. Topics in Quantum Electron.*, vol. 8, pp. 1405-1411, Nov. 2002.
- [180] E.J. Klein *et al.*, “Densely integrated microring resonator based photonic devices for use in access networks”, *OSA Optics Expr.*, vol. 15, pp. 10346-10355, Aug. 2007.
- [181] V. Roncin *et al.*, “Patterning Effects in All-Optical Clock Recovery: Novel Analysis Using a Clock Remodulation Technique”, *IEEE J. Sel. Topics in Quantum Electron.*, vol. 16, pp. 1495-1502, Sept. 2010.
- [182] R.K. Staubli, and P. Gysel, “Crosstalk Penalties Due to Coherent Rayleigh Noise in Bidirectional Optical Communication Systems”, *IEEE/OSA J. Lightwave Technol.*, vol. 9, pp. 375-380, Mar. 1991.
- [183] E.T. Lopez, J.A. Lazaro, C. Arellano, V. Polo, and J. Prat, “Optimization of Rayleigh-Limited WDM-PONs With Reflective ONU by MUX Positioning and Optimal ONU Gain”, *IEEE Photonics Technol. Lett.*, vol. 22, pp. 97-99, Jan. 2010.
- [184] A. Chiuchiarelli *et al.*, “Enhancing Resilience to Rayleigh Crosstalk by Means of Line Coding and Electrical Filtering”, *IEEE Photonics Technol. Lett.*, vol. 22, pp. 85-87, Jan. 2010.
- [185] D. Jorgesen, C.F. Marki, and S. Esener, “Improved High Pass Filtering for Passive Optical Networks”, *IEEE Photonics Technol. Lett.*, vol.22, pp.1144-1146, Aug. 2010.
- [186] J.A. Lazaro, C. Arellano, V. Polo, and J. Prat, “Rayleigh Scattering Reduction by Means of Optical Frequency Dithering in Passive Optical Networks With Remotely Seeded ONUs”, *IEEE Photonics Technol. Lett.*, vol. 19, pp. 64-66, Jan. 2007.

- [187] T. Yoshida, S. Kimura, H. Kimura, K. Kumozaki, and T. Imai, "A New Single-Fiber 10-Gb/s Optical Loopback Method Using Phase Modulation for WDM Optical Access Networks", *IEEE/OSA J. Lightwave Technol.*, vol. 24, pp. 786-796, Feb. 2006.
- [188] C.W. Chow, G. Talli, and P. D. Townsend, "Rayleigh Noise Reduction in 10-Gb/s DWDM-PONs by Wavelength Detuning and Phase-Modulation-Induced Spectral Broadening", *IEEE Photonics Technol. Lett.*, vol. 19, pp. 423-425, Mar. 2007.
- [189] P.J. Urban, A.M.J. Koonen, G.D. Khoe, and H. de Waardt, "Interferometric Crosstalk Reduction in an RSOA-based WDM Passive Optical Network", *IEEE/OSA J. Lightwave Technol.*, vol. 27, pp. 4943-4953, Nov. 2009.
- [190] B. Schrenk, G. de Valicourt, J.A. Lazaro, R. Brenot, and J. Prat, "Rayleigh Scattering Tolerant PON Assisted by Four-Wave Mixing in SOA-based ONUs", *IEEE/OSA J. Lightwave Technol.*, vol. 28, pp. 3364-3371, Dec. 2010.
- [191] M. Kato *et al.*, "40-channel transmitter and receiver photonic integrated circuits operating at per channel data rate 12.5 Gbit/s", *IEE Electron. Lett.*, vol. 43, pp. 468-469, Apr. 2007.
- [192] X.S. Yao, L.S. Yan, B. Zhang, A.E. Willner, and J. Jiang, "All-optic scheme for automatic polarization division demultiplexing", *OSA Optics Expr.*, vol. 15, pp. 7407-7414, Jun. 2007.
- [193] H.J. Thiele, R.I. Killey, and P. Bayvel, "Investigation of Cross-Phase Modulation-Induced Transmission Penalties Using the Pump-Probe Technique", *Optical Fiber Technology*, vol. 8, pp. 71-81, Jan. 2002.
- [194] C. Fürst, J.P. Elbers, C. Scheerer, and C. Glingener, "Limitations of dispersion-managed DWDM systems due to cross-phase modulation", in *Proc. LEOS'00*, pp. 23-24, Rio Grande, Puerto Rico, Nov. 2000.
- [195] D.F. Geraghty, R.B. Lee, M. Verdiell, M. Ziari, A. Mathur, and K.J. Vahala, "Wavelength Conversion for WDM Communication Systems Using Four-Wave Mixing in Semiconductor Optical Amplifiers", *IEEE J. of Sel. Topics Quantum Electron.*, vol. 3, pp. 1146-1155, Oct. 1997.
- [196] H. Simos, A. Bogris, and D. Syvridis, "Investigation of a 2R All-Optical Regenerator Based on Four-Wave Mixing in a Semiconductor Optical Amplifier", *IEEE/OSA J. Lightwave Technol.*, vol. 22, pp. 595-604, Feb. 2004.
- [197] J.M. Kahn, and K.P. Ho, "Spectral Efficiency Limits and Modulation/Detection Techniques for DWDM Systems", *IEEE J. Sel. Topics in Quantum Electron.*, vol. 10, pp. 259-272, Mar. 2004.
- [198] R.J. Essiambre, G. Kramer, P.J. Winzer, G.J. Foschini, and B. Goebel, "Capacity Limits of Optical Fiber Networks", *IEEE/OSA J. Lightwave Technol.*, vol. 28, pp. 662-701, Feb. 2010.
- [199] J.J. Martinez *et al.*, "Novel WDM-PON Architecture Based on a Spectrally Efficient IM-FSK Scheme Using DMLs and RSOAs", *IEEE/OSA J. Lightwave Technol.*, vol. 26, pp. 350-356, Feb. 2008.

[200] B. Schrenk, J.A. Lazaro, C. Kazmierski, and J. Prat, "Colorless FSK Demodulation and Detection With Integrated Fabry-Pérot Type SOA/REAM", *IEEE Photonics Technol. Lett.*, vol. 22, pp. 1002-1004, Jul. 2010.

[201] A. Garreau *et al.*, "10 Gbit/s Drop and Continue Colorless Operation of a 1.5 μ m AlGaInAs Reflective Amplified Electroabsorption Modulator", in *Proc. ECOC'06*, We.1.6.5, Cannes, France, Sept. 2006.

[202] B. Schrenk, J.A. Lazaro, C. Kazmierski, and J. Prat, "Colourless FSK/ASK Optical Network Unit Based on a Fabry Pérot Type SOA/REAM for Symmetrical 10 Gb/s WDM-PONs", in *Proc. ECOC'09*, We.7.5.6, Vienna, Austria, Sept. 2009.

[203] B. Schrenk, G. de Valicourt, J.A. Lazaro, and J. Prat, "Colourless FSK+ASK/ASK Operation for 20/10 Gbps Access Networks with Simple Reflective User Terminals", in *Proc. OFC'11*, JWA79, Los Angeles (CA), United States, Mar. 2011.

[204] T. Mizuochi *et al.*, "Forward Error Correction Base on Block Turbo Code With 3-Bit Soft Decision for 10-Gb/s Optical Communication Systems", *IEEE J. Sel. Topics in Quantum Electron.*, vol. 10, pp. 376-385, Mar. 2004.

[205] S.P. Jung, Y. Takushima, and Y.C. Chung, "Transmission of 1.25-Gb/s PSK signal generated by using RSOA in 110-km coherent WDM PON", *OSA Optics Expr.*, vol. 18, pp. 14871-14877, Jul. 2010.

[206] S.P. Jung, Y. Takushima, and Y.C. Chung, "Generation of 5-Gbps QPSK Signal using Directly Modulated RSOA for 100-km Coherent WDM PON", in *Proc. OFC'11*, OTuB3, Los Angeles (CA), United States, Mar. 2011.

[207] P.S. Cho and J.B. Khurgin, "Suppression of cross-gain modulation in SOA using RZ-DPSK modulation format", *IEEE Photonics Technol. Lett.*, vol. 15, pp. 162-164, Jan. 2003.

[208] B. Schrenk, J.M. Fabrega, C. Kazmierski, J.A. Lazaro, and J. Prat, "SOA/REAM as Vector Modulator for QAM Upstream", in *Proc. OFC'11*, OThK1, Los Angeles (CA), United States, Mar. 2011.

[209] P. Healey *et al.*, "Spectral slicing WDM-PON using wavelength-seeded reflective SOAs", *IEE Electron. Lett.*, vol. 37, pp. 1181-1182, Sept. 2001.

[210] E. Wong, K.L. Lee, and T.B. Anderson, "Directly Modulated Self-Seeding Reflective Semiconductor Optical Amplifiers as Colorless Transmitters in Wavelength Division Multiplexed Passive Optical Networks", *IEEE/OSA J. Lightwave Technol.*, vol. 25, pp. 67-74, Jan. 2007.

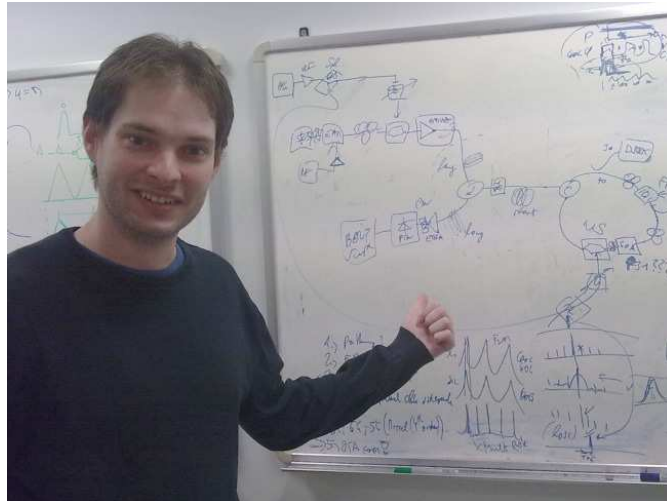
[211] C. Bock, J.A. Lazaro, J. Prat, "Extension of TDM-PON Standards to a Single-Fiber Ring Access Network Featuring Resilience and Service Overlay", *IEEE/OSA J. Lightwave Technol.*, vol. 25, pp. 1416-1421, Jun. 2007.

[212] J.A. Lazaro, C. Bock, V. Polo, R.I. Martinez, and J. Prat, "Remotely amplified combined ring-tree dense access network architecture using reflective RSOA-based ONU", *OSA J. of Optical Netw.*, vol. 6, pp. 801-807, Jun. 2007.

- [213] C.L. Zhao, H.Y. Tam, B.O. Guan, X. Dong, P.K.A. Wai, and X. Dong, "Optical automatic gain control of EDFA using two oscillating lasers in a single feedback loop", *Optics communications*, vol. 225, pp. 157-162, Sept. 2003.
- [214] A.D. McCoy, P. Horak, B.C. Thomsen, M. Ibsen, and D.J. Richardson, "Noise Suppression of Incoherent Light Using a Gain-Saturated SOA: Implications for Spectrum-Sliced WDM Systems", *IEEE/OSA J. Lightwave Technol.*, vol. 23, pp. 2399-2409, Aug. 2008.
- [215] K. Ogawa, "Analysis of mode partition noise in laser transmission systems", *IEEE J. Quantum Electron.*, vol. 18, pp. 849-855, May 1982.
- [216] N. S. Bergano, F.W. Kerfoot, and C. R. Davidso, "Margin measurements in optical amplifier systems", *IEEE Photonics Technol. Lett.*, vol. 5, pp. 304-306, Mar. 1993.
- [217] J.L. Gimlett *et al.*, "Impact of Multiple Reflection Noise in Gbit/s Lightwave Systems with Optical Fiber Amplifiers", *IEE Electron. Lett.*, vol. 25, pp. 1393-1394, Sept. 1989.
- [218] M.D. Feuer *et al.*, "Remotely-pumped self-amplified star network for local access", in *Proc. OFC'96*, pp. 146-147, San Jose (CA), United States, Feb. 1996.
- [219] B. Schrenk, F. Bonada, J.A. Lazaro, and J. Prat, "Fortistis: Split Extension in Dense Passive Optical Networks by Inline Amplification with Remote ASE-Shaped Pump Delivery via Colorless Optical Network Units", in *Proc. OFC'10*, JThA33, San Diego (CA), United States, Mar. 2010.
- [220] B. Schrenk, F. Bonada, J. Bauwelinck, X.Z. Qiu, J. Prat, and J.A. Lazaro, "Energy-Efficient Optical Access Networks Supported by a Noise-Powered Extender Box", *IEEE J. Sel. Topics in Quantum Electron.*, to be published
- [221] D.P. Shea and J.E. Mitchell, "Long-Reach Optical Access Technologies", *IEEE Network*, vol. 21, no. 5, pp. 5-11, Sept. 2007.
- [222] B. Baekelandt *et al.*, "OSNR Penalty Imposed by Linear In-Band Crosstalk Caused by Interburst Residual Power in Multipoint-To-Point Networks", *IEEE Photonics Technol. Lett.*, vol. 20, pp. 587-589, Apr. 2008.
- [223] Z. Huang, H.P. Chan, and M.A. Uddin, "Low-loss ultracompact optical power splitter using a multistep structure", *OSA Appl. Opt.*, vol. 49, pp. 1900-1907, Apr. 2010.
- [224] B.H. Choi, H.H. Park, and M.J. Chu, "New Pump Wavelength of 1540-nm Band for Long-Wavelength-Band Erbium-Doped Fiber Amplifier (L-Band EDFA)", *IEEE J. Quantum Electron.*, vol. 39, pp. 1272-1280, Oct. 2003.
- [225] S. Appathurai, R. Davey, and D. Nettet, "Next Generation Fibre-to-the-Home Solutions", in *Proc. Broadnets '08*, pp. 232-235, London, United Kingdom, Sept. 2008.
- [226] F. Saliou *et al.*, "Reach Extension Strategies for Passive Optical Networks [Invited]", *IEEE/OSA J. Opt. Comm. Netw.*, vol. 1, pp. C51-C60, Sept. 2009.
- [227] M. Forzati, and C.P. Larsen, "On the symmetry requirements for tomorrow's fibre access networks", in *Proc. ICTON'09*, Tu.B5.3, Ponta Delgada, Portugal, Jun. 2009.

- [228] C. Bock, J. Prat, and S. Walker, "Hybrid WDM/TDM PON Using the AWG FSR and Featuring Centralized Light Generation and Dynamic Bandwidth Allocation", *IEEE/OSA J. Lightwave Technol.*, vol. 23, pp. 3981-3988, Dec. 2005.
- [229] P. Chanclou, S. Gosselin, J. Fernandez, V. Lopez, and E. Zouganeli "Overview of the Optical Broadband Access Evolution: A Joint Article by Operators in the IST Network of Excellence e-Photon/ONe", *IEEE Comm. Mag.*, pp. 29-35, Aug. 2006.
- [230] Q.T. Nguyen *et al.*, "24 channels colorless WDM-PON with L-band 10 Gb/s downstream and C-band 2.5 Gb/s upstream using multiple-wavelengths seeding sources based on mode-locked lasers", in *Proc. OFC'10*, OThG6, San Diego (CA), United States, Mar. 2010.
- [231] J. Prat, C. Arellano, V. Polo, C. Bock, "Optical Network Unit Based on a Bidirectional Reflective Semiconductor Optical Amplifier for Fiber-to-the-Home Networks", *IEEE Photonics Technol. Lett.*, vol. 17, pp. 250-252, 2005.
- [232] P. Chanclou *et al.*, "Demonstration of RSOA-based remote modulation at 2.5 and 5 Gbit/s for WDM PON", in *Proc. OFC'07*, OWD1, Anaheim (CA), United States, Mar. 2007.
- [233] M.J. Connelly, and R.F. O'Dowd, "Travelling-wave semiconductor laser amplifier detector noise characteristics", *IEE Proc. Optoelectron.*, vol. 142, pp. 23-28, Feb. 1995.
- [234] M. Gustavsson, A. Karlsson, and L. Thylen, "Traveling Wave Semiconductor Laser Amplifier Detectors", *IEEE/OSA J. Lightwave Technol.*, vol. 8, pp. 610-617, Apr. 1990.
- [235] C. Kazmierski, "Advances in Remote Amplified Modulator Developments for Applications from 10Gb/s WDM Access to 100Gb/s Core Networks", in *Proc. ECOC'10*, Mo.1.F.1, Torino, Italy, Sept. 2010.

Biography



Bernhard Schrenk was born in Mistelbach, Austria, in 1982 and holds the BSc ('05) and the MSc ('07) in microelectronics, both given by the Technical University of Vienna, Austria.

During his undergraduate study he focused on photonics and carried out his diploma thesis at the Institute of Experimental Physics of Prof. Anton Zeilinger, where he was involved in the realization of a first commercial prototype for a quantum cryptography system, based on an entangled photon source, within the European SECOQC project.

The work presented in this Ph.D. thesis was performed from 2007 to 2011 at the Department of Signal Theory and Communications at the Technical University of Catalonia (UPC) in Barcelona, Spain. The research topics cover a wide range of novel techniques for optical network units in high data rate Fiber-to-the-Home applications and their impact on the overall transmission performance within long-reach and high-split access networks. The work was carried out within the European SARDANA, EURO-FOS and BONE projects.